REPUBLIC OF TURKEY MINISTRY OF JUSTICE

COUNCIL OF FORENSIC MEDICINE

ATLAS OF FORENSIC HISTOPATHOLOGY

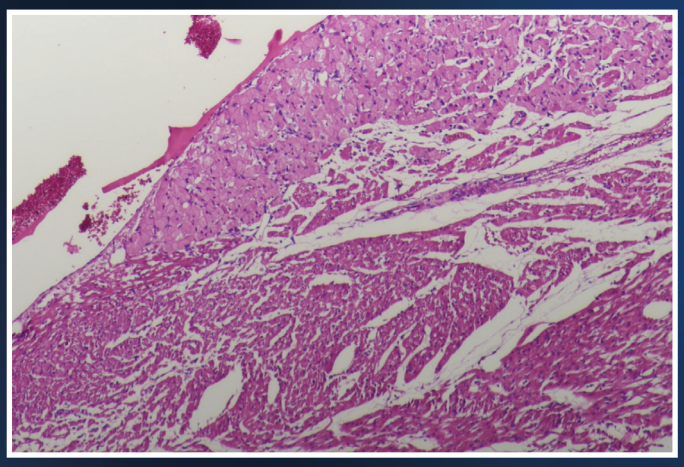

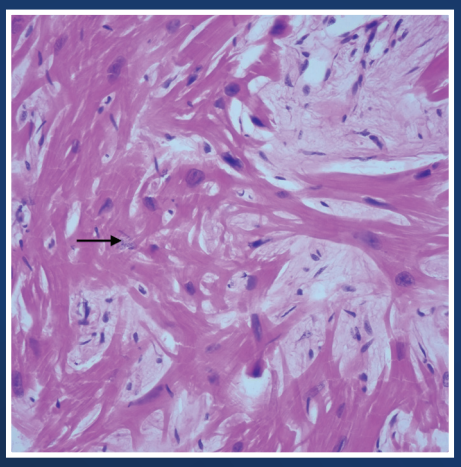

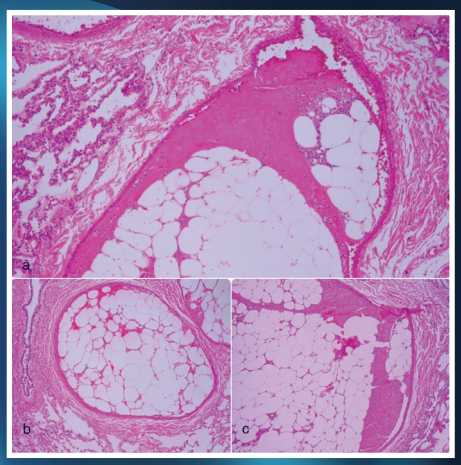

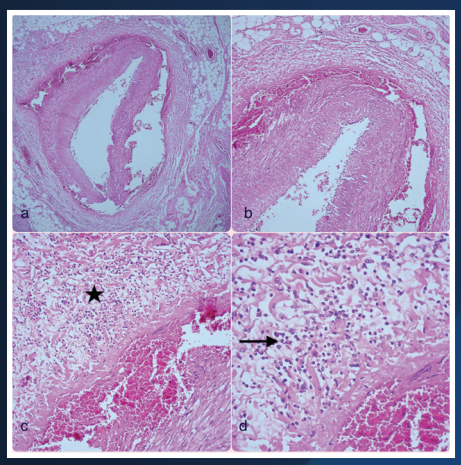

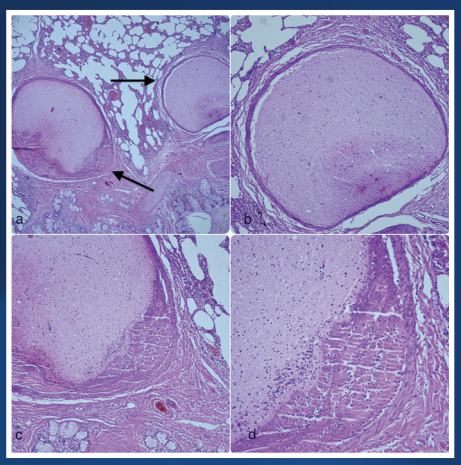

Assoc. Prof. Taner DAŞ
Assoc. Prof. Ferah KARAYEL
Asst. Prof.Hızır ASLIYÜKSEK

REPUBLIC OF TURKEY MINISTRY OF JUSTICE

COUNCIL OF FORENSIC MEDICINE

ATLAS OF FORENSIC HISTOPATHOLOGY

EDITORS
Taner DAŞ, MD
Associate Professor of Pathology
Republic of Turkey Ministry of Justice
Council of Forensic Medicine, Morgue Unit
Director of Histopathology Department

Hızır ASLIYÜKSEK, MD
Assistant Professor of Forensic Medicine
Republic of Turkey Ministry of Justice
President of Council of Forensic Medicine

AUTHORS
Taner DAŞ, MD
Associate Professor of Pathology
Republic of Turkey Ministry of Justice
Council of Forensic Medicine, Morgue Unit
Director of Histopathology Department

Ferah KARAYEL, MD
Associate Professor of Pathology
PhD, Forensic Medicine
Republic of Turkey Ministry of Justice
Council of Forensic Medicine
First Expertise Board, Pathology Member

ATLAS OF FORENSIC HISTOPATHOLOGY **© Republic of Turkey Ministry of Justice**
Council of Forensic Medicine
Yenibosna Çobançeşme Mah. Sanayi Cad.
Kımız Sok. No:1 Bahçelievler/İSTANBUL 34196

Council of Forensic Medicine Publications
Republic of Turkey Ministry of Justice
Council of Forensic Medicine

COUNCIL OF FORENSIC MEDICINE PUBLICATIONS - 4
Republic of Turkey Ministry of Justice
Council of Forensic Medicine
on behalf of the owner and editor-in-chief
Hızır ASLIYÜKSEK, MD
Assistant Professor of Forensic Medicine

Yenibosna Çobançeşme Mh. Sanayi Cd. Kımız Sk. No:1
Bahçelievler/İSTANBUL 34196

EDITORS
Taner DAŞ, MD
Associate Professor of Pathology
Hızır ASLIYÜKSEK, MD
Assistant Professor of Forensic Medicine

AUTHORS
Taner DAŞ, MD
Associate Professor of Pathology
Ferah KARAYEL, MD, PhD
Associate Professor of Pathology

DESIGN PREPARATION
Nihat YILMAZ

PRINTING
Natural Printing Publishing and Advertising Services Industry and Trade Ltd. Şti.
Maltepe Mah. Davutpaşa Cad. Emintaş Kazım Dinçol Industrial Site
Floor: 2 No: 226/274 Topkapı/Zeytinburnu/İSTANBUL
CERTIFICATE NUMBER: 68512

ISBN
978-605-2163-03-0

SEPTEMBER 2024

REPUBLIC OF TURKEY
MINISTRY OF JUSTICE
COUNCIL OF FORENSIC MEDICINE

ATLAS OF FORENSIC HISTOPATHOLOGY

REPUBLIC OF TURKEY MINISTRY OF JUSTICE

COUNCIL OF FORENSIC MEDICINE

CONTENTS

FOREWORD Minister of Justice Yılmaz TUNÇ 09

PREFACE President of the Council of Forensic Medicine Asst.Prof.Dr.Hızır ASLIYÜKSEK 11
PREFACE Assoc. Prof. Dr. Taner DAŞ 13
PREFACE Assoc. Prof. Dr. Ferah KARAYEL 15

CHAPTER 1 CARDIOVASCULAR SYSTEM 17
Assoc. Prof. Taner DAŞ

CHAPTER 2 RESPIRATORY SYSTEM 77
Assoc. Prof. Taner DAŞ / Assoc. Prof. Ferah KARAYEL

CHAPTER 3 LIVER 113
Assoc. Prof. Taner DAŞ / Assoc. Prof. Ferah KARAYEL

CHAPTER 4 KIDNEY 127
Assoc. Prof. Taner DAŞ

CHAPTER 5 SPLEEN 149
Assoc. Prof. Taner DAŞ / Assoc. Prof. Ferah KARAYEL

CHAPTER 6 PANCREAS 155
Assoc. Prof. Taner DAŞ / Assoc. Prof. Ferah KARAYEL

CHAPTER 7 GASTROINTESTINAL SYSTEM 161
Assoc. Prof. Taner DAŞ / Assoc. Prof. Ferah KARAYEL

CHAPTER 8 EFFECTS OF ELECTRICITY AND HEAT (Skin) 169
Assoc. Prof. Taner DAŞ / Assoc. Prof. Ferah KARAYEL

CHAPTER 9 VITALITY AND WOUND AGE 173
Assoc. Prof. Taner DAŞ / Assoc. Prof. Ferah KARAYEL

CHAPTER 10 CENTRAL NERVOUS SYSTEM 183
Assoc. Prof. Ferah KARAYEL

CHAPTER 11 PEDIATRIC PATHOLOGY 225
Assoc. Prof. Ferah KARAYEL

INDEX 247

REPUBLIC OF TURKEY MINISTRY OF JUSTICE

COUNCIL OF FORENSIC MEDICINE

FOREWORD

Dear Readers,

The importance of scientific accuracy and objective findings in the pursuit of justice is an undeniable truth. The Council of Forensic Medicine, in this regard, serves as one of the most crucial and reliable cornerstones of our justice system.

Our institution plays a critical role in elucidating forensic cases, uncovering crimes and criminals, and ultimately ensuring the establishment of justice.

The "Atlas of Forensic Histopathology" is a significant work that transforms the scientific expertise and experience of the Council of Forensic Medicine into a tangible resource.

I extend my gratitude to all the esteemed editors and authors who contributed to the preparation of this atlas. I firmly believe that this valuable work will serve as an important reference in the field of forensic sciences and contribute to the accurate and swift administration of justice.

I am confident that this work, which contributes to the advancement of our justice system and the proliferation of scientific studies, will provide benefits for many years to come. I hope that this significant contribution to the forensic sciences community and our justice system will be auspicious.

Yılmaz TUNÇ
Minister of Justice

REPUBLIC OF TURKEY MINISTRY OF JUSTICE

COUNCIL OF FORENSIC MEDICINE

PREFACE

Dear Colleagues and Esteemed Readers,

The role of scientific findings in the pursuit of justice is indisputable, and among these findings, the work carried out in the field of forensic histopathology is of paramount importance. As the Council of Forensic Medicine, we are delighted to share with you the "Atlas of Forensic Histopathology," prepared through our meticulous efforts and extensive scientific knowledge accumulated over the years.

This atlas aims to enhance the knowledge and skills of our forensic medicine experts and pathologists by providing a detailed examination and accurate interpretation of pathological findings encountered in forensic cases. The comprehensive visuals and explanations included are designed to be understood and applied by experts at all levels.

I believe that the "Atlas of Forensic Histopathology" will serve as a significant resource and guide for forensic medicine and pathology specialists, students in forensic medicine training, and all professionals involved in the administration of justice. I hope this work will contribute to the advancement of knowledge in the field of forensic sciences, thereby aiding in the accurate realization of justice.

I wish that this meticulously prepared work will illuminate the field of forensic sciences for many years to come.

Asst.Prof.Dr.Hızır ASLIYÜKSEK
President of the Council of Forensic Medicine

REPUBLIC OF TURKEY MINISTRY OF JUSTICE

COUNCIL OF FORENSIC MEDICINE

PREFACE

Forensic histopathology, as an important and delicate branch of forensic sciences, contributes to the delivery of justice in many cases. The work in this field requires medical and forensic expertise and must therefore be conducted with utmost precision. This atlas reviewed the lesions we frequently encounter in forensic histopathology and their microscopic findings.

Histopathological examinations are of great importance in achieving accurate and definitive results in forensic cases. Histopathological findings play a key role in elucidating many complex incidents, determining causes of death, and revealing how crimes are committed. In this context, forensic histopathology holds a unique position with its role in both medical and forensic aspect.

With this atlas, we have evaluated a wide range of cases in forensic pathology, from commonly seen to rare ones, and aimed to provide a comprehensive source that covers both theoretical knowledge and practical aspect for the readers.

I would like to thank the Head of the Council of Forensic Medicine, Dr. Hızır Asliyüksek, who supported us throughout the preparation of the Atlas of Forensic Histopathology.

I hope this work will take its place as an important reference source in the field of forensic histopathology and will continue to be beneficial for many years.

Assoc. Prof. Dr. Taner DAŞ
Head of the Histopathology Branch
Council of Forensic Medicine, Morgue,
Histopathology Department

REPUBLIC OF TURKEY MINISTRY OF JUSTICE

COUNCIL OF FORENSIC MEDICINE

PREFACE

Forensic Pathology, though a sub-discipline of Medical Pathology, differs from surgical pathology. Histopathological examination in forensic autopsies plays a significant role in determining the cause, mechanism, and manner of death. Histopathological examination of tissues sampled during autopsies guides the accurate evaluation of cases in many situations, such as forensic traumatology, sudden cardiac deaths, sudden unexpected infant deaths, and the assessment of wound age and vitality.

Over the years, the number of forensic autopsies with pathological examination has steadily increased in our country. An increasing number of pathology specialists in Turkey are working in the field of forensic pathology. Currently, forensic pathology is not included in medical pathology specialty training. Additionally, autopsy practices in institutions providing pathology specialty training are limited to a few pediatric autopsies. For this reason, we aimed to share the pathologies we have identified over the years in tissue samples taken from autopsies conducted at the Council of Forensic Medicine, an exemplary institution worldwide in terms of the number and variety of cases, to provide educational and practical guidance for pathology residents and specialists, as well as forensic medicine residents and specialists.

We thank the Head of the Council of Forensic Medicine, Dr. Hızır Asliyüksek, who supported us during the preparation of the Atlas of Forensic Histopathology.

Assoc. Prof. Dr. Ferah KARAYEL
Council of Forensic Medicine
First Specialization Board, Pathology member

CARDIOVASCULAR SYSTEM

Assoc. Prof. Taner DAŞ

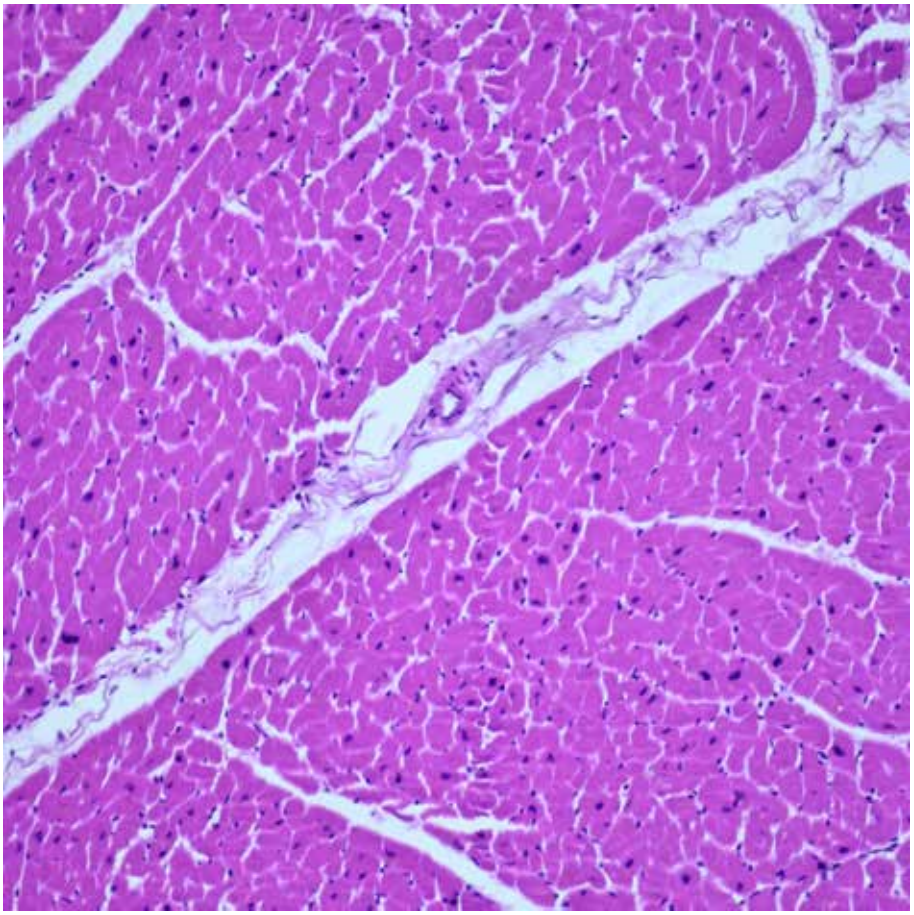

Figure 1.1
Normal microscopic view of myocardial fibers, (H&E, x200). Normal heart muscle, a type of striated muscle, consist of cardiac muscle cells, called cardiomyocytes, with a centrally located nucleus and large eosinophilic cytoplasm.

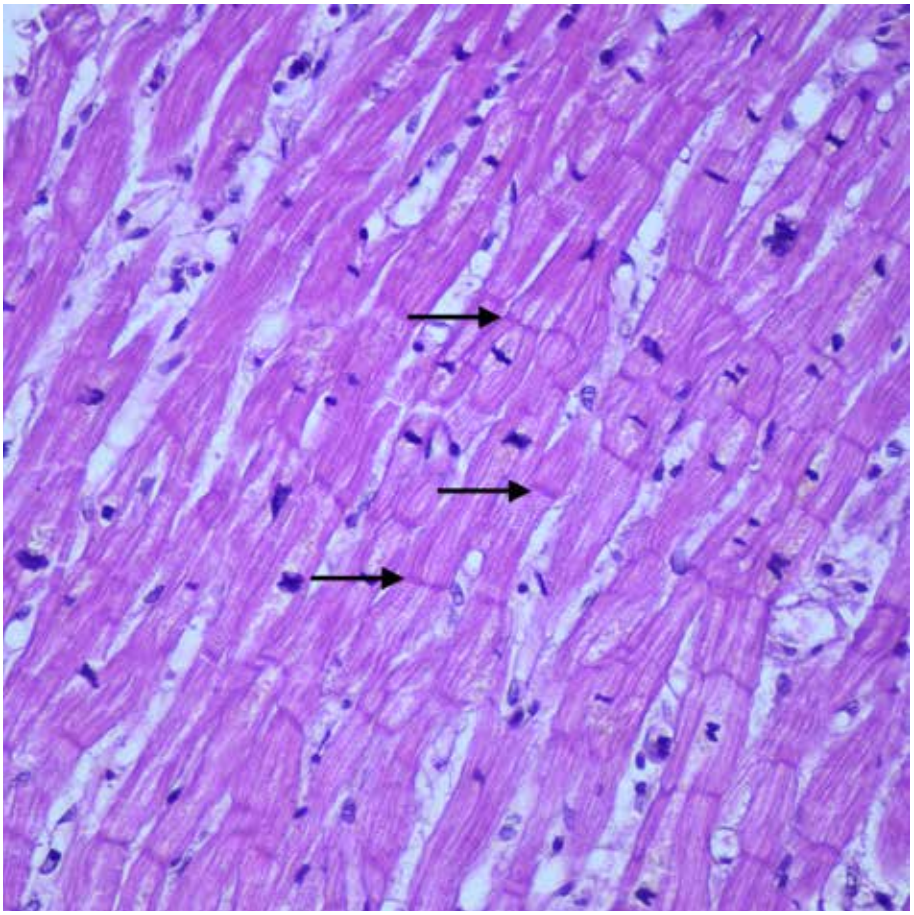

Figure 1.2
Intercalated discs, (H&E, x400). There are intercellular junctions between cardiomyocytes named "Intercalated disks" (arrows) that allow the transmission of mechanical and electrical activity from one myocyte to another during heartbeat. There are "gap junctions" on these disks that permit ion movements.

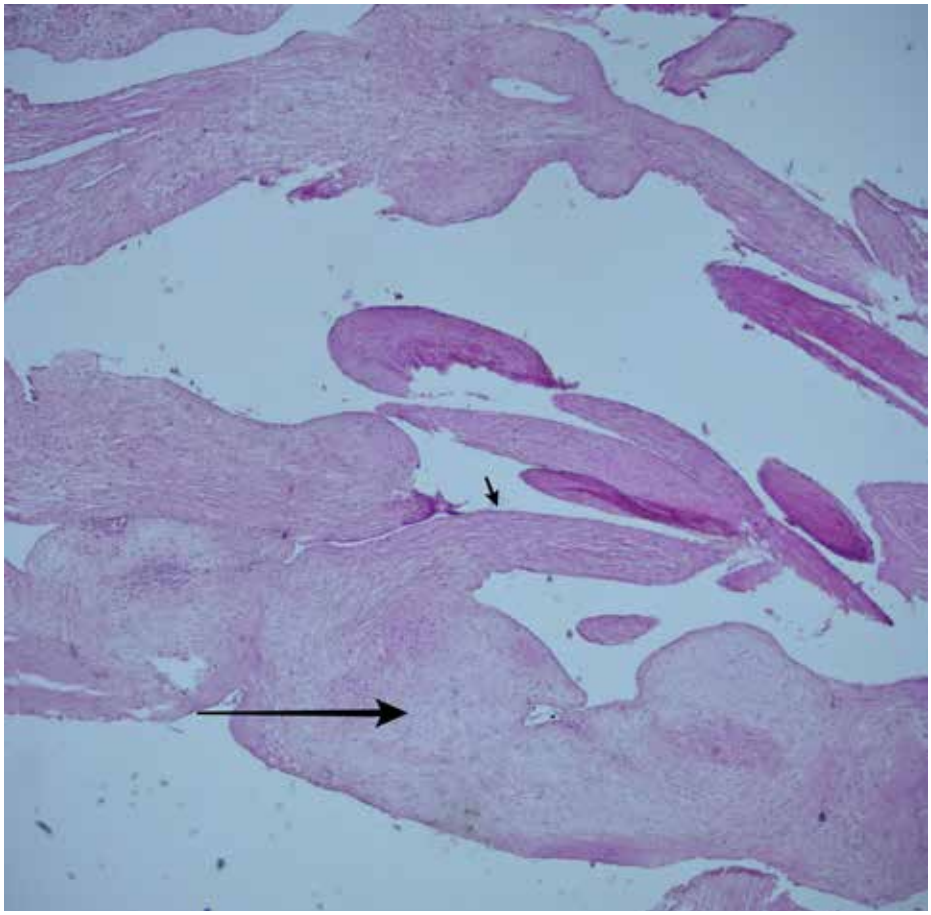

Figure 1.3
Normal heart valves, (H&E, x40).
Heart valves have a similar layered structure. It consists of a dense collagenized layer (fibrosa) (short arrow) near the outer flow surface, a central loose connective tissue (spongiosa) (long arrow) containing elastin and an endothelial layer on the free surface.

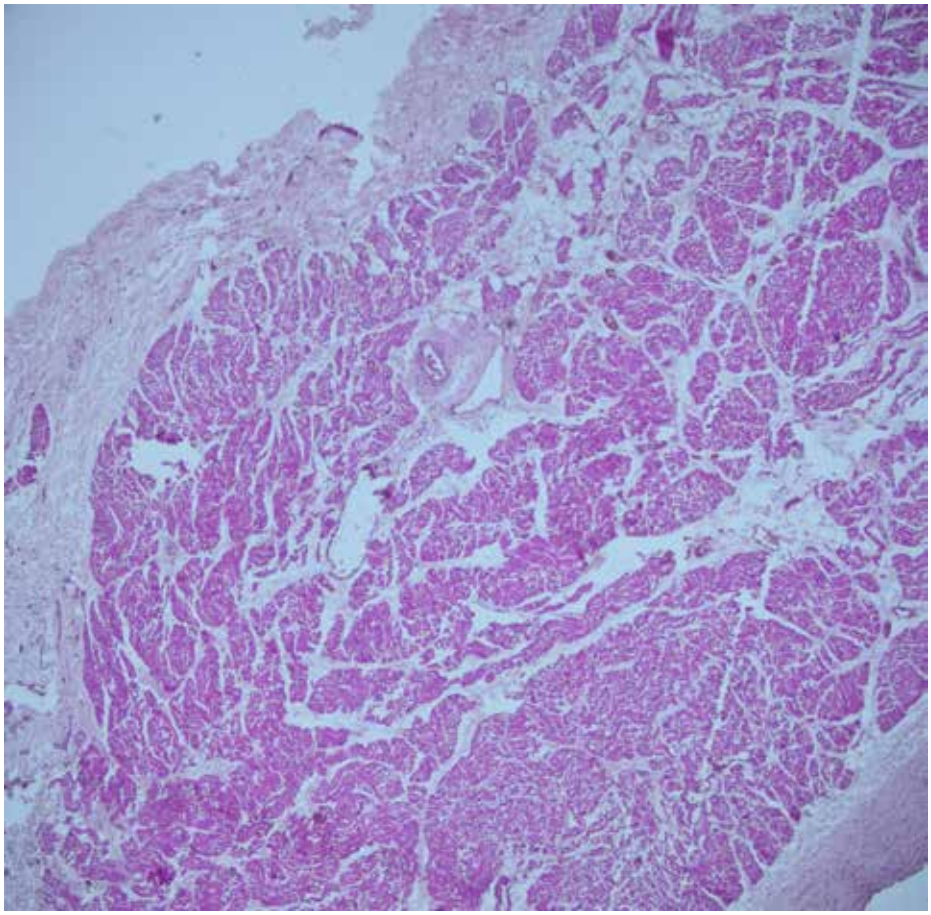

Figure 1.4
Normal SA (Sinoatrial) node, (H&E, x40).
The sinoatrial (SA) node consists of cardiomyocytes specialized to transmit electrical and mechanical activity. Nodal cells (P cells) are small, oval cells with pale staining cytoplasm compared to other cardiomyocytes.

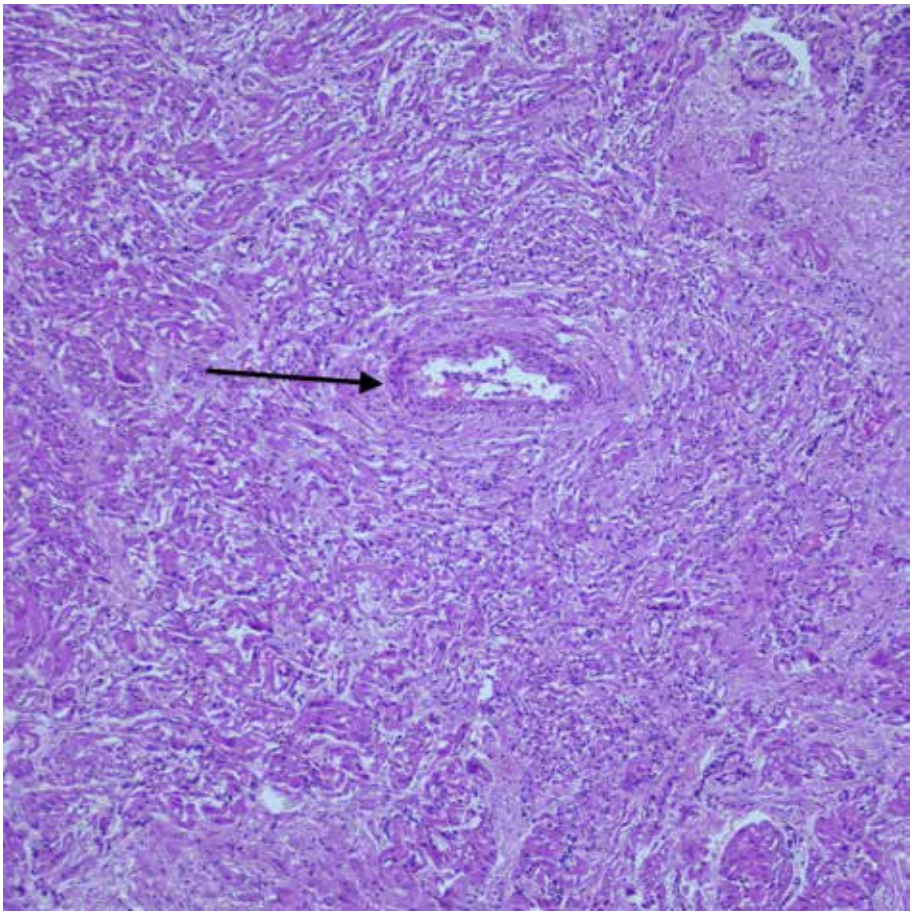

Figure 1.5
Normal SA (Sinoatrial) node, (H&E, x100). The sinoatrial (SA) node is located subepicardially and the sinoatrial node artery (arrow) passes through its center.

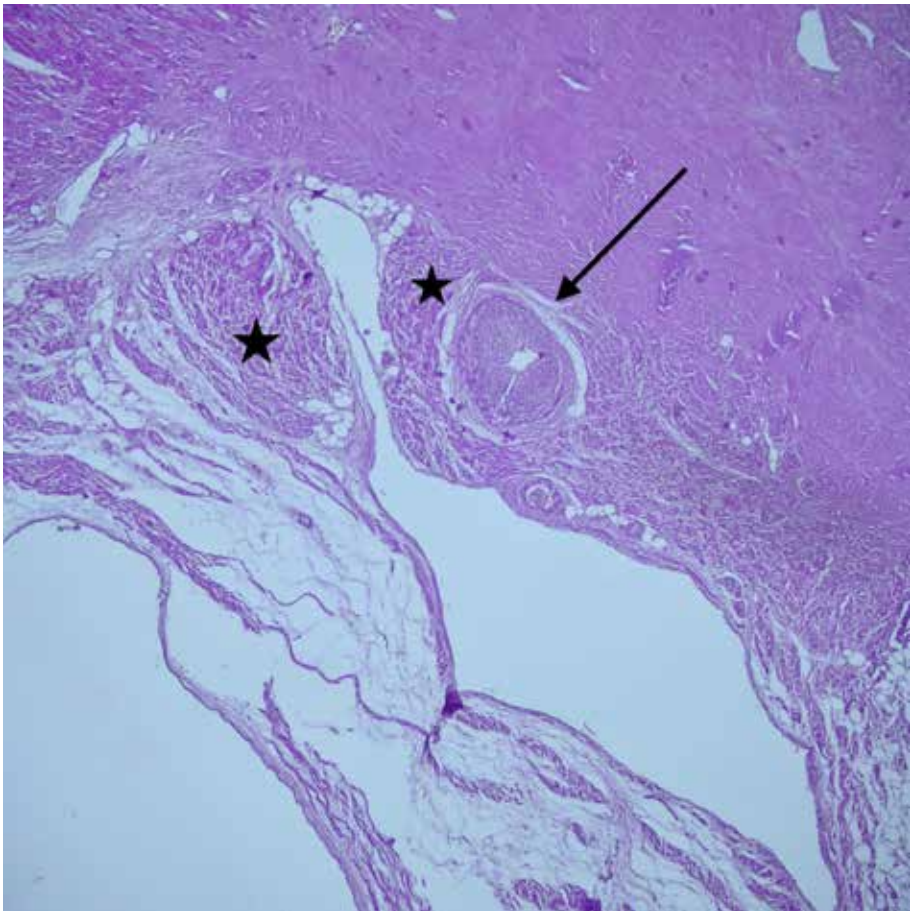

Figure 1.6
Normal atrioventricular (AV) node (H&E, x40). The atrioventricular (AV) node is a structure in the right atrium that resembles the cardiomyocytes located in the atrium. The atrioventricular (AV) node (asterisk) is situated subendocardially, and the atrioventricular nodal artery (arrow), unlike the sinus nodal artery, may not be located intranodally. The atrioventricular (AV) node consists of small, oval-shaped nodal (P cells) cells with pale cytoplasm.

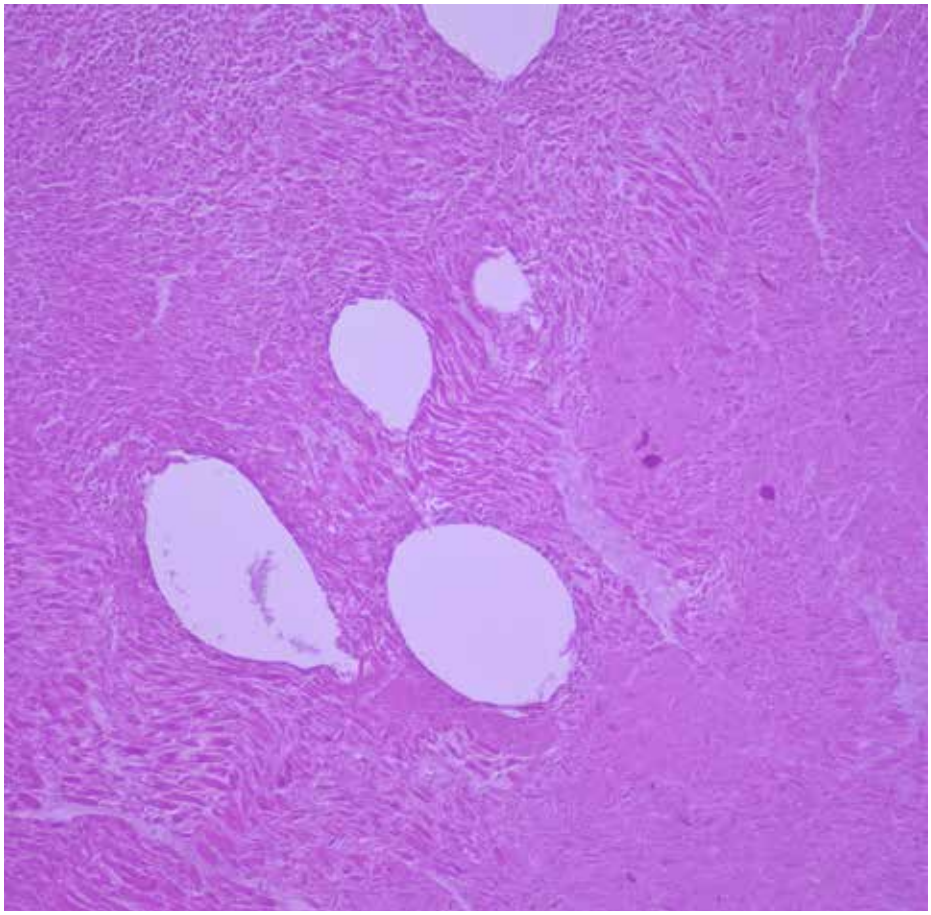

Figure 1.7
Cardiac autolysis, (H&E, x100). Autolysis is the digestion of the dead or dying cells by its own enzymes. It is distinguished from necrosis by the absence of inflammatory cell infiltration. During autolysis and decomposition, with the spread of intestinal and other bacteria, liquid and gas is released, causing tissue cavities.

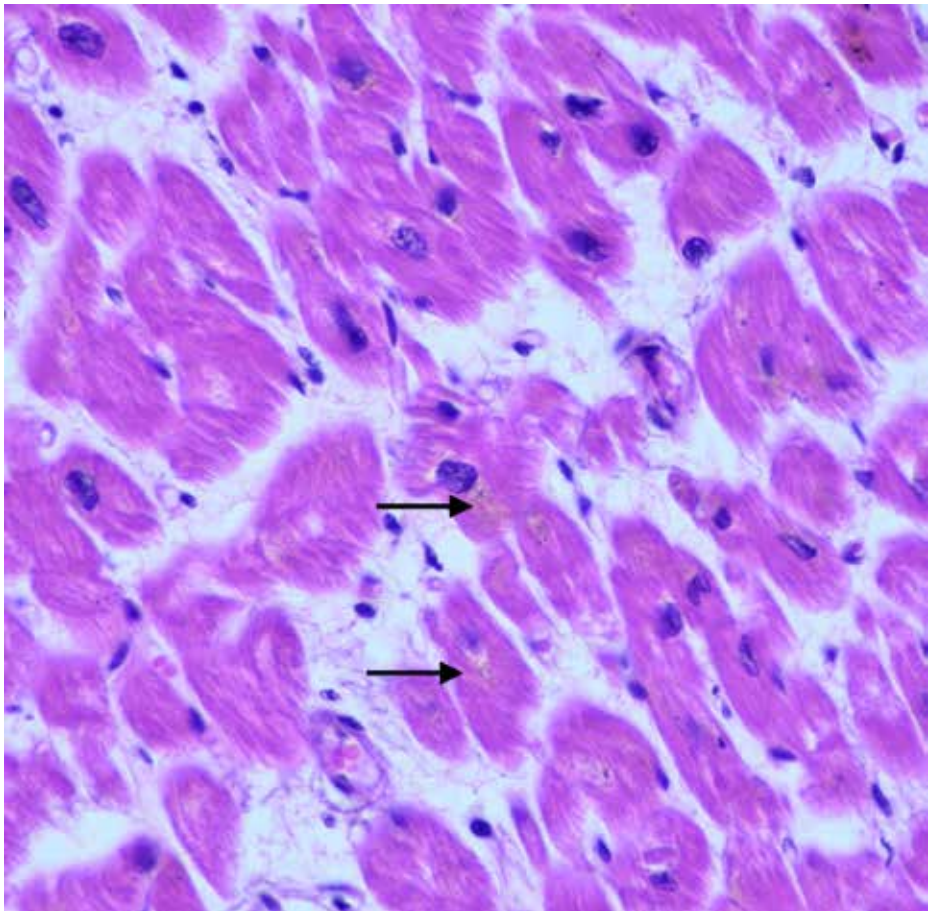

Figure 1.8
Lipofuscin pigment accumulation, (H&E, x600). With increasing age, perinuclear-located, granular, golden-brown lipofuscin (lipochrome) pigment accumulation (arrows) is observed in cardiomyocytes. It consists of lipid-containing residues originating from lysosomal digestion as a result of autophagocytosis (Wear and tear pigment).

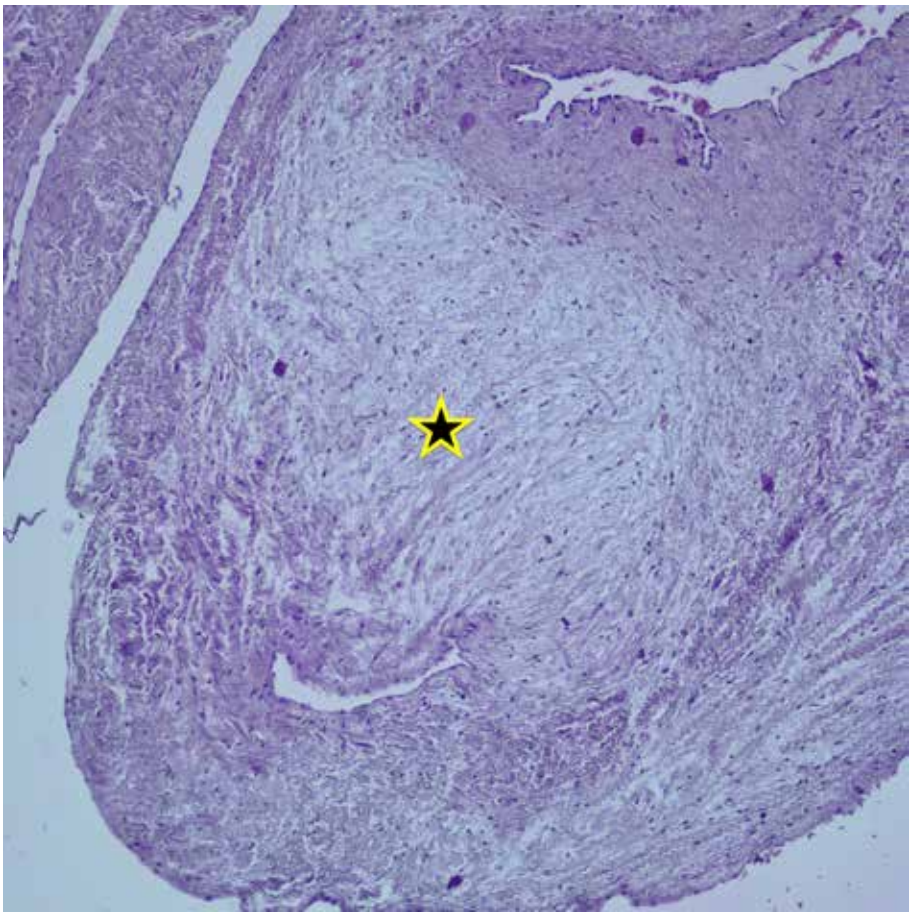

Figure 1.9
Myxoid degeneration of the heart valve,
(H&E, x100).
Myxoid degeneration detected in heart valves disrupts the mechanical strength and structure of the valve due to changes in the synthesis and remodeling of collagen.
The microscopic view shows an area of myxomatous degeneration (asterisk)
in the mitral valve.

Table 1-1 Development of Morphological Findings in Myocardial Infarction.

Time	Macroscopic Features	Microscopic Features
1/2-4 hours	No feature	No feature, waviness of fibers
4-12 hours	Dark mottling (occasional)	Early coagulation necrosis, edema, hemorrhage
12-24 hours	Dark mottling	Coagulation necrosis, pyknosis of nuclei, cardiomyocyte hipereosinophilia, contraction band necrosis, beginning of neutrophils infiltration
1-3 days	Mottling with yellow infarct center	Coagulation necrosis, dense interstitial neutrophils infiltration
3-7 days	Central yellow necrotic softening, hyperemic borders	Beginning disintegration of dead cardiomyocytes, early phagocytosis of dead cells by macrophages at infarct borders
7-10 days	Yellow, soft necrotic center, depressed red margins	Phagocytosis of dead cells, and granulation tissue formation at the borders of lesion
10-14 days	Red-gray depressed infarct borders	Granulation tissue formation with neovascularization and collagen deposition
2-8 weeks	Gray-white scar formation from borders of lesion to the center	Increased collagen deposition, decreased cellularity
More than 2 months	Total scar tissue formation	Dense collagenous scar formation

Reference :

1.Kumar, V., Abbas, A. K., & Aster, J. C. (2015). Robbins & Cotran Pathologic Basis of Disease (9th ed.). Elsevier. Section 12, The Heart, p. 544.

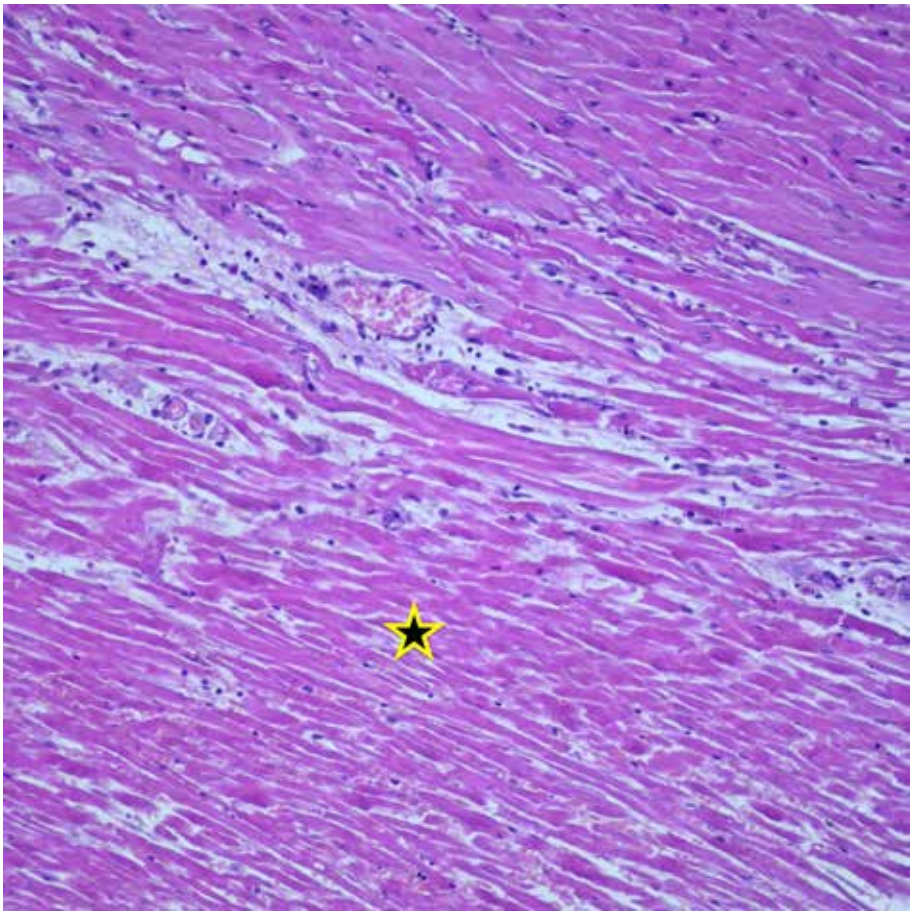

Figure 1.10
Acute myocardial infarction (within first 24 hours), (H&E, x100). The obvious hypereosinophilic appearance in cardiomyocytes (asterisk) is noteworthy in the microscopic view.

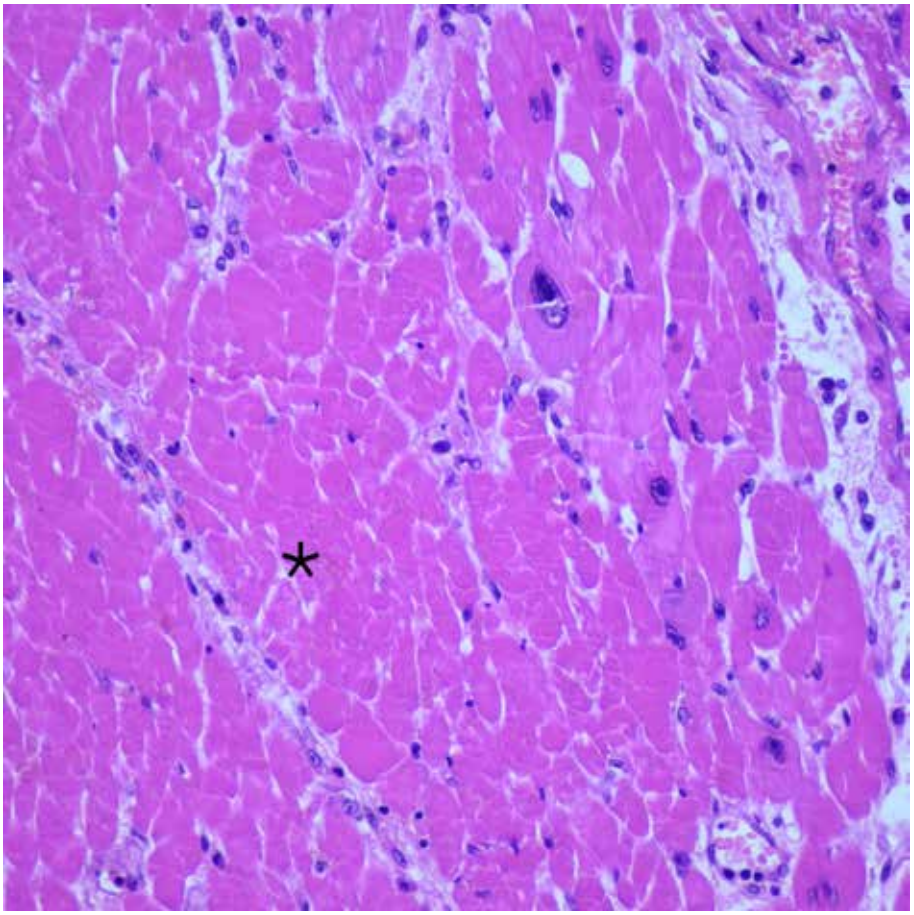

Figure 1.11
Acute myocardial infarction (MI) (within first 24 hours), (H&E, x200). The pronounced hypereosinophilic appearance in cardiomyocytes is clearly visible when compared with the normal surrounding muscle fibers. There is also nucleus loss in necrotic muscle fibers with a hypereosinophilic appearance (asterisk). Nucleus loss is evidence that cellular damage is irreversible.

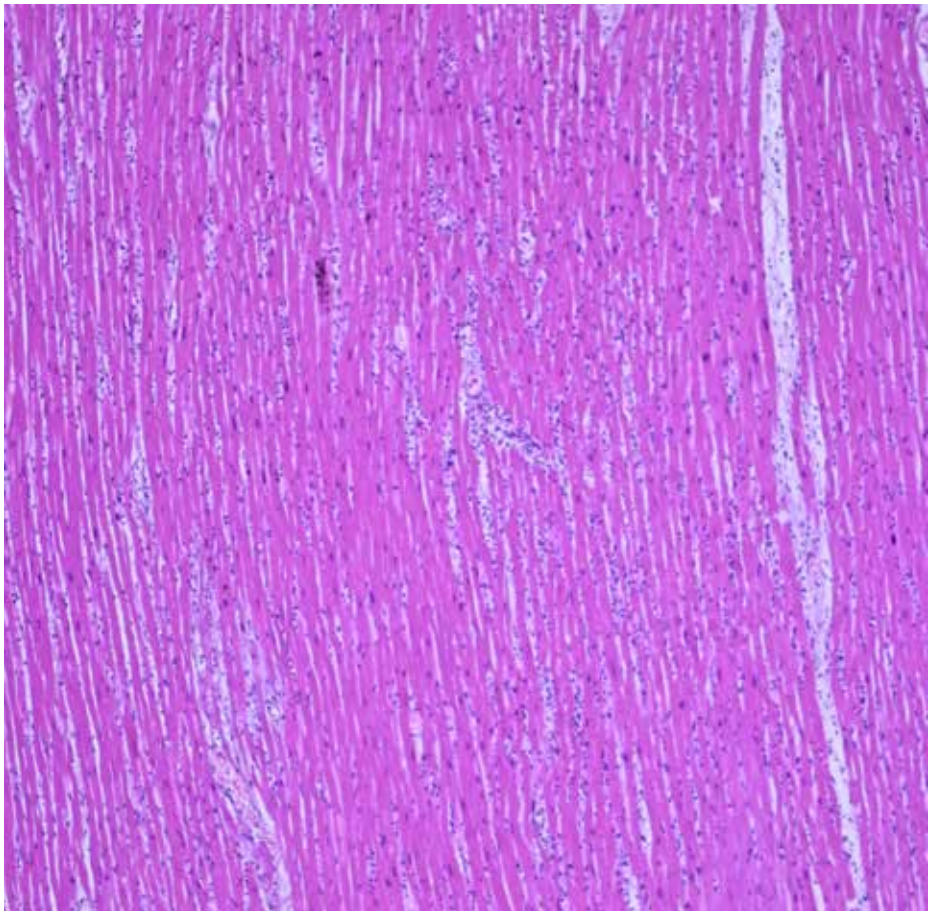

Figure 1.12
Myocardial infarction (within first 24 hours), (H&E, x100). Neutrophil infiltration is notable in the infarct area.

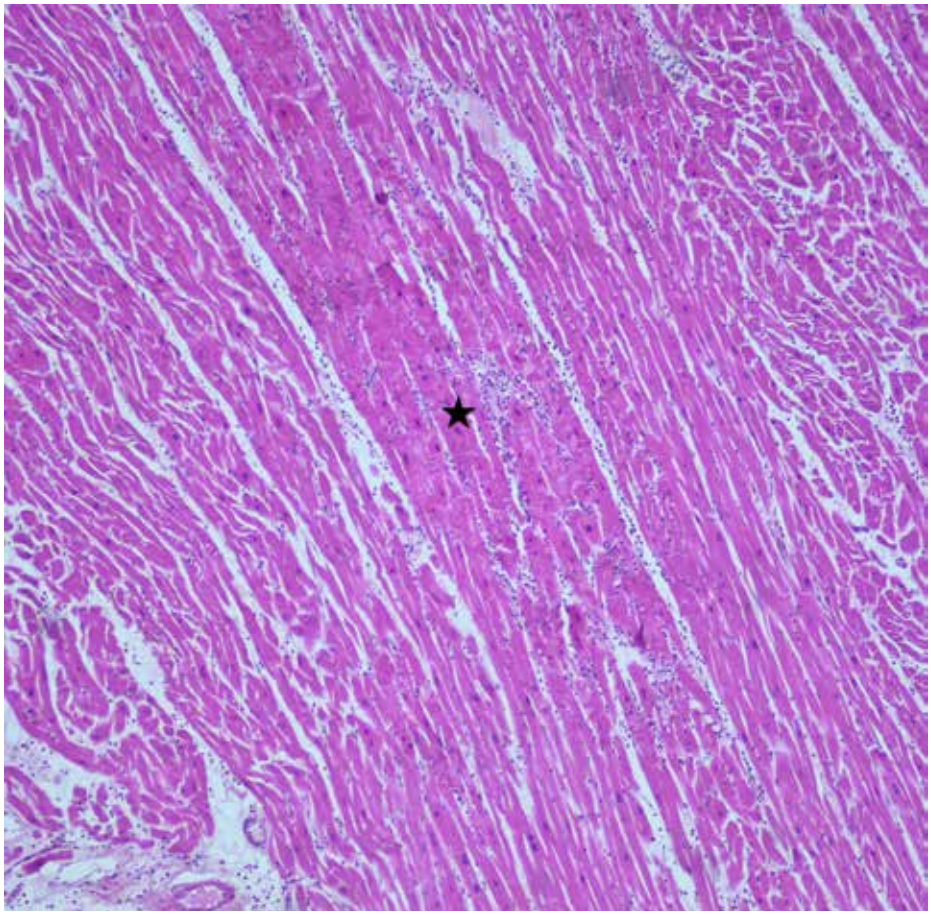

Figure 1.13
Myocardial infarction (within first 24 hours), (H&E, x100). The acute myocardial infarction seen in this microscopic view is within the first 24 hours. In addition to the hypereosinophilic appearance, contraction band necrosis is also observed in cardiomyocytes. Additionally, increased neutrophils are noted in the myocardial infarct area. (asterisk)

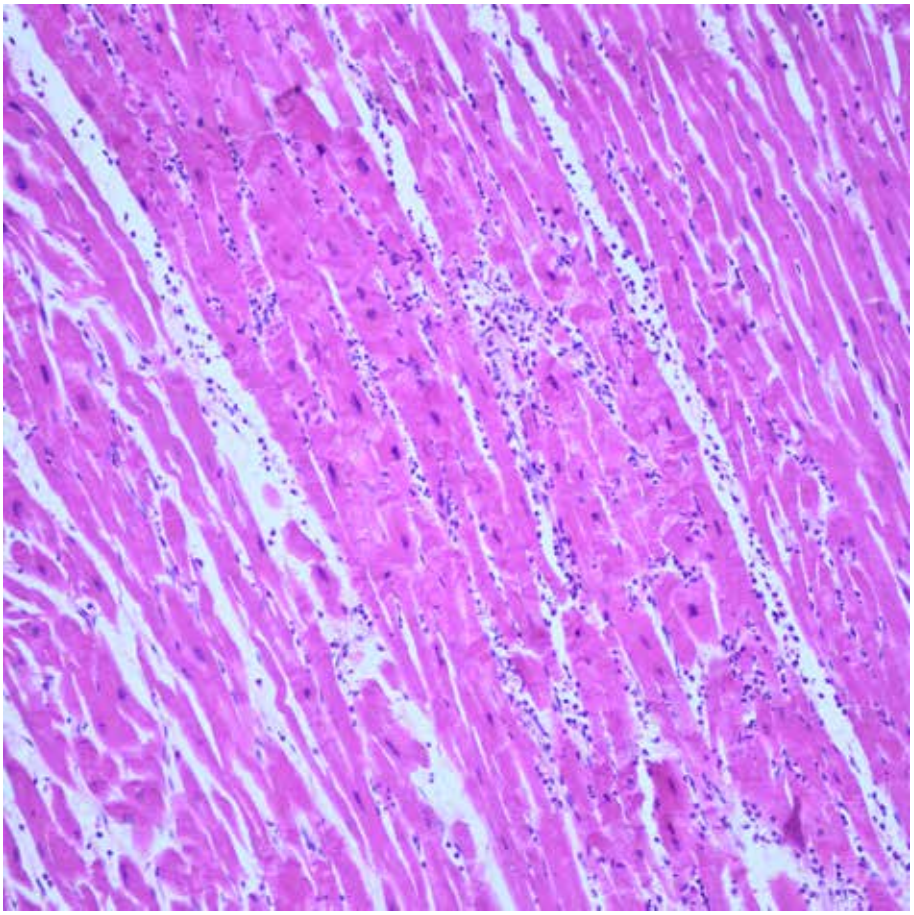

Figure 1.14 Myocardial infarction (within first 24 hours), (H&E, x200). Hypereosinophilic appearance in cardiomyocytes, contraction band necrosis, neutrophil infiltration and edema are noteworthy in the infarcted myocardium.

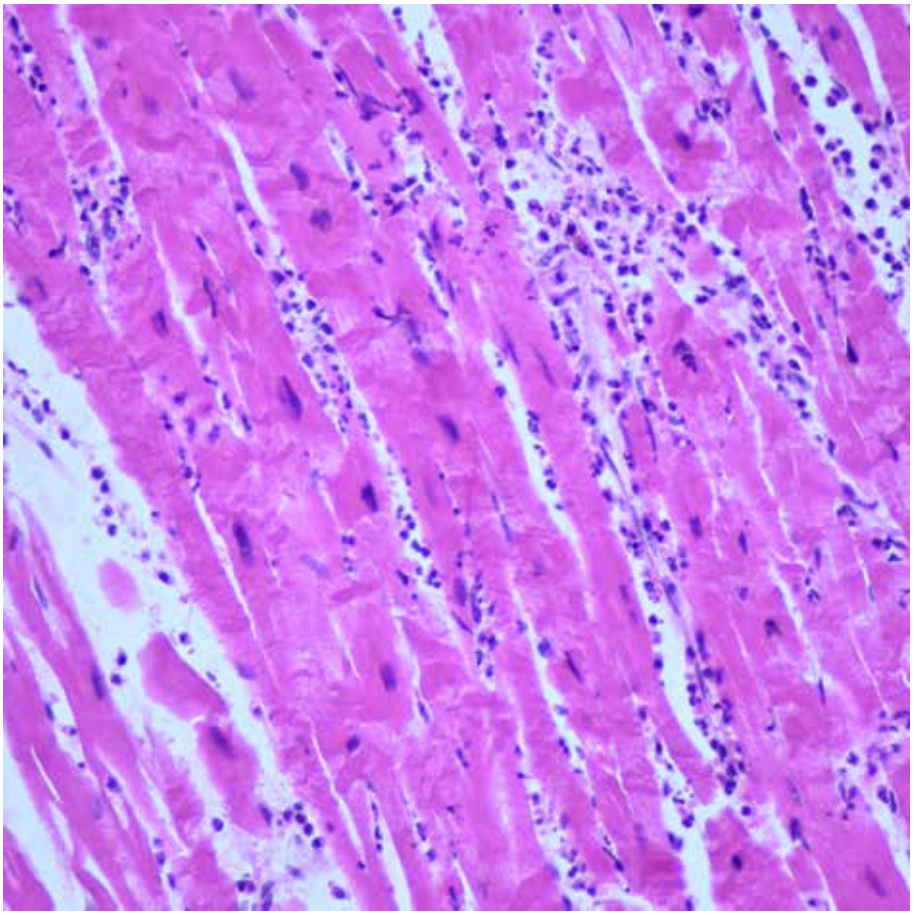

Figure 1.15 Myocardial infarction (within first 24 hours), (H&E, x400). Contraction band necrosis and edema is observed in the infarct area. In addition, there is karyolysis in some necrotic muscle fibers and their nuclei no longer visible. There is neutrophil infiltration within necrotic myocardium.

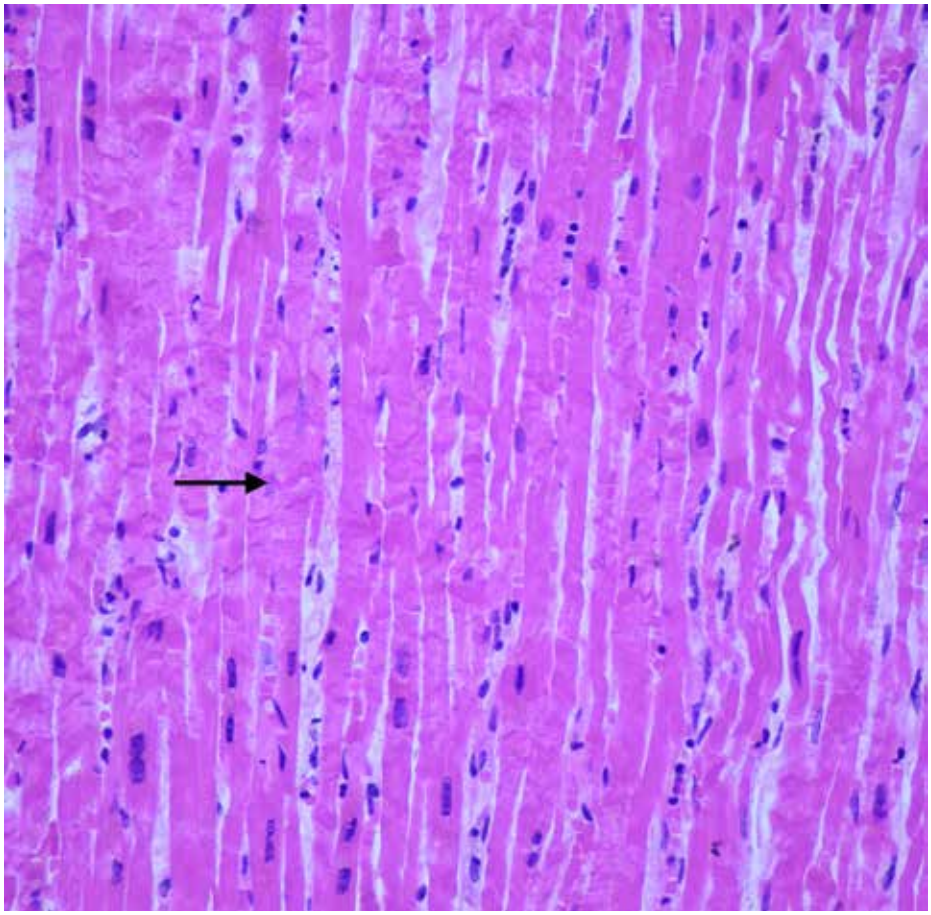

Figure 1.16
Myocardial infarction (within first 24 hours), (H&E, x400). Contraction band necrosis and nucleus loss are observed in the microscopic view. Dark pink, irregularly shaped contraction band necrosis (arrow) across numerous muscle fibers is seen. Neutrophils have not yet reached the infarcted area. This indicates that the infarction is less than 12 hours old.

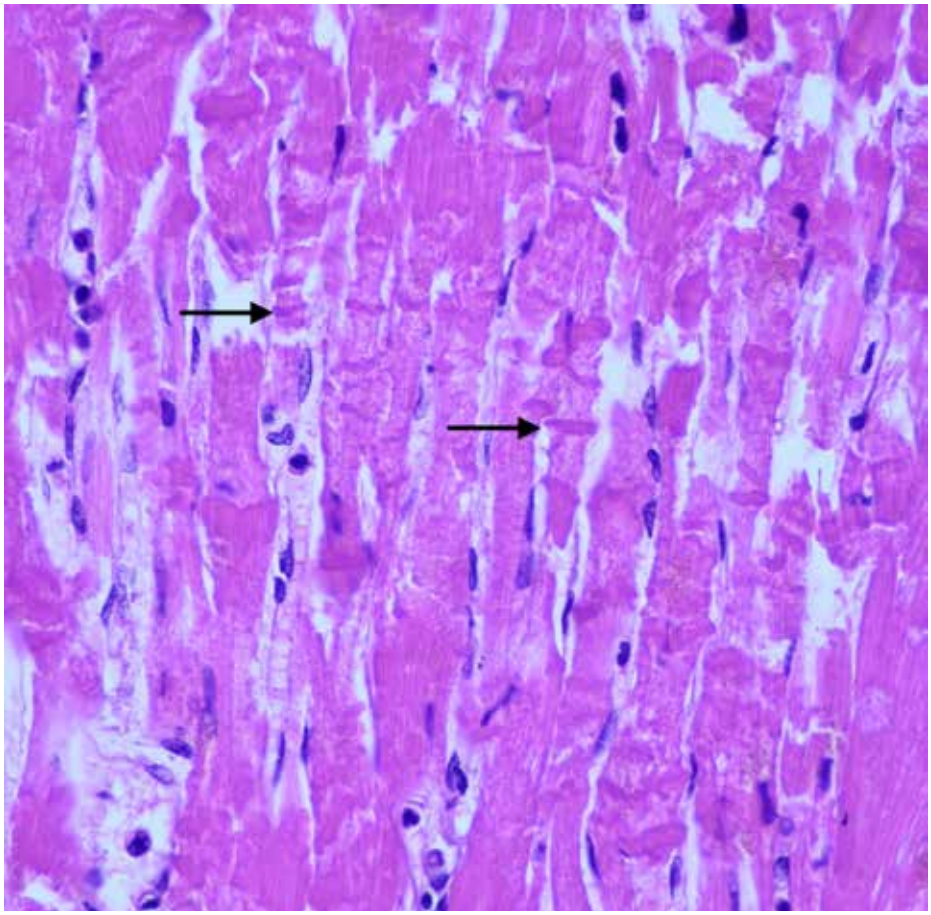

Figure 1.17
Contraction band necrosis (Coagulative myocytolysis), (H&E, x600). Contraction bands indicate focal pathological spasm. Contraction band necrosis (arrows) is an important finding of early ischemia, if reperfusion has occurred. However, it can be detected in people who died during cardiac surgery, shocks due to electrical effects, catecholamine use and potassium deficiency.

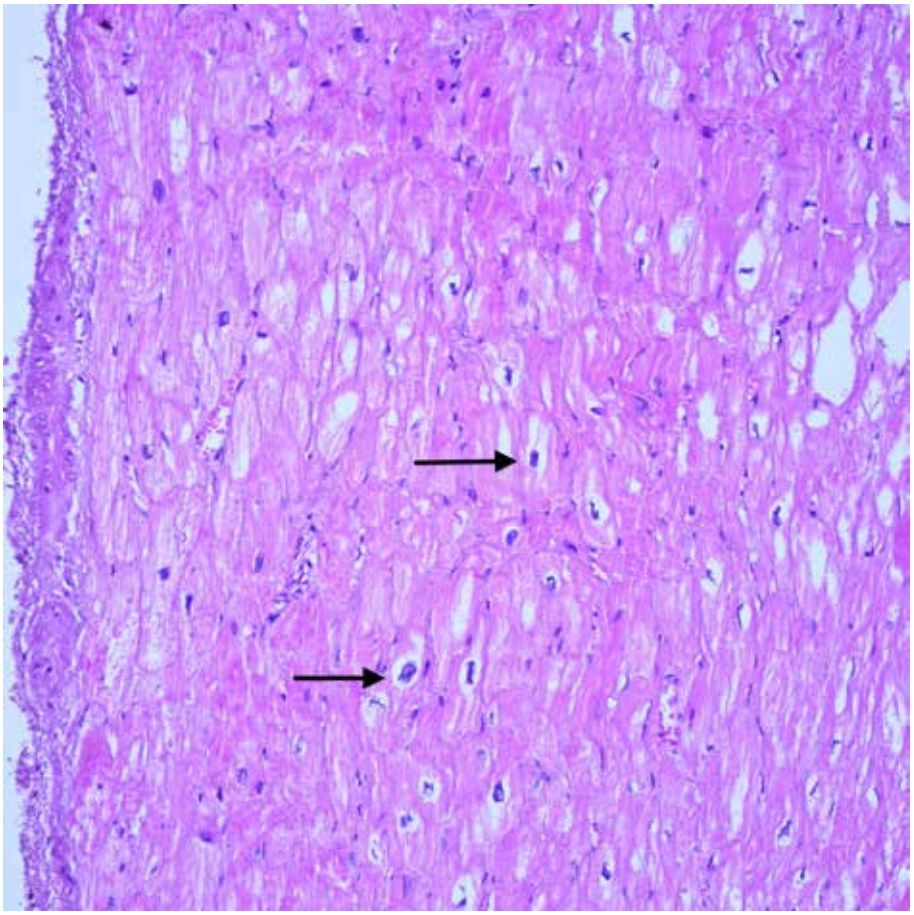

Figure 1.18
Colliquative myocytolysis, (H&E, x200). Colliquative myocytolysis is also called "vacuolar degeneration", "ballooning degeneration" or "myocytolysis". It is mostly used to describe focal lesions in the subendocardial and perivascular areas. It appears as clear halo around cardiomyocyte nuclei (arrow). These spaces contain water, glycogen or lipid, which have an arrhythmogenic effect.

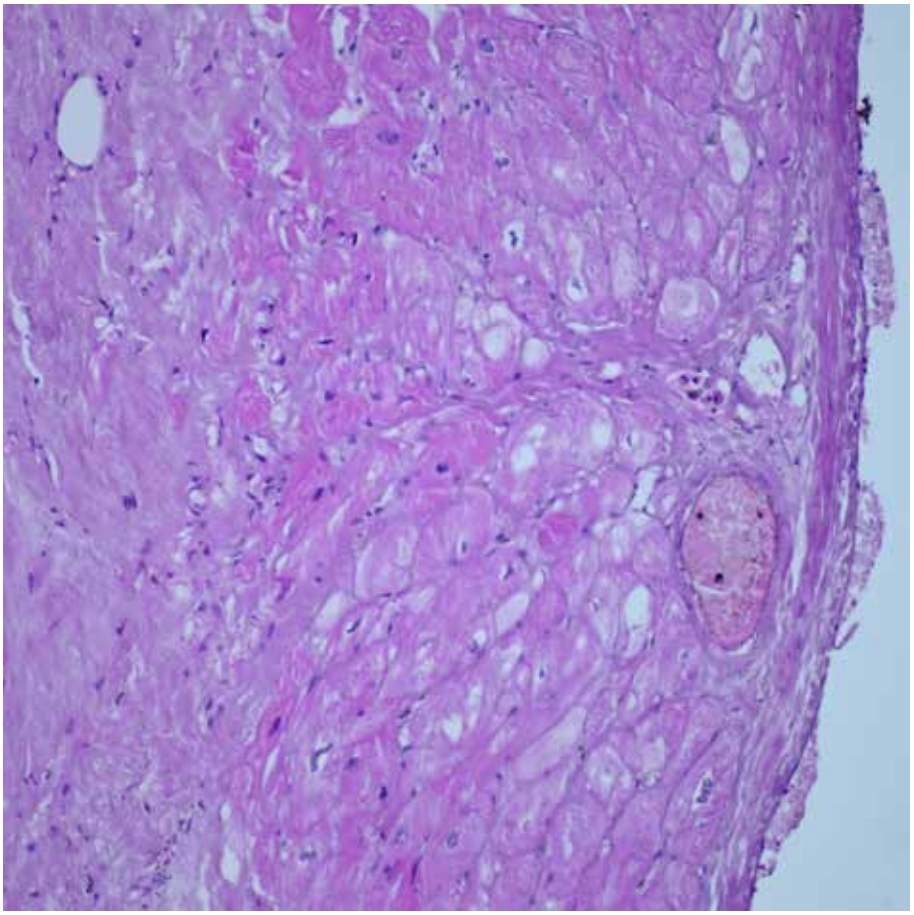

Figure 1.19
Colliquative myocytolysis, (H&E, x200). It may develop due to isolated hypoxic, ischemic and toxic damage. It is a reversible cellular damage in its early stages.

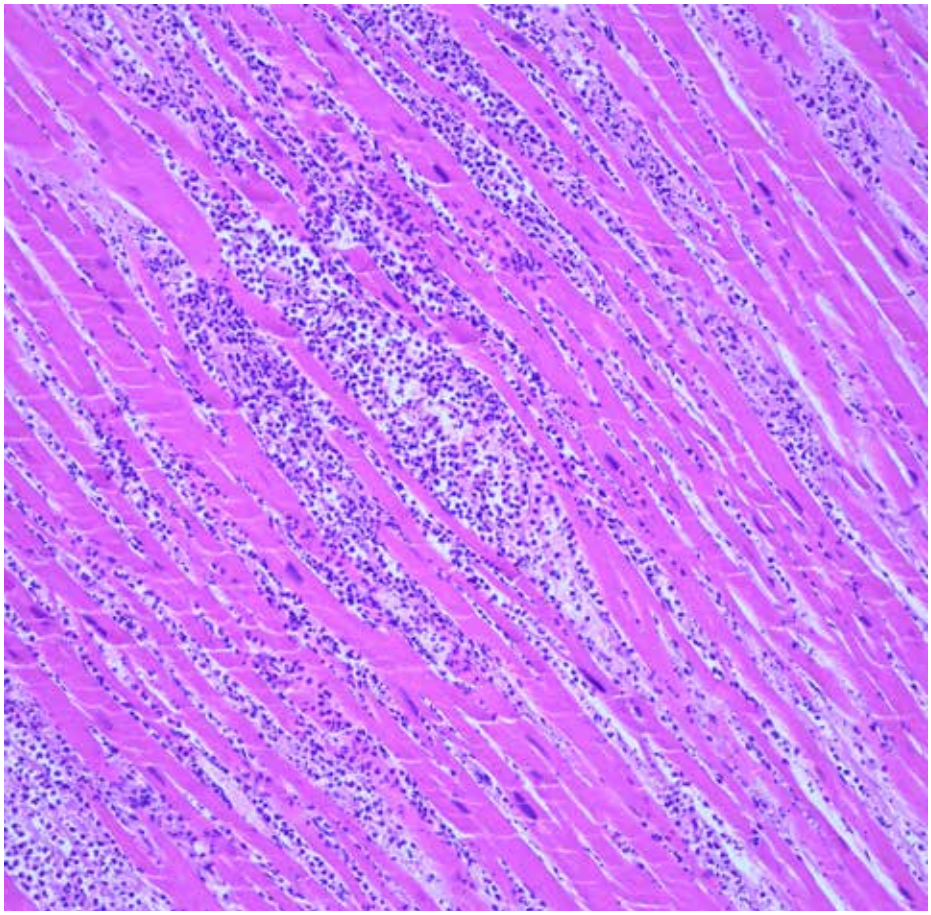

Figure 1.20
Myocardial infarction (within 1-3 days), (H&E, x200).
In advanced stages of coagulation necrosis, cardiomyocyte nuclei dissolve and disappear. Dense neutrophil infiltration is observed within the myocardium in microscopic view.

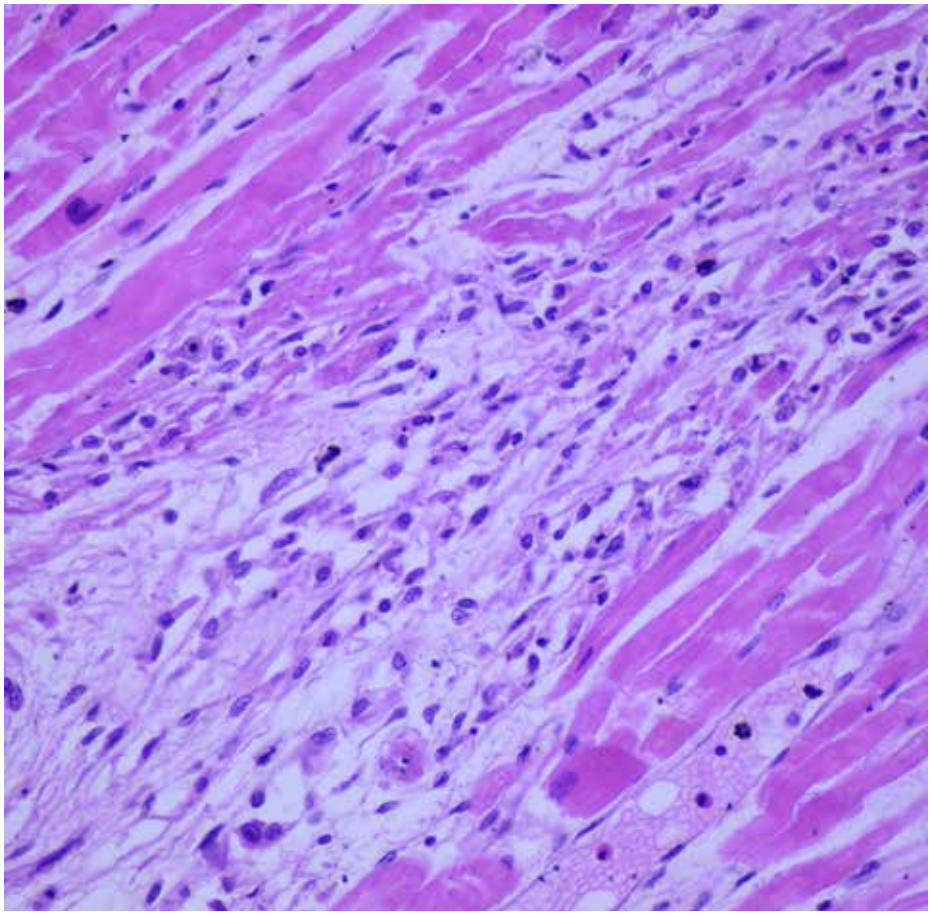

Figure 1.21
Myocardial infarction (within 3-7 days), (H&E, x400).
After the 3rd day of myocardial infarction, necrotic muscle fibers disintegrate. At the edges of the infarct, disintegrated muscle fibers are phagocytosed by macrophages.

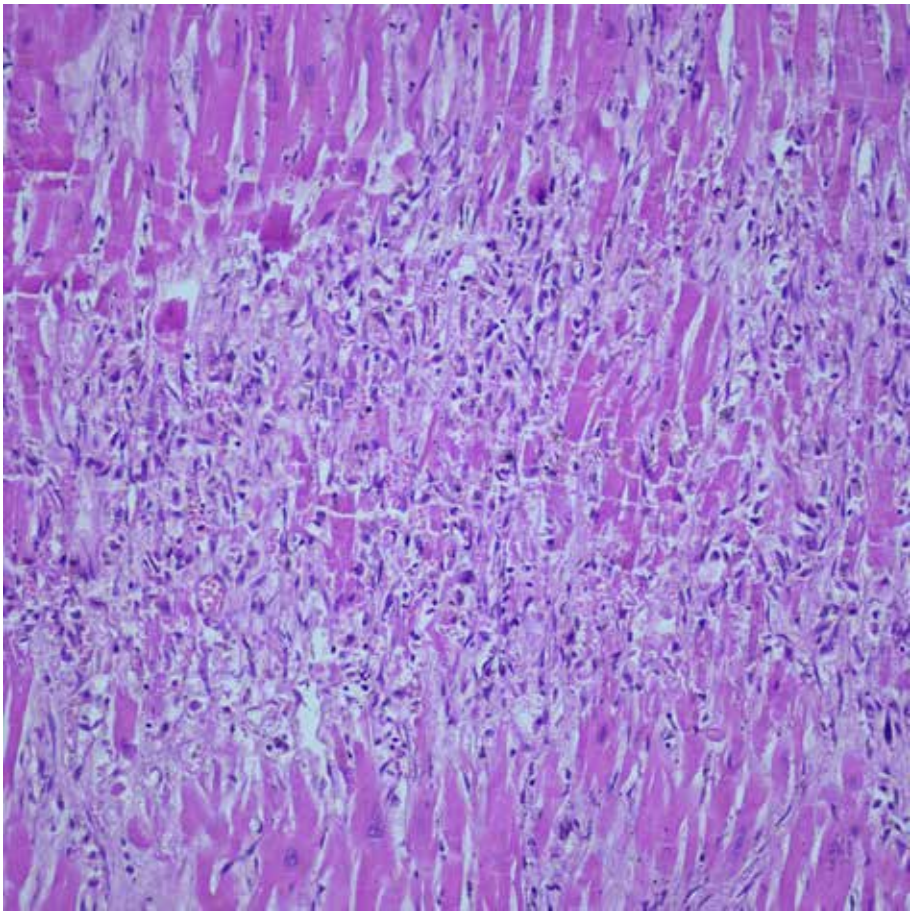

Figure 1.22
Myocardial infarction (within 3-7 days), (H&E, x200). In the 1st week, healing of the infarcted area becomes more evident with hemosiderin pigment-laden macrophages, neovascularization and fibroblast proliferation.

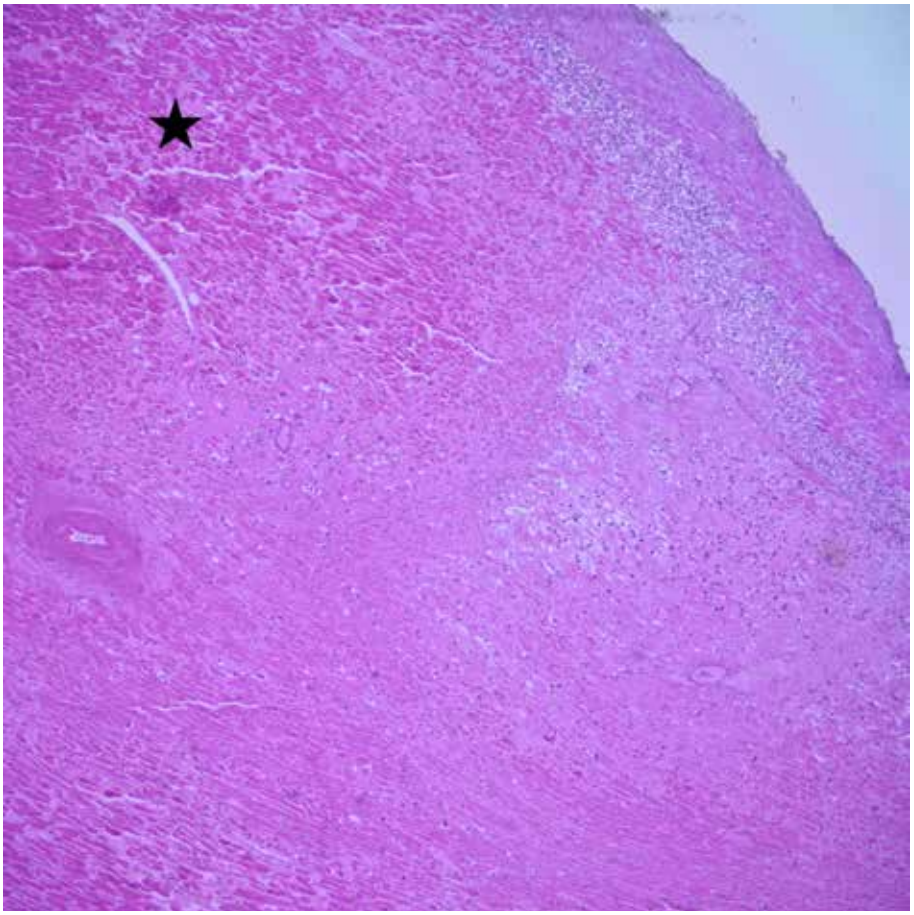

Figure 1.23
Myocardial infarction (within 1-2 weeks), (H&E, x40). Myocardial infarction containing areas of granulation tissue in the periphery with necrotic cardiomyocytes observed in the central part of infarcted area (asterisk).

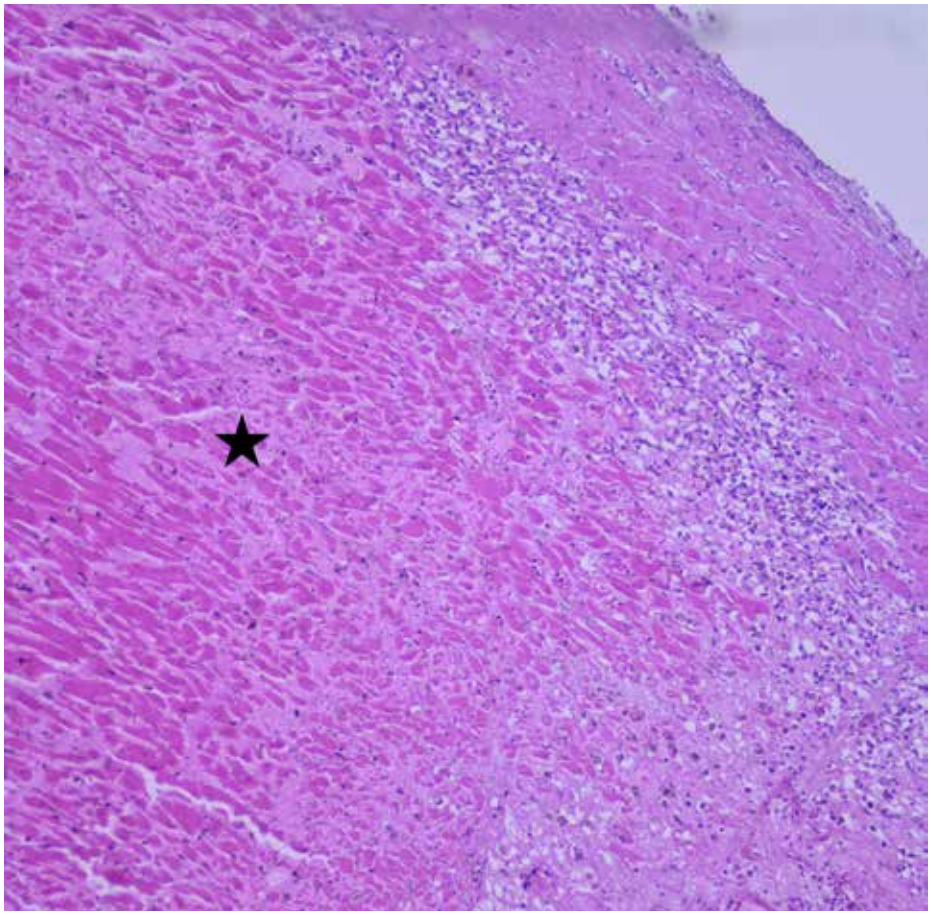

Figure 1.24
Myocardial infarction (within 1-2 weeks), (H&E, x100).
At higher magnification, granulation tissue with coagulative necrosis in its center (arrow) is seen.
Determining the timing of the myocardial infarction is based on the infarct periphery.

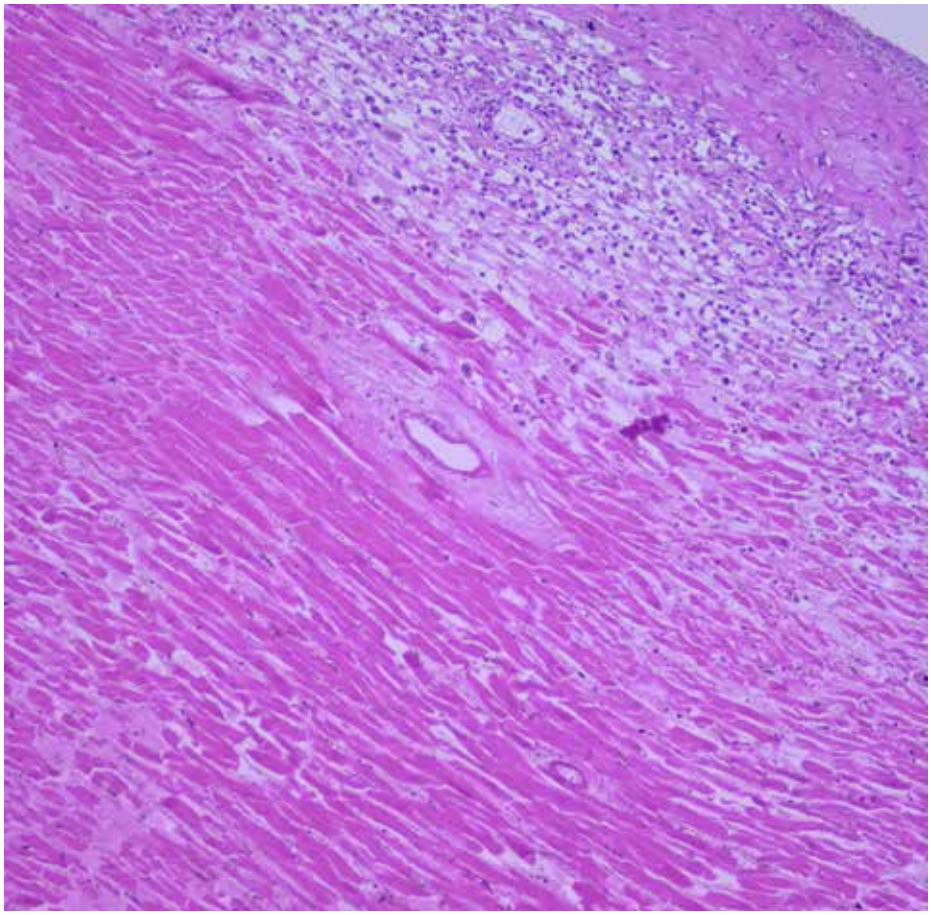

Figure 1.25
Myocardial infarction (within 1-2 weeks), (H&E, x100).
Granulation tissue with coagulative necrosis in its center.

Figure 1.26
Myocardial infarction (within 1-2 weeks), (H&E, x100). In the microscopic view, peripherillay localized granulation tissue (arrow) adjacent to the center of infarcted area is seen.

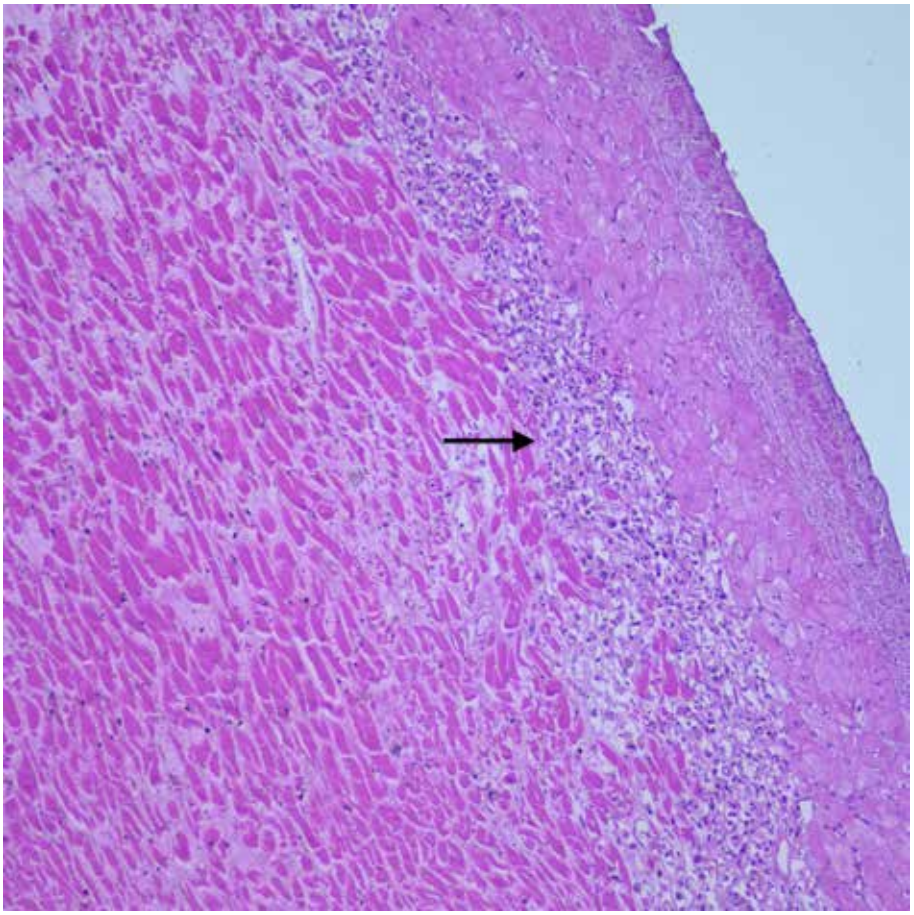

Figure 1.27
Myocardial infarction (within 1-2 weeks), (H&E, x200). In the microscopic view, granulation tissue formation is seen.

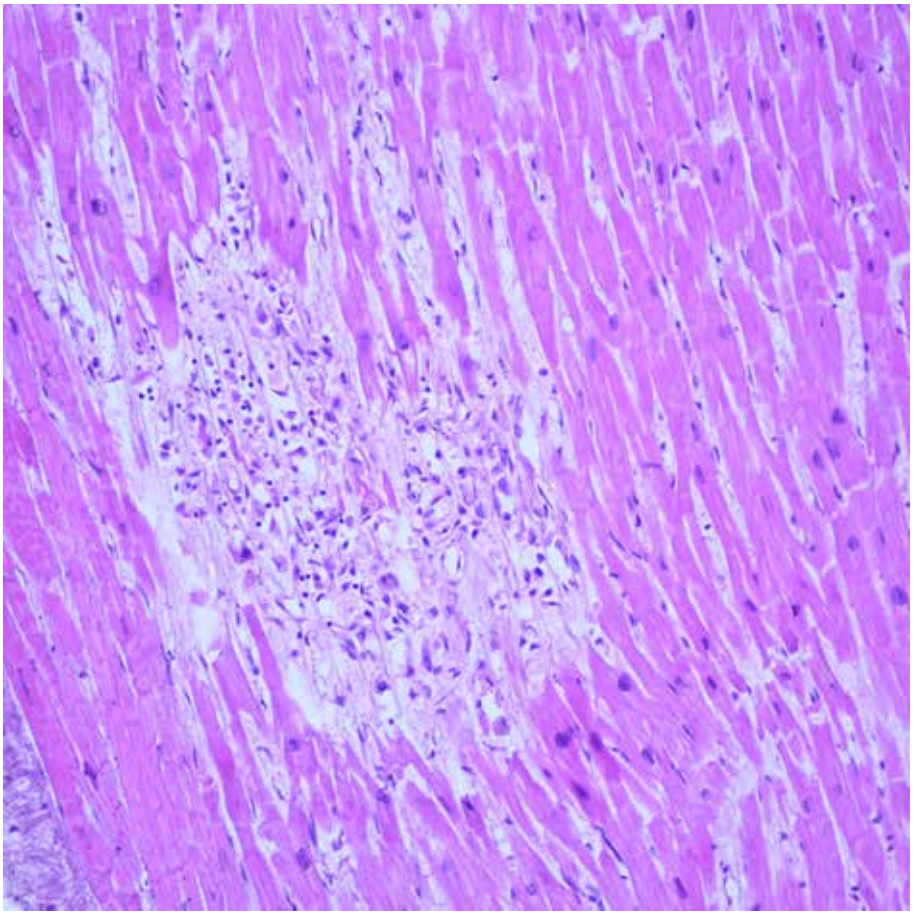

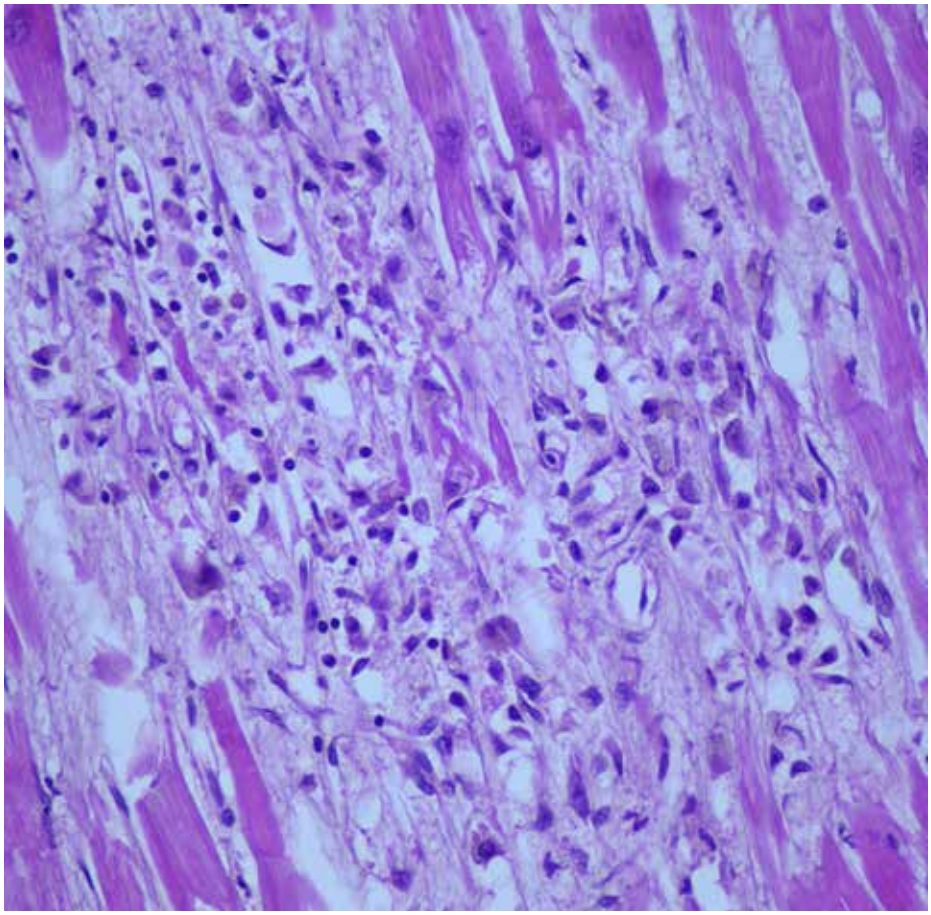

Figure 1.28
Myocardial infarction (within 1-2 weeks), (H&E, x400).
At higher magnification.
During the healing of myocardial infarction, hemosiderin-laden histiocytes, fibroblast proliferation and neovascularization is seen.

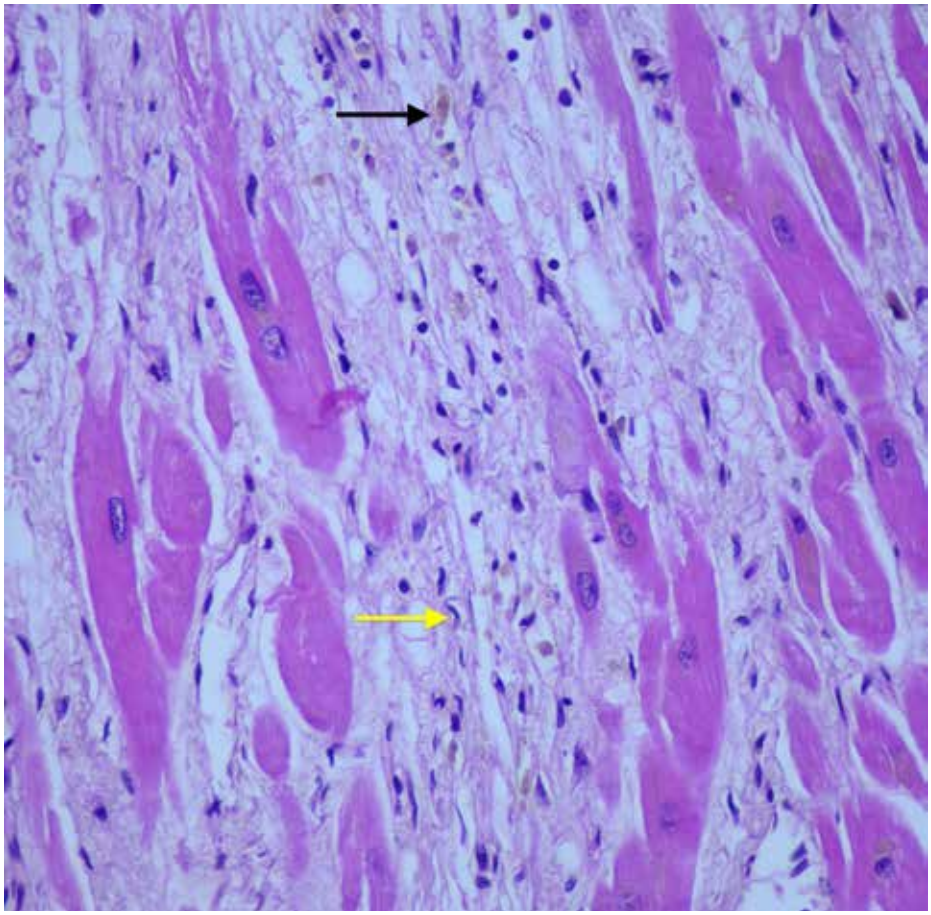

Figure 1.29
Myocardial infarction (2 weeks of MI), (H&E, x400).
During the healing process, pigment-laden histiocytes (black arrow), fibroblasts (yellow arrow) and increased collagen deposition are noteworthy.

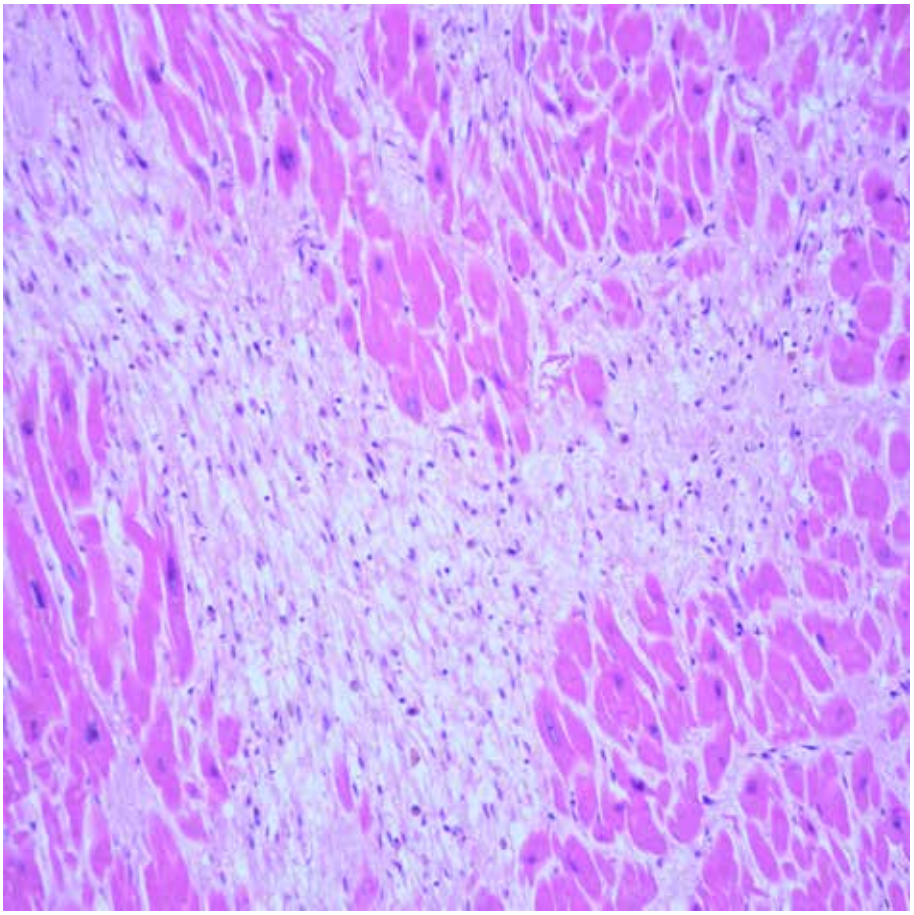

Figure 1.30
Myocardial infarction (2 weeks of MI), (H&E, x400). In the microscopic view, collagen deposition is evident, and there are occasional hemosiderin-laden histiocytes. Cellularity decreased.

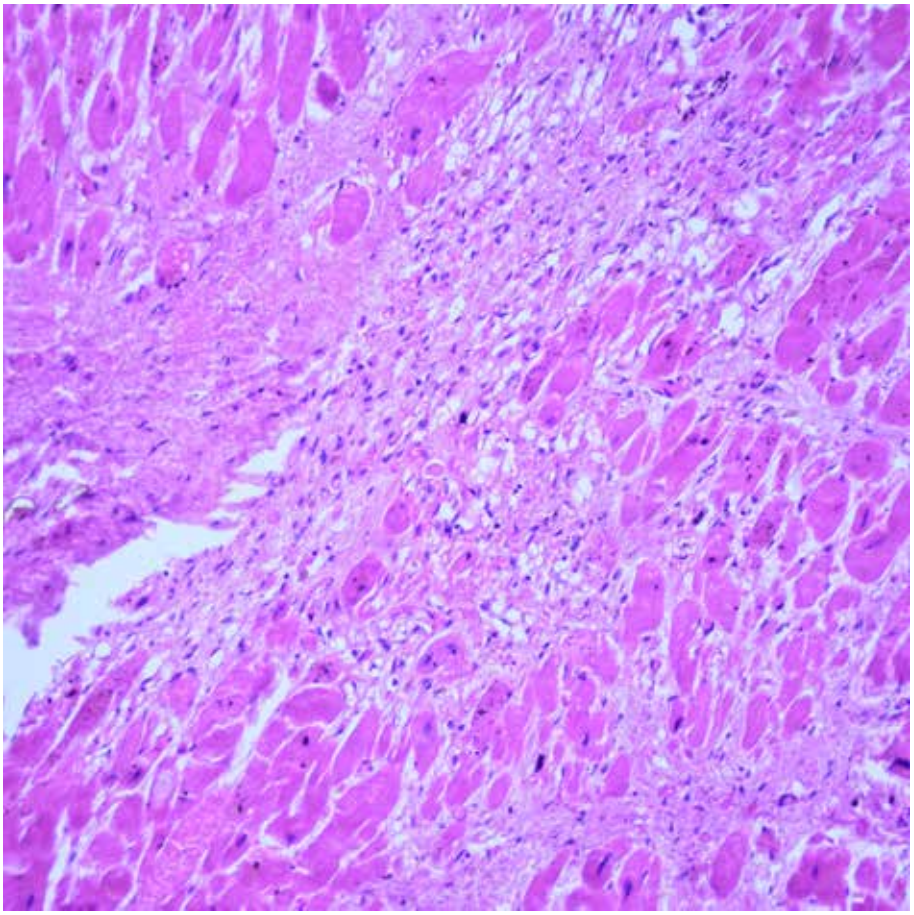

Figure 1.31
Myocardial infarction (2-8 weeks of MI), (H&E, 200). With the healing process of myocardial infarction, cellularity decreases and extensive collagen deposition becomes evident.

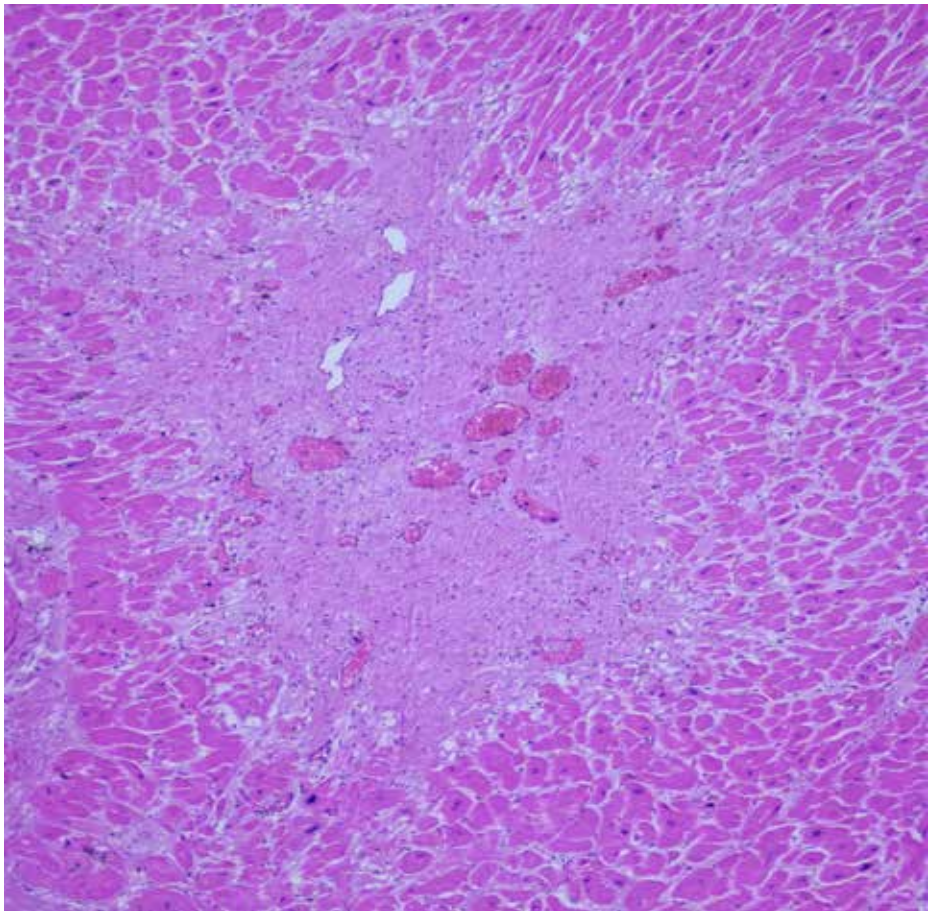

Figure 1.32
Myocardial infarction (2-8 weeks of MI), (H&E, 40).
The microscopic view shows widespread collagen deposition, significantly reduced cellularity, occasional fibroblast proliferation and dilated congested vascular structures.

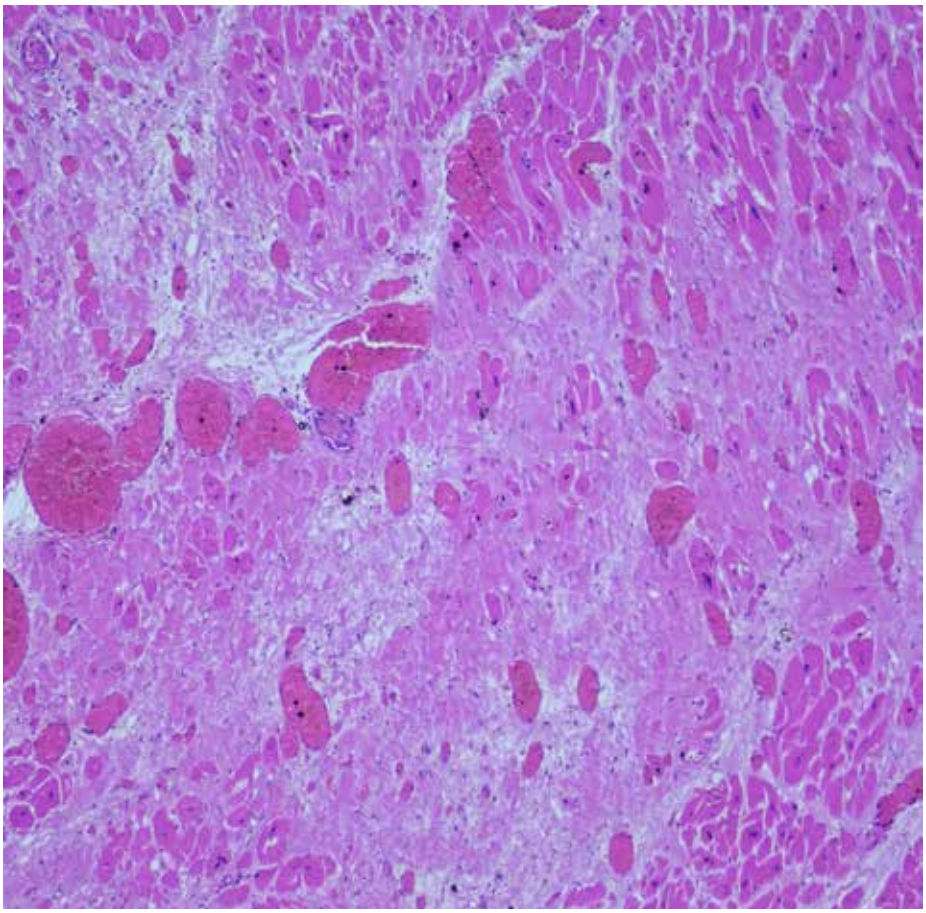

Figure 1.33
Myocardial infarction (around 2 months), (H&E, x100).
2 months after myocardial infarction, dense collagenized fibrous scar tissue was formed.

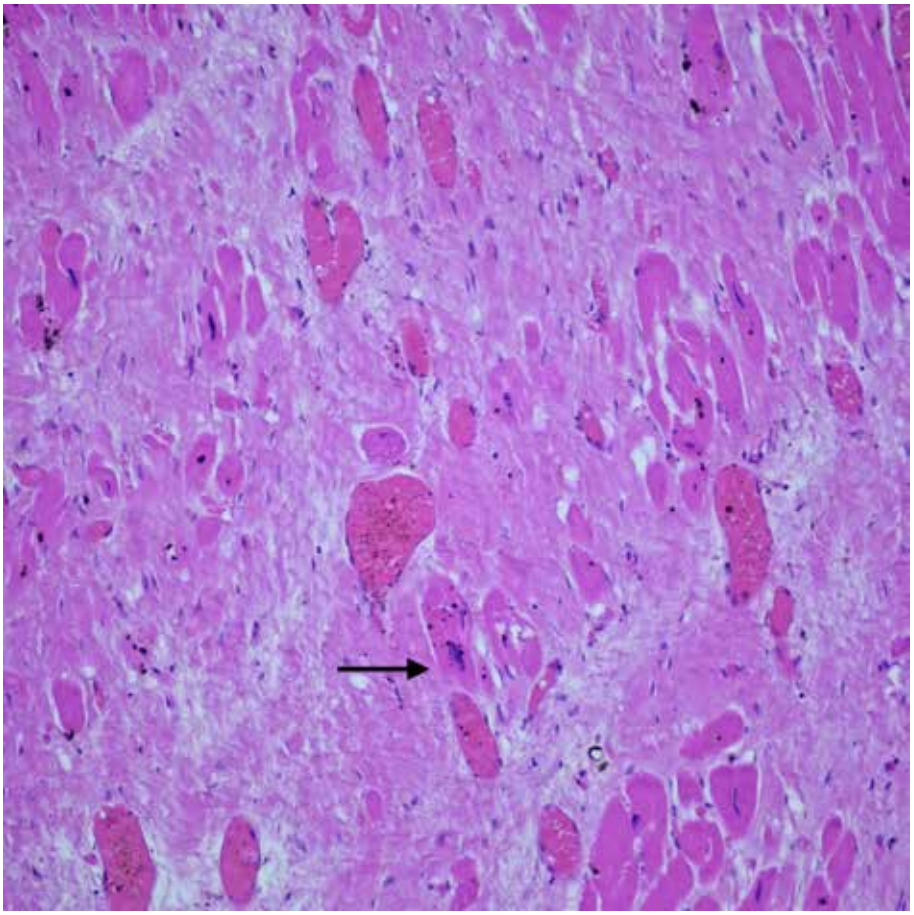

Figure 1.34 Myocardial infarction (around 2 months), (H&E, x200). Two months after myocardial infarction, dense collagenized fibrous scar tissue is fully formed. After this stage, timing of myocardial infarction cannot be made accurately. The microscopic view shows residual hypertrophic muscle fibers (arrow) trapped in the scar area. This is related to predisposition to arrhythmia.

Figure 1.35 Coronary artery bridging, macroscopic view. In transverse sections, the coronary artery (arrow) was found to be within the myocardium. Cases with myocardial bridging are prone to vasospasm.

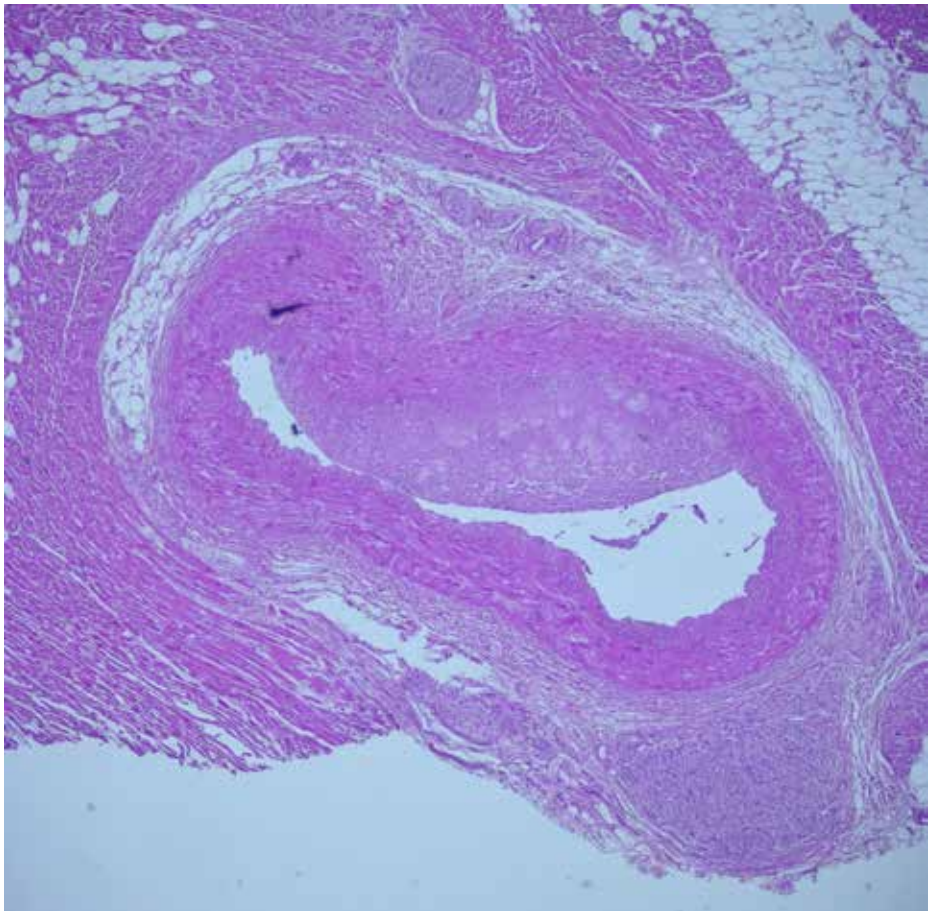

Figure 1.36
Coronary artery bridging, (H&E, x40).
Bridging is when the coronary artery passes from the epicardial adipose tissue through the myocardium and emerges back into the epicardial adipose tissue after traveling a certain distance.
It is most commonly detected in the middle segment of the descending branch of the left coronary artery.

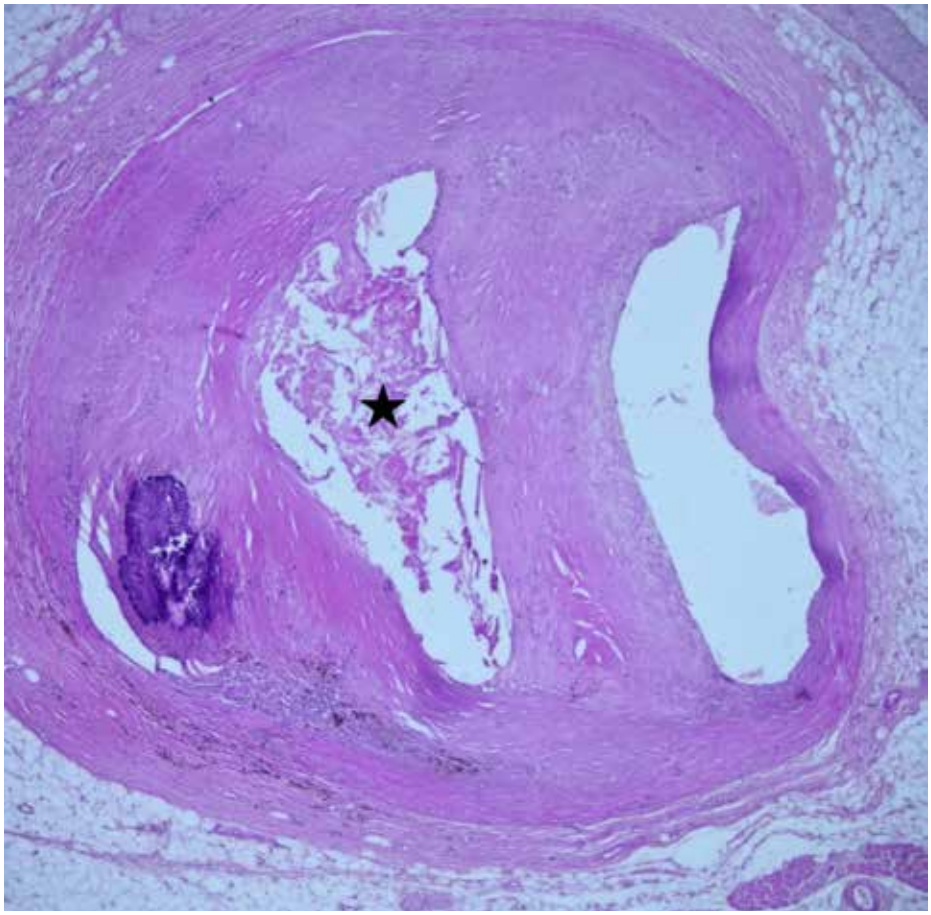

Figure 1.37
Calcified atheroma plaque that severely narrows the coronary artery lumen, (H&E,40).
Atherosclerotic plaque consists of a necrotic core in the center (asterisk) and a fibrotic capsule in the periphery. If the stenosis of the coronary artery lumen is more than 75%, acute coronary syndrome may develop. In the microscopic view, since there is a coronary artery segment that does not contain plaque, this lesion is described as “eccentric”, not “concentric”.

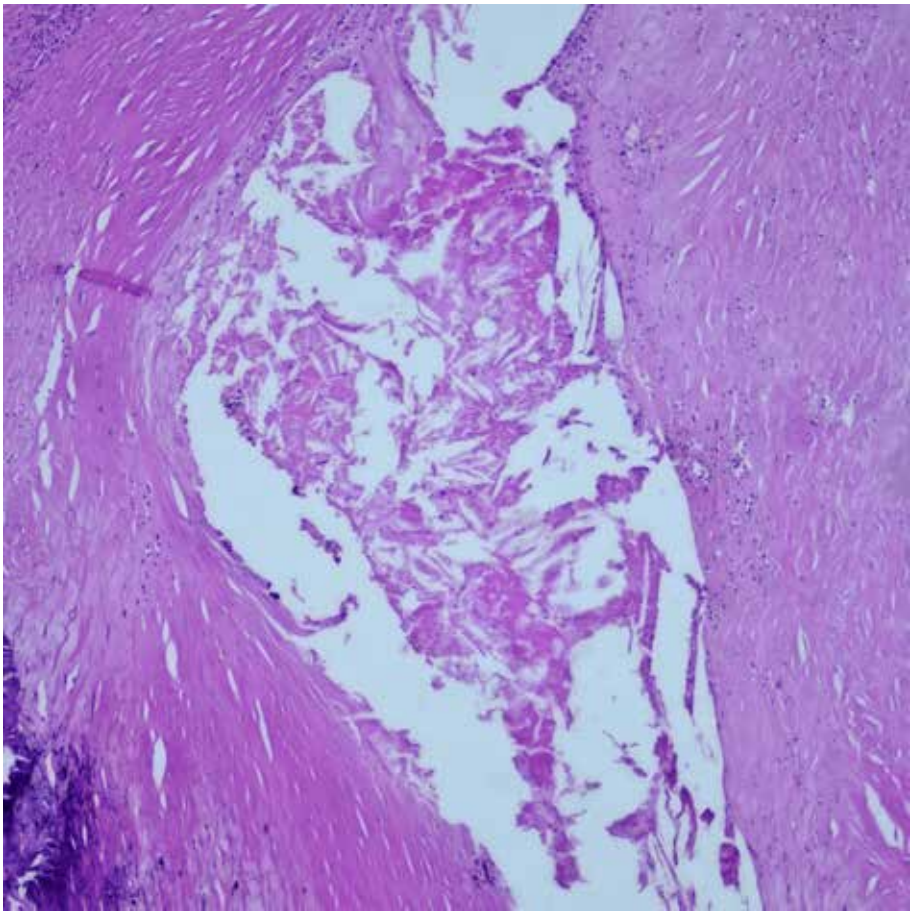

Figure 1.38 Coronary artery atheroma plaque necrotic core, (H&E, x100). Lipid-containing necrotic core in which cholesterol clefts are also observed in the center of the atherosclerotic plaque.

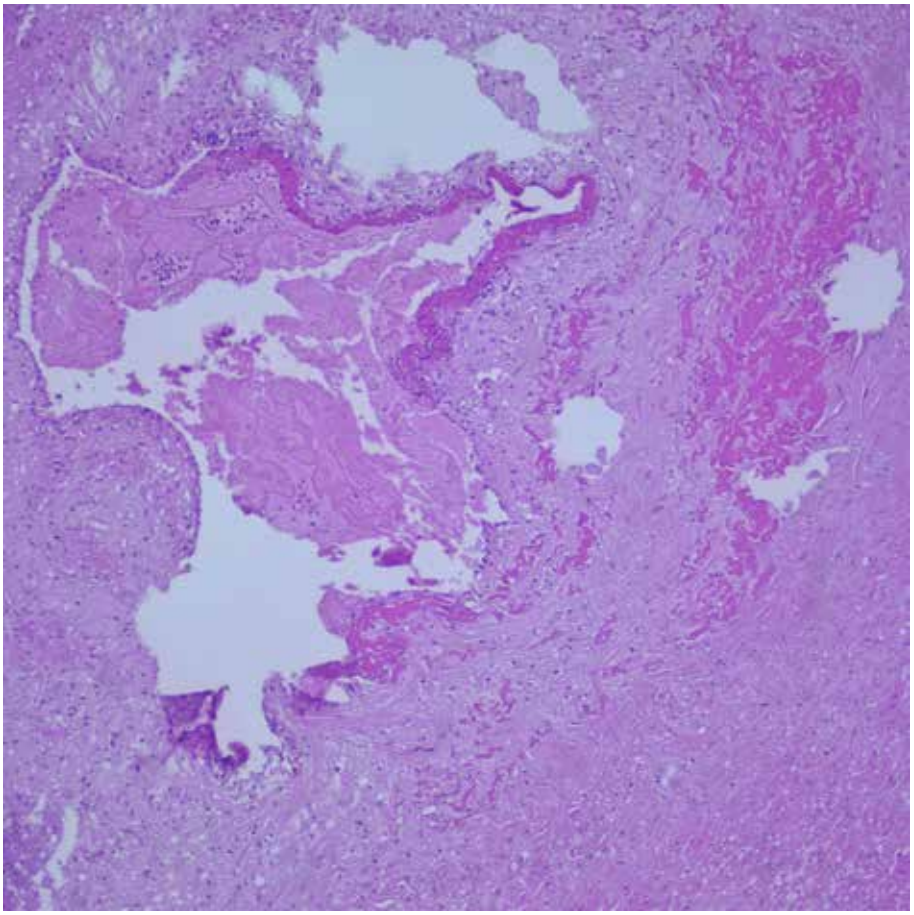

Figure 1.39 Coronary atherosclerosis with fibrin thrombus in the lumen, (H&E, x100). Atheroma plaque causes thrombosis due to endothelial damage, rupture, erosion and ulceration. The microscopic view shows an antemortem fibrin thrombus attached to the vessel wall on the luminal surface and obstructing almost the entire lumen.

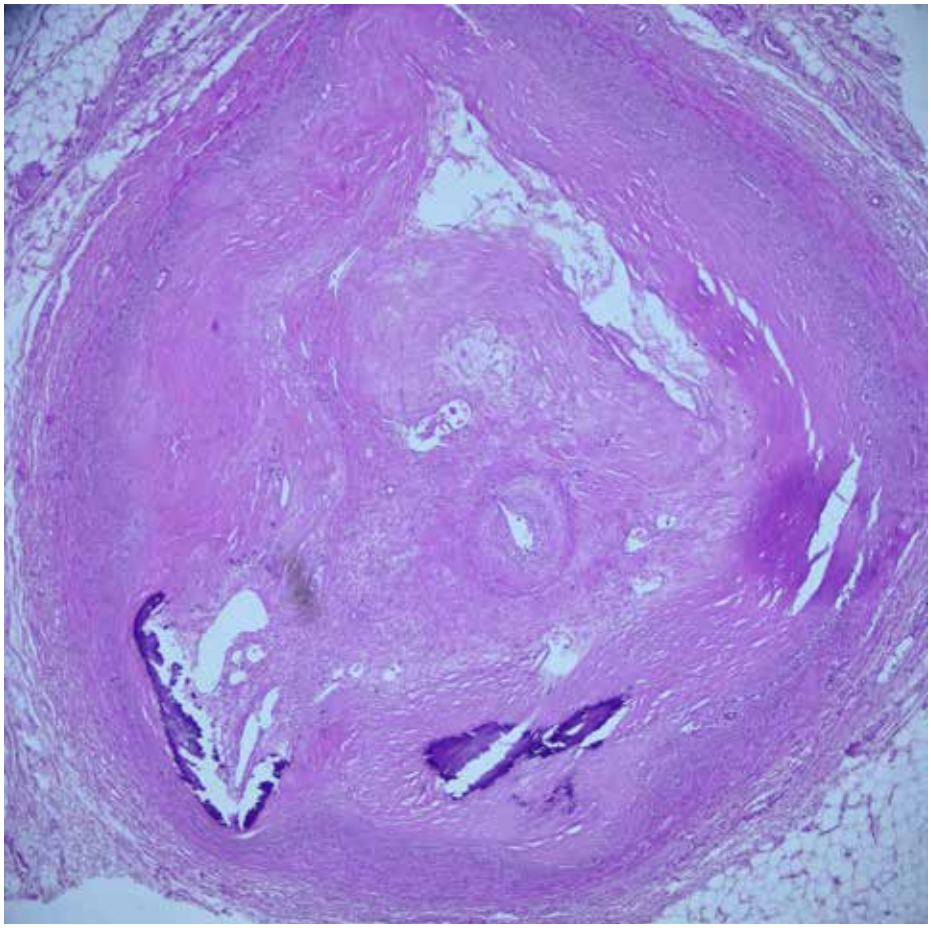

Figure 1.40
Calcified atheroma plaque that narrows almost the entire lumen, (H&E, x40).
More than 75% of myocardial infarctions are caused by almost complete narrowing of the coronary artery with atheroma plaque, rupture and eroded atheroma plaque. In cases where there is no atherosclerotic plaque, myocardial infarction may develop due to vasospasm, vasculitis, thromboembolic diseases, coronary artery dissection and myocardial bridging.

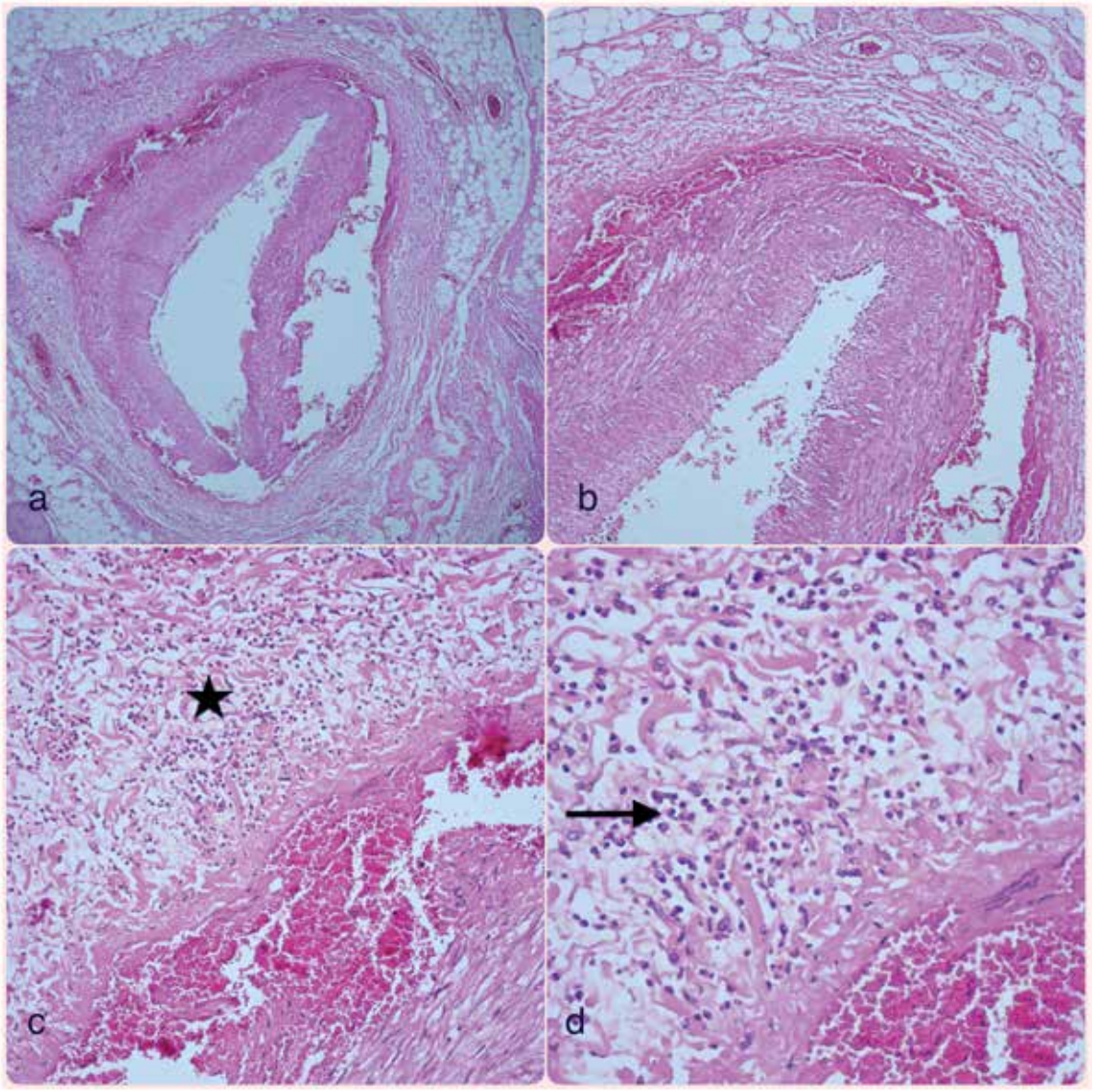

Figure 1.41
Coronary artery dissection,
a,b) (H&E, x40), (H&E, x100).
Dissecting hematoma formation is observed between the coronary artery media and adventitia layers. Intramurally located hematoma narrows the lumen by applying external pressure to the vessel wall.
c,d) (H&E, x200), (H&E, x400).
At the higher magnification dense eosinofil infiltration is demostrated in the adventitia. Coronary artery dissection can occur spontaneously (especially during pregnancy or postpartum period), traumatic or iatrogenic (e.g. coronary angiography, balloon angioplasty). Traumatic dissection of the coronary artery is extremely rare. Coronary artery disseciton may be accompanied by eosinophil infiltration in the adventitia, angiomatosis and cystic medial necrosis.

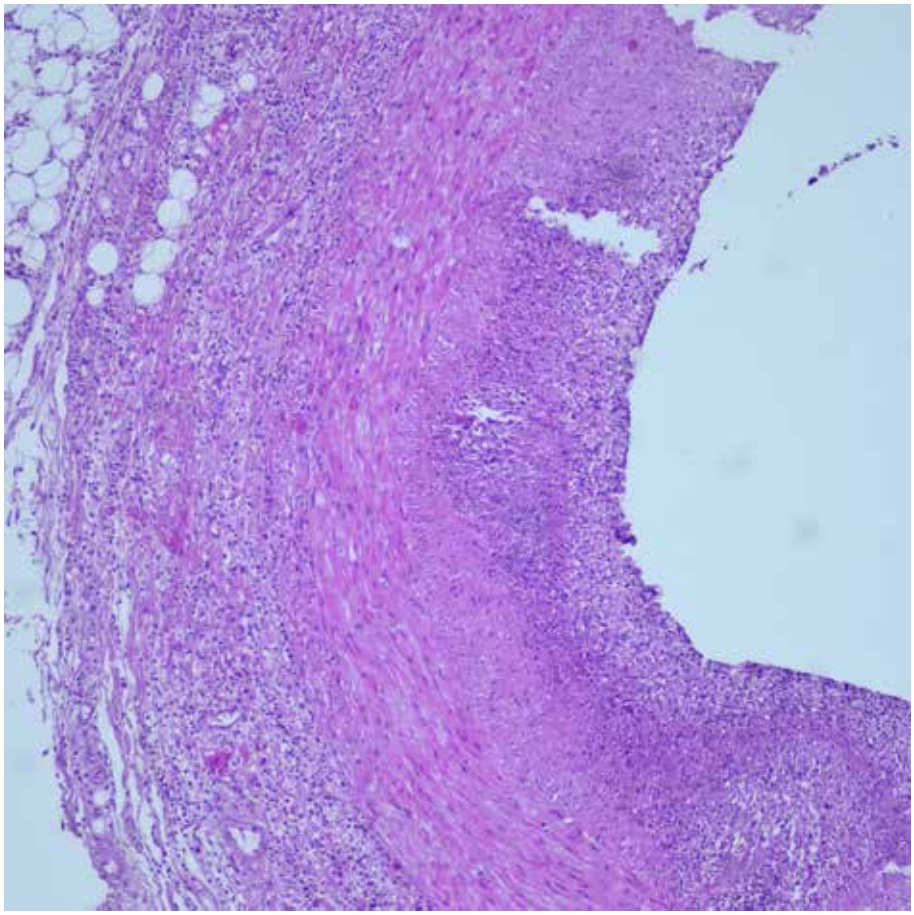

Figure 1.42
Coronary arteritis, (H&E, x100). Mixed inflammatory cell infiltration is observed in the vascular wall.

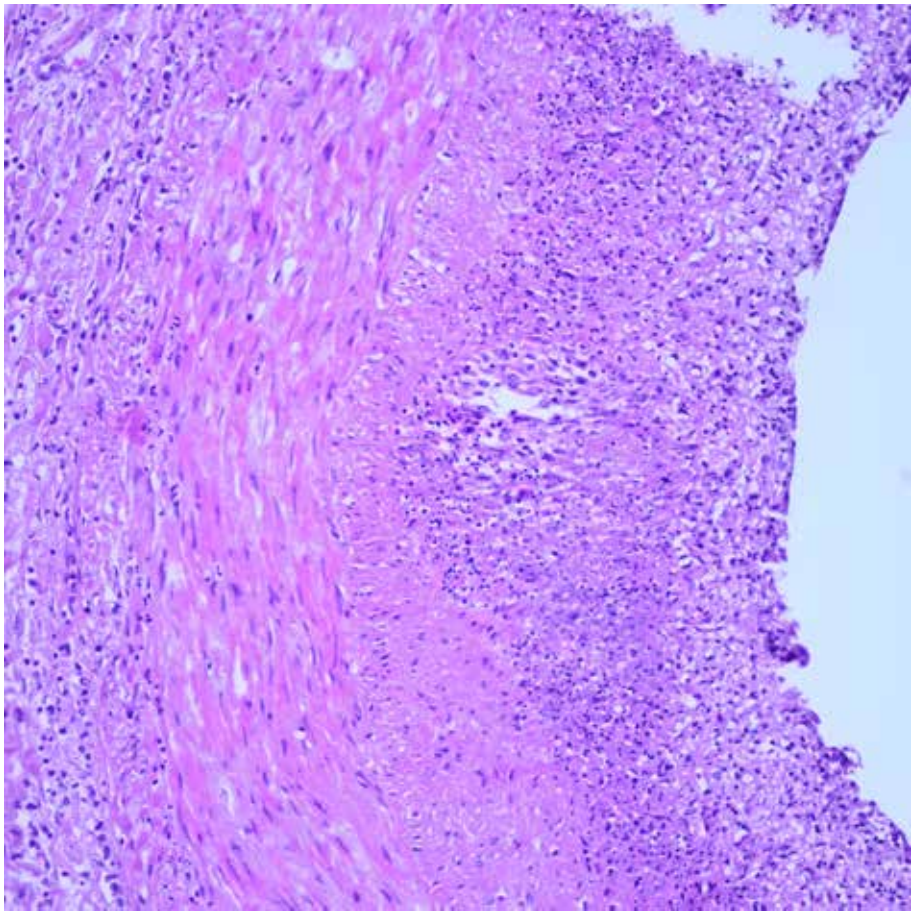

Figure 1.43
Coronary arteritis, (H&E, x200). At higher magnification, detailed microscopic view of coronary artery involvement by the mixed inflammatory cells.

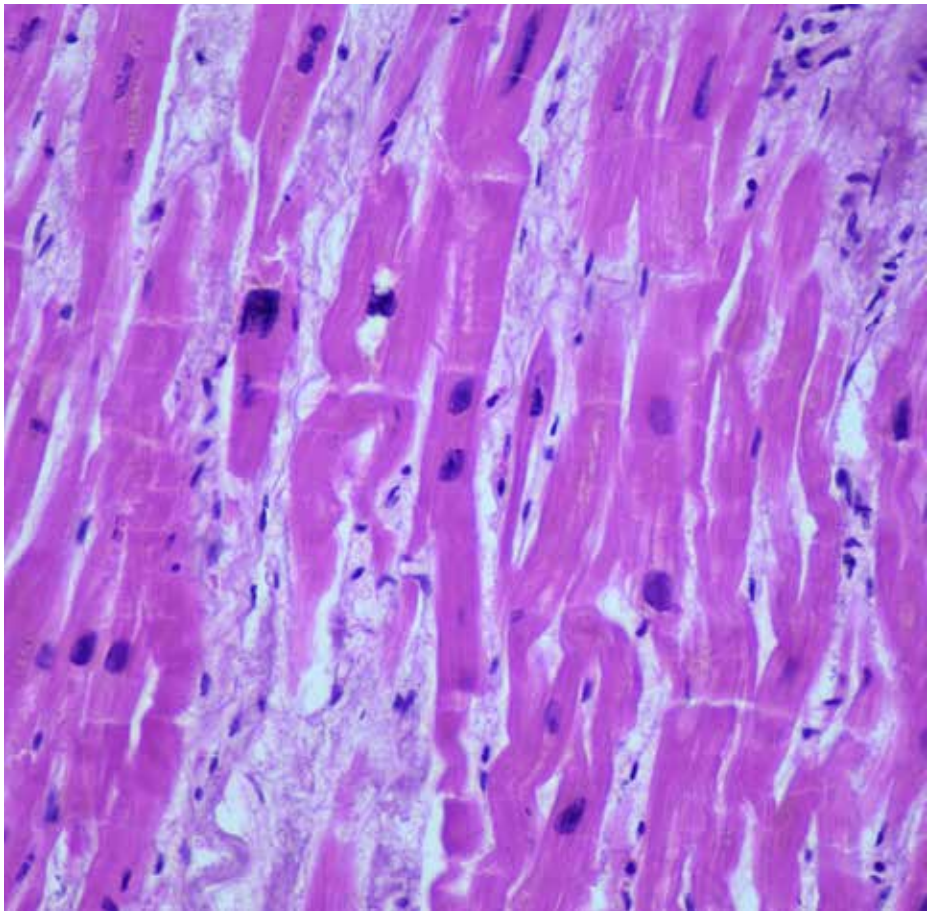

Figure 1.44 Hypertrophic cardiomyocyte, (H&E, x400). The microscopic view shows cardiomyocyte with a large, irregular, hyperchromatic nucleus.

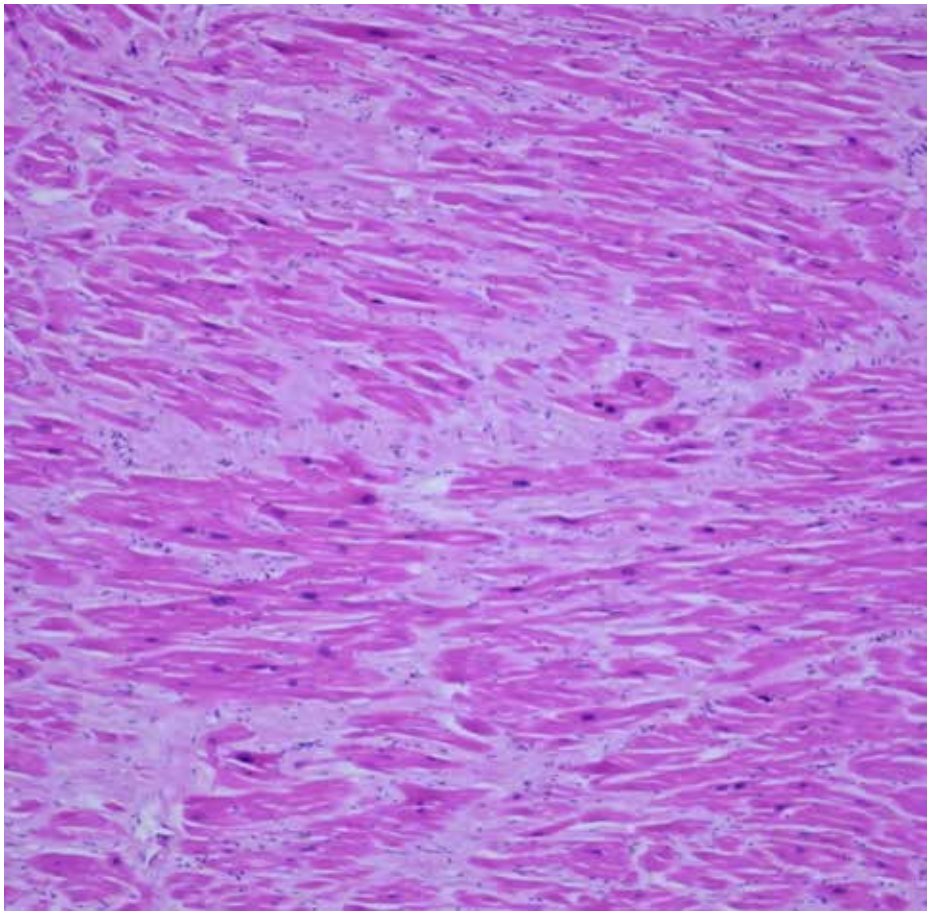

Figure 1.45 Marked interstitial fibrosis and surrounding hypertrophic cardiomyocytes, (H&E, x100). Interstitial fibrosis refers to dense collagen accumulation that disrupts myocardial interstitial architecture. It is a common finding in conditions that cause heart failure, such as hypertensive heart diseases, aortic stenosis, hypertrophic cardiomyopathy, diabetic cardiomyopathy, and nonischemic dilated cardiomyopathy. Cardiomyocyte death is the triggering factor for the onset of interstitial fibrosis in reperation process.

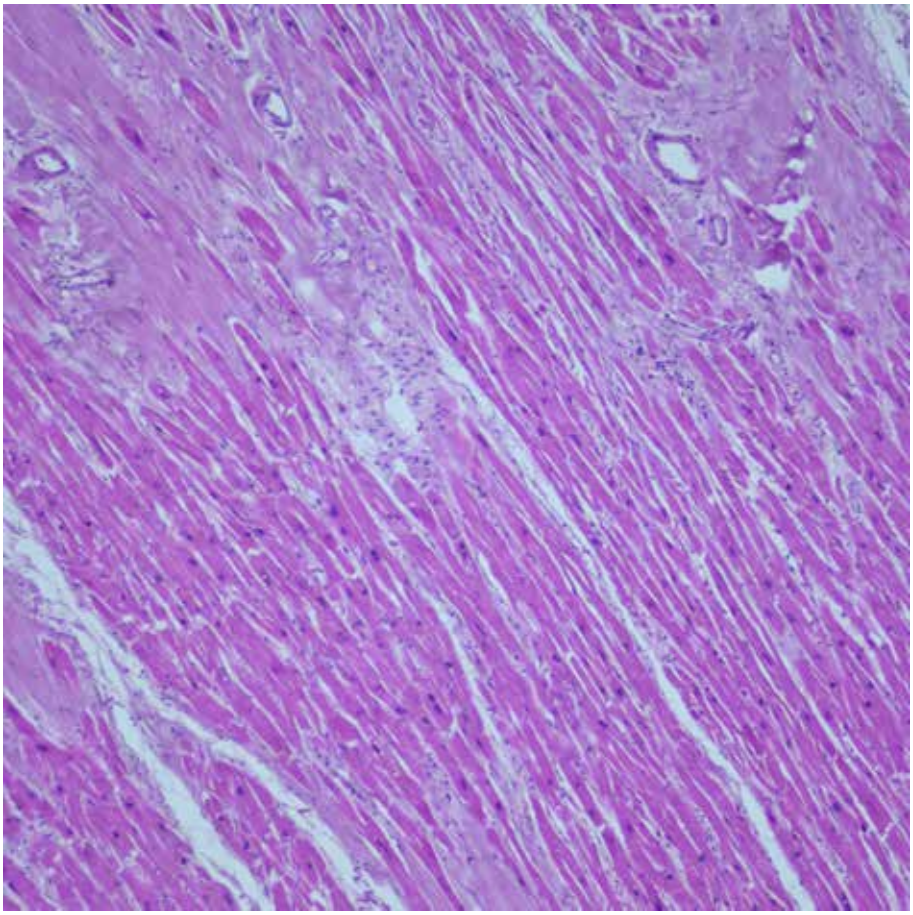

Figure 1.46
Marked perivascular fibrosis, (H&E, x40). Myocardial interstitial fibrosis may also occur in the form of thick intramural bands around intramural coronary arteries, as seen in the microscopic view.

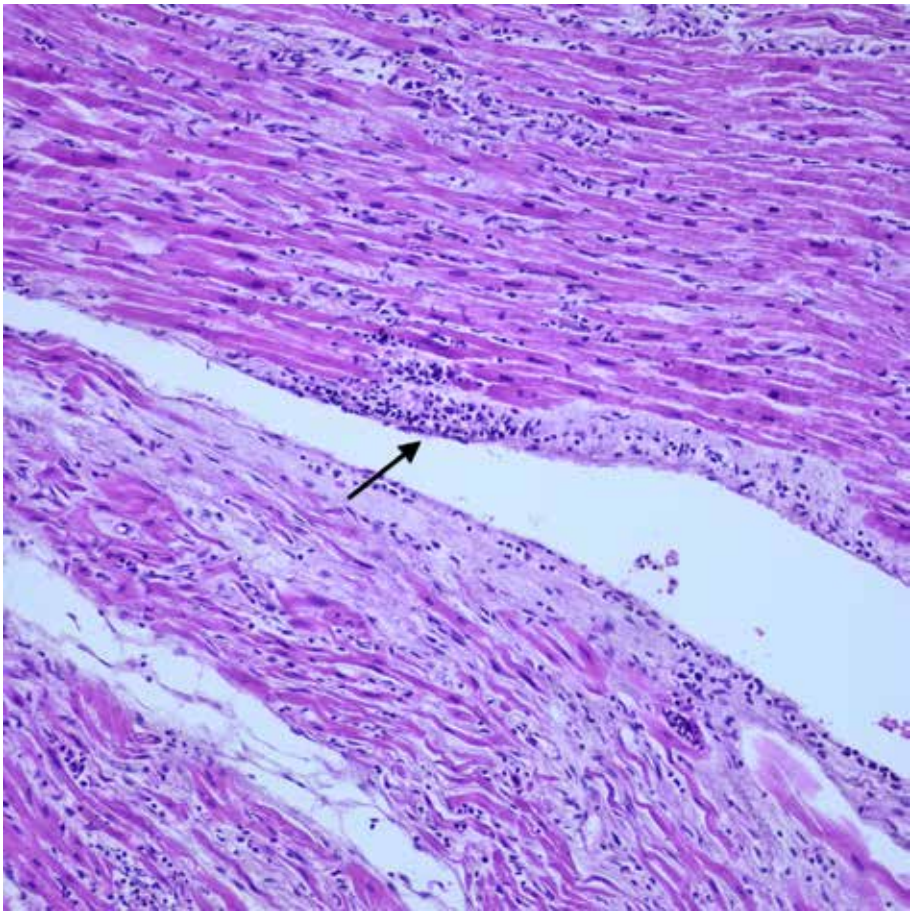

Figure 1.47
Endocarditis, (H&E, x100). Lymphocytic inflammatory cell infiltration in the endocardium (arrow) in a case of pancarditis.

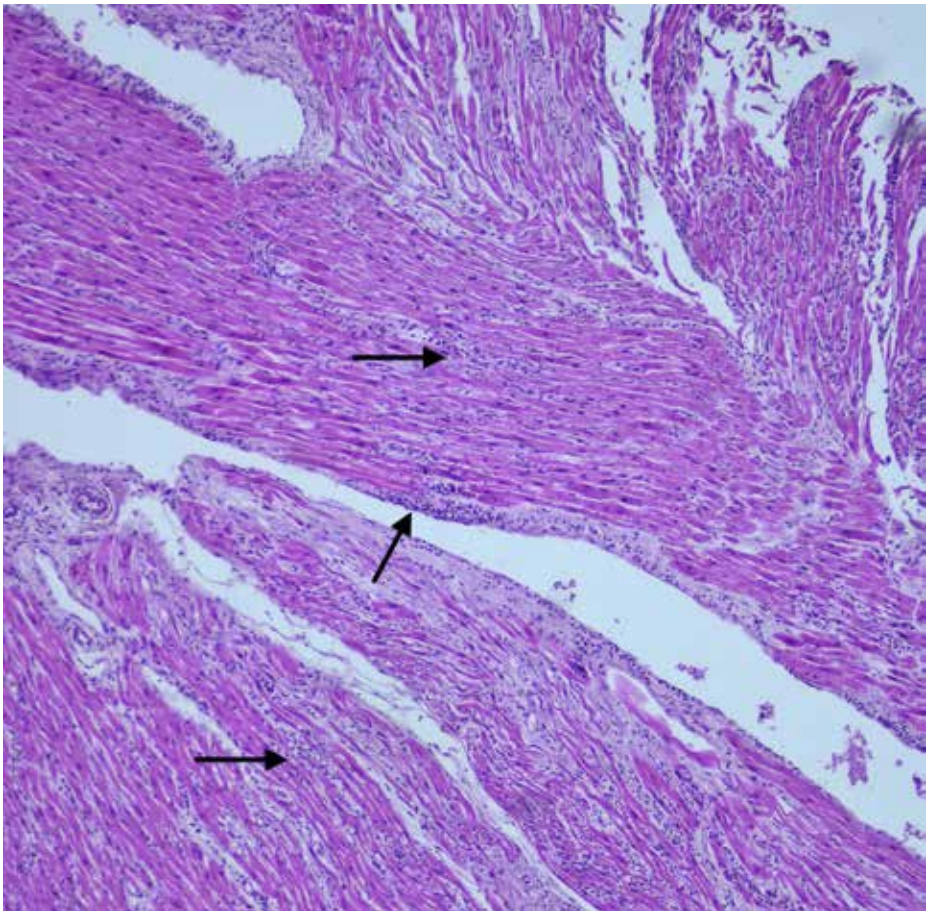

Figure 1.48 Pancarditis, (H&E, x100). In the case of pancarditis, dense lymphocytic inflammatory cell infiltration is observed in the endocardium (arrow) and myocardium (arrow), which also causes cardiomyocyte necrosis.

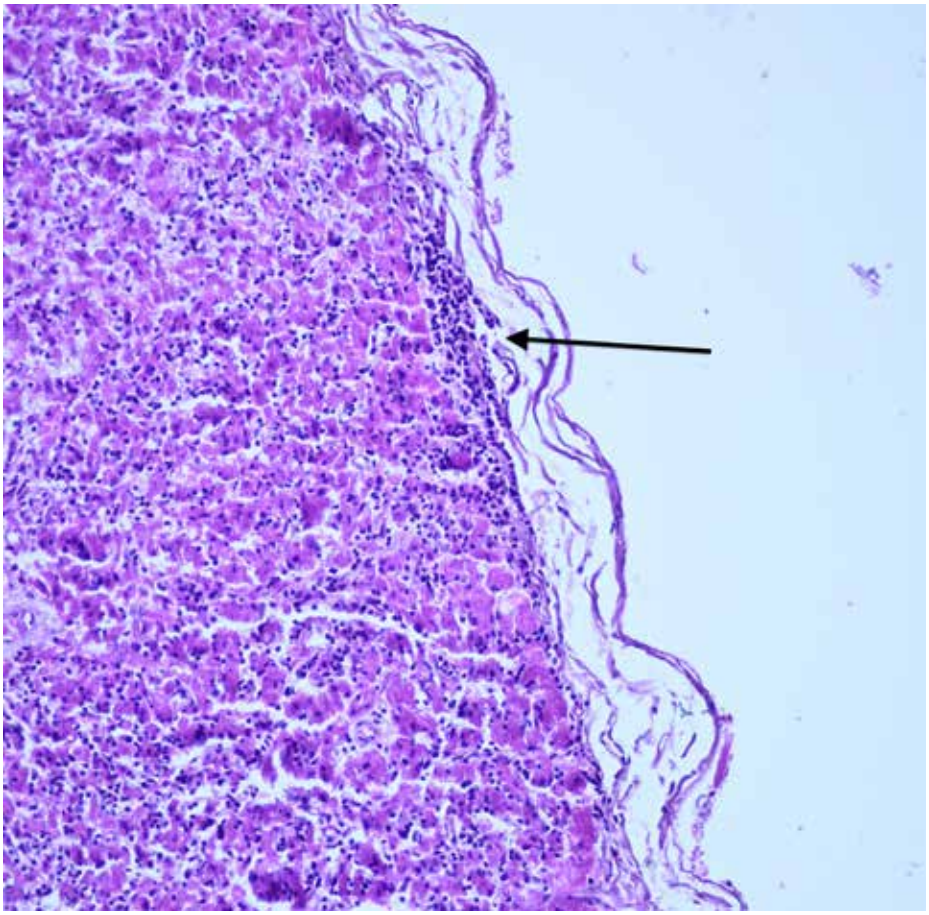

Figure 1.49 Pancarditis, (H&E, x200). Lymphocytic inflammatory cell infiltration in the epicardium (arrow) in a case of pancarditis. In pancarditis, we detect inflammatory cell infiltration in the endocardium, myocardium and epicardium and also associated cardiomyocyte necrosis.

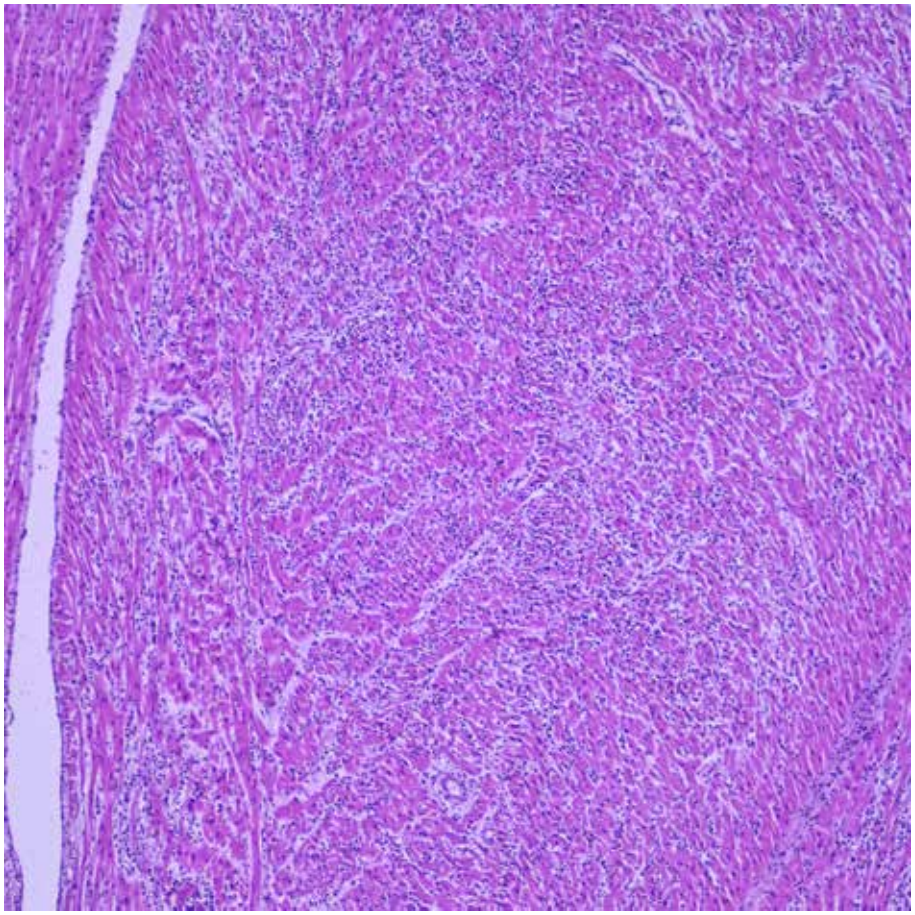

Figure 1.50
Lymphocytic Myocarditis, (H&E, x100).
In the microscopic view, myocarditis with lymphocyte infiltration accompanied by cardiomyocyte necrosis. Conditions that are not accompanied by myocyte necrosis are called "borderline myocarditis".

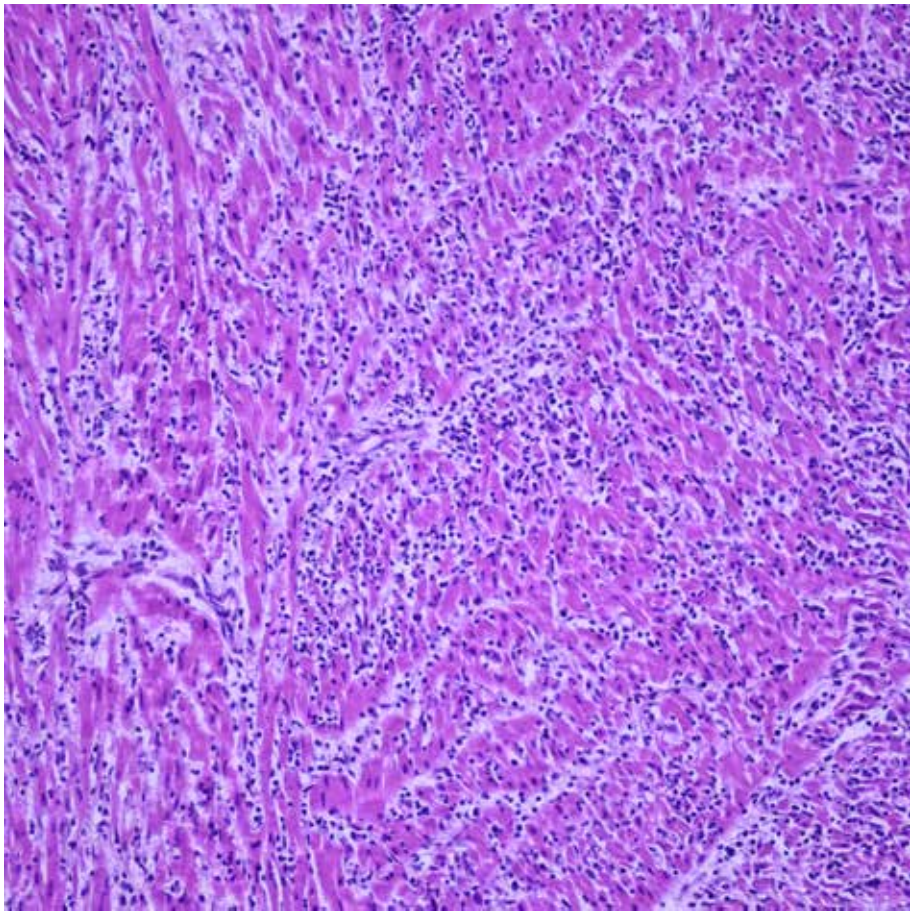

Figure 1.51
Lymphocytic Myocarditis, (H&E, x200).
Higher magnification of the previous case. Myocyte necrosis and lymphocyte infiltration are seen in details in the higher magnification.

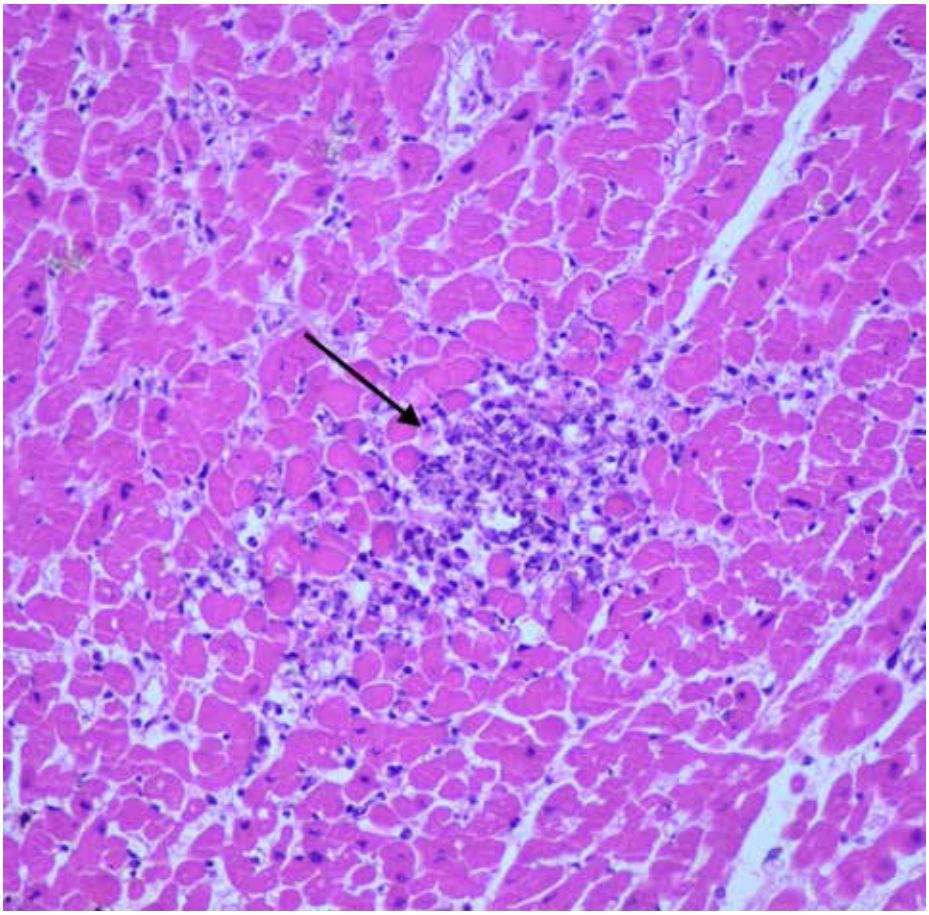

Figure 1.52 Neutrophilic myocarditis (compatible with septic focus), (H&E, x400). In the microscopic view, focal neutrophilic accumulation and significant myocyte damage are observed, forming microabscesses (arrow) within the myocardium. This pattern of myocarditis is most frequently detected in disseminated bacteremia and sepsis.

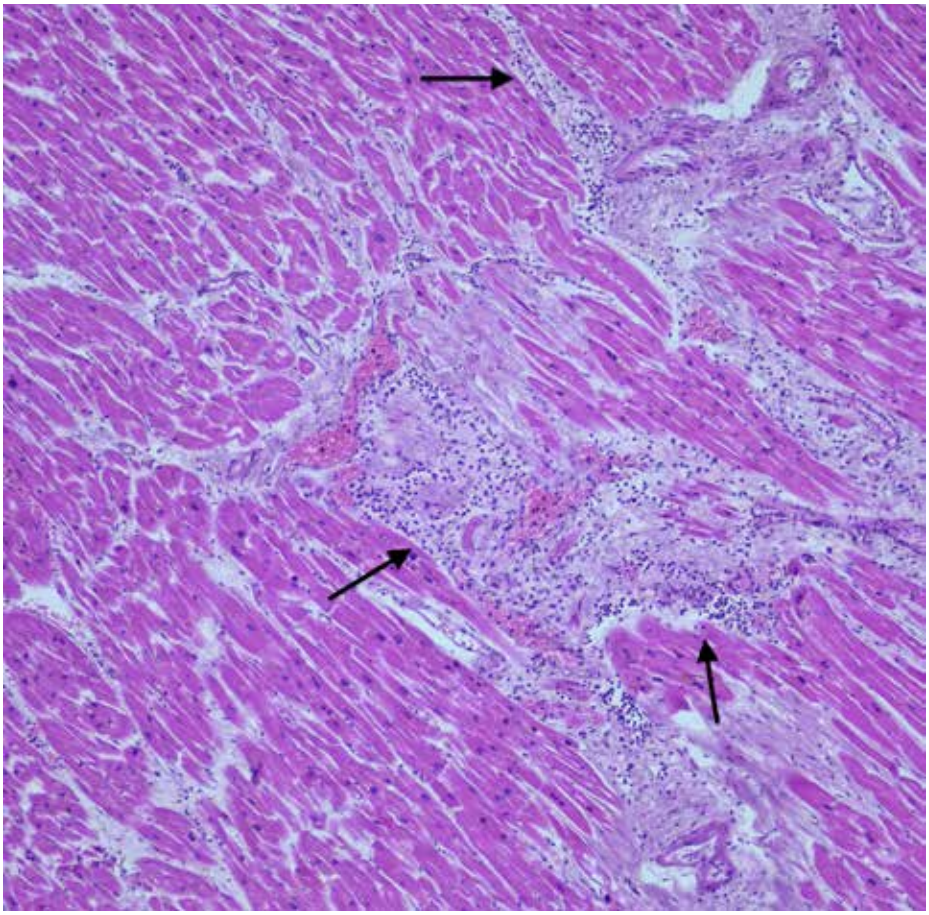

Figure 1.53 Toxic myocarditis, (H&E, x100). This microscopic view shows mixed inflammatory cell infiltration (arrows) in the perivascular and interstitial areas without myocyte necrosis.

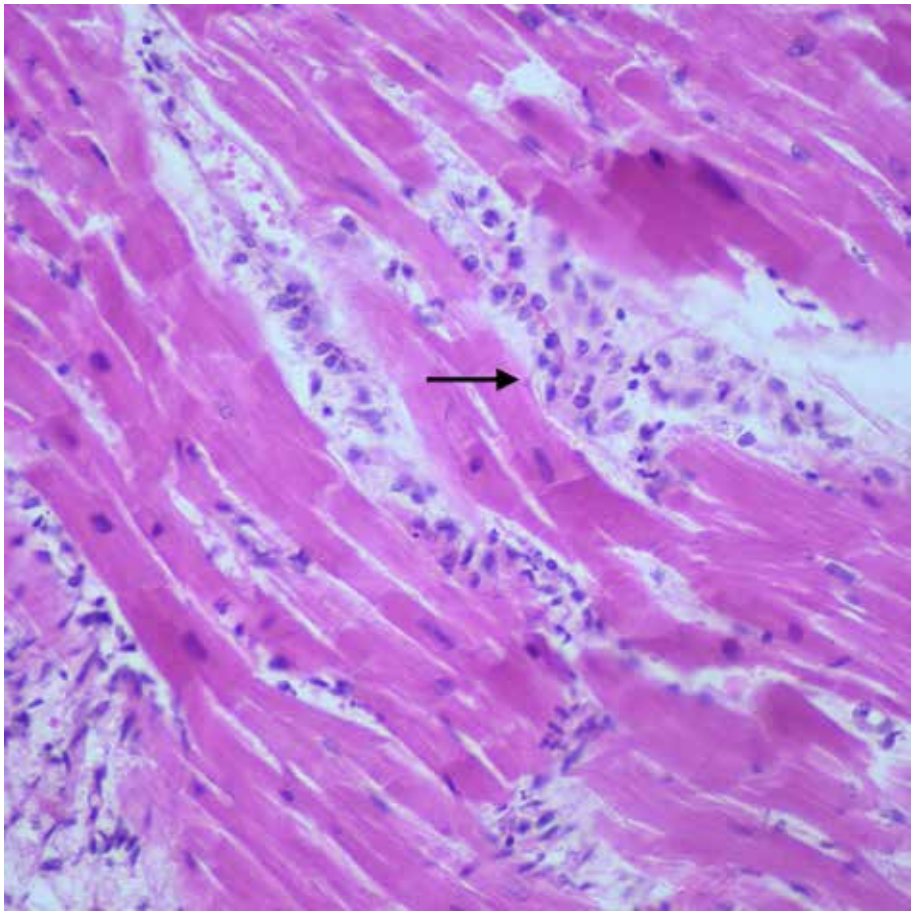

Figure 1.54
Toxic myocarditis (H&E, x400). Mixed inflammatory cell infiltration in perivascular areas (arrow) at higher magnification.

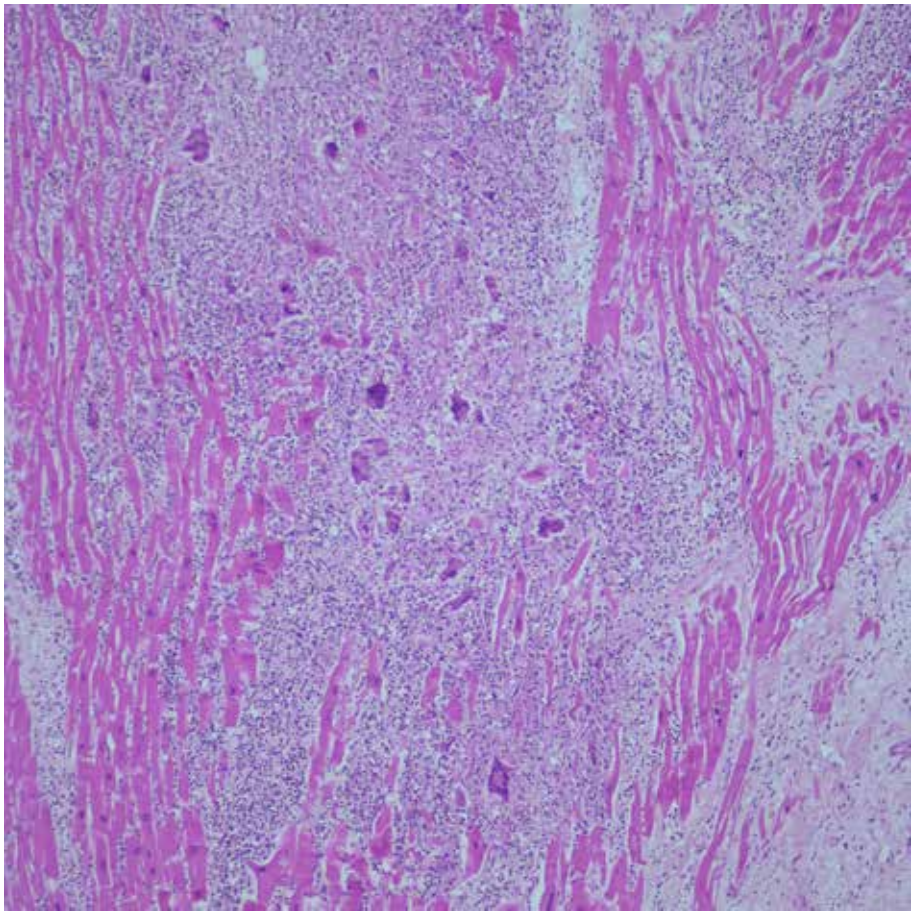

Figure 1.55
Lymphohistiocytic myocarditis with giant cells (Giant cell myocarditis), (H&E, 100x). Extensive myocyte necrosis, many giant cells, and mixed inflammatory cells consisting of lymphocytes, plasma cells, and eosinophils are observed in the myocardium. Granulomas were not detected.

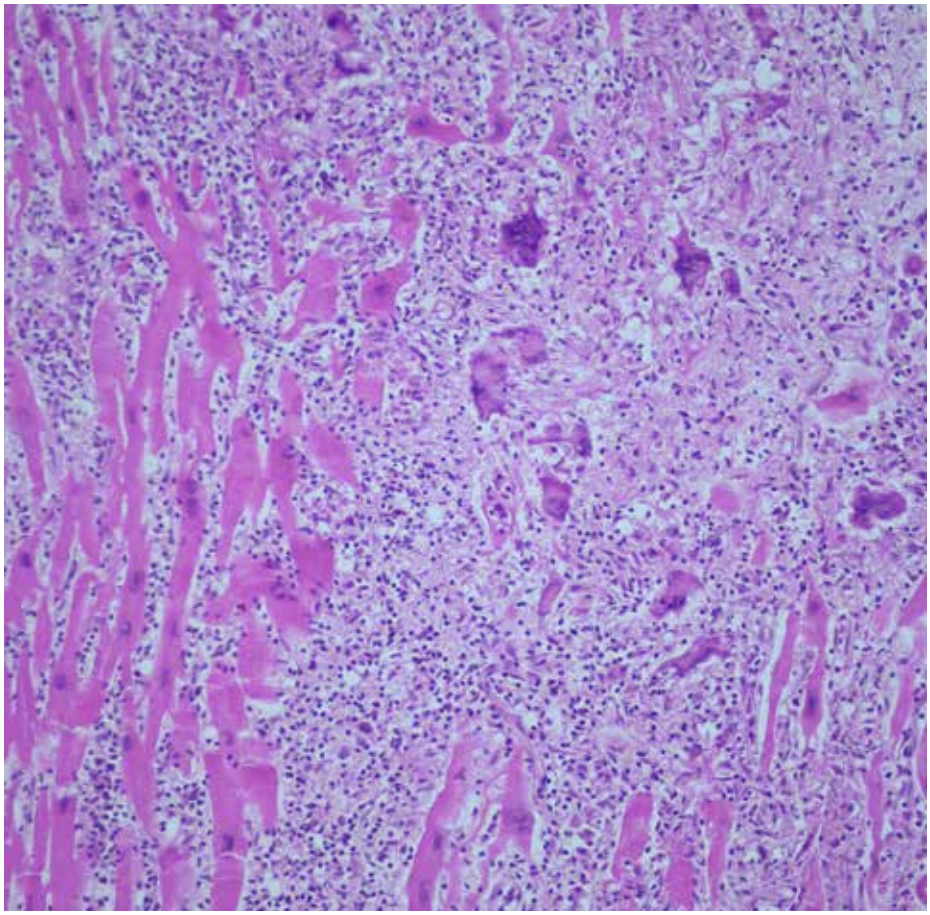

Figure 1.56 Lymphohistiocytic myocarditis with giant cells (Giant cell myocarditis), (H&E, x200). Giant cell myocarditis is considered a major form of lymphohistiocytic myocarditis.

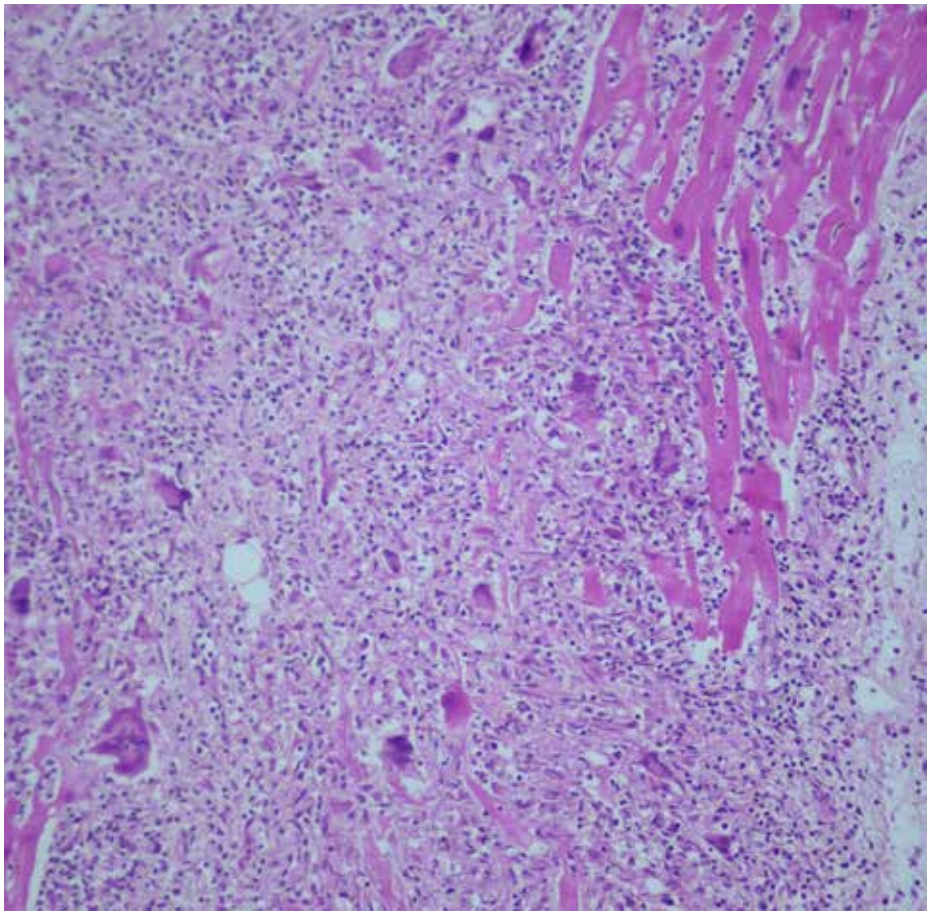

Figure 1.57 Lymphohistiocytic myocarditis with giant cells (Giant cell myocarditis), (H&E, x200). In the microscopic view, lymphohistiocytic inflammatory cell infiltration and giant cells associated with myocyte necrosis is seen.

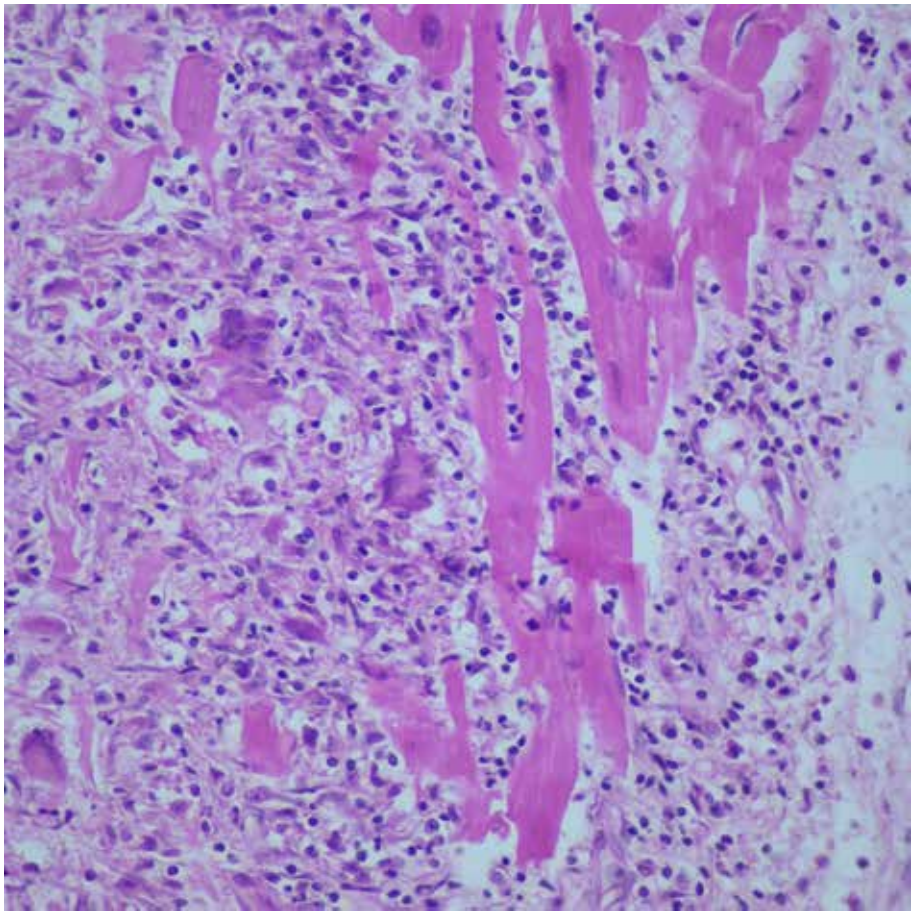

Figure 1.58
Lymphohistiocytic myocarditis with giant cells (Giant cell myocarditis), (H&E, x400). At higher magnification.

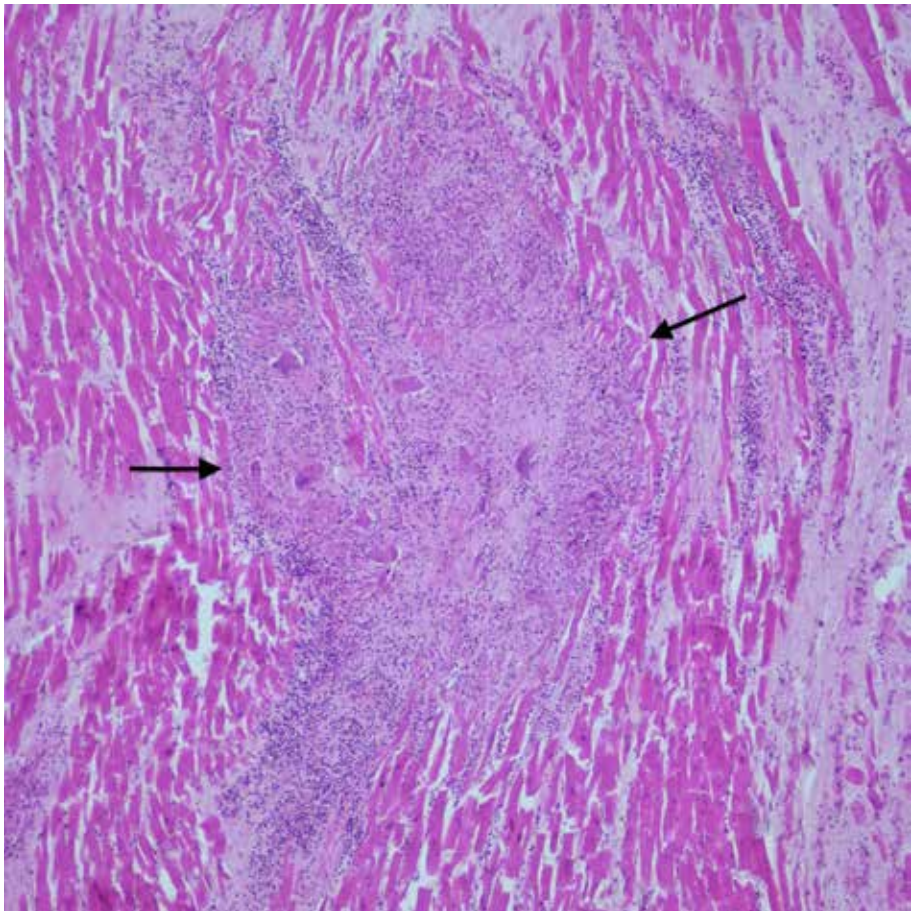

Figure 1.59
Myocarditis with granulomas (Cardiac Sarcoidosis and other granulomatous diseases) (H&E, x100). It is the second major form of lymphohistiocytic myocarditis. Mostly these granulomas are nonnecrotizing and small. The microscopic view shows nonnecrotizing granulomas (arrows) within the myocardium.

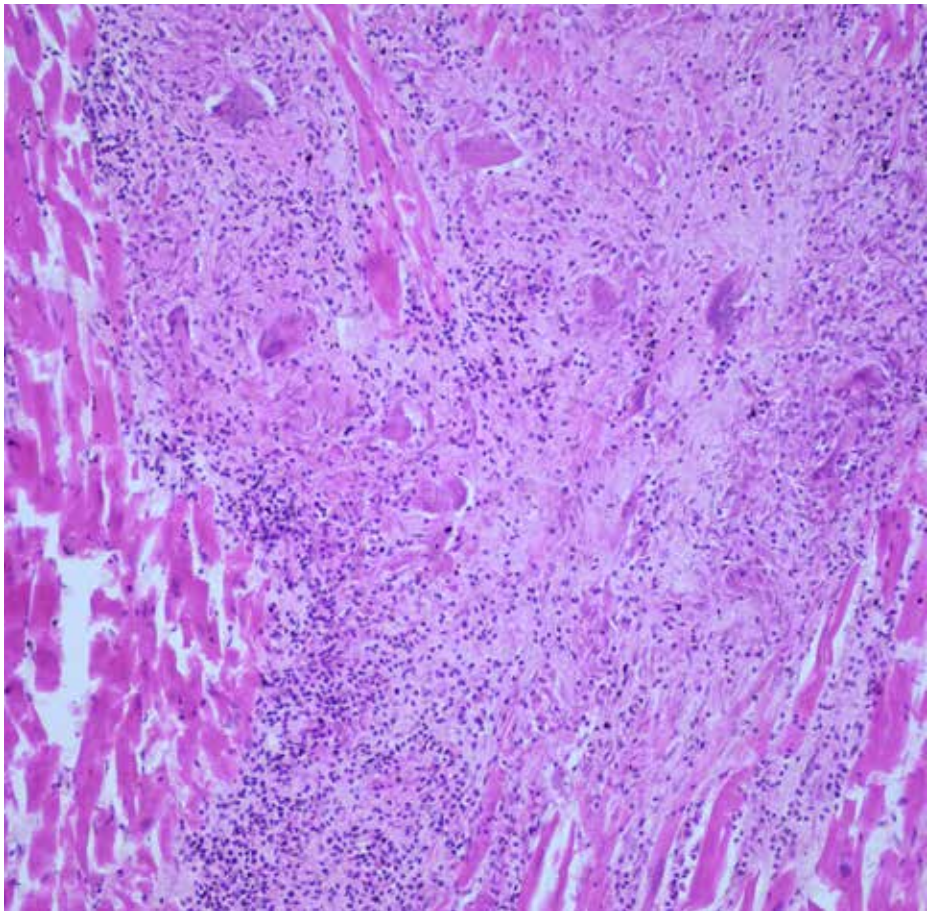

Figure 1.60 Myocarditis with granulomas (Cardiac Sarcoidosis and other granulomatous diseases), (H&E, x200). At higher magnification.

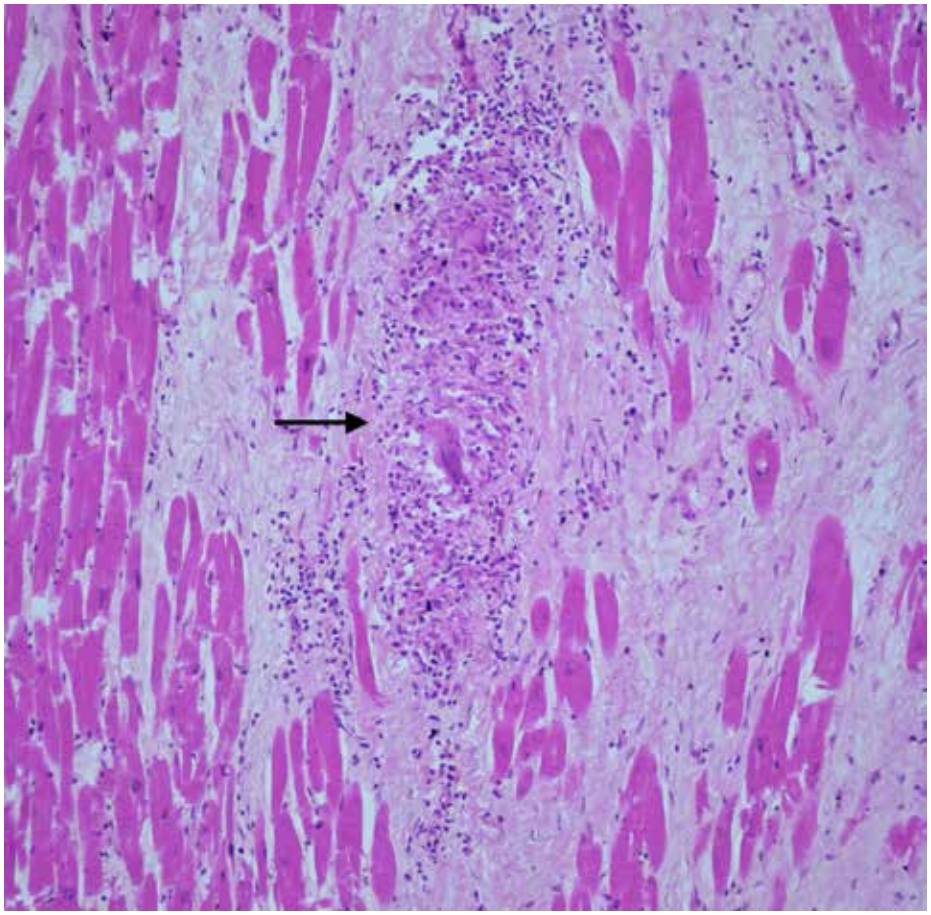

Figure 1.61 Myocarditis with granulomas (Cardiac Sarcoidosis and other granulomatous diseases), (H&E, x200). The microscopic view shows a typical nonnecrotizing granuloma.

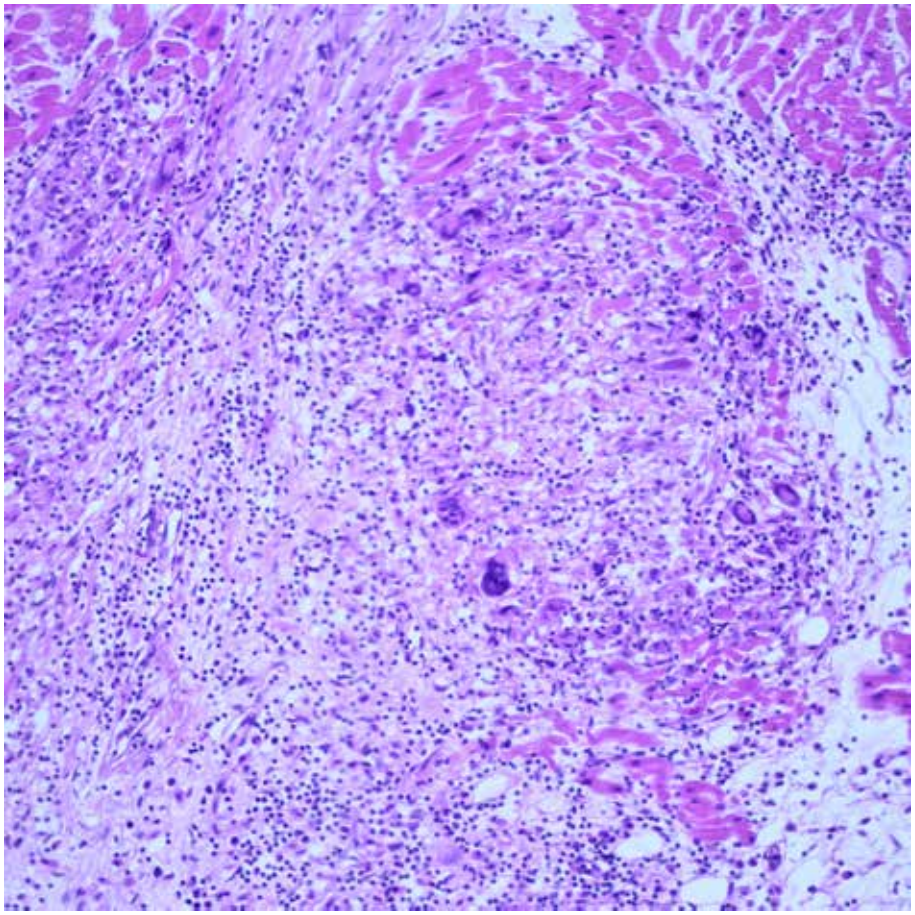

Figure 1.62
Lymphohistiocytic myocarditis with giant cells (Giant cell myocarditis), (H&E, x200).
In the case, Parvovirus B-19 was detected positive by rt-PCR in the postmortem cardiac tissue. Giant cell myocarditis is a clinicopathological term and should be used when histopathological findings are accompanied by a classical fulminant course and poor prognosis. When clinicopathological findings do not comply with this classical picture, "Lymphohistiocytic myocarditis with giant cells" should be used.

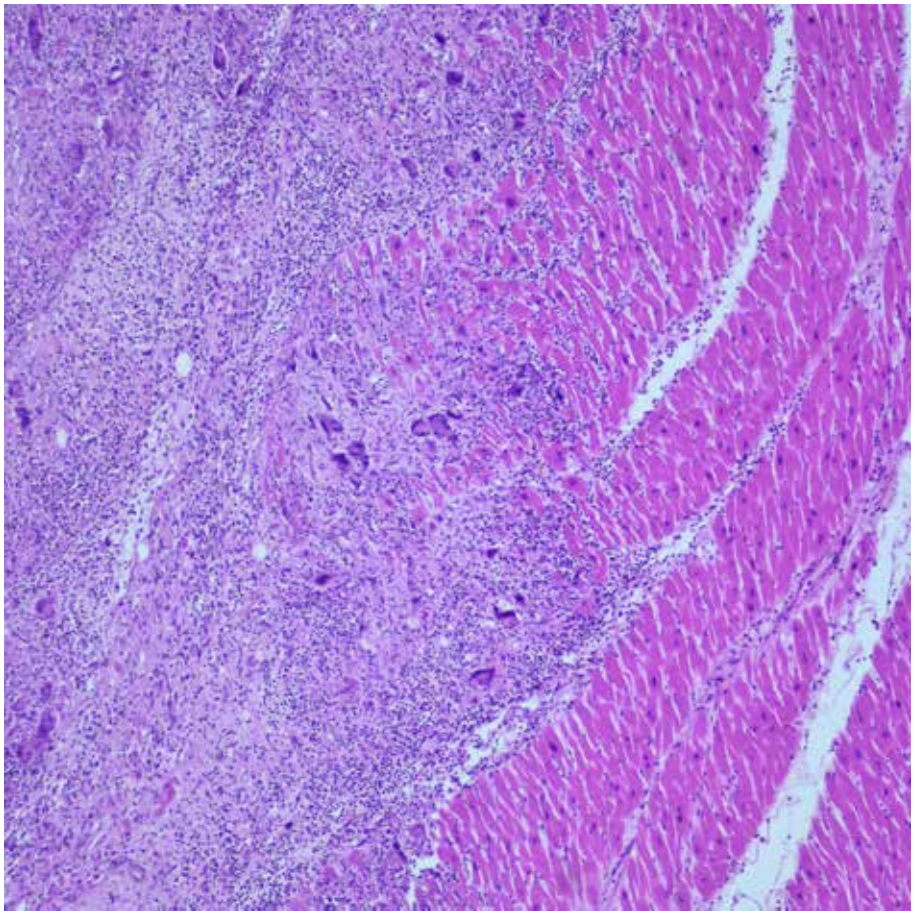

Figure 1.63
Lymphohistiocytic myocarditis with giant cells (Giant cell myocarditis), (H&E, x100).

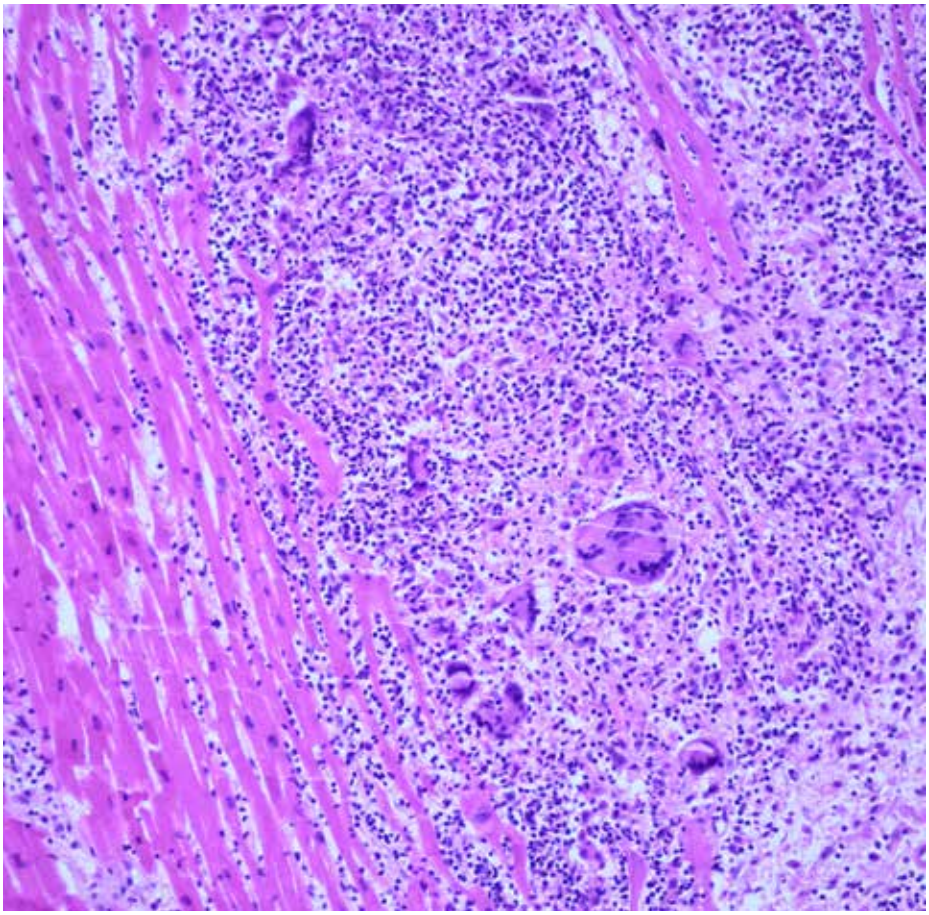

Figure 1.64 Lymphohistiocytic myocarditis with giant cells (Giant cell myocarditis), (H&E, x200). At higher magnification, dense lymphohistiocytic inflammatory cell infiltration, accompanied by giant cells and myocyte necrosis are noted.

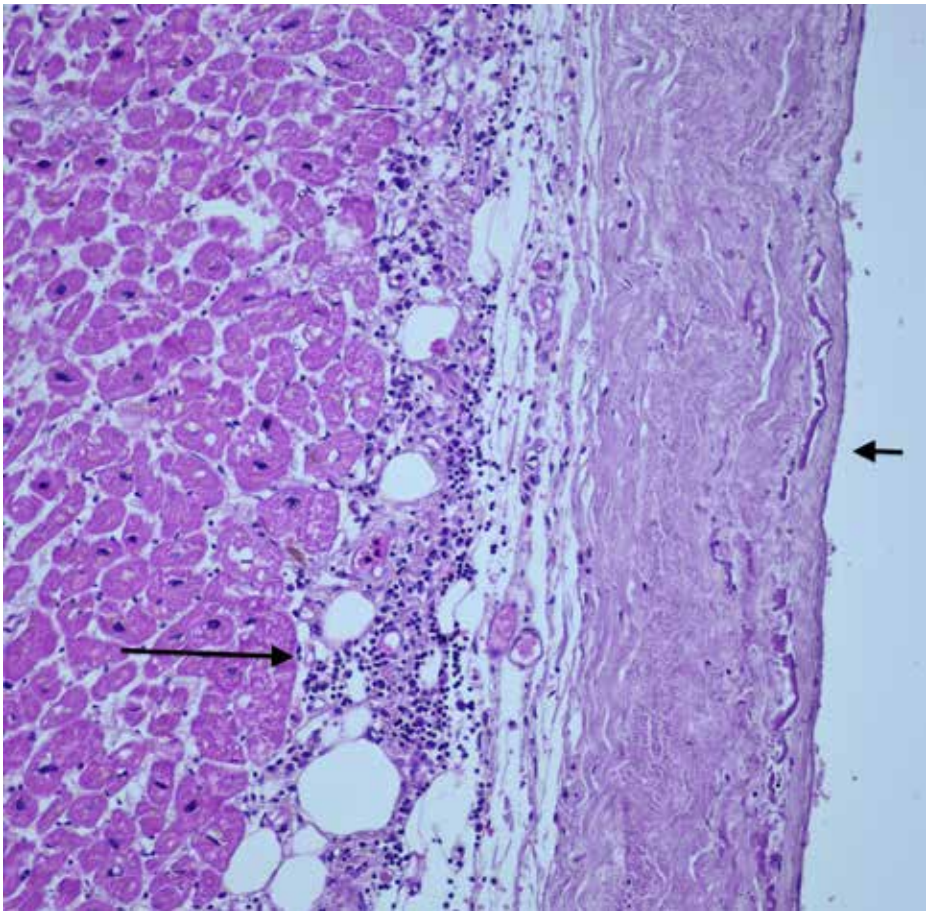

Figure 1.65 Chronic pericarditis, (H&E, x200). Mononuclear inflammatory cell infiltration (long arrow) and fibrous thickening (short arrow) are noteworthy in the pericardial fatty tissue.

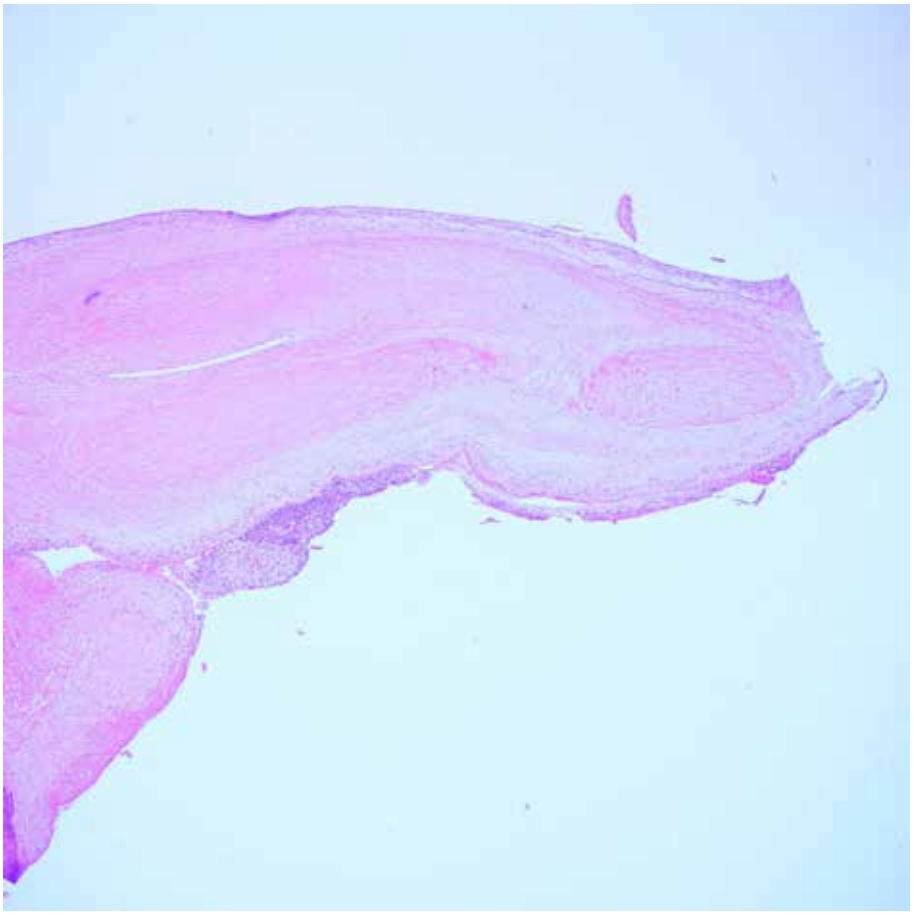

Figure 1.66
Infective Endocarditis, (H&E, x40).
Infective endocarditis is a microbial infection of endovascular cardiac structures, typically the heart valves.

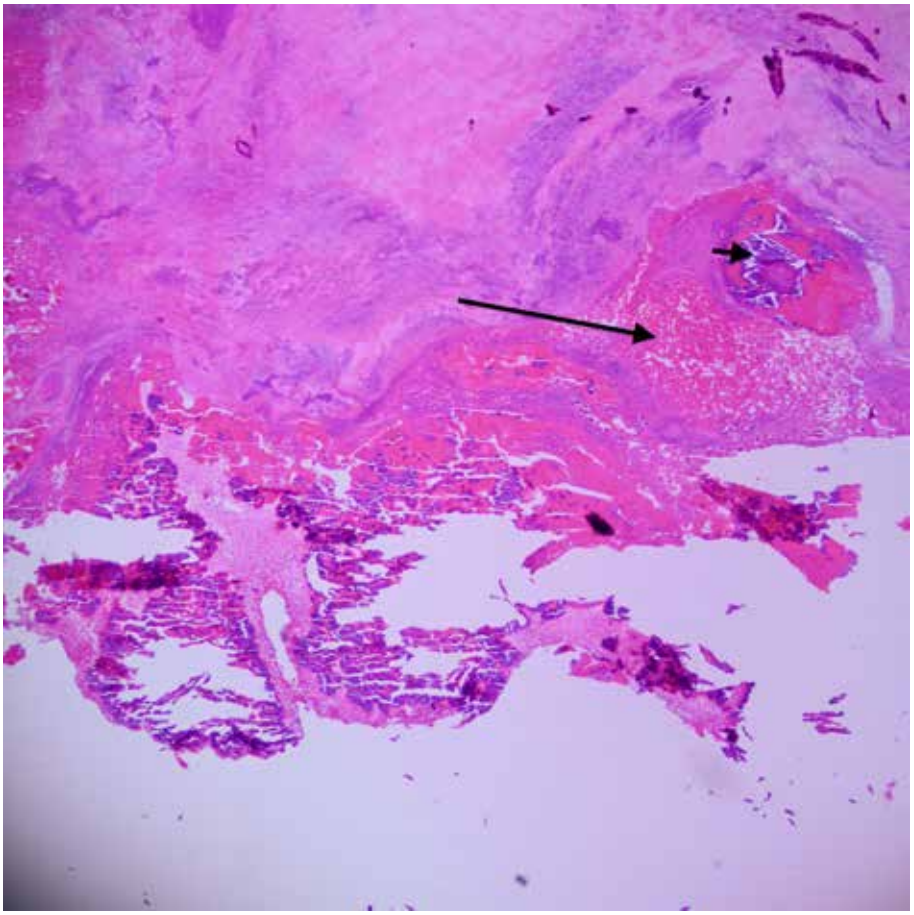

Figure 1.67
Infective Endocarditis, (H&E, x40).
Fibrin and platelets (long arrow), together with bacterial colonies and inflammatory cells (short arrow), formed fragile vegetations on the valve. These fragile vegetations may disintegrate and embolize.

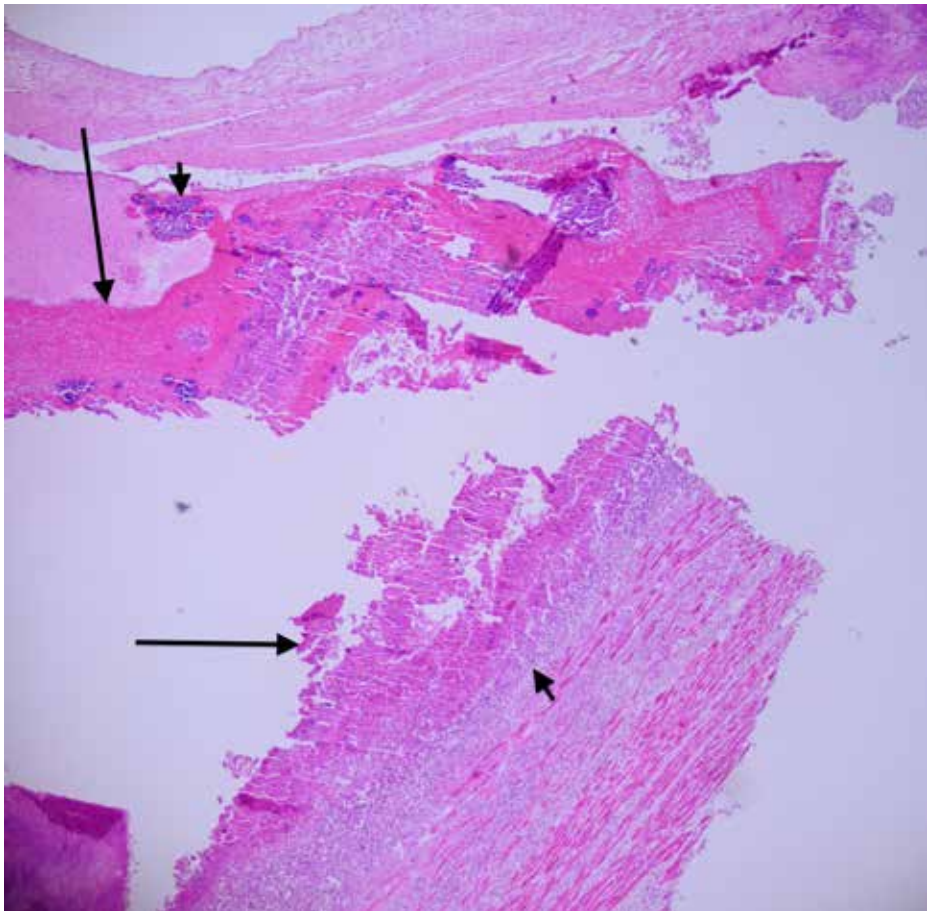

Figure 1.68
Infective Endocarditis, (H&E, x40). In the microscopic view, fibrin (long arrow), bacterial colonies (short arrow) are seen.

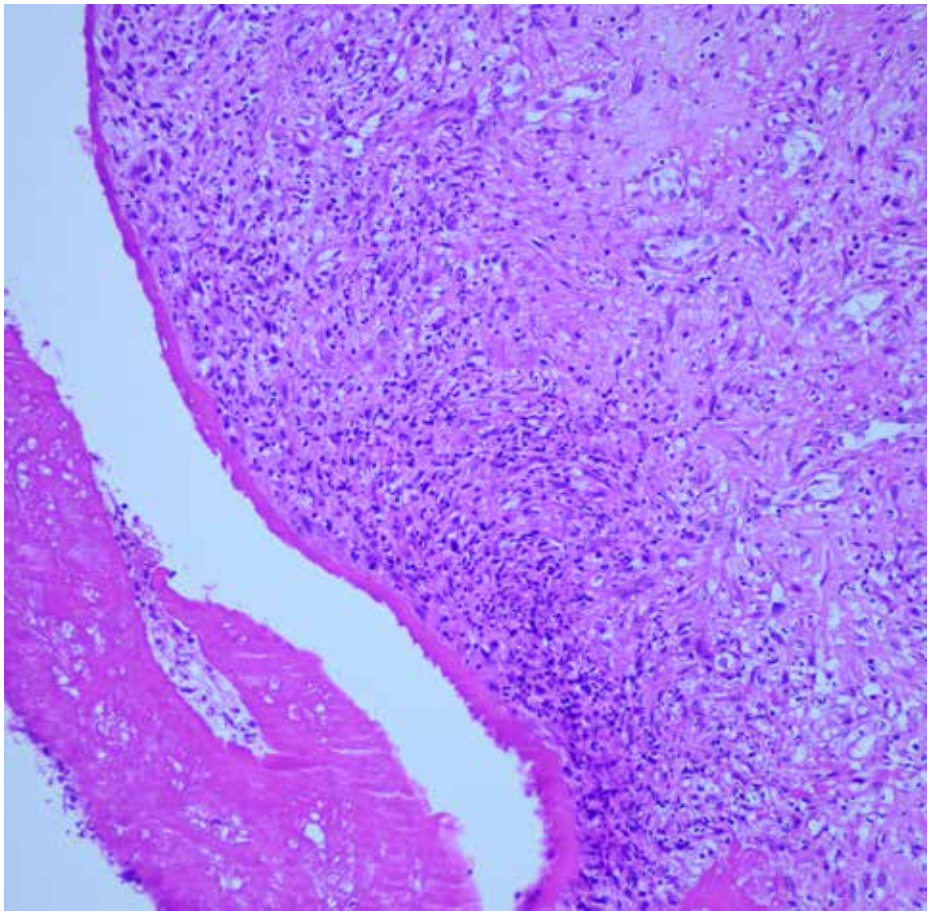

Figure 1.69
Infective Endocarditis, (H&E, x100). Fibrovascular proliferation is observed in the endocardium and subendocardial region.

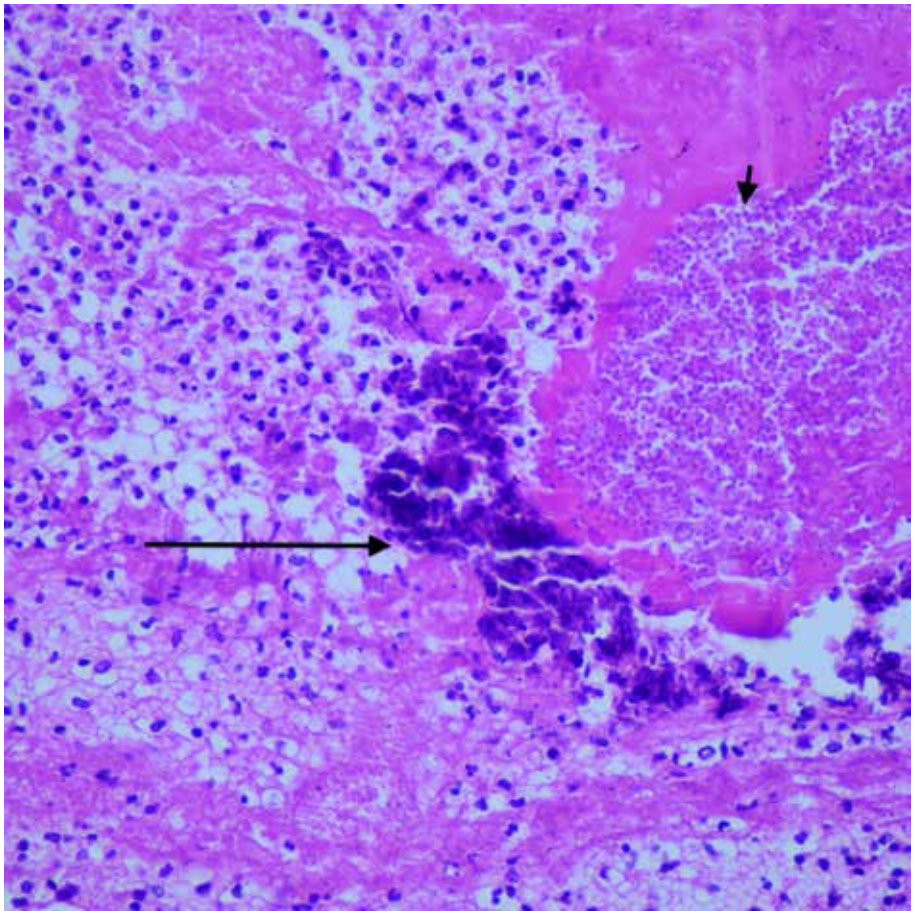

Figure 1.70
Infective Endocarditis, (H&E, x400). Fibrin, erythrocytes, bacteri colonies (long arrow), fungal hyphae and spores (short arrow), mixed inflammatory cell infiltration accompanied by dense neutrophils are observed in thrombotic debris.

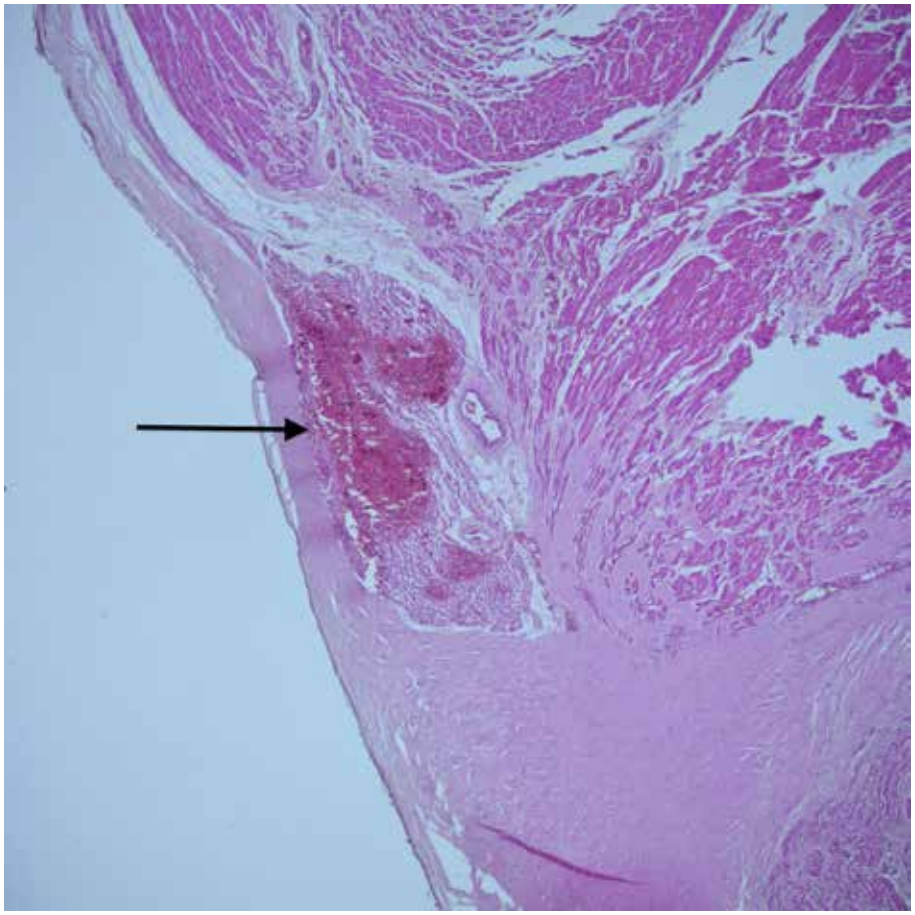

Figure 1.71
Hemorrhage in the AV node, (H&E, x40). AV node hemorrhage (arrow) is seen in the microscopic view.

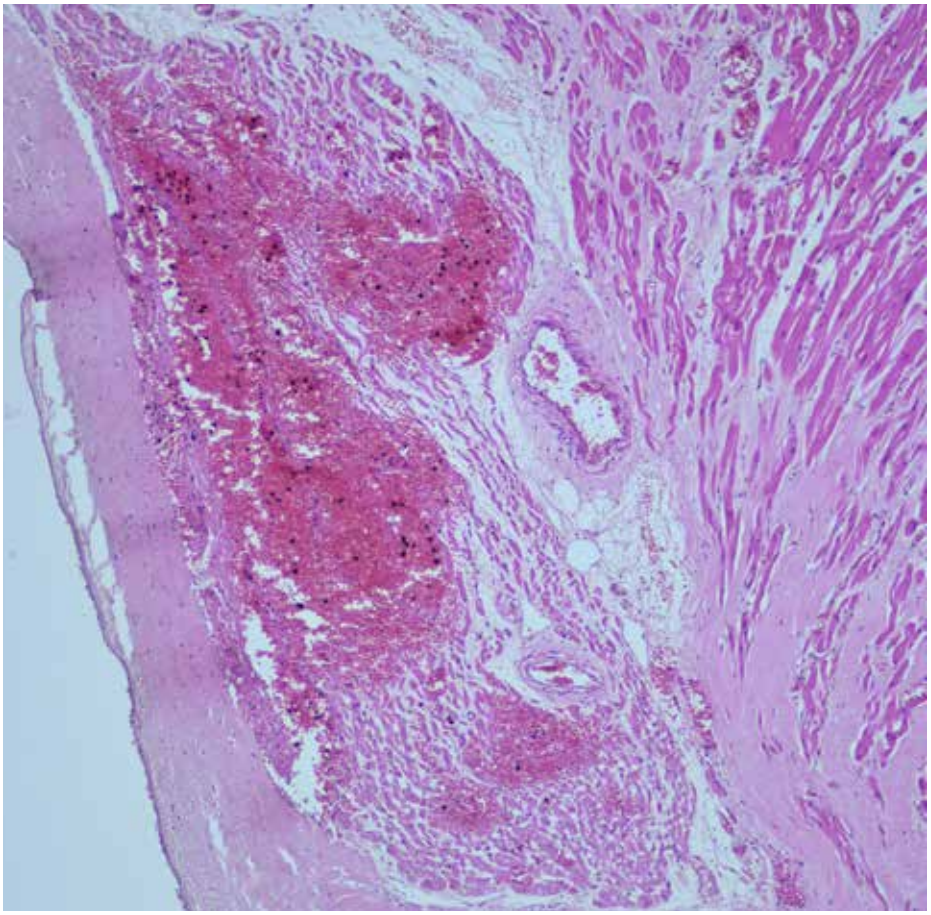

Figure 1.72 Hemorrhage in the AV node, (H&E, x100). At higher magnification.

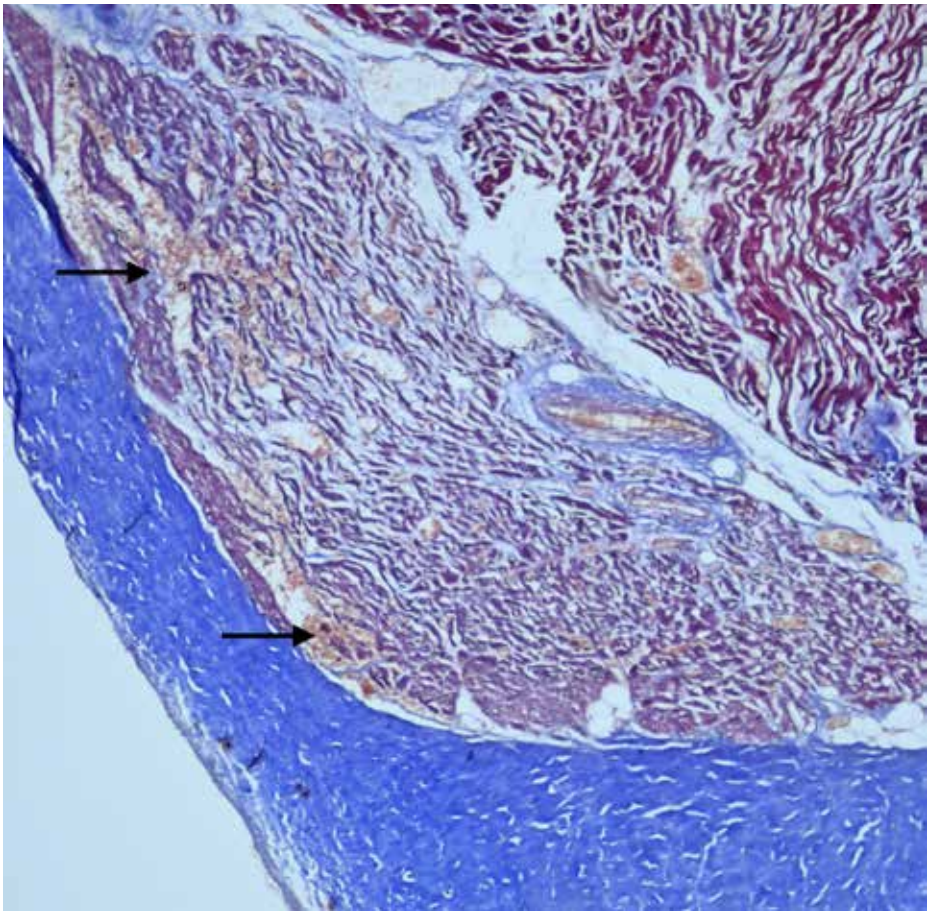

Figure 1.73 Hemorrhage in the AV node, (Masson Trichrome, x100). Hemorrhage in the AV node (arrow).

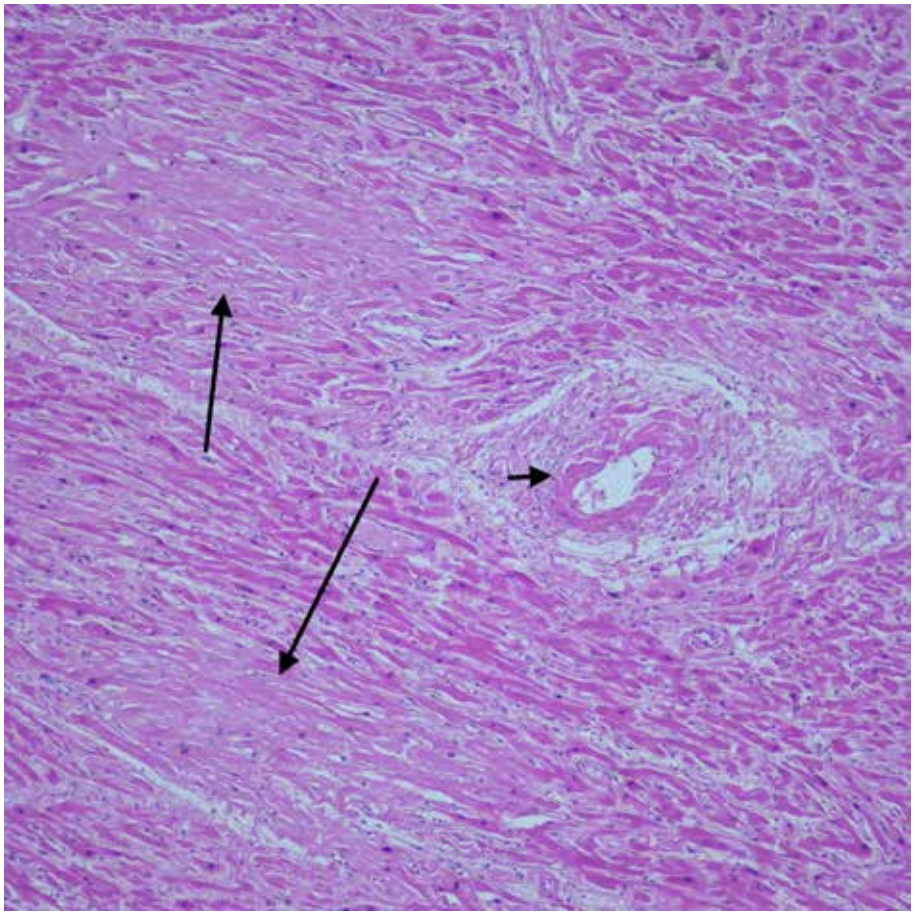

Figure 1.74
Cardiac amyloidosis, (H&E, x100). Amyloid can accumulate in the atrium and ventricle myocardium, vascular walls, heart valves, and pericardium. It is an important cause of heart failure. Cardiac involvement is an important cause of mortality in amyloidosis. The microscopic view shows amyloid accumulation in the interstitial space (long arrow) and the vessel wall (short arrow). Microscopically, it is seen as amorphous, eosinophilic, homogeneous pale areas. It is important to distinguish it from fibrosis foci.

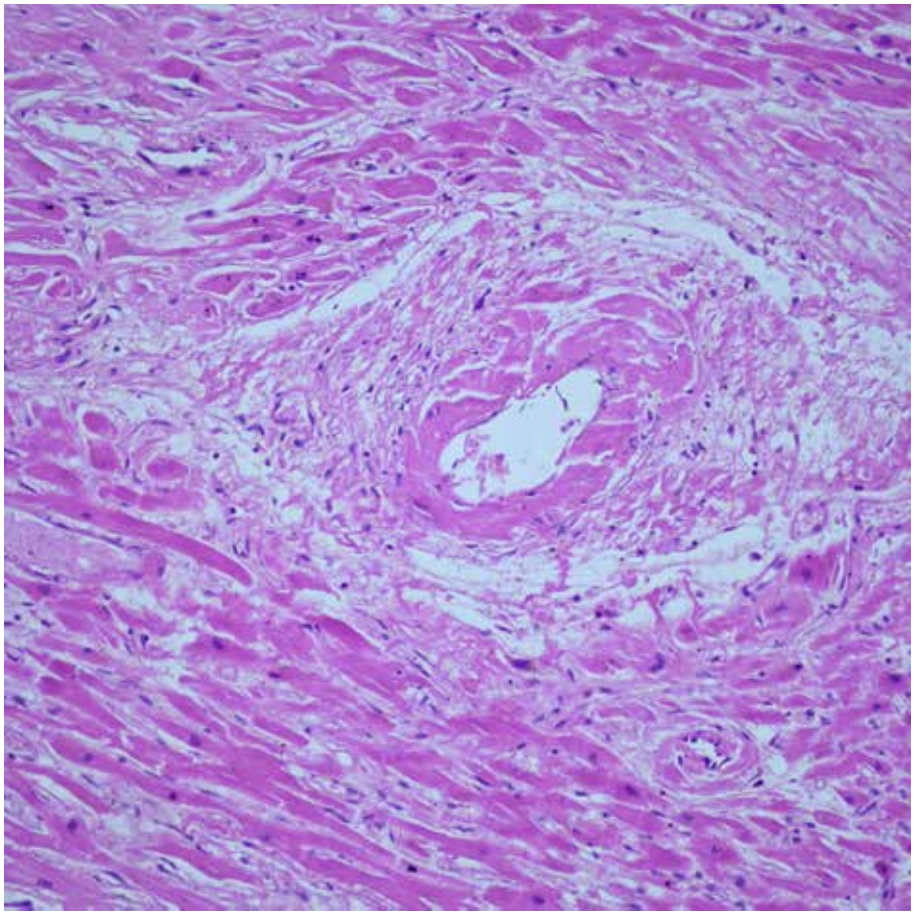

Figure 1.75
Cardiac amiloidosis, (H&E, x200). At higher magnification, eosinophilic amorphous amyloid accumulation is seen in the intramyocardial vessel wall.

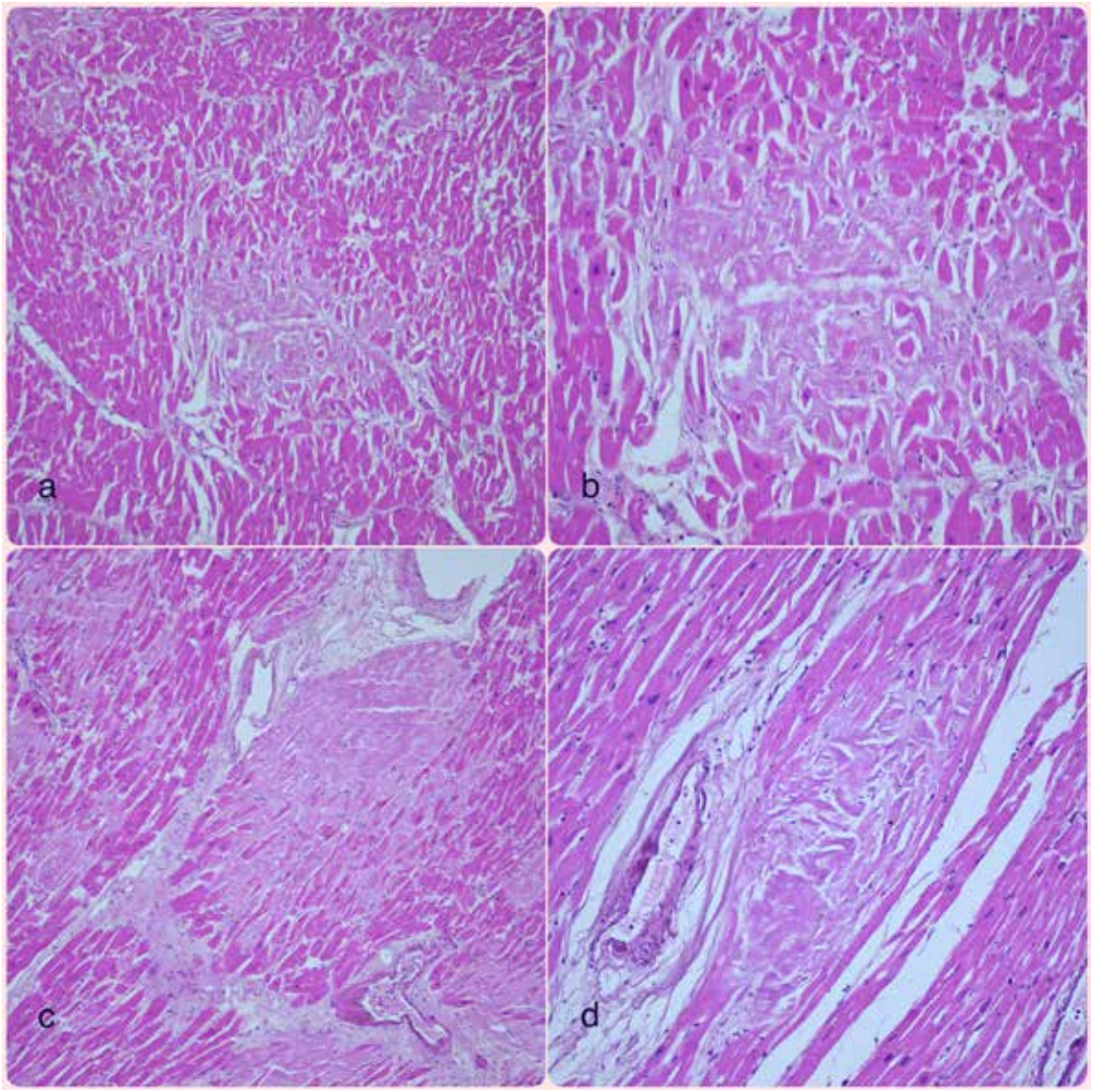

Figure 1.76
Cardiac amyloidosis .
a) (H&E, x100). Amorphous, pale eosinophilic amyloid deposition in the interstitium
b) (H&E, x200). At higher magnification.
c) (H&E, x100). Amyloid deposition in the perivascular areas.
d) (H&E, x200). At higher magnification.

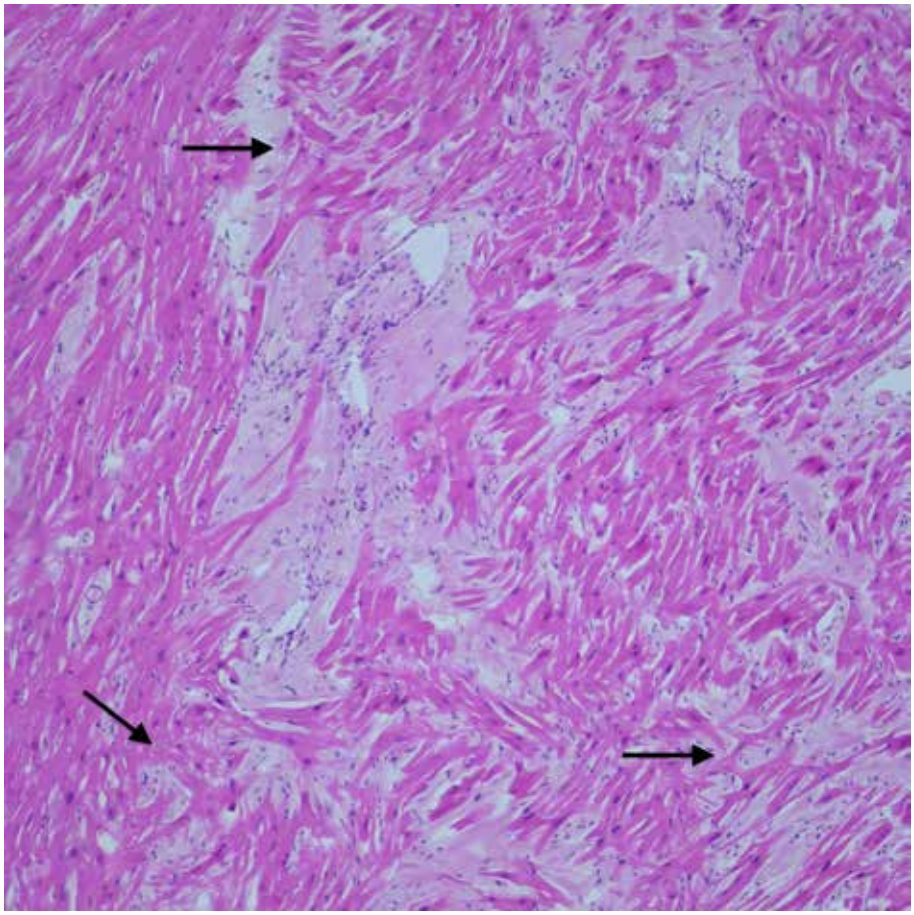

Figure 1.77
Hypertrophic Cardiomyopathy, (H&E, x100). Hypertrophic cardiomyopathy is the most common inherited heart disease. Macroscopically, the ratio of septum thickness to posterior wall thickness is greater than 1,3 cm in normotensive individuals and greater than 1,5 cm in hypertensive individuals. Myocardial disarray (arrow) is a specific finding for hypertrophic cardiomyopathy when it is diffuse.

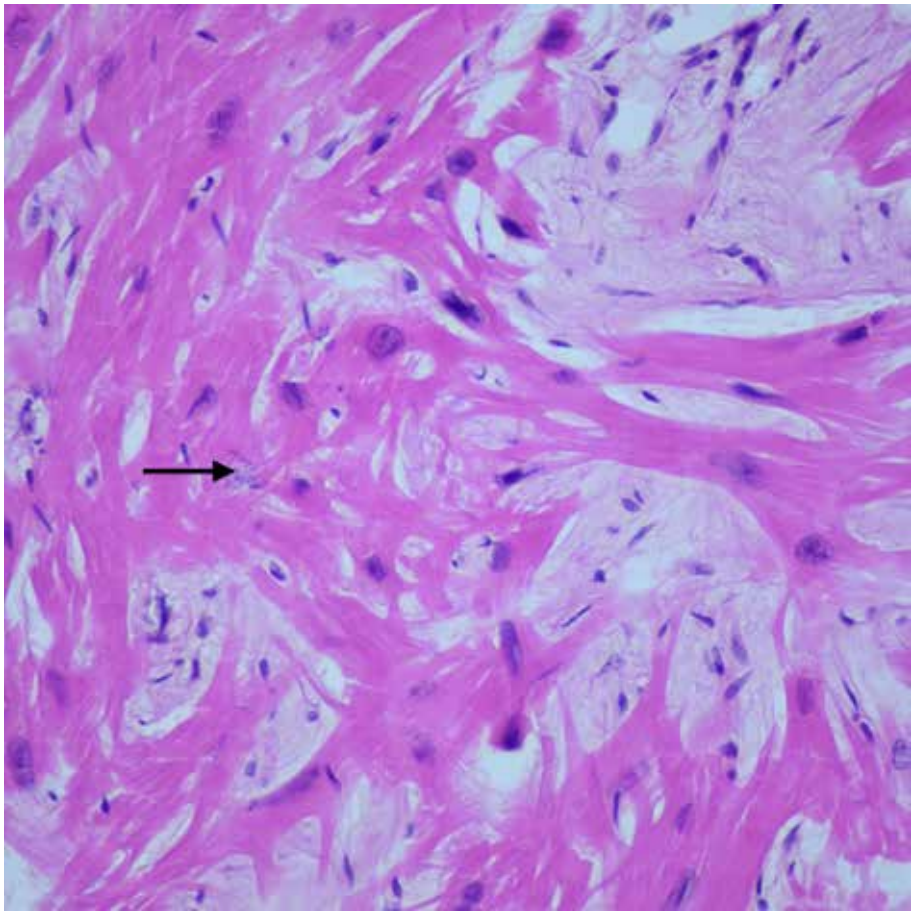

Figure 1.78
Hypertrophic Cardiomyopathy, (H&E, x400). Myocardial disarray (arrow) (The arrangement of myocytes perpendicularly or obliquely at an angle to each other is called "myofibrillar disarray").

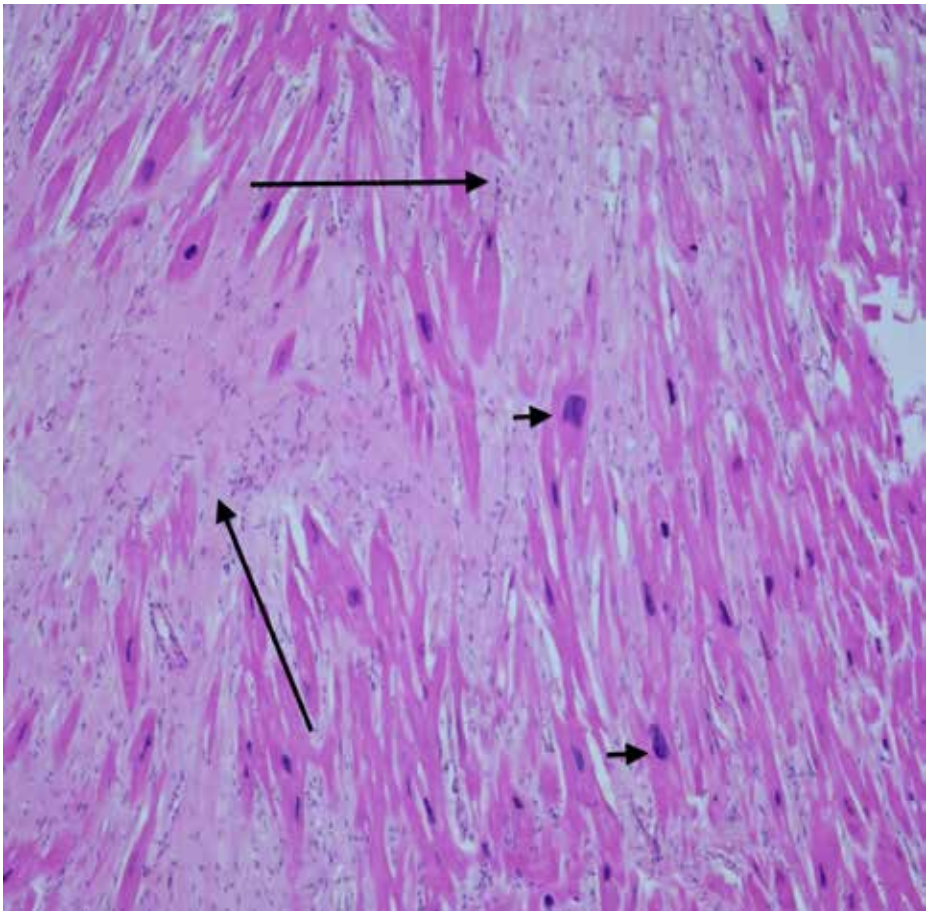

Figure 1.79 Hypertrophic Cardiomyopathy, (H&E, x100). Both interstitial and replacement fibrosis may be seen in hypertrophic cardiomyopathy. In the microscopic view, distinct areas of replacement fibrosis are shown with long arrows. Short arrows indicate hypertrophic cardiomyocytes with large, hyperchromatic and irregular nuclei.

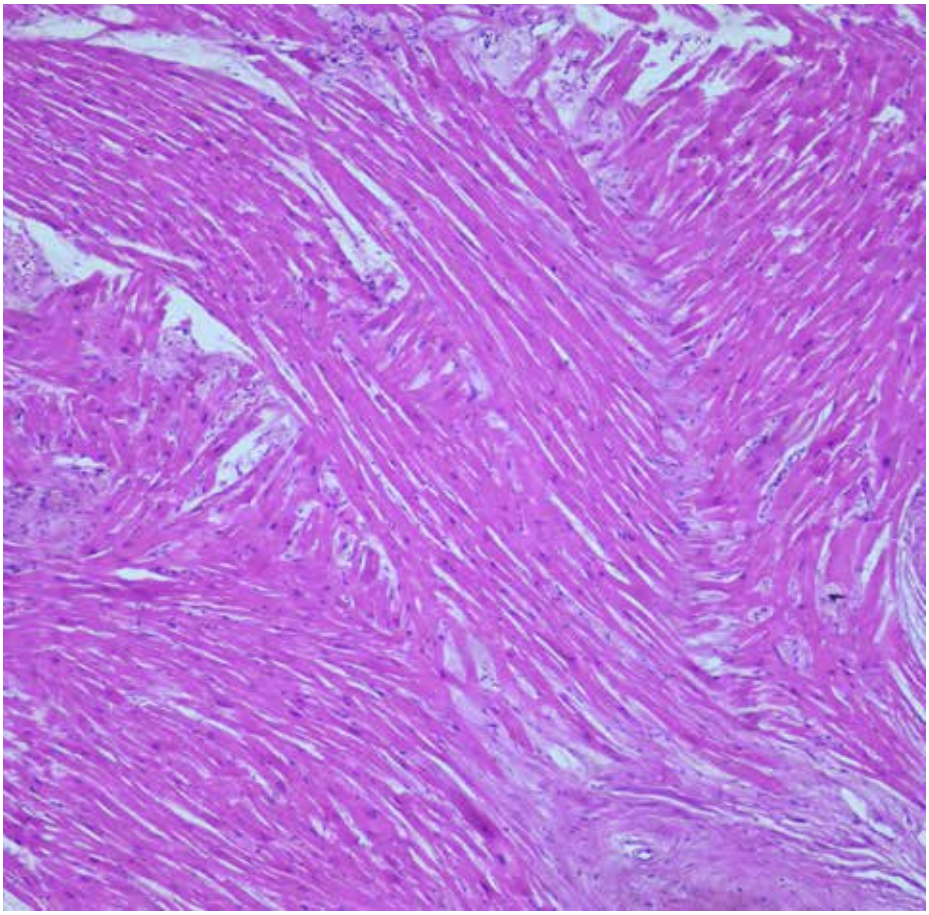

Figure 1.80 Crossing of muscle fibers in the septum, (H&E, x100). In the septum, a microscopic appearance that can be confused with myofibrillar disarray may be detected as a result of muscle fibers crossing each other. This is the normal appearance of muscle fibers in the septum. The microscopic view shows muscle fibers coming from the ventricular free wall converge at acute angle at septum.

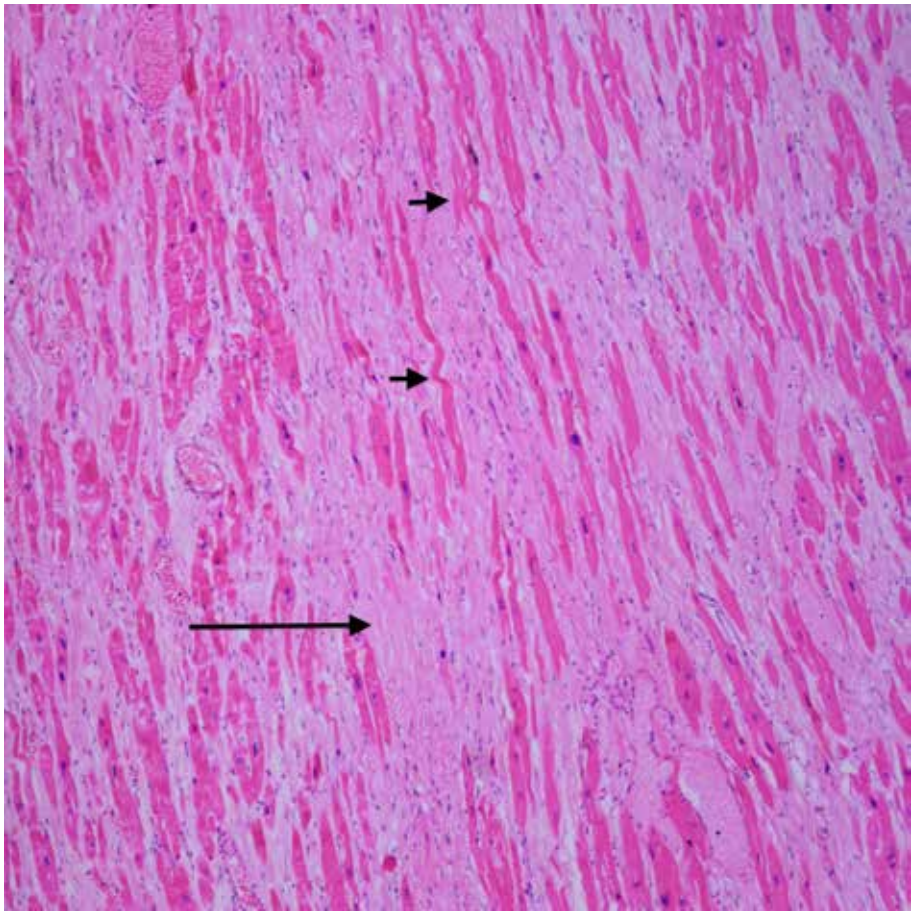

Figure 1.81
Dilated cardiomyopathy, (H&E, x100).
In microscopic view, there is thinning and a wavy appearance of cardiomyocytes (short arrows). Interstitial fibrosis is also an important feature of dilated cardiomyopathy and may take the form of replacement fibrosis (long arrow).

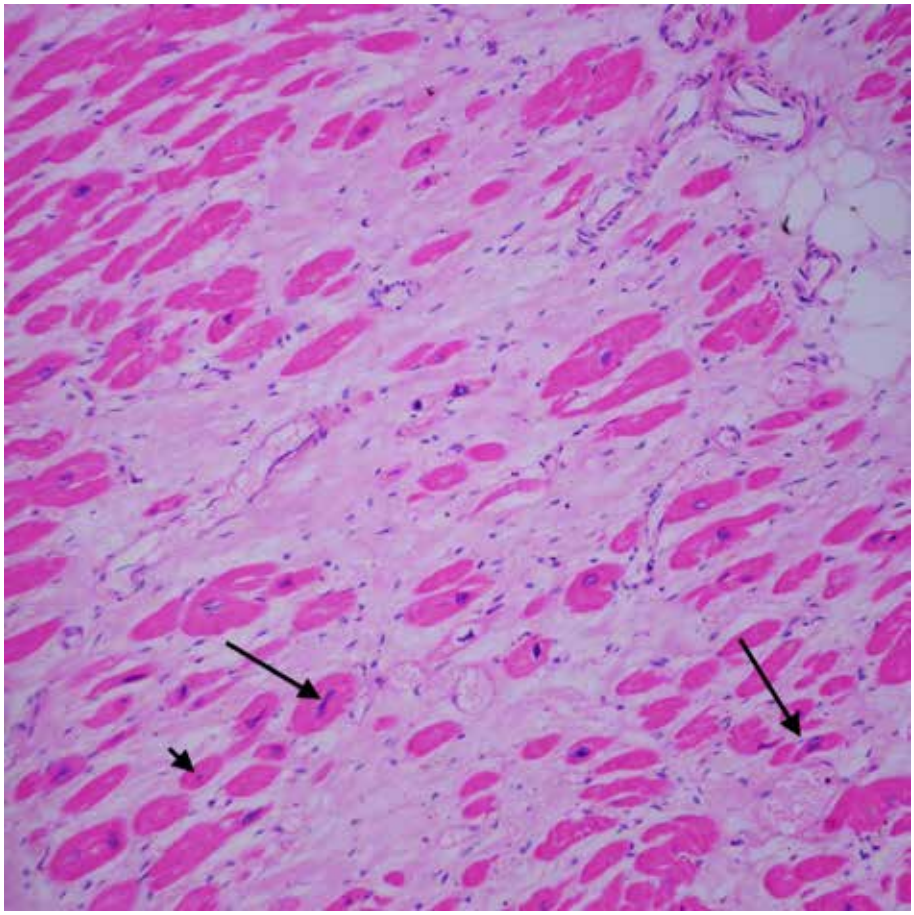

Figure 1.82
Dilated cardiomyopathy, (H&E, x100).
The microscopic view demostrates small cardiomyocytes (short arrow) intermingled with hypertrophic cardiomyocytes with a bizarre shaped hyperchromatic nucleus (long arrows).

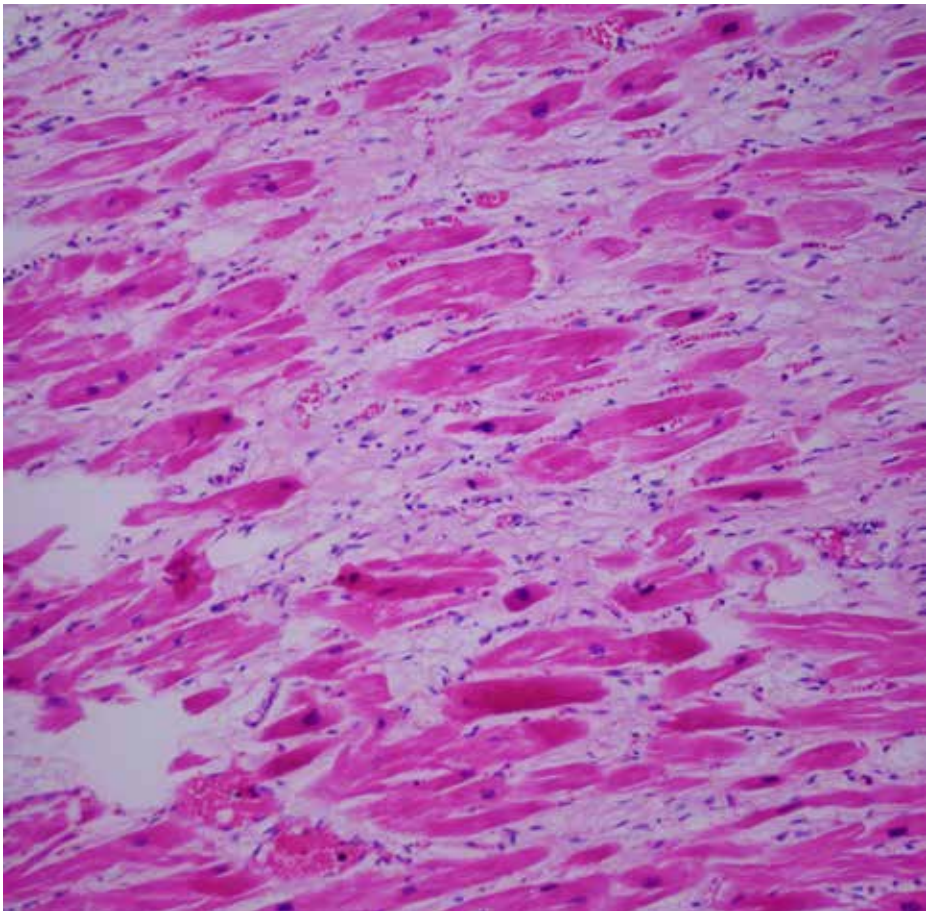

Figure 1.83 Dilated cardiomyopathy, (H&E, x200). In the microscopic view, areas of interstitial fibrosis and intermingled hypertrophic and small cardiomyocytes are seen.

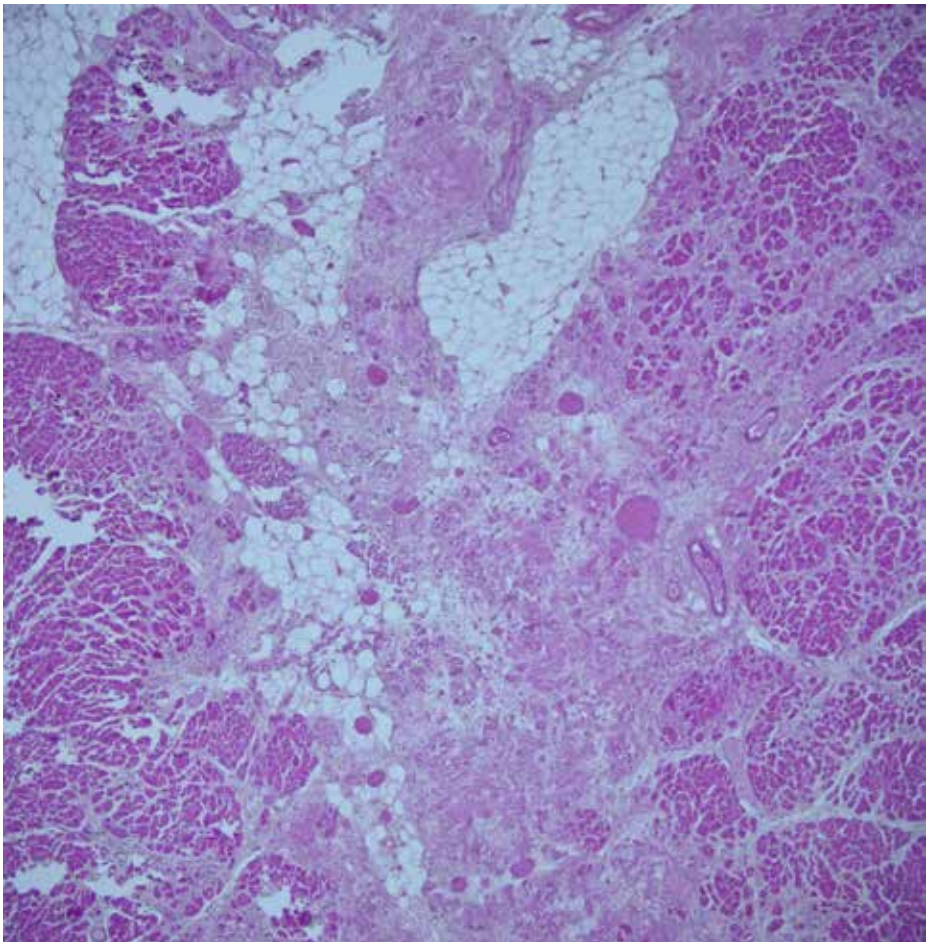

Figure 1.84 Arrhythmogenic cardiomyopathy, (H&E, x40). Cardiomyocyte loss and fibroadipose tissue replacement is obvious in the microscopic view.

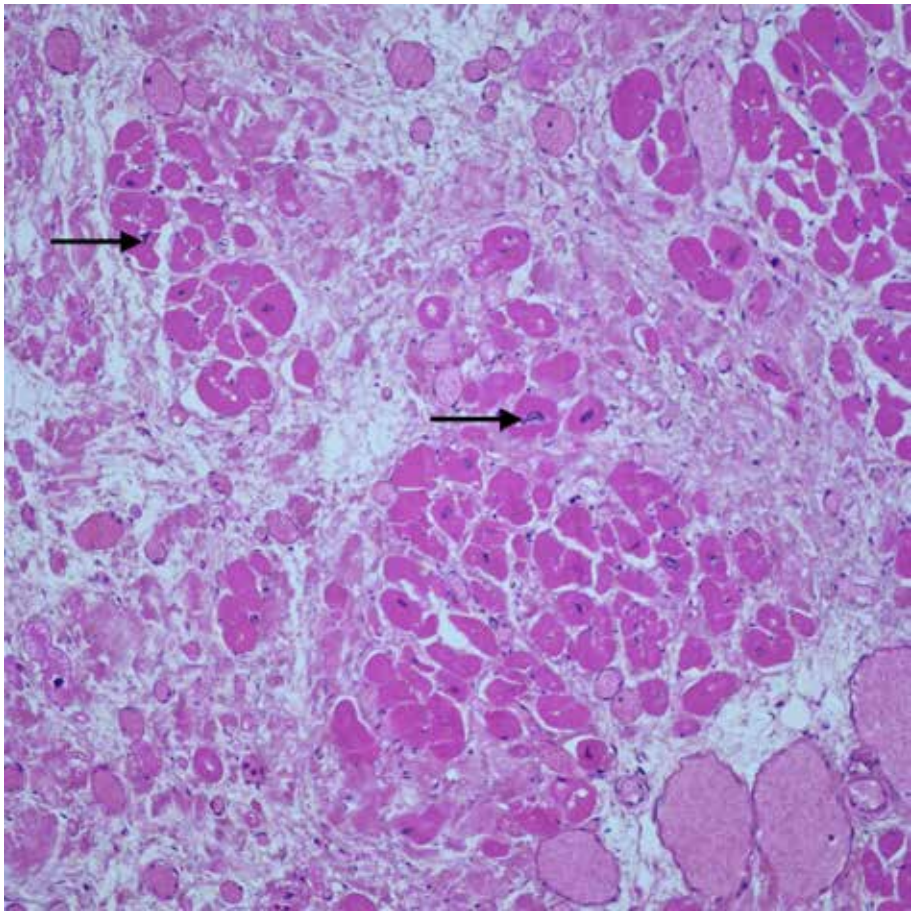

Figure 1.85
Arrhythmogenic cardiomyopathy, (H&E, x200). Cardiomyocyte loss, fibroadipose tissue replacement and dystrophic myocytes (arrows) are seen in the microscopic view.

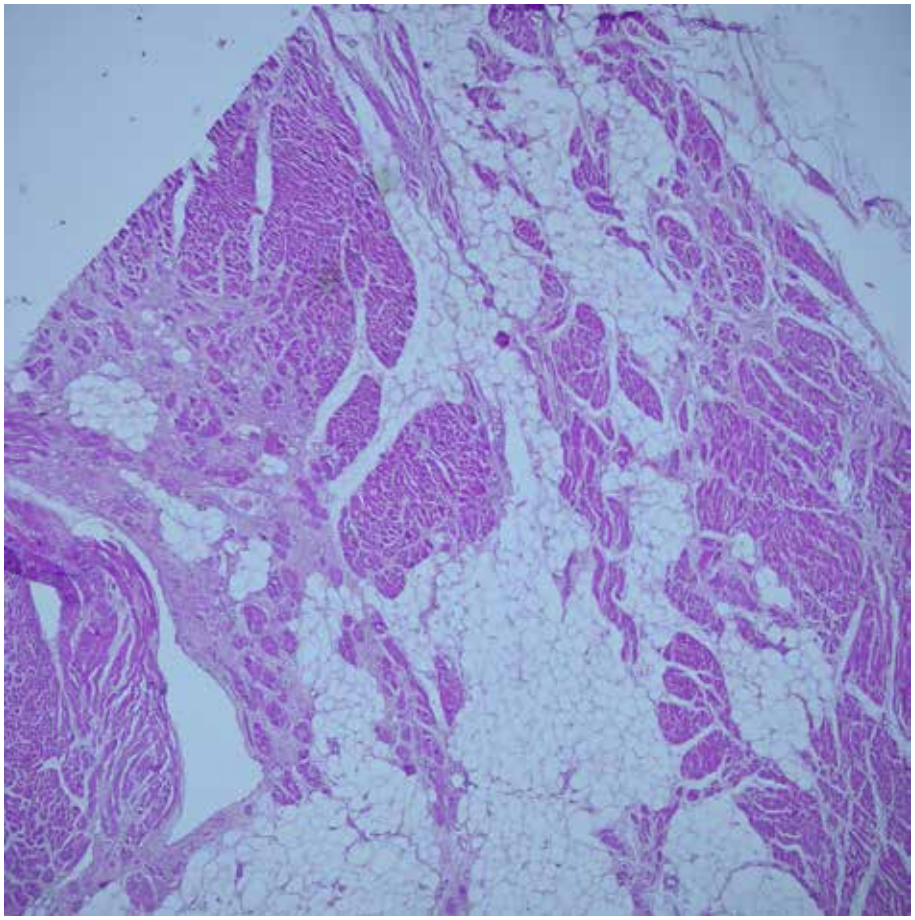

Figure 1.86
Arrhythmogenic cardiomyopathy, (H&E, x40). In the microscopic view, fibroadipose tissue is seen in the myocardium.

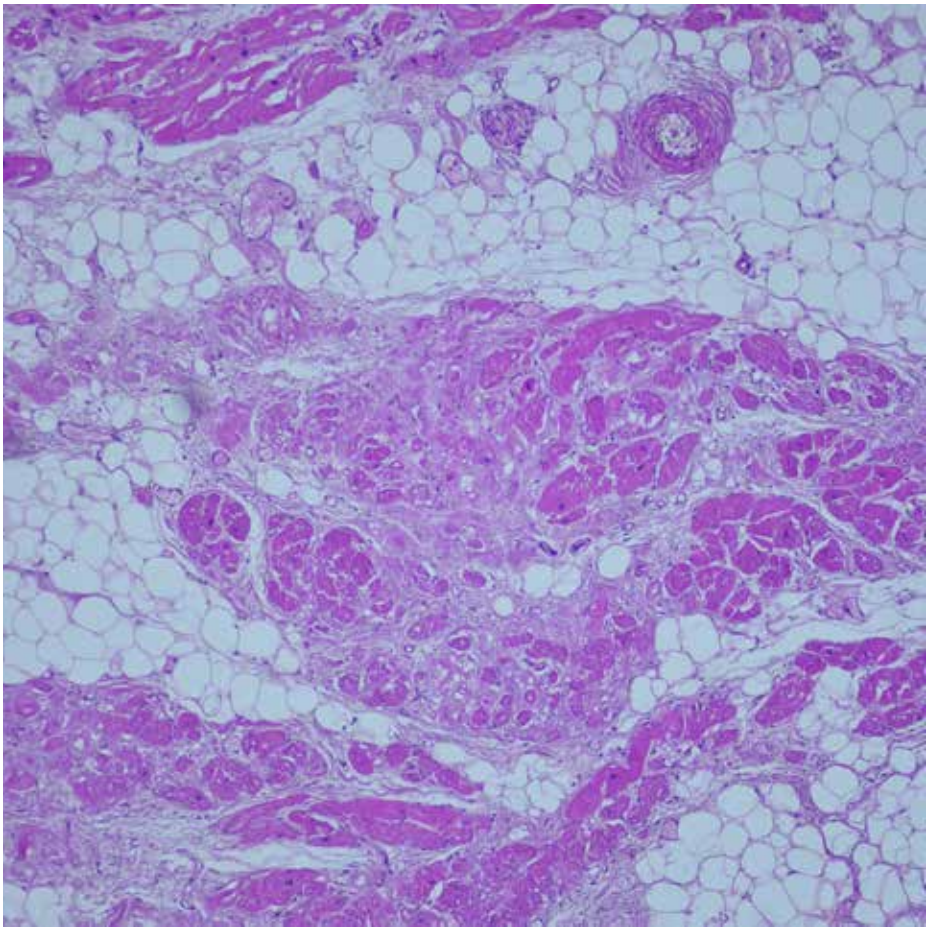

Figure 1.87 Arrhythmogenic cardiomyopathy, (H&E, x40). In the microscopic view, fibroadipose tissue infiltration in the right atrium wall is noteworthy.

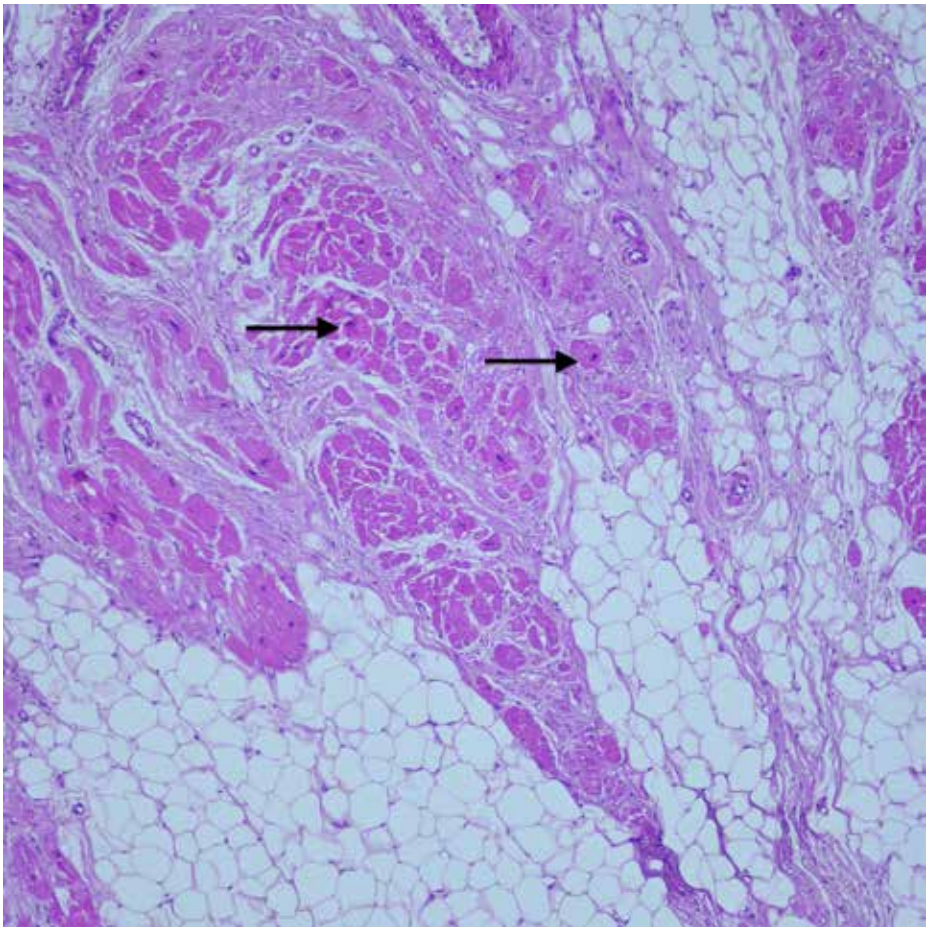

Figure 1.88 Arrhythmogenic cardiomyopathy, (H&E, x40). In the microscopic view, fibroadipose tissue infiltration in the right atrium wall and dystrophic cardiomyocytes (arrows) in the fibrotic area are noteworthy.

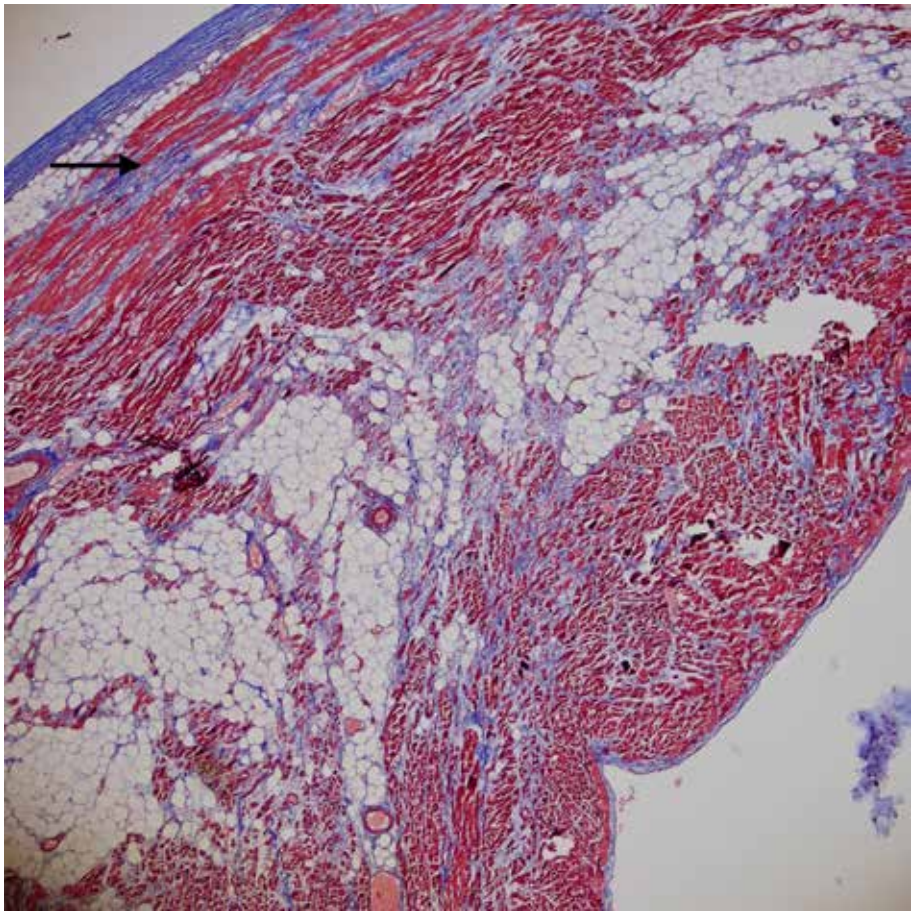

Figure 1.89
Arrhythmogenic cardiomyopathy, (Masson trichrome, x40). Areas of fibrosis (arrow).

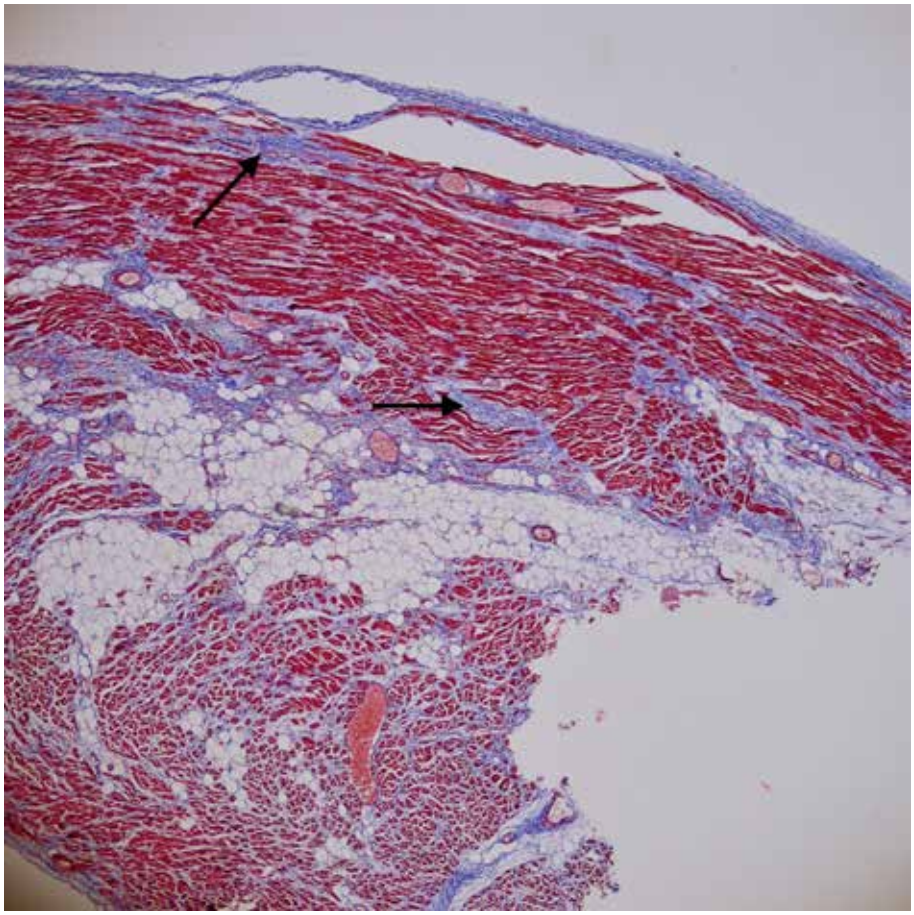

Figure 1.90
Arrhythmogenic cardiomyopathy, (Masson trichrome, x40). The microscopic view shows cardiomyocyte loss and fibroadipose tissue replacement. Areas of fibrosis (arrow).

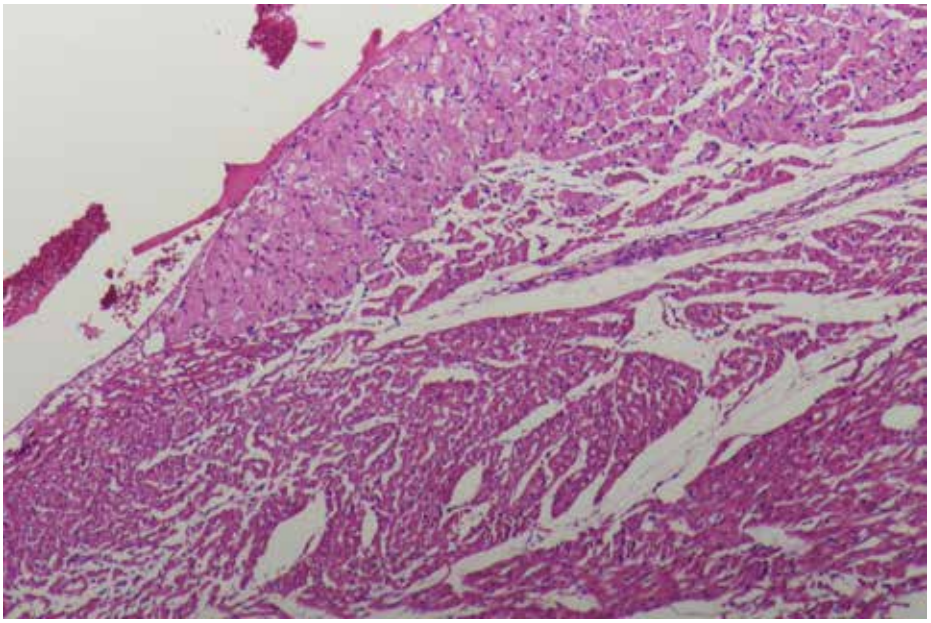

Figure 1.91 Histiocytoid cardiomyopathy (Purkinje cell tumor, Idiopathic infantile cardiomyopathy), (H&E, x100). The microscopic view shows a group of cells with eosinophilic vacuolated cytoplasm in the subendocardial region.

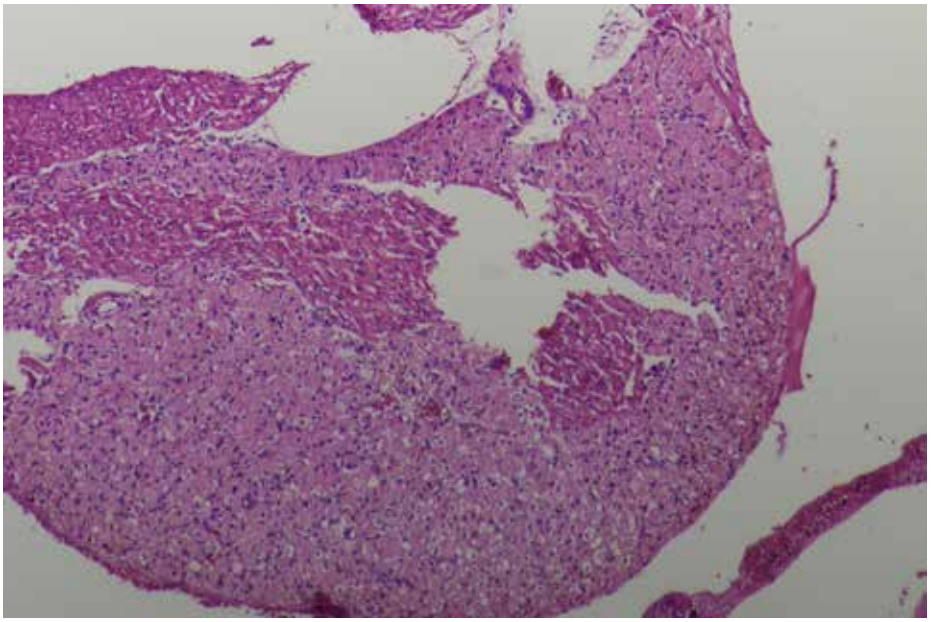

Figure 1.92 Histiocytoid cardiomyopathy (Purkinje cell tumor, Idiopathic infantile cardiomyopathy), (H&E, x100). Although it considered as mitochondrial cardiomyopathy, it is now considered a cardiomyocyte or Purkinje cell-derived hamartoma. Microscopically, it consists of vacuolated histiocyte-like cells within the myocardium.

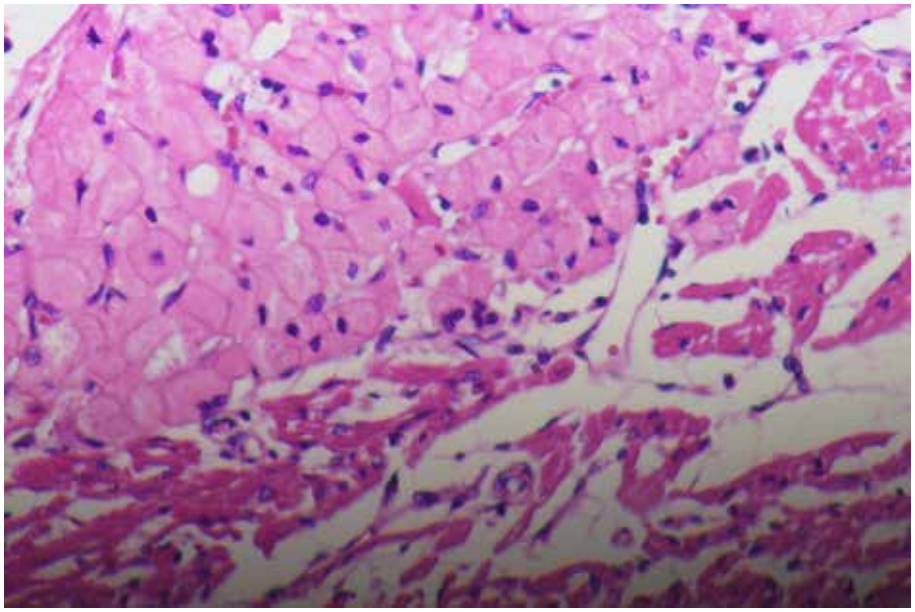

Figure 1.93
Histiocytoid cardiomyopathy, (H&E, x200).
The microscopic view demostrates vacuolated histiocyte-like cells within the myocardium.

Figure 1.94
Cystic Tumor of AV (atrioventricular) node, macroscopic view. Macroscopic view of the cystic tumor located in the AV node region (arrow).
Tumor size is often range from 2 mm to 2 cm. It is the primary cardiac tumor that most often causes sudden death.

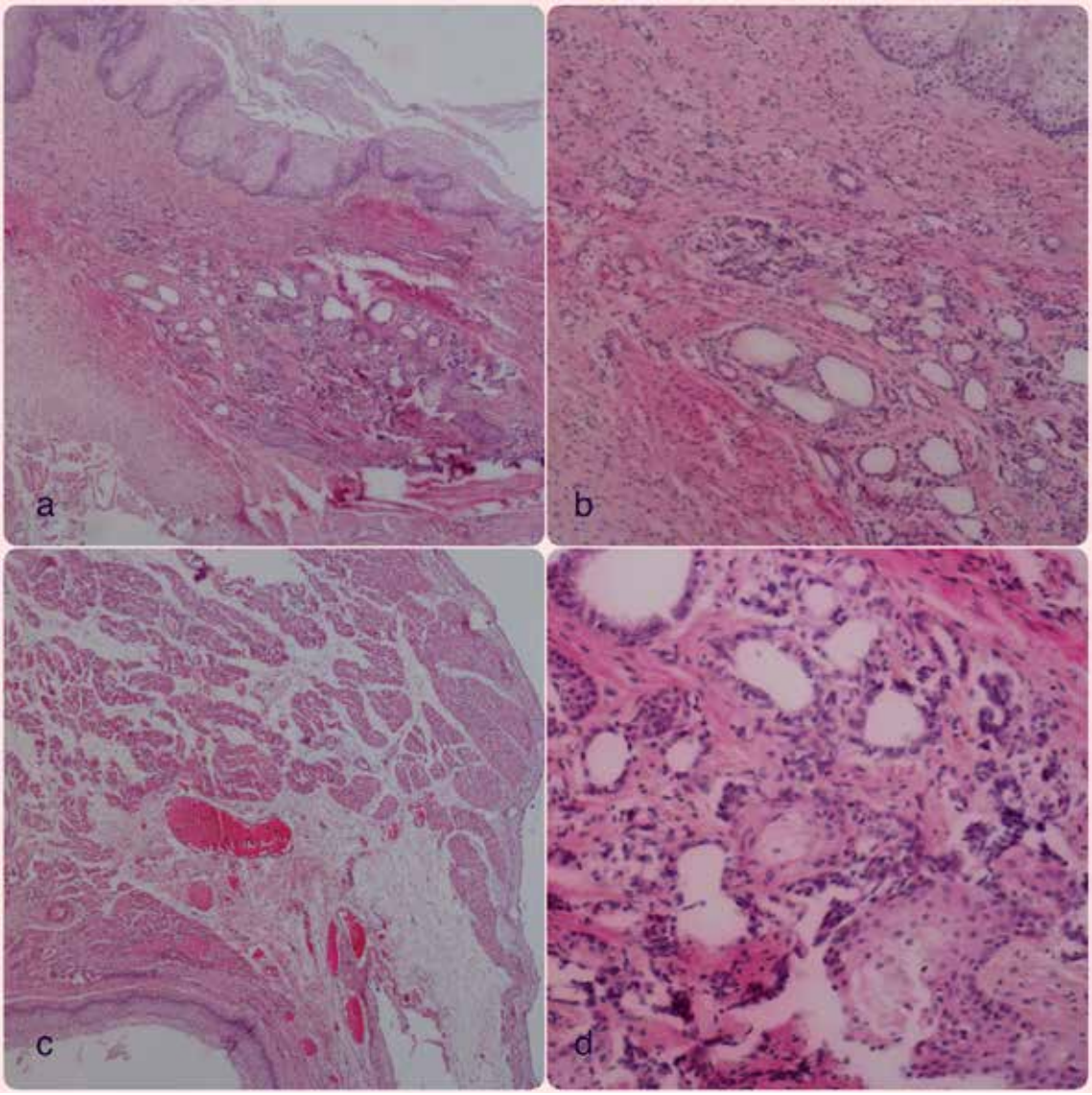

Figure 1.95
Cystic tumor of the AV node. The tumor occurs in cysts, ducts and solid cell islands.
a,c) (H&E, x40), (H&E, x40).
Cystic structures lined with epithelium showing squamous differentiation.
b,d) (H&E, x100), (H&E, x200).
Irregular cyst and duct structures are seen within the fibrous stroma.

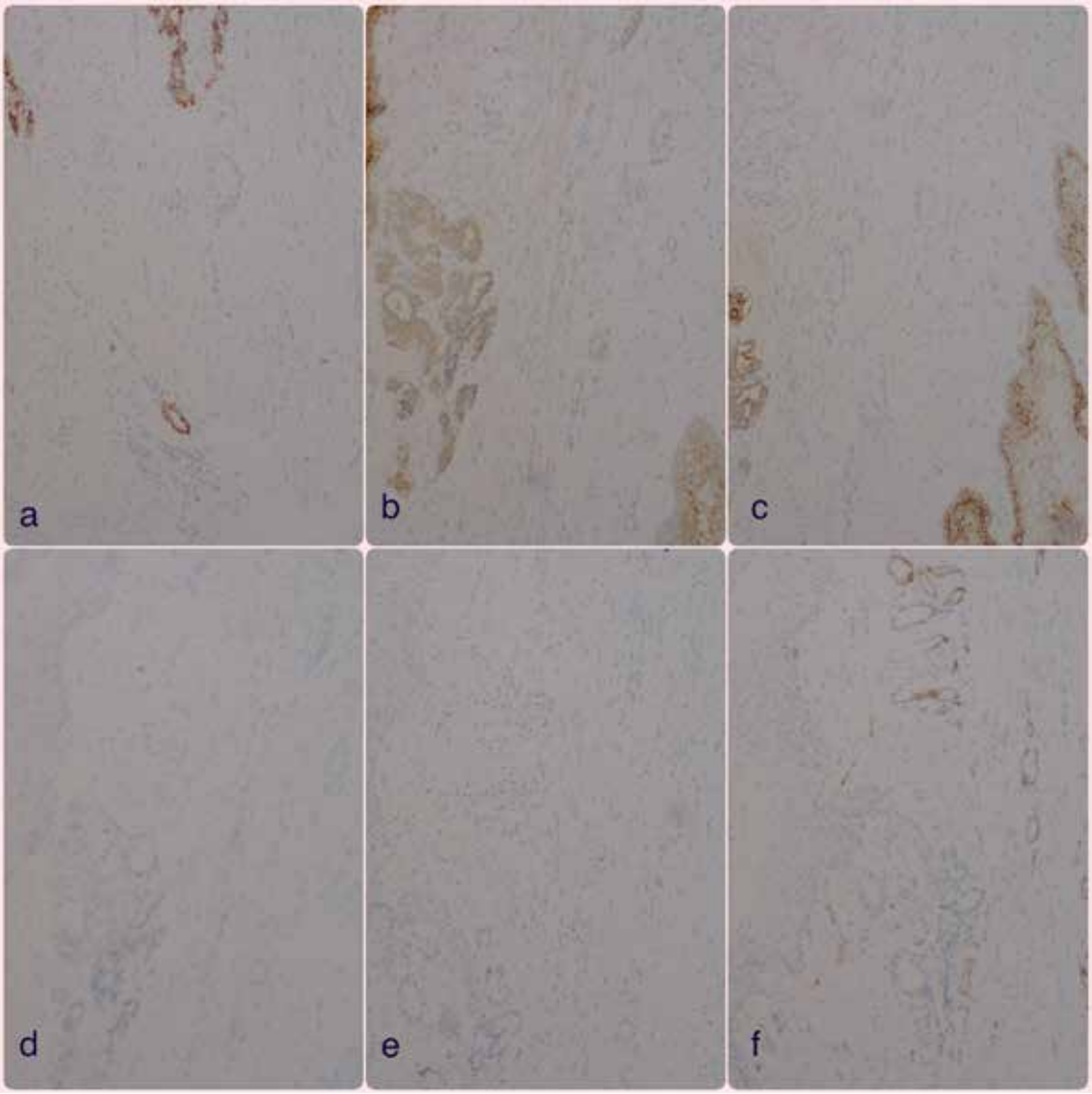

Figure 1.96
Cystic tumor of the AV node, immunohistochemical staining,
a) CK7. Stain positive for CK7 (Cytokeratin 7) in tumor cells.
b) CEA. Stain positive for CEA (Carcinoembryogenic antigen) in tumor cells.
c) EMA. Tumor cells stain positive for EMA (Epithelial Membrane Antigen).
d) CK20. Tumor cells do not stain for CK-20 (Cytokeratin 20).
e) NSE. Tumor cells do not stain for NSE (Neuron specific enolase).
f) CD31. No staining was detected for CD31 in tumor cells.

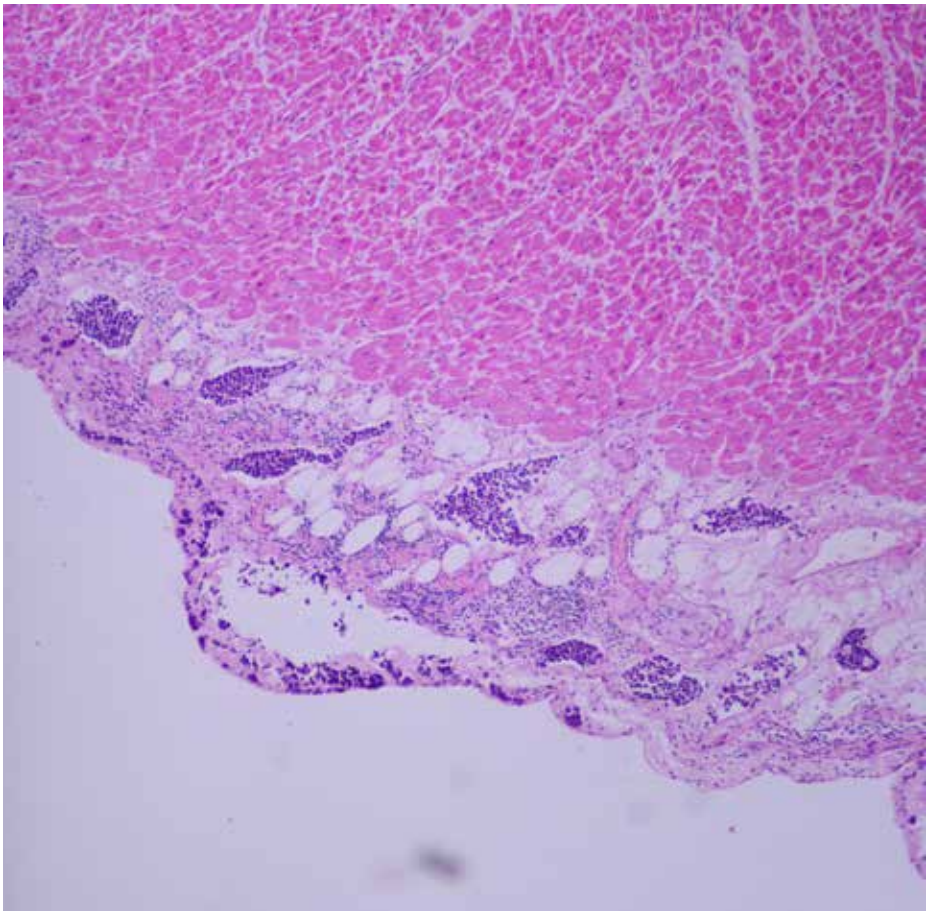

Figure 1.97
Leukemic infiltration in the epicardium, (H&E, x100). In the microscopic view, leukemic infitration in the epicardium is demostrated.

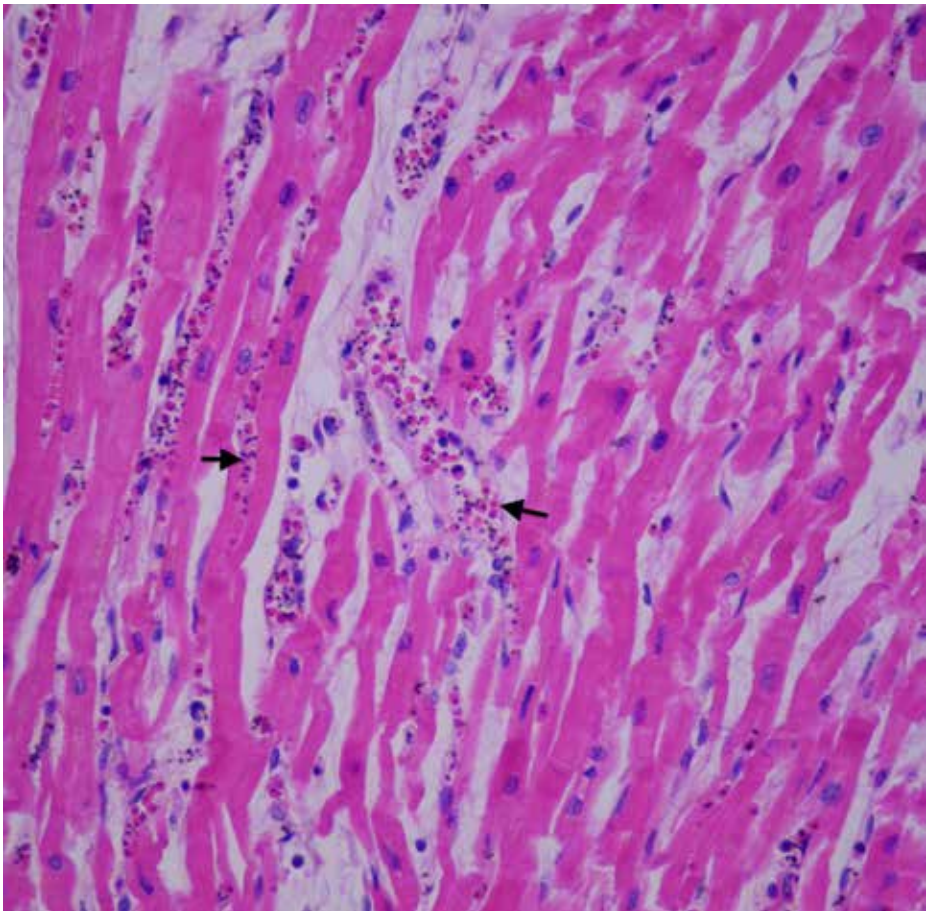

Figure 1.98
Malaria, (H&E, x200). Many black-dark brown, coarse parasite pigments (hemozoin pigment) (arrows) are seen in the erythrocytes located in the capillary lumen of the myocardium. It has a structure similar to formalin pigment and is distinguished by its selective localization within erythrocytes.

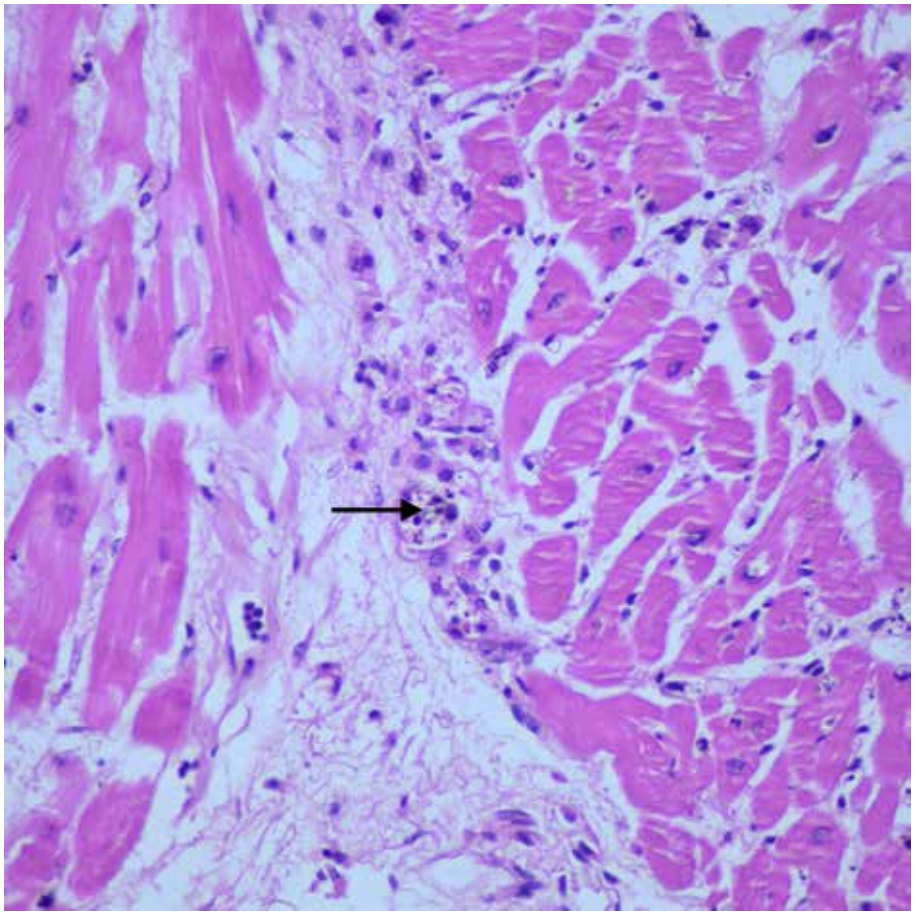

Figure 1.99
Malaria,
(H&E, x400).
At higher
magnification, black-
dark brown, coarse
parasite pigments
(hemozoin pigment)
(arrow)
are seen in the
erythrocytes.

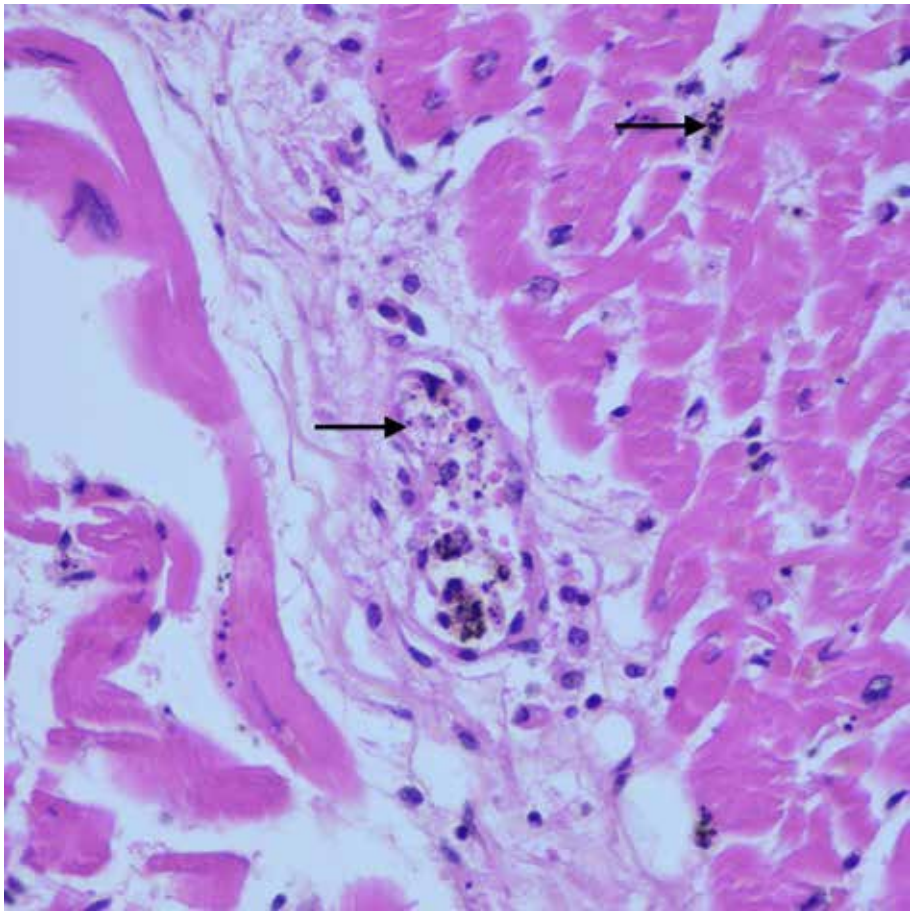

Figure 1.100
Malaria,
(H&E, x600).
At higher
magnification parasite
pigments
(hemozoin pigment)
(arrows).

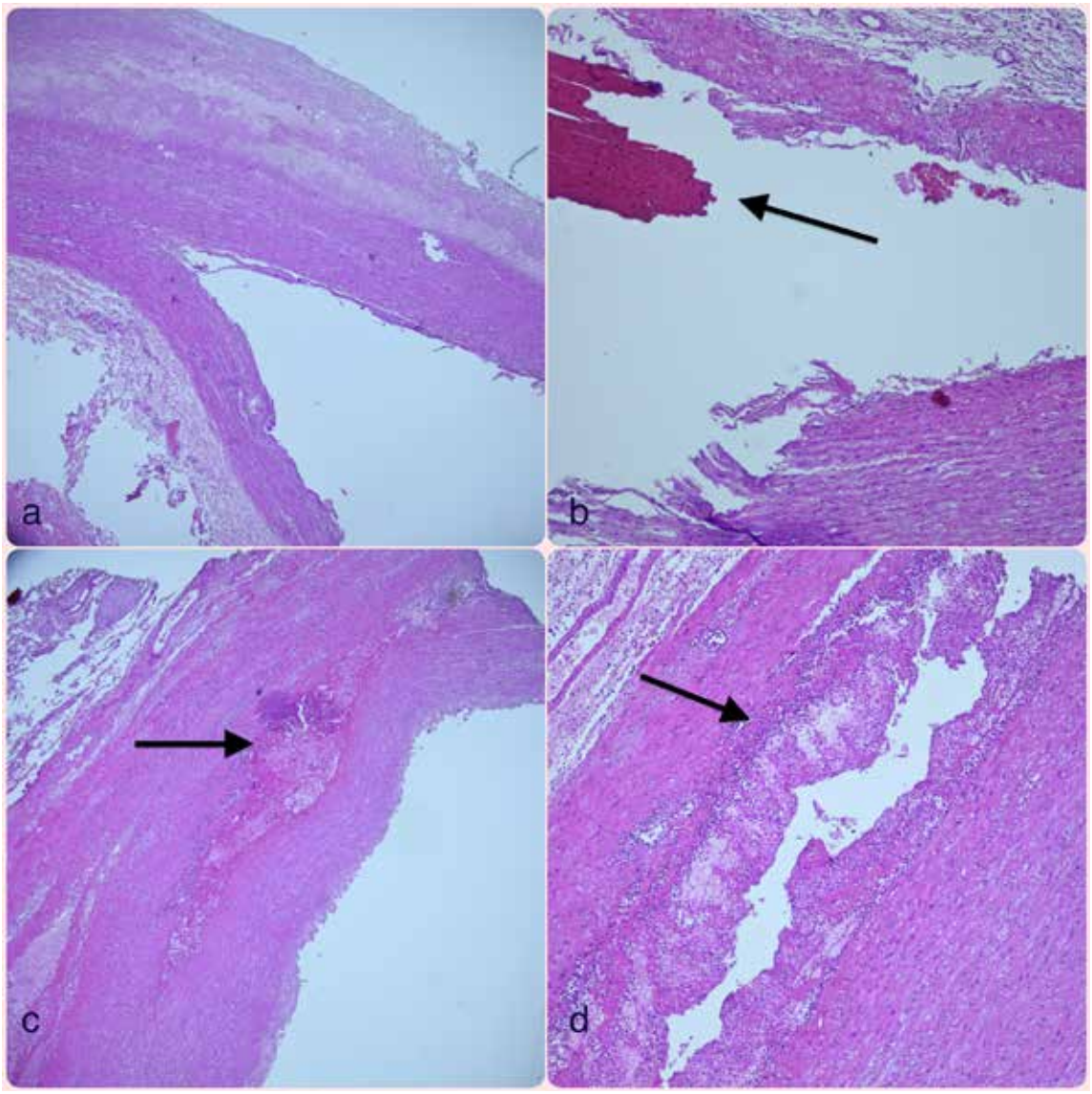

Figure 1.101
Aort dissection.
a) (H&E, x40). Dissection is observed in the aortic media layer.
b) (H&E, x100). Dissection of aorta demostrating an aortic intramural hematoma (arrow).
c) (H&E, x40). Dissection in the media layer, intramural hemorrhage and hematoma formation (arrow) are seen.
d) (H&E, x100). Intramural fibrin and neutrophil accumulation in the dissected aort.

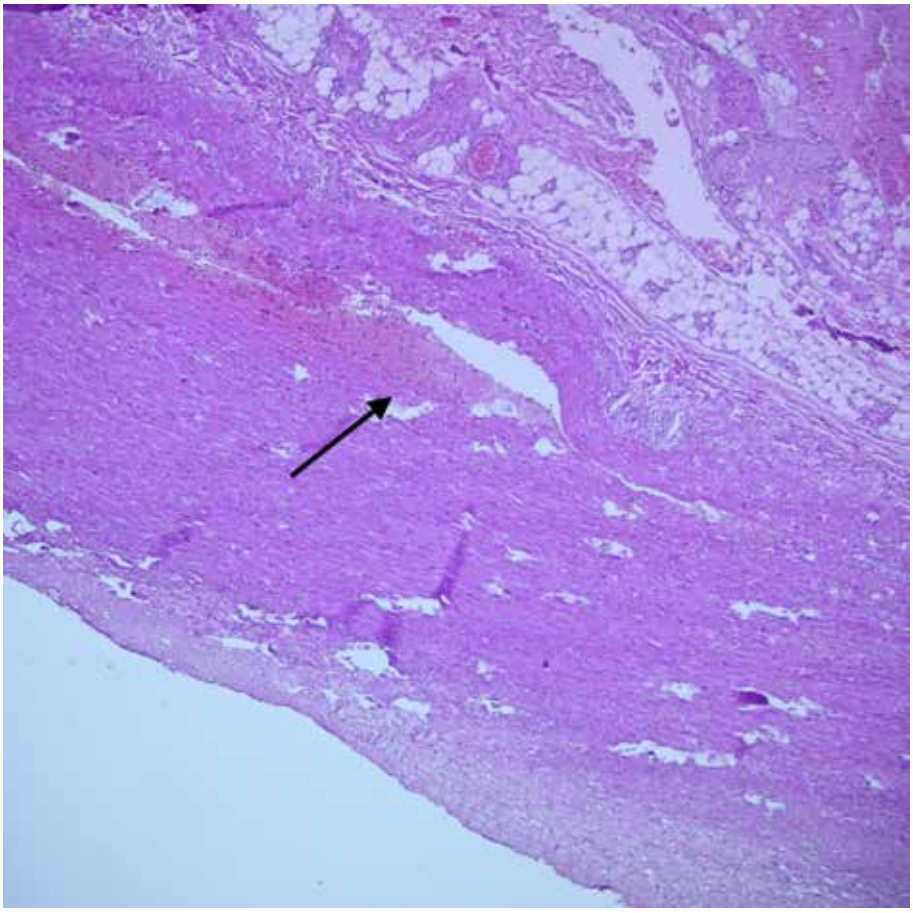

Figure 1.102
Aort dissection, (H&E, x40). Dissection and hemorrhage (arrow) are seen in the media layer.

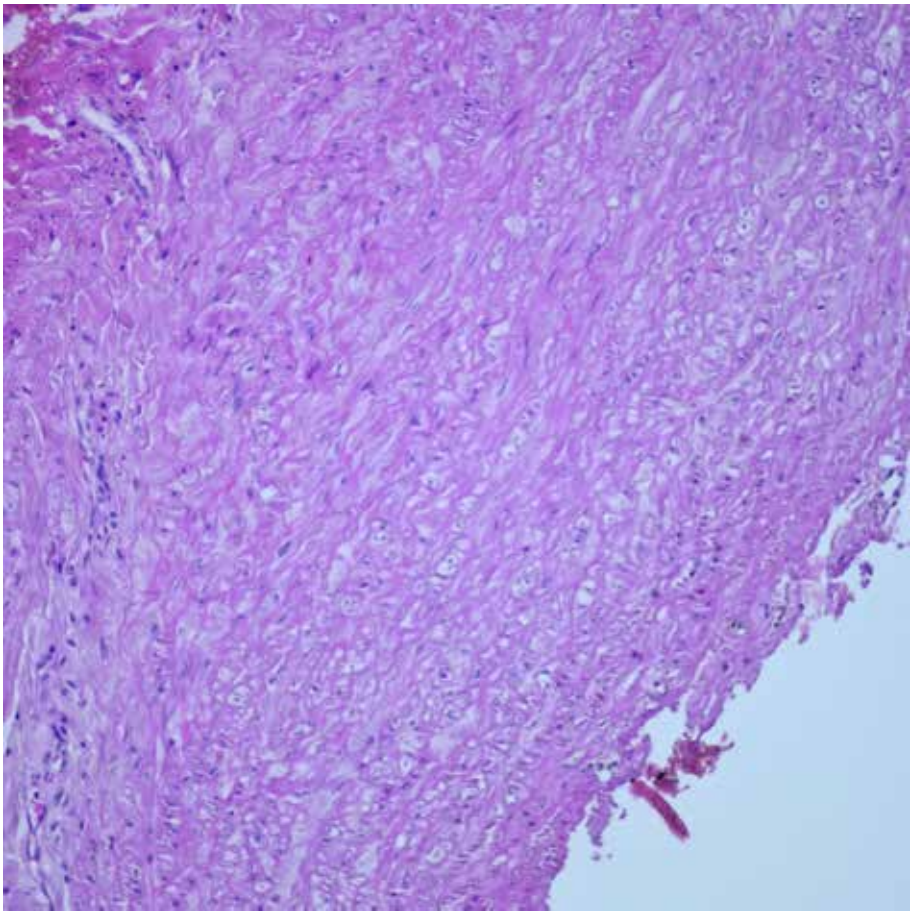

Figure 1.103
Cystic medial degeneration, (H&E, x200). Ischemia occurs in the media layer as a result of atherosclerotic thickening of the intima and narrowing of the vaso vasorum as a result of systemic hypertension. Medial ischemia causes degenerative changes in the aorta and results weakening of the aortic wall with loss of smooth muscle cells, and elastic fibers in media layer. These changes are called “cystic medial degeneration”.

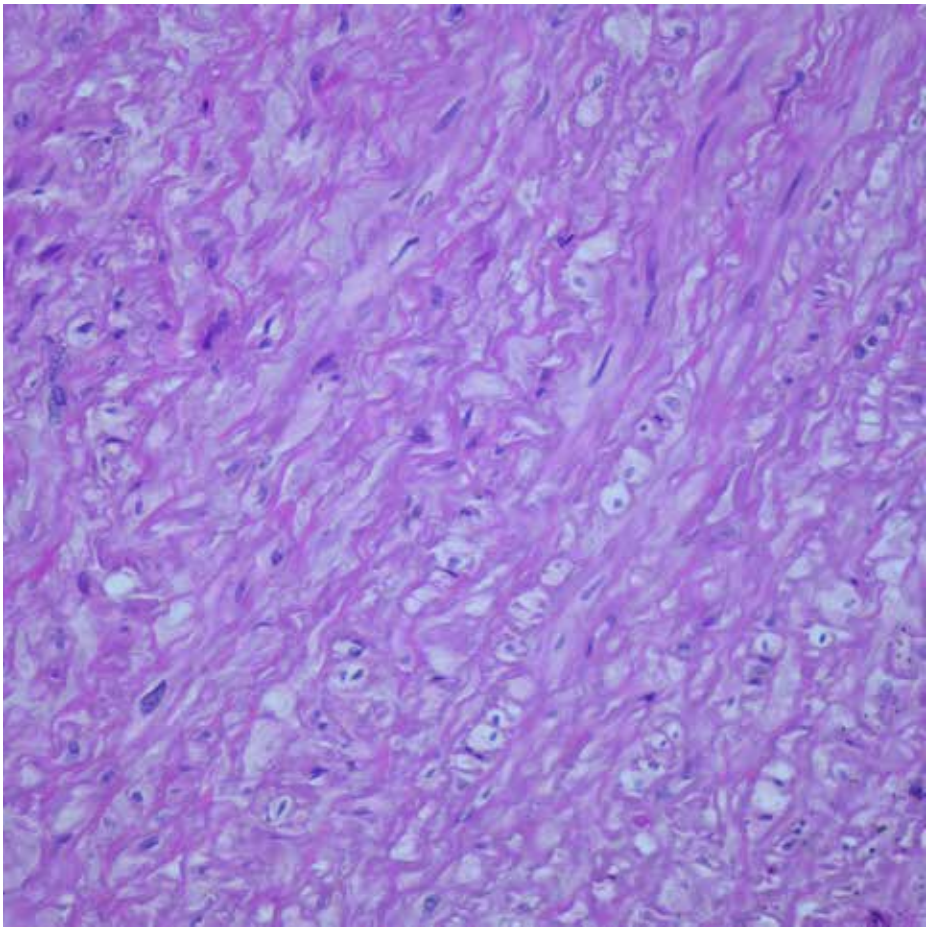

Figure 1.104 Cystic medial degeneration, (H&E, x400). At higher magnification.

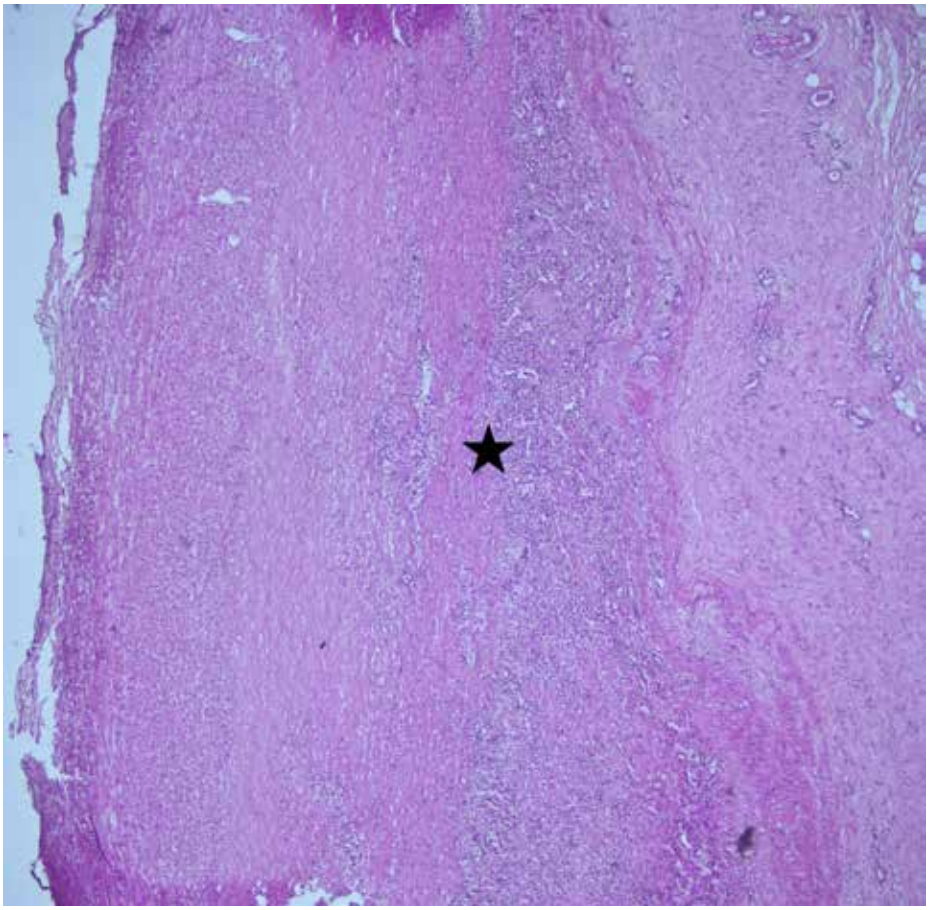

Figure 1.105 Aortitis, (H&E, x40). Dense mononuclear inflammatory cell infiltration (asterisk) is seen in the media and adventitia layers of aort. Damage to smooth muscle bundles in the media layer and weakening of the vessel wall are obvious.

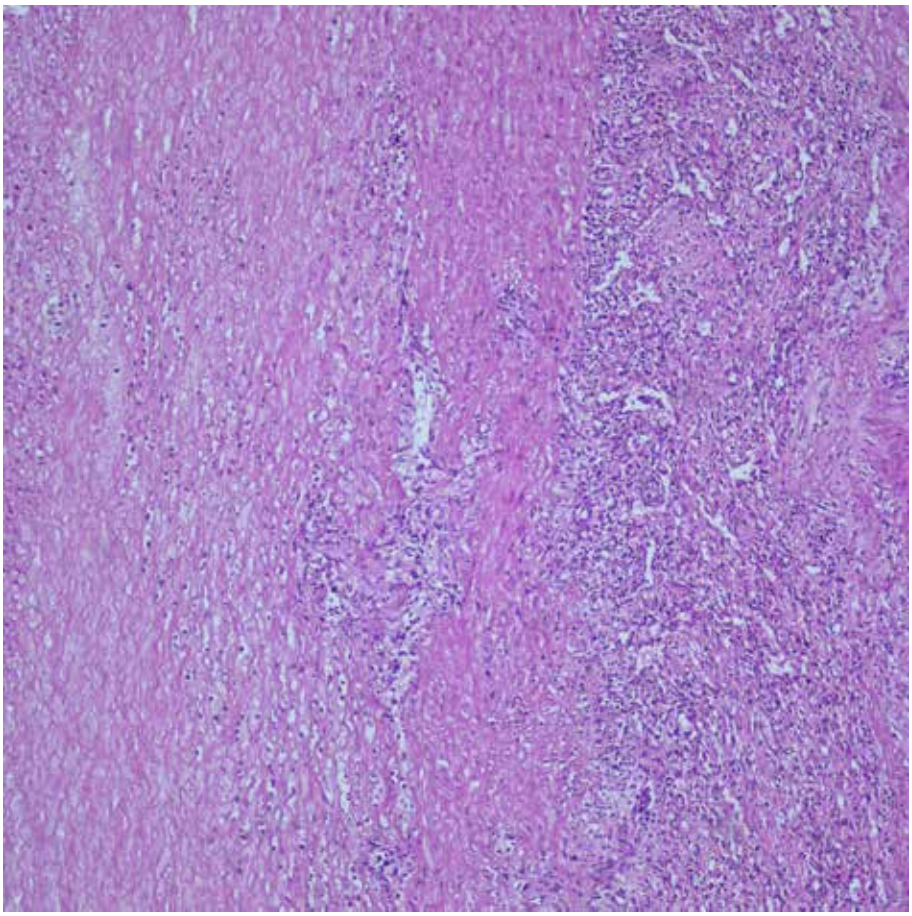

Figure 1.106
Aortitis,
(H&E, x100).
At higher magnification.

RESPIRATORY SYSTEM

Assoc. Prof. Taner DAŞ
Assoc. Prof. Ferah KARAYEL

STAGES OF LUNG DEVELOPMENT

Lung development goes through five main histological stages, and each stage has a specific time interval:

1. Embryonic Stage (3-6 weeks).
- Basic lung structures such as trachea, bronchi and bronchioles are formed.

2. Pseudoglandular Stage (5-17 weeks)
- Thick airways lined with cuboidal epithelium are seen.
- Cartilage, smooth muscle and mucus glands develop.
-There is no gas exchange yet.

3. Canalicular Stage (16-25 weeks)
- Bronchioles and alveolar ducts develop.
-The epithelium begins to change into Type 1 and 2 pneumocytes.
- Pulmonary vessels are formed.
-At this stage, some respiration is possible; therefore, infants born at this stage can survive if provided with intensive care.

4. Saccular Stage (24- birth)
- Saccules (primitive alveoli) are formed.
- Type I and Type II pneumocytes develop.
- Type II pneumocytes produce surfactant.
-Pulmonary surfactant production begins in the 24th week; however, sufficient production does not occur until the 32nd week. Therefore, babies born after the 32nd week have a much higher chance of survival.

5. Alveolar Stage (36 weeks- 8 years)
- Alveoli mature and proliferate.
- After birth, the number of alveoli increases and develops structurally.

Reference :
1. Rehman S, Bacha D. Embryology, Pulmonary. [Updated 2023 Aug 14]. In: StatPearls [Internet]. Treasure Island (FL): StatPearls Publishing; 2024 Jan-. Available from: https://www.ncbi.nlm.nih.gov/books/NBK544372/

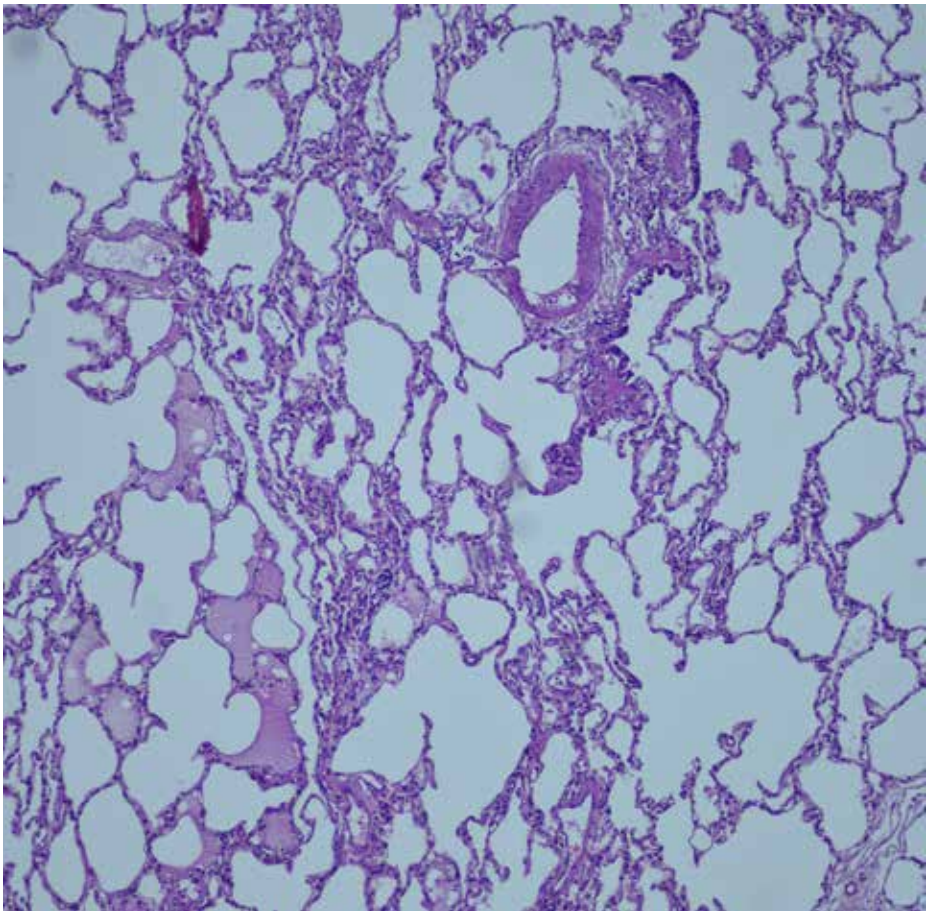

Figure 2.1
Adult lung tissue, (H&E, x100).
The lung alveolar surface is composed of flat type 1 pneumocytes and round type 2 pneumocytes that synthesize pulmonary surfactant.
The interstitium consists of thin elastic fibers, short collagen bundles, a small number of fibroblast-like cells, smooth muscle cells, mast cells, and occasional mononuclear cells.
There are a few alveolar macrophages in the alveolar spaces.

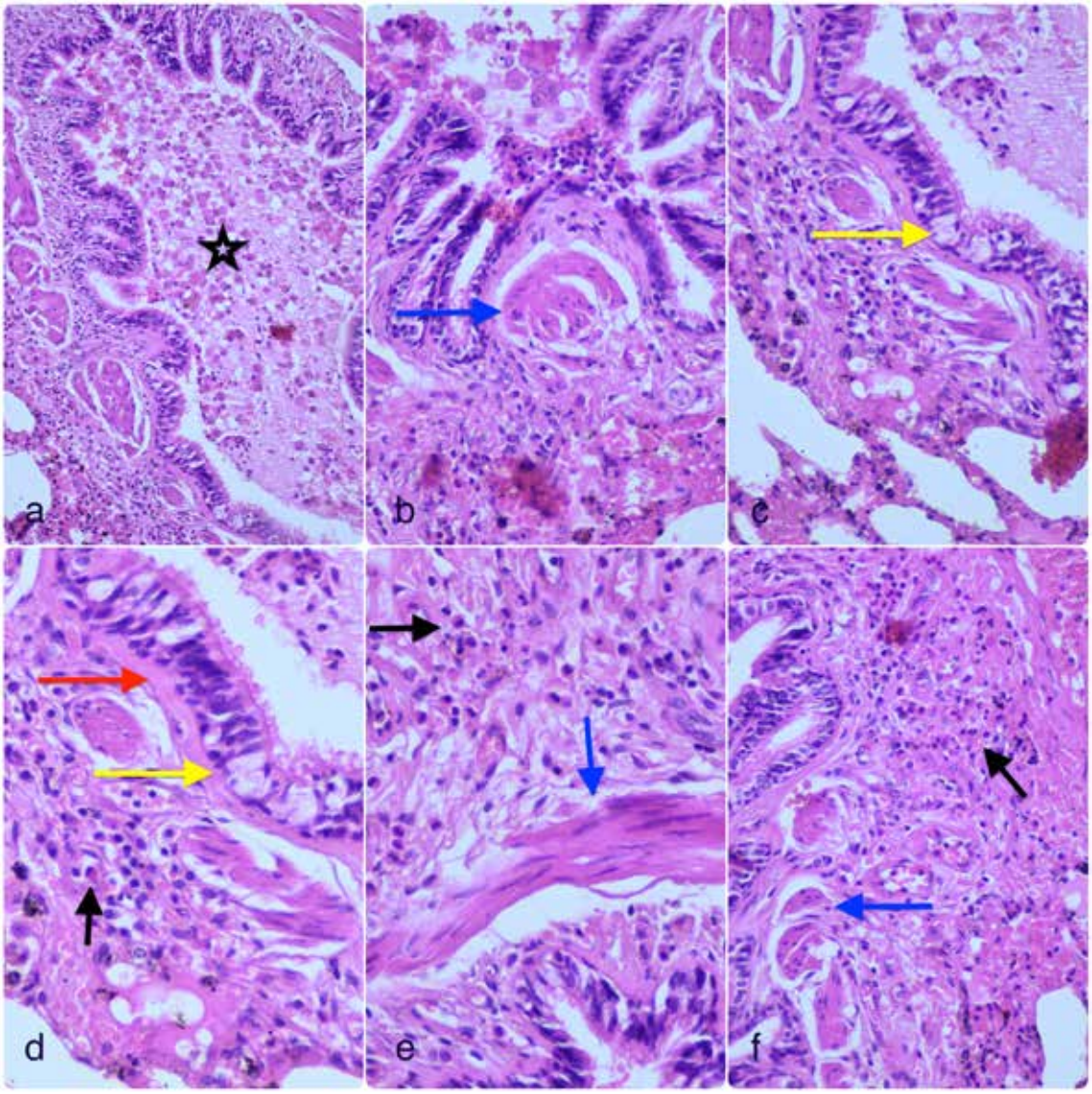

Figure 2.2
Asthma,
a,b,c,d,e,f,) (H&E, x200, x400, x400, x600, x600, x400).
Goblet cell metaplazisi (yellow arrow) due to epithelial irritation are observed in the bronchioles. Smooth muscle hyperplasia (blue arrow), thickening of the basement membranes (red arrow), and mixed inflammatory cell infiltration rich in eosinophils (black arrow) are observed in the peribronchiolar areas. There is a mucus plug in the bronchiolar lumen (asterisk).

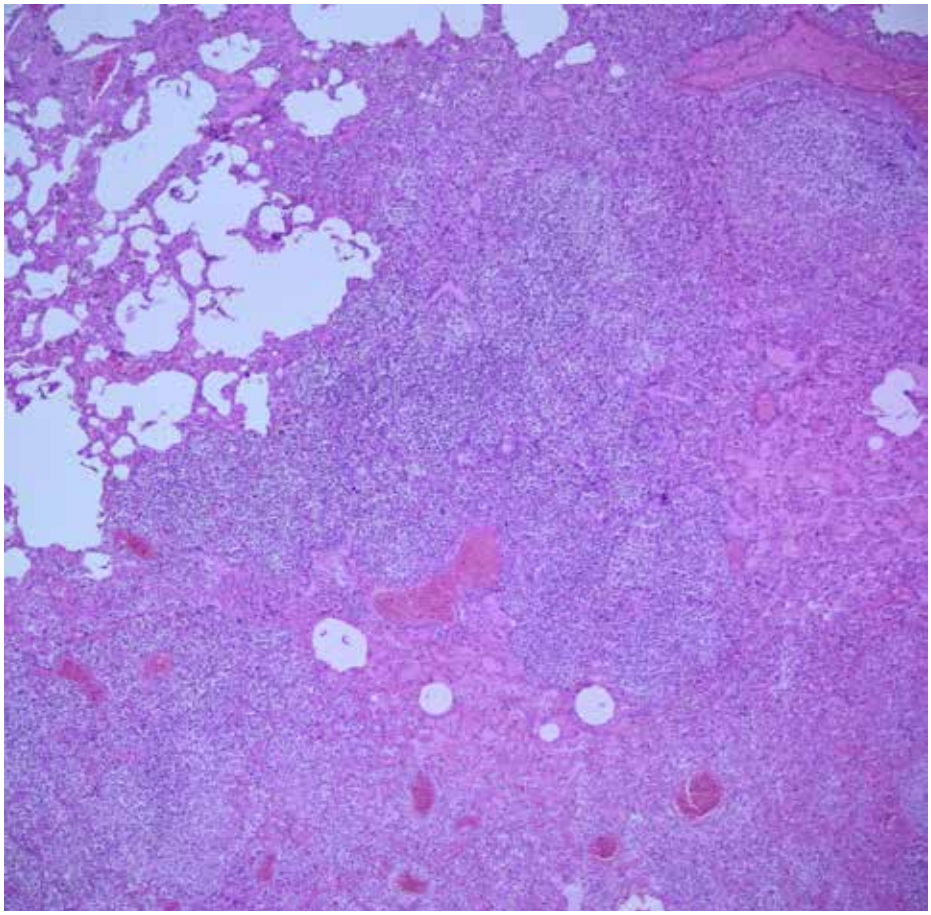

Figure 2.3
Acute pneumonia, (H&E, x40).
Dense neutrophil infiltration is observed in the alveolar lumens.

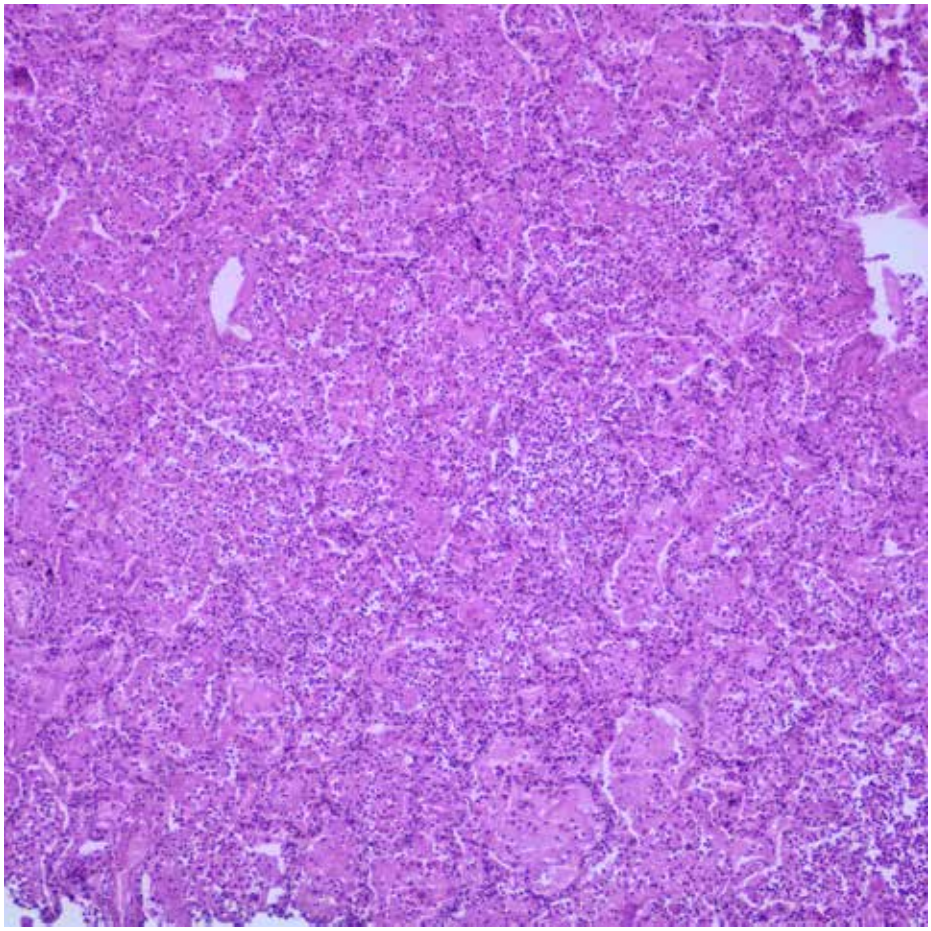

Figure 2.4
Acute pneumonia, (H&E, x100).
At higher magnification exudation of serum and neutrophils can be observed in the alveolar lumens.

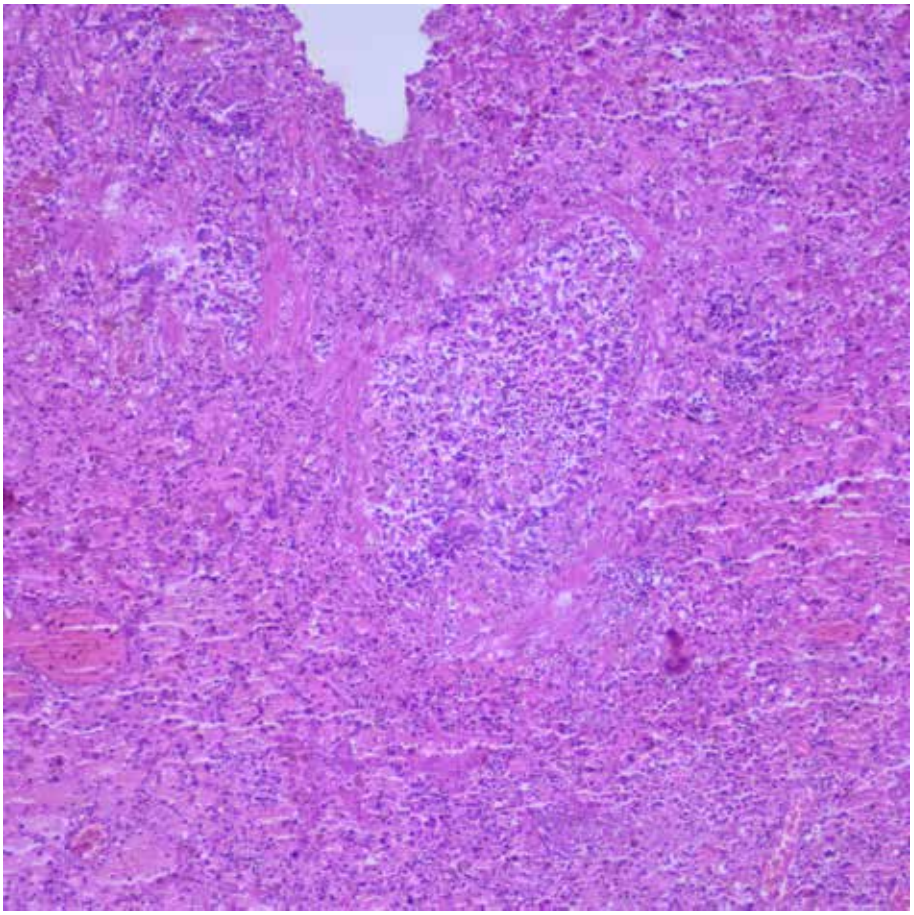

Figure 2.5
Acute bronchopneumonia, (H&E, x100). Exudation of serum and neutrophils is observed in the alveolar lumens, along with neutrophils infiltrating the bronchial epithelium and filling the lumen.

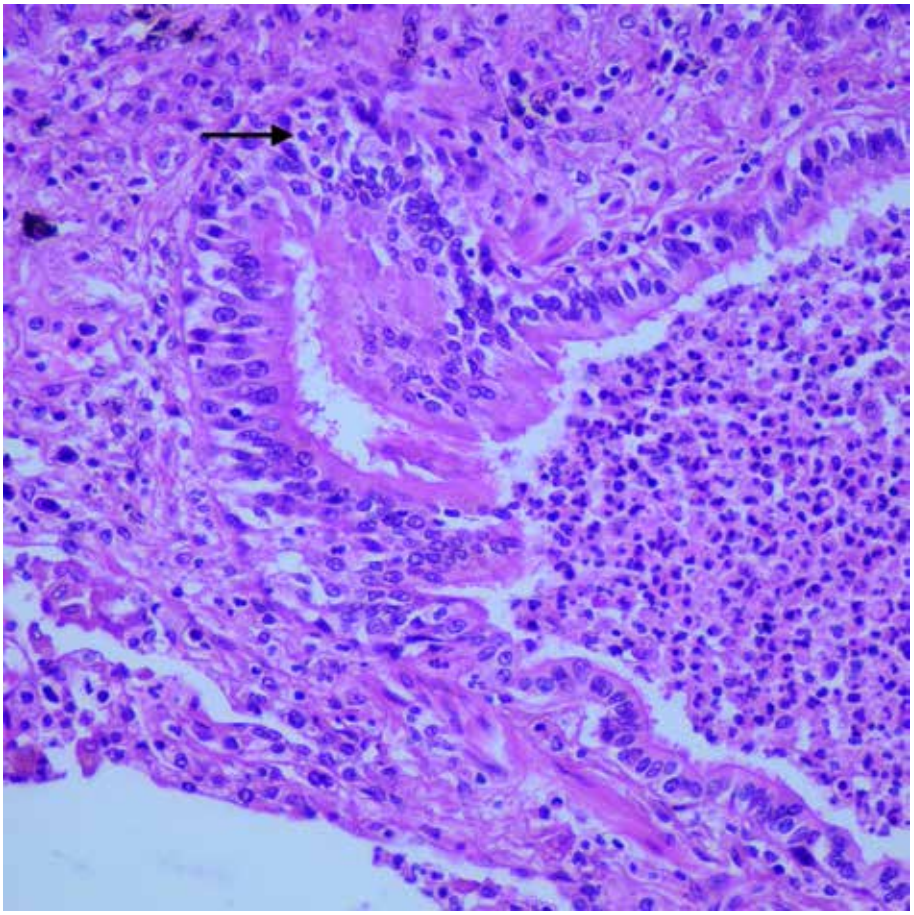

Figure 2.6
Acute bronchitis, (H&E, x400). At higher magnification, neutrophils infiltrating the bronchial epithelium (arrow) and filling the alveolar lumen.

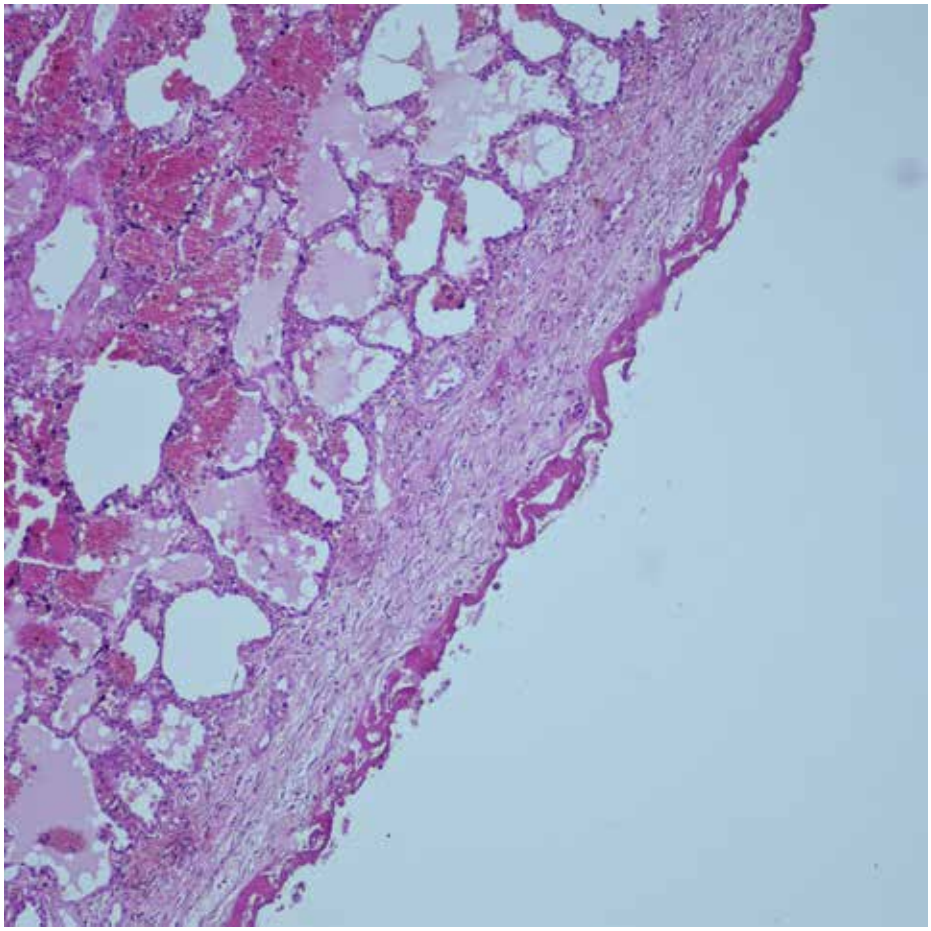

Figure 2.7
Fibrinous pleuritis, (H&E, x100). Bright eosinophilic fibrin exudation is observed in the pleura. Pleural reaction (pleuritis) may resolve or organize into fibrous thickening and adhesions.

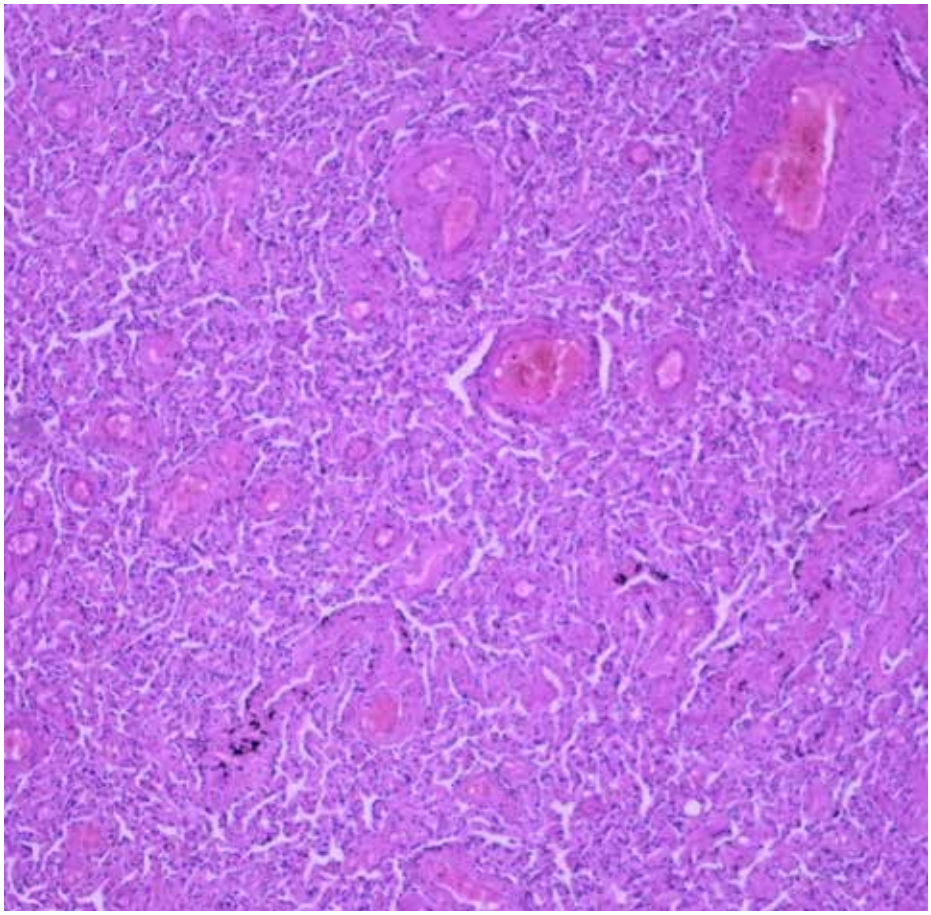

Figure 2.8
Atelectasis, (H&E, x100). At the microscopic view, a collapsed appearance of alveolar spaces is observed.

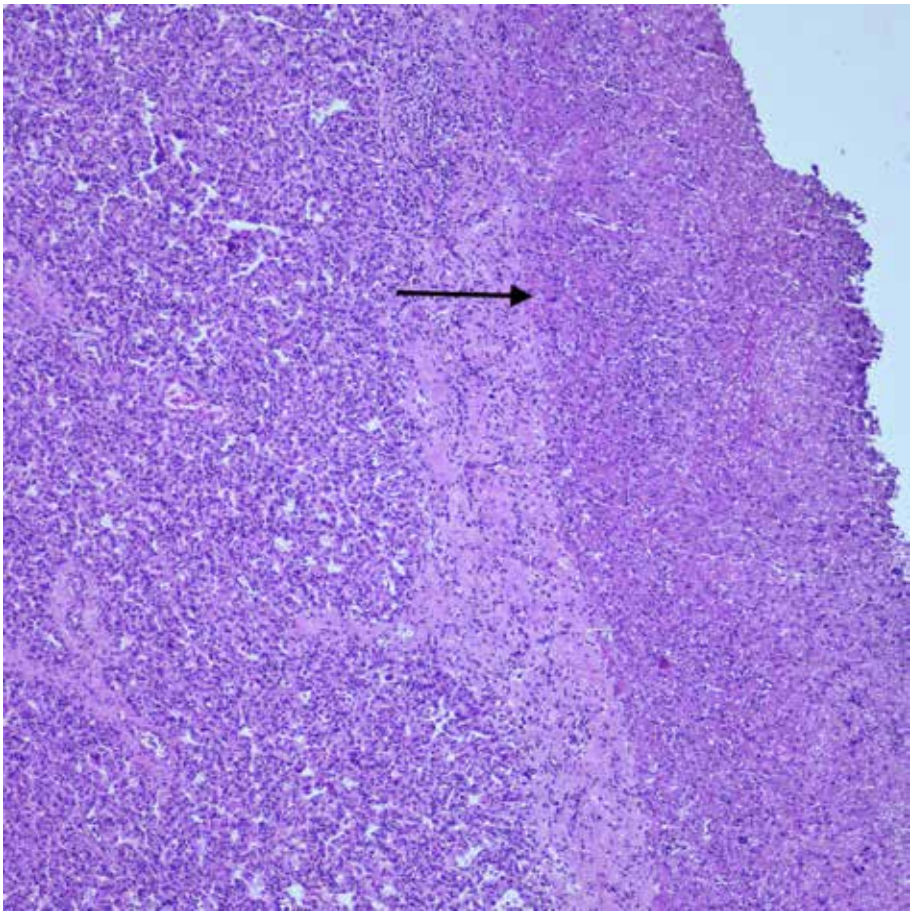

Figure 2.9
Atelectasis, purulent fibrinous pleuritis, (H&E, x100). Alveolar spaces collapsed. Neutrophil and fibrin exudation (arrow) are observed in the pleura.

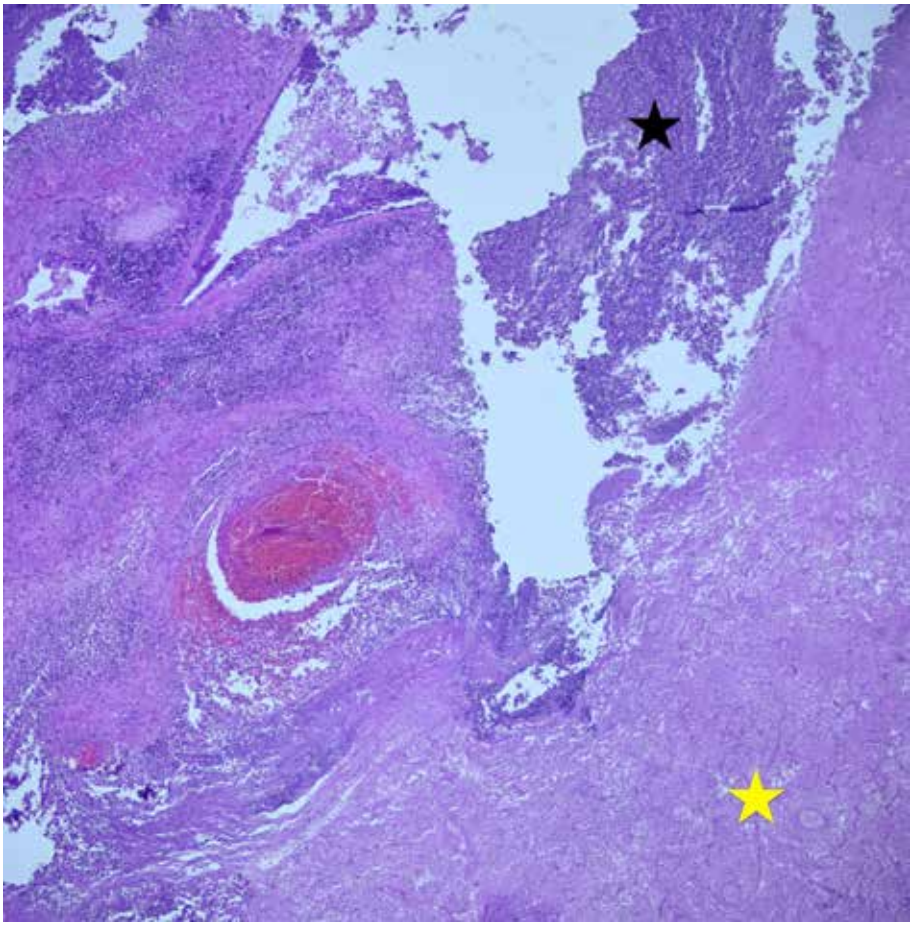

Figure 2.10
Lobular pneumonia associated with abscess and necrotic areas, (H&E, x40). The alveolar septa are destroyed, and an abscess (black asterisk) formation consisting of neutrophils and nuclear debris is observed, surrounded by necrotic lung tissue (yellow asterisk).

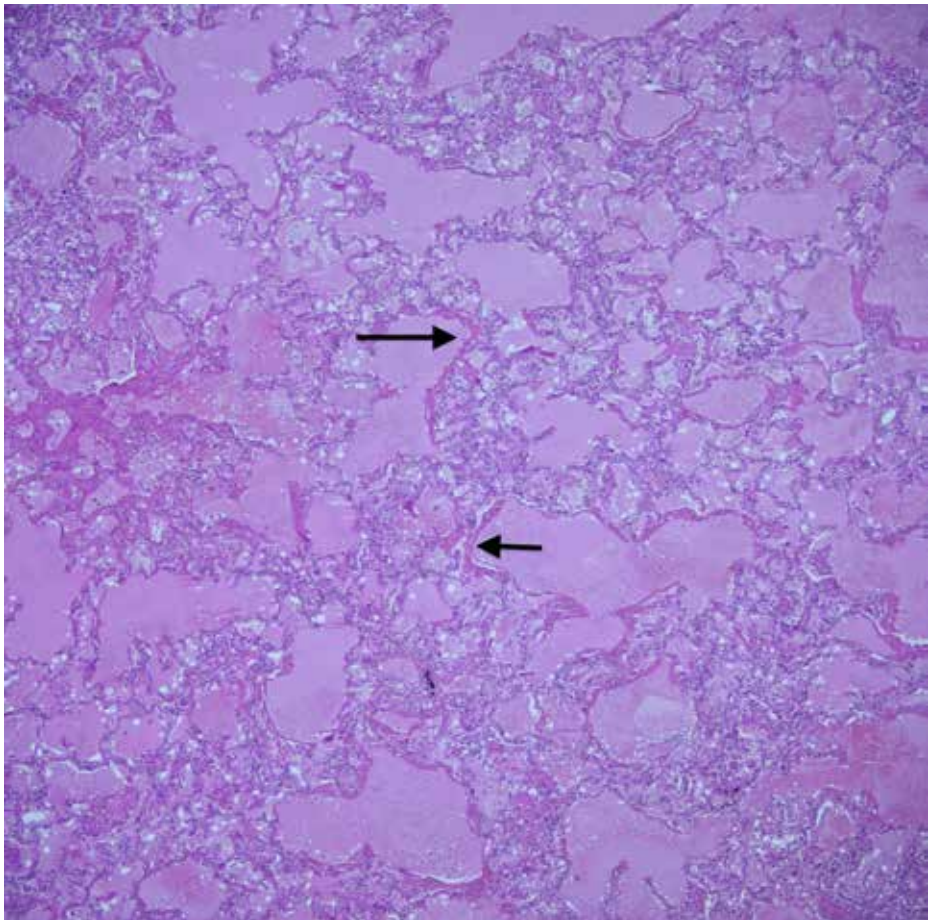

Figure 2.11
Pulmonary edema and formation of hyaline membrane in the lung, (H&E, x40).
Serum exudation is observed in the alveolar lumens, and bright pink hyaline membranes are seen in some alveolar walls in a lining pattern (arrows).

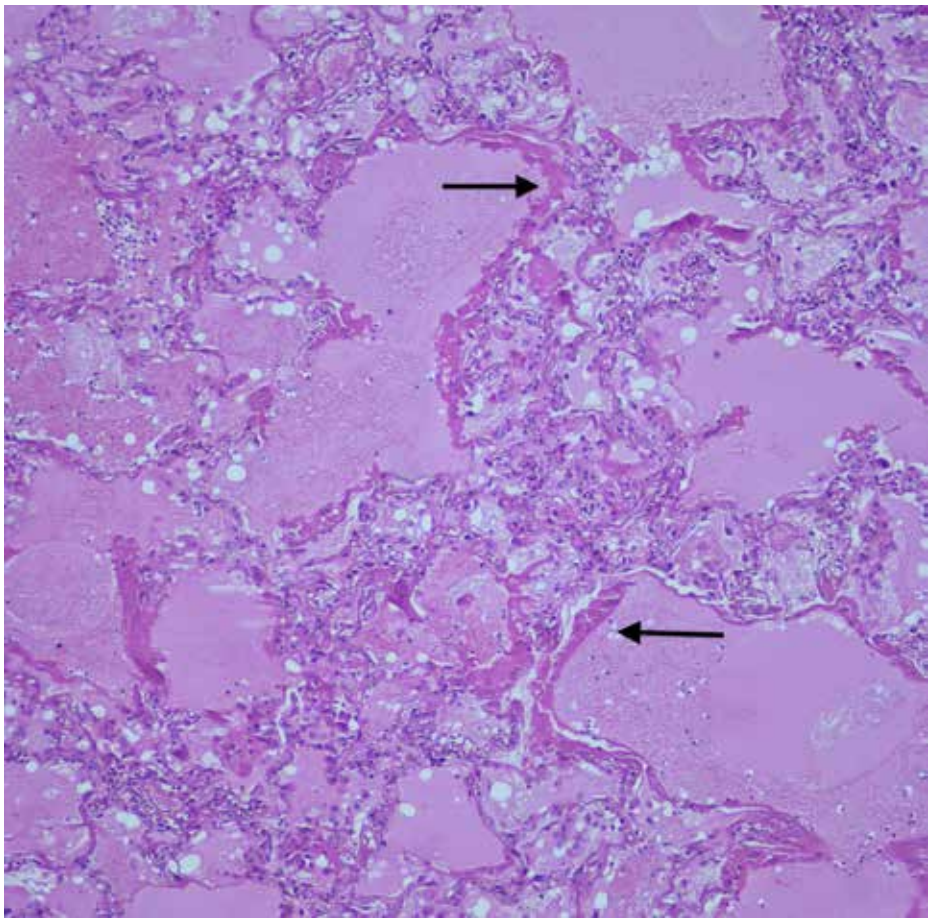

Figure 2.12
Pulmonary edema and formation of hyaline membrane in the lung, (H&E, x100).
At higher magnification, edema in alveolar lumens and hyaline membrane formation in the alveolar walls (arrows).

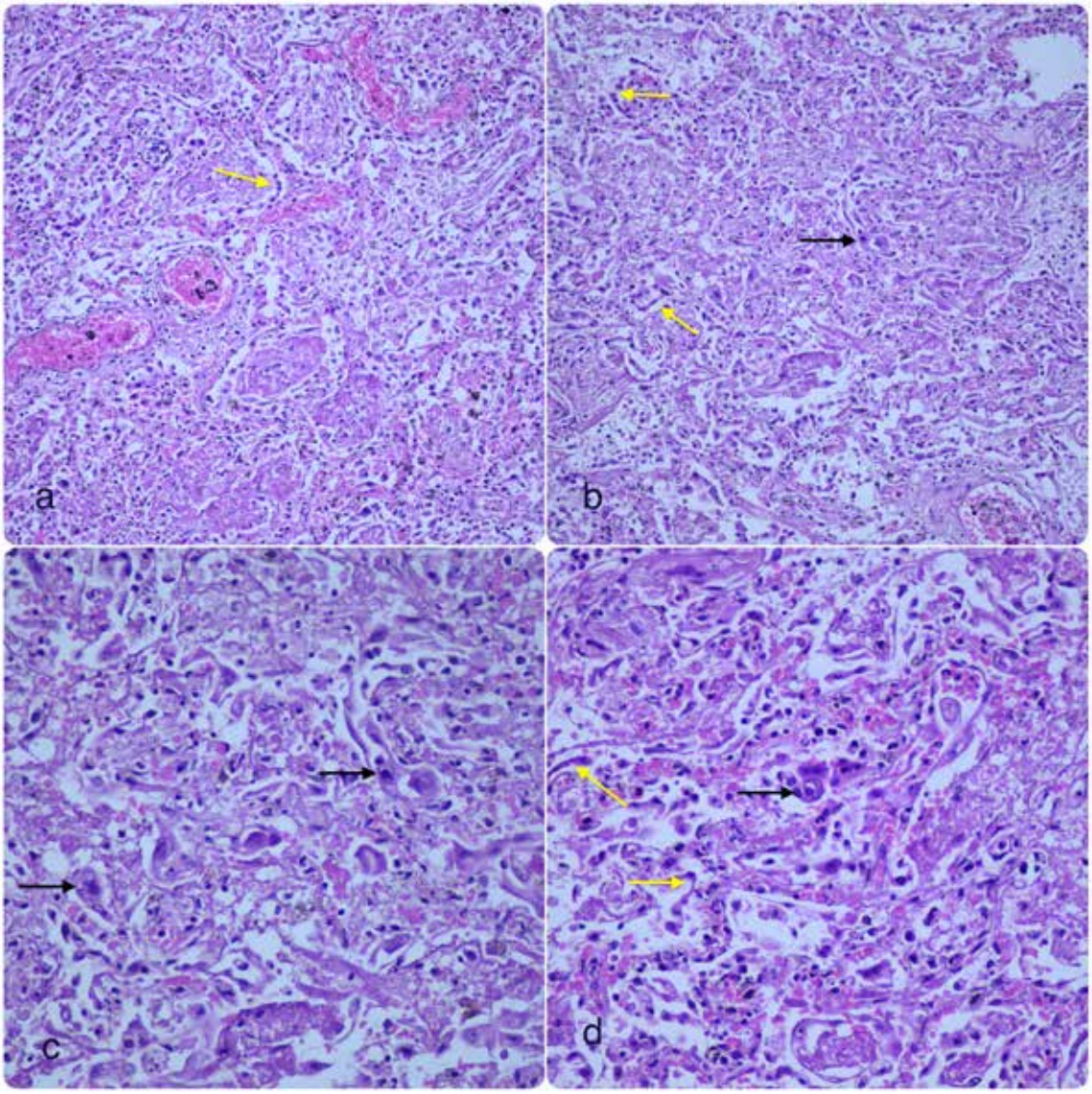

Figure 2.13
CMV pneumonia,
a) (H&E, x200). In interstitial pneumonias, the inflammatory reaction is primarily limited to the alveolar walls. While alveolar exudate is not observed, cytoplasmic and intranuclear viral inclusions indicative of the cytopathic effect of viruses may be seen. In the early stage of diffuse alveolar damage associated with these infections, the alveolar walls are lined with hyaline membranes. During the organization phase of injury, type 2 epithelial cell hyperplasia (yellow arrow) and intraalveolar fibrosis develop.
b) (H&E, x200). Type 2 pneumocyte hyperplasia (yellow arrows) and viral cytopathic effect-related viral inclusions (black arrow) are observed in the alveolar walls.
c) (H&E, x400). At higher magnification, viral inclusions specific to CMV infection (black arrows).
d) (H&E, x400). At higher magnification, viral inclusions specific to CMV infection (black arrows) and type 2 epithelial cell hyperplasia in the alveolar walls (yellow arrows)
[CMV was verified by rt-PCR at the postmortem lung tissues in all CMV cases in this book].

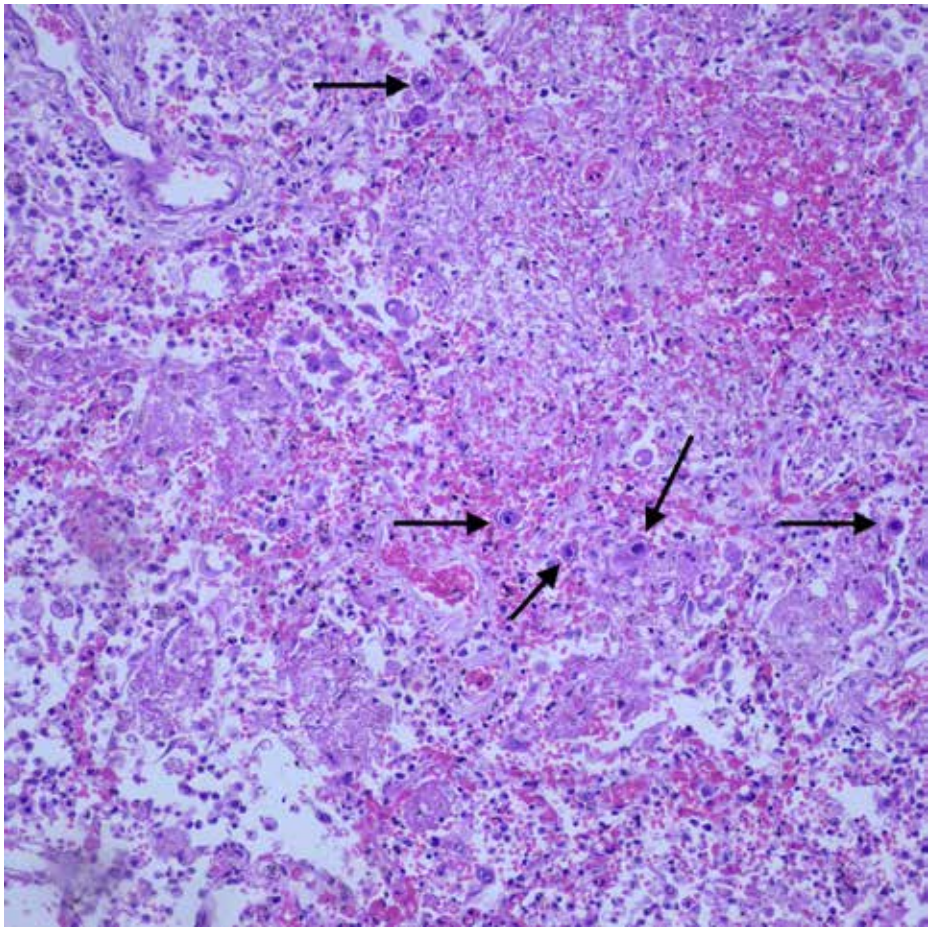

Figure 2.14
CMV pneumonia, (H&E, x200).
In CMV infection, endothelial cells, mesenchymal cells, and macrophages are most commonly affected. The affected cells can enlarge up to 4 times their normal size. They exhibit large pleomorphic nuclei containing basophilic intranuclear inclusions (Cowdry bodies) surrounded by clear halos (owl's eye appearance). Also, they contain red coarse intracytoplasmic granules. In the microscopic view, basophilic intranuclear inclusions surrounded by clear halos (arrows) are observed.

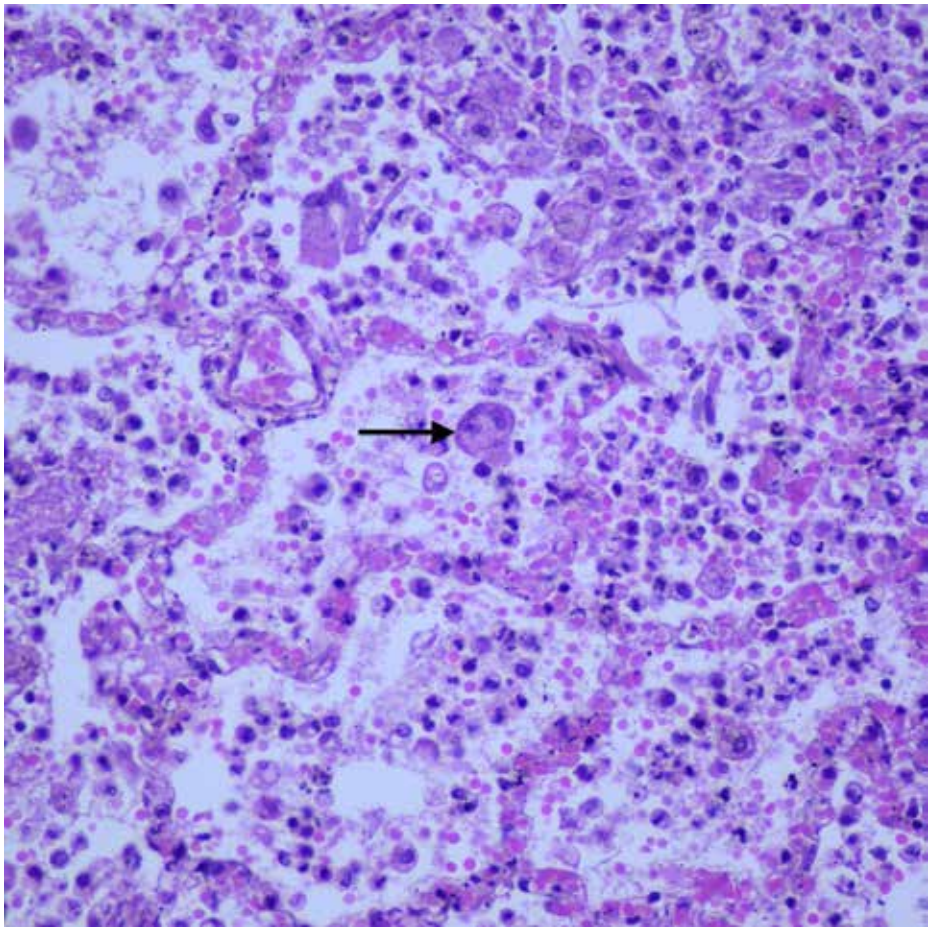

Figure 2.15
CMV pneumonia, (H&E, x400).
In viral pneumonias, histiocytic-origin multinucleated syncytial giant cells (arrow) can be seen due to viral cytopathic effect.

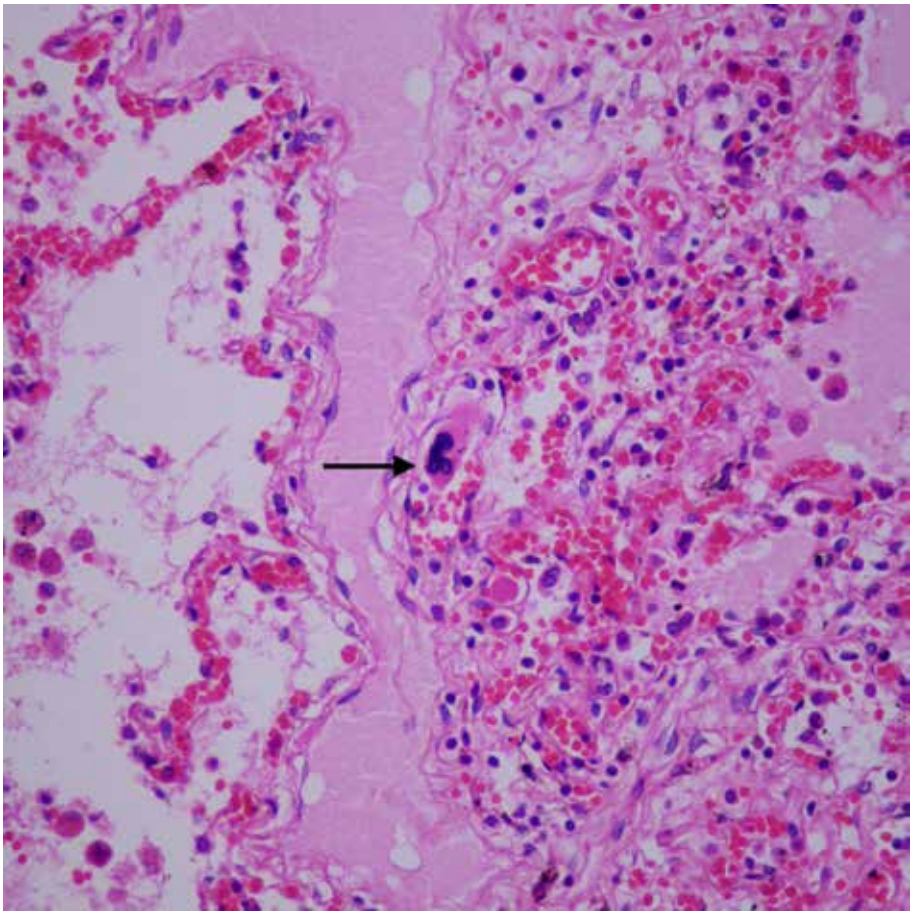

Figure 2.16
Megakaryocytes in the pulmonary capillary lumen, (H&E, x400). In some atypical pneumonias, megakaryocytes and fibrin thrombi can be observed in pulmonary vascular lumens. Megakaryocytes can be detected in the lungs in diffuse alveolar damage, shock, sepsis, and burns. In SARS-CoV-2 infection, megakaryocytes are found in the capillary vascular lumens of the lungs. This condition is associated with activation of the coagulation system and thrombus formation in distal pulmonary vessels. In pulmonary embolism, we can observe interstitial megakaryocytes. In the microscopic view, a megakaryocyte in the capillary vascular lumen is shown (arrow).

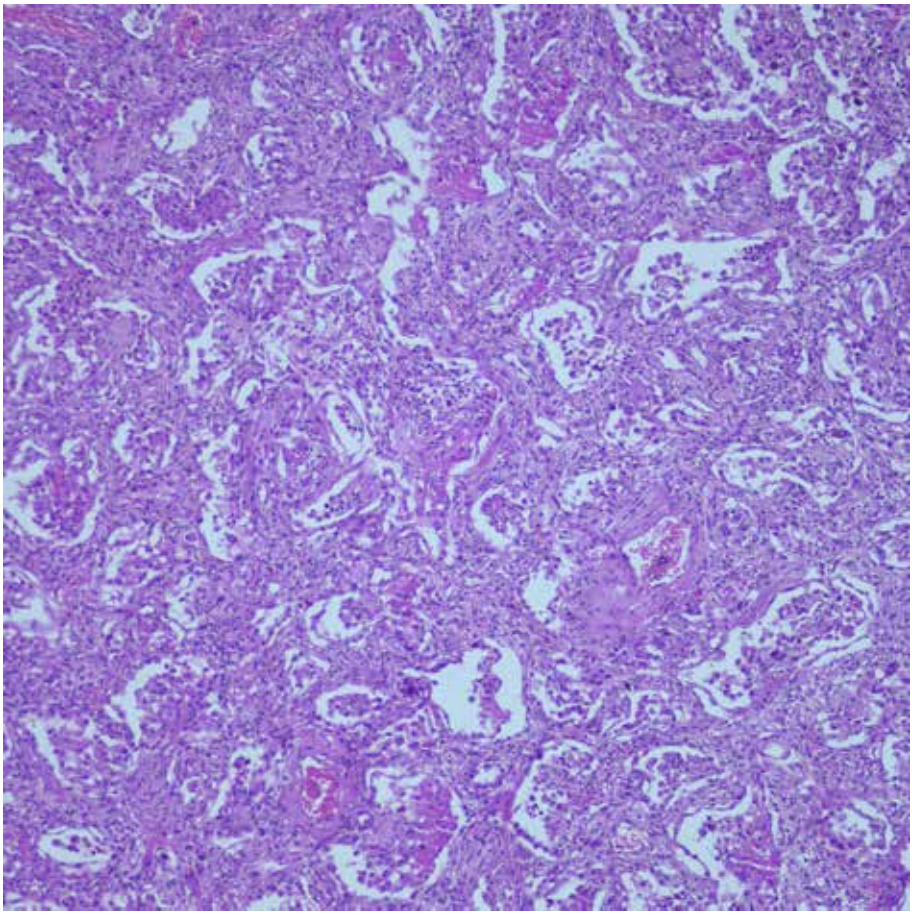

Figure 2.17
Diffuse alveolar epithelial damage in the late proliferative-fibrotic stage, (H&E, x100). Diffuse alveolar epithelial damage consists of early exudative (acute) phase, subacute proliferative (organizing) phase, and late fibrotic phase. The exudative phase is most prominent in the first week. Approximately one week after the injury, proliferative phase begin. Type 2 pneumocyte hyperplasia and fibroblastic proliferation is detected in the interstitium and alveolar spaces. Collagen accumulation is minimal at this stage. While in some cases diffuse alveolar epithelial damage resolves without significant sequelae, in others, honeycomb appearance due to fibrosis is observed in the lungs.

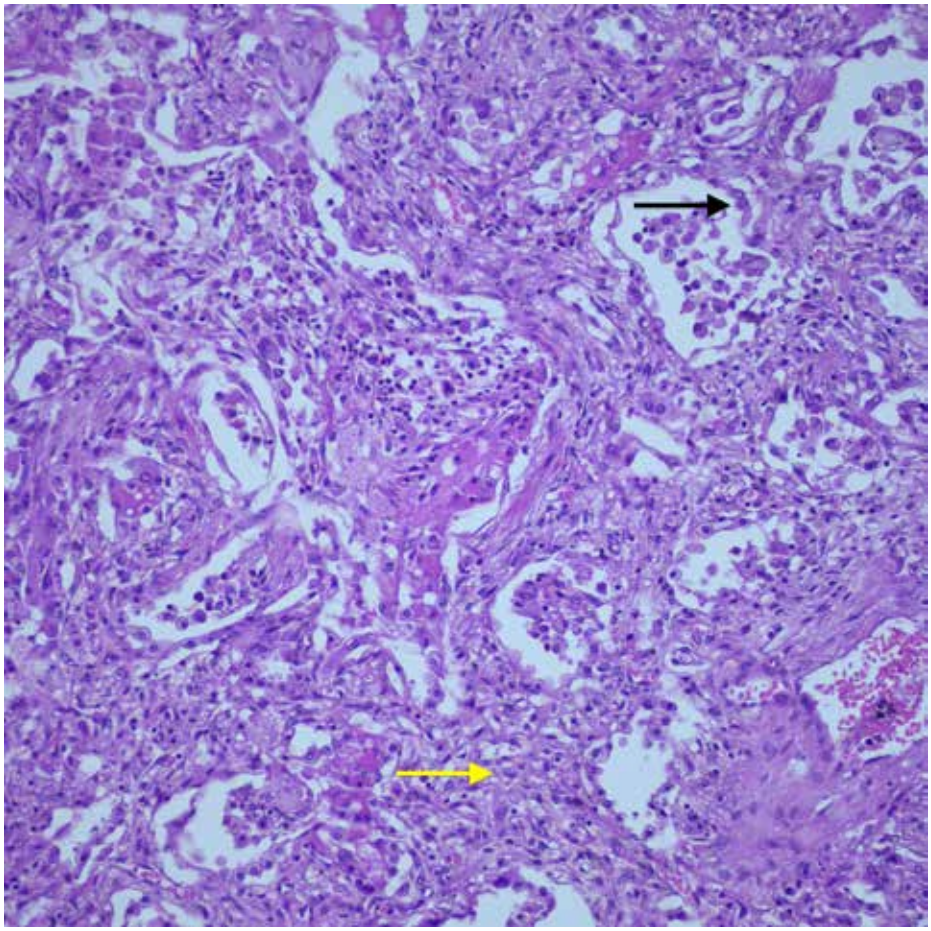

Figure 2.18
Diffuse alveolar epithelial damage in the late proliferative-fibrotic stage, (H&E, x200). At higher magnification, type 2 pneumocyte hyperplasia (black arrow) and fibroblastic proliferation in the interstitium (yellow arrow) are observed.

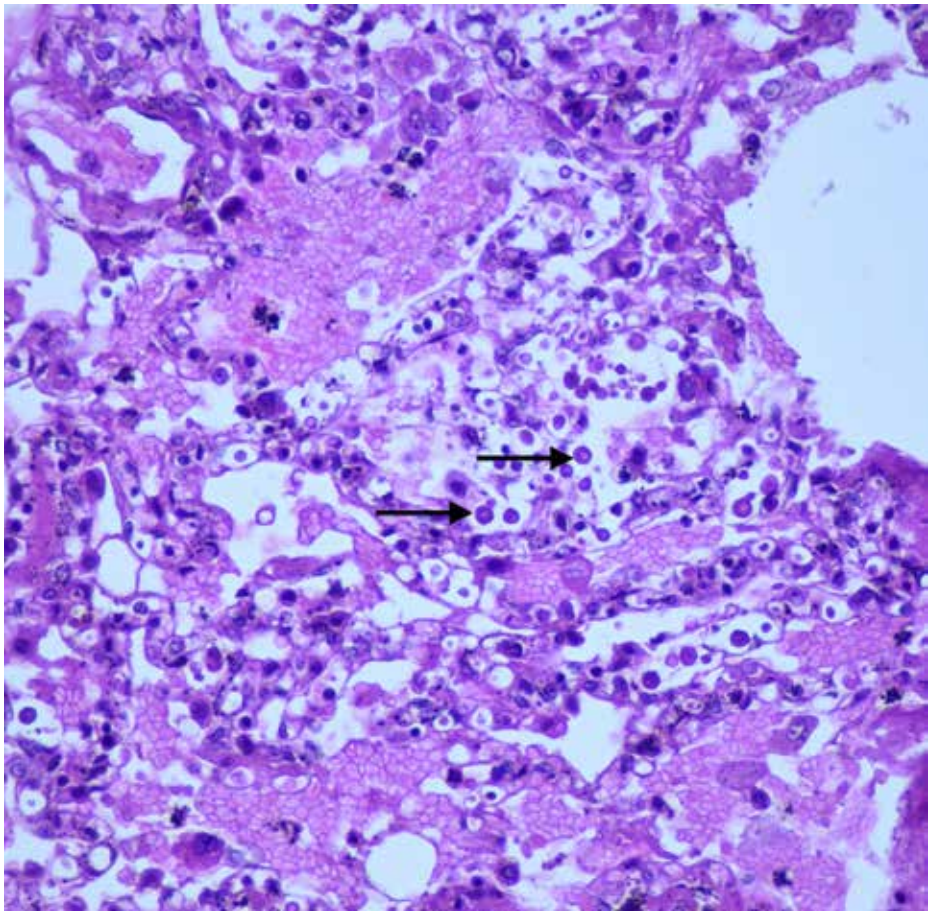

Figure 2.19
Fungal pneumonia, (H&E, x400). While most fungal infections presented as granulomas, in others, only minimal changes, interstitial pneumonia, and intraalveolar foamy material may be observed. The findings detected in most cases depend on the individual's immune status and the type of fungal organism. In the microscopic view, cryptococcal yeast forms (arrows) are observed in the interstitium and alveolar lumens.

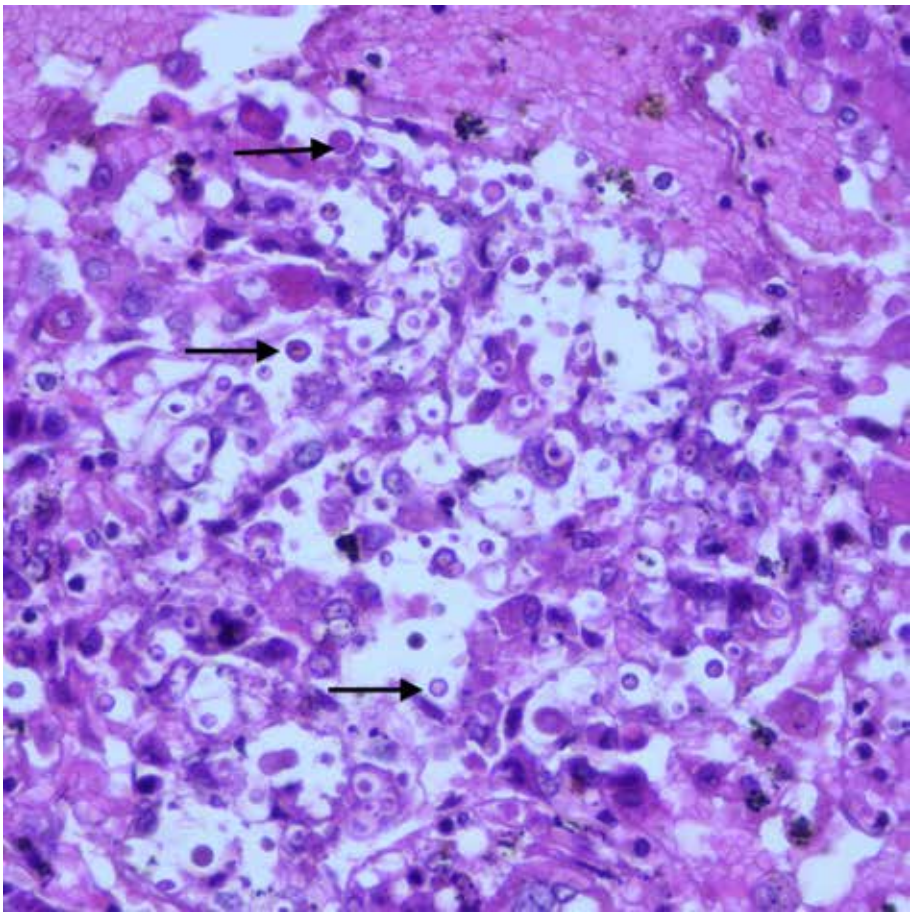

Figure 2.20
Fungal pneumonia,
(H&E, x600).
At higher magnification, cryptococcal yeast forms (arrows) are seen.

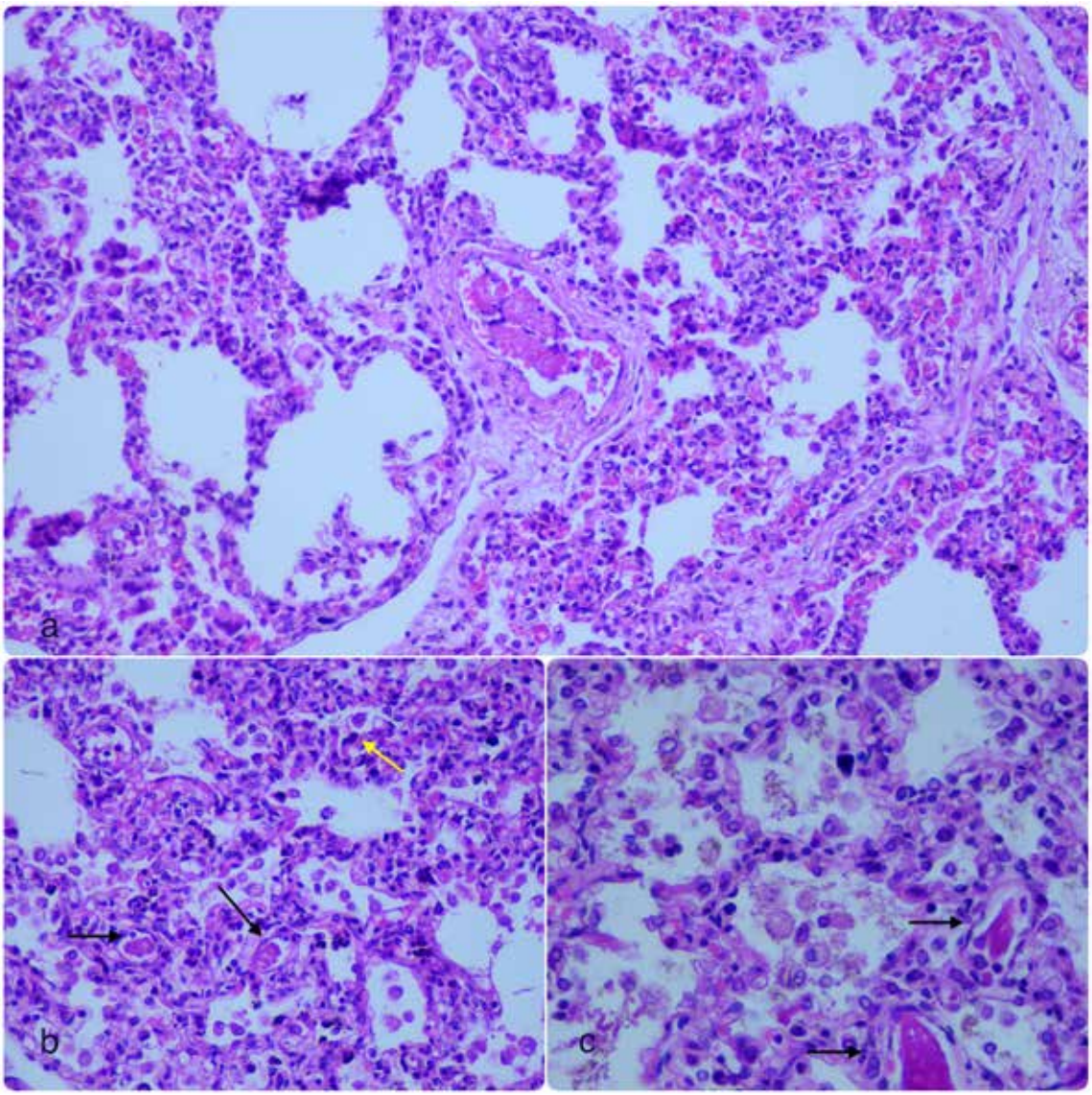

Figure 2.21
RSV (Respiratory Syncytial Virus) pneumonia,
a) (H&E, x200). RSV can cause severe infections, particularly in early childhood, resembling influenza. In the microscopic view, a case with RSV infection detected by PCR demostrates a fibrin thrombus in the vascular lumen.
b) (H&E, x400). RSV infection and resultant DIC (disseminated intravascular coagulation), numerous capillary vascular lumens show fibrin thrombi (black arrows), and smudge-like cells due to viral cytopathic effect (yellow arrow) are observed.
c) (H&E, x600). At higher magnification, fibrin thrombi (black arrows) in capillary vascular lumens.
[RSV was verified by rt-PCR at the postmortem lung tissues in this case].

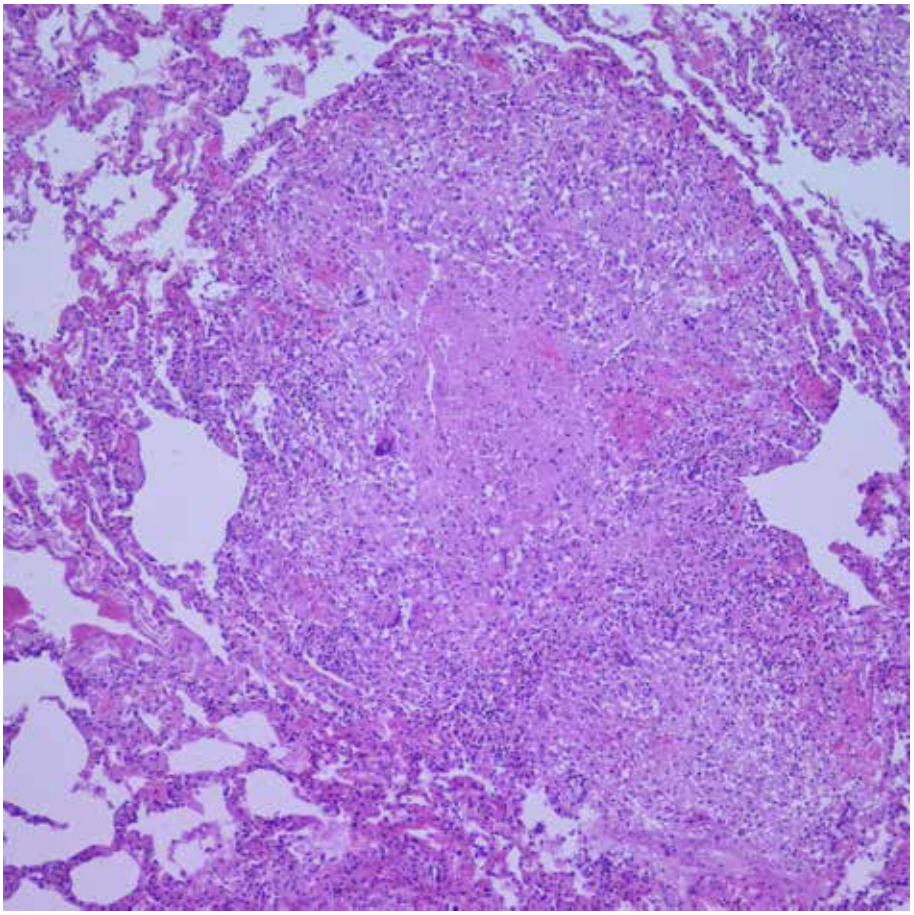

Figure 2.22 Tuberculosis granuloma, (H&E, x100). In the microscopic view, a tuberculosis granuloma is seen with central caseous necrosis surrounded by epithelioid histiocytes, giant cells, and lymphocytes.

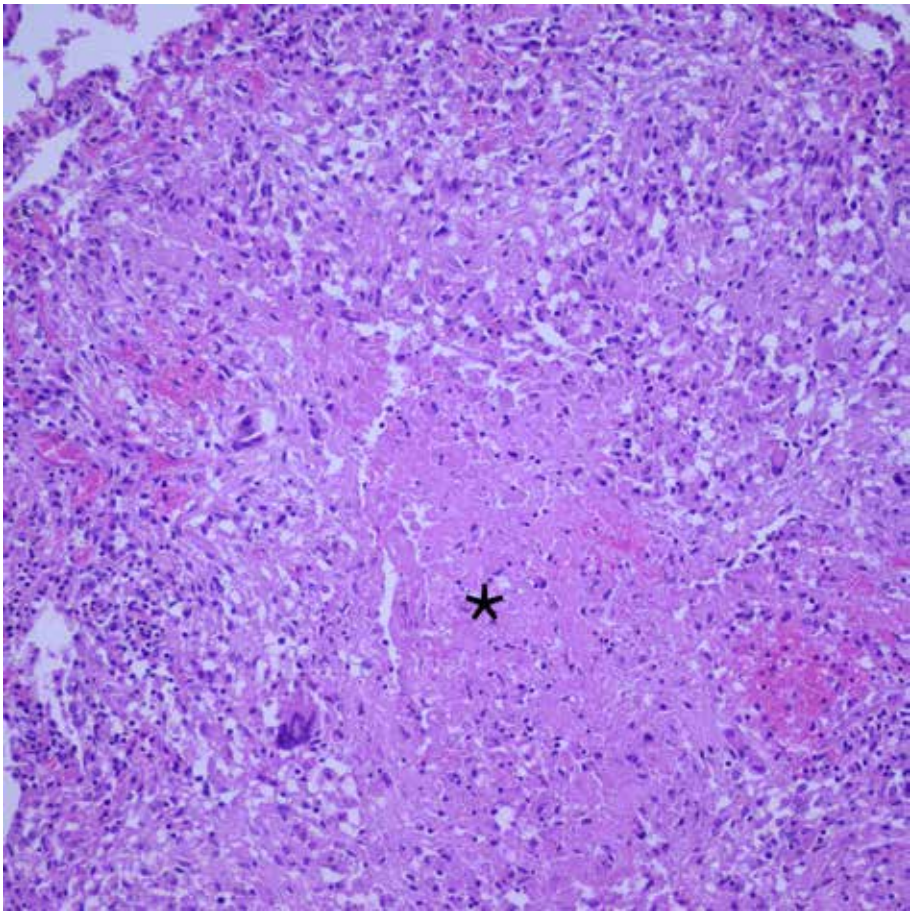

Figure 2.23 Tuberculosis granuloma, (H&E, x200). At higher magnification, a tuberculosis granuloma is observed with central caseous necrosis (asterisk) surrounded by epithelioid histiocytes, giant cells, and lymphocytes.

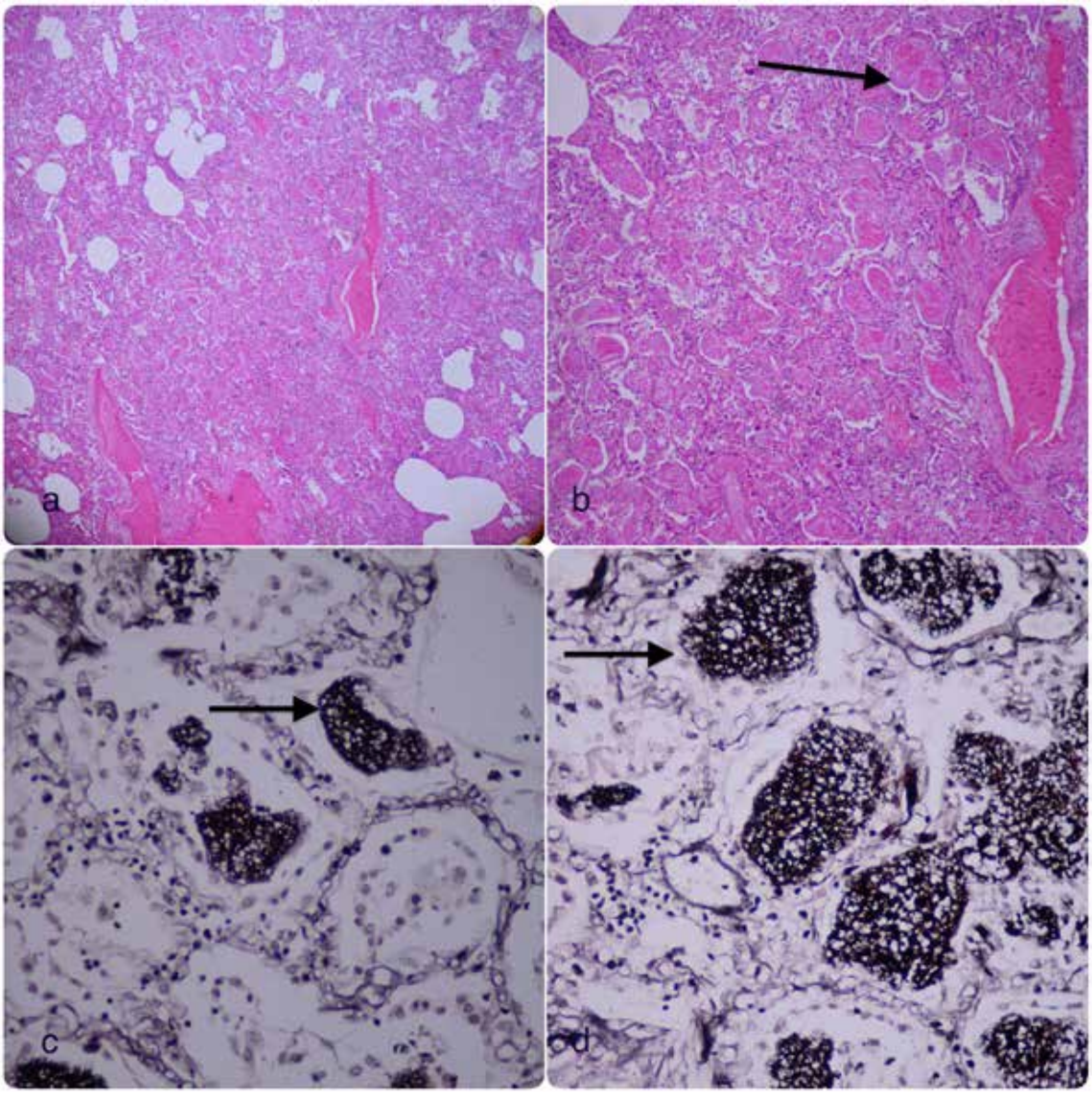

Figure 2.24
Pneumocystis Jiroveci pneumonia,
a) (H&E, x40). In people with HIV infection, acellular eosinophilic foamy exudate is observed in the alveolar lumens and thickening with mild mononuclear inflammatory cell infiltration is observed in the interstitium. Pneumocystis jiroveci is the fungus that most commonly causes diffuse alveolar epithelial damage.
b) (H&E, x100). At higher magnification, acellular eosinophilic foamy exudate (arrow) is seen in the alveolar lumens.
c) (Silver Methenamine, x400). Silver stain shows organisms in groups in the alveolar lumens.
d) (Silver Methenamine, x400). Groups of Pneumocystis jiroveci in alveolar lumens with silver stain.

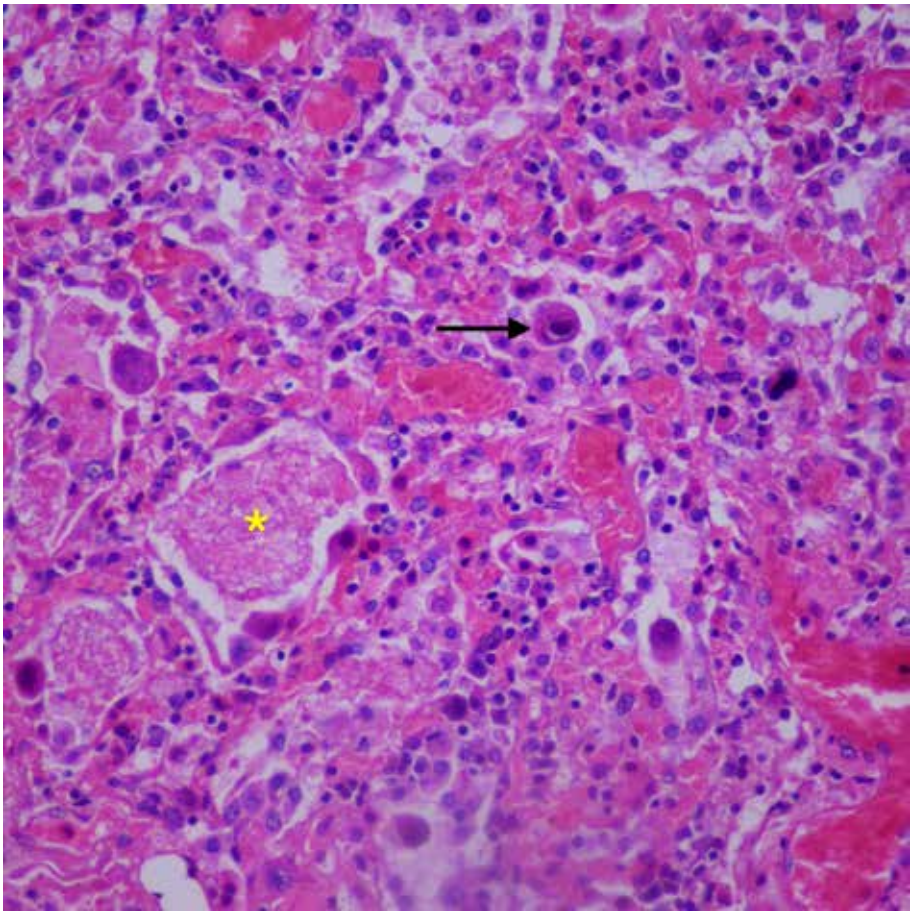

Figure 2.25
Pneumocystis jiroveci and CMV pneumonia (H&E, x400). In the same case with HIV infection, asellular eosinophilic foamy exudate (asterisk) is observed in the alveolar lumens, along with mild mononuclear inflammatory cell infiltration and thickening in the interstitium, and CMV inclusion (arrow).

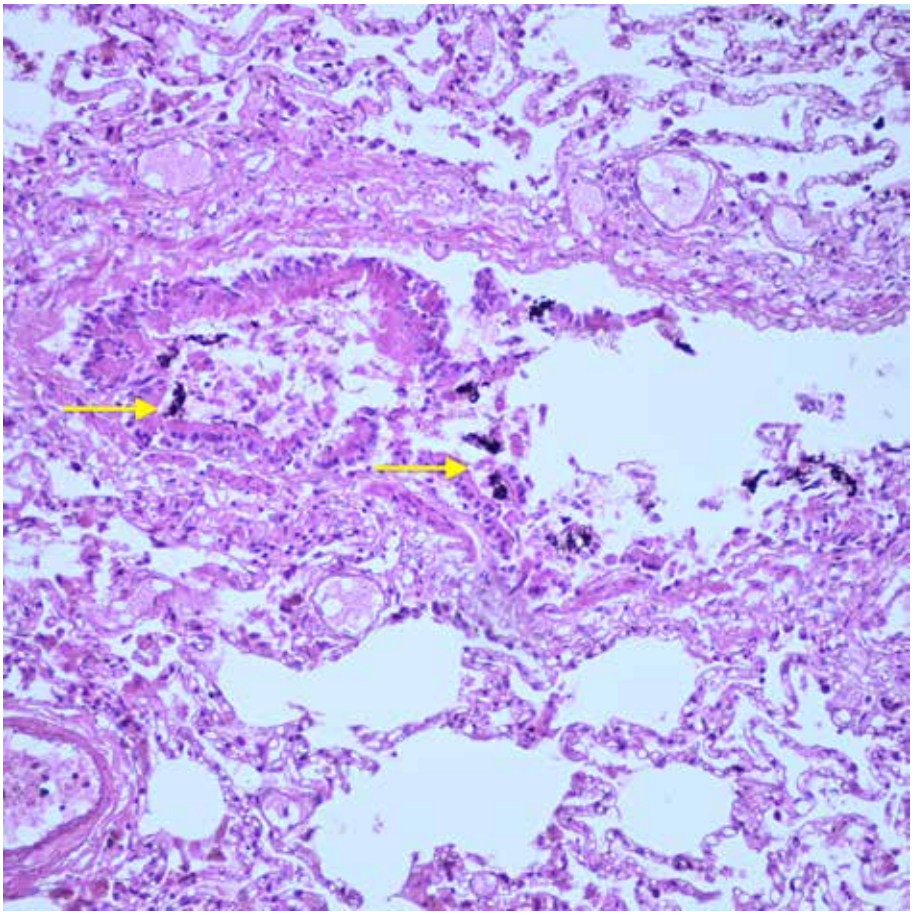

Figure 2.26
Soot in bronchioles, (H&E, x200). Due to inhalation during a fire, soot can be detected in the bronchiolar lumens adjacent to the wall. Soot can reach the oral cavity, nasal cavity and throat passively, even without breathing. However, when soot reaches distal to the vocal cord, it is an indicator of breathing during the fire. In the microscopic view, a black pigmented accumulation (soot) (arrows) adjacent to the surface epithelium is seen in the bronchiolar lumen of a person taken out of the fire environment.

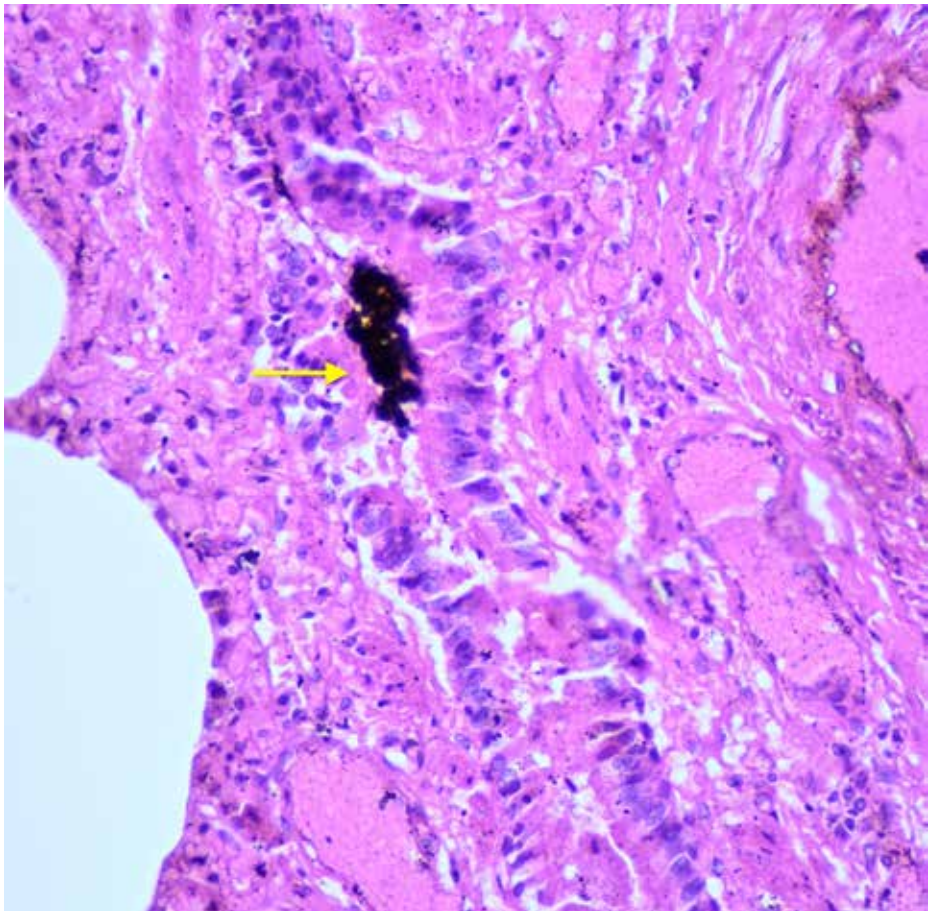

Figure 2.27
Soot in the bronchioles, (H&E, x400).
At higher magnification in the microscopic view, black pigment (soot) accumulation (arrow) can be seen in the bronchiolar lumen.

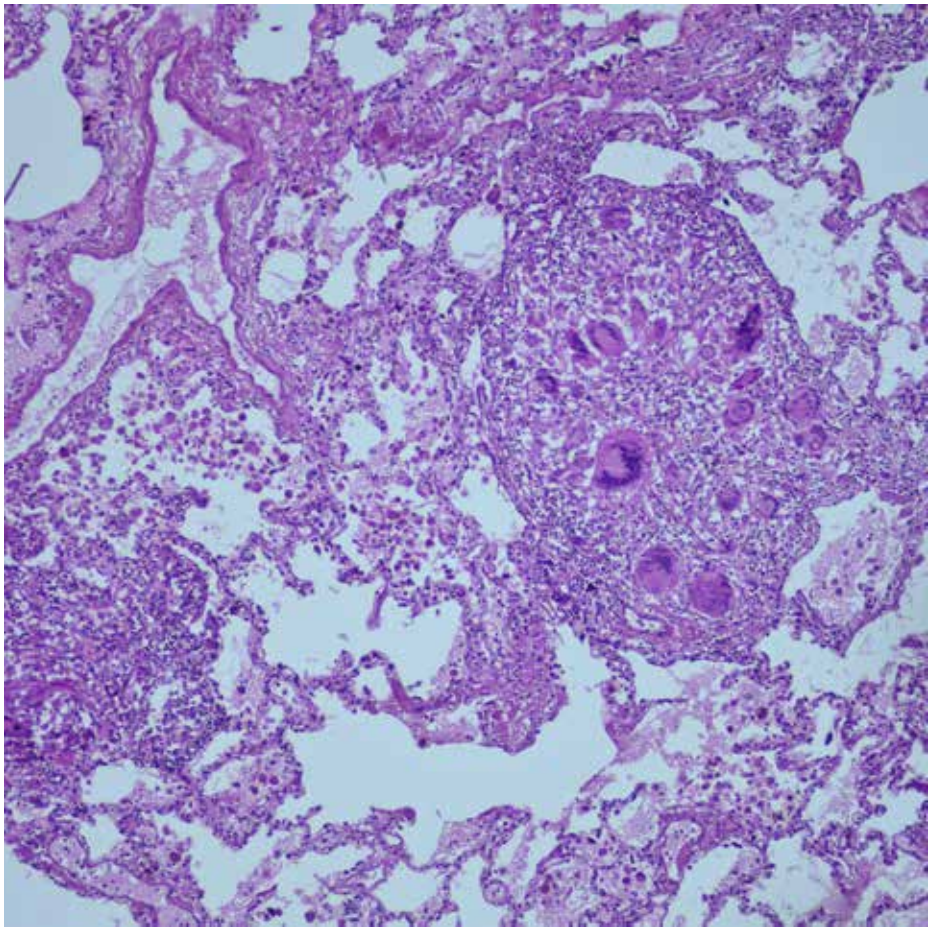

Figure 2.28
Foreign body granuloma, (H&E, x100).
A foreign body granuloma is observed in the lung.

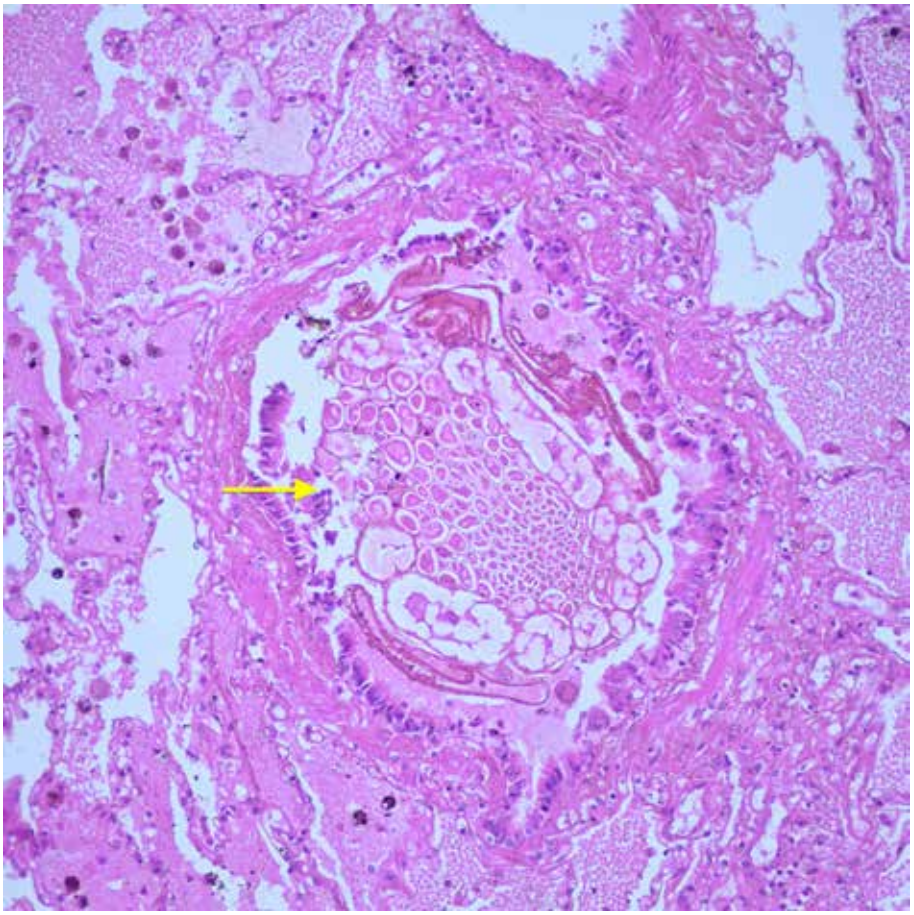

Figure 2.29
Aspiration of food in the bronchiolar lumen, (H&E, x200). The microscopic view shows food (vegetable material) aspiration (arrow) in the bronchiolar lumen.

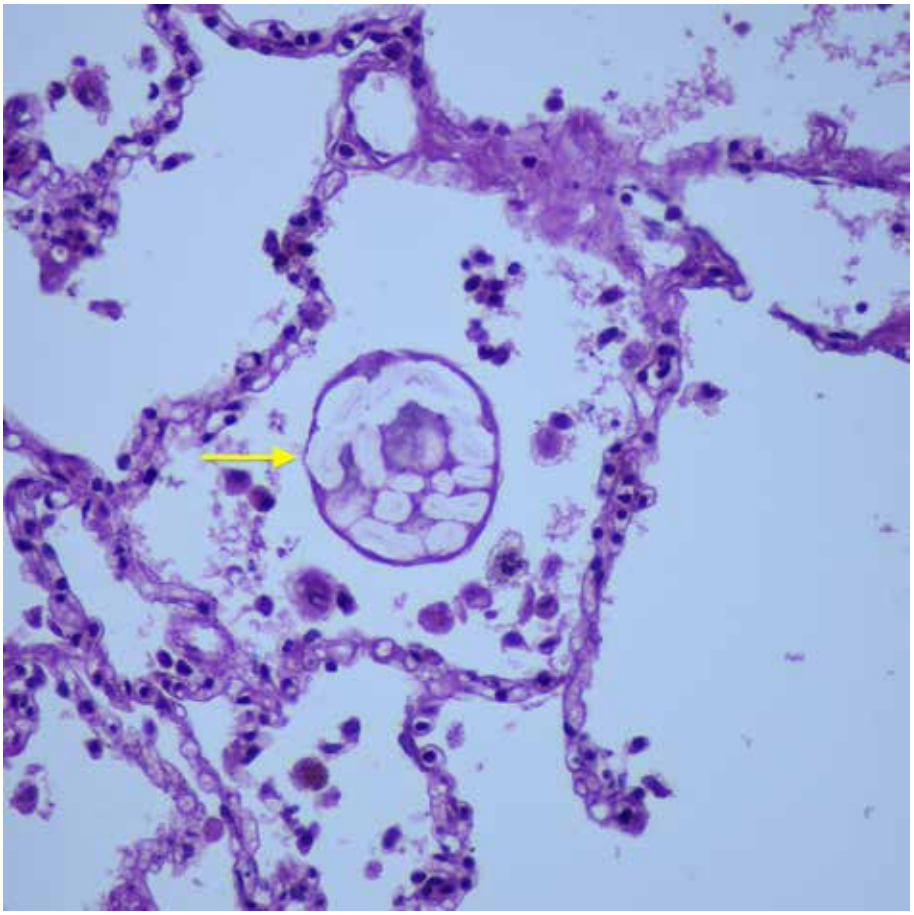

Figure 2.30
Food aspiration in the alveolar lumen, (H&E, x400). The microscopic view demostrates food (vegetable material) aspiration (arrow) in the alveolar lumen. The absence of an inflammatory reaction in this image indicates that aspiration is a terminal or preterminal event.

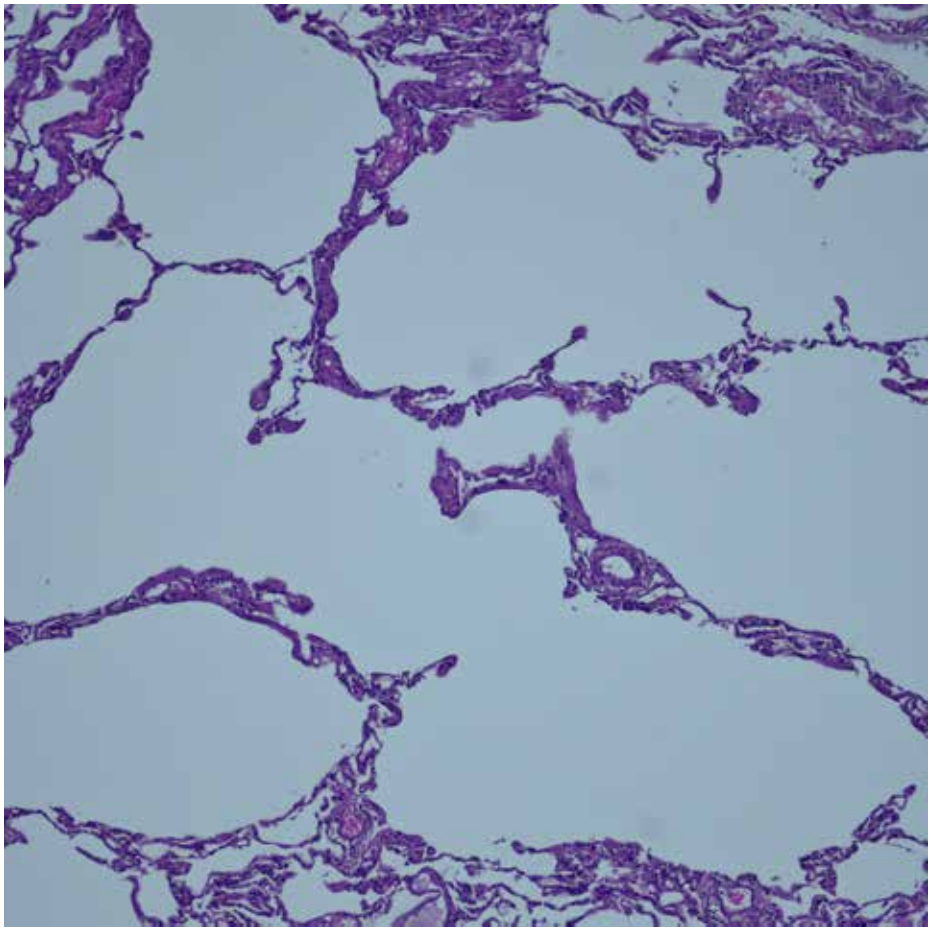

Figure 2.31
Emphysema, (H&E, x100). Emphysema is described as abnormal expansion of the air spaces distal to the terminal bronchioles with minimal alveolar fibrosis. The microscopic view demostrates emphysematous changes due to fragmentation and expansion of the alveolar walls.

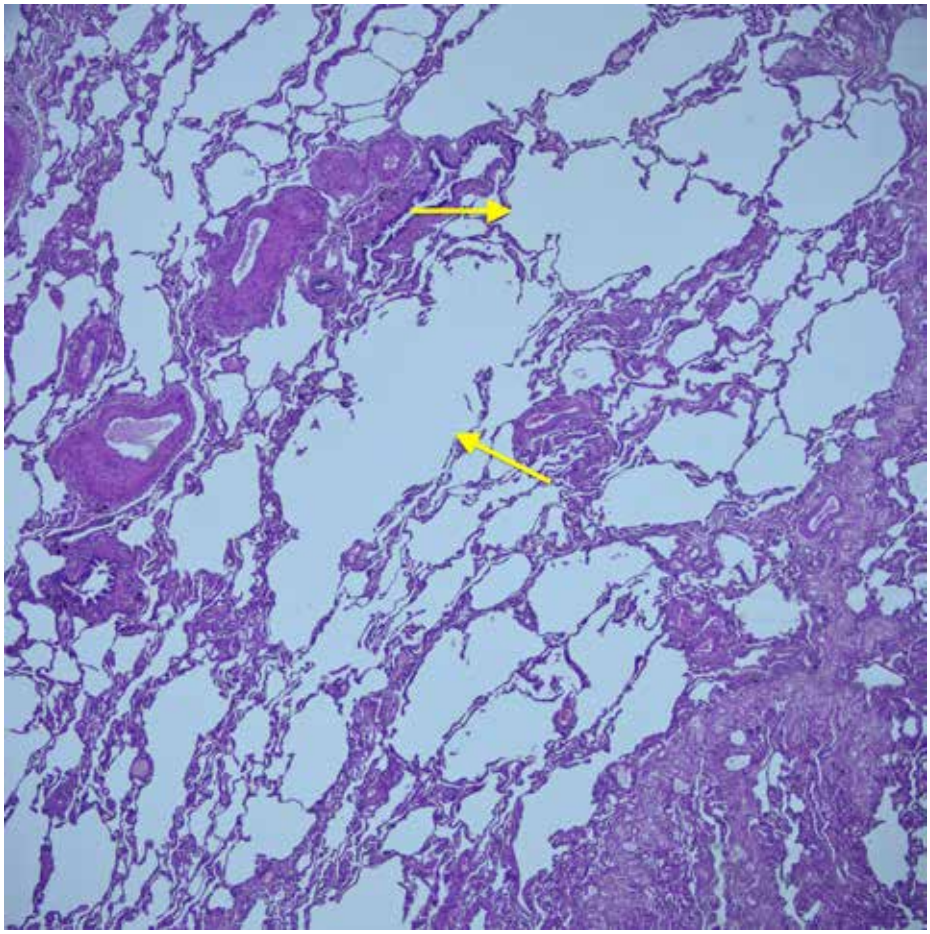

Figure 2.32
Emphysema, (H&E, x40). At lower magnification, emphysematous changes due to fragmentation and expansion of the alveolar walls (arrows) can be seen.

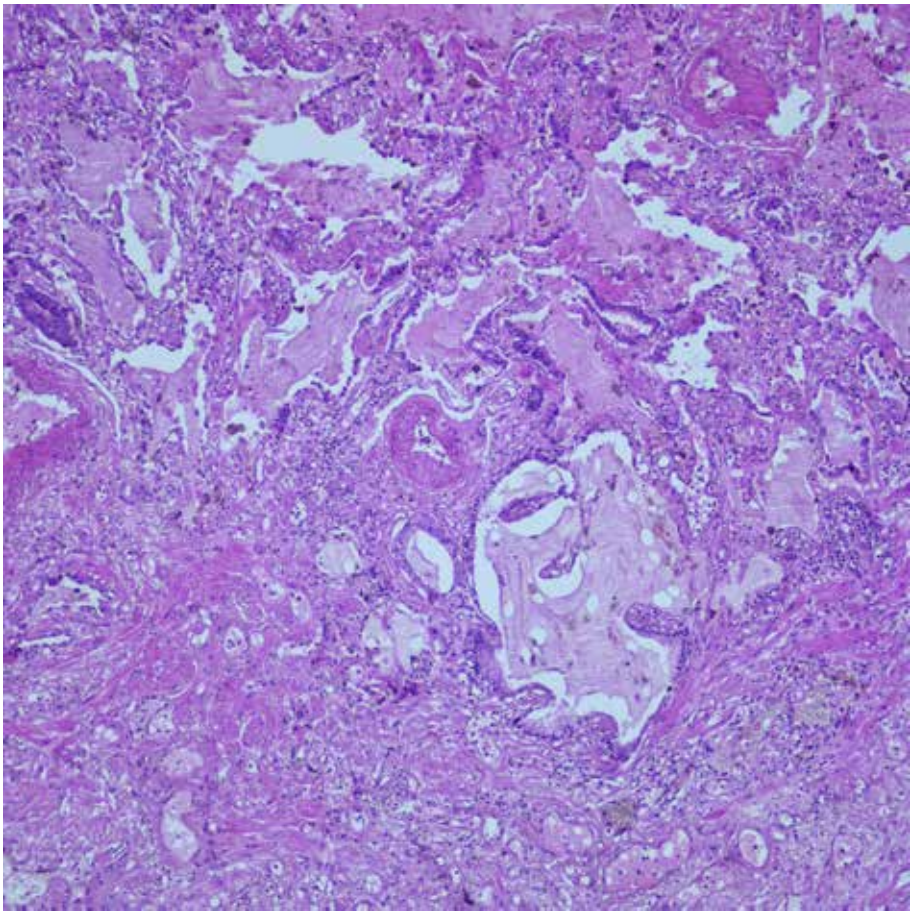

Figure 2.33
Honeycomb lung, (H&E, x100). Microscopically, the enlarged air spaces are lined with hyperplastic and bronchiolar-type epithelium and are surrounded by fibrosis. These changes can be observed in numerous interstitial lung diseases and are non-specific. Even in early stages of disease, microscopic honeycomb foci can be detected. The localization is important in distinguishing these microscopic honeycomb foci from bronchiolar metaplasia. Microscopic honeycomb foci are located at the periphery of lobules and are associated with fibrosis, whereas bronchiolar metaplasia occurs in the centers of lobules.

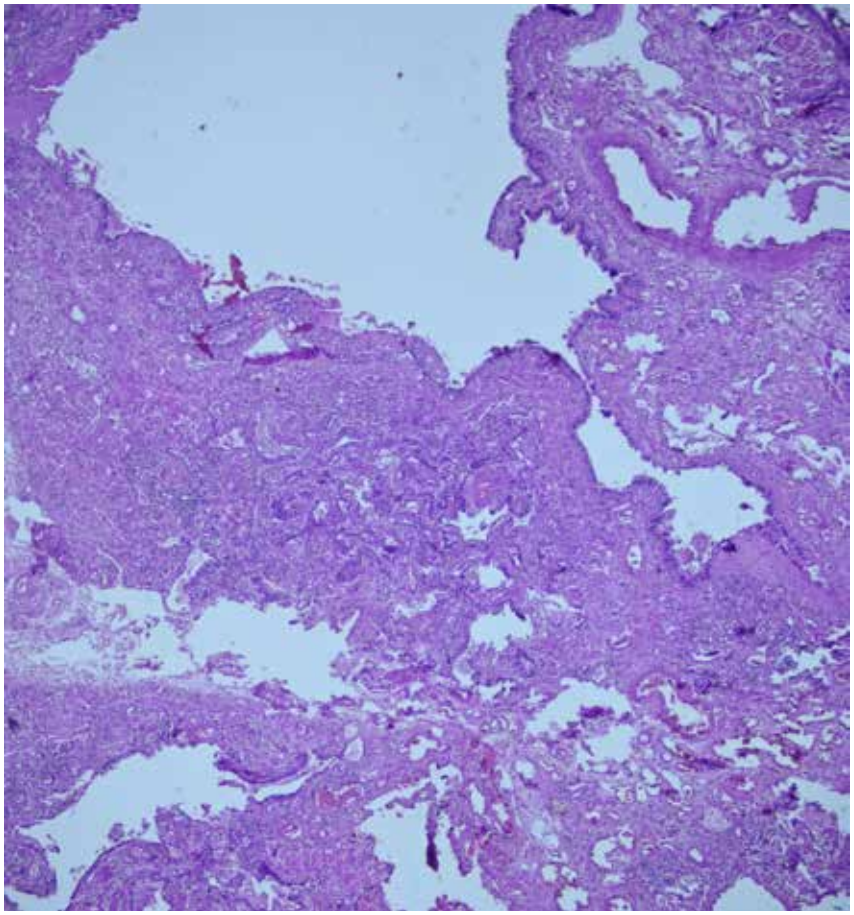

Figure 2.34
Bronchiectasis, (H&E, x40). Bronchiectasis is the permanent dilation of bronchi, often accompanied by acute and chronic inflammation. The microscopic view demostrates a marked enlargement of the bronchial lumen.

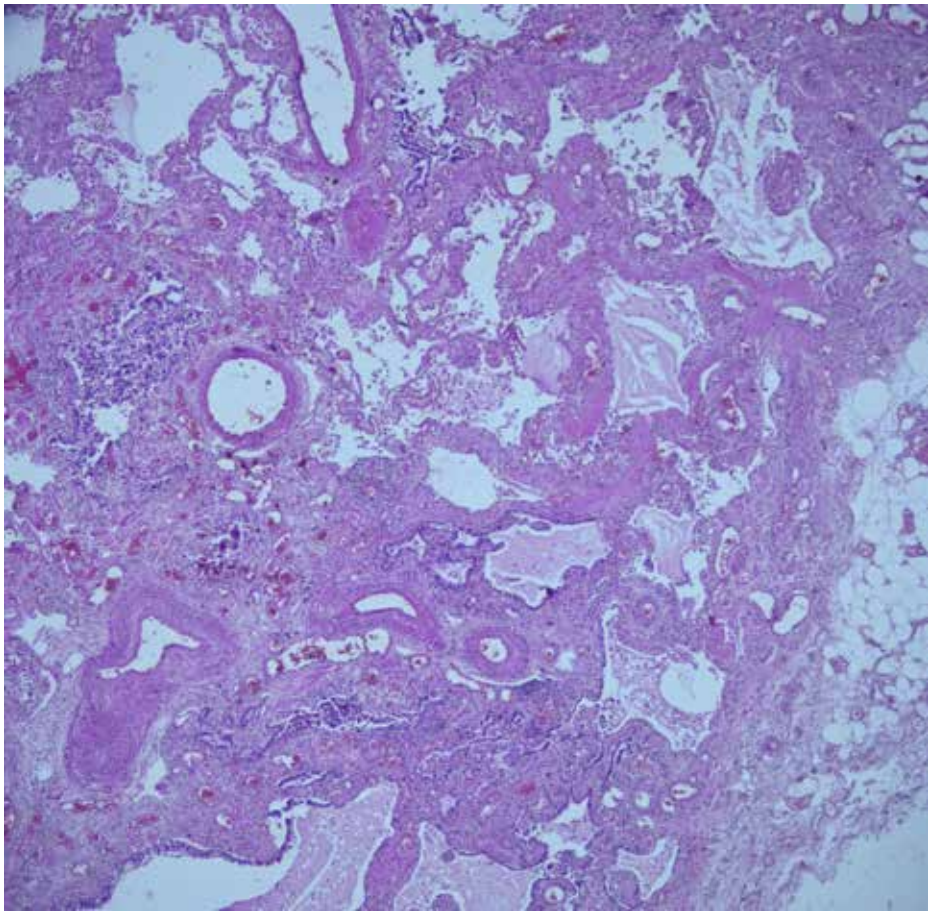

Figure 2.35
Usual interstitial pneumonia, (H&E, x40).
In the early stage of usual interstitial pneumonia, fibroblastic foci characterized by fibers parallel to the surface, along with cystic spaces lined by bronchiolar epithelium due to alveolar wall collapse. The microscopic view demostrates a honeycomb appearance.

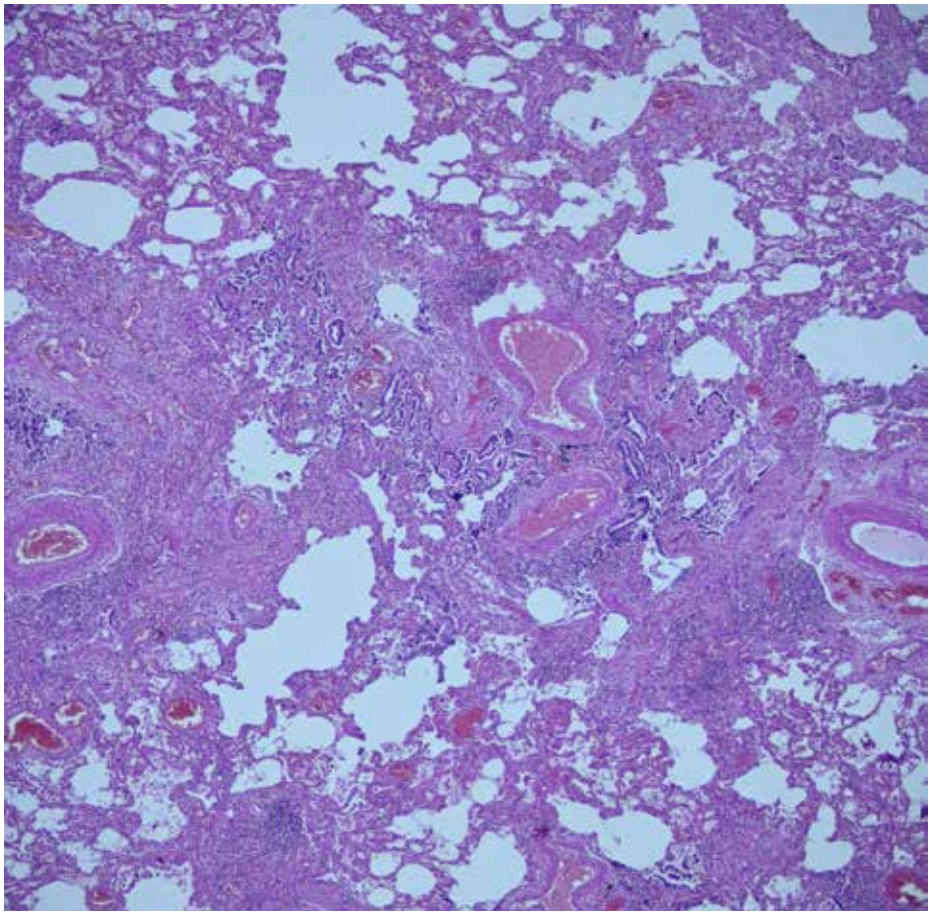

Figure 2.36
Usual interstitial pneumonia, (H&E, x40).
The microscopic view shows prominent fibrosis, architectural destructions, and a honeycomb appearance in the lung.

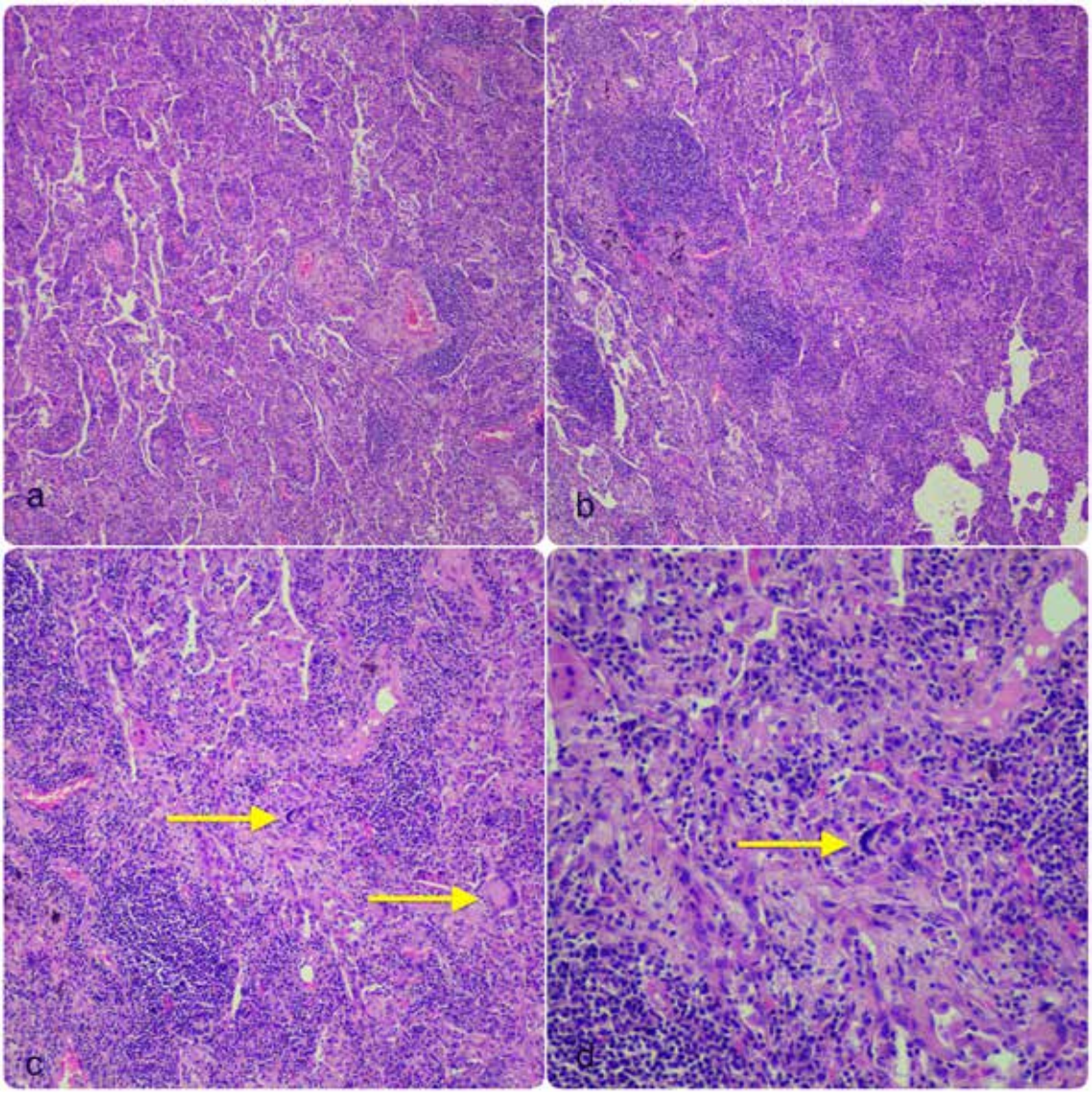

Figure 2.37
Lymphoid interstitial pneumonia,
a) (H&E, x100). Lymphoid interstitial pneumonia is characterized by dense and diffuse infiltration of alveolar septa by lymphocytes, histiocytes, and plasma cells. Multinucleated giant cells and non-necrotizing granulomas may be seen. The microscopic view demostrates dense lymphocyte infiltration in the interstitium.
b) (H&E, x100). Dense lymphocyte infiltration in the interstitium and atelectasis.
c) (H&E, x200). At higher magnification, giant cells (yellow arrows)
d) (H&E, x400). At higher magnification, giant cells (yellow arrows).

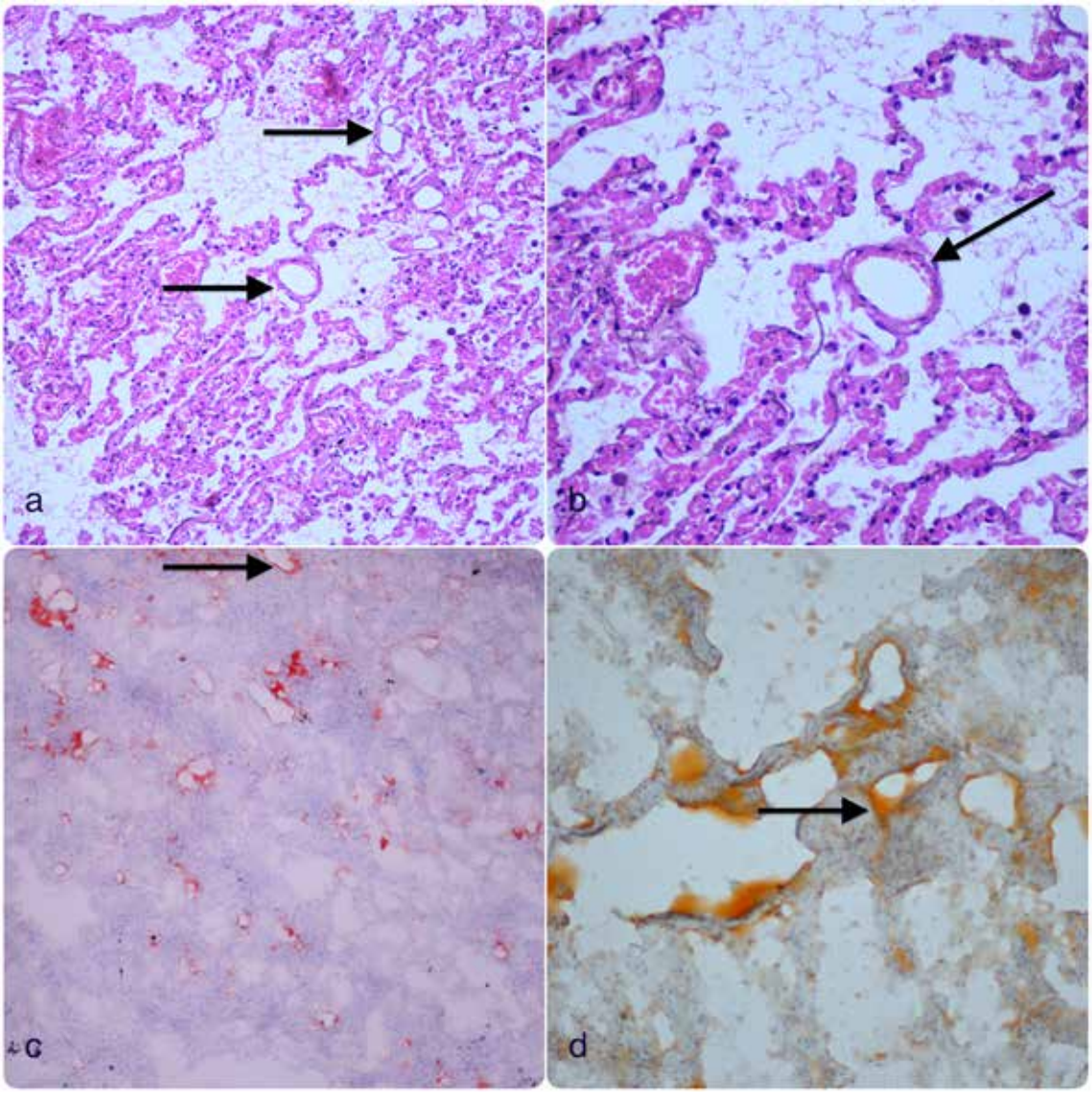

Figure 2.38
Pulmonary fat embolism,
a) (H&E, x200). The microscopic view shows ring-shaped, hollow-appearing fat globules (arrows) in the lumens of interstitial capillaries. Fat and bone marrow embolism most commonly occur as a result of soft tissue crush injuries, long bone fractures, and cardiopulmonary resuscitation.
b) (H&E, x400). At higher magnification, the compression of erythrocytes by a fat globule (arrow) in the vascular lumen is noticeable.
c) (Oil Red O, x100). Fat globules in the lumens of capillary vessels are stained red-orange with Oil Red O stain.
d) (Oil Red O, x200). At higher magnification, fat globules in the lumens of capillary vessels are stained red-orange (arrow) with Oil Red O stain.

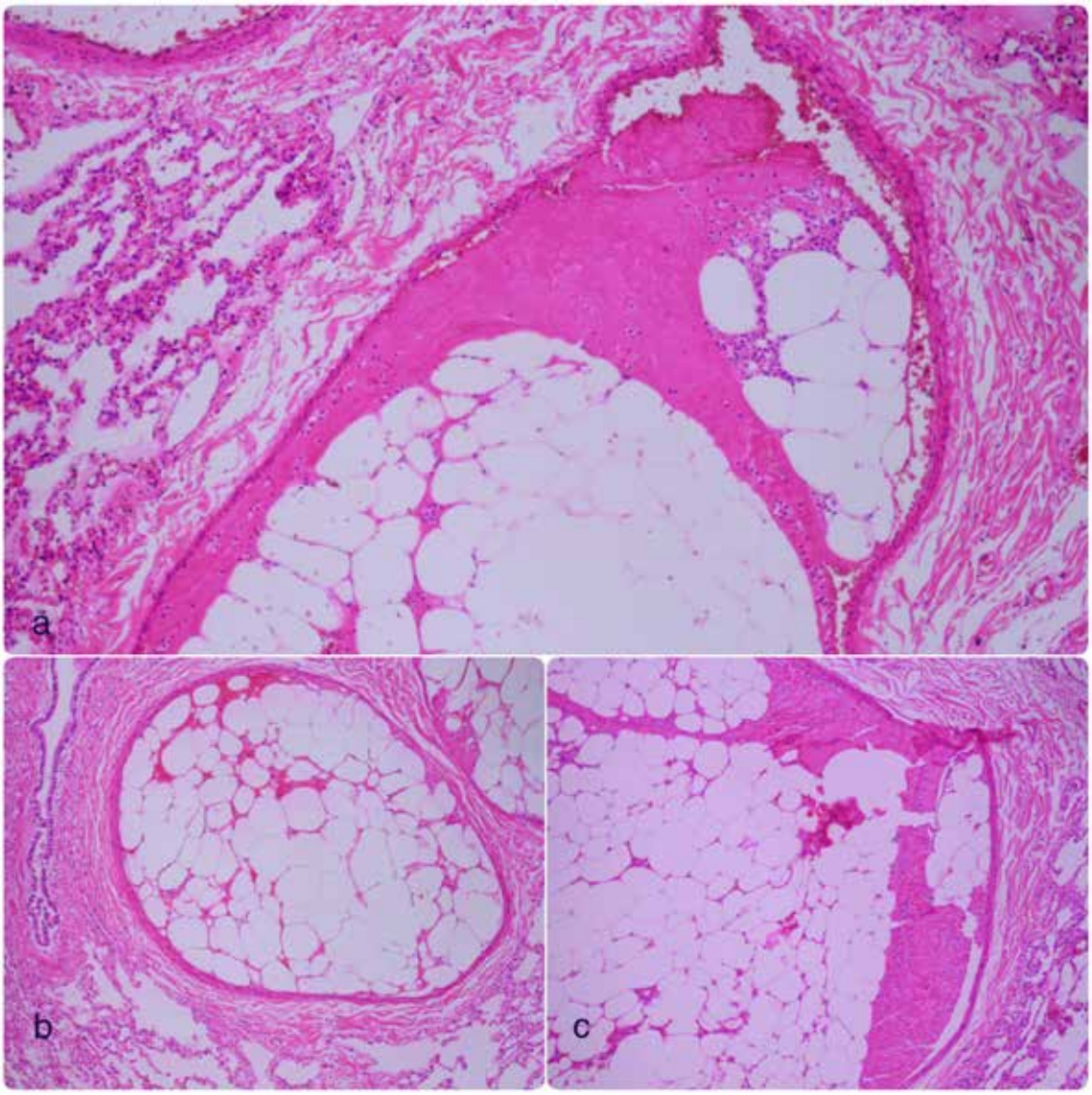

Figure 2.39
Gross fat emboli in the lung vascular lumens,
a) (H&E, x100). Following liposuction operation in the chest region, the microscopic view shows fat globule mass in the vascular lumens with fibrin thrombus formation on this fat globules mass.
b) (H&E, x100). The microscopic view shows a gross fat mass completely filling the vascular lumen.
c) (H&E, x200). At higher magnification, a gross fat mass and fibrin thrombus are observed in the vascular lumen.

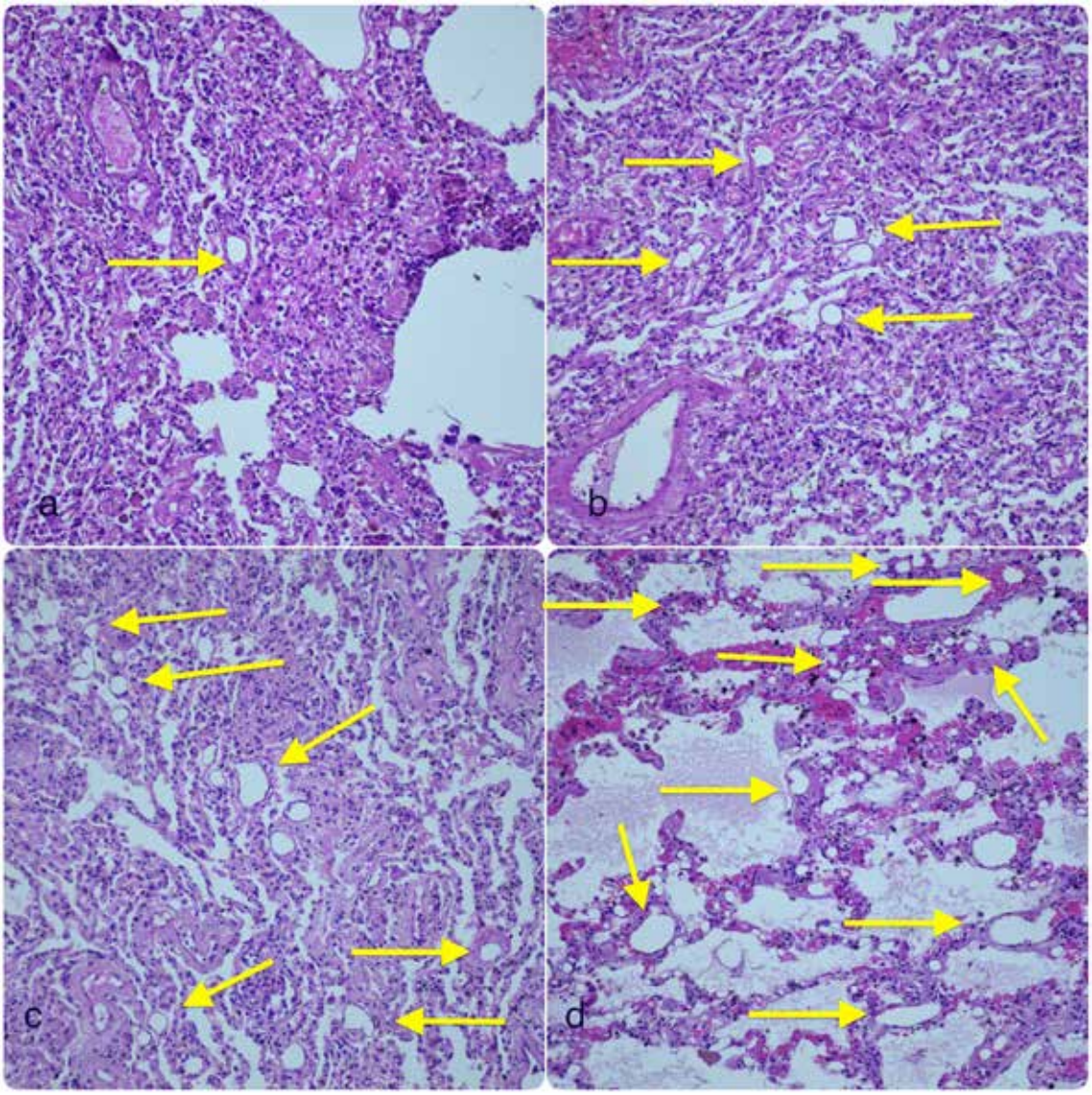

Figure 2.40
Pulmonary fat embolism.
According to the Mason grading system, fat embolisms are graded from 0 to 4. In Grade 0, there is no fat embolism; in Grade 1, fat emboli are not immediately apparent when 2 or 3 microscopic fields are examined; in Grade 2, fat emboli are easily detectable; in Grade 3, numerous fat emboli are observed; and in Grade 4, potentially fatal levels of fat emboli are present.
a) Grade 1 fat embolism, (H&E, x200). Microscopically, a few fat emboli are observed when examining several fields at higher magnification.
b) Grade 2 fat embolism, (H&E, x200). Microscopically, fat emboli are easily seen when examining several fields at higher magnification.
c) Grade 3 fat embolism, (H&E, x200). Microscopically, numerous fat emboli are prominent in a single field at higher magnification.
d) Grade 4 fat embolism, (H&E, x200). Microscopically, an excessive number of fat emboli are observed in a single field at higher magnification.

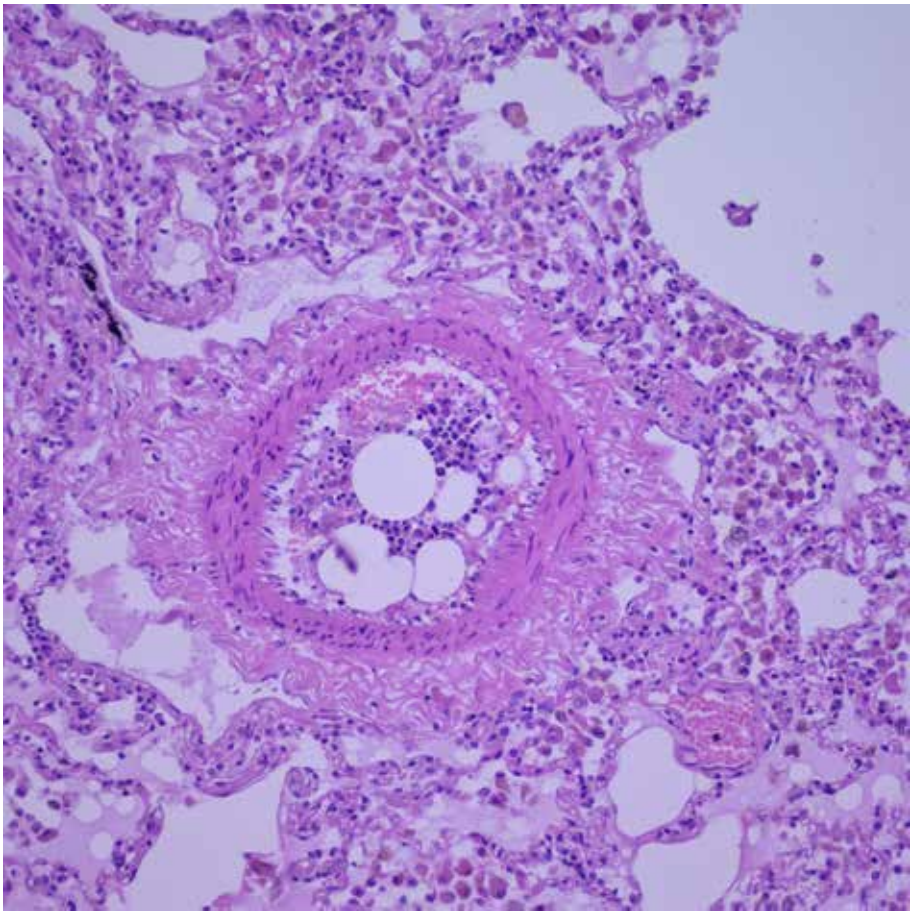

Figure 2.41 Bone marrow embolism, (H&E, x200). The microscopic view demostrates hematopoietic cells, bone marrow, and fat cells in the lumen of a pulmonary vessel.

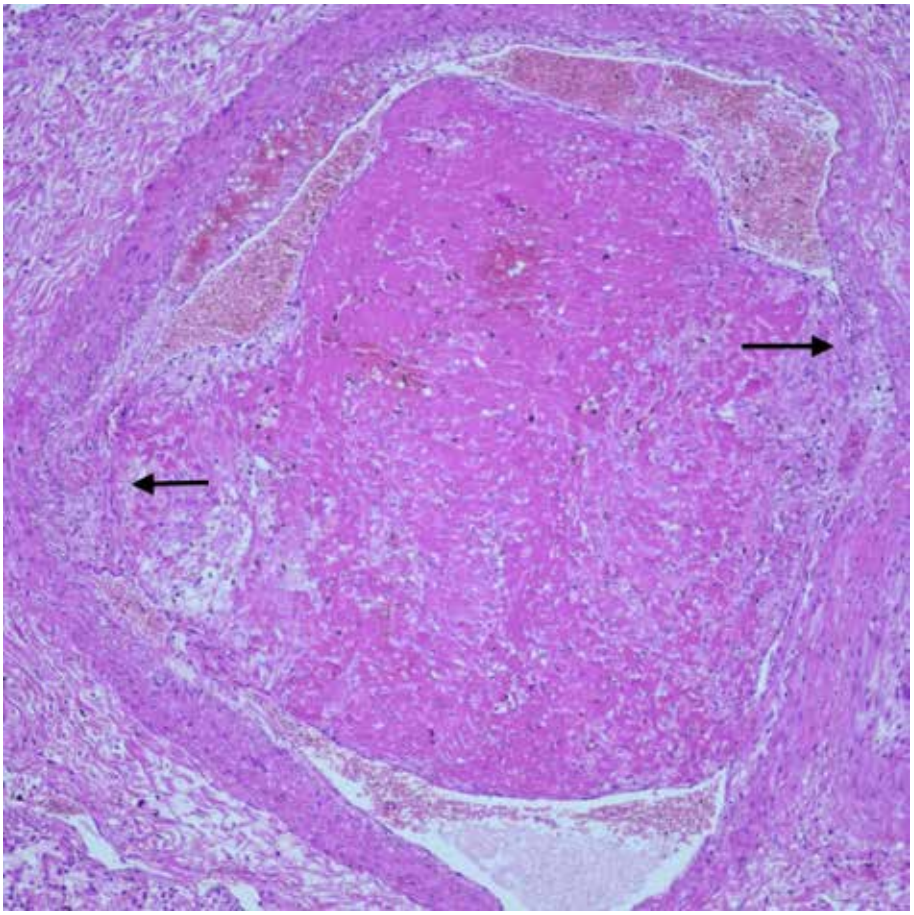

Figure 2.42 Organized fibrin thrombus in the pulmonary vessel lumen, (H&E, x100). In the microscopic view, a fibrin thrombus adherent to the wall of the pulmonary vessel is observed, with fibroblastic proliferation noted at the edges.

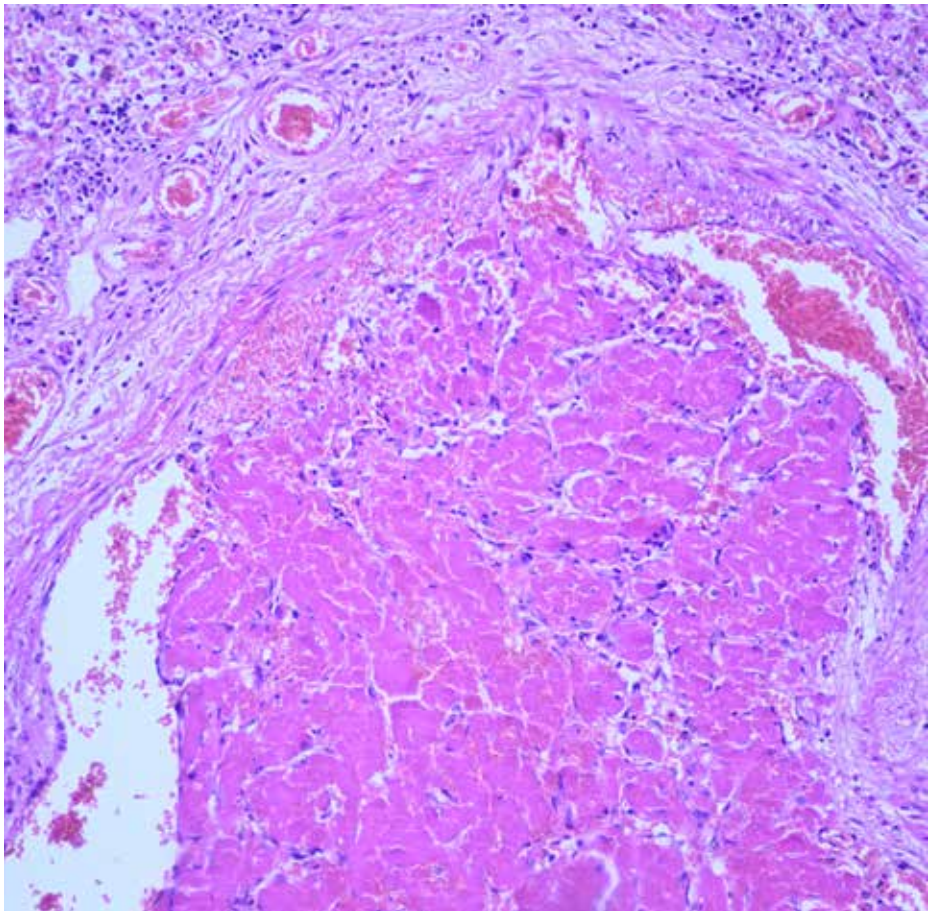

Figure 2.43
Partially organized fibrin thrombus in the pulmonary vessel lumen, (H&E, x200). At higher magnification, a fibrin thrombus adherent to the vessel wall with fibroblastic proliferation observed.

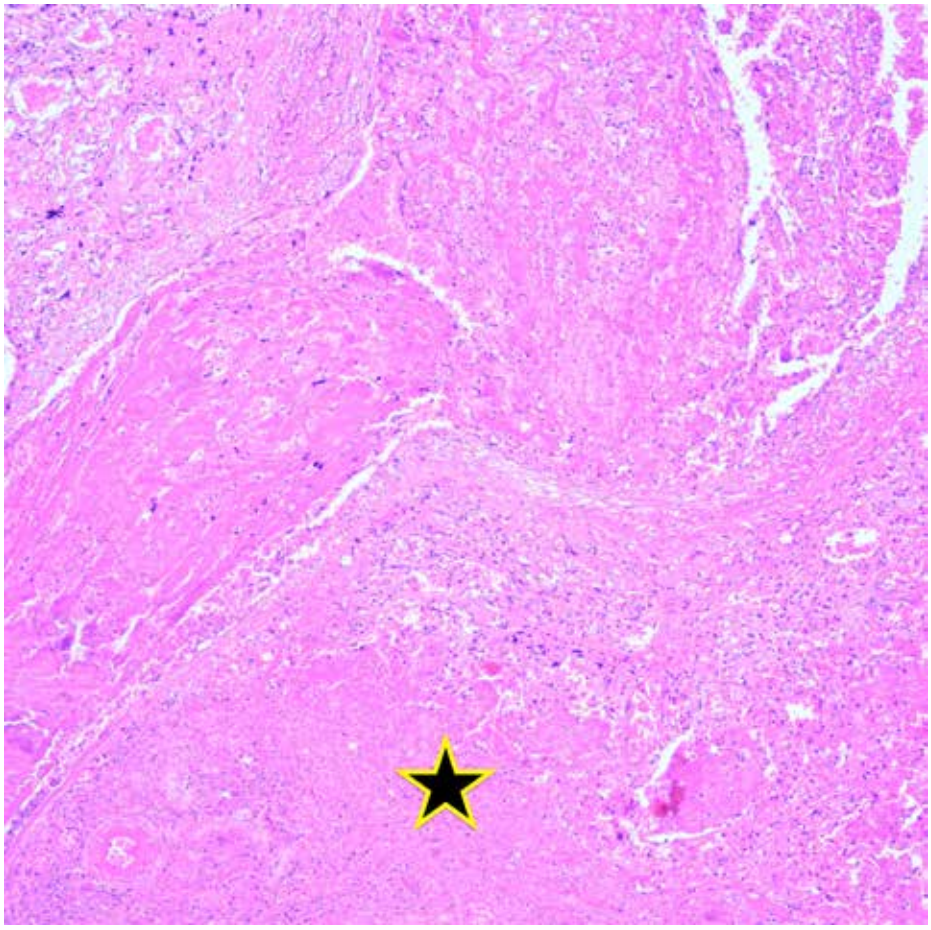

Figure 2.44
Pulmonary fibrin thrombus and pulmonary infarction (H&E, x100). Blood elements (fibrin, platelets, erythrocytes, and leukocytes) attach to the inner surface of the vessel, forming a thrombus. The origin of large pulmonary artery thrombi is typically the deep veins of the legs. While most emboli are asymptomatic, a smaller proportion leads to acute cor pulmonale, shock, death, or pulmonary infarction. In the microscopic view, a fibrin thrombus is observed in the pulmonary vessel lumen, with areas marked by asterisks indicating pulmonary infarction.

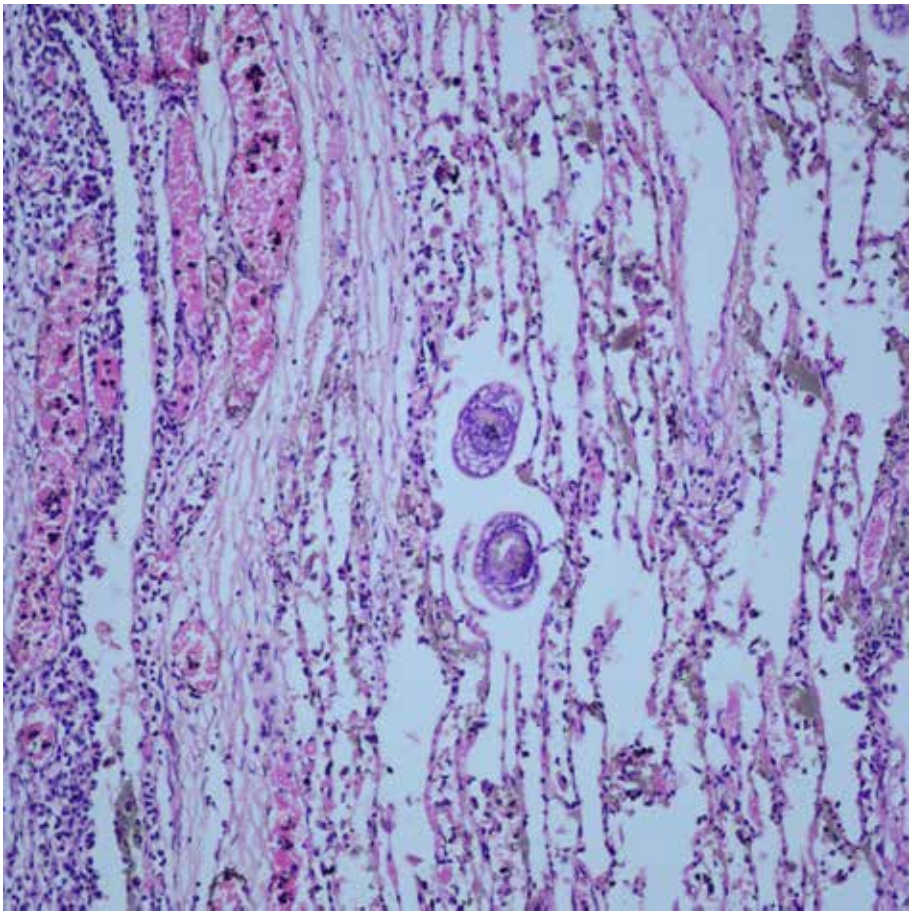

Figure 2.45
Presence of scolex in the alveolar lumens in a case with anaphylaxis due to pulmonary hydatid cyst rupture,
(H&E, x200).
In the microscopic view, scolices can be seen in the alveolar lumen.

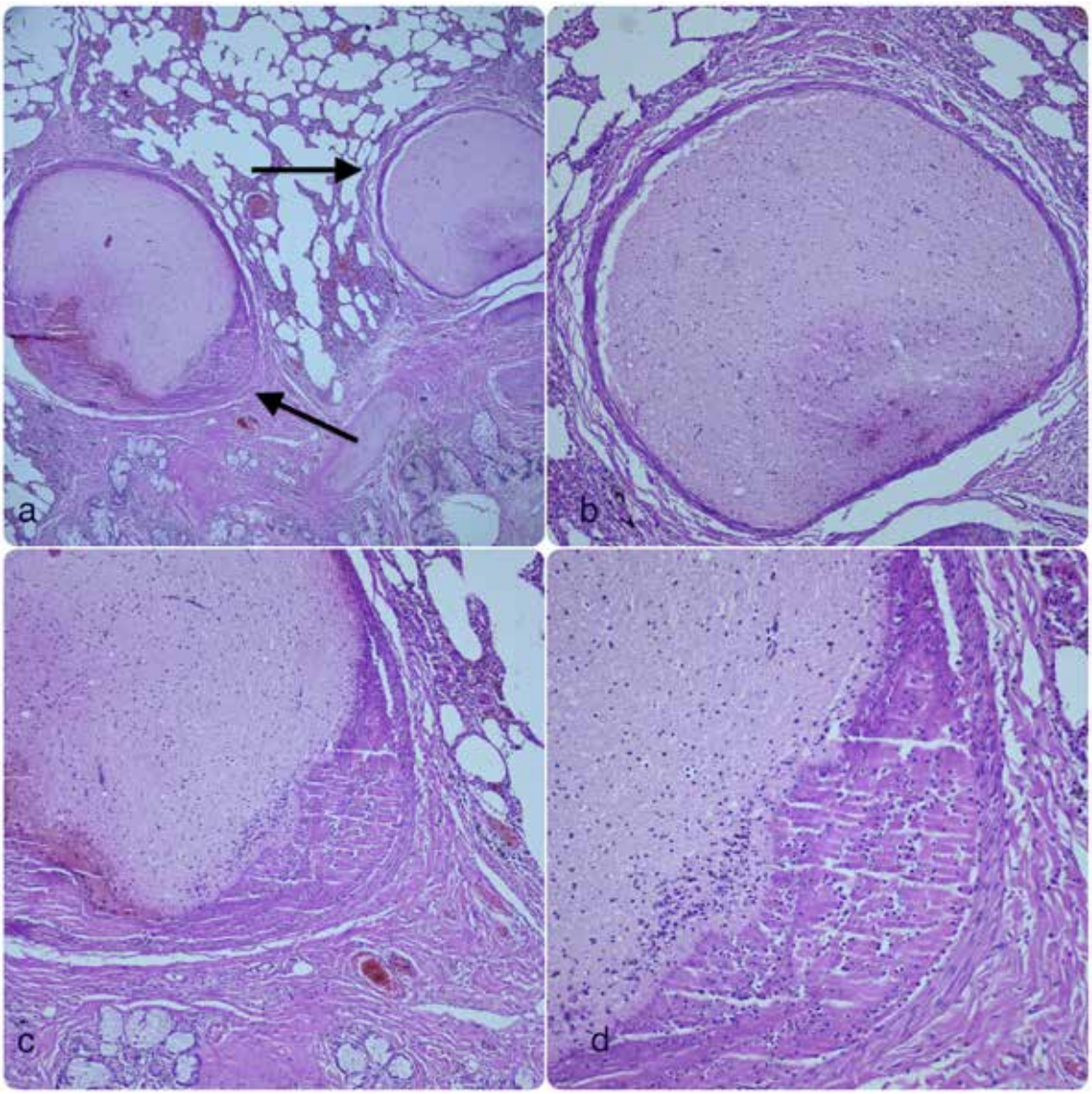

Figure 2.46
Brain tissue embolism in pulmonary vessel lumens,
a) (H&E, x40). Motorcycle accident and head trauma resulting in fractures in the skull and brain tissue damage, brain tissue embolism (arrows) is observed in the pulmonary vessel lumens.
b) (H&E, x100). At higher magnification microscopic view.
c) (H&E, x100). Brain tissue embolism with fibrin thrombus formation on top is observed. **d)** (H&E, x200). At higher magnification microscopic view of brain tissue embolism with associated fibrin thrombus formation on top.

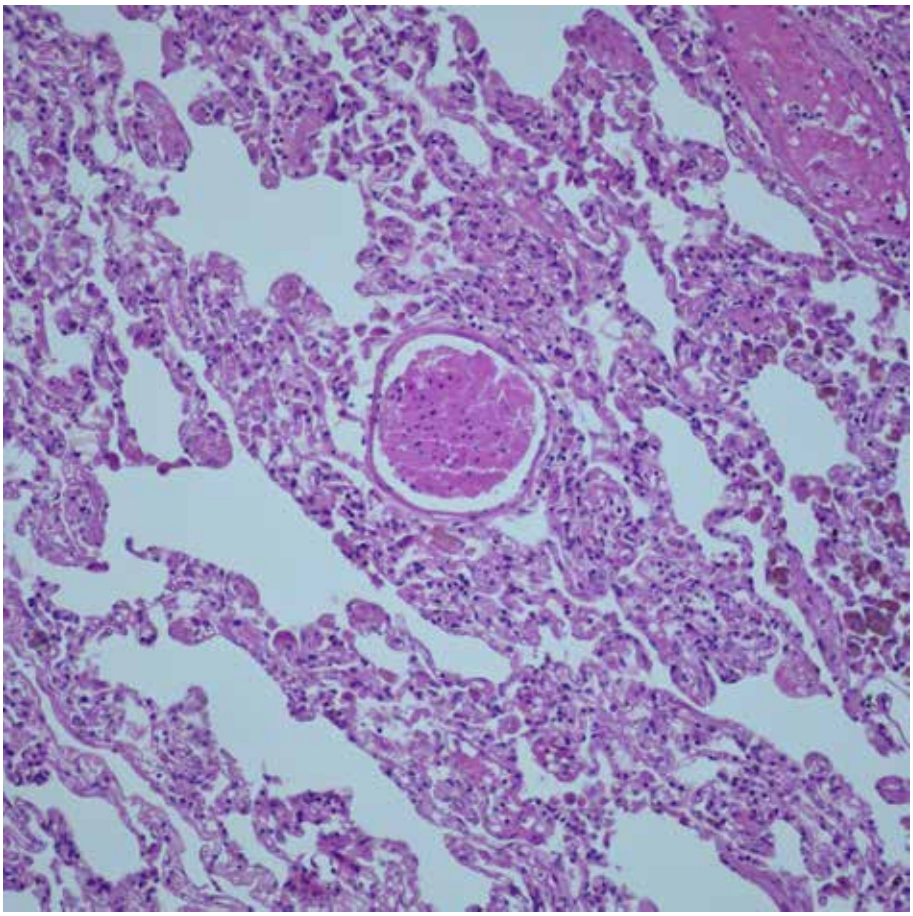

Figure 2.47
Liver tissue embolism in pulmonary vessel lumens,
(H&E, x200).
In an individual with liver tissue damage and laseration resulting from a motorcycle accident and liver trauma, liver tissue embolism is observed in the pulmonary vessel lumen.

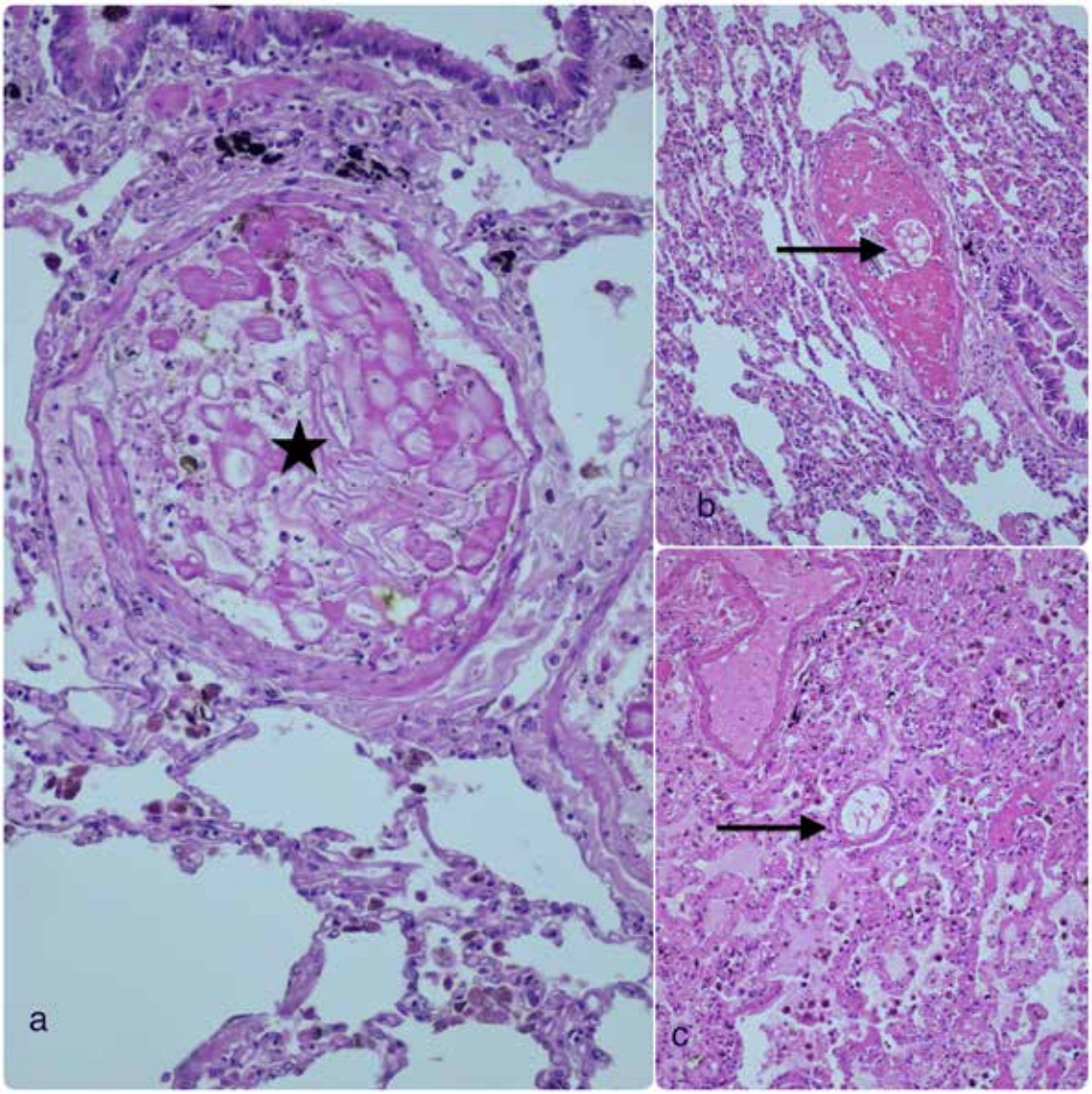

Figure 2.48
Food embolism,
a) (H&E, x400). In an individual with extensive tissue trauma and damage resulting from a motorcycle accident, food tissue embolism (asterisk) is observed in the pulmonary vessel lumen.
b,c) (H&E, x200). Food material embolism (arrow) with visible plant fibers is observed in the vessel lumen.

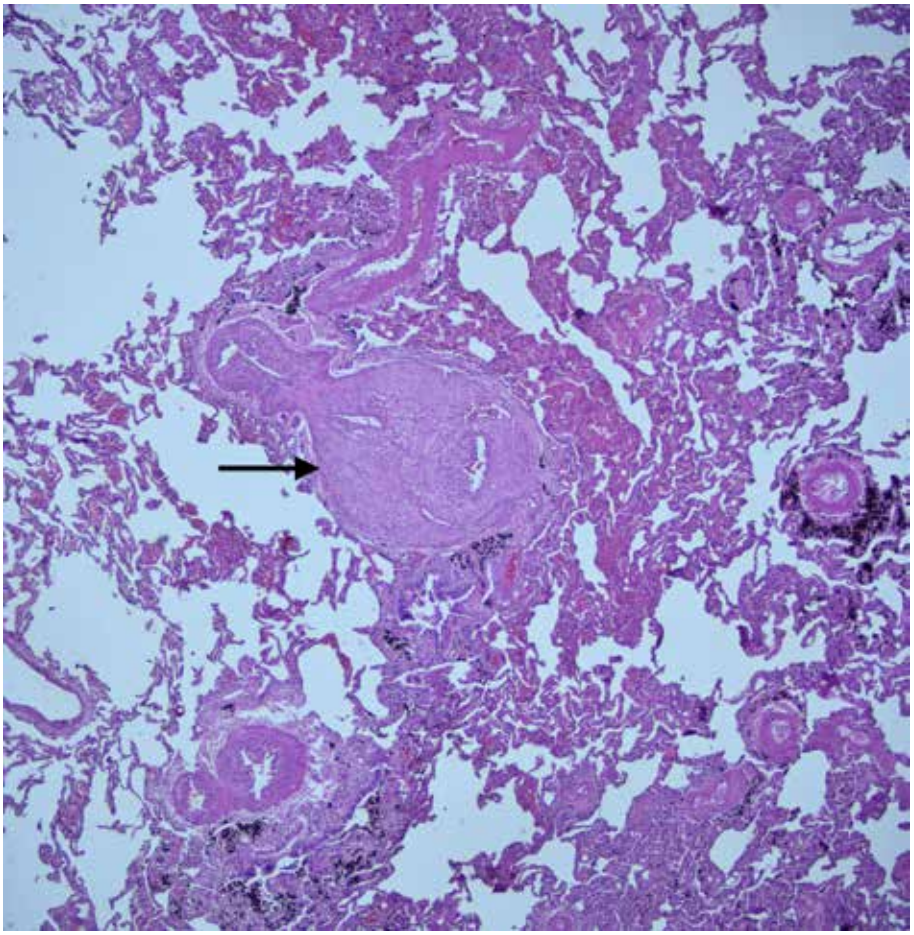

Figure 2.49 Pulmonary hypertension, (H&E, x40). Narrowing of the vessel lumen is observed due to myointimal and smooth muscle cell proliferation in the medium-sized muscular artery, resulting in thickening of the intima and media. In advanced cases, plexiform lesions (arrow), characterized by the formation of numerous lumens within the vessel, occur at branching points where medium-sized vessels divide into smaller arteries.

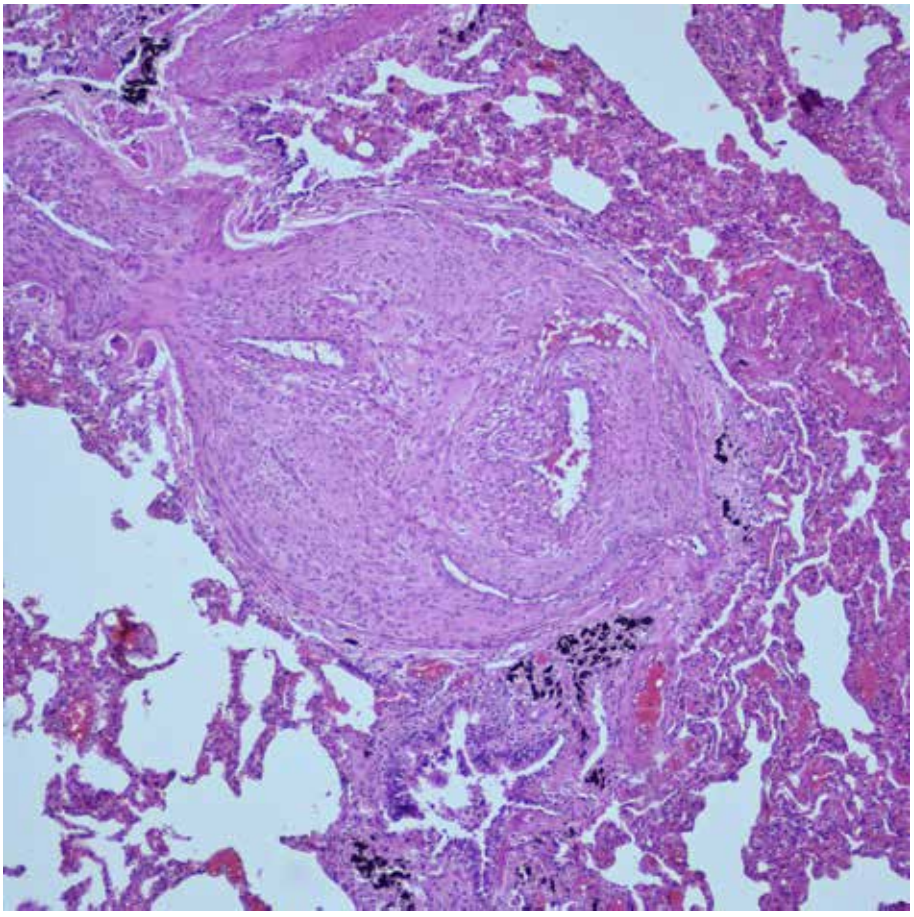

Figure 2.50 Pulmonary hypertension, (H&E, x100). At higher magnification.

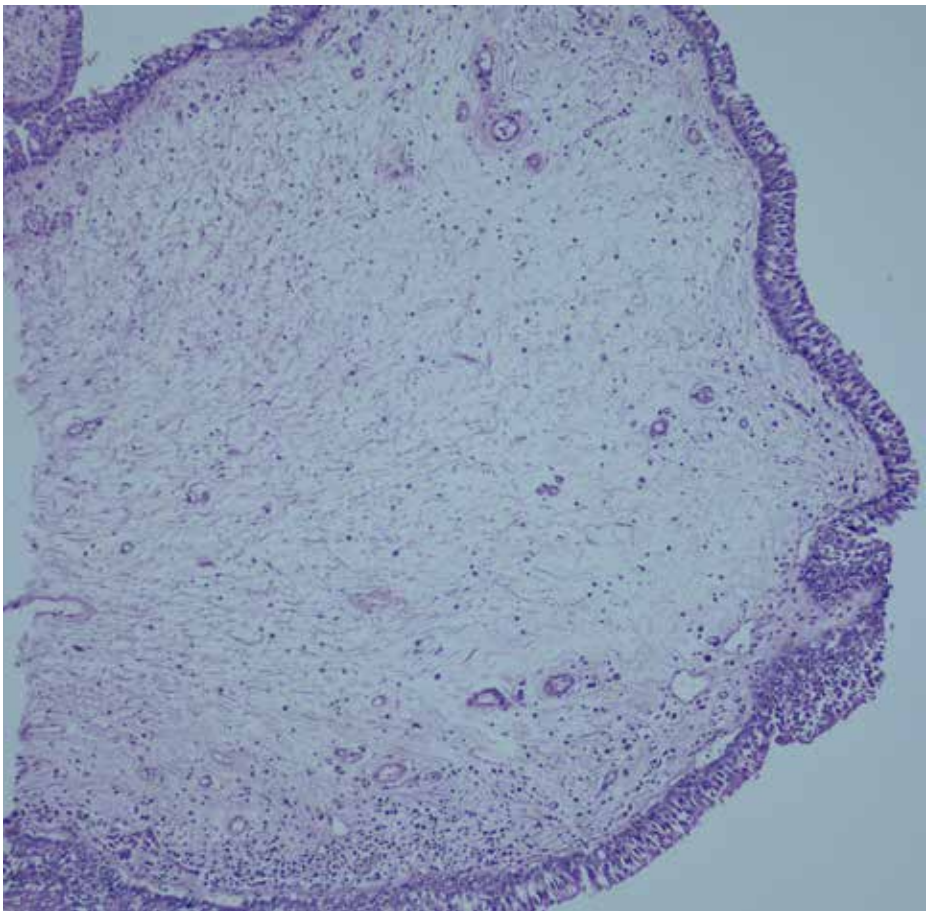

Figure 2.51
Laryngeal edema,
(H&E, x100).
In an individual died due to massive laryngeal edema and resultant respiratory obstruction. The larynx exhibits massive edema, with few mononuclear inflammatory cells seen in the subepithelial area.

LIVER

Assoc. Prof. Taner DAŞ
Assoc. Prof. Ferah KARAYEL

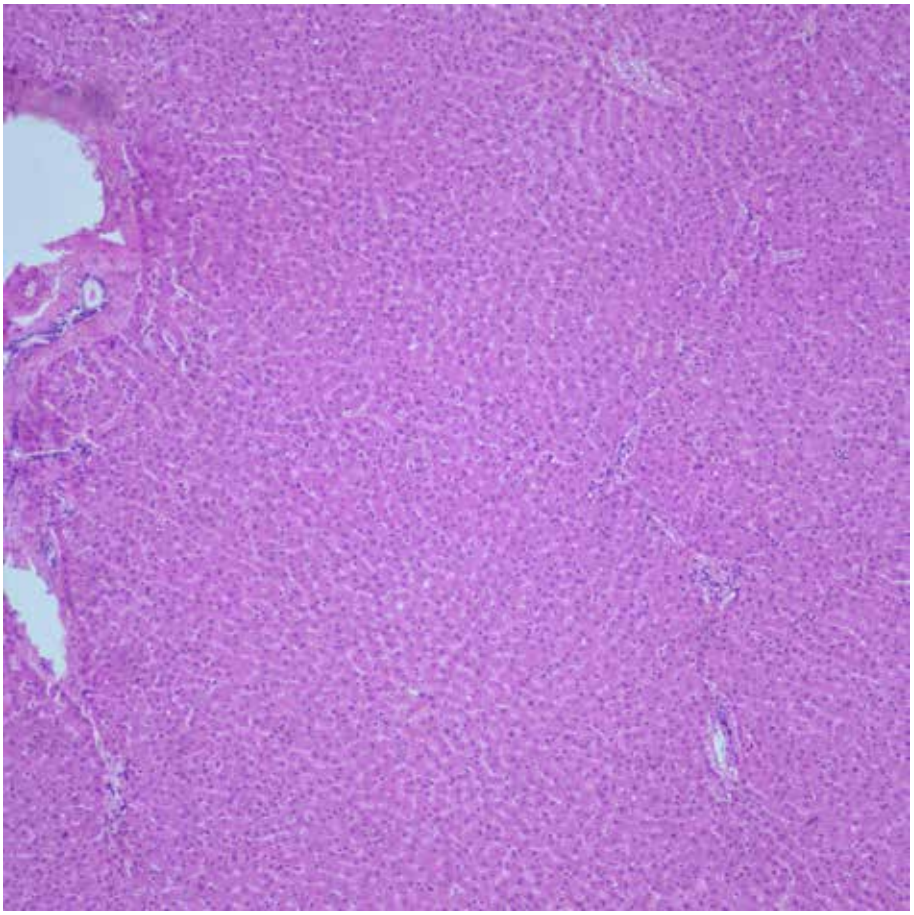

Figure 3.1 Normal liver histology, (H&E, x100). The liver consists of lobules, and the central canal is seen in the center and the portal tracts is in the periphery of lobule.

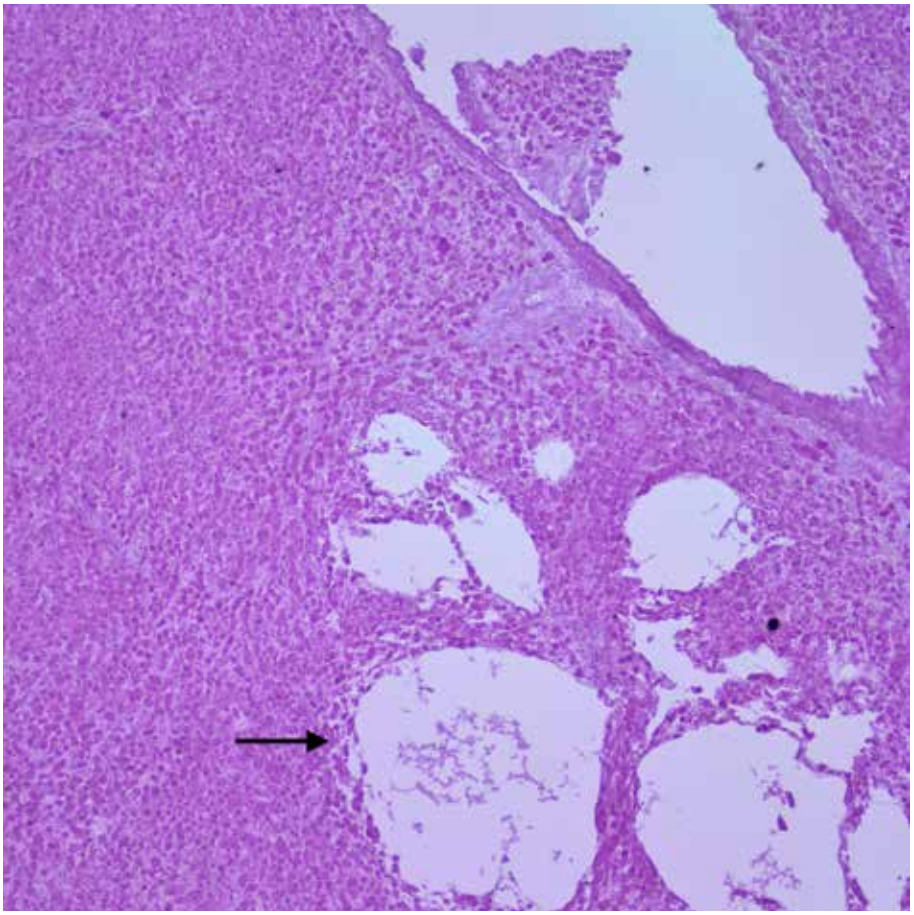

Figure 3.2 Liver autolysis, (H&E, x100). Autolysis is the digestion of the dead or dying cell by its own enzymes. During autolysis and decomposition, with the spread of intestinal and other bacteria, liquid and gas is released, causing tissue cavities (ok).

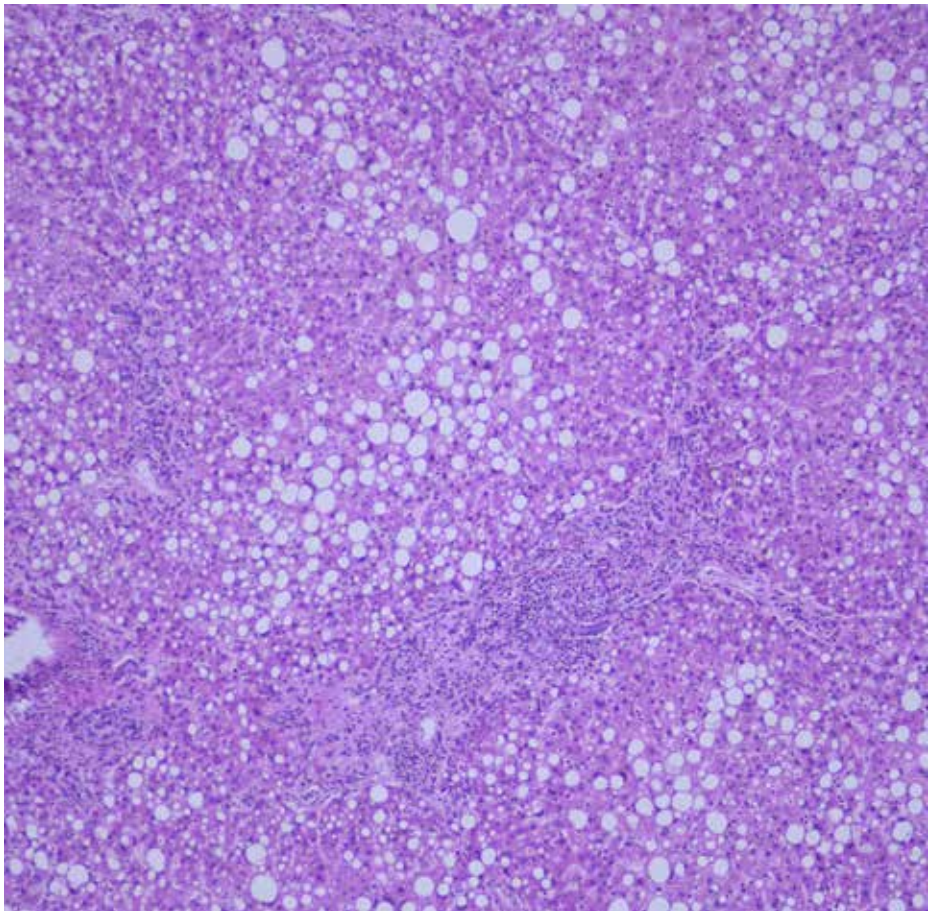

Figure 3.3
Steatohepatitis, (H&E, x100). Steatosis, ballooning degeneration of hepatocytes and inflammation are necessary histologic findings for diagnosis steatohepatitis.

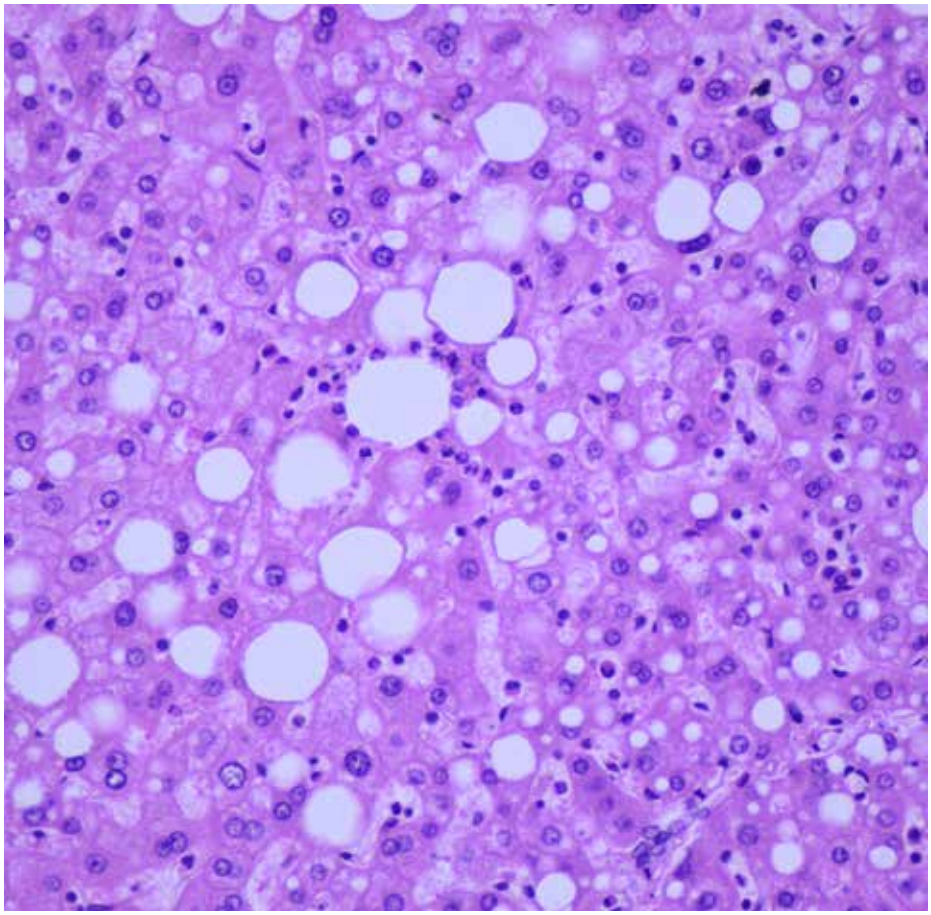

Figure 3.4
Steatohepatitis, (H&E, x400)
At higher magnification.

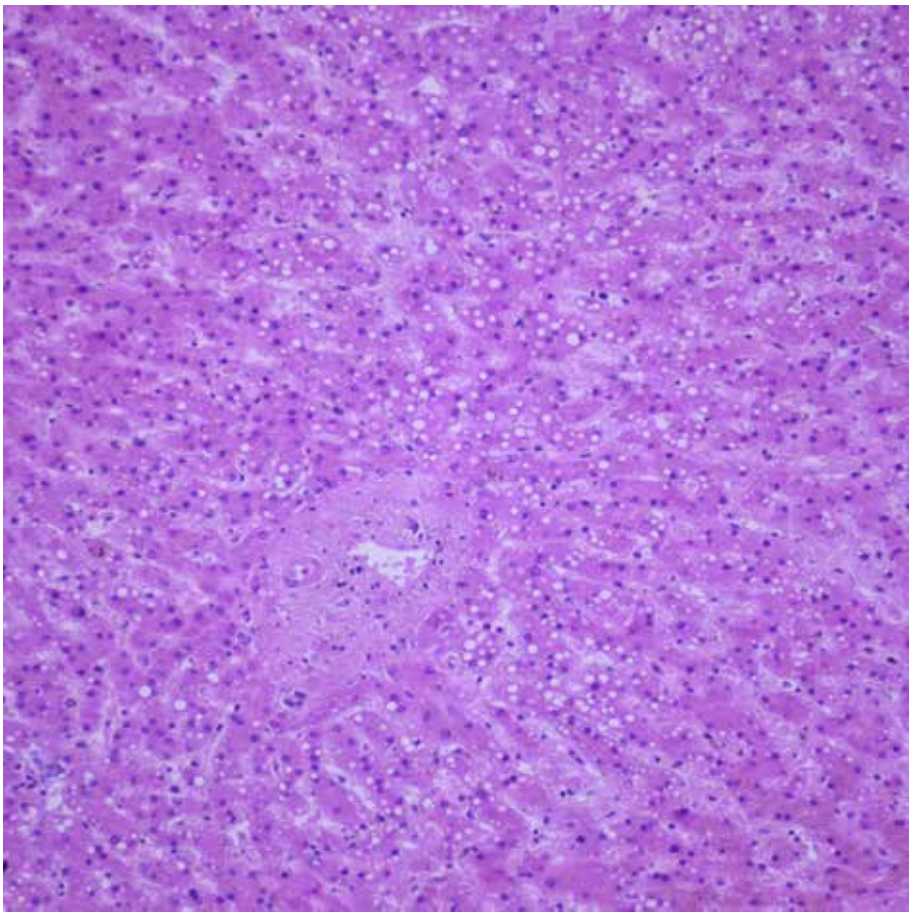

Figure 3.5
Microvesicular steatosis,
(H&E, x200).
Microvesicular steatosis is a serious condition that progresses to liver failure and coma when it is diffuse. Microscopically, they are numerous lipid droplets with a diameter of 1-2 micrometers.
Microvesicular steatosis seen in drug reactions, congenital metabolic diseases, and parental nutrition, acute fatty liver of pregnancy.

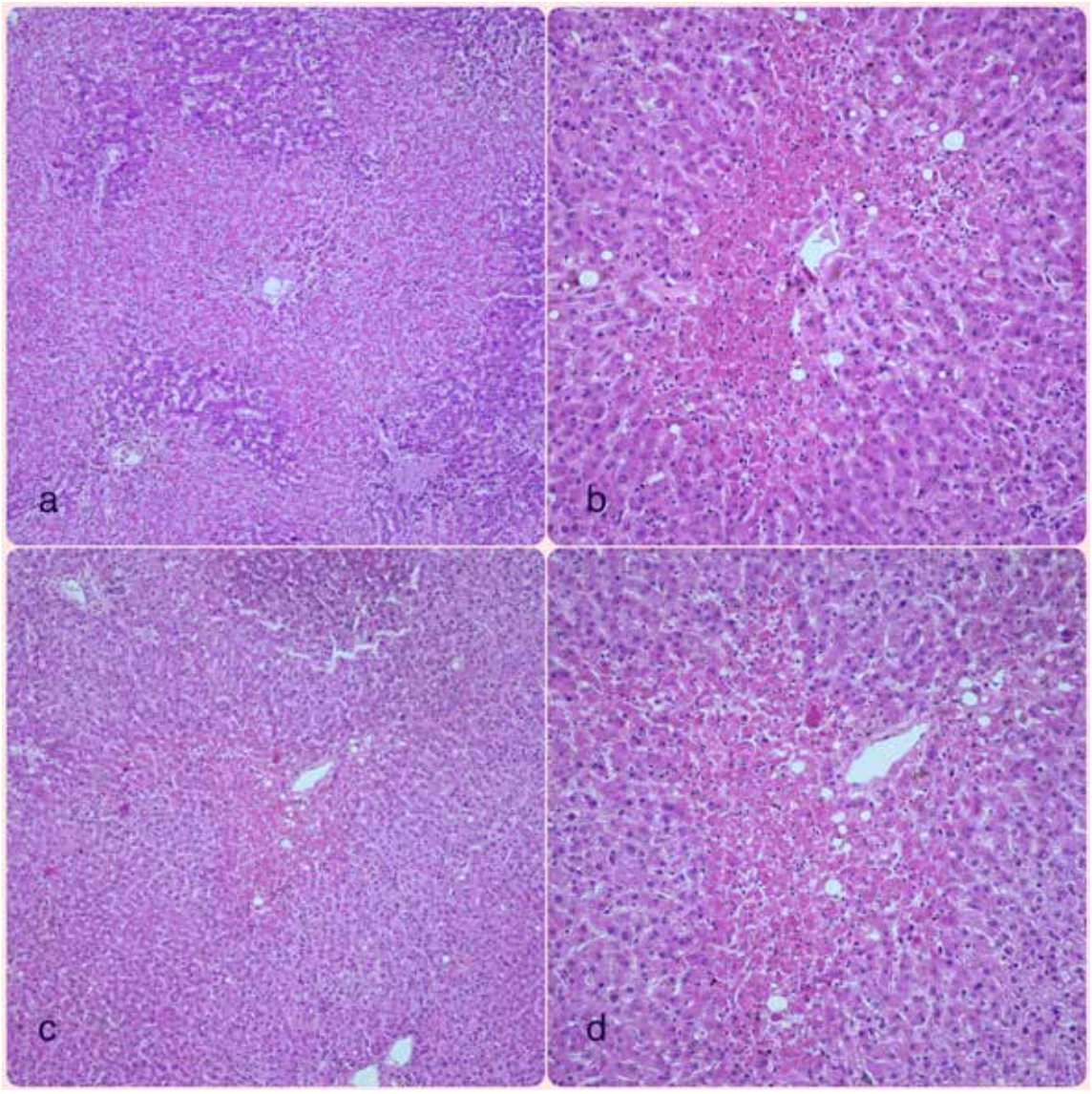

Figure 3.6
Chronic passive congestion and centrilobular hemorrhagic necrosis.
a,b,c,d) (H&E, x100, x200, x40, x100).
In chronic passive hepatic congestion, the centrilobular regions are dark brown and slightly depressed from the surface, and macroscopically they have a "nutmeg" appearance. The most common causes are congestive heart failure, severe hypovolemia, septic shock, and pulmonary embolism.
Microscopically, centrilobular hepatocyte necrosis, hemorrhage, and pigment-laden histiocytes observed.

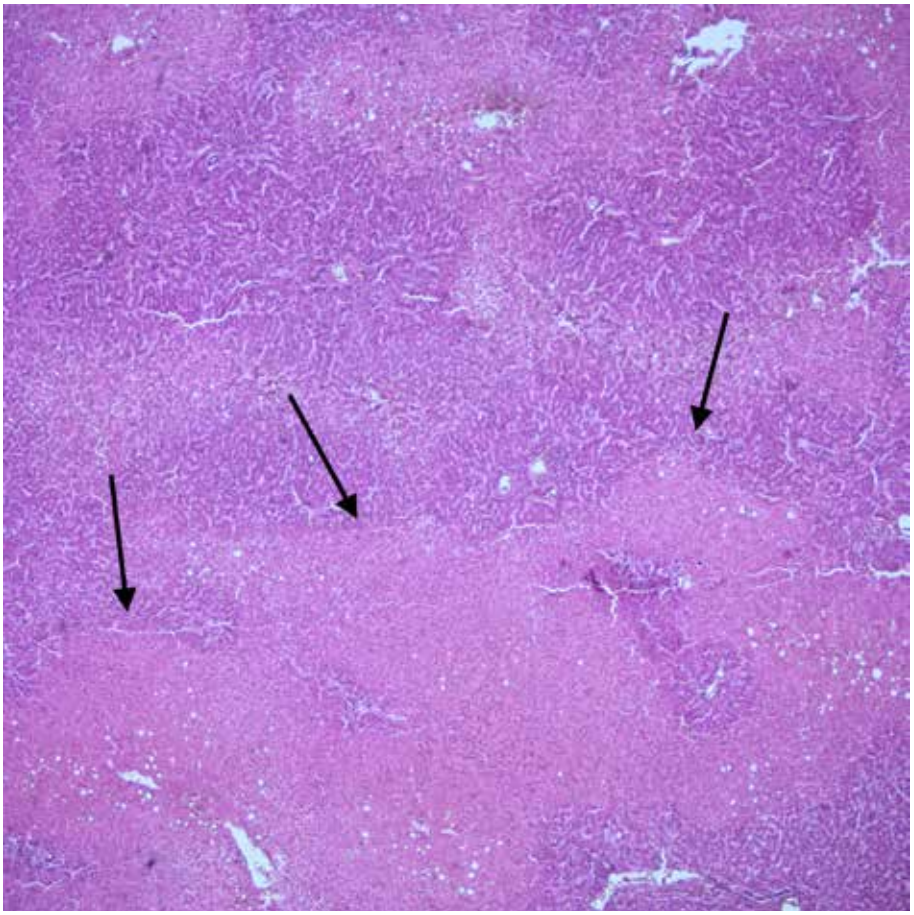

Figure 3.7
Submassive necrosis, (H&E, x40). Submassive necrosis (Confluent necrosis) refers to large areas of hepatocyte necrosis. It is most commonly seen with viral, autoimmune or drug-induced severe hepatitis. Rarely, it may develop due to hypoperfusion caused by shock and left heart failure. Massive and submassive necrosis is seen in acetaminophen poisoning, which is also used for suicide, and in mushroom poisoning. The microscopic view demostrates submassive hepatocyte necrosis (arrows).

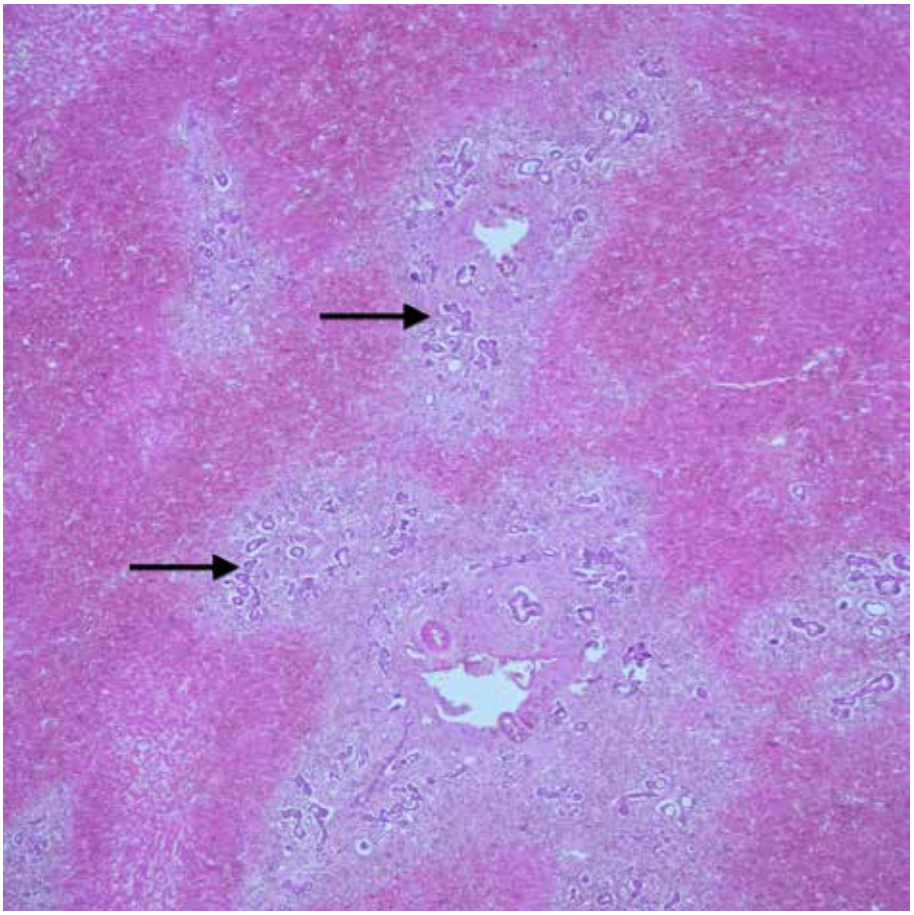

Figure 3.8
Submassive liver necrosis with reactive bile duct proliferation, (H&E, x40). Reactive bile duct proliferation (arrows) may develop in submassive necrosis. If the person survives, these areas progress to fibrosis.

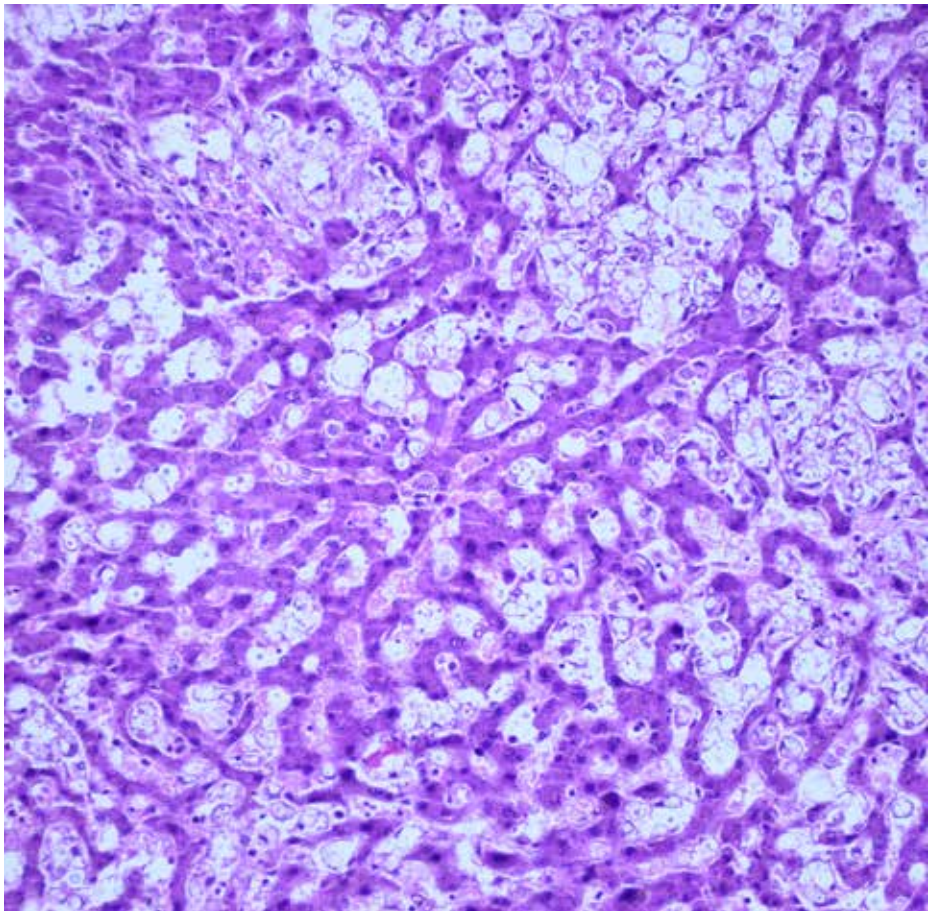

Figure 3.9
Fungal hepatitis, (H&E, x200). In the microscopic view, cryptococci are seen in the parenchyma. Cryptococcus is a common opportunistic infection in people with HIV infection.

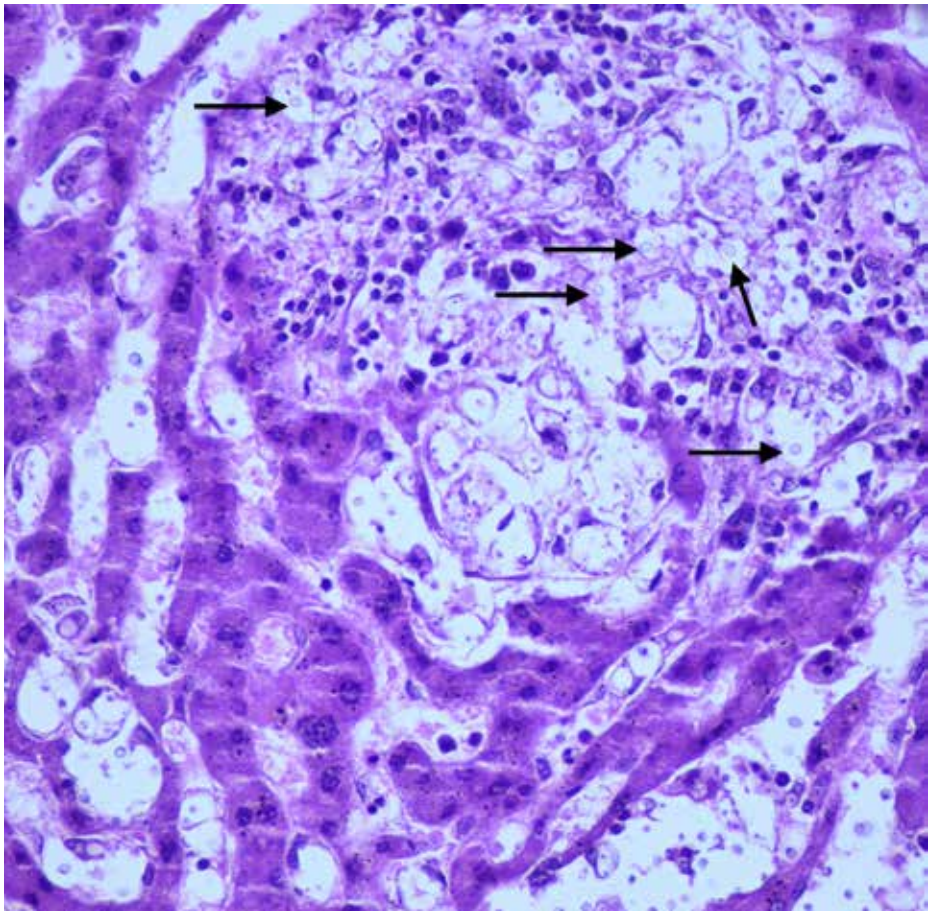

Figure 3.10
Fungal hepatitis, (H&E, x400). At higher magnification, round or oval-shaped cryptococci (arrows) with thin walls seen between the inflammatory cells.

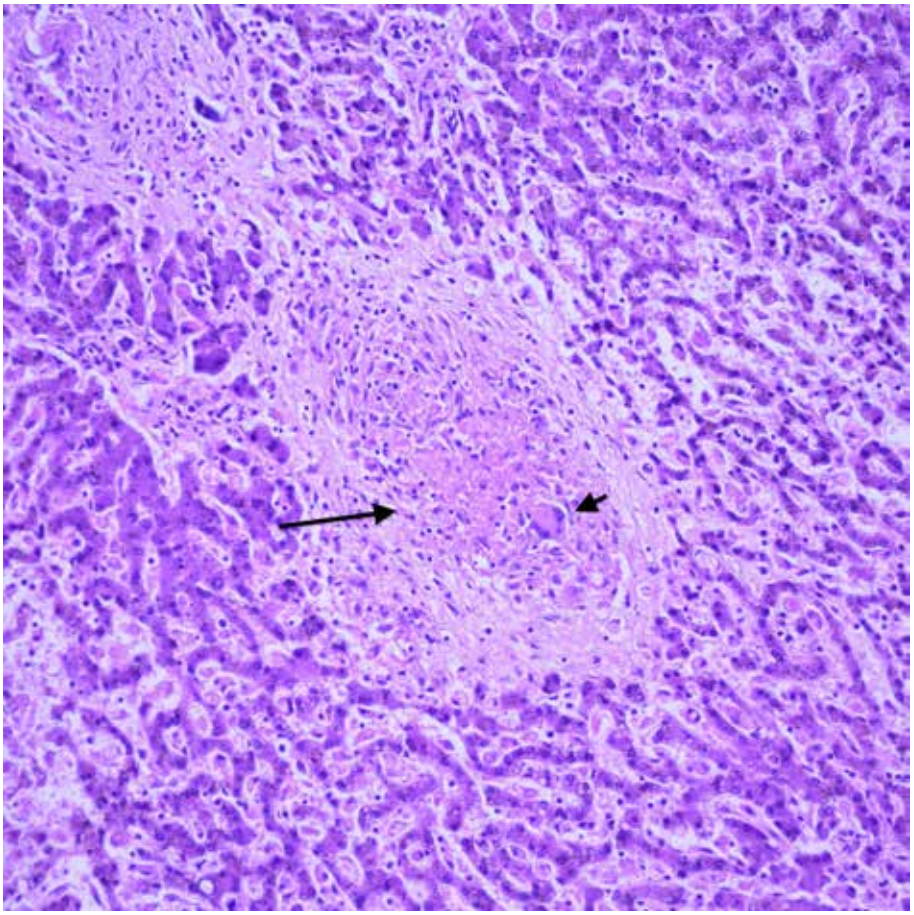

Figure 3.11 Granuloma in the liver, (H&E, x200). In the microscopic view, granuloma (long arrow) is seen in the liver parenchyma. The short arrow points to the Langhans-type giant cell. Granulomas seen in the liver as a result of infectious (tuberculosis, fungal infections etc.) and non-infectious causes (drug-induced liver damage, foreign body reaction, sarcoidosis and other granulomatous diseases).

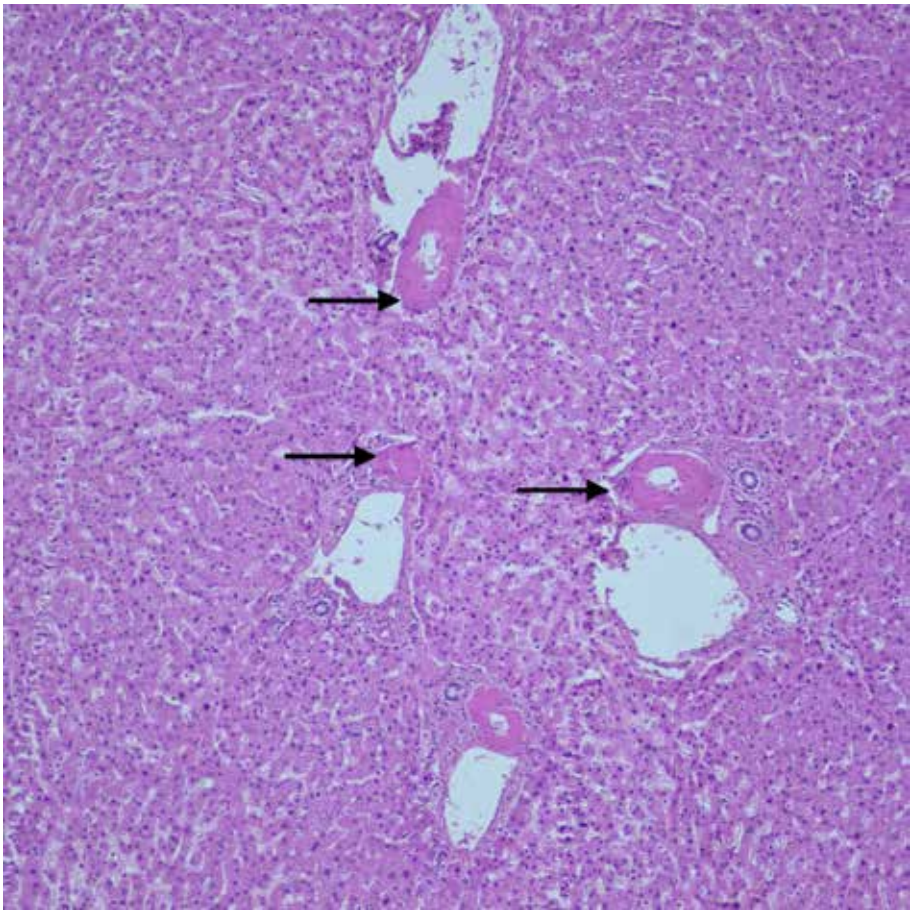

Figure 3.12 Amyloid deposition in liver vascular walls, (H&E, x100). The microscopic view shows eosinophilic amorphous amyloid accumulation on the vessel walls (arrows) in the parenchyma. Systemic amyloidosis often involves the liver. Accumulation often occurs in hepatic artery branches and sinusoids. We can also see amyloid-like homogeneous portal deposits in light chain deposition disease. Congo red helps in differential diagnosis.

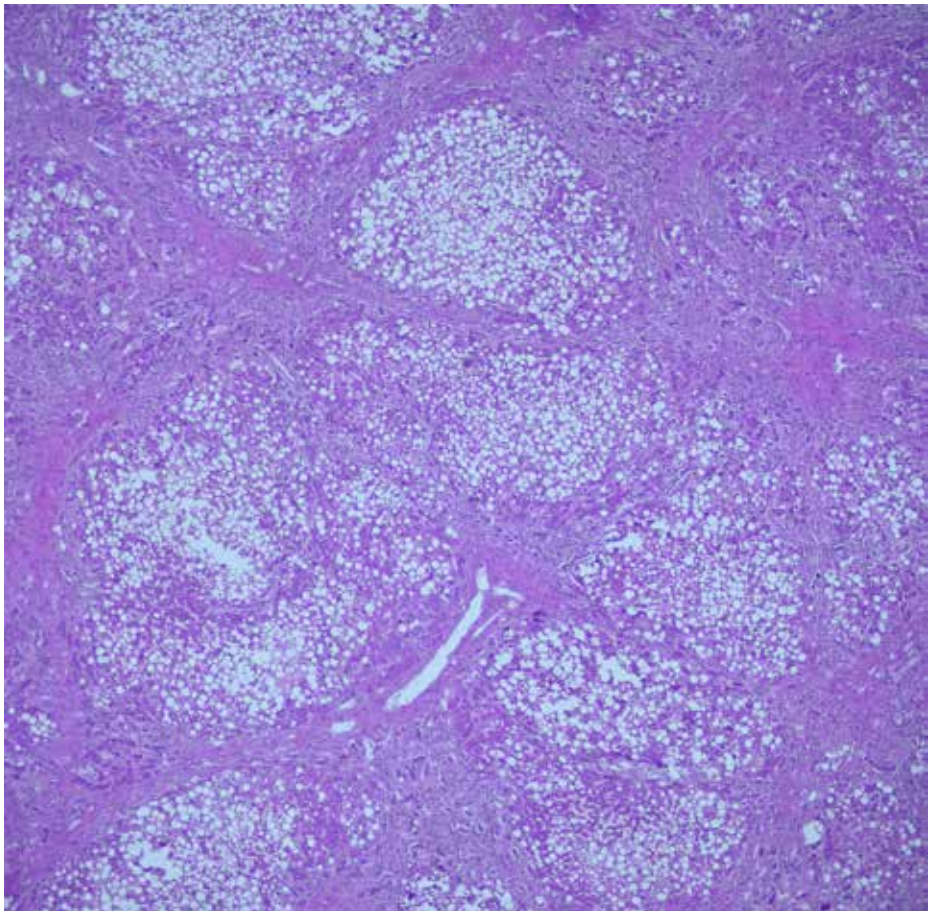

Figure 3.13
Cirrhosis,
(H&E, x40).
Diffuse nodulation surrounded by fibrous bands is observed in the liver parenchyma.

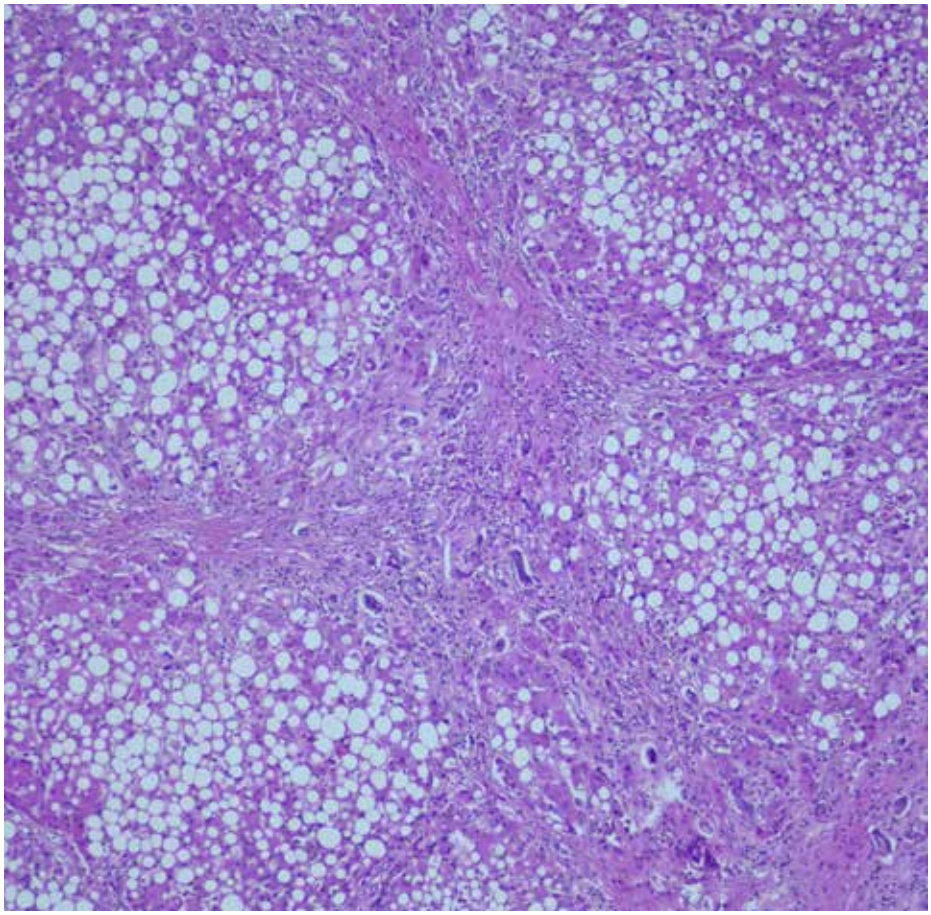

Figure 3.14
Cirrhosis,
(H&E, x100).
At higher magnification, fibrous bands along with bile duct proliferation and mononuclear inflammatory cell infiltration are notable.

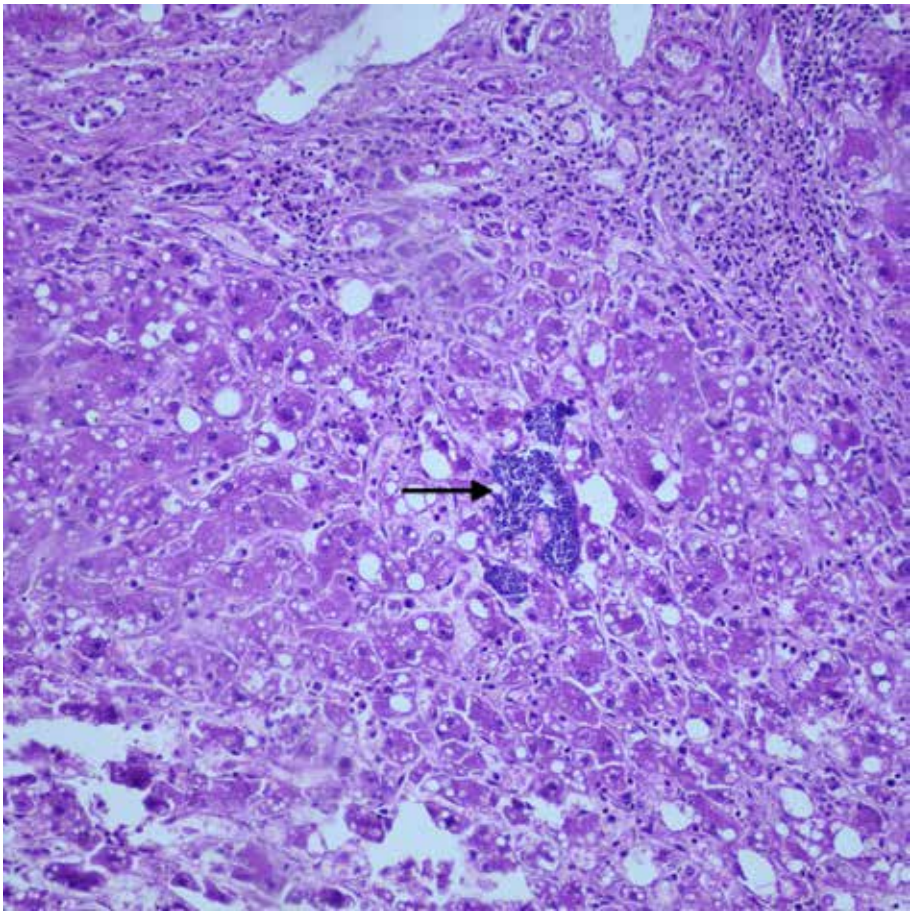

Figure 3.15
Postmortem bacteria clusters in the liver, (H&E, x200). Especially in cases with a long postmortem period, basophilic bacterial clusters (arrow) without an inflammatory response may be seen.

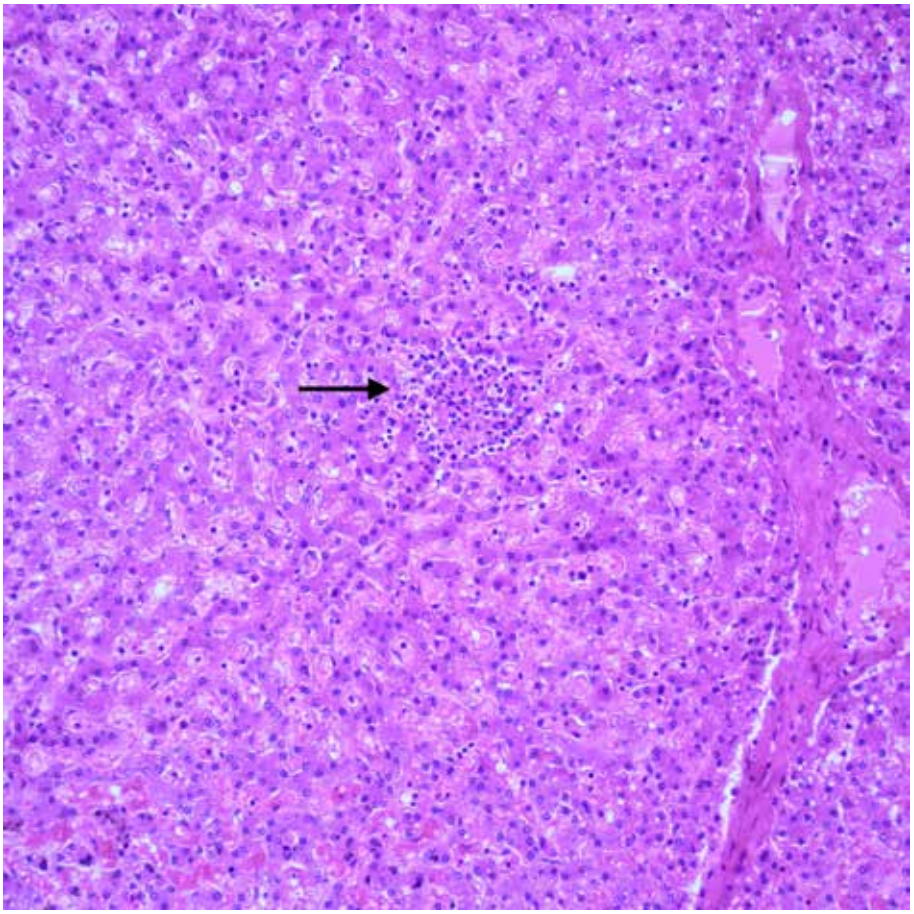

Figure 3.16
Septic focus in the liver, (H&E, x200). A microabscess (arrow) consisting of neutrophils and necrotic hepatocytes is seen in the liver parenchyma. In the case, there were septic foci in many organs and the procalcitonin level was found to be high.

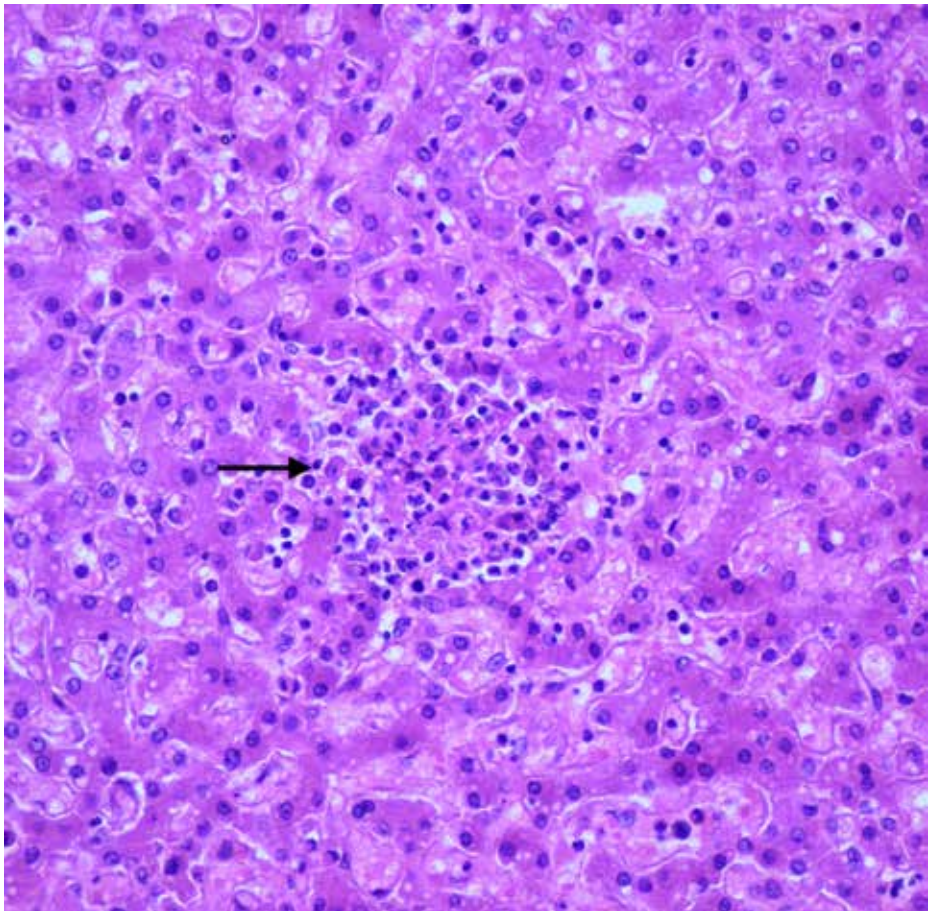

Figure 3.17
Septic focus in the liver,
(H&E, x400)
At higher magnification (arrow).

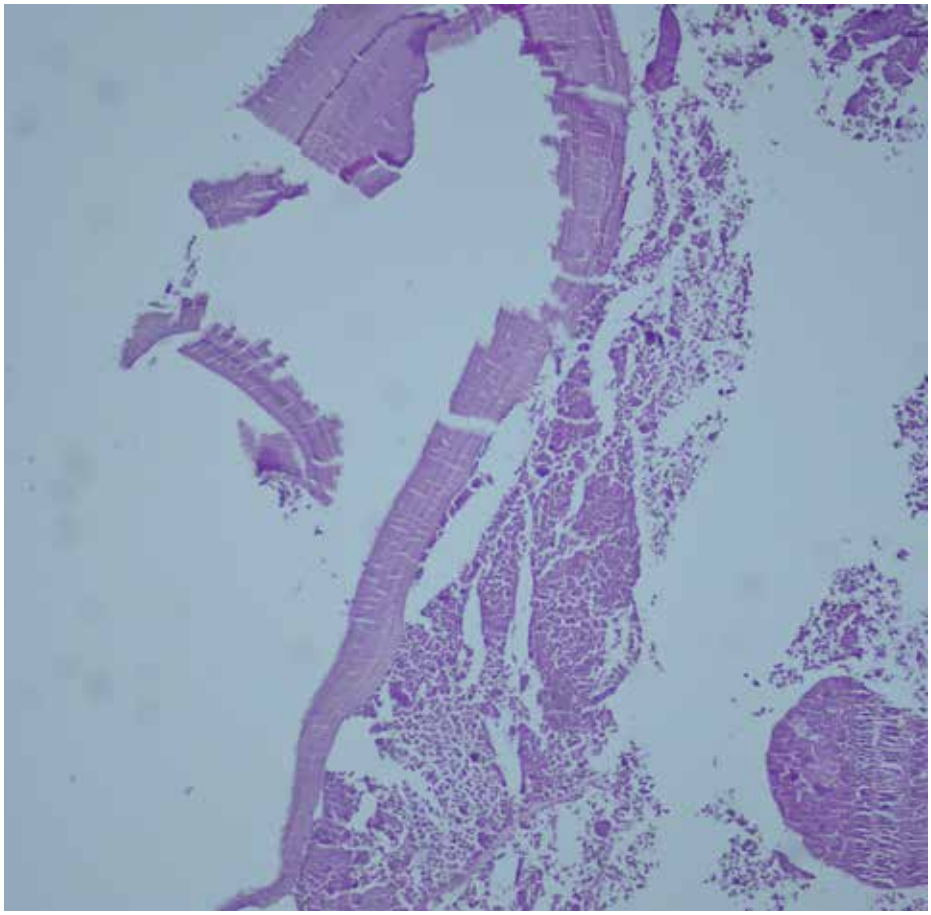

Figure 3.18
Liver hydatid cyst,
(H&E, x100).
Hydatid cyst contains inner germinal layer.

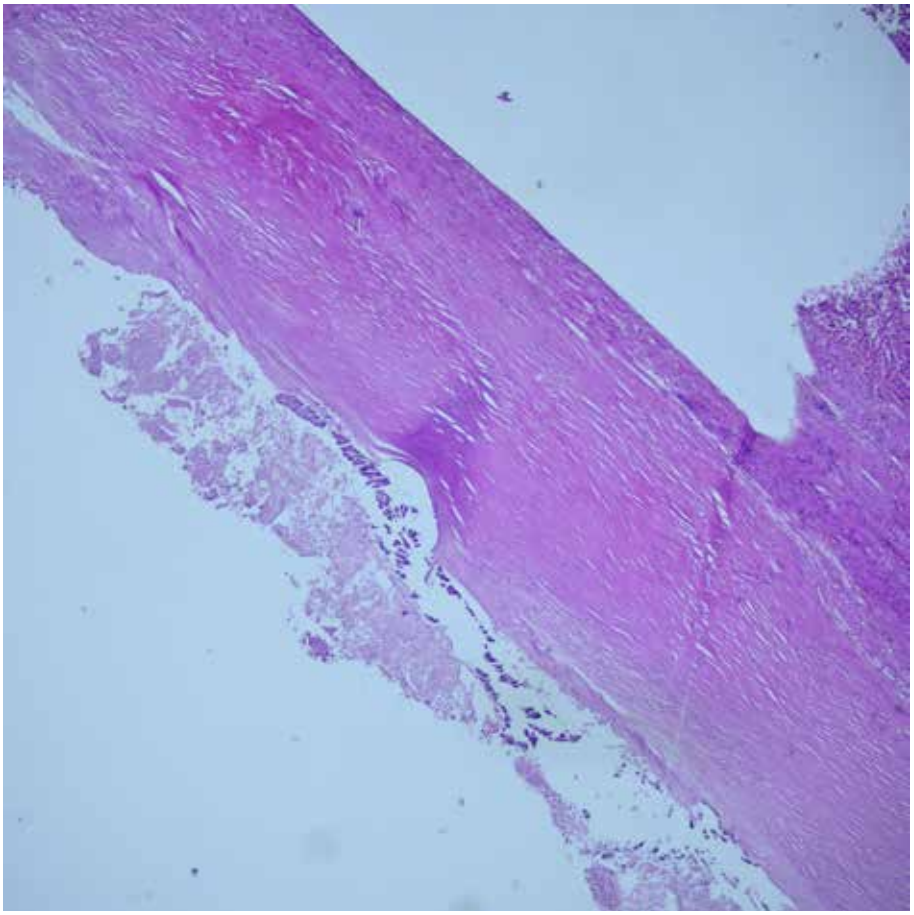

Figure 3.19 Fibrous laminar layer of liver hydatid cyst, (H&E, x40). Hydatid cyst wall contains outer fibrous laminar (chitinous) layer.

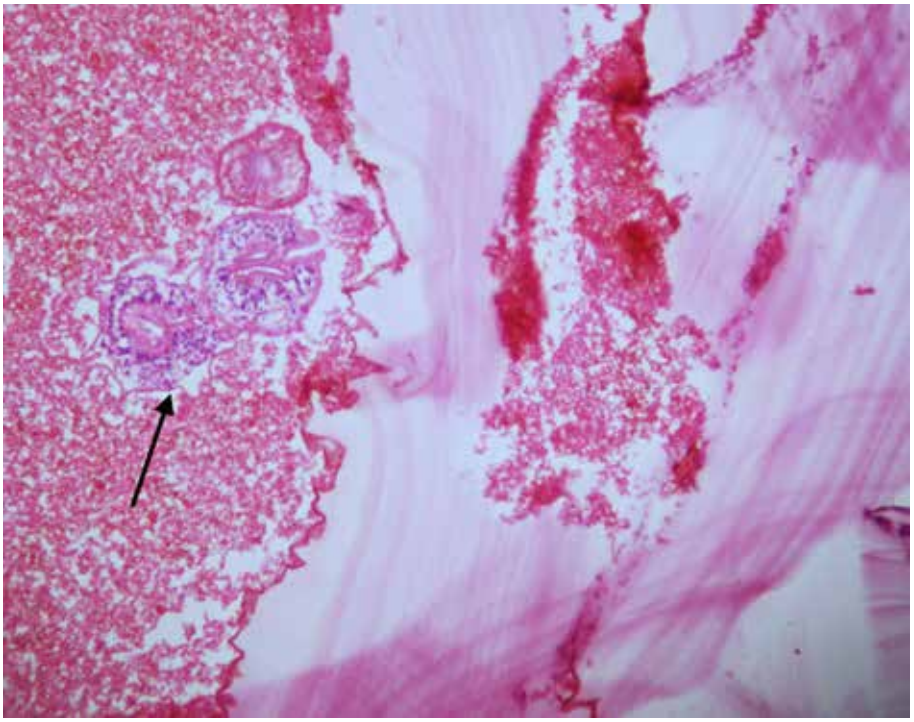

Figure 3.20 Hydatid cyst scolex, (H&E, x400). Scolex (arrow) surrounded by germinal membrane lining the hydatid cyst.

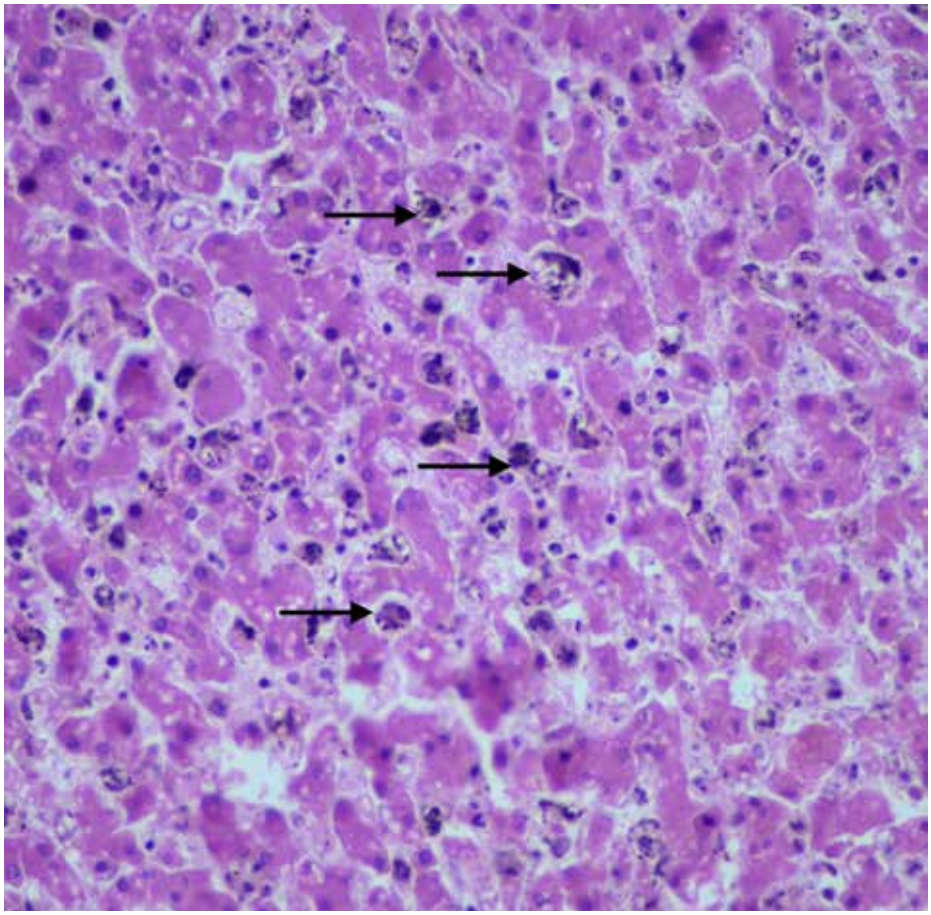

Figure 3.21
Malaria,
(H&E, x400).
The Kupffer cells in the sinusoids contain brown parasite pigment (hemozoin) (arrows).

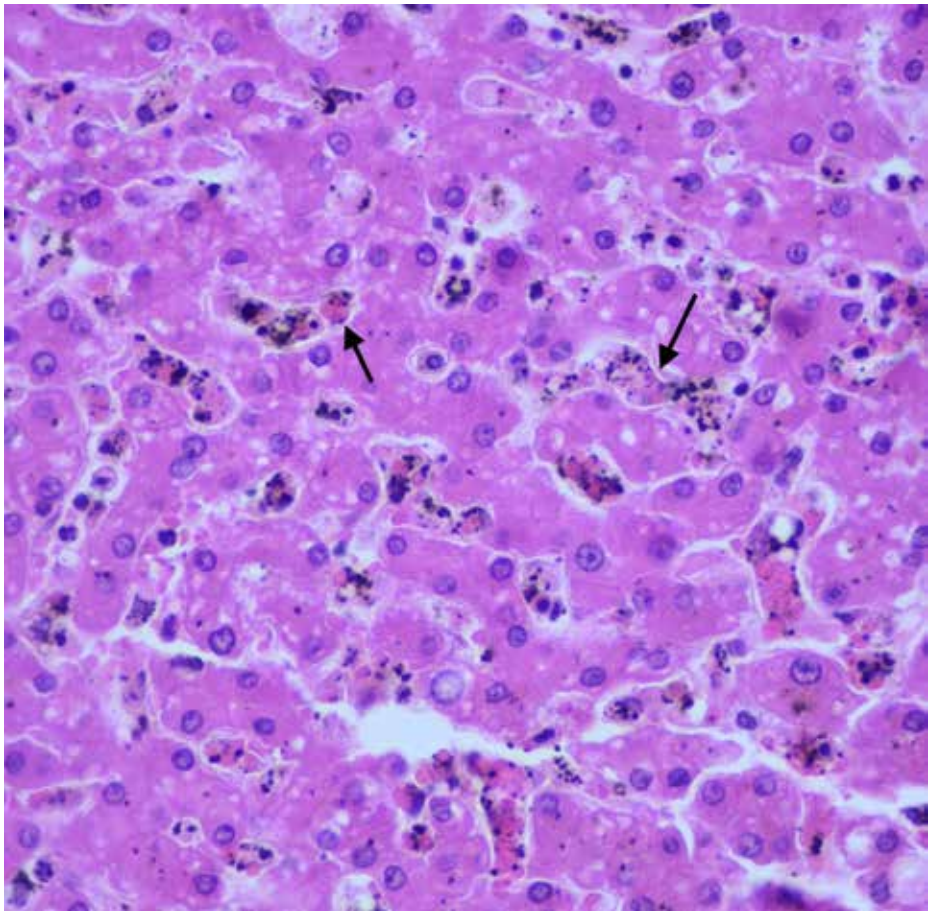

Figure 3.22
Malaria,
(H&E, x600).
At higher magnification.
Many black-dark brown, coarse parasite pigments (hemozoin pigment) (arrows) are seen in the erythrocytes located in the capillary lumen.

KIDNEY

Assoc. Prof. Taner DAŞ

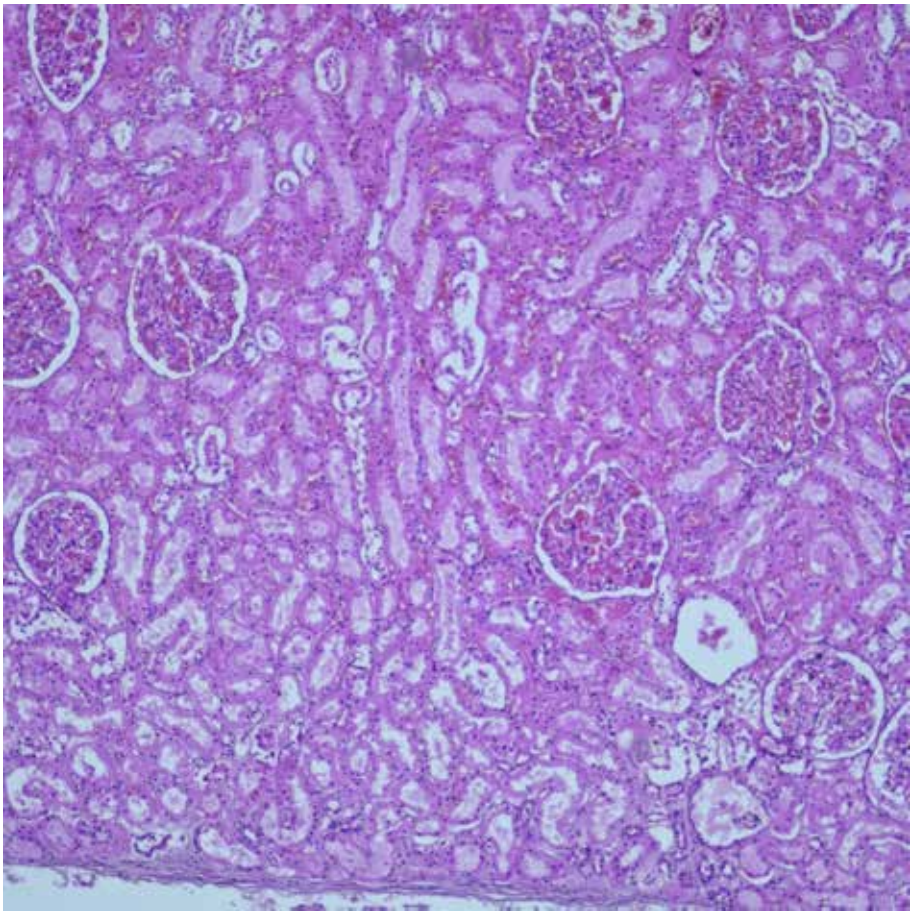

Figure 4.1
Normal renal histology, (H&E, x100)
In the microscopic view of the kidney, normal appearance of glomeruli, tubules, interstitium and vascular structures are seen.

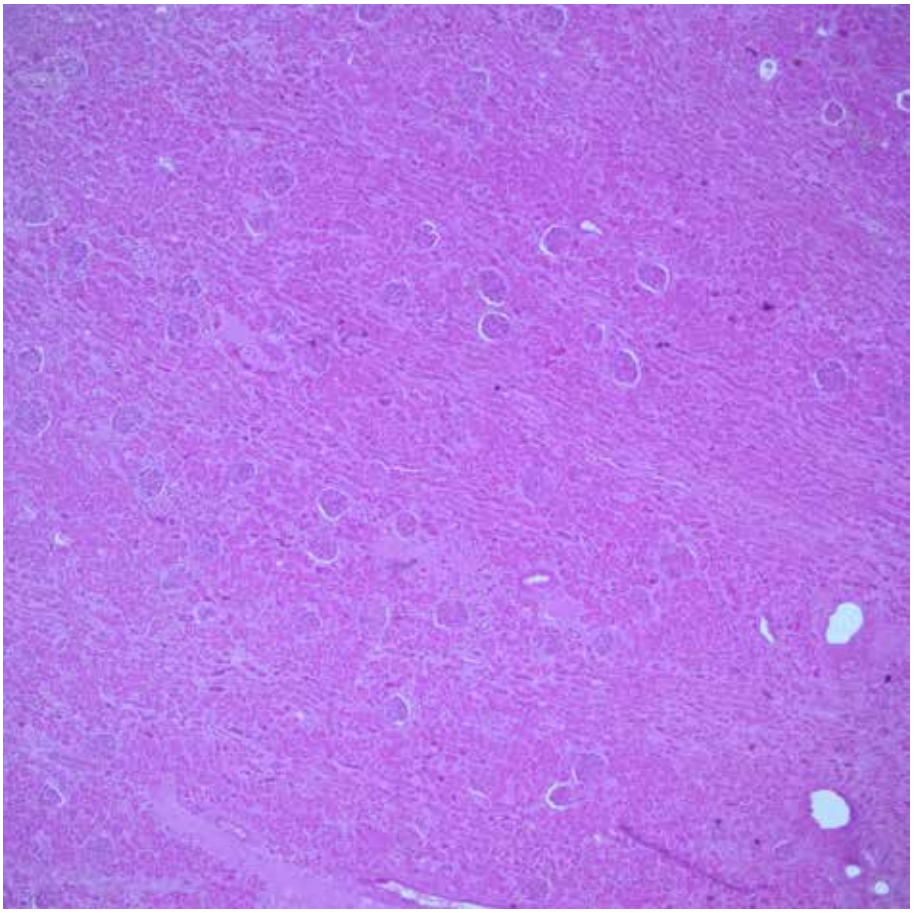

Figure 4.2
Kidney autolysis, (H&E, x40).
Autolysis is the digestion of the dead or dying cell by its own enzymes.

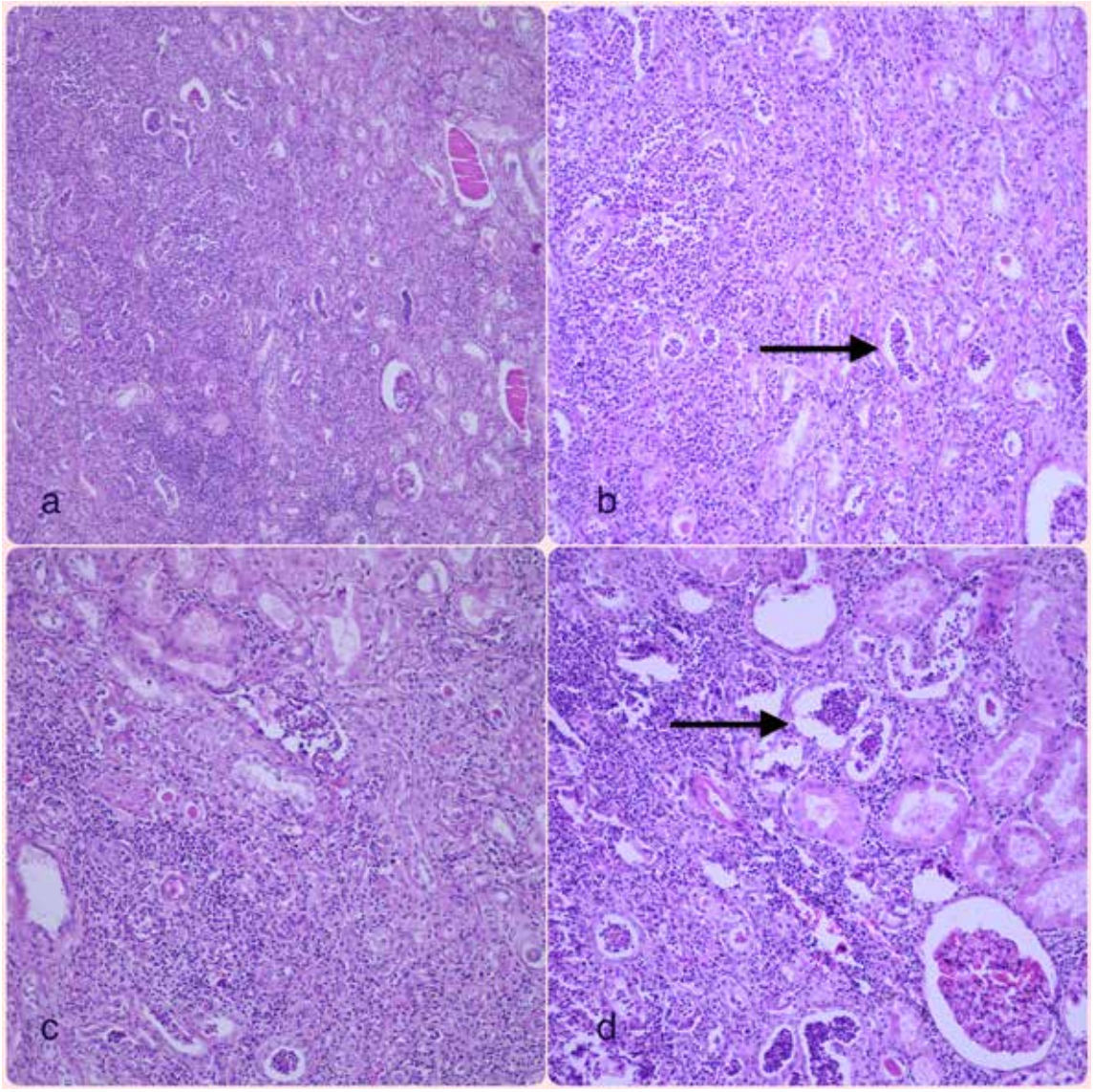

Figure 4.3
Acute tubulointerstitial nephritis,
a,b,c,d) (H&E, x100,x200,x200,x200).
Acute tubulointerstitial nephritis is the acute inflammation of the tubular and interstitial compartments of kidney. Infection, drugs and autoimmune diseases may cause acute tubulointersititial nephritis. Approximately 70% of all tubulointerstitial nephritis is due to drugs. In the images, dense neutrophil infiltration is seen in the interstitium and tubule lumens (arrows).

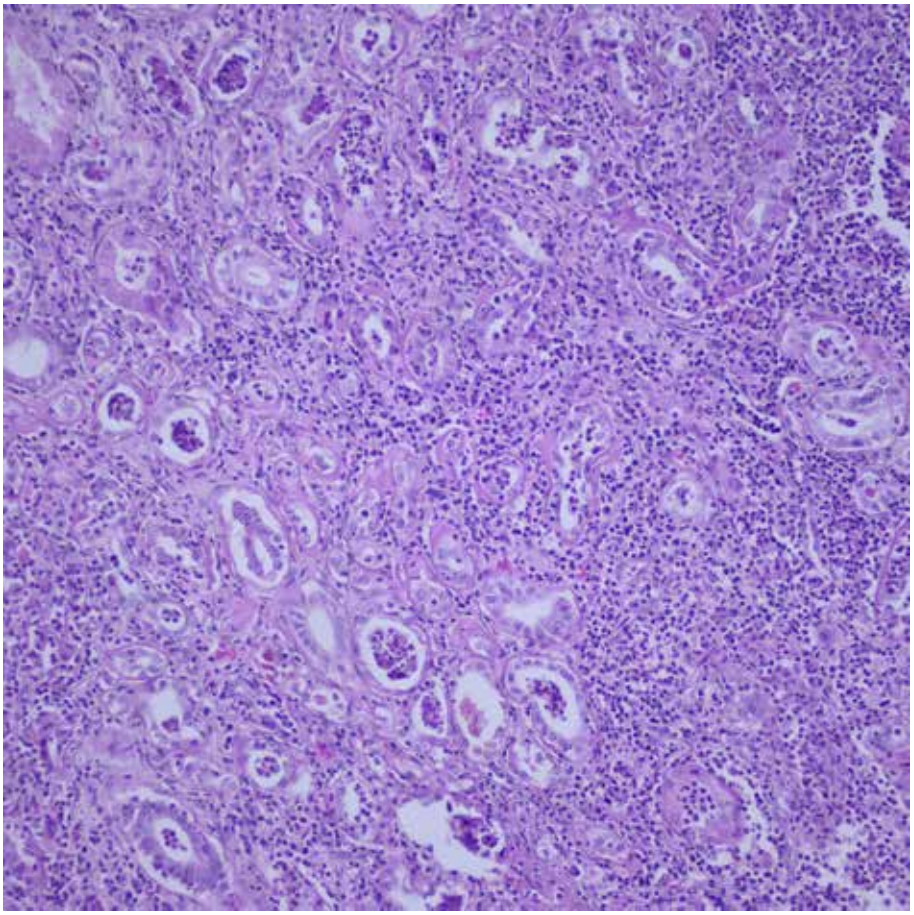

Figure 4.4
Acute tubulointerstitial nephritis, (H&E, x200). Abundant neutrophil infiltration is seen in the intersititium and tubule lumen.

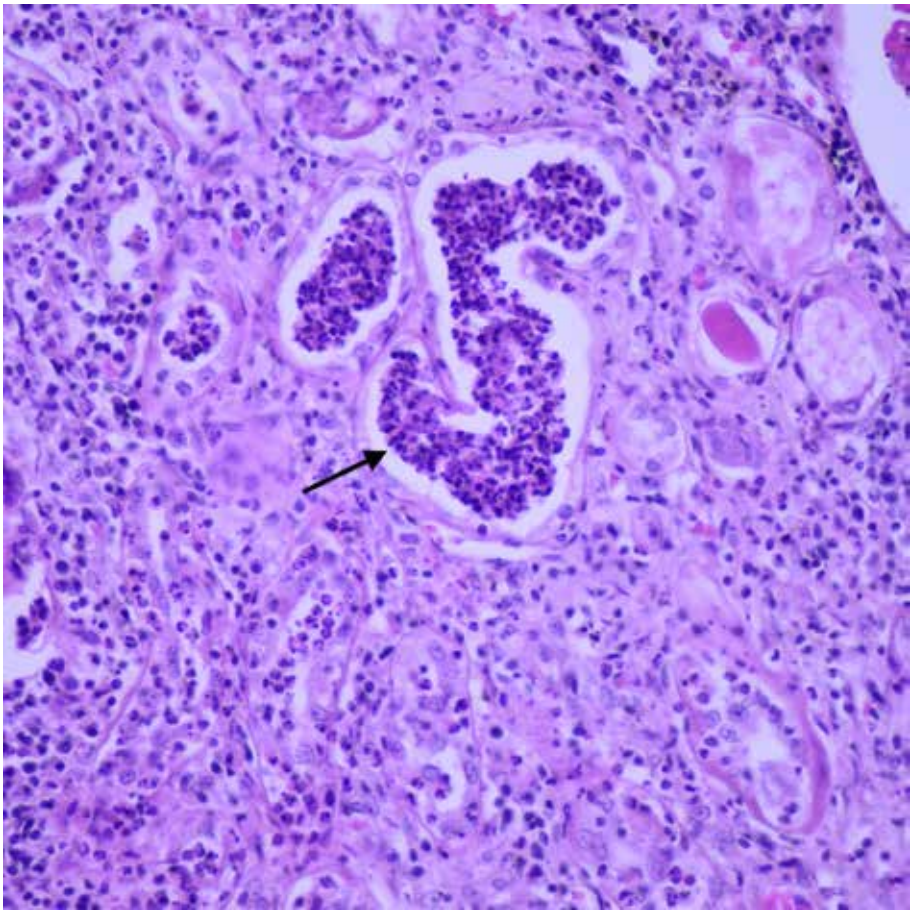

Figure 4.5
Acute tubulointerstitial nephritis, (H&E, x400). Abundant neutrophil accumulation (arrow) in the tubule lumens.

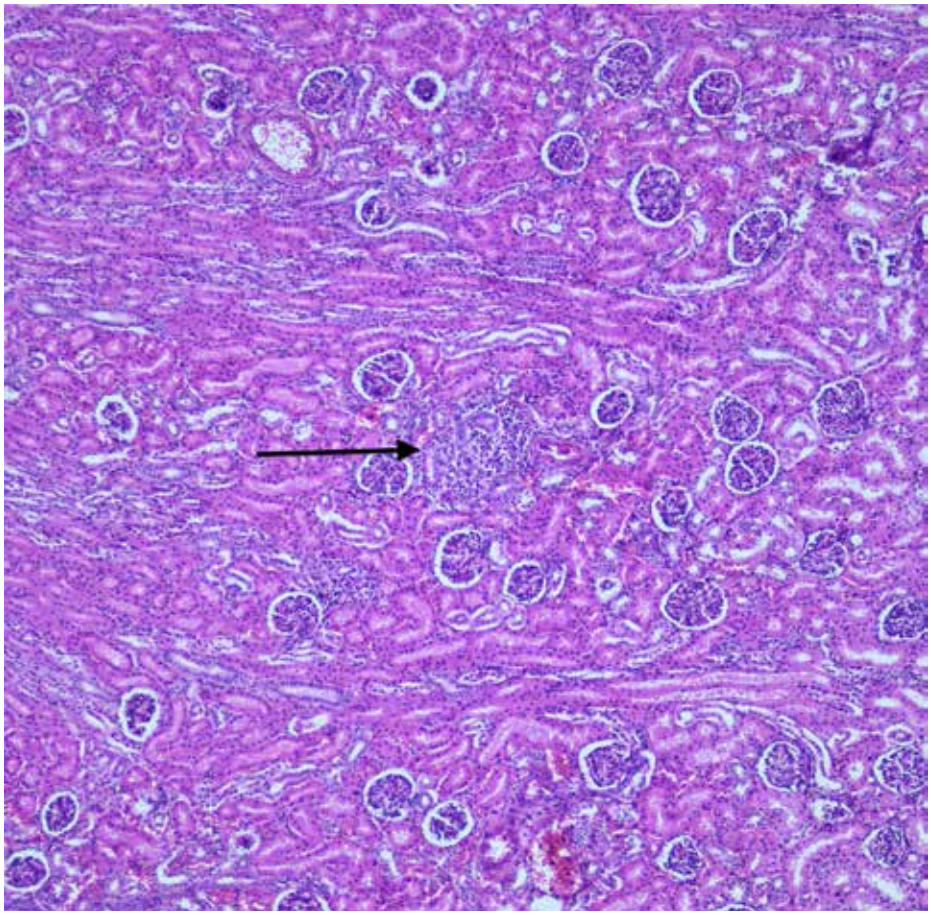

Figure 4.6
Interstitial nephritis (CMV), (H&E, x100). Mononuclear inflammatory cell infiltration (arrow) is observed in the interstitial area of the renal parenchyma (interstitial nephritis). [CMV was verified by rt-PCR at the postmortem renal tissue].

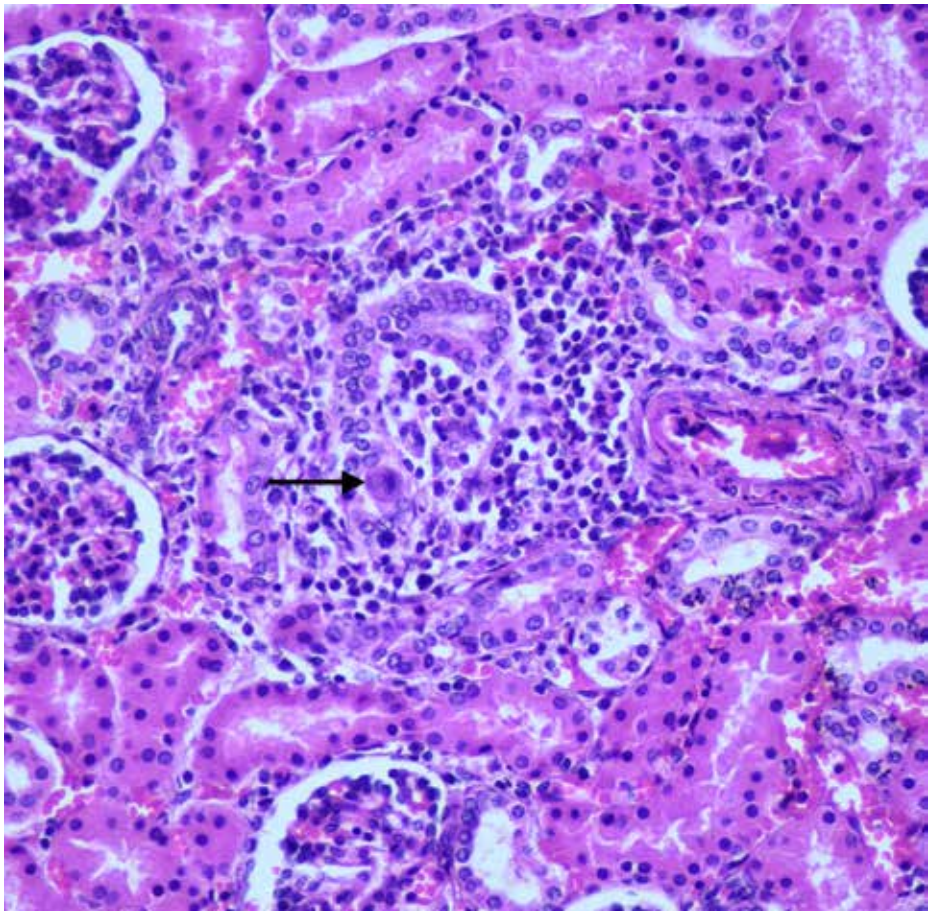

Figure 4.7
Interstitial nephritis (CMV), (H&E, x400). Interstitial mononuclear inflammatory cell infiltration and enlarged tubule epitelial cell due to viral cytopathic effect, and "owl-eye type intranuclear inclusion" (arrow) and intracytoplasmic basophilic inclusions are observed.

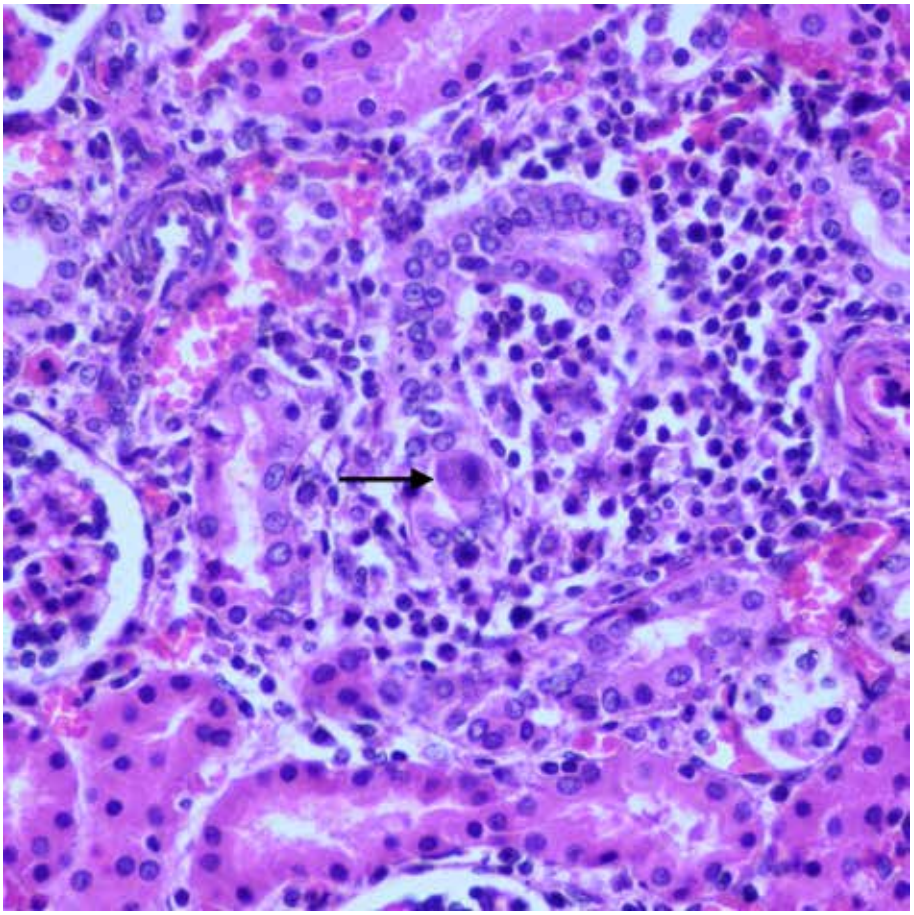

Figure 4.8 Interstitial nephritis (CMV), (H&E, x600). At higher magnification enlargement of the tubule epithelium due to the viral cytopathic effect and owl-eye type intranuclear inclusion and intracytoplasmic basophilic inclusion. (arrow)

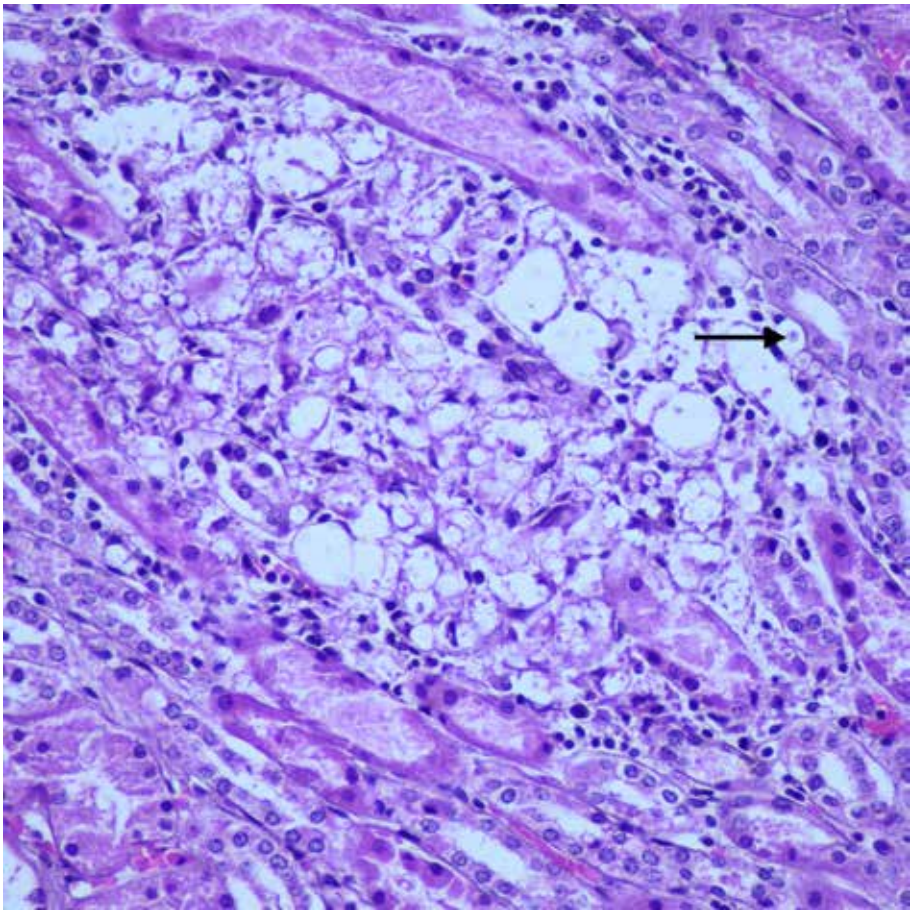

Figure 4.9 Fungal nephritis, (H&E, x200). In the microscopic view, cryptococci (arrow) are seen in the parenchyma. Cryptococcus is a common opportunistic infection in people with HIV infection.

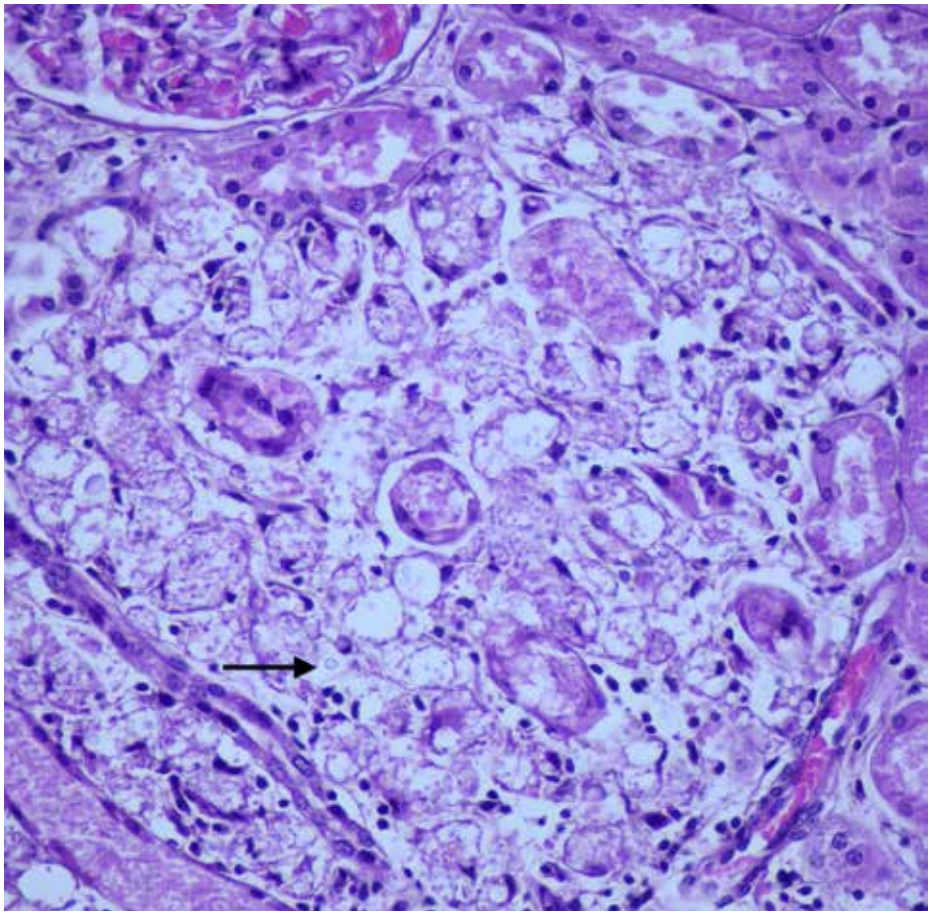

Figure 4.10
Fungal nephritis, (H&E, x400). At higher magnification, round or oval-shaped cryptococci (arrow) with thin walls seen.

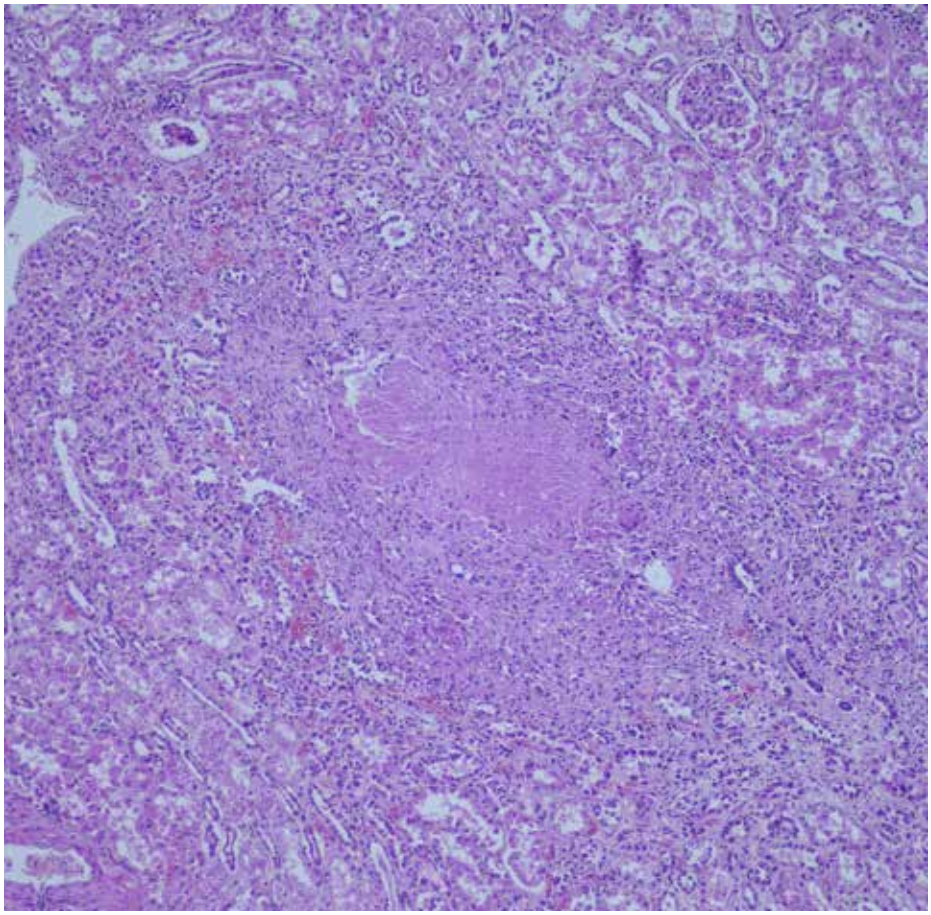

Figure 4.11
Necrotizing granuloma in the kidney, (H&E, x100). A granuloma with central necrosis is observed in the kidney parenchyma.

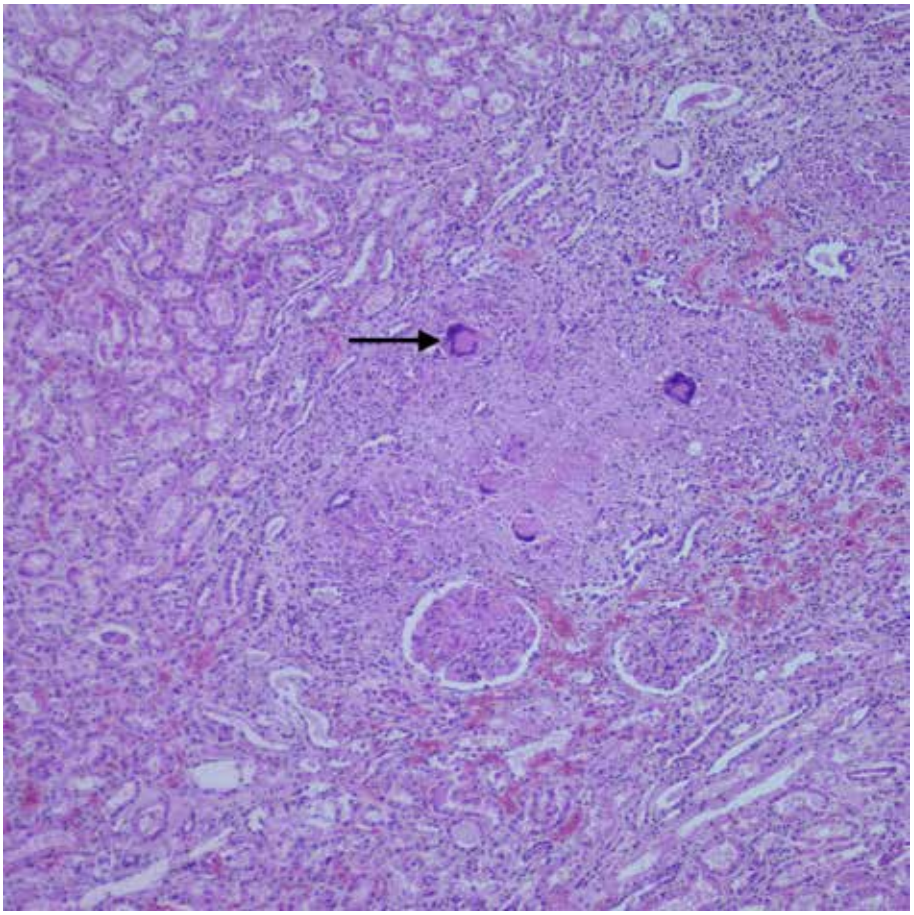

Figure 4.12
Necrotizing granuloma in the kidney, (H&E, x100). Necrotizing granuloma with central necrosis and surrounding epithelioid histiocytes and Langhans-type giant cells (arrow).

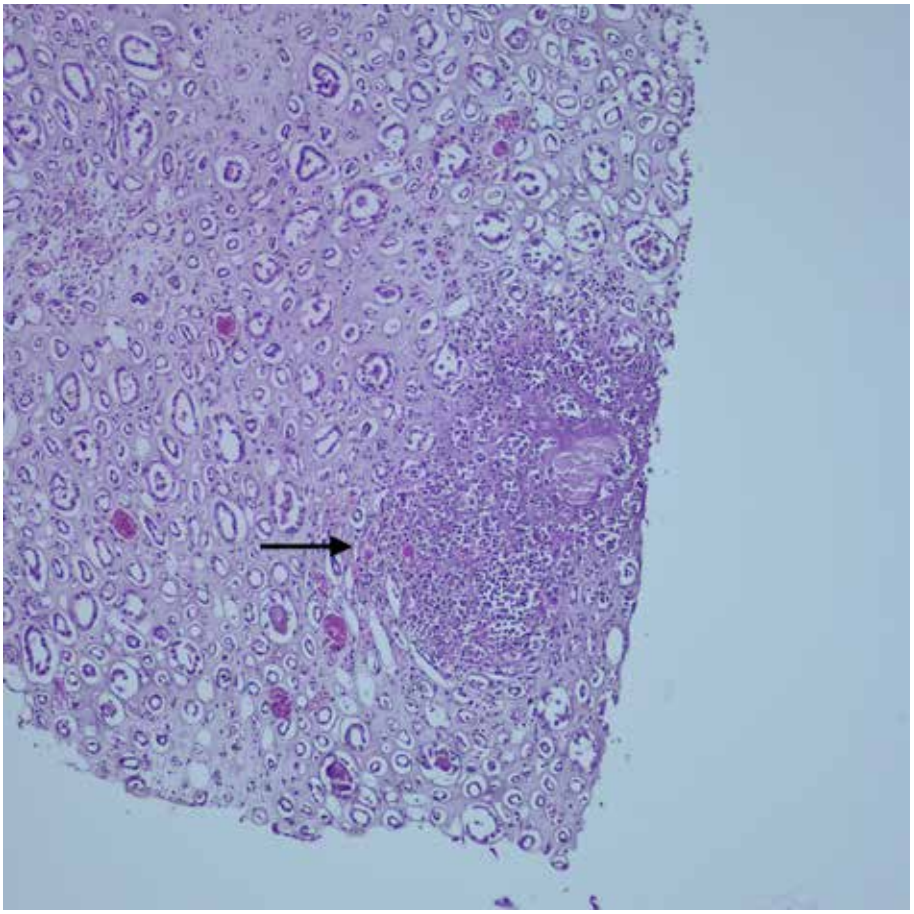

Figure 4.13
Renal septic focus (microabscess), (H&E, x100). A microabscess (arrow) consisting of neutrophils is seen in the renal parenchyma.

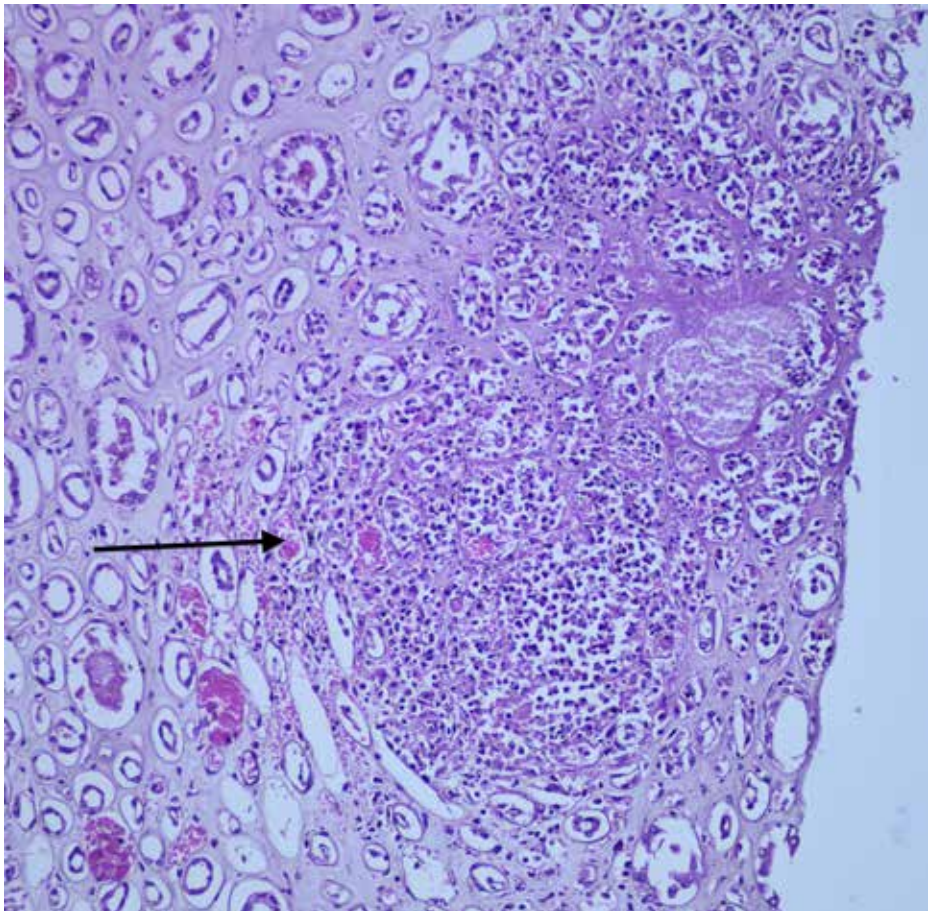

Figure 4.14
Renal septic focus (microabscess), (H&E, x200). At higher magnification.

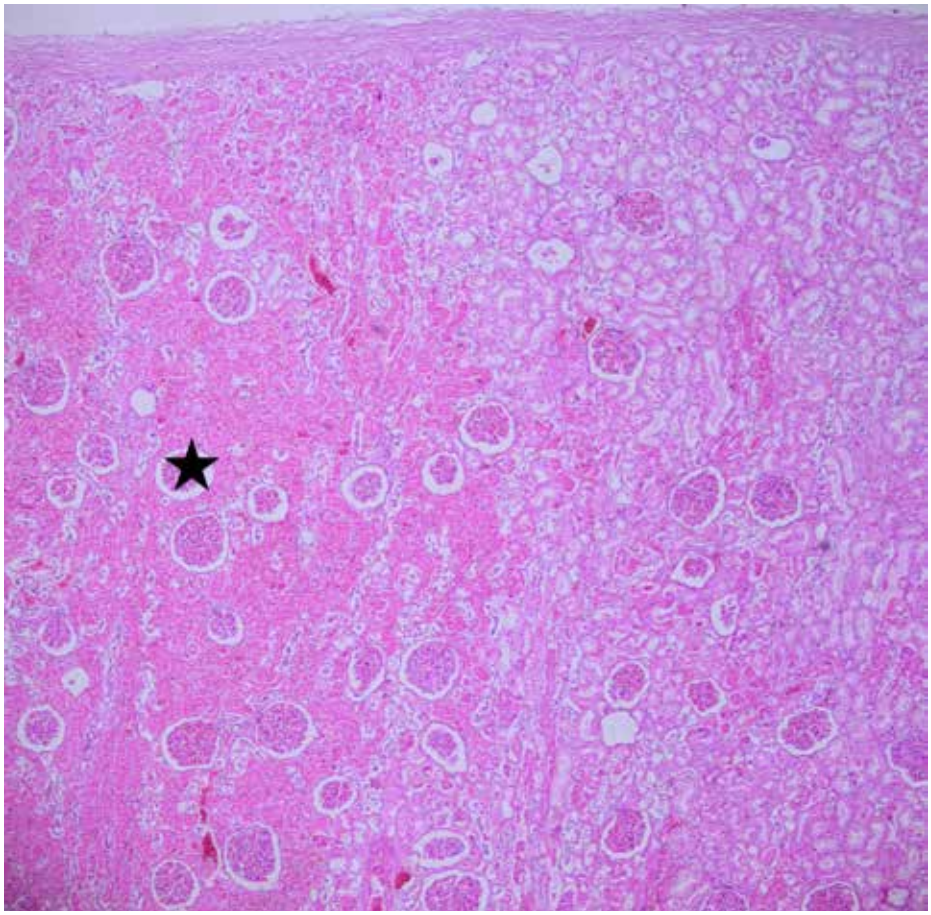

Figure 4.15
Acute Tubular Necrosis (Injury, Damage), (H&E, x40).
Acute tubular necrosis mostly develops due to ischemic (50%) and toxic (25%) causes. Since necrosis is rarely seen, "acute tubular injury" is a more appropriate terminology. In the microscopic view, on the left side, there is necrotic appearance in the tubular epithelium, with hypereosinophilia and loss of nuclei (asterisk).
Necrosis can be evaluated more clearly when compared to the normal tubular structures on the right side of the image.

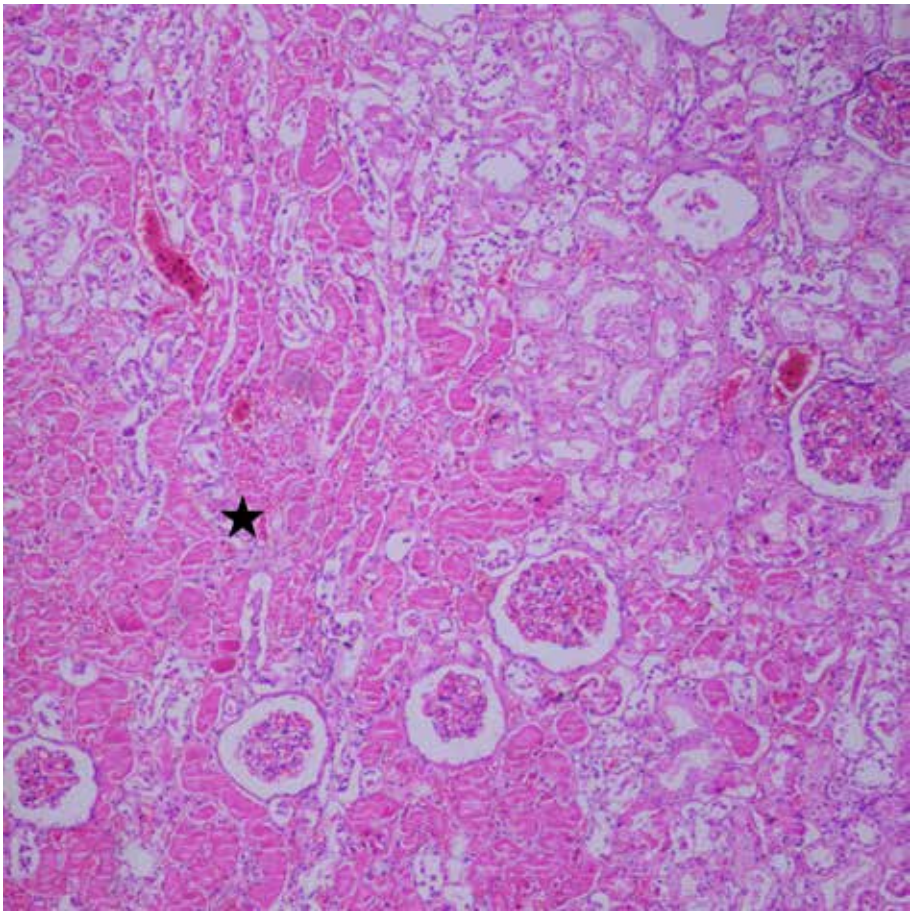

Figure 4.16 Acute Tubular Necrosis (Injury, Damage), (H&E, x100). At higher magnification. Acute tubular necrosis (asterisk).

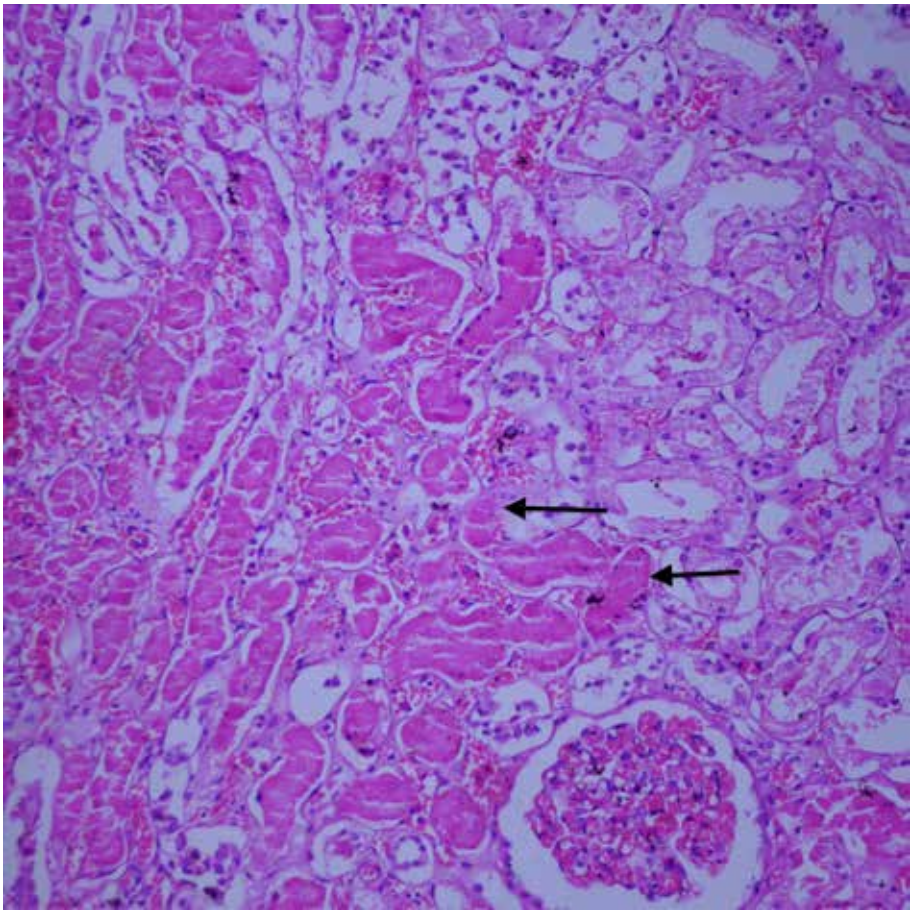

Figure 4.17 Acute Tubular Necrosis (Injury, Damage), (H&E, x200). At higher magnification. Necrotic changes at the tubular epithelium (arrows). Necrosis occurs more frequently in ATN that develop due to toxic causes.

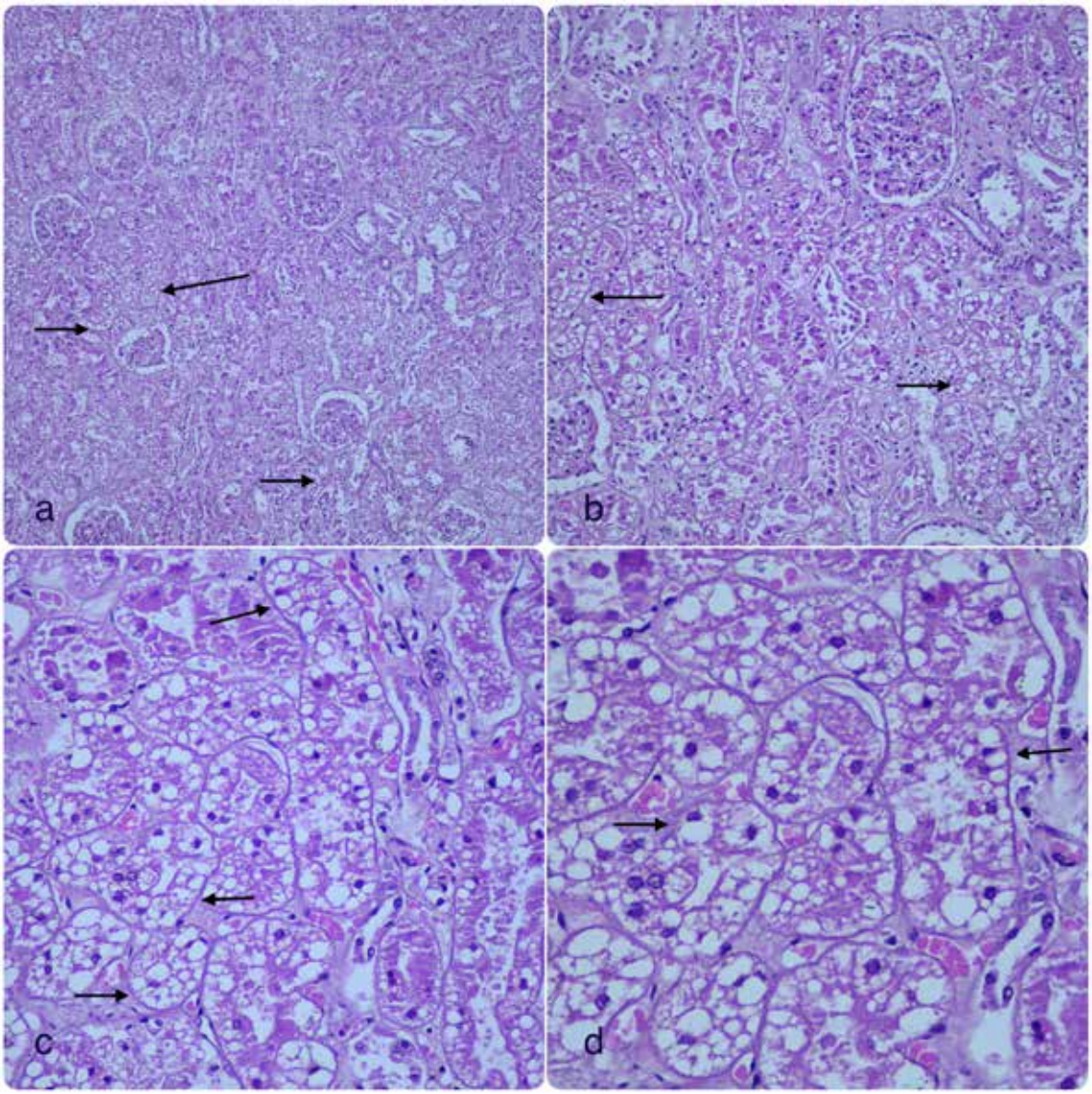

Figure 4.18
Toxic Acute Tubuler Injury,
a,b,c,d) (H&E, x100,200,400,400).
Subnuclear vacuoles in renal tubules are considered as histological signs of ketoacidosis. In addition to being detected in diabetic ketoacidosis, subnuclear tubular vacuolization is also detected in starvation, hypothermia and alcoholic ketoacidosis.
They occur in the majority of deaths due to alcohol use disorders. Although it has been seen in deaths due to alcoholic ketoacidosis, it is not specific.
In the microscopic view, subnuclear vacuolization (arrows) in the renal tubules of an alcoholic person due to cologne use is noteworthy.
Similarly, in carbon tetrachloride poisoning, lipid accumulation and subsequent necrosis may develop in damaged tubule epithelial cells.

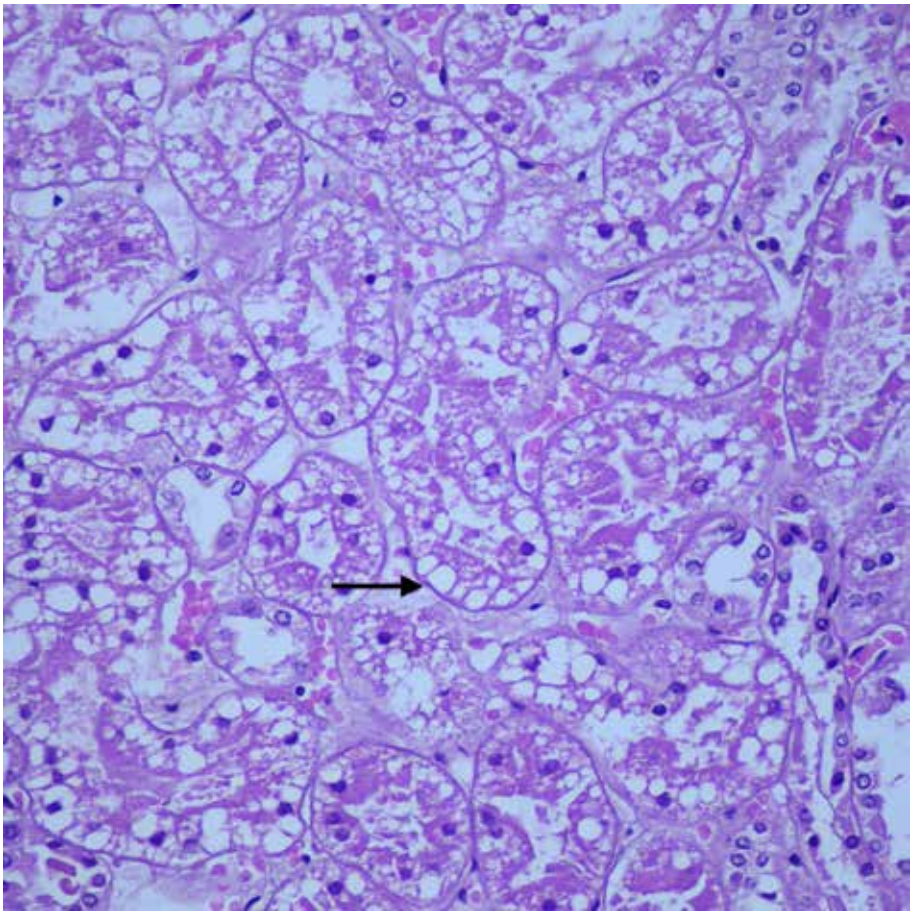

Figure 4.19 Toxic Acute Tubuler Injury, (H&E, x400). Subnuclear vacuolization (arrow) in the renal tubules.

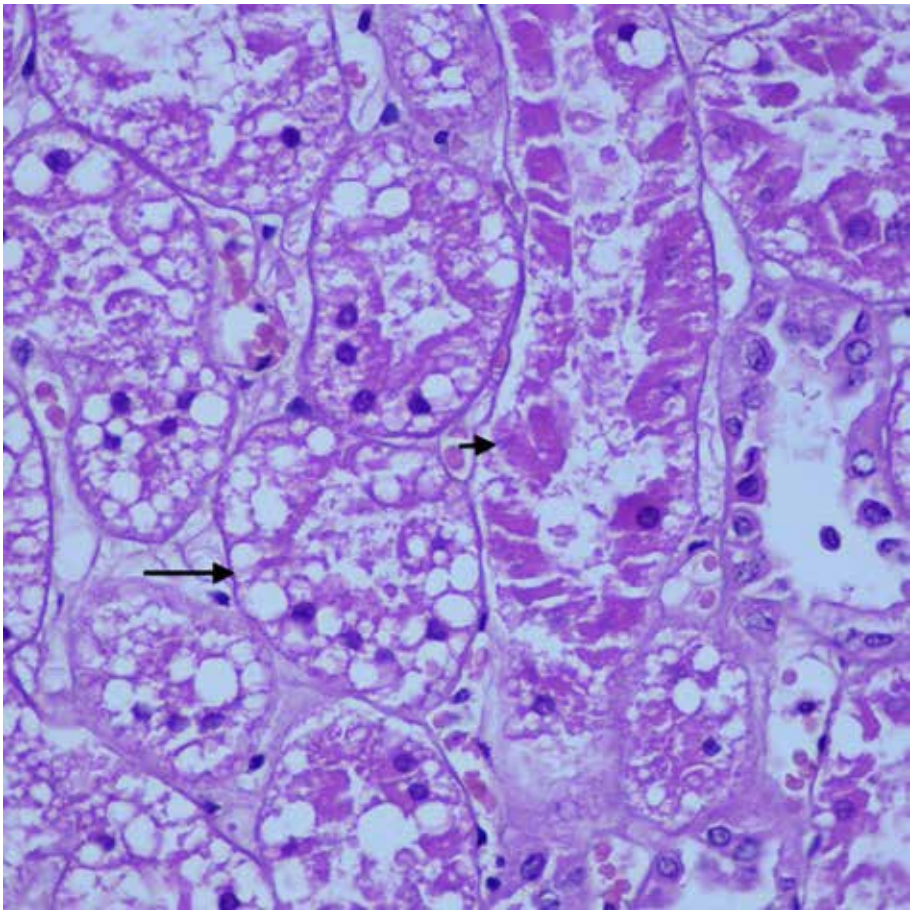

Figure 4.20 Toxic Acute Tubuler Injury, (H&E, x600). At higher magnification, subnuclear vacuolization (long arrow) is seen in the renal tubules. Necrotic changes in the tubule epithelium, indicated by the short arrow, are noteworthy.

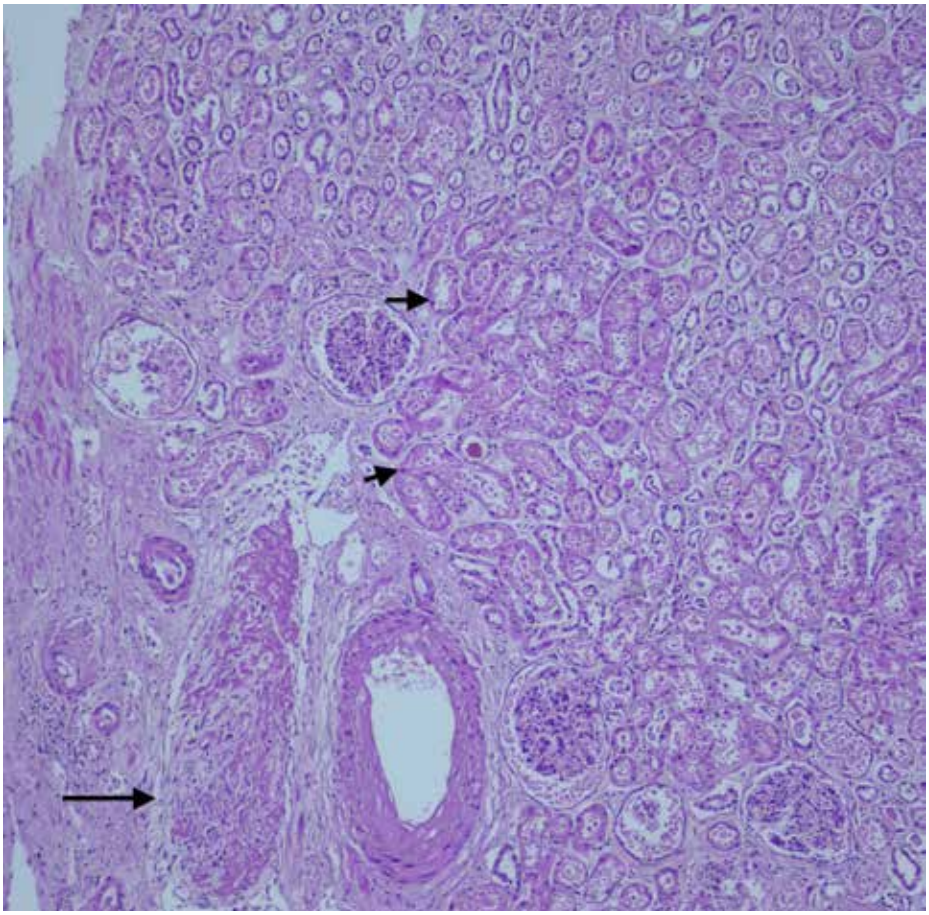

Figure 4.21
Renal thrombus,
(H&E, x100).
The microscopic view demostrates a fibrin thrombus (long arrow) showing signs of organization in the vascular lumen. There is acute tubular damage (short arrow)
in the surrounding tubules.

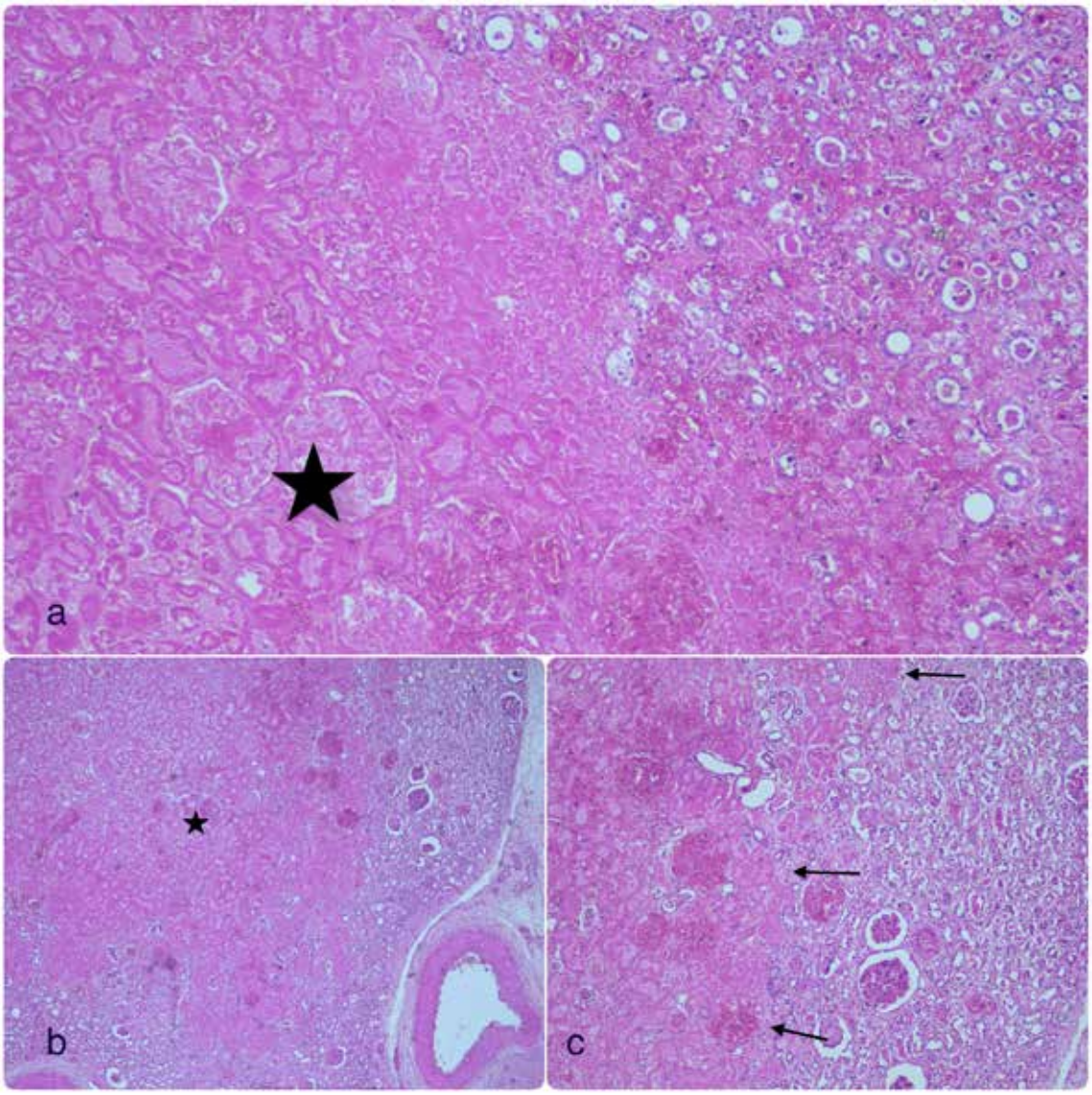

Figure 4.22
Renal infarction,
a) (H&E, x100). Renal infarction on the left side of the image marked with an asterisk. Renal infarction most commonly occurs due to embolism or in situ thrombosis.
b) (H&E, x40) Renal infarct area marked with an asterisk at lower magnification
c) (H&E, x40) Normal kidney parenchyma is seen on the right side of the image, and the renal infarct area is shown with arrows on the left side.

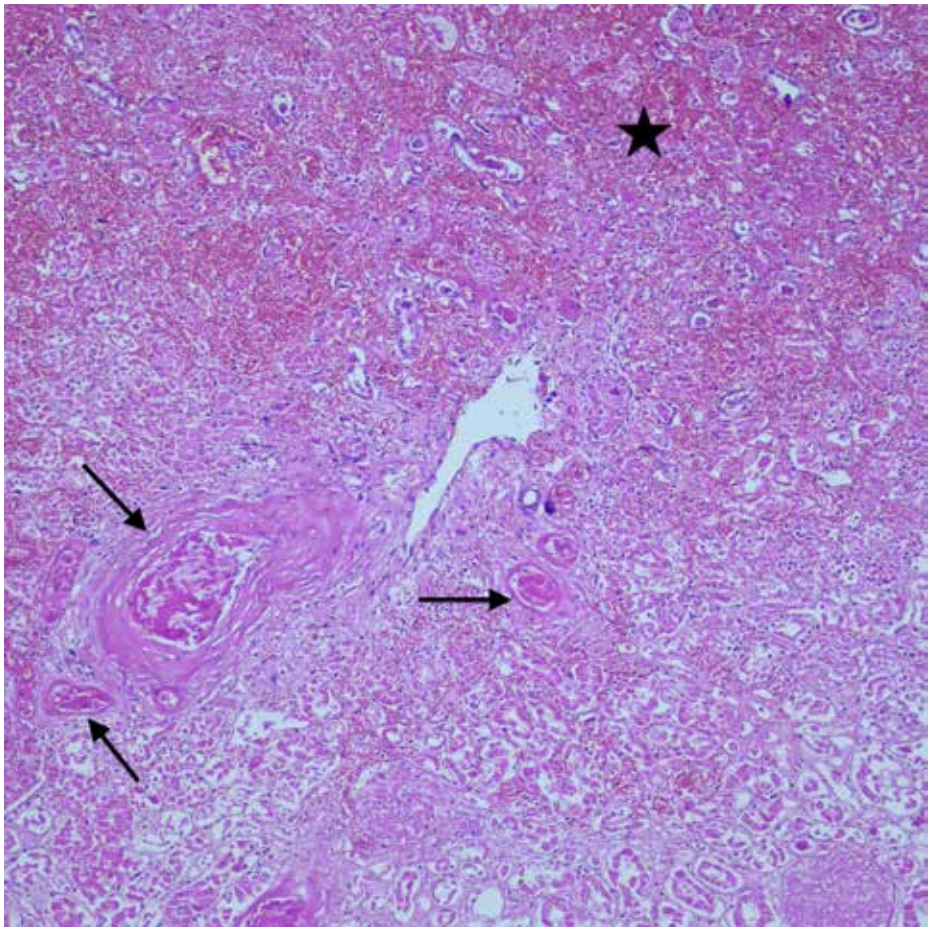

Figure 4.23
Renal infarction, (H&E, x100). Fibrin thrombi (arrows) are seen in the lumen of many vessels. The area of renal infarction is marked with an asterisk.

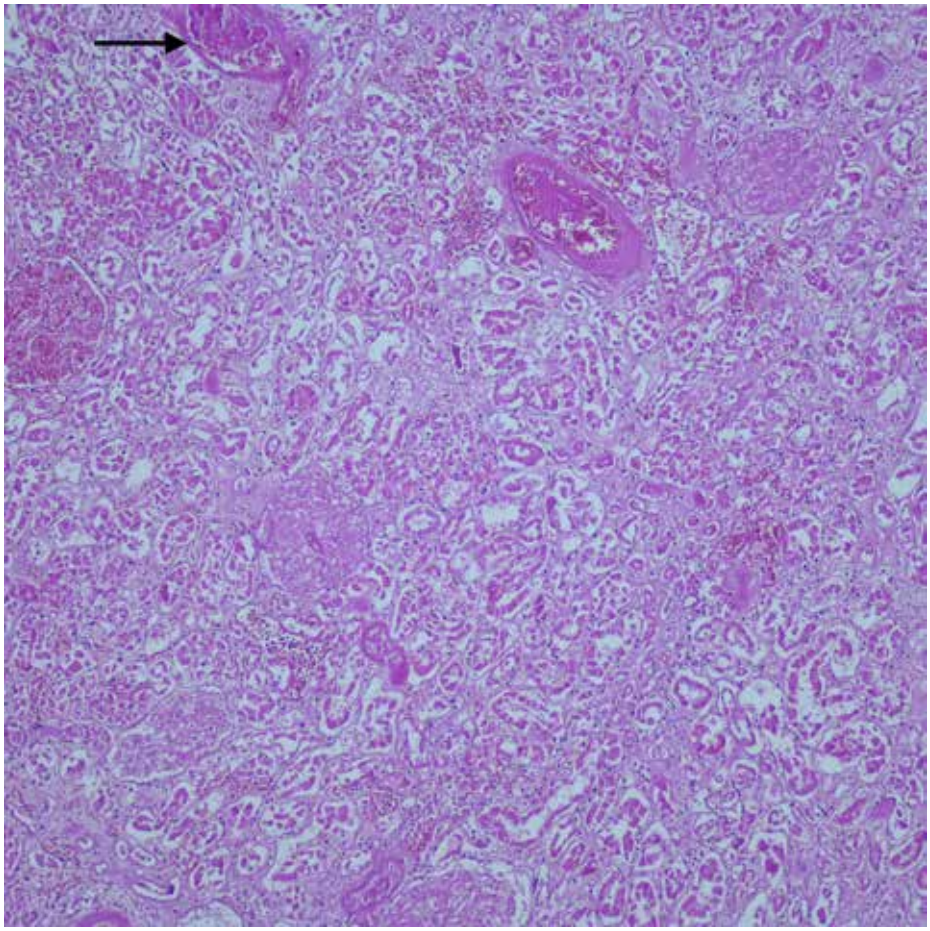

Figure 4.24
Renal infarction, (H&E, x100). Fibrin thrombus (arrow) in the vascular lumen and renal infarction.

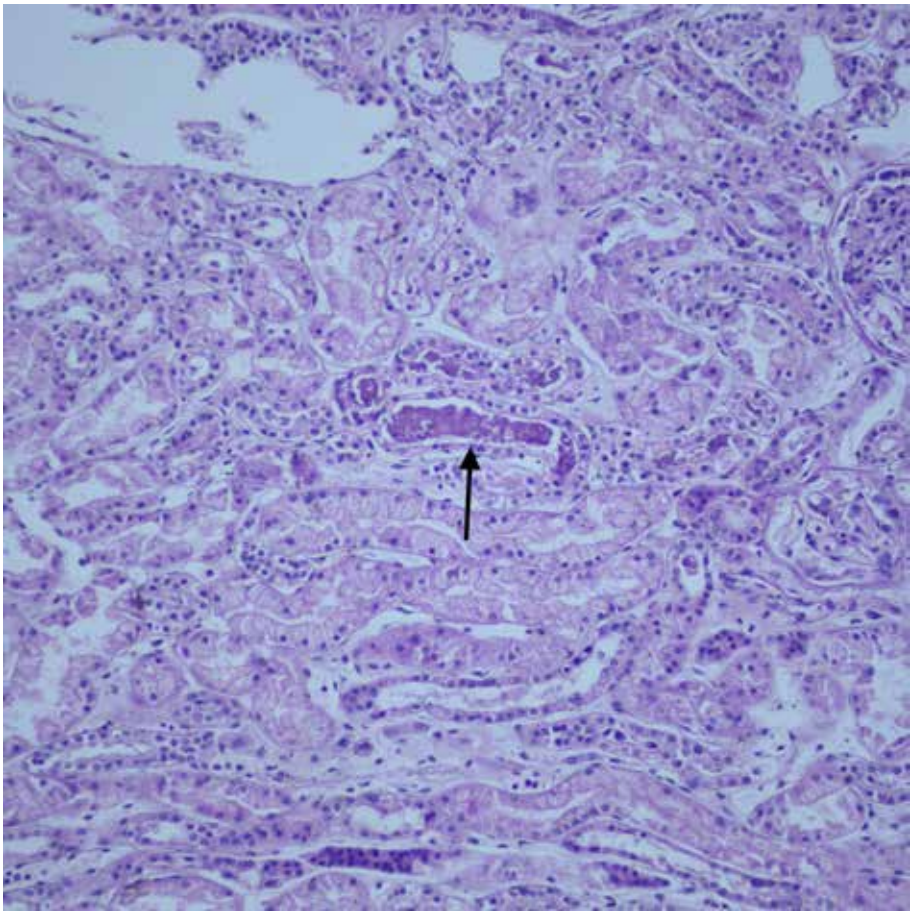

Figure 4.25
Rhabdomyolysis, (H&Ex200). In rhabdomyolysis, acute tubular damage and myoglobulin-containing casts are seen in the tubule lumen. It is also called pigment nephropathy. Acute renal failure develops in approximately 40% of severe rhabdomyolysis cases. Rhabdomyolysis results from muscle injury caused by traumatic, toxic, drug related and electrical effects. The microscopic view demostrates pigmented, basophilic, granular tubular cast (myoglobulin) in the tubule lumen (arrow).

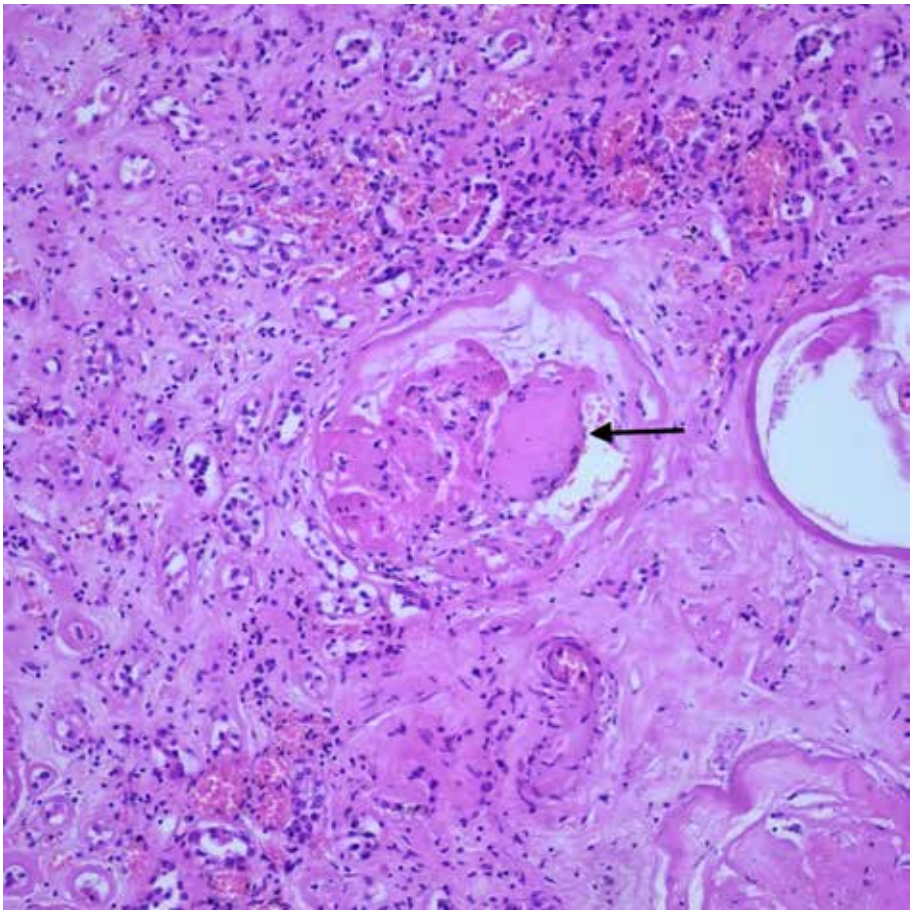

Figure 4.26
Rhabdomyolysis, (H&Ex200). In rhabdomyolysis, acute tubular damage and myoglobulin-containing casts are seen in the tubule lumen. It is also called pigment nephropathy. Acute renal failure develops in approximately 40% of severe rhabdomyolysis cases. Rhabdomyolysis results from muscle injury caused by traumatic, toxic, drug related and electrical effects. The microscopic view demostrates pigmented, basophilic, granular tubular cast (myoglobulin) in the tubule lumen (arrow).

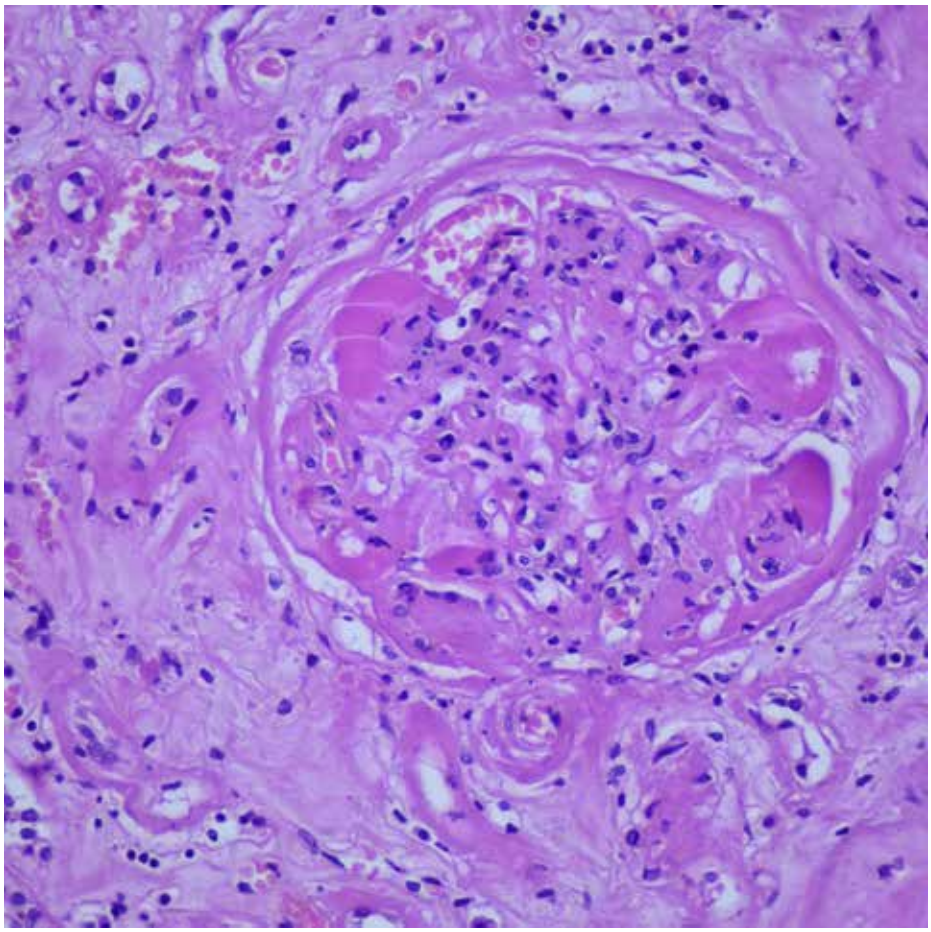

Figure 4.27
Diabetic Glomerulosclerosis (Diffuse and nodular glomerulosclerosis), (H&E, x400).
At higher magnification.

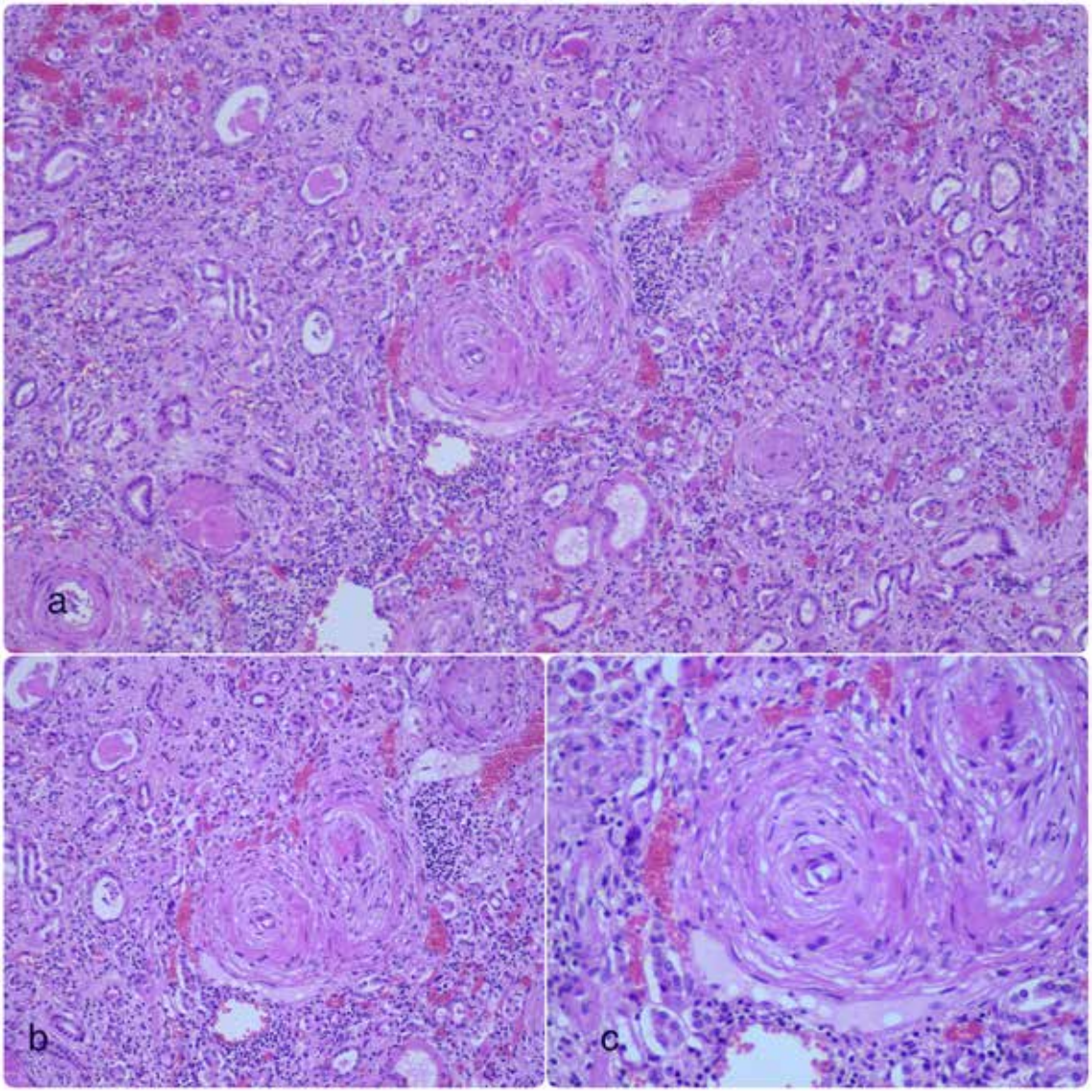

Figure 4.28
Hyperplastic arteriolosclerosis,
a) (H&E, x100). Hyperplastic arteriolosclerosis are onion skin-like laminated lesions seen on the vessel wall in severe hypertension. This lamination consists of smooth muscle cells and basement membrane. Malignant hypertension may be accompanied by necrotizing arteriolitis. The microscopic view shows hyperplastic arteriolosclerosis, which causes significant narrowing of the vascular lumen.
b) (H&E, x200). At higher magnification
c) (H&E, x400). At higher magnification.

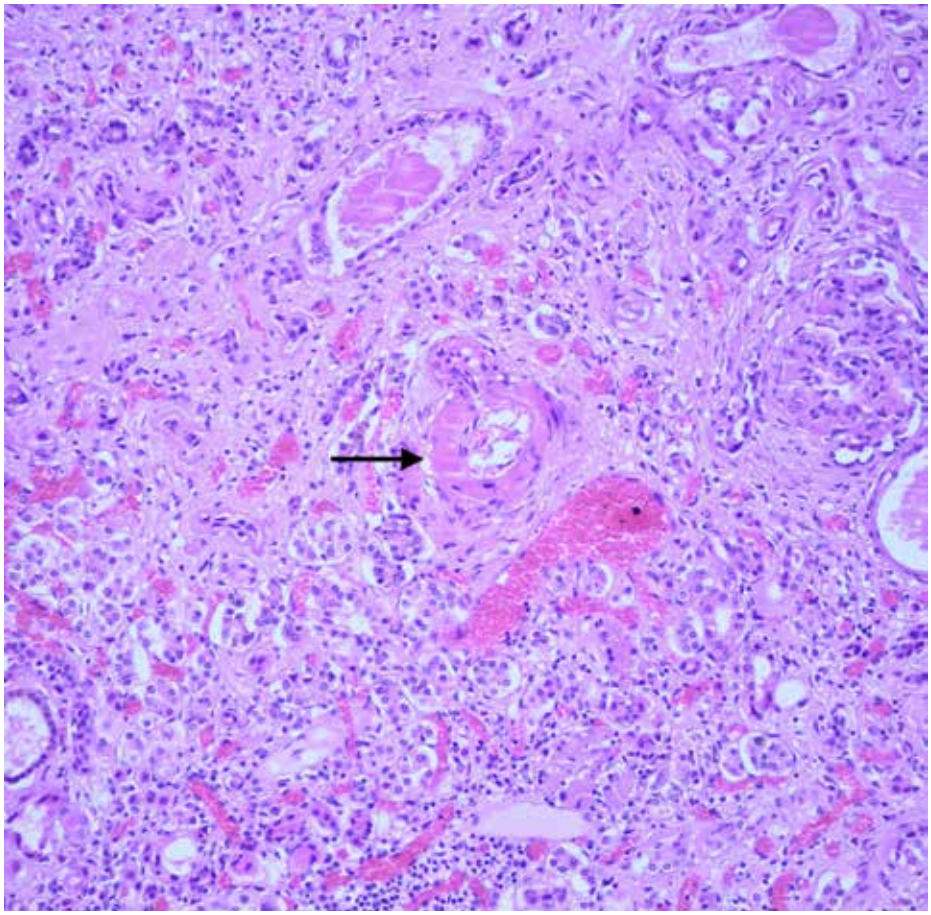

Figure 4.29
Hyaline arteriolosclerosis, (H&E, x200). Although it is frequently seen in elderly people, it is more common and severe in hypertensive people. It is seen as a pink, homogeneous hyaline thickening on the wall of arteriole, and causes luminal narrowing. Similar lesions may also be seen in diabetic microangiopathy. The microscopic view demostrates an eosinophilic, amorphous, hyaline thickening on the arteriole (arrow).

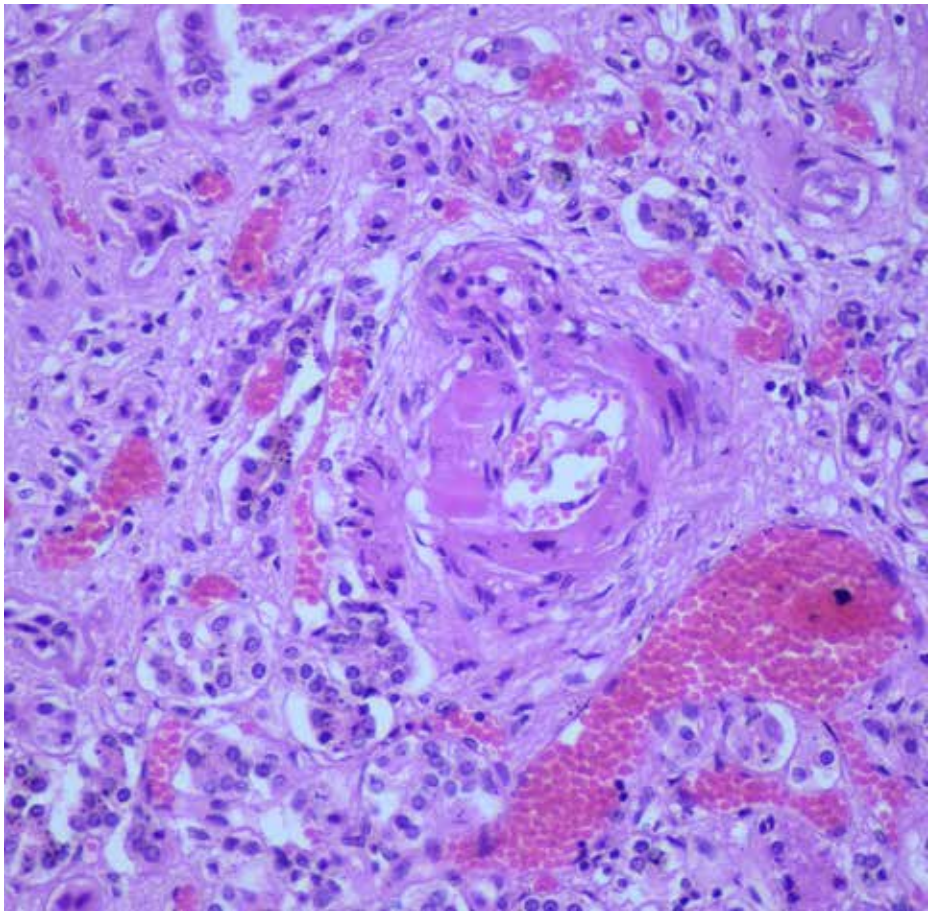

Figure 4.30
Hyaline arteriolosclerosis, (H&E, x400). At higher magnification.

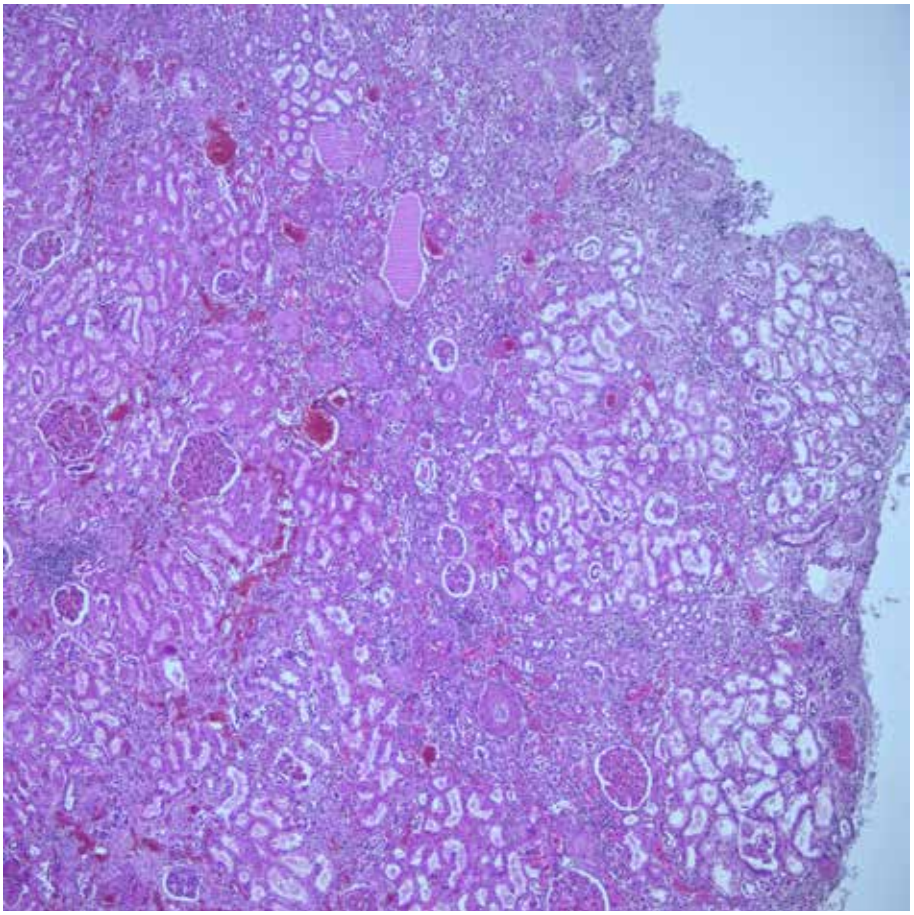

Figure 4.31 Chronic pyelonephritis, (H&E, x40). Chronic plelonephritis is a diffuse and patchy tubulointerstitial inflammation of the kidney. The microscopic view demostrates dense chronic inflammatory cell infiltration in the intersititium.

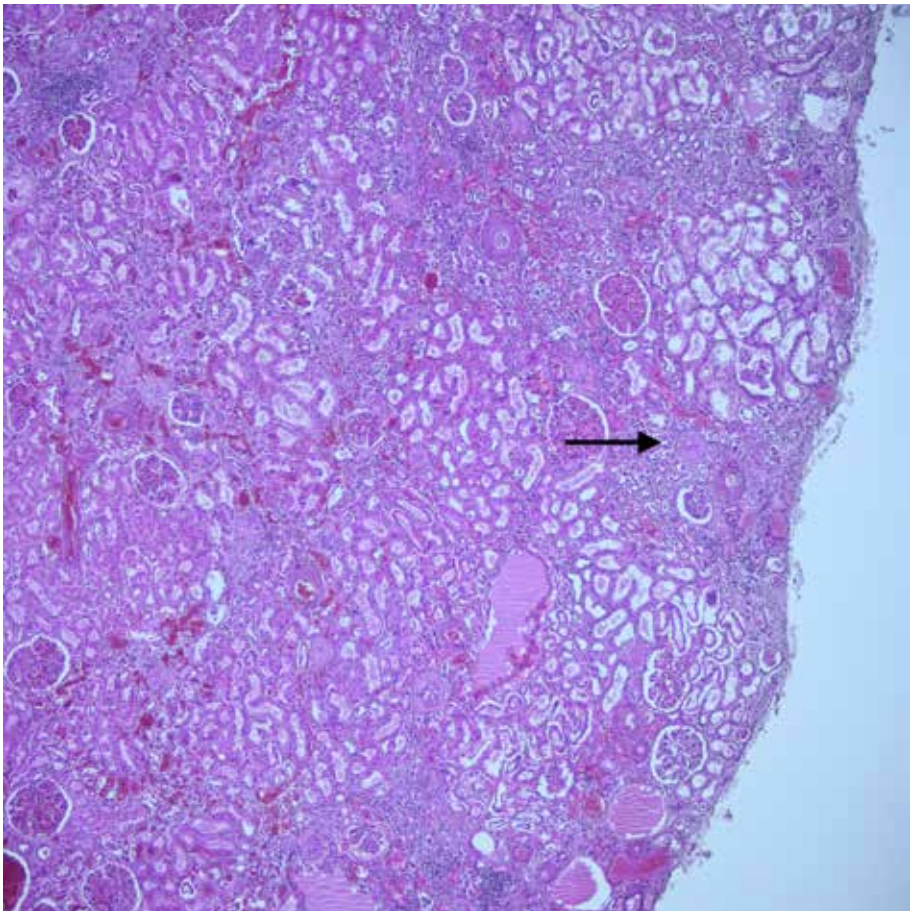

Figure 4.32 Chronic pyelonephritis, (H&E, x40). The microscopic view demostrates chronic inflammatory cell infiltration in the interstitium and sclerotic glomerulus (arrow).

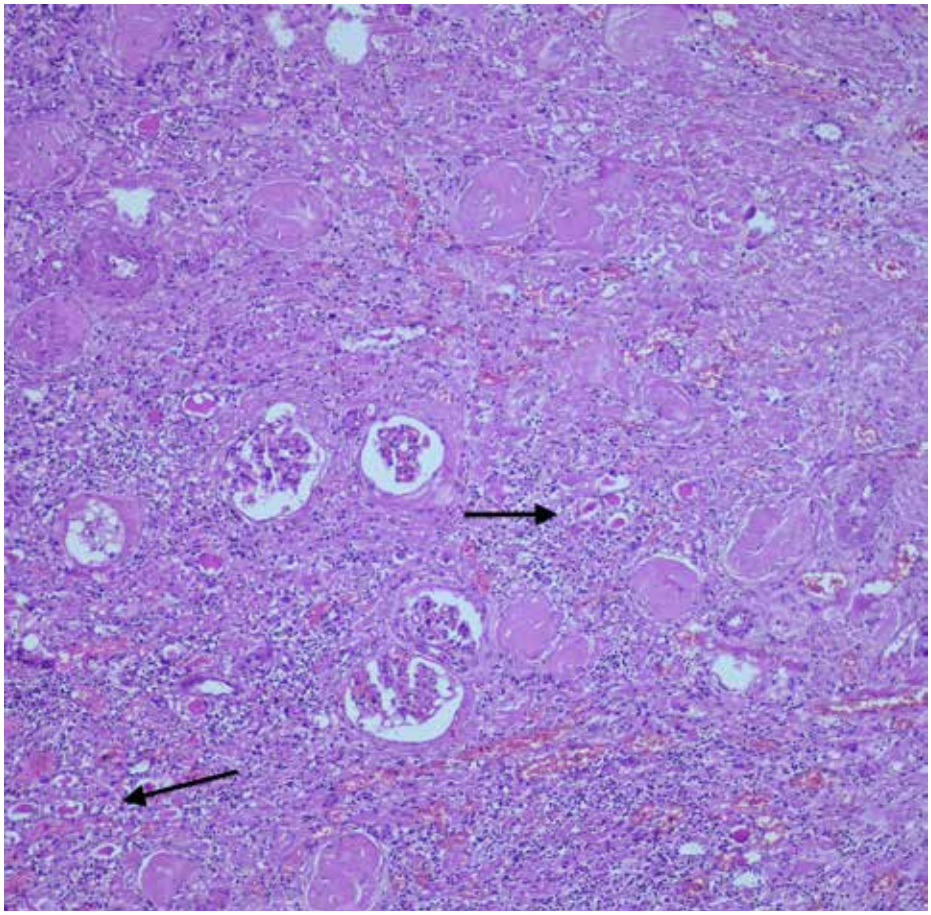

Figure 4.33
Chronic pyelonephritis, (H&E, x100). At higher magnification, the microscopic view demostrates chronic inflammatory cell infiltration in the interstitium, numerous sclerotic glomeruli, as well as renal tubular atrophy and cast formation (thyroidization) (arrow).

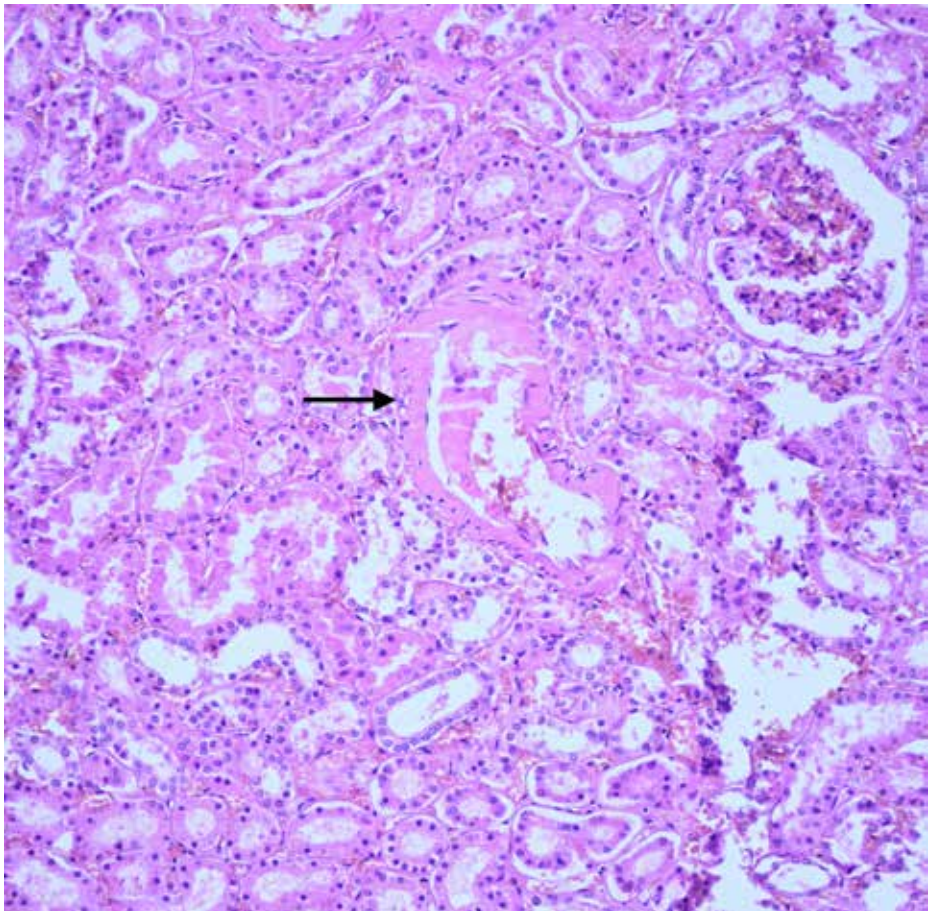

Figure 4.34
Amyloid accumulation in the renal vascular wall, (H&E, x200). The microscopic view demostrates amorphous eosinophilic amyloid accumulation in the vessel wall (arrow). Verification by Congo red is necessary.

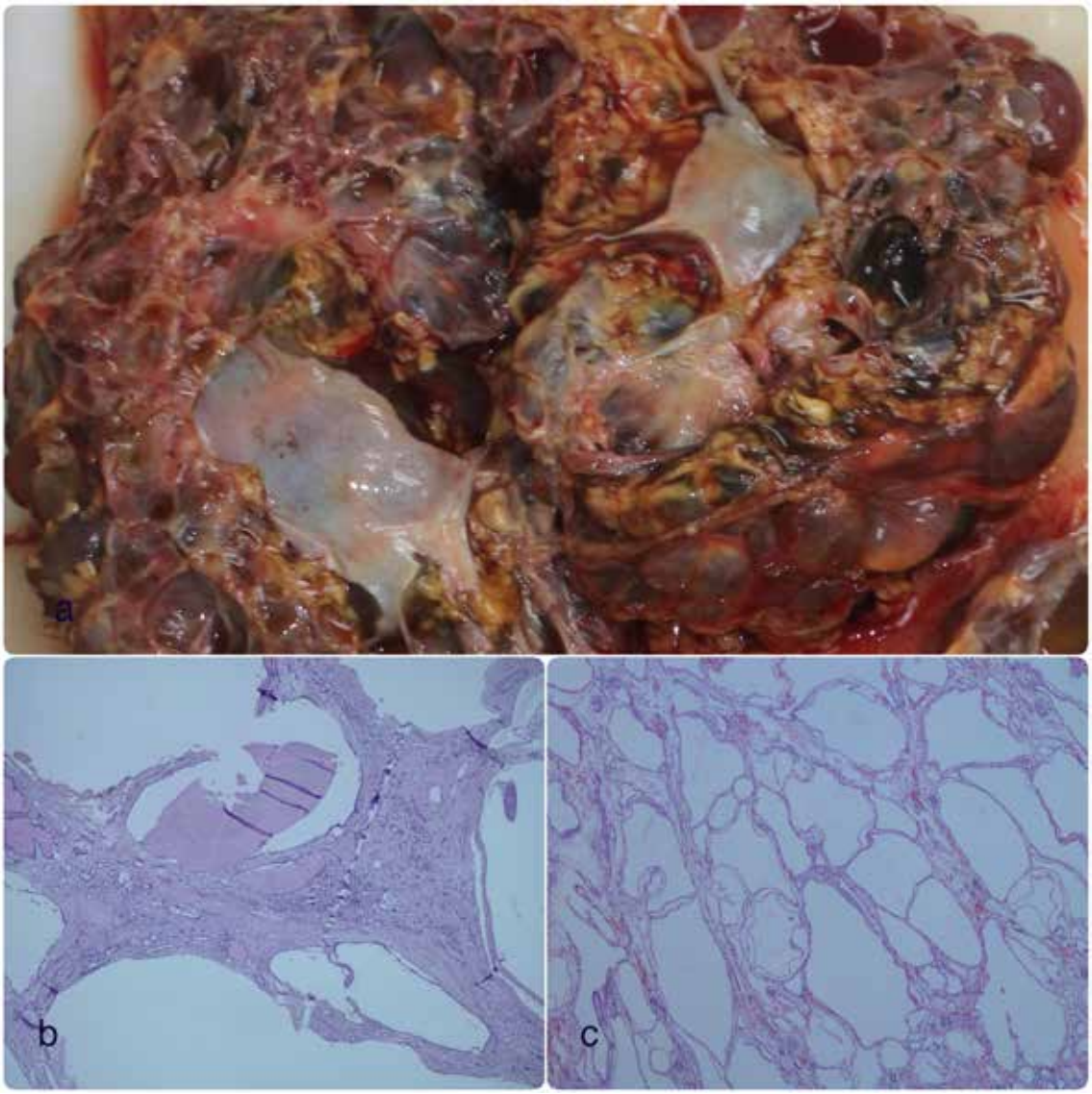

Figure 4.35
Adult Type Polycystic Kidney Disease,
a) The macroscopic image demostrates significantly enlarged kidney with many cysts filled with clear fluid.
b,c) (H&E, x40). Microscopic view reveals many cystic structures lined with cuboidal and flattened epithelium. Among the cysts, there is interstitial fibrosis, chronic inflammatory cell infiltration, sclerosis and atrophy of the tubules.

SPLEEN

Assoc. Prof. Taner DAŞ
Assoc. Prof. Ferah KARAYEL

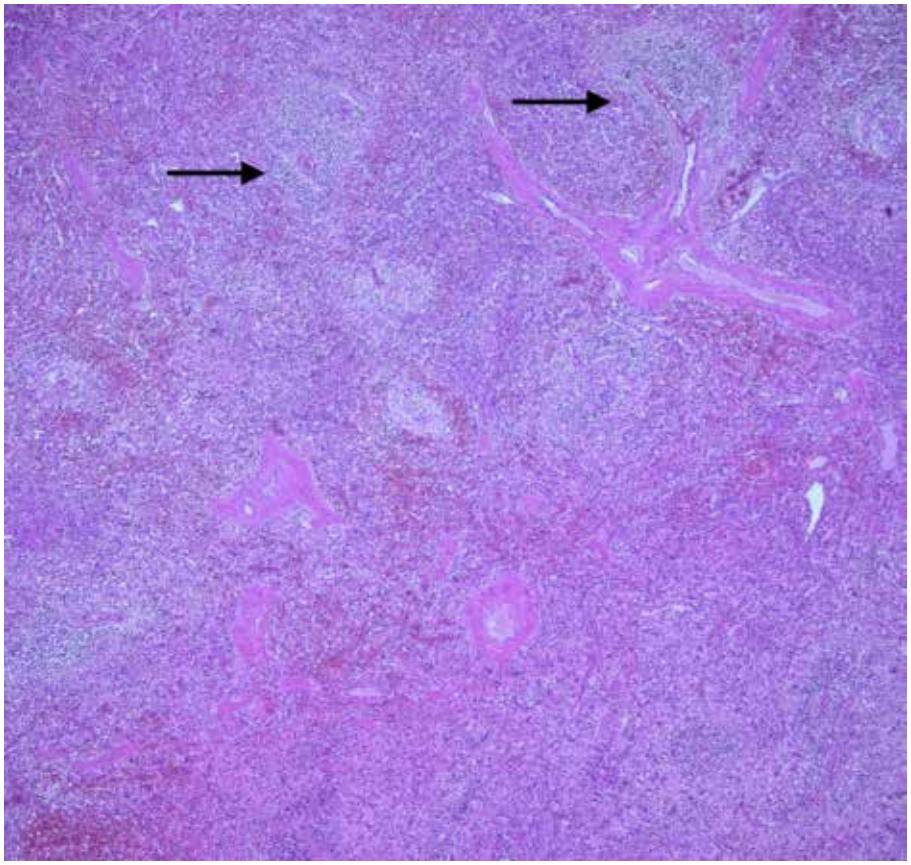

Figure 5.1
Normal Spleen, (H&E, x100). The spleen consists of white (arrow) and red pulp (¾ of its volume).

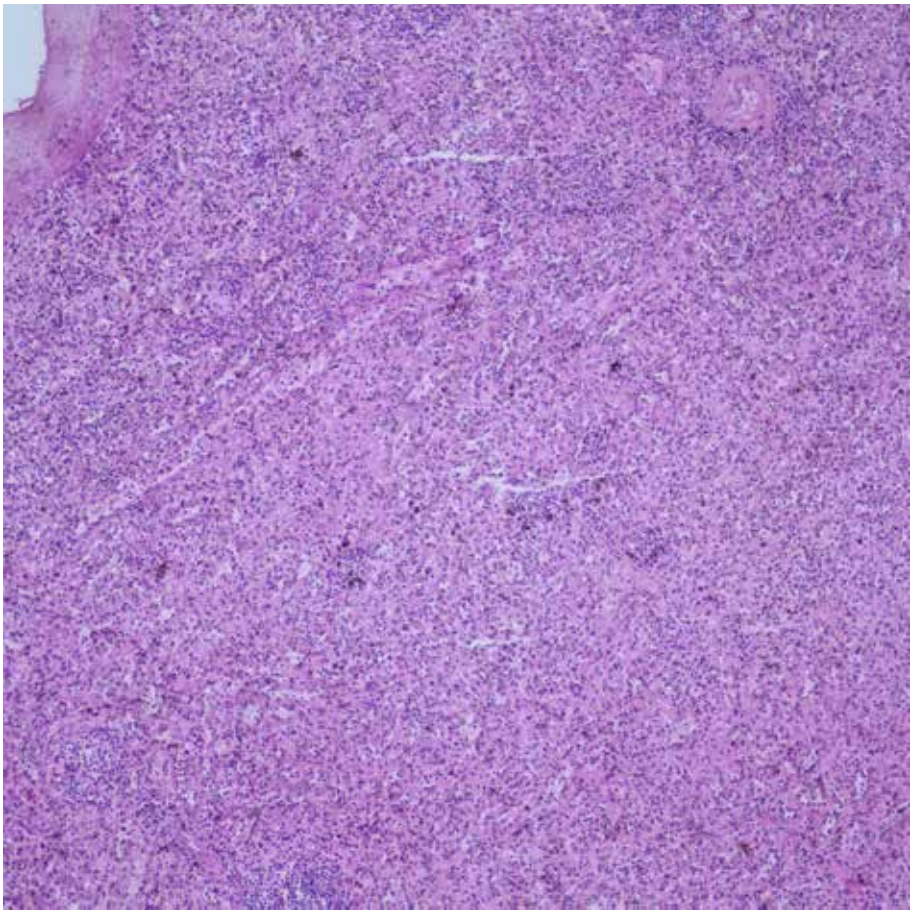

Figure 5.2
Atrophy, (H&E, x40). There is decrease in the white and/or red pulp of the spleen. Follicles disappear.

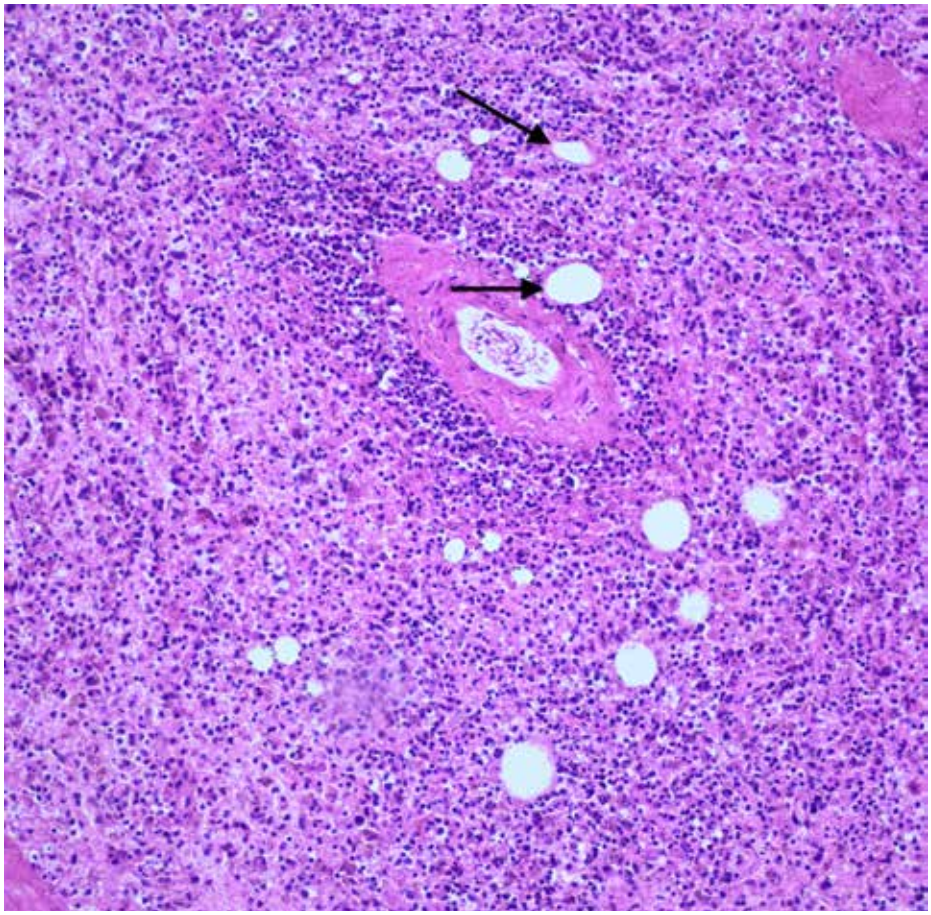

Figure 5.3
Fat embolism, (H&E, x200). Although rare, fat embolism may be seen in the spleen.

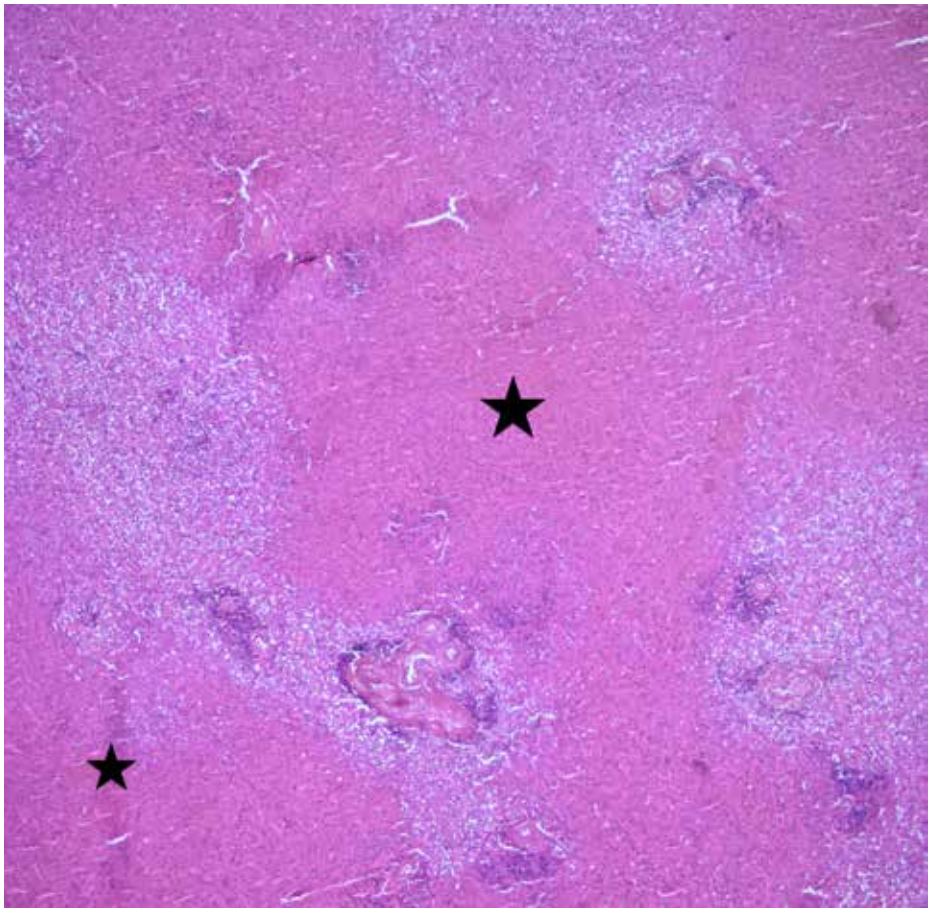

Figure 5.4
Splenic infarct, (H&E, x40). Splenic infarct is most commonly seen due to thromboembolic and infiltrative hematological diseases. In the microscopic view, the infarcted area is demostrated with an asterisk.

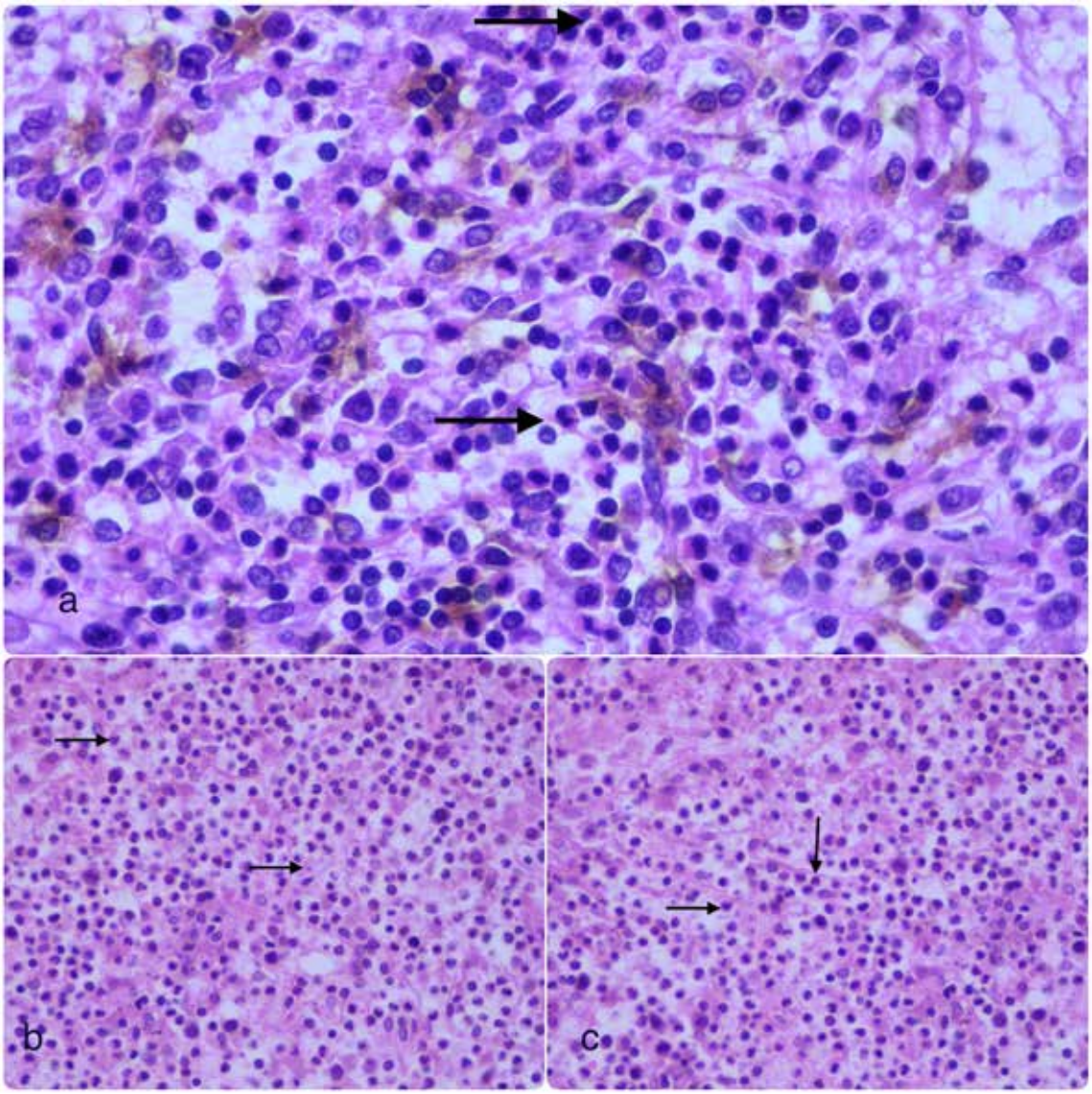

Figure 5.5
Septic splenitis,
a,b,c) (H&E, x600, x400, x400).
Septic splenitis is defined histopathologically as neutrophil infiltration (arrows) and congestion in the red pulp. It is often accompanied by splenomegaly.

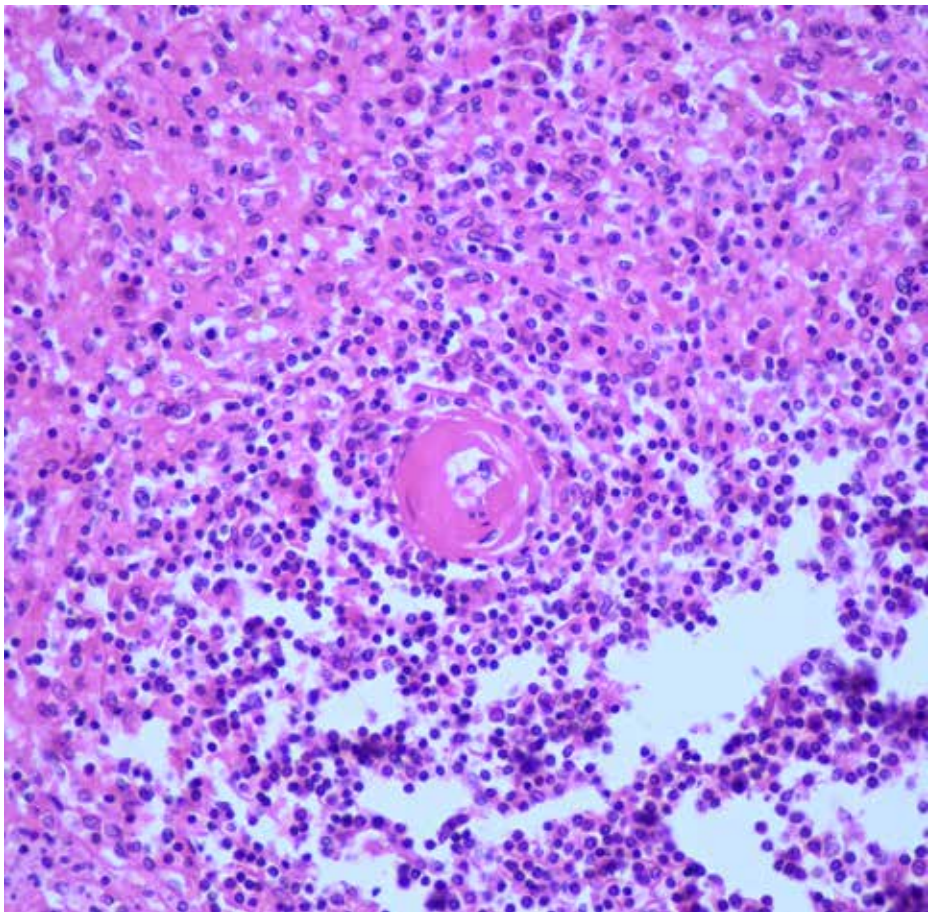

Figure 5.6
Amyloid accumulation in the splenic vascular wall,
(H&E, x400).
The microscopic view demostrates amorphous eosinophilic amyloid accumulation in the vessel wall. Verification by Congo red is necessary.

PANCREAS

Assoc. Prof. Taner DAŞ
Assoc. Prof. Ferah KARAYEL

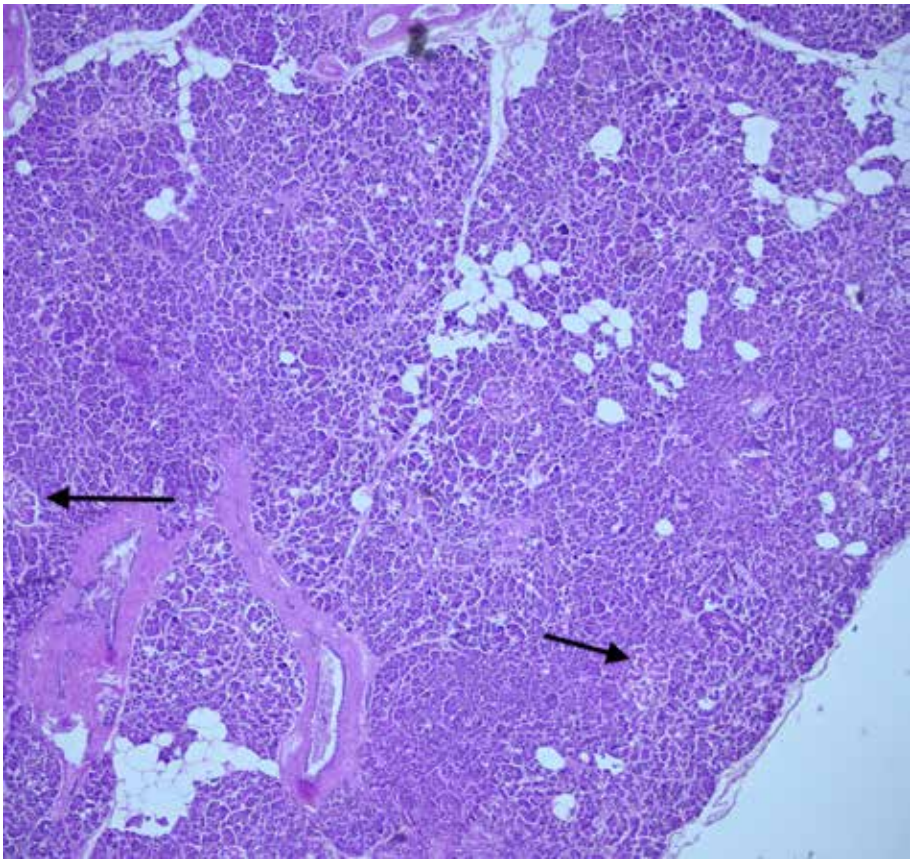

Figure 6.1
Normal Pancreas, (H&E, x40). The pancreas is an organ with exocrine and endocrine components. The exocrine component consists of serous acini. The endocrine component consists of pancreatic islets (islets of Langerhans) (arrow).

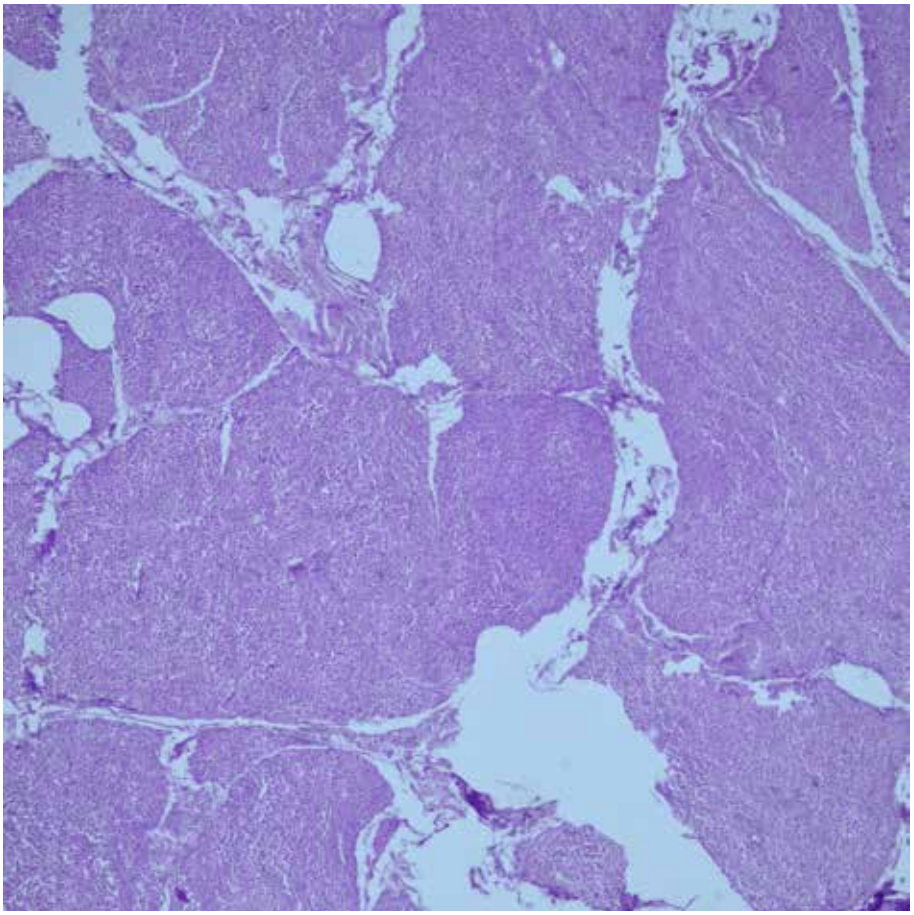

Figure 6.2
Pancreas autolysis, (H&E, x100). Postmortem interval is the most important factor for autolysis. Autolysis is the digestion of the dead or dying cell by its own enzymes. It shows features similar to necrosis. The absence of inflammatory cell infiltration is important in distinguishing it from necrosis. In addition, caseous debris, liquefaction, coagulative material, fibrin and mineral are commonly accompany in necrosis.

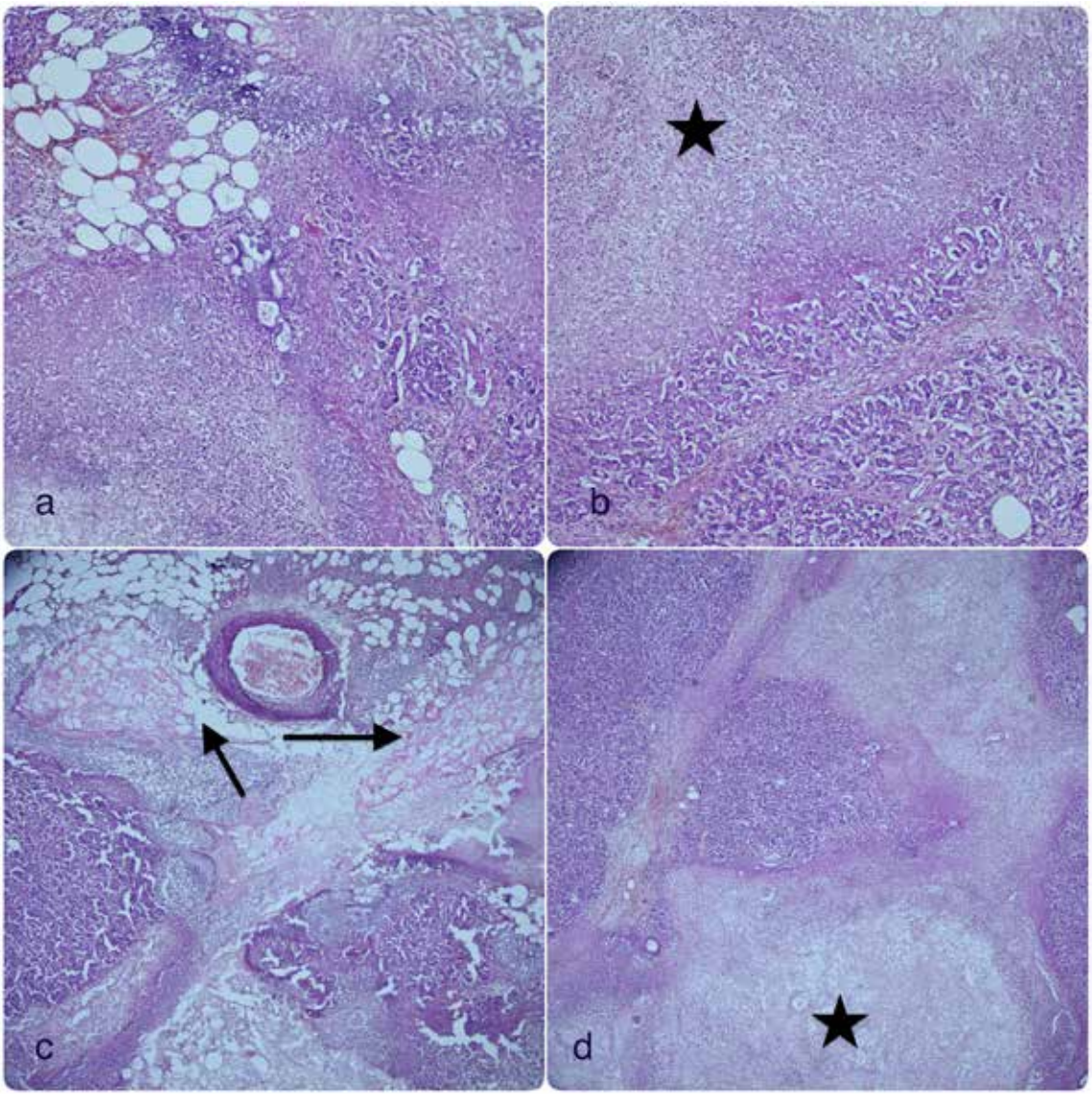

Figure 6.3
Acute necrotizing pancreatitis,
a) (H&E, x40). The picture shows dense neutrophil infiltration with widespread necrosis extending into the peripancreatic fat tissue.
b,d) (H&E, x100), (H&E, x40). Extensive necrosis (asterisks) are noted.
c) (H&E, x40). Fat necrosis (arrows) and neutrophil infiltration extending into the peripancreatic fatty tissue.

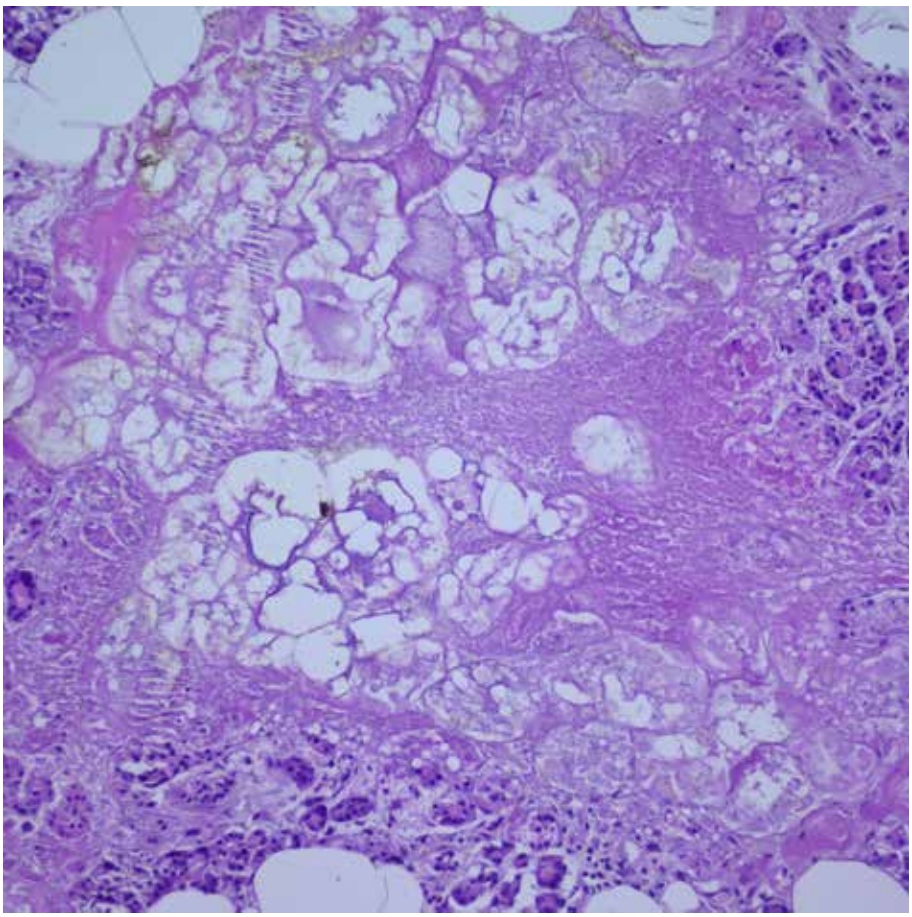

Figure 6.4
Fat necrosis,
(H&E, x200).
Lipase enzyme is released as a result of acute pancreatitis or pancreatic trauma, causing fat necrosis.

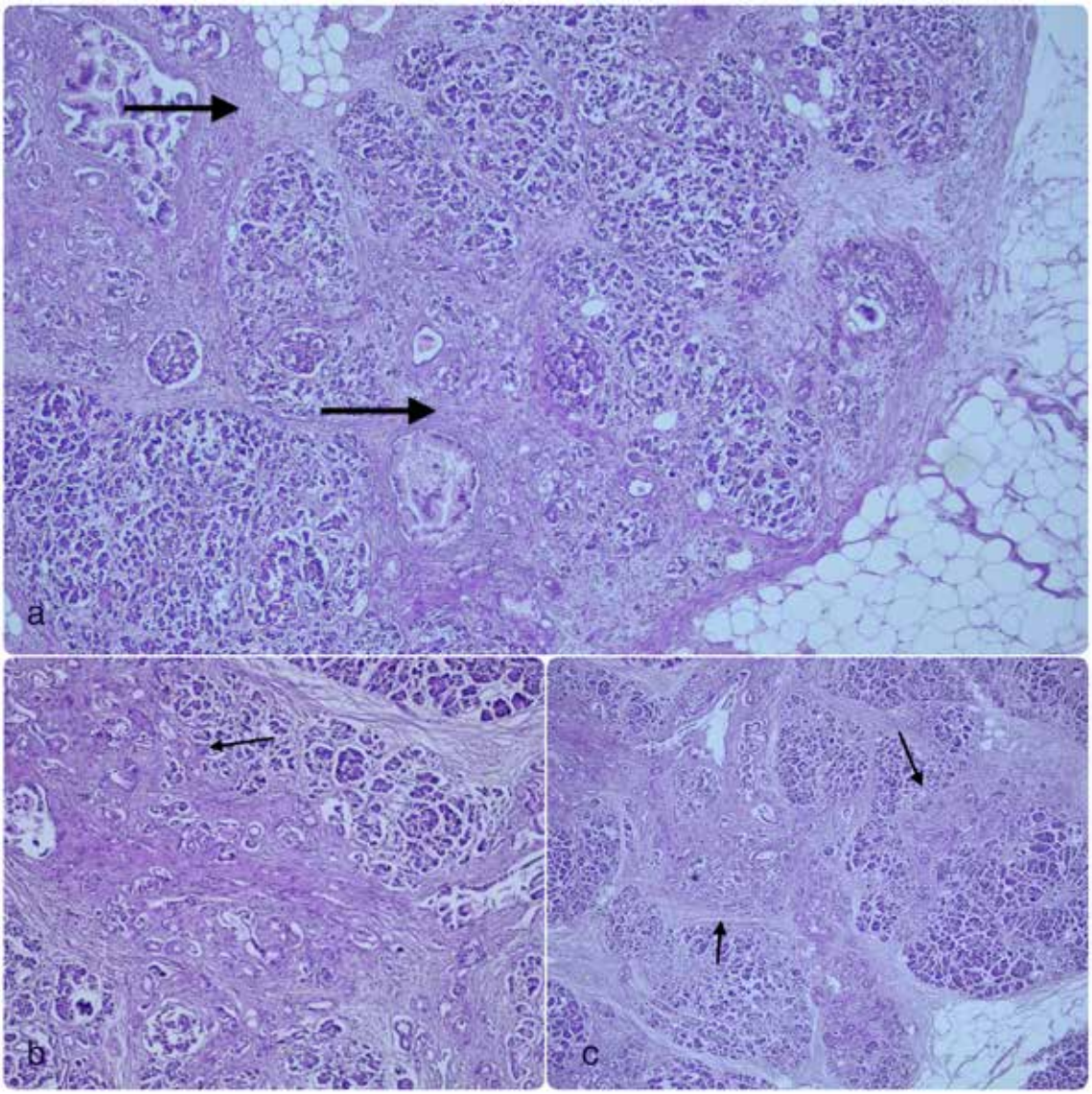

Figure 6.5
Chronic pancreatitis,
a) (H&E, x40). It is a chronic fibroinflammatory disease of the pancreas in which parenchymal fibrosis, atrophy and ductal changes (ectasia, distortion, intraluminal amorphous accumulations, squamous metaplasia) are observed. Clinical and radiology are necessary for diagnosis. The microscopic view demostrates areas of fibrosis (arrows), acinar loss in the parenchyma, and ductal changes.
b,c) (H&E, x100), (H&E, x40). Acinar ductal metaplasia (arrows) is seen.

GASTROINTESTINAL SYSTEM

Assoc. Prof. Taner DAŞ
Assoc. Prof. Ferah KARAYEL

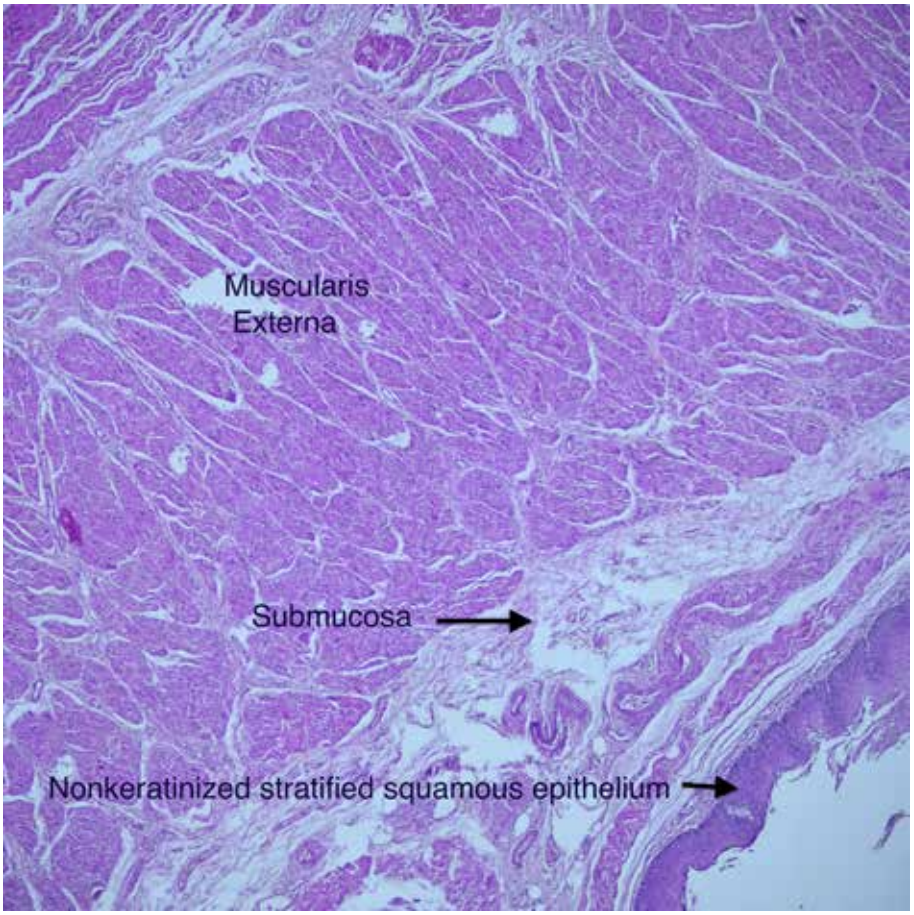

Figure 7.1
Esophagus, (H&E, x40). It consists of 4 layers: esophageal mucosa (which includes nonkeratinized stratified squamous epithelium on the surface, lamina propria and muscularis mucosa), submucosa, muscularis externa and adventitia.

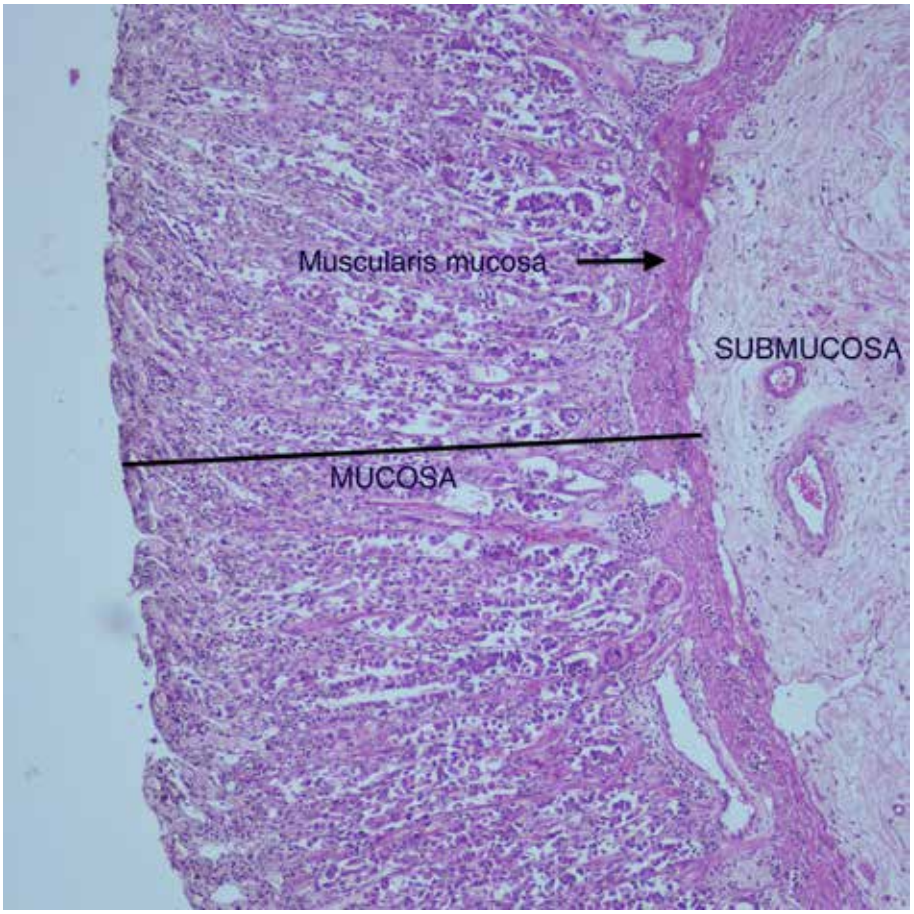

Figure 7.2
Gastric mucosa, (H&E, x100). Histologically, the stomach contains 4 layers: mucosa (surface epithelium, lamina propria and muscularis propria), submucosa, muscularis externa and serosa (visceral peritoneum).

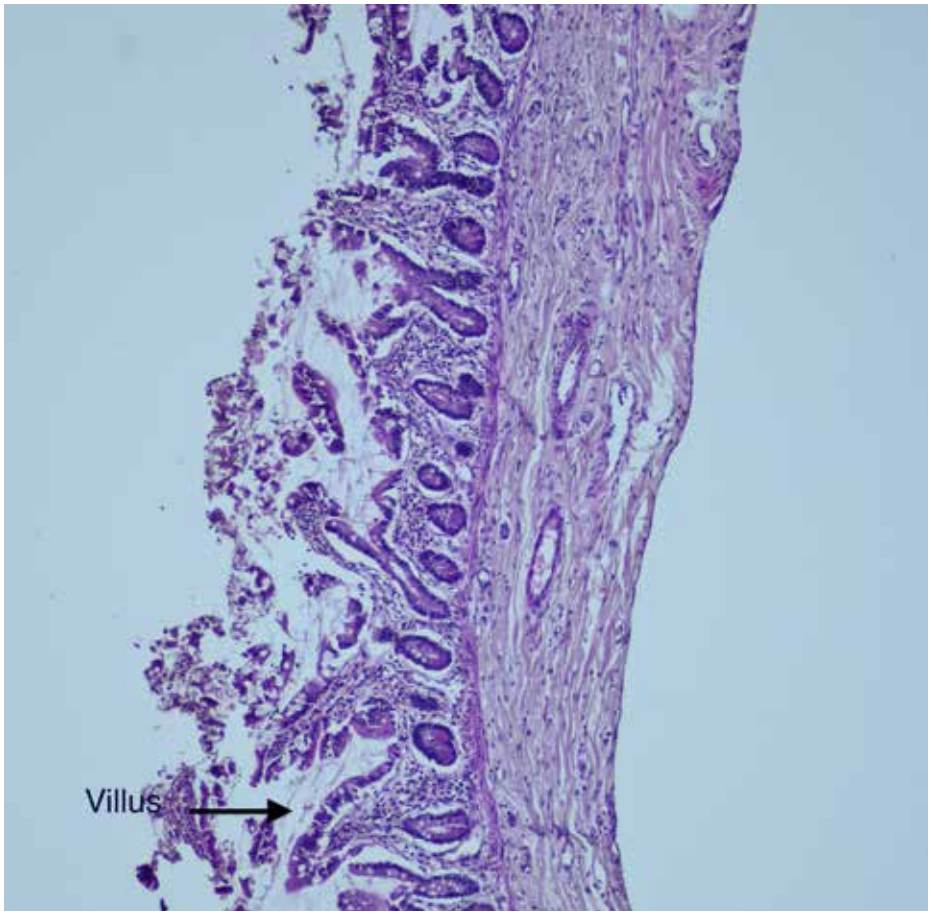

Figure 7.3
Small intestine, (H&E, x100).
The small intestine, like the entire gastrointestinal tract, is histologically composed of the mucosa (consisting of surface epithelium, lamina propria and muscularis mucosa), submucosa, muscularis externa (circular and longitudinal), and serosa (visceral peritoneum).
The small intestine has many finger-like projections called villi.

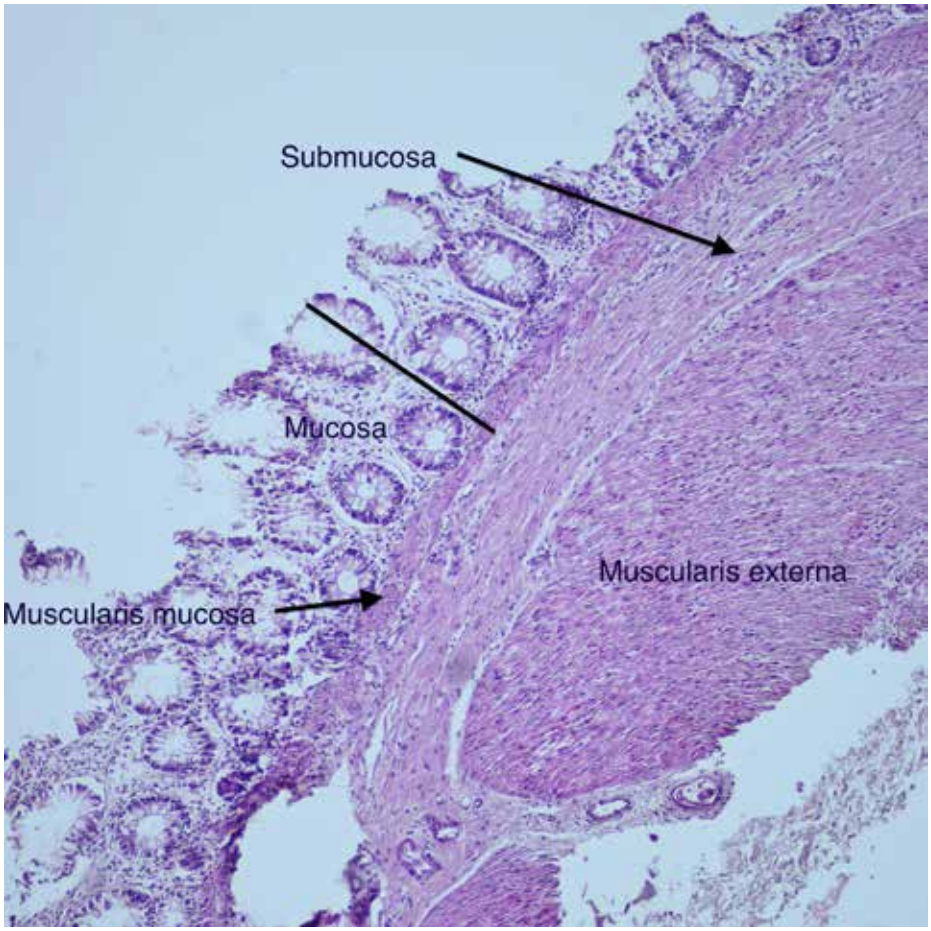

Figure 7.4
Large intestine, (H&E, x100).
The large intestine is histologically composed of mucosa (surface epithelium, intestinal glands, lamina propria, and muscularis mucosa), submucosa (containing connective tissue, blood vessels, and nerves), muscularis externa (inner circular, outer longitudinal muscle layer), and serosa (visceral peritoneum).

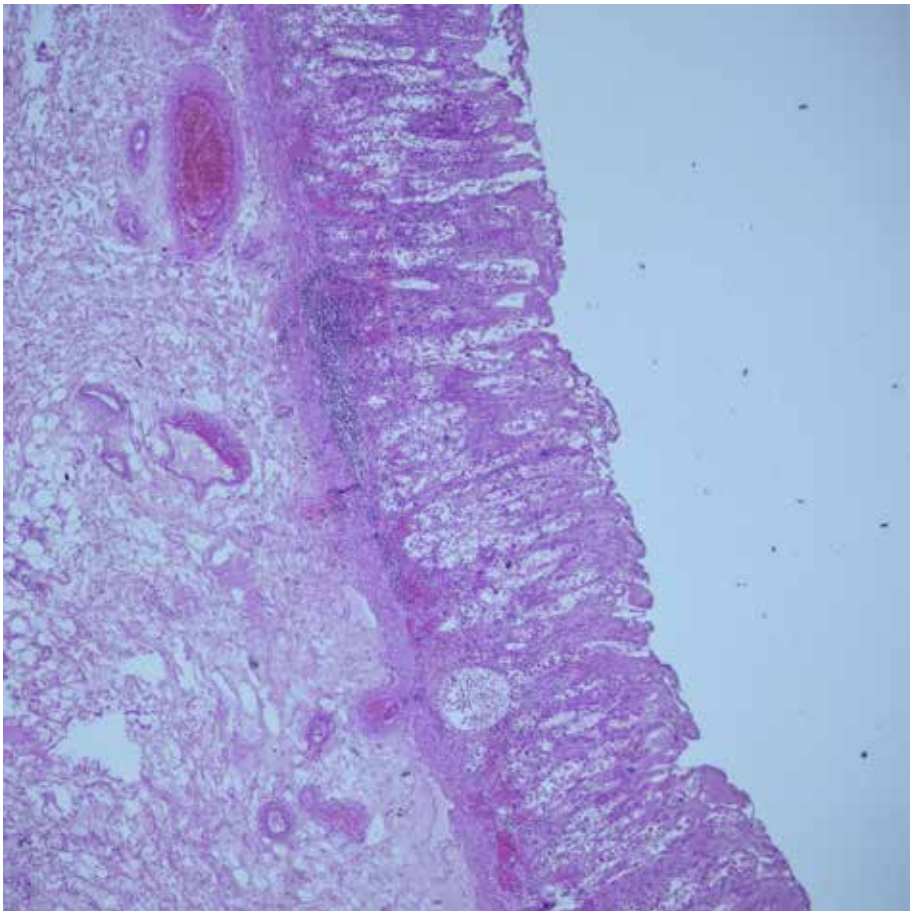

Figure 7.5
Mucosal infarction, (H&E, x40). Mucosal infarction in the stomach is very rare. In the microscopic view, fibrin thrombus is seen in the vascular lumens in the submucosa in a person with sepsis and associated fibrin thrombi in multiple organs, with transmural infarcts in the intestines. Necrotic changes in epithelial cells, inflammatory cell infiltration and hemorrhage are observed in the mucosa.

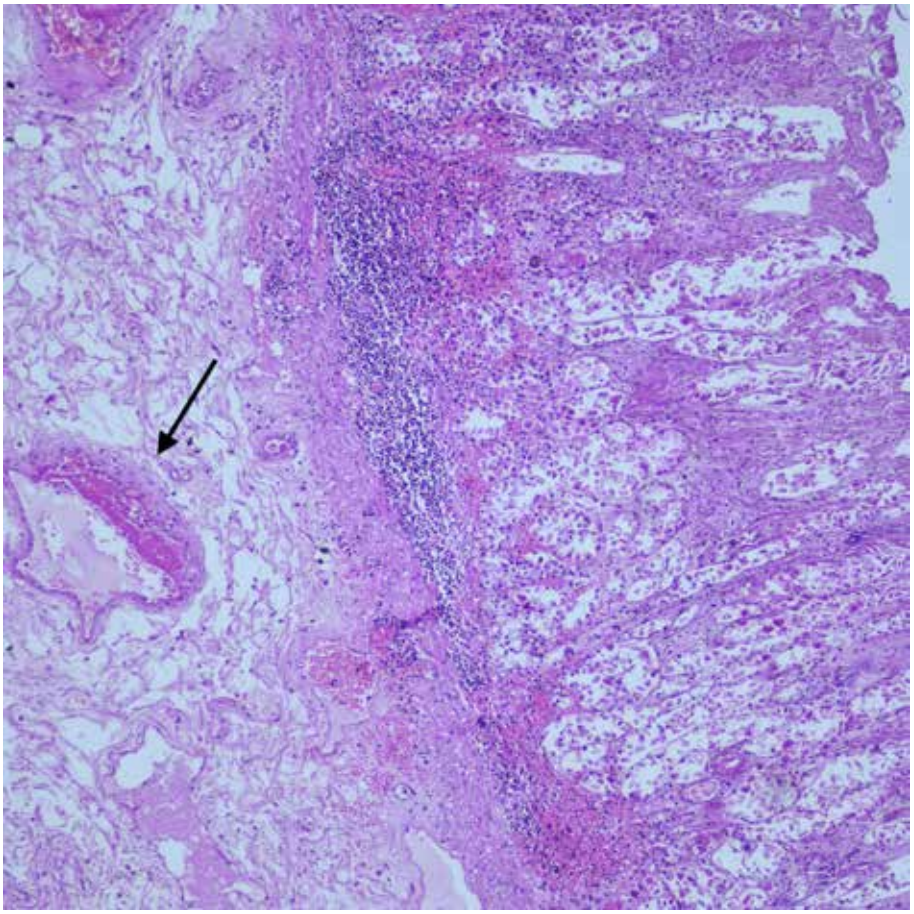

Figure 7.6
Mucosal infarction, (H&E, x100). At higher magnification. Fibrin thrombus (arrow) is seen in the vascular lumen in the submucosa. Necrotic changes in epithelial cells, inflammatory cell infiltration and hemorrhage are observed in the mucosa.

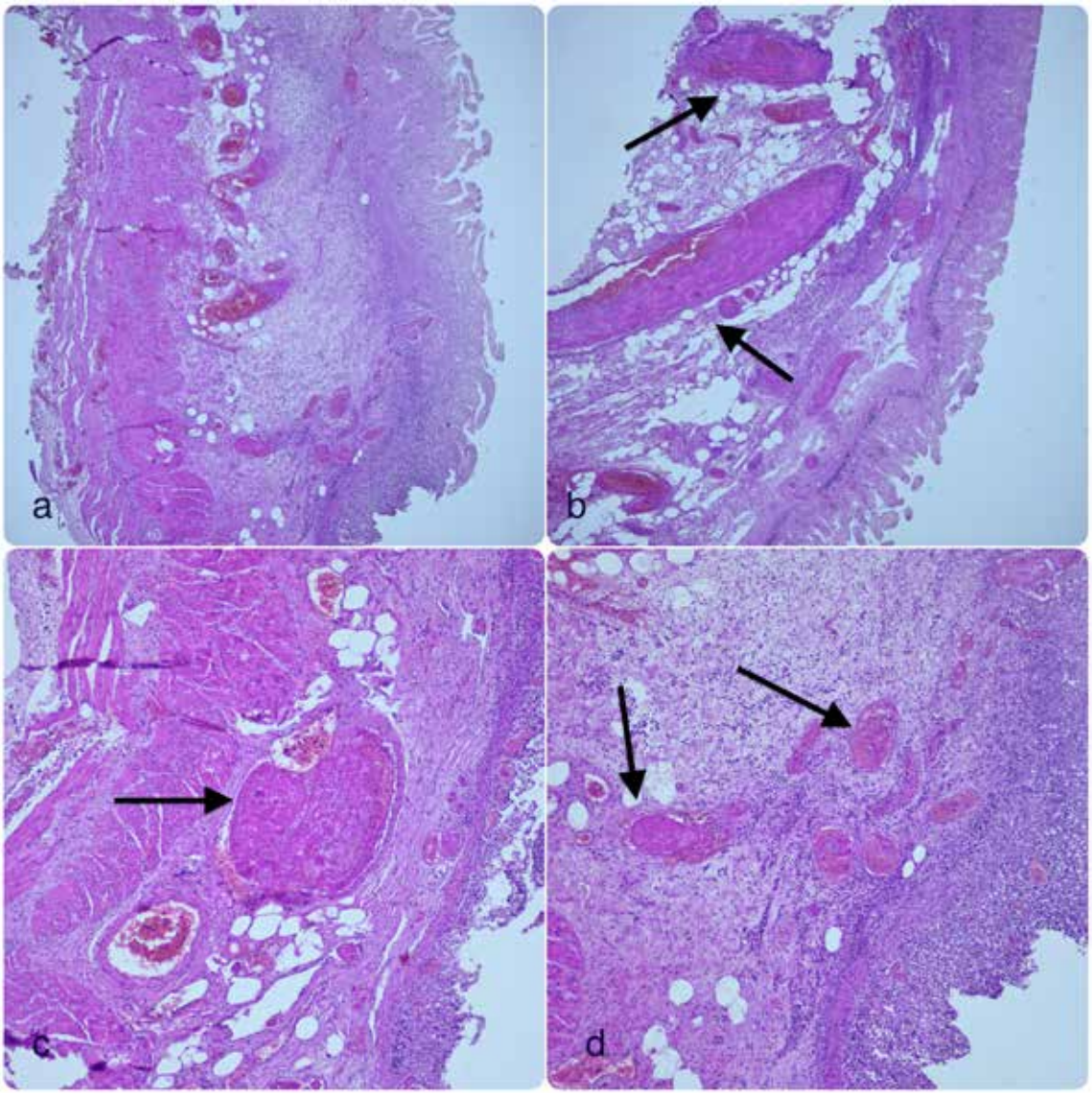

Figure 7.7
Small intestine transmural infarction.
a) (H&E, x40). The microscopic view demostrates infarct in the all layers (transmural) of small intestine.
b) (H&E, x40). Fibrin thrombi (arrows) are seen in the lumen of many vessels in the serosal fatty tissue.
c,d) (H&E, x100), (H&E, x40). There are fibrin thrombus (arrows) in the vascular lumens in the submucosa and inflammatory cell infiltration in all wall layers.

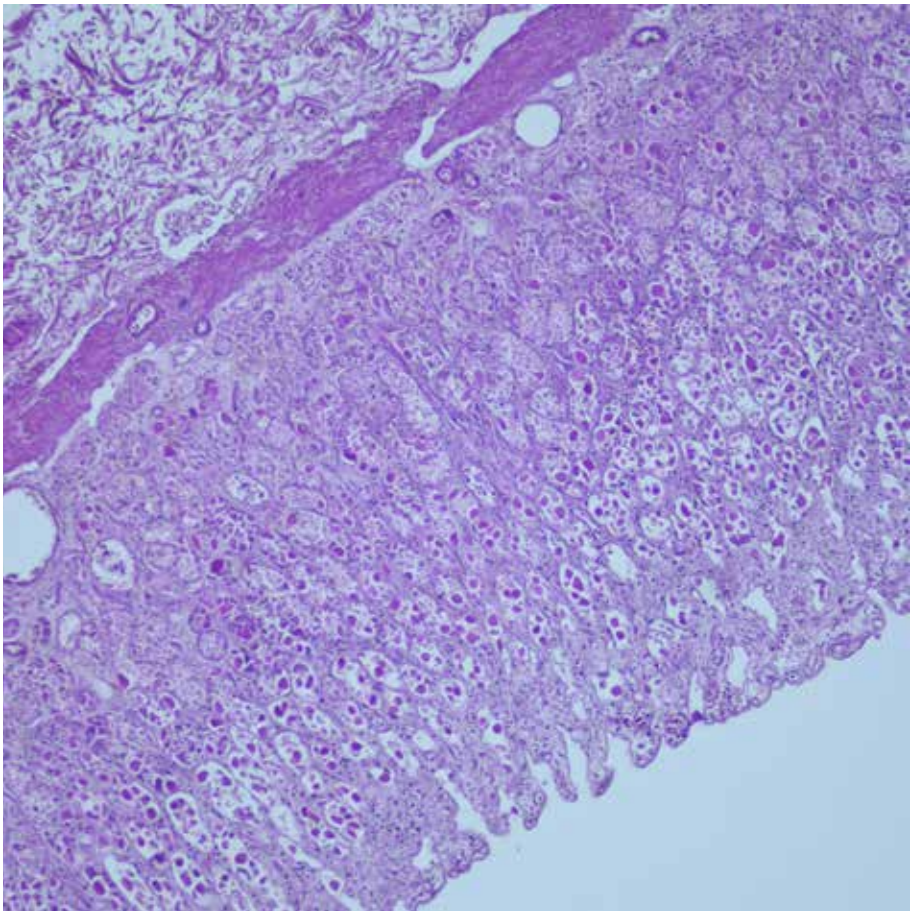

Figure 7.8
Stomach autolysis, (H&E, x100). Autolysis is the digestion of the dead or dying cell by its own enzymes. It shows features similar to necrosis. The absence of inflammatory cell infiltration is important in distinguishing it from necrosis. In addition, caseous debris, liquefaction, coagulative material, fibrin and mineral are commonly accompany in necrosis.

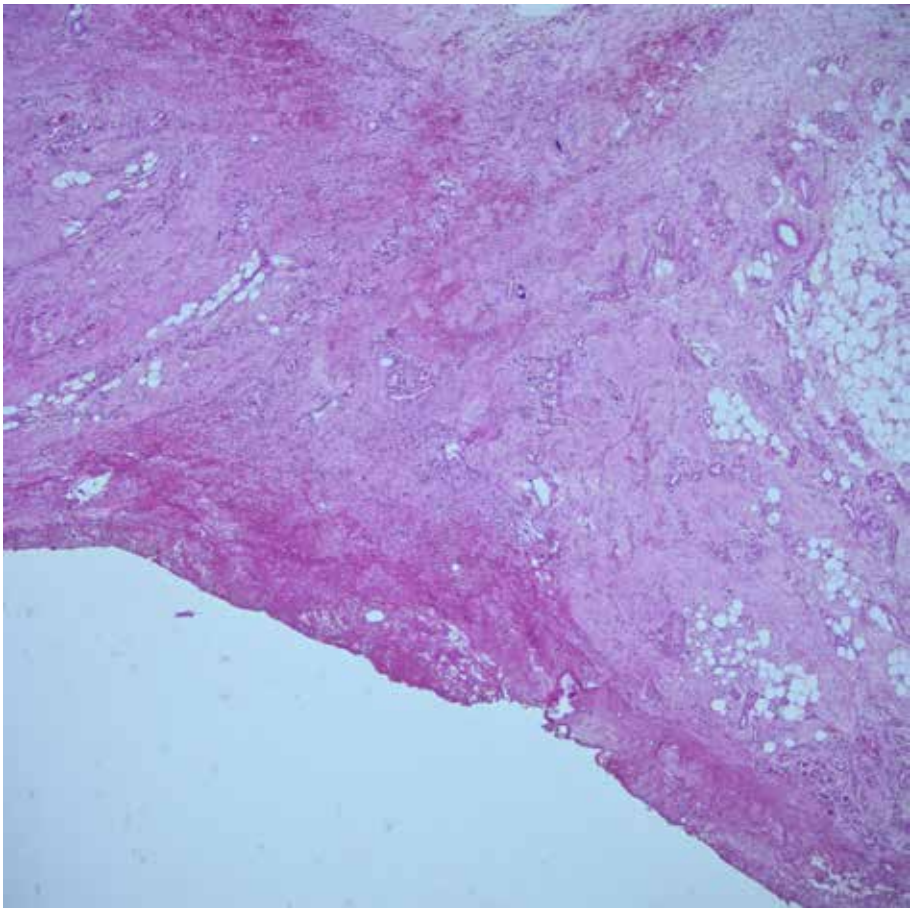

Figure 7.9
Fibrinous peritonitis and organization, (H&E, x40). The microscopic view demostrates hemorrhage, and fibrinous peritonitis showing organization such as fibroblast proliferation and neovascularization in the intestinal serosal layer.

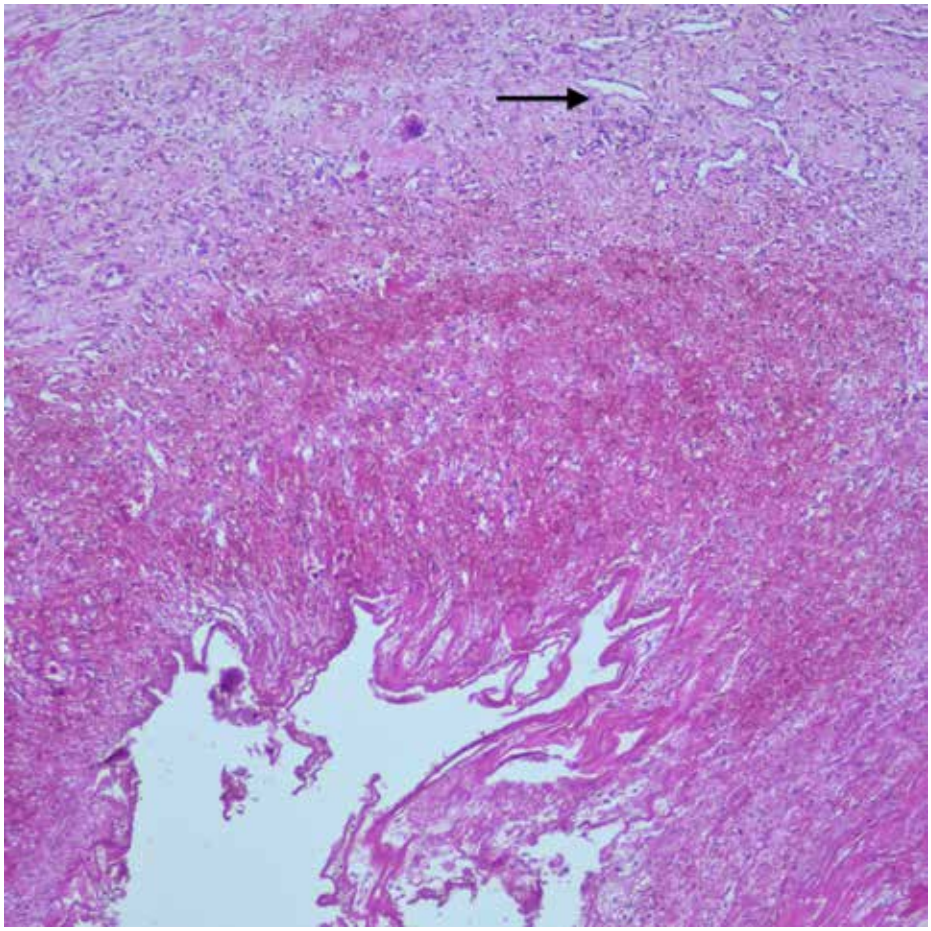

Figure 7.10
Fibrinous peritonitis and organization,
(H&E, x100).
Fibrinous peritonitis accompanied with fibroblast proliferation and neovascularization
(arrow).
At higher magnification.

EFFECTS OF ELECTRICITY AND HEAT

Assoc. Prof. Taner DAŞ
Assoc. Prof. Ferah KARAYEL

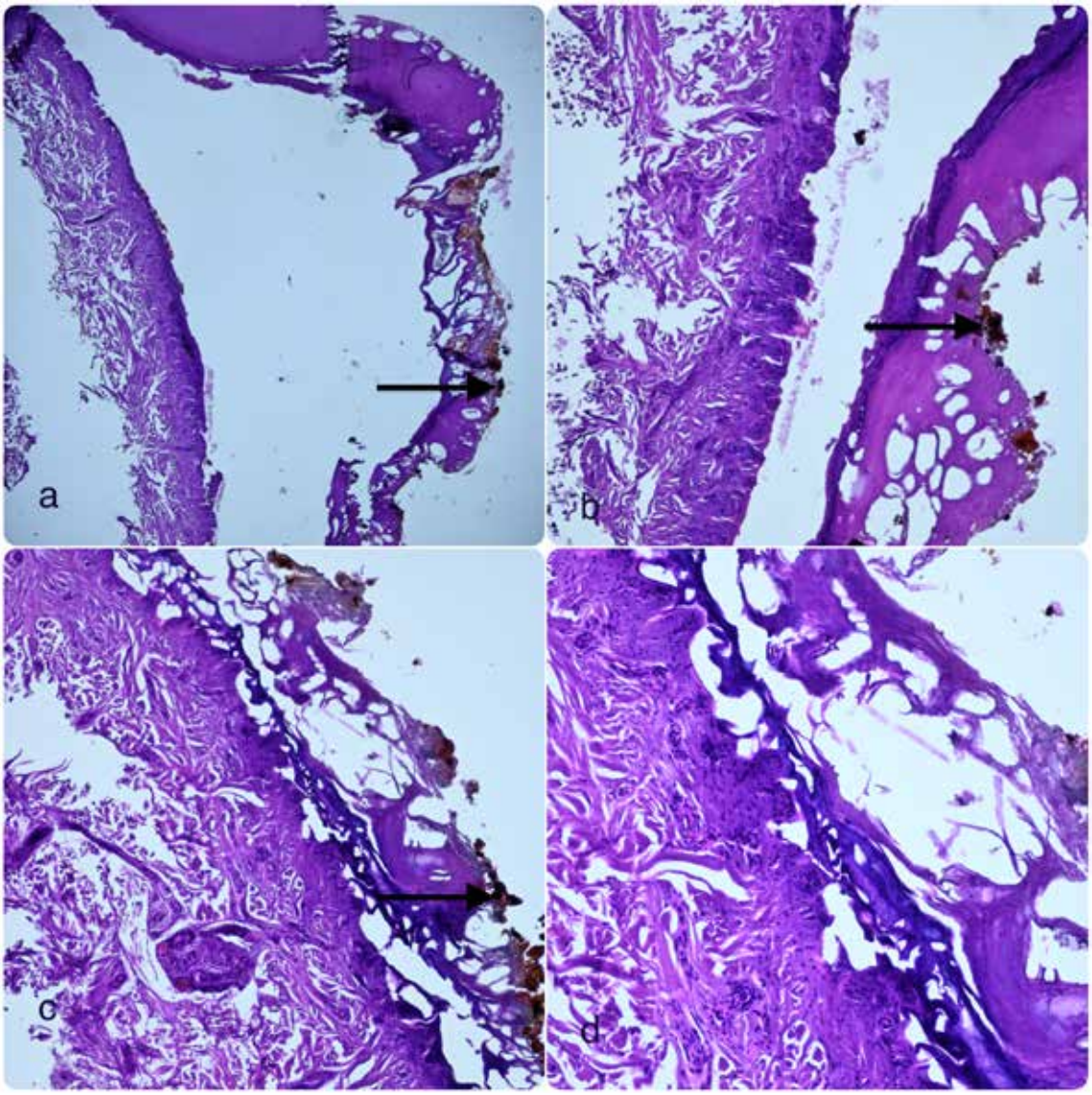

Figure 8.1
Skin electric effect,
a,b,c,d) (H&E, x40, x100, x100, x200).
Intraepidermal and subepidermal separations in the skin due to electric shock, many small gaps in the epidermis (Swiss cheese appearance), thin and elongated (spindle-shaped) parallel appearance in the epidermal cells, and homogenization in the dermis are observed in the the microscopic view.
Prolonged exposure of the skin to electricity may cause blackish carbonization of the metallic conductor in the epidermis and subepidermal soft tissue. These small, blackish particles are called "electrical metallization."
These findings originate from the formation of metal particles as a result of the atomization of the metallic electrical cable, especially as a result of the heat released during high voltage electric shock. In "thermal metallization", black particles are located in the center of the injury area, while in "electrical metallization" they are located at the periphery of the lesion.
This finding is helpful in distinguishing between thermal and electrical metallization.
In image a, b, and c, brown-black pigment accumulation
(arrows) due to electrical metallization can be seen.

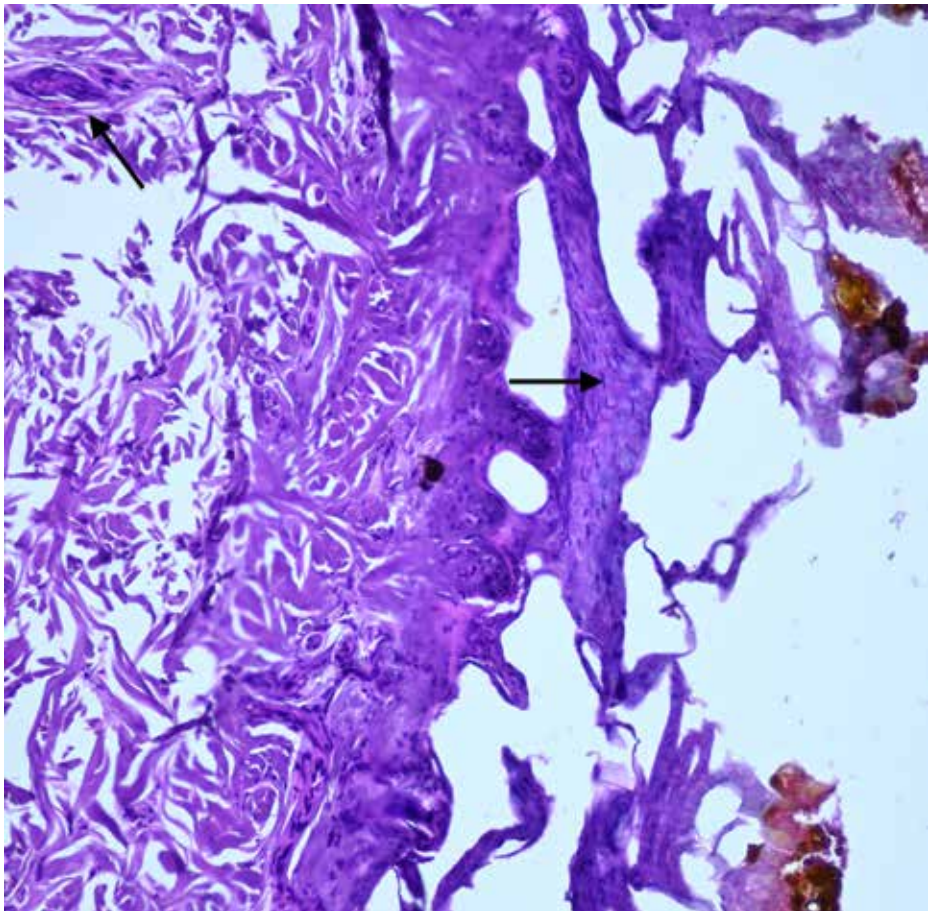

Figure 8.2
Skin electric effect, (H&E, x200).
At higher magnification, elongation, thinning and hyperchromatic spindle appearance (arrow) in the epidermal cells in the epidermis and skin appendages are noted. In addition to electrical lesions, elongation and spindle appearance of epidermal cells can also be seen at the blister edges in barbiturate poisoning, heat burns, blunt dermal trauma (crush), cauterization, desiccation, and freezing. Antemortem electrical burns cannot be distinguished from postmortem electrical burns because it takes around 8-14 hours for vital reactions to develop.

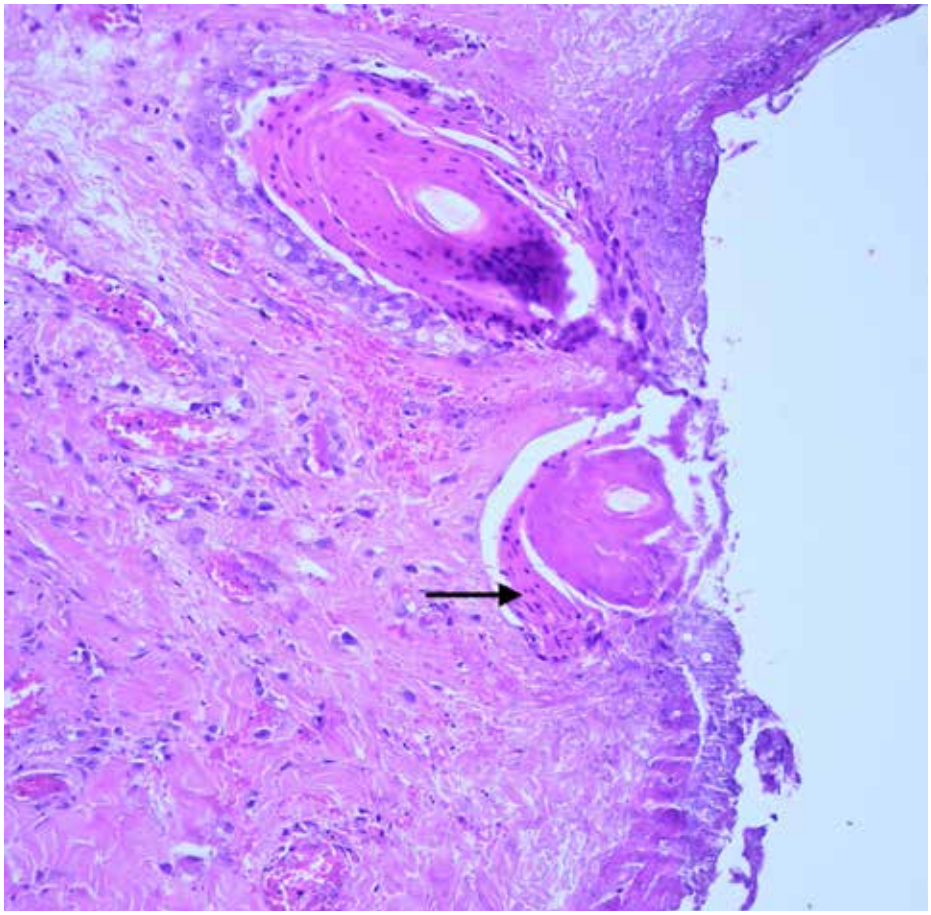

Figure 8.3
Skin thermal injury, (H&E, x100).
Spindle formation in epidermal cells is remarkable in skin appandages.

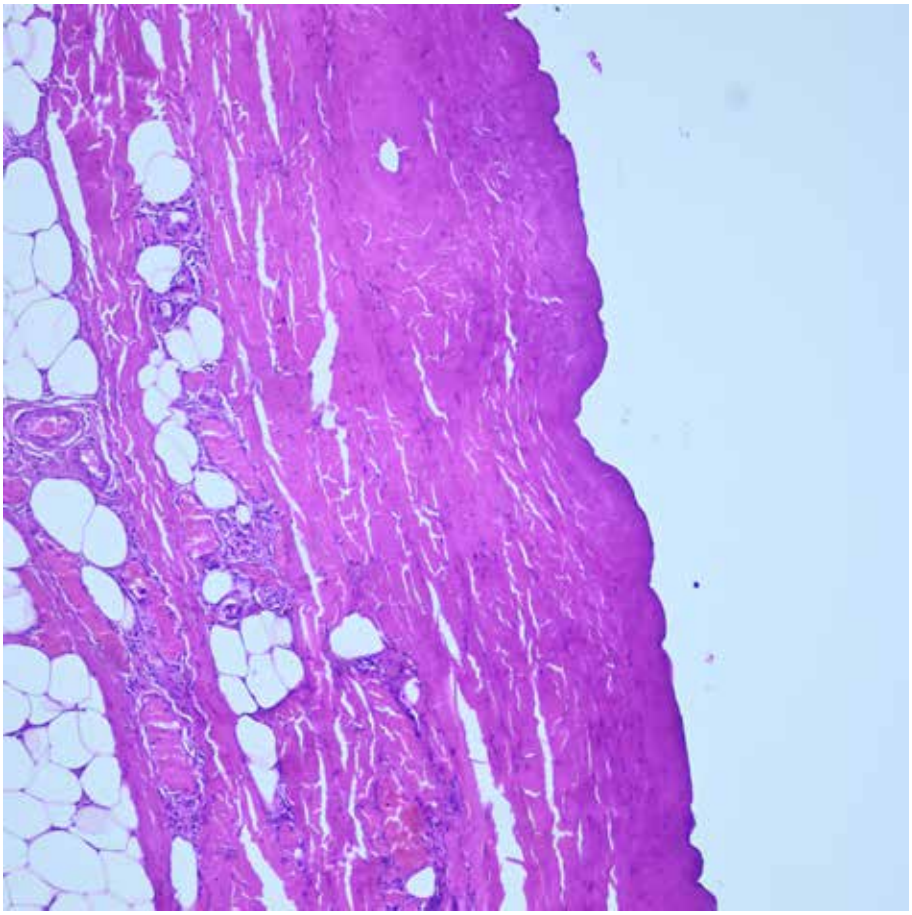

Figure 8.4
Skin thermal injury,
(H&E, x100).
In the case of skin burns and 13 days of hospital treatment, loss of epidermis and homogenization of the dermis are observed in this decedant. In thermal burns, antemortem and postmortem discrimination generally cannot be made clearly. Because even living for a certain period of time after the incident, vital reaction (inflammmatory cell infiltration) may not occur due to heat thrombosis in the dermal vessels.

VITALITY AND WOUND AGE

Assoc. Prof. Taner DAŞ
Assoc. Prof. Ferah KARAYEL

EVALUATION OF WOUND AGE WITH HISTOLOGICAL FINDINGS

It is important from a forensic perspective whether the wound occurred while alive or after death. It is necessary to determine the time between trauma and death, thus determining the causality between the wound and the trauma. Additionally, detecting wounds at different ages in cases of violence is important to show the continuity of the event.

Because of the multitude of factors that influence wound age (such as age, genetics, nutritional status, environmental conditions, and wound type), it is prudent to determine wound age based solely on histological studies. Unless special staining and immunohistochemical examinations are performed, description of wound age should be limited to the time periods specified in Table 9.1.

The most important problem is distinguishing wounds that occur just before or after death. In this case, examining tissue sections stained with Hematoxylin Eosin may not be sufficient. Detection of antigens released in the early vascular phase of the wound healing process, when the cellular response has not yet started, by immunohistochemical method provides important information. For this purpose, extracellular matrix proteins such as fibronectin, tenascin, laminin, collagen, adhesion molecules, growth factors, and proinflammatory cytokines such as interleukins can be investigated.

Table 9.1 Use of vitality terminology and approximate wound age findings with conventional histological staining

Statement	Histopathological findings
Wound shortly before or after death	No active wound healing or immune reaction. Vitality and wound age determination is not possible.
Vital wound, during life	Signs of active immune reaction present (neutrophils, macrophages and fibroblasts infiltration) Hemorrhage, fibrin and platelet accumulation alone do not indicate a vital wound. The presence of the hyperemic zone at the edge of the wound is also not sufficient to describe as vital injury.
Fresh vital wound (hours-a few days)	Neutrophil infiltration is obvious, and early wound repair signs, such as macrophages, fibroblasts, branched capillary vessels, hemosiderin deposits, foreign body giant cells. The accumulation of fibrin and platelets alone does not permit a reliable statement on wound age.
Vital wound, not longer fresh (a few days-weeks)	Signs of resorption and wound repair spreading from wound margin to the deep center, invading macrophages, lymphocytes, pigment laden macrophages, foreign body type giant cells, granulation tissue, and scar area with decreased cellularity
Vital wound, not very old (weeks-months)	Wound repaired and scar tissue formed.
Vital wound, old, healed (many months-years)	Dense collagen scar tissue, no (or few) blood vessels, residual hemosiderin and calcium pigment deposition

Reference :

1.Dettmeyer, R. B. (2011). Forensic Histopathology: Fundamentals and Perspectives. Springer. Section 10, p. 194.

Table 9.2 Stages of fracture healing

Time	Histopathological Findings
1 day	Hematoma and traumatic inflammation: Acute hemorrhage at the fracture site due to vascular rupture, hematoma formation surrounding and joining the ends of the bone
1-2 days	Organization: Fibrin deposition in hematoma, inflammatory response with edema, accumulation of neutrophils
2-3 days	The emergence of fibroblasts, mesenchymal cells, gradual development of granulation tissue; necrosis of the bone adjacent to the fracture becomes evident; empty lacunes due to death of osteocytes; clear line between dead bone (empty lacuna) and living bone
3-6 days	Temporary fibrous callus, blood vessels in the bone marrow space and musculature After about 3 days, dead bone fragments are reabsorbed. Marked proliferation of cells of the periosteum and endostium
7-14 days	Temporary bone callus: The morphology of connective tissue cells undergoes modification. Osteoid matrix accumulates between proliferating cells. Transformation of fibrous callus into temporary bony callus: connective tissue cells form collagen fibers; fibroblasts transform into osteoblasts produce osteoid; chondroblasts are affected, cartilage islands develop in the fibrous stroma; bone formation, transformation into lamellar bone via osteoclasts and osteoblasts (this bone forms the final callus)
2-3 weeks	The callus reaches its maximum size.
3-4 weeks	A hard bony callus is formed.
More than 4 weeks	Rearrangement of callus and bone junction: remodeling of new bone from woven appearance to mature bone; Histologically, ossification and new bone may be found.

Reference :

1.Dettmeyer, R. B. (2011). Forensic Histopathology: Fundamentals and Perspectives. Springer. Section 10, p. 203.

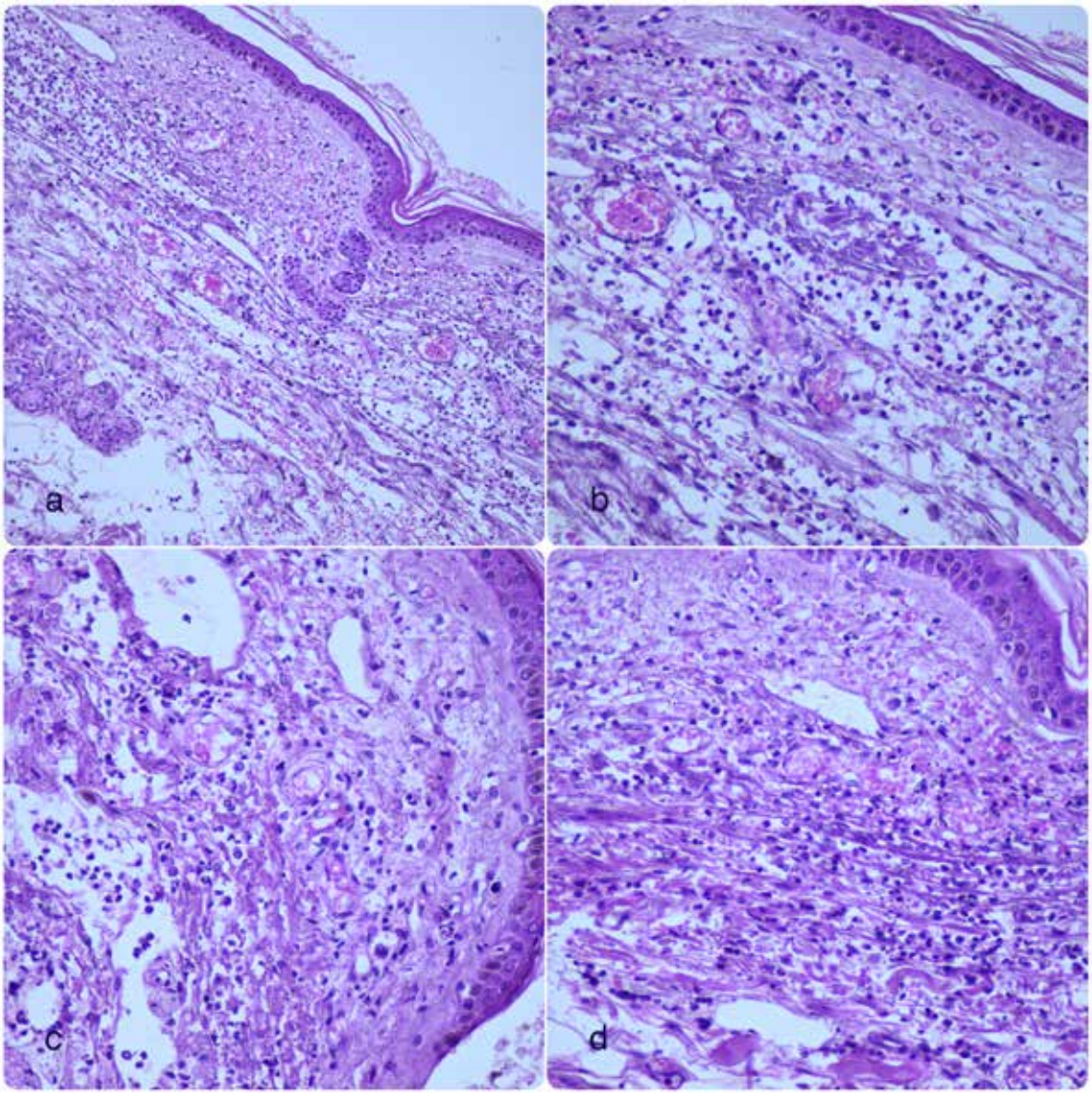

Figure 9.1
Wound age,
a) (H&E, x200). In this microscopic view, containing skin and subcutaneous tissue, proliferation of neutrophils, erythrocytes extravasation, and proliferation of capillaries is observed. These findings are consistent with a fresh vital wound that has formed within a few hours to a few days.
b,c,d) (H&E, x400). At higher magnification.

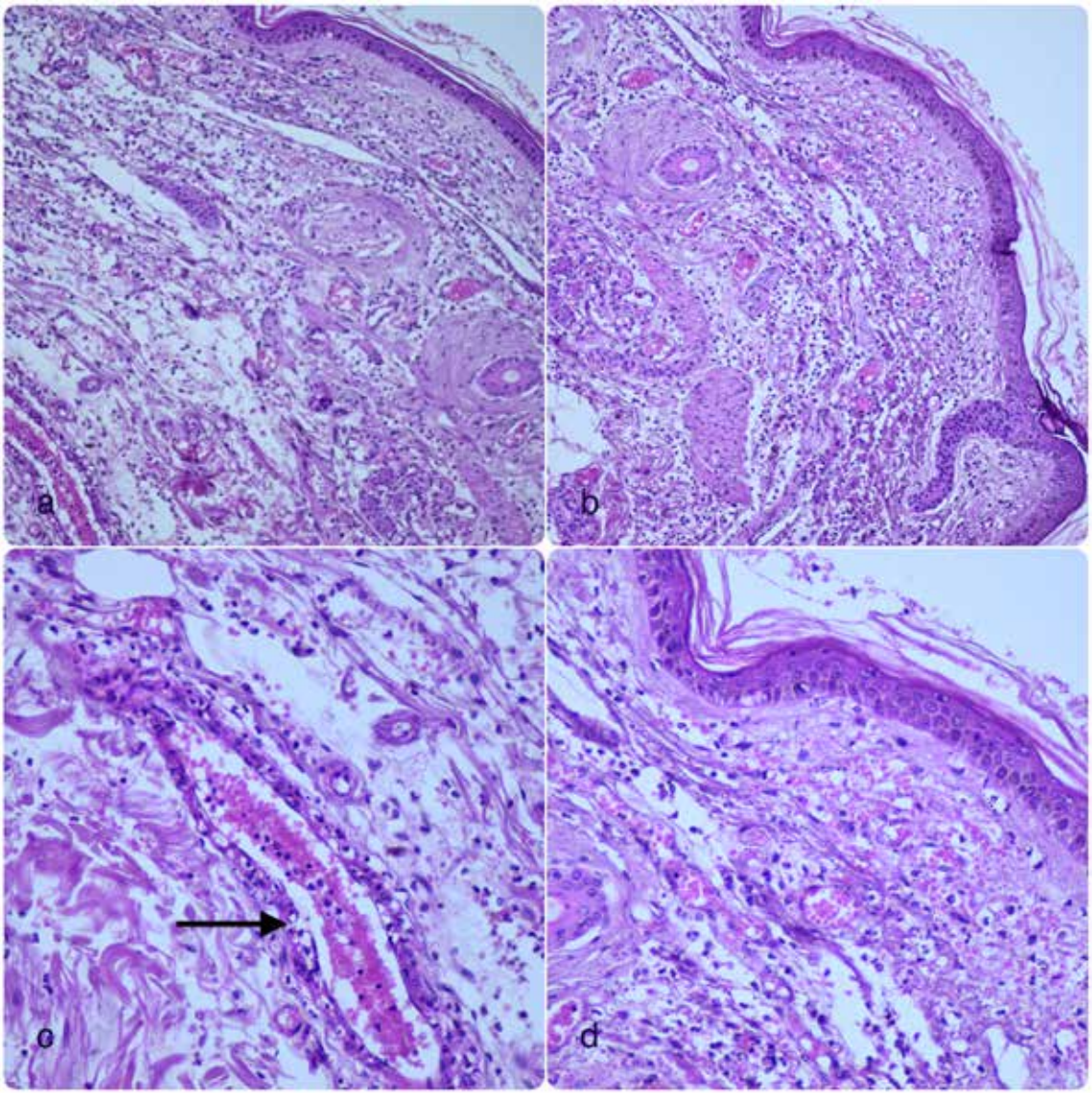

Figure 9.2
Wound age.
a) (H&E, x200). Microscopic view reveals neutrophil infiltration, erythrocytes, and capillary vessel proliferation in skin and subcutaneous tissue. These findings are consistent with a fresh vital wound that has developed within a few hours to a few days.
b) (H&E, x400) At higher magnification.
c) (H&E, x200). Neutrophil margination (arrow) is visible on the dermal vessel wall.
d) (H&E, x400) Erythocyte extravasation and neutrophil infiltration are observed in the dermis.

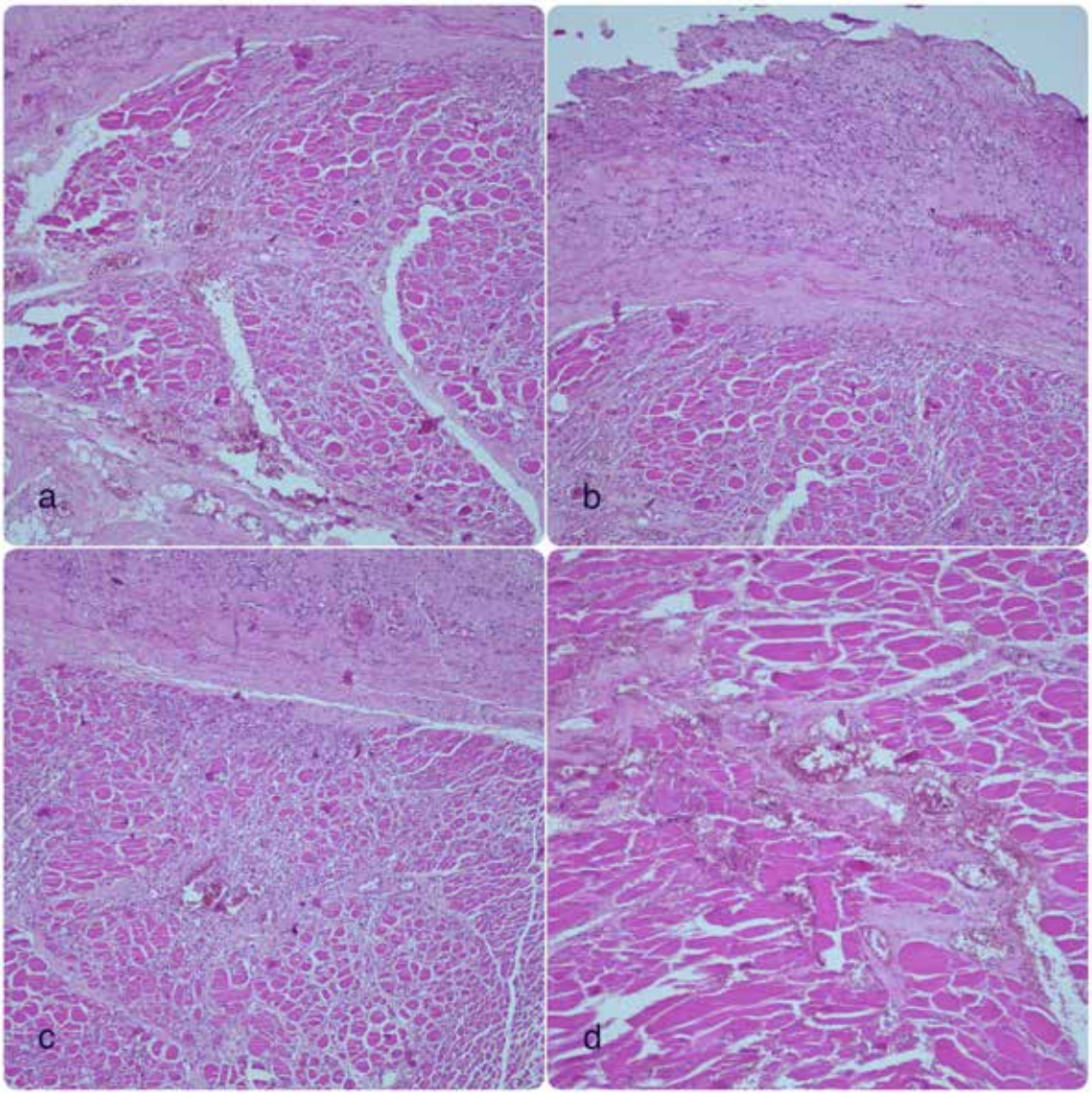

Figure 9.3
Wound age.
a,b,c,d) (H&E, x100).
Hemorrhage, neovascularization, fibroblast proliferation, and granulation tissue development are observed between the striated muscle bundles. It is compatible with a wound that is no longer fresh (few days to a few weeks of injury).

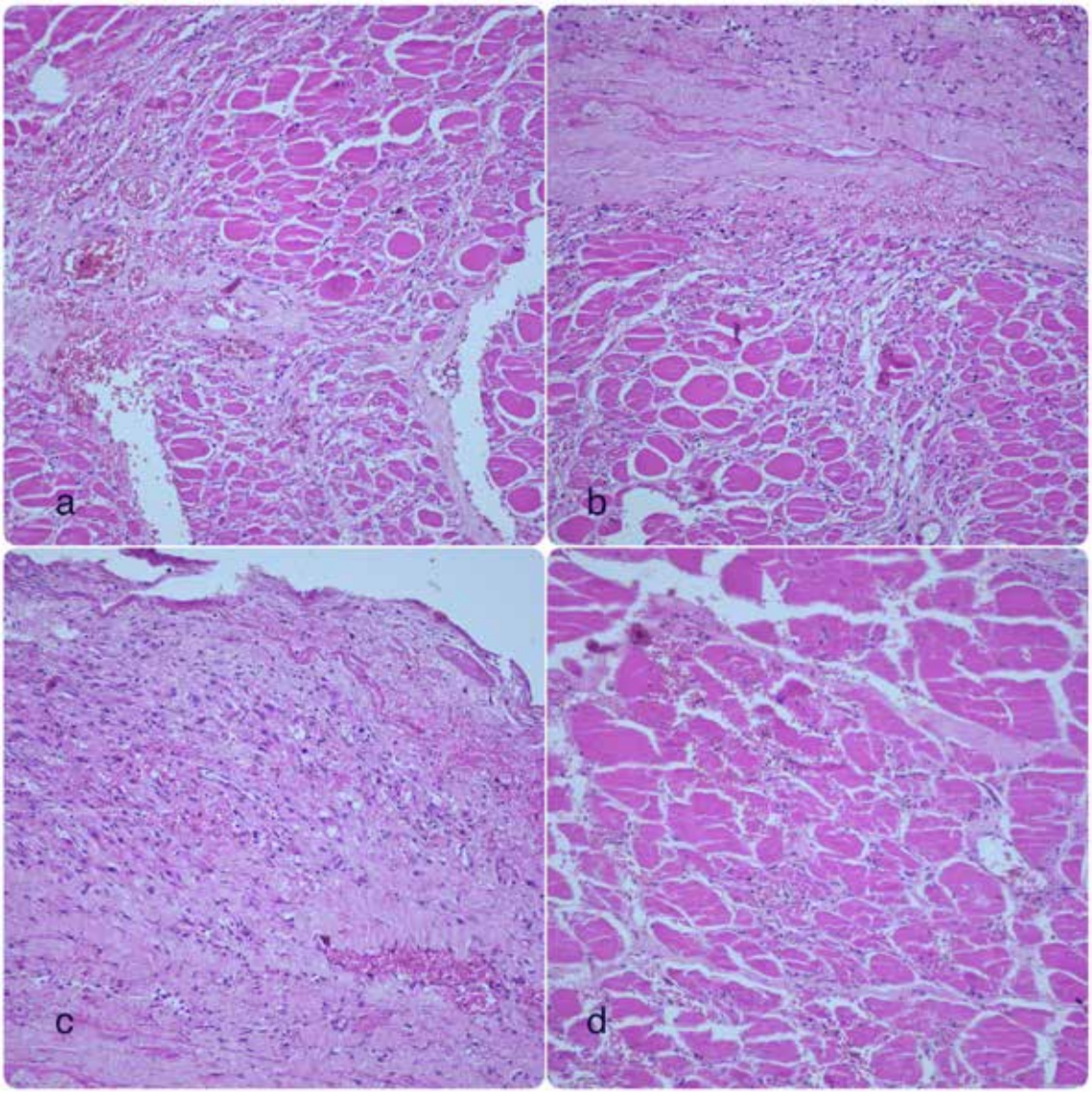

Figure 9.4
Wound age.
a,b,c,d) (H&E, x200).
At higher magnification, a wound compatible for a few days to a few weeks of injury (no longer fresh).

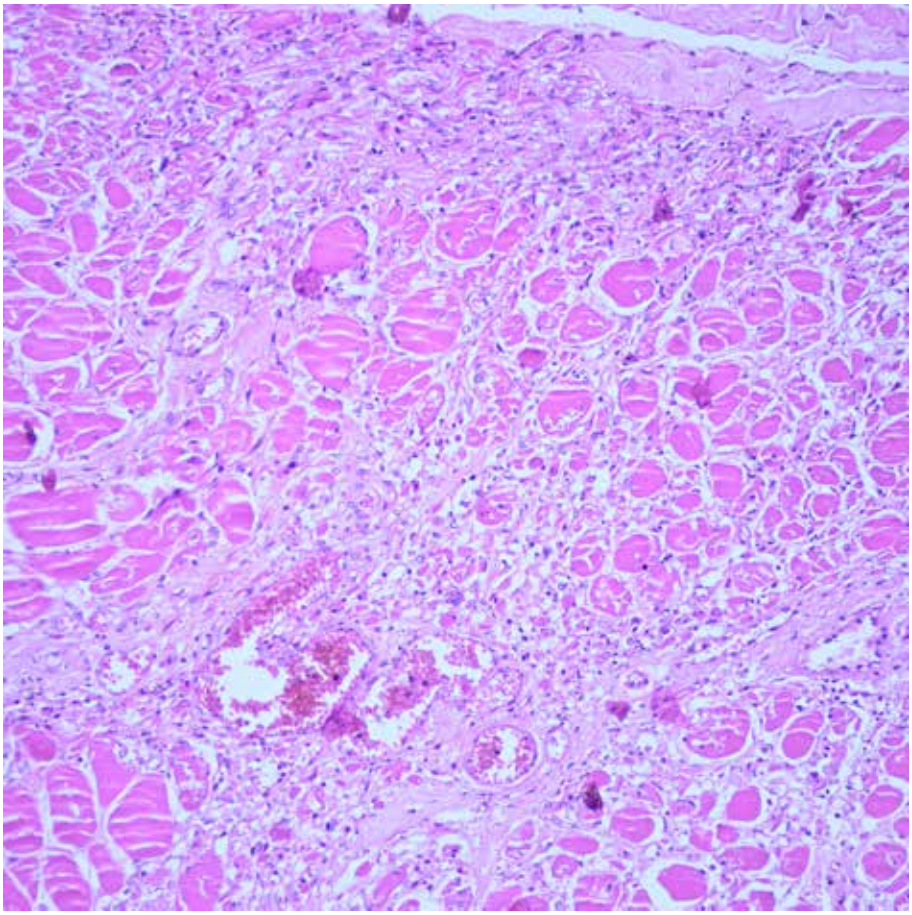

Figure 9.5
Wound age,
(H&E, x200).
Neovascularization, and fibroblast proliferation observed between the striated muscle bundles. It is compatible for a few days to a few weeks of injury.

CENTRAL NERVOUS SYSTEM

Assoc. Prof. Ferah KARAYEL

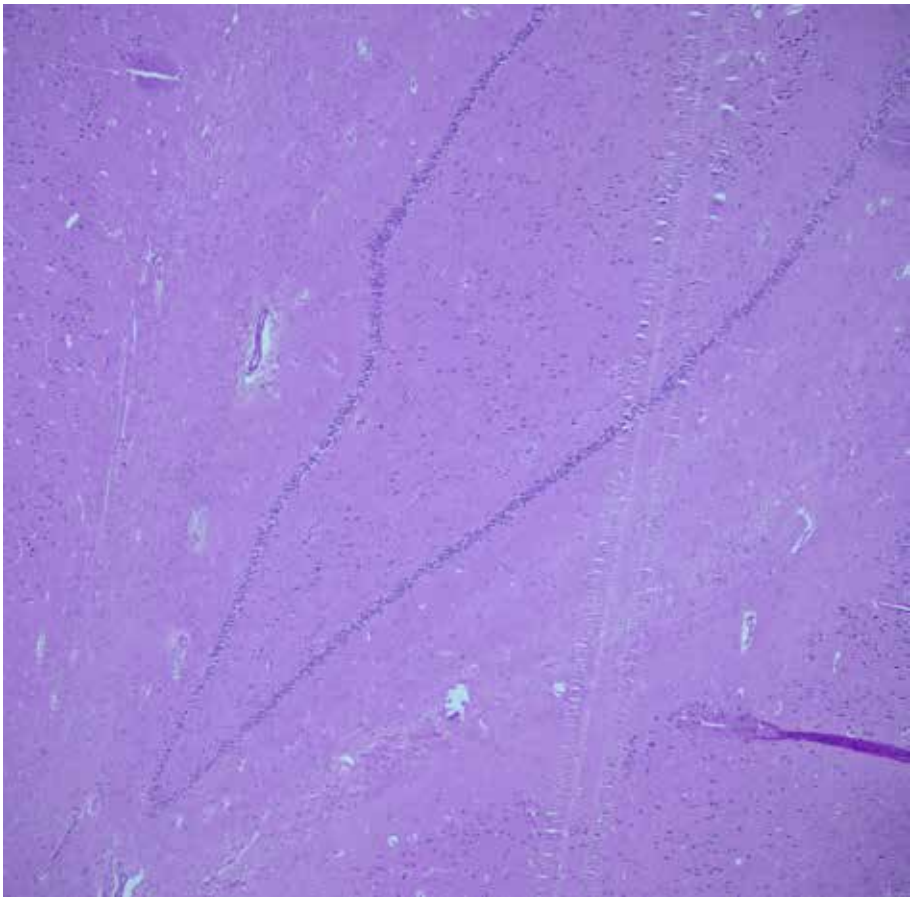

Figure 10.1
CA4 region in the brain, (H&E, x40). The hippocampus region of the brain is located at the base and medial of the lateral ventricle. The CA4 region located in the hippocampus is one of the regions that must be sampled in systematic brain sampling, especially in epilepsy cases.

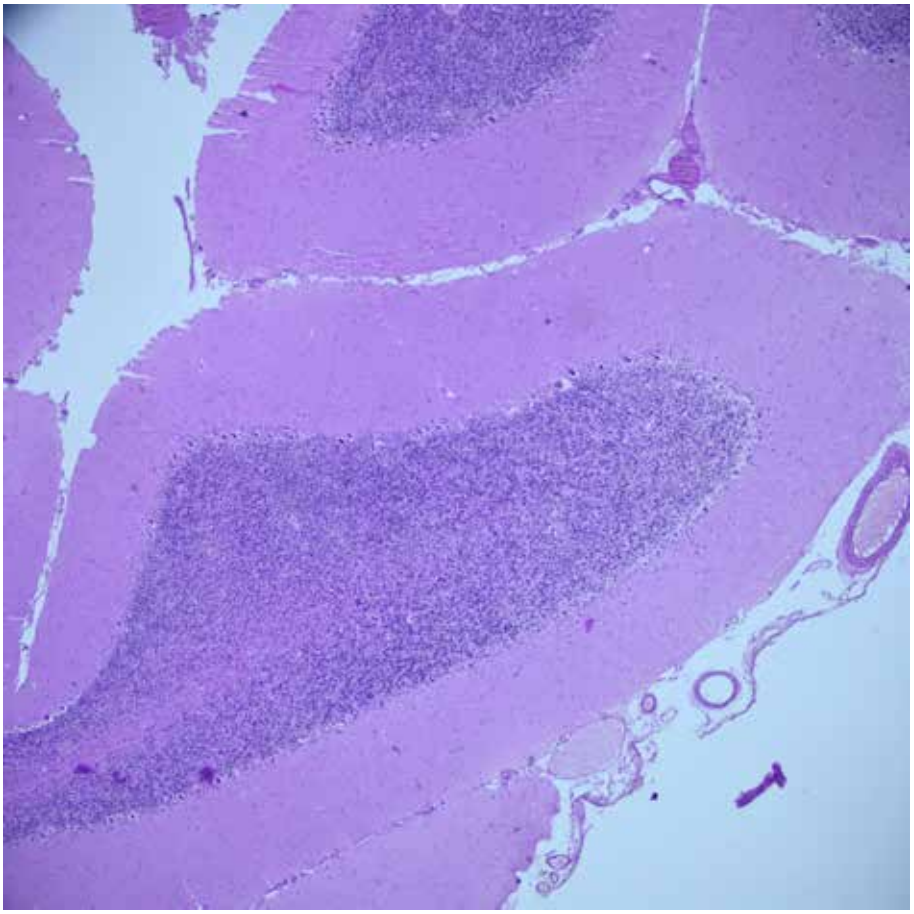

Figure 10.2
Cerebellum, (H&E, x40). The cerebellar cortex contains gray matter on the outside and white matter (medulla) on the inside. It has 3 layers. There are granular cells in the stratum granulosum, Purkinje cells in the stratum gangliosum, stellate cells on the surface in the stratum moleculare, and basket cells in the depths.

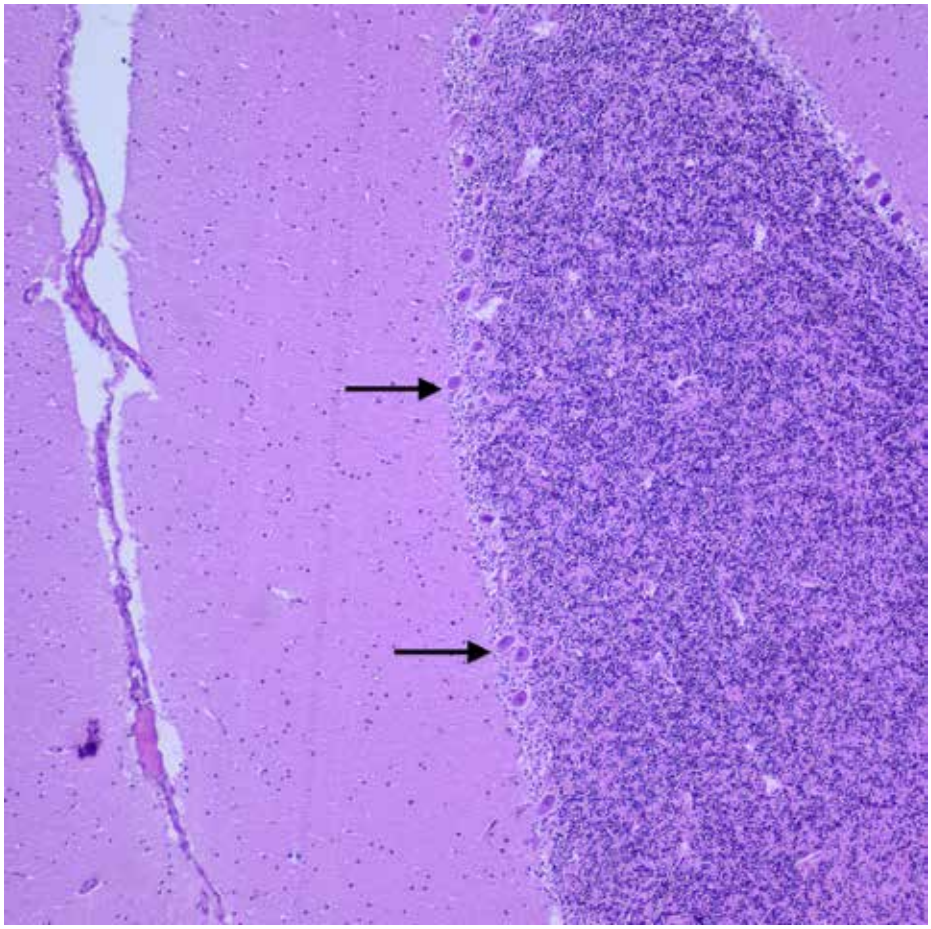

Figure 10.3
Purkinje cells in the cerebellum, (H&E, x100).
Purkinje cells are located in a single row in the stratum gangliosum.
While these cells extend to the molecular layer with their branching dendrites, they also reach the medulla with their axons.
Thus, they provide transmission by establishing connections with the neurons located there.

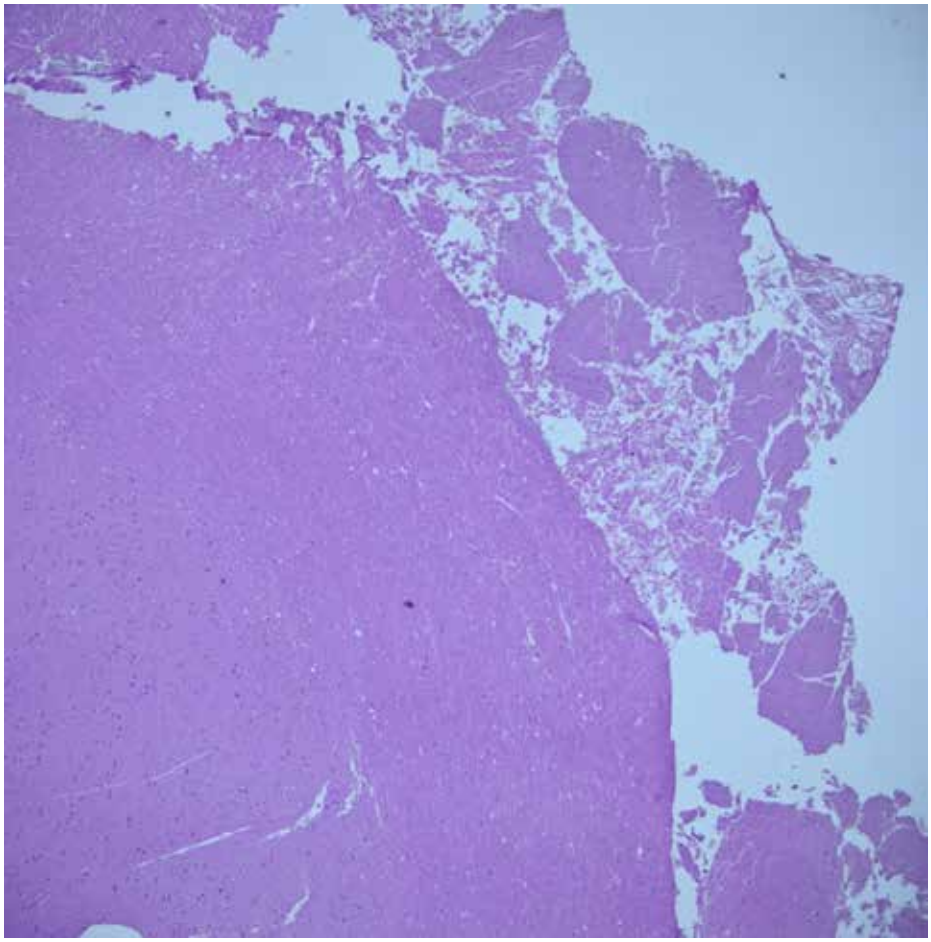

Figure 10.4
Brain autolysis, (H&E, x40).
This is the microscopic appearance of the brain in cases showing signs of decay, as well as in cases that have received intensive care treatment, also called respiratory brain, and have been exposed to severe hypoxia.

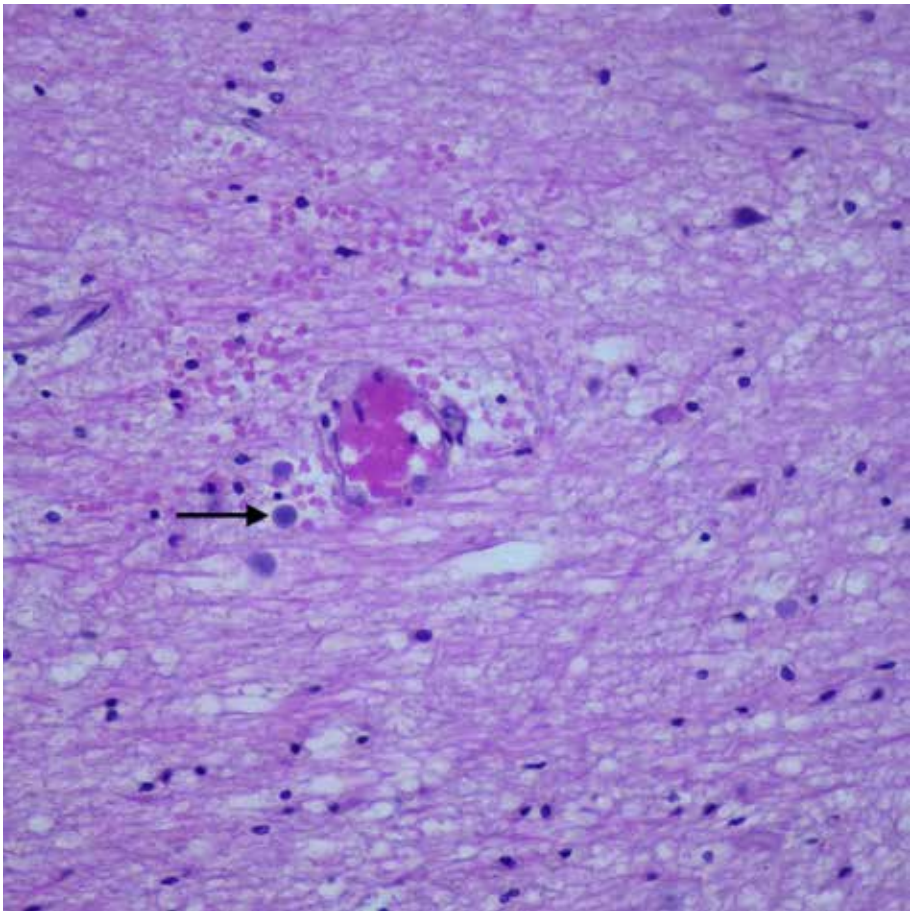

Figure 10.5
Corpora amylecea, (H&E, x400). These structures, which are seen in the brain due to aging and degenerative changes, are round, weakly basophilic, concentric lamellar bodies consisting of glycosaminoglycans, heat shock proteins and ubiquitin. They are often found in perivascular (arrow), subpial and subependymal regions.

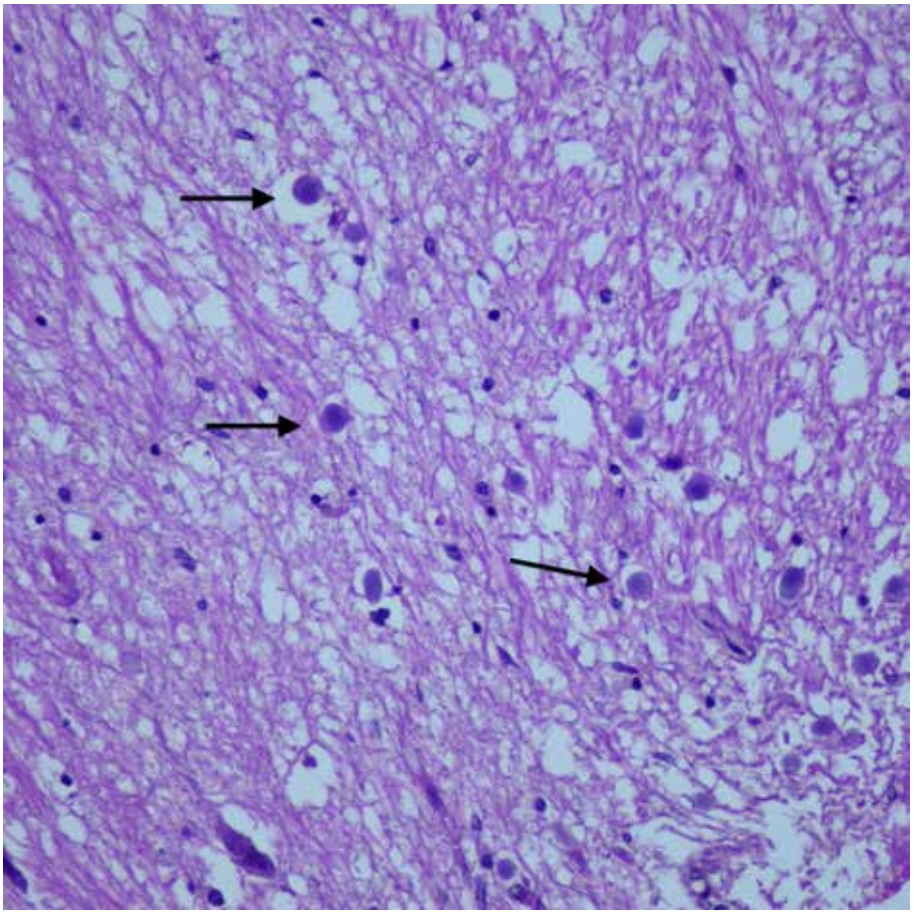

Figure 10.6
Corpora amylecea, (H&E, x400). Appearance of corpora amylecea in a different area of the brain. Corpora amylecea (arrow) is known to increase with aging and is frequently seen in neurodegenerative conditions such as Alzheimer's disease.

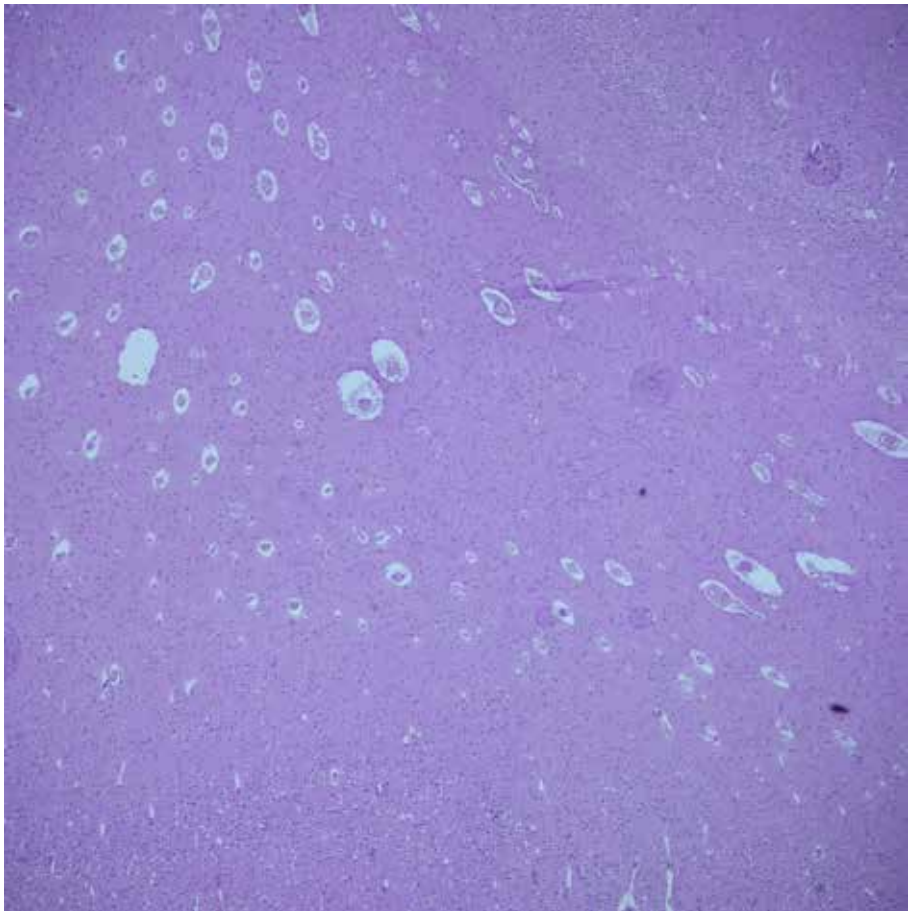

Figure 10.7
Areas of brain perivascular expansion, edema, (H&E, x40).
Expansion and hollow appearance in the perivascular areas are observed in the brain tissue in this microscopic view. Extracellular edema (vasogenic edema) appears as enlarged perivascular spaces around blood vessels. Intracellular edema (cytotoxic edema) is detected as significant swelling in cells such as neurons, astrocytes and oligodendrocytes. Macroscopically, the edematous brain has increased in weight and appears soft, wet and shiny. The sulci are narrowed, the gyri are flattened, and the ventricular cavities are compressed.

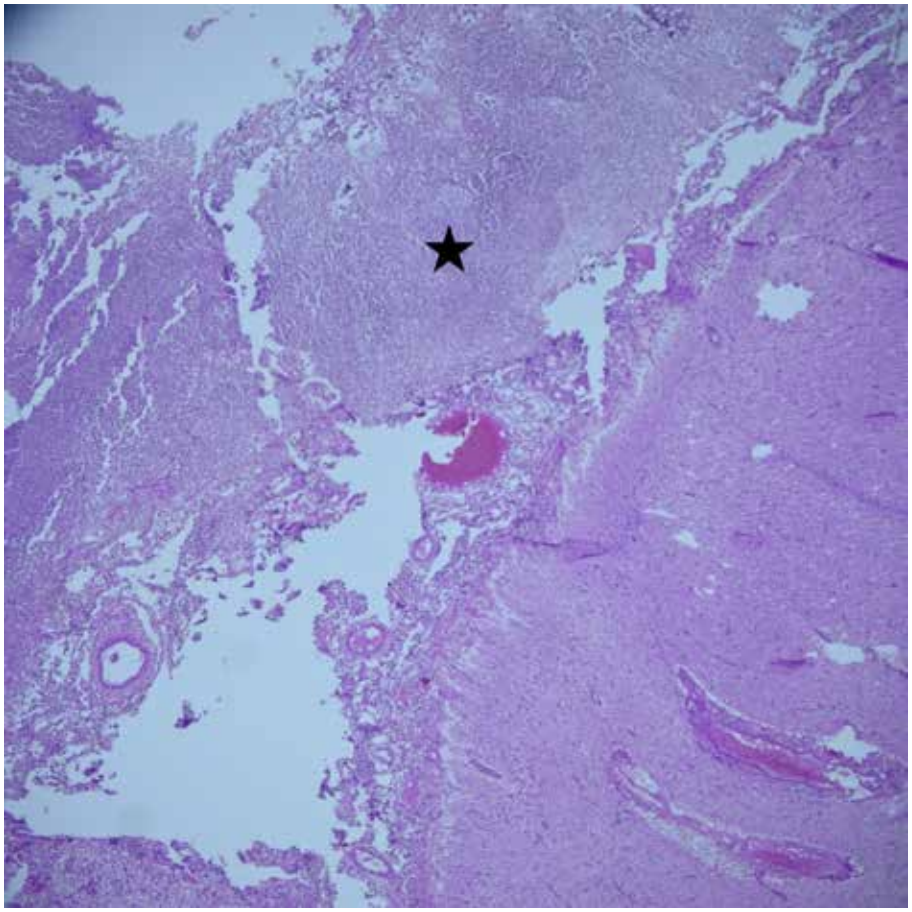

Figure 10.8
Acute (purulent) meningitis, (HE, x40).
Exudate consisting of dense neutrophils filling the subarachnoidal space (asterisk) is seen at image.
Acute meningitis shows various microscopic findings depending on the type of inflammation. While neutrophilic infiltration and fibrin accumulation are common in bacterial meningitis, lymphocytic infiltration is prominent in viral meningitis. Granuloma formation is seen in fungal and tuberculous meningitis.

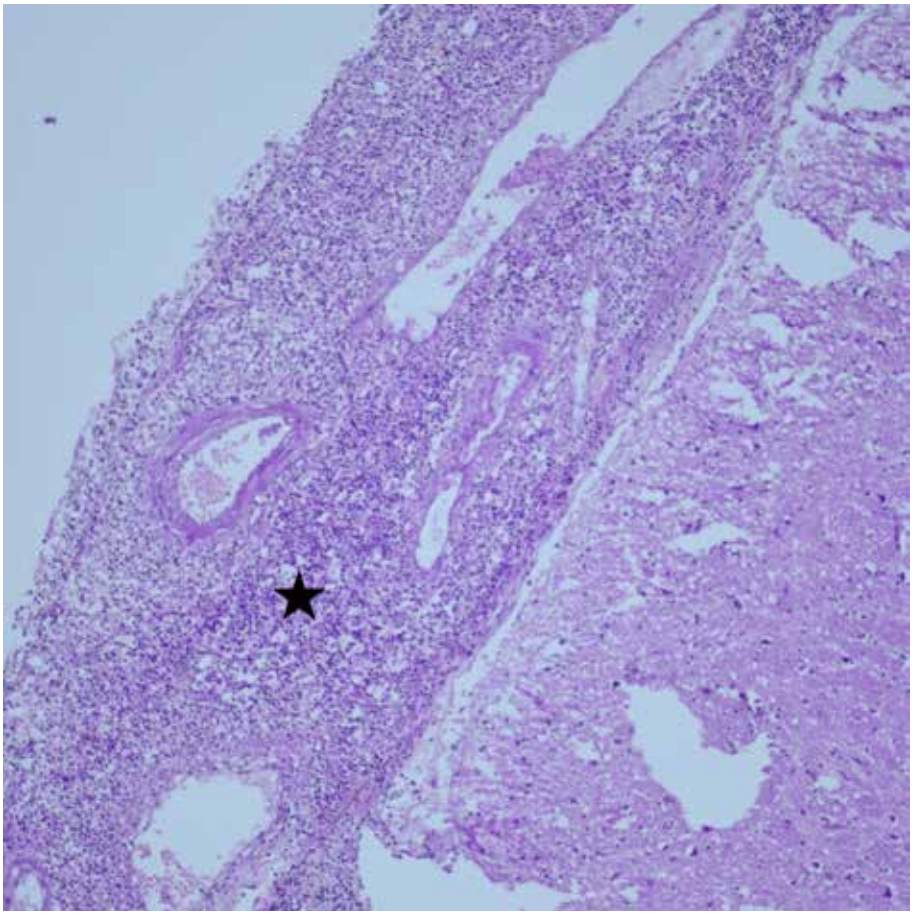

Figure 10.9 Acute meningitis, (H&E, x100). At higher magnification, an exudate (asterisk) consisting of dense neutrophils filling the subarachnoidal space is seen on the brain surface.

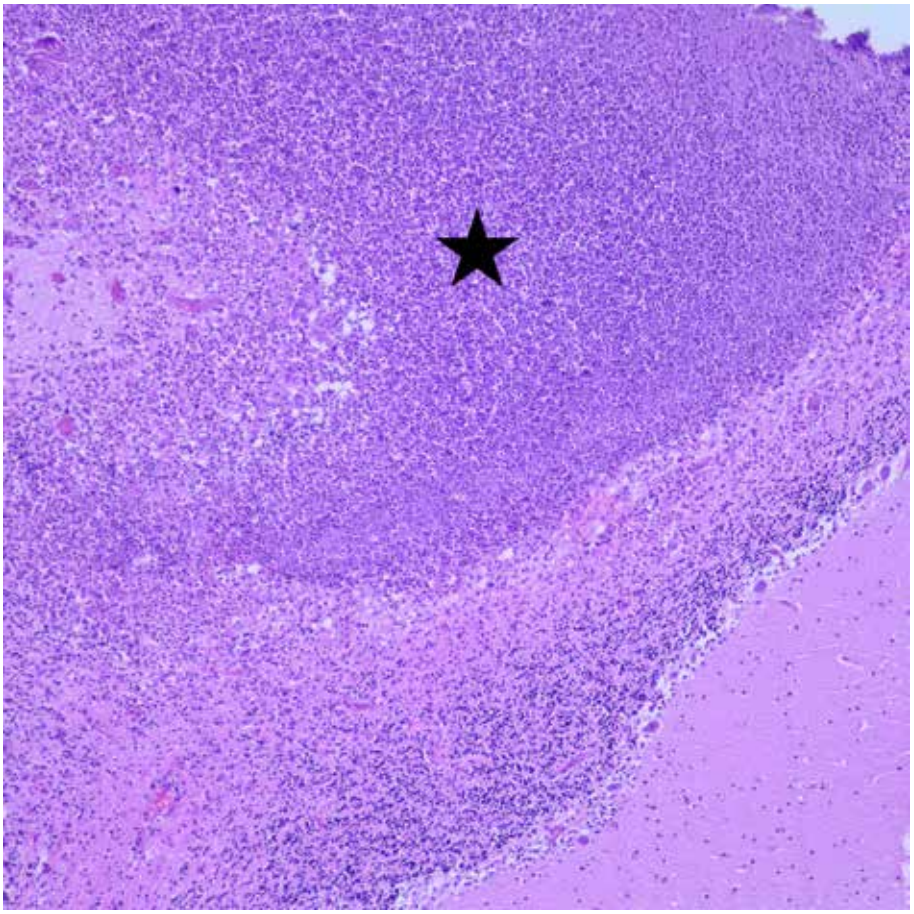

Figure 10.10 Cerebellum, abscess formation, (H&E, x100). In the cerebellum, an abscess focus (asterisk) consisting of necrosis and dense neutrophils is seen in the parenchyma. Cerebellar abscess is an accumulation of pus, often caused by bacterial infection. In addition to edema in the surrounding parenchyma, capsule formation may be observed around the abscess in later periods.

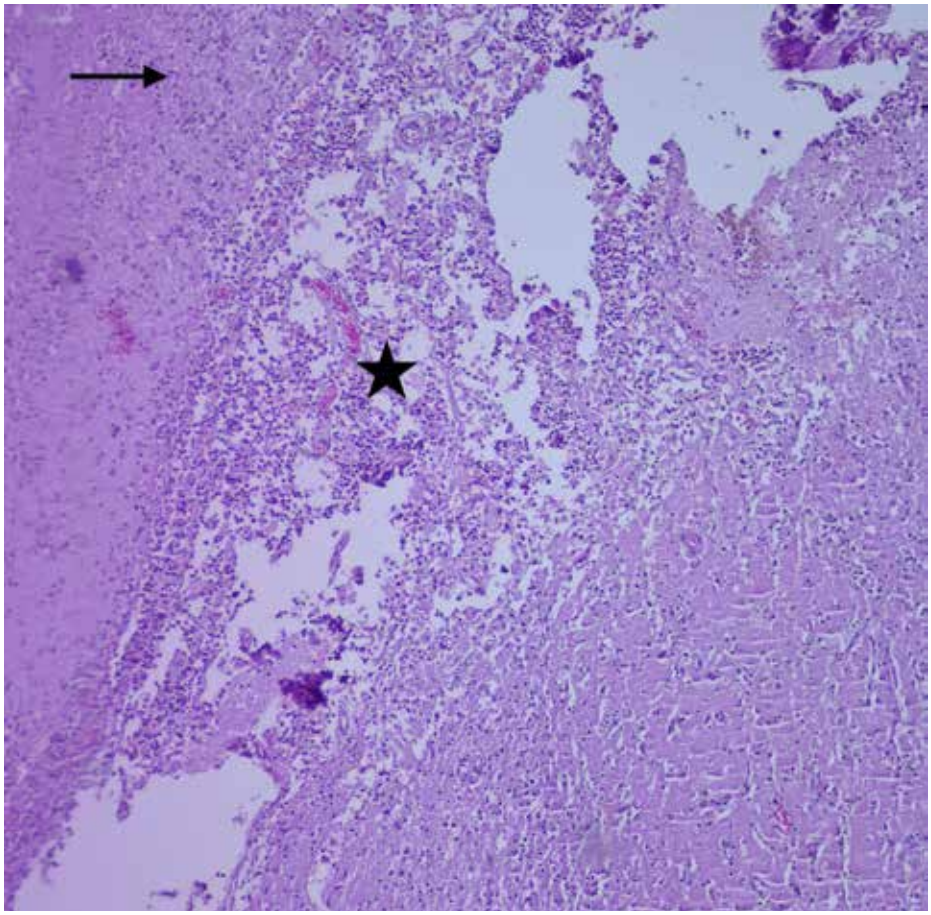

Figure 10.11
Brain, acute meningoencephalitis, (H&E, x100).
In this microscopic view, neutrophils are seen in the subarachnoidal space (asterisk), perivascular areas, and parenchyma (arrow).
Acute meningoencephalitis is inflammation of the brain (encephalitis) and meninges (meningitis). It is often caused by viral, bacterial, fungal or parasitic infections. Microscopic findings of meningoencephalitis may vary depending on the cause of the infection. Dense neutrophils, lymphocytes and plasma cells infiltration in the brain membranes (especially in the leptomeninges), microglial nodules, perivascular lymphocytic cuffing, neuronal necrosis and astrocytic proliferation are detected in the brain parenchyma.

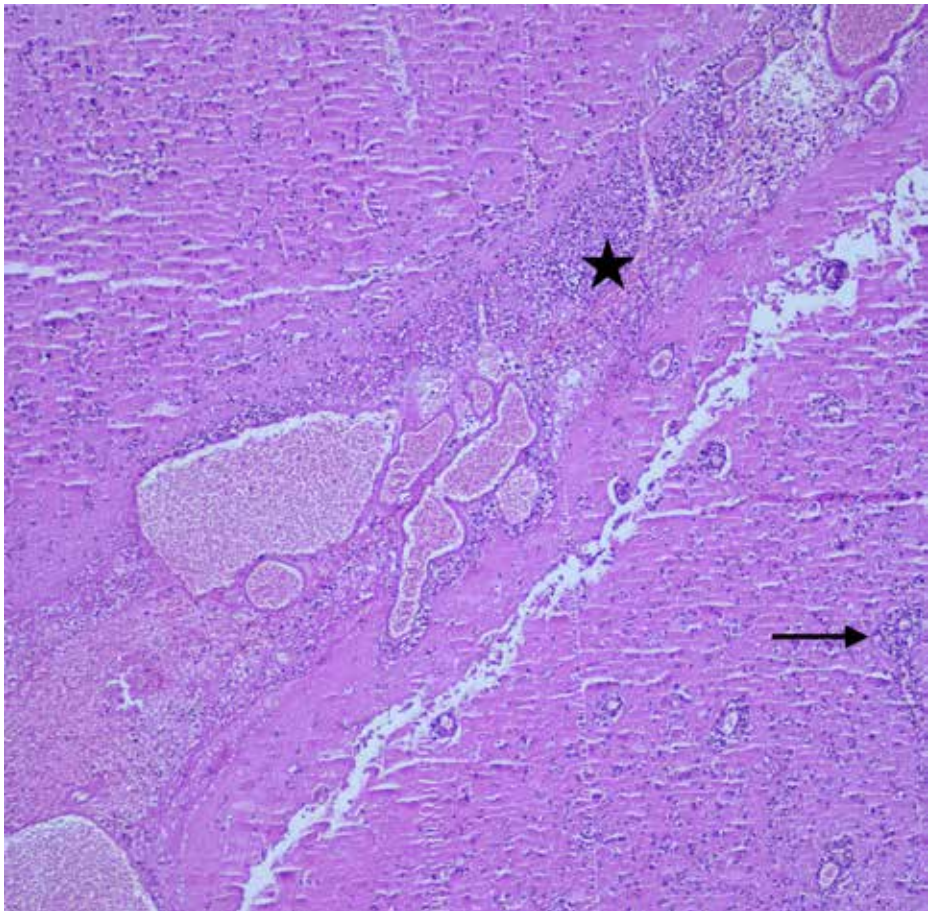

Figure 10.12
Brain, acute meningoencephalitis, (H&E, x100).
Neutrophil infiltration is seen in the subarachnoidal space (asterisk), perivascular areas (arrow) and parenchyma.

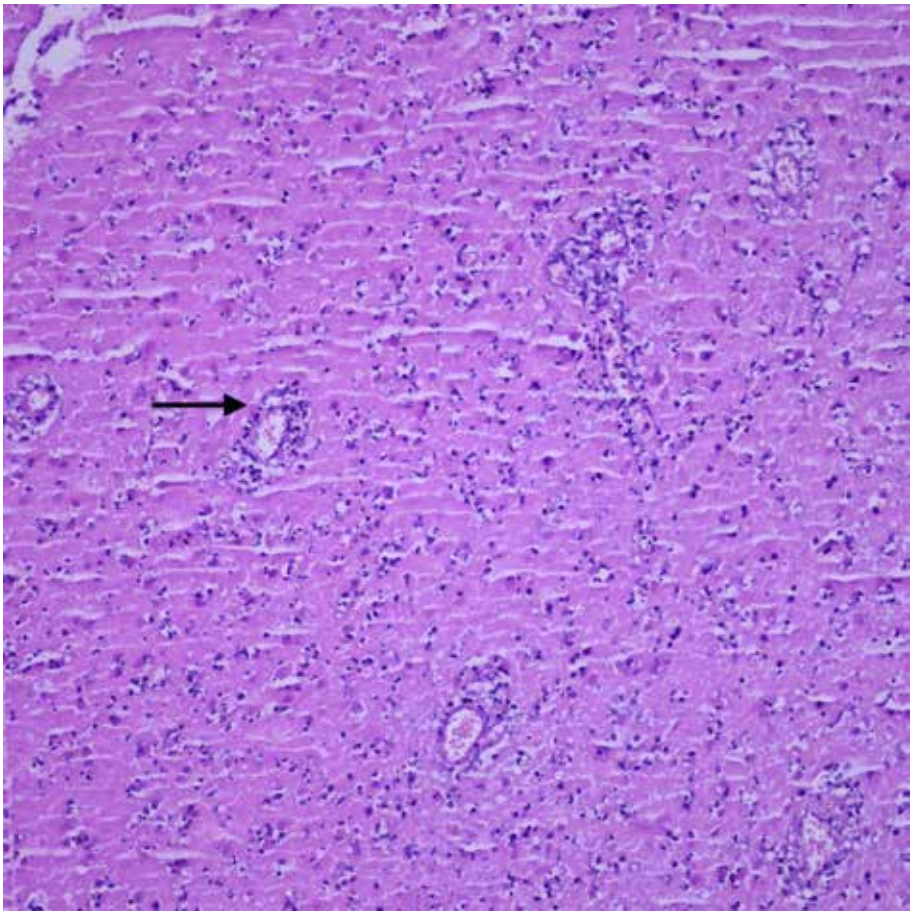

Figure 10.13
Brain, acute meningoencephalitis, (H&E, x200). At higher magnification, neutrophil infiltration is seen within the brain parenchyma and perivascular areas (arrow).

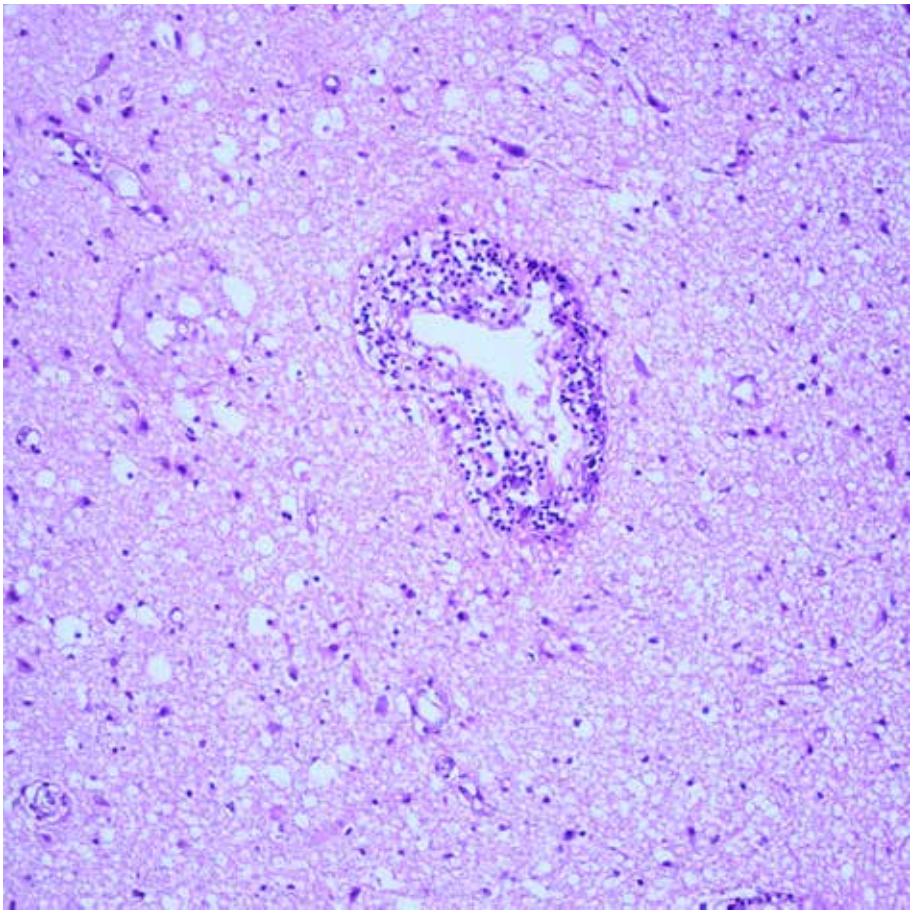

Figure 10.14
Brain, encephalitis, (H&E, x200). Mononuclear inflammatory cells are seen in the parenchyma and around the vessels and scattered singly or in small groups.

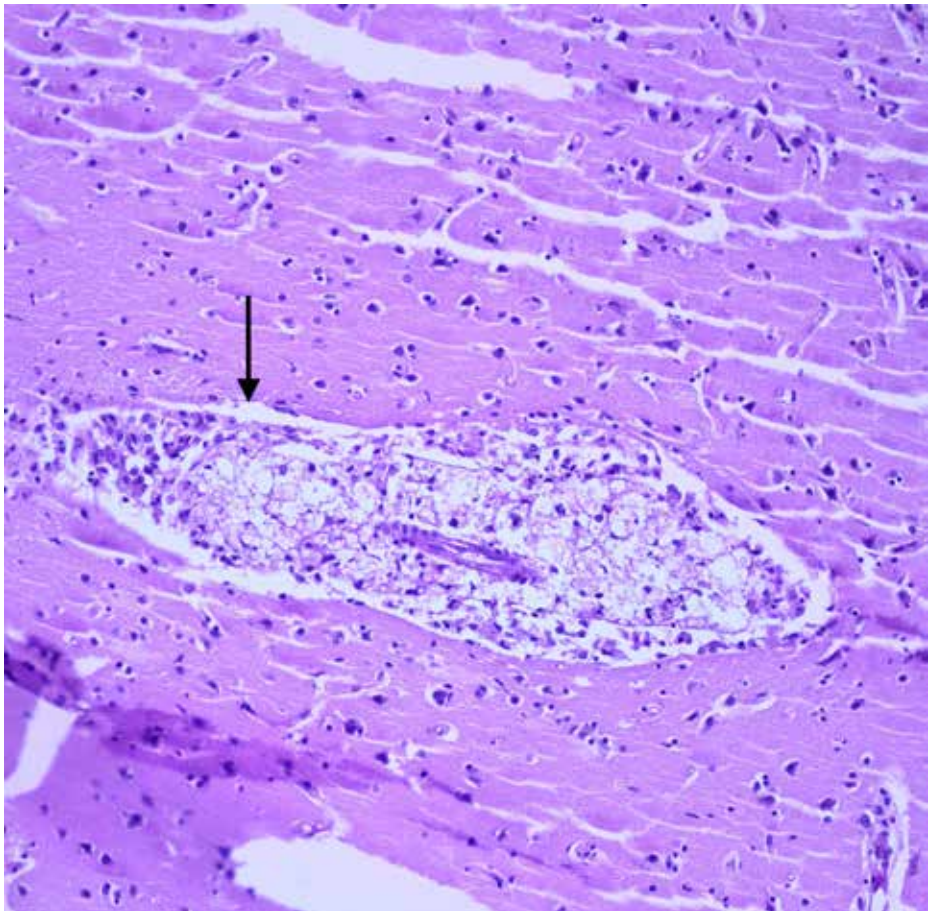

Figure 10.15
Fungal meningoencephalitis, (H&E, x200). Yeast form in the intraparenchymal perivascular spaces (arrow) are seen.

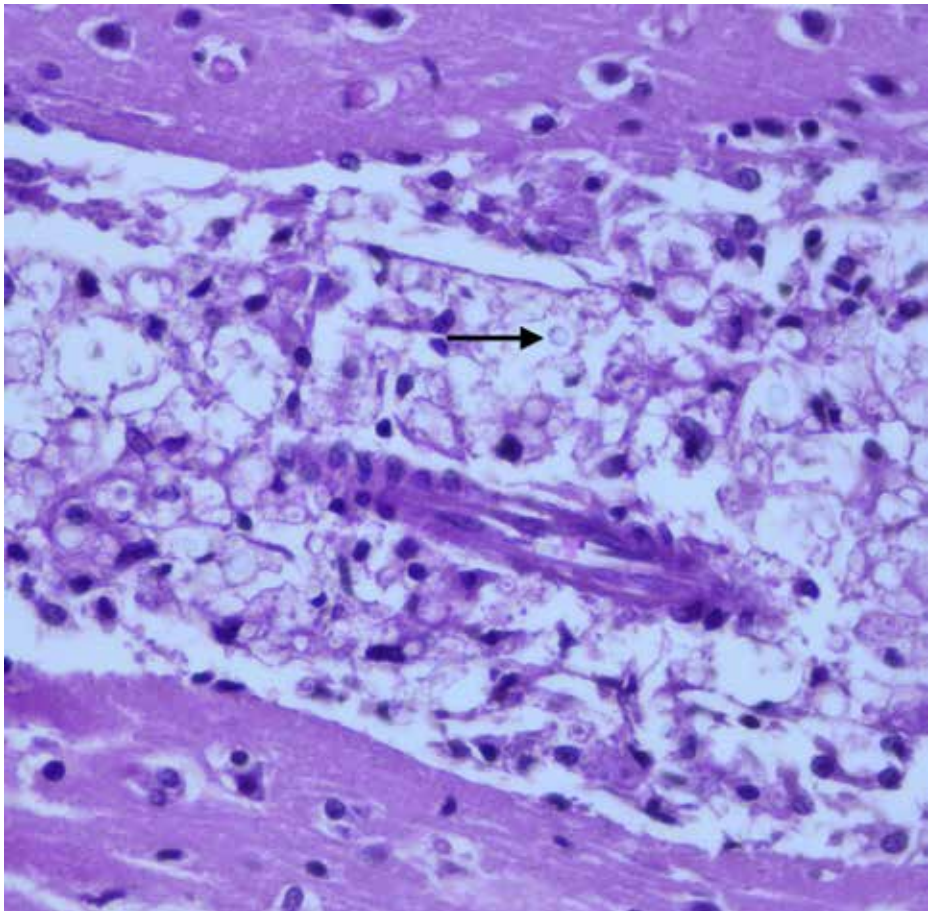

Figure 10.16
Fungal meningoencephalitis, (H&E, x600). At higher magnification, yeast form in the intraparenchymal perivascular spaces are seen. The organism appears as spherical structures with a clear halo (arrow) around it (cryptococci).

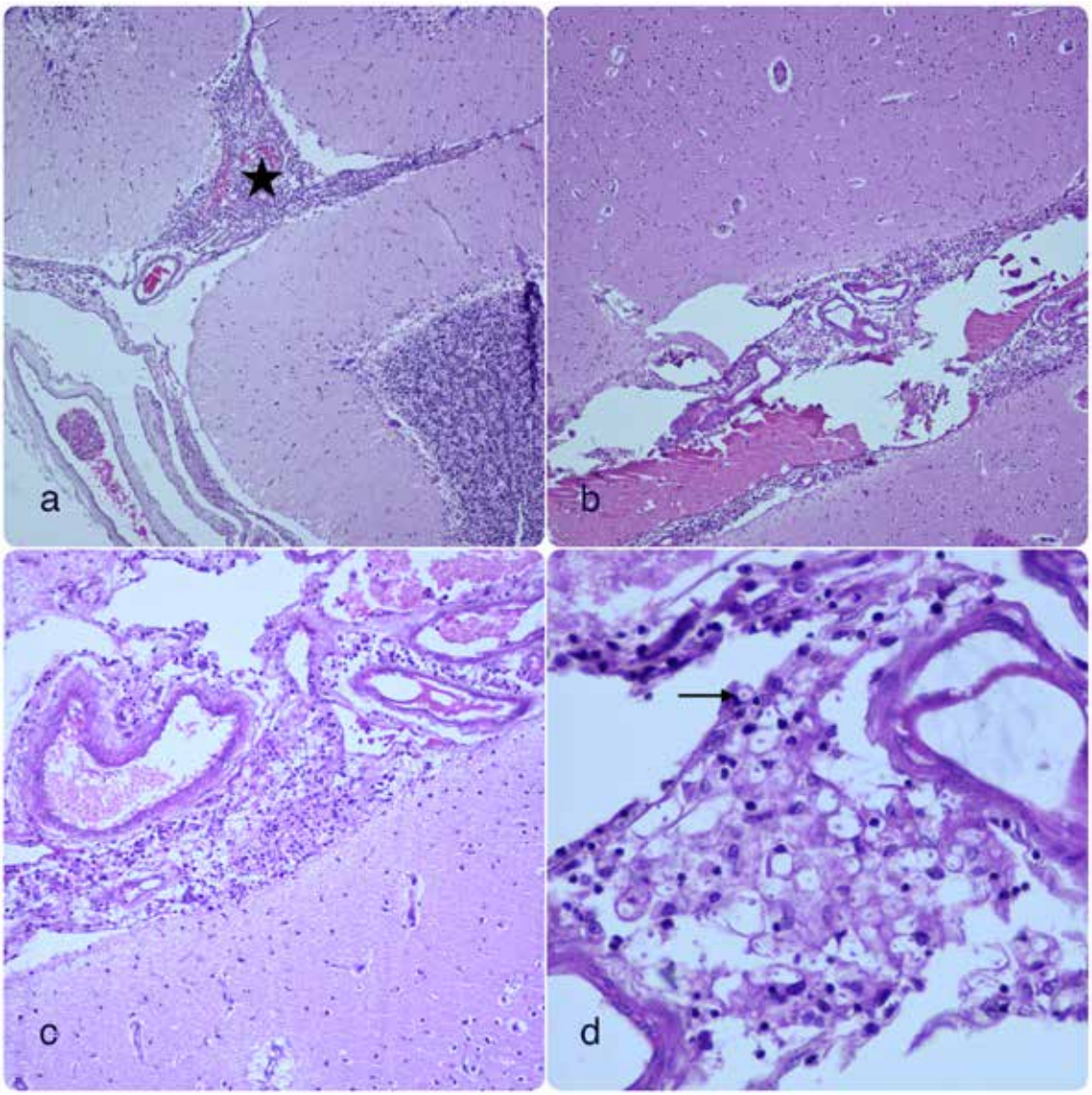

Figure 10.17
Fungal meningoencephalitis,
a) (H&E, x100). Criptococcus neoformans, one of the common causes of fungal encephalitis, is usually the causative agent in immunosuppressed people. They appear as round or oval-shaped, encapsulated yeast cells in the brain parenchyma. There is a transparent halo around the capsules. They form chronic inflammatory cell infiltration, microglial nodules and sometimes small granuloma structures. The microscopic view shows dense mononuclear inflammatory cell infiltration (asterisk) in the subarachnoid space of the cerebellum.
b) (H&E, x100). The microscopic view shows mononuclear inflammatory cell infiltration in the subarachnoid space.
c) (H&E, x200). At higher magnification.
d) (H&E, x600). At higher magnification.
The microscopic view shows cryptococcal yeast forms (arrow).

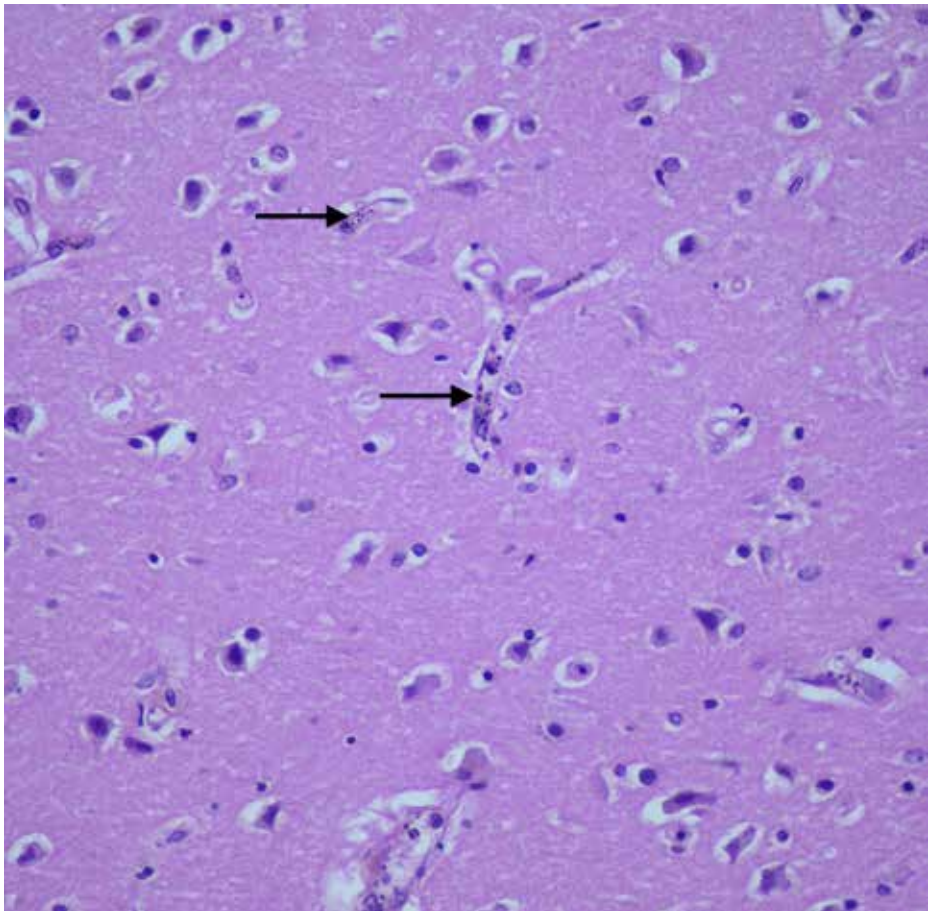

Figure 10.18
Malaria,
(H&E, x400).
Black, dark brown, coarse, numerous parasite pigments (hemozoin pigment) (arrows) are seen in the erythrocytes located in the capillary lumen of the brain parenchyma.

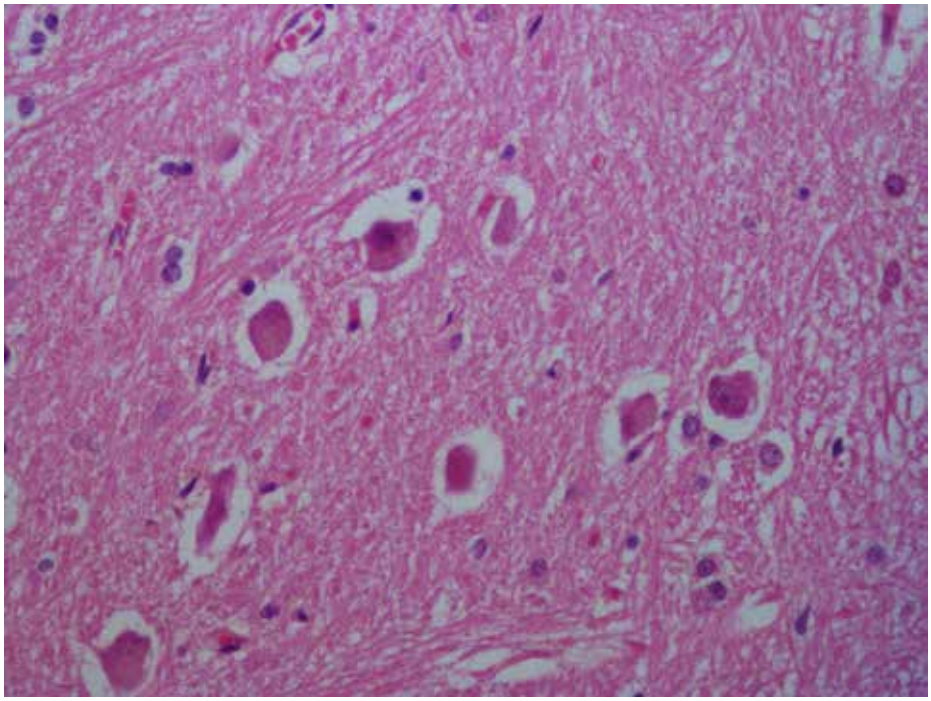

Figure 10.19
Rabies,
(H&E, x400).
Eosinophilic, round intracytoplasmic inclusions (Negri bodies) are detected in neurons in the brain parenchyma, pyramidal cells in the hippocampus and cerebellar Purkinje cells.

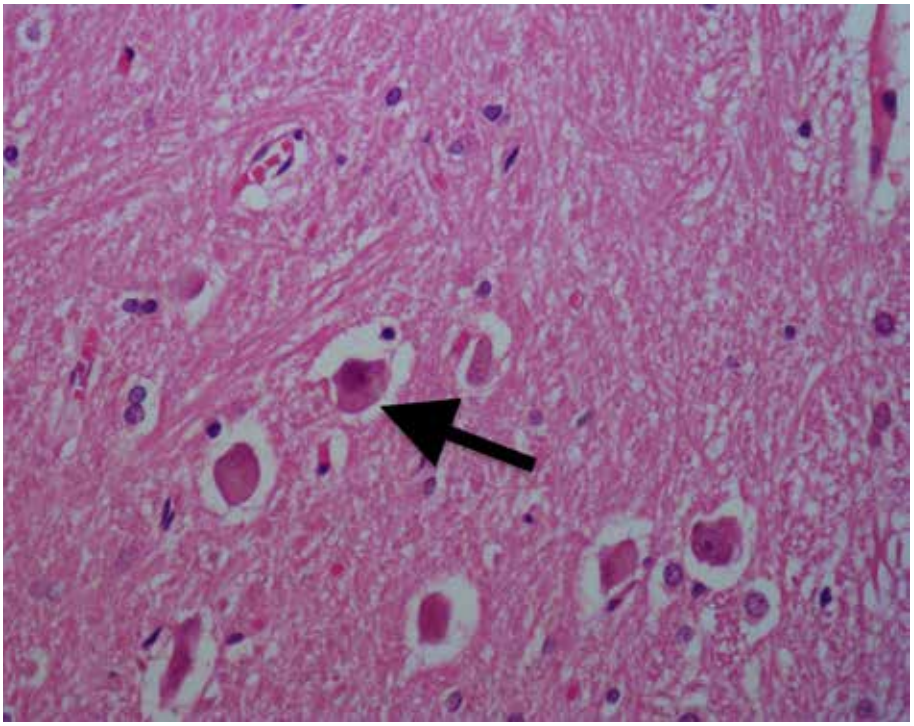

Figure 10.20 Rabies, (H&E, x400). Eosinophilic, round intracytoplasmic inclusions (Negri bodies) (arrow) are detected in neurons in the brain parenchyma.

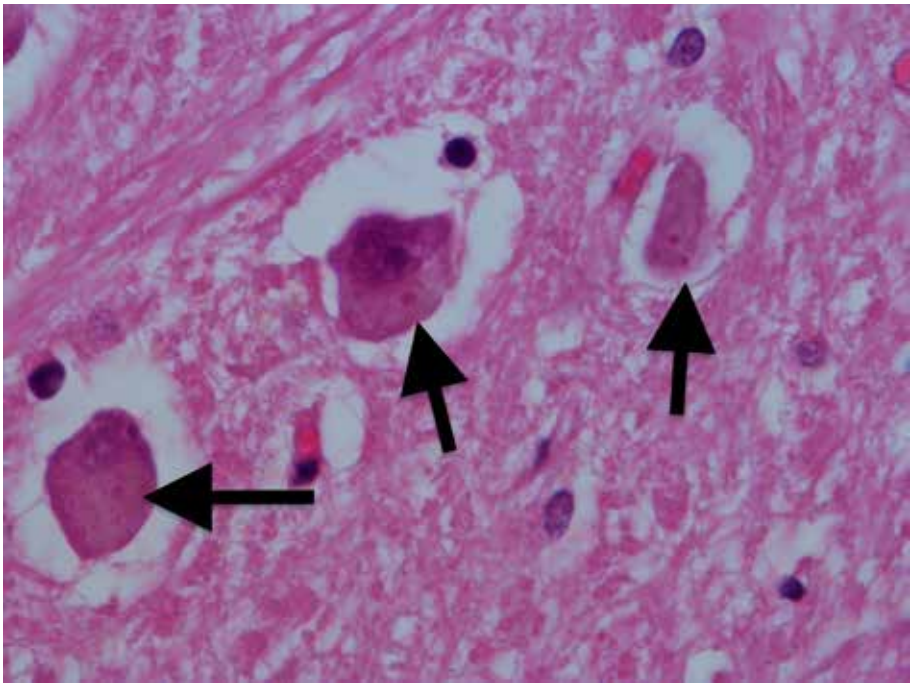

Figure 10.21 Rabies, (H&E, x1000). At higher magnification eosinophilic, round intracytoplasmic inclusions (Negri bodies) (arrow) are detected in neurons in the brain parenchyma.

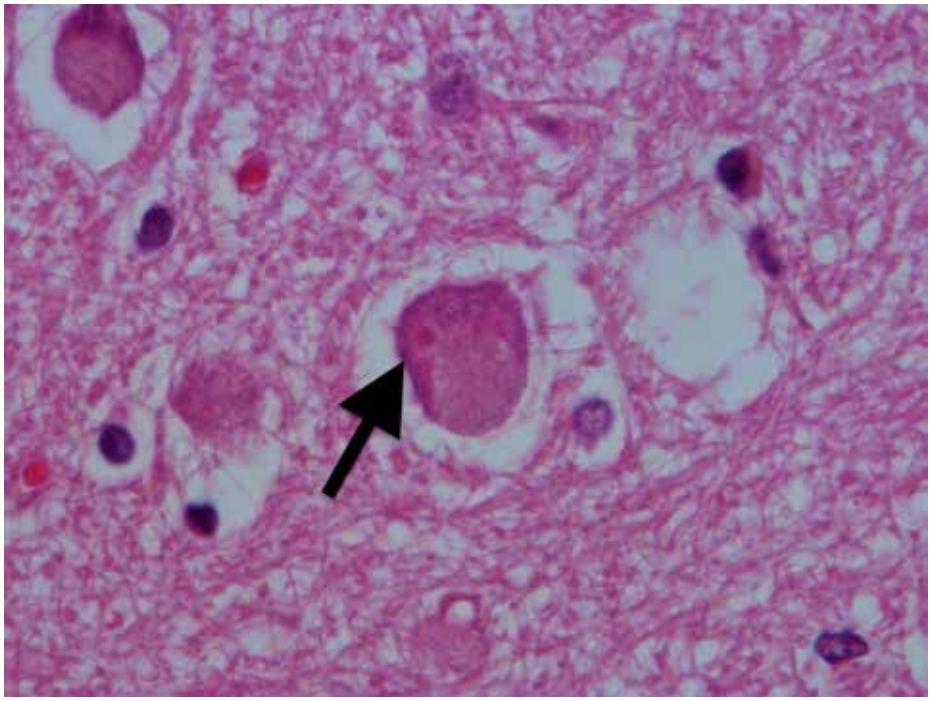

Figure 10.22
Rabies,
(H&E, x1000).
At higher
magnification
eosinophilic, round
intracytoplasmic
inclusions
(Negri bodies)
(arrow)
in neurons in the brain
parenchyma.

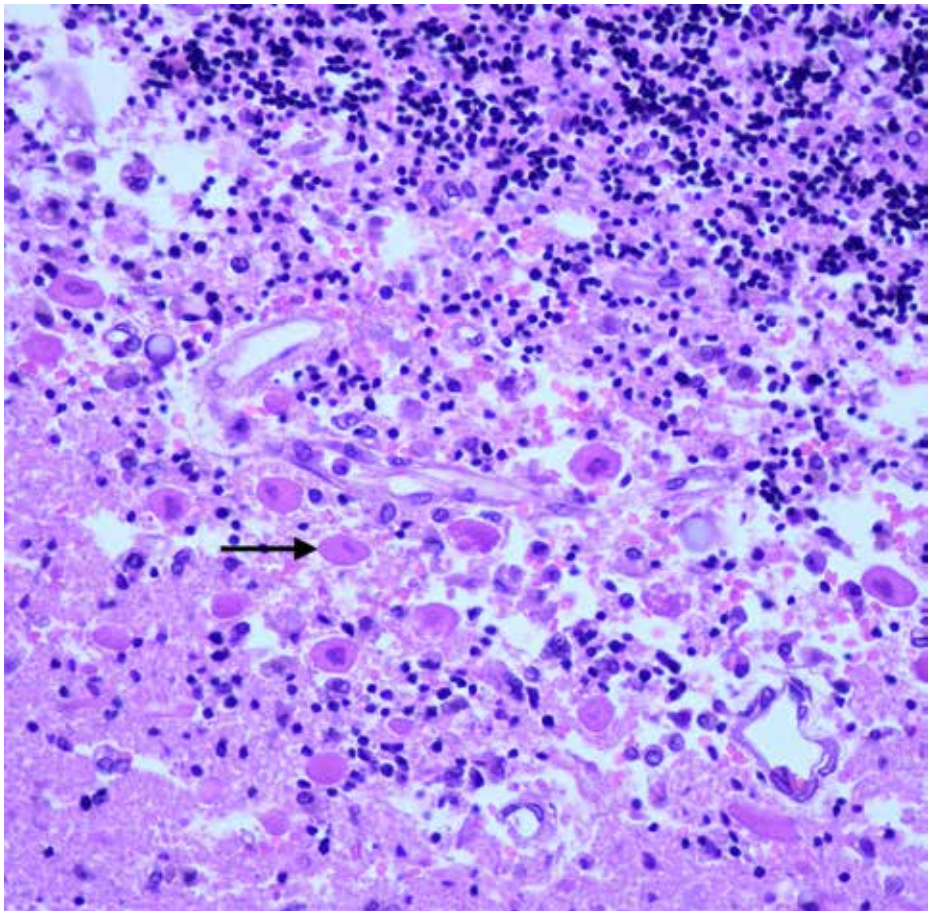

Figure 10.23
Acute hypoxic-ischemic
changes in the cerebellum,
(H&E, x400).
In the microscopic view,
significant vacuolization
in the area adjacent to
the granular layer in the
cerebellum, a significant
decrease in the number of
Purkinje cells, a pyknotic
appearance in the Purkinje
cell nuclei, and an increase
in eosinophilia in their
cytoplasm
(arrow)
are observed. Acute
hypoxic-ischemic changes
in the cerebellum involve
cellular and tissue damage
resulting from inadequate
oxygen and blood flow.
Microscopically, findings
such as red neurons,
reactive astrogliosis and
microglial activation are
seen.

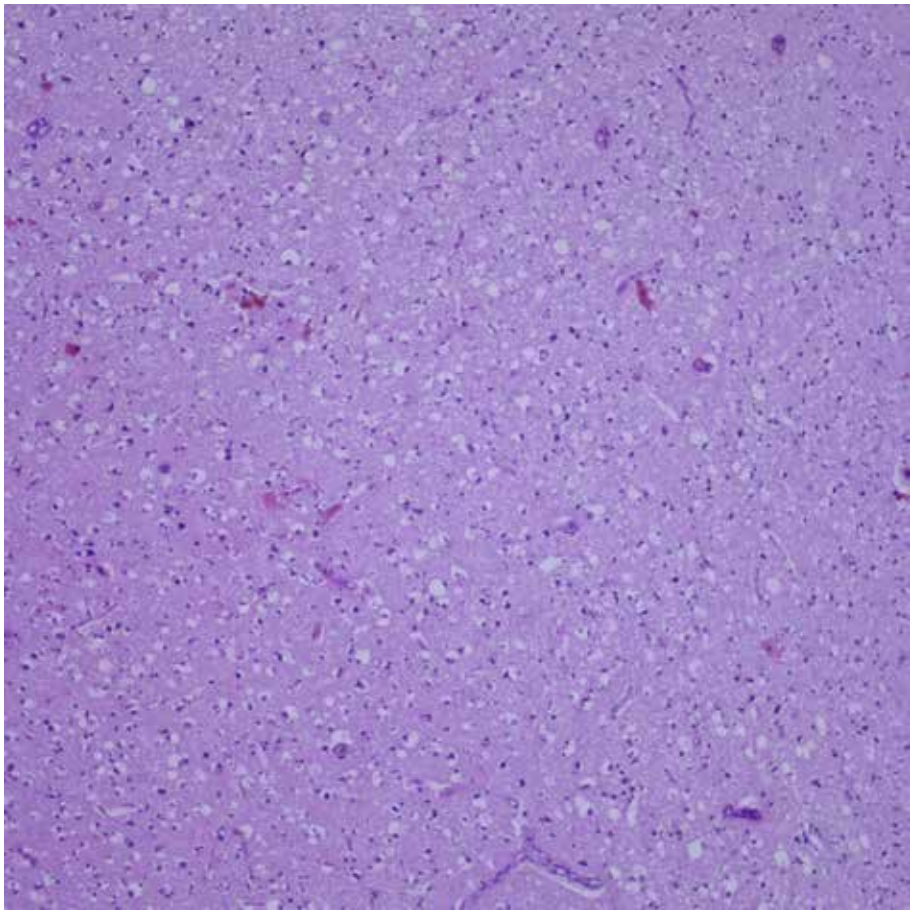

Figure 10.24
Brain acute-hypoxic ischemic changes, (H&E, x100). Vacuolization occurs as a result of cellular damage and edema. Due to lack of oxygen and energy, the integrity of the cellular membrane is disrupted, which causes intracellular fluids to leak out and create spaces (vacuoles) between cells. Additionally, in hypoxic conditions, cell damage and vacuolization occur as a result of the activation of lysosomal enzymes. Microscopically, cellular vacuolization is detected as small, round spaces (vacuoles) in cells, especially in neurons. In the microscopic view, the cells have a vacuolar appearance.

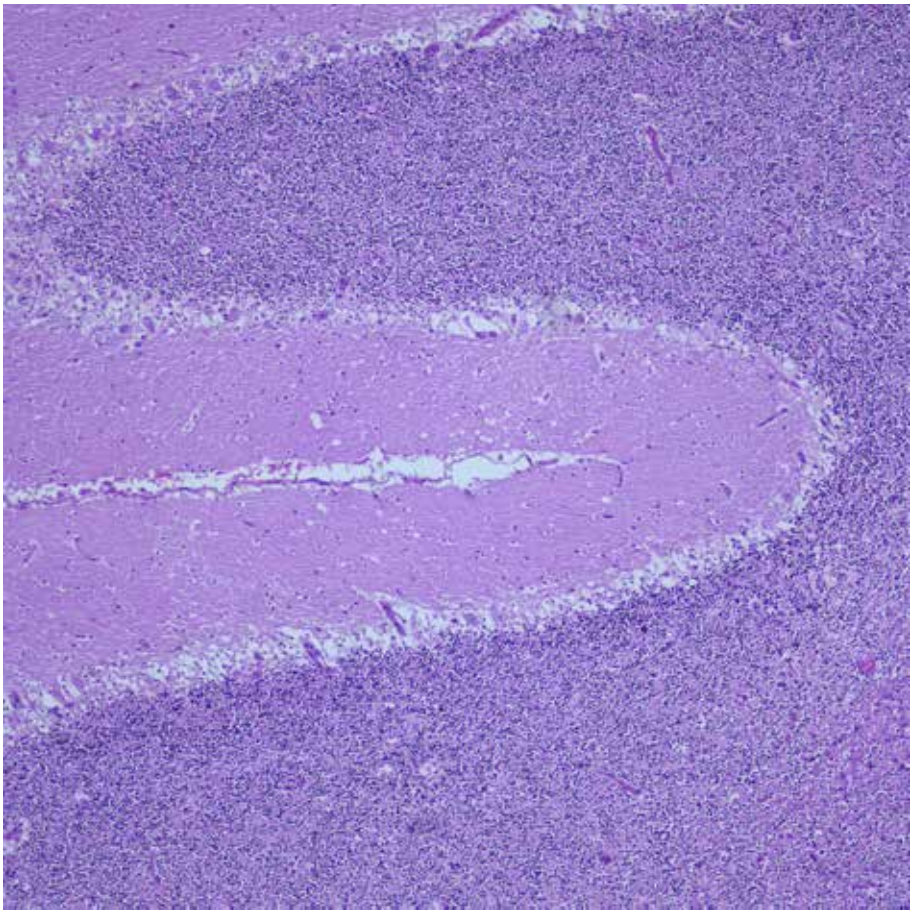

Figure 10.25
Acute-hypoxic ischemic changes in the cerebellum, (H&E, x100). In the microscopic view, significant vacuolization in the area adjacent to the granular layer in the cerebellum, a significant decrease in the number of Purkinje cells are observed.

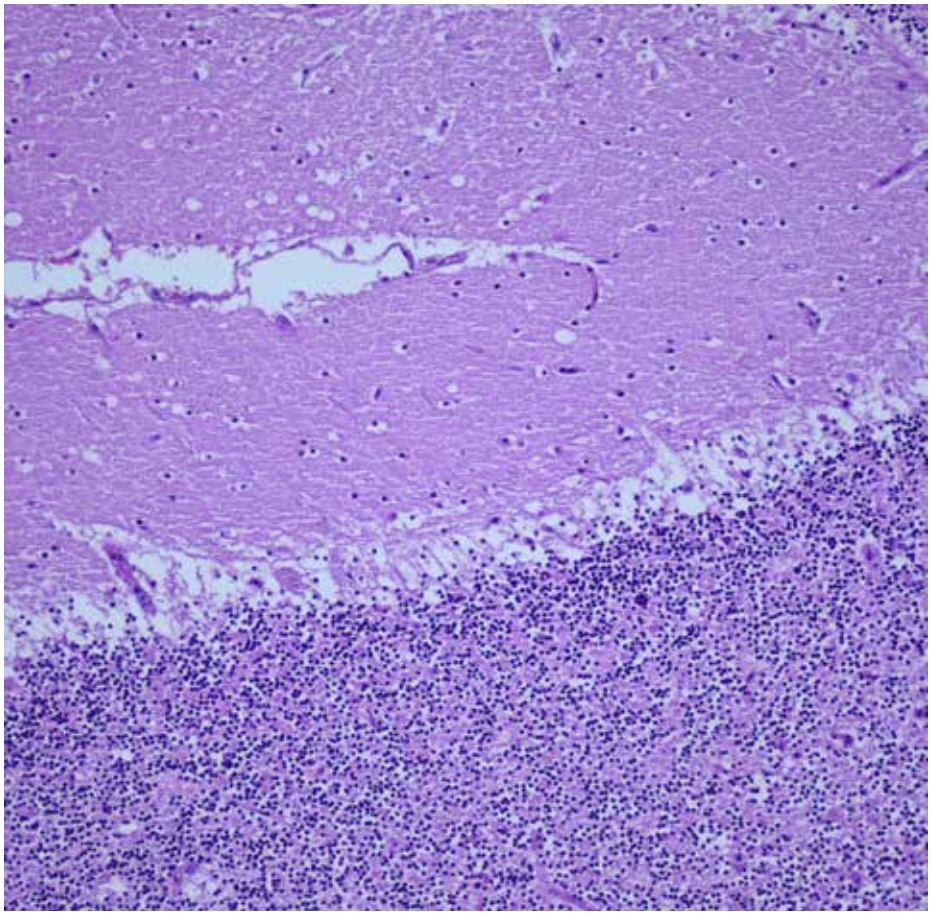

Figure 10.26
Cerebellum acute-hypoxic ischemic changes, (H&E, x200). At higher magnification.

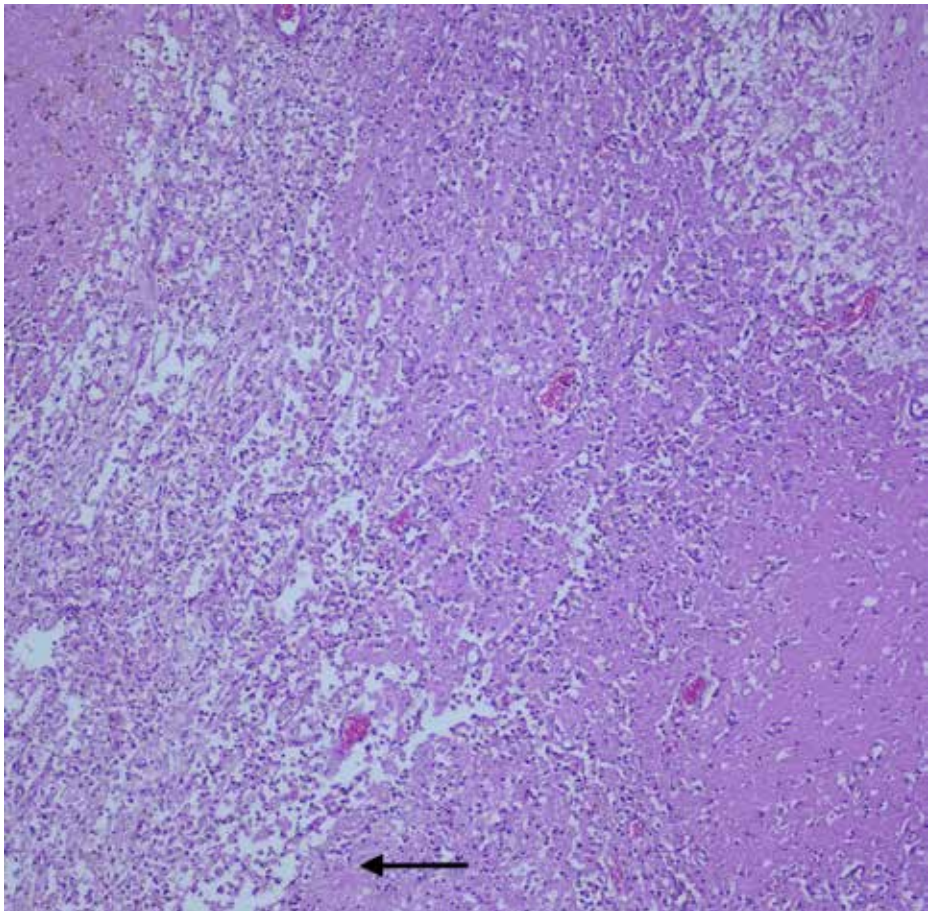

Figure 10.27
Brain subacute infarction, (H&E, x100). The microscopic view shows dense macrophage infiltration (arrow) in the parenchyma and neovascularization and reactive endothelial cells in the necrotic tissue. These findings are compatible with subacute period (5-14 days) brain infarction.

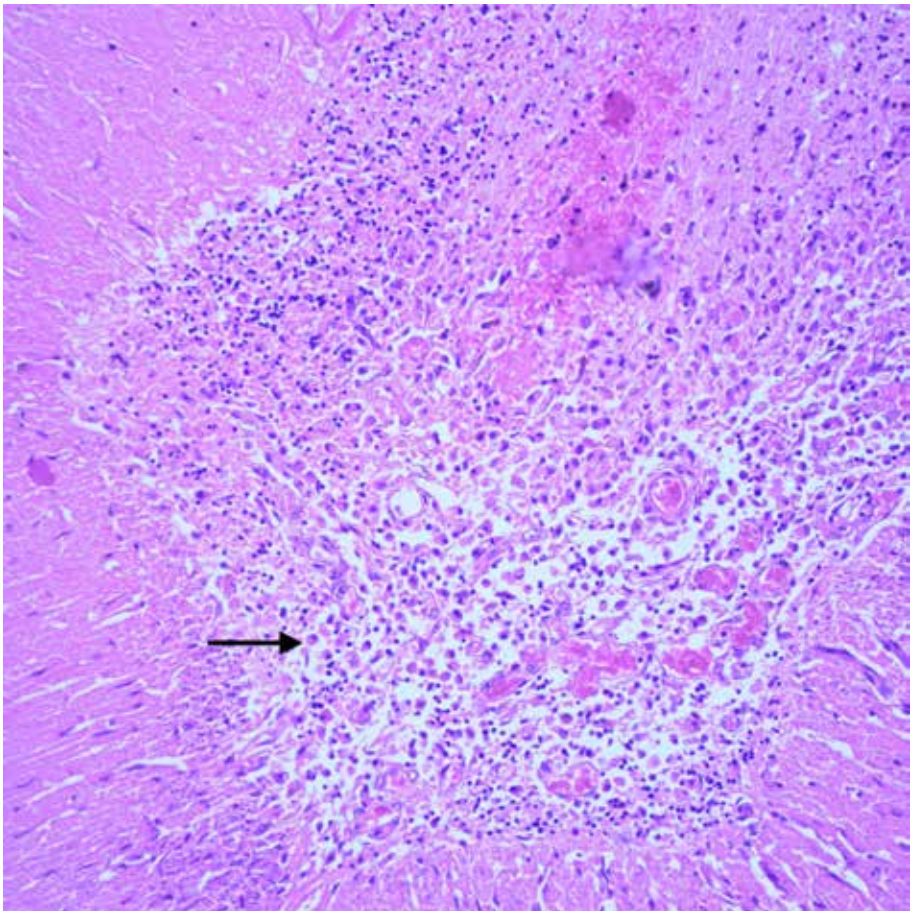

Figure 10.28
Cerebellum, subacute infarction, (H&E, x200). At higher magnification, dense macrophage infiltration (arrow) in the parenchyma of the cerebellum, loss of Purkinje cells, neovascularization and reactive endothelial cells in the necrotic tissue are seen.

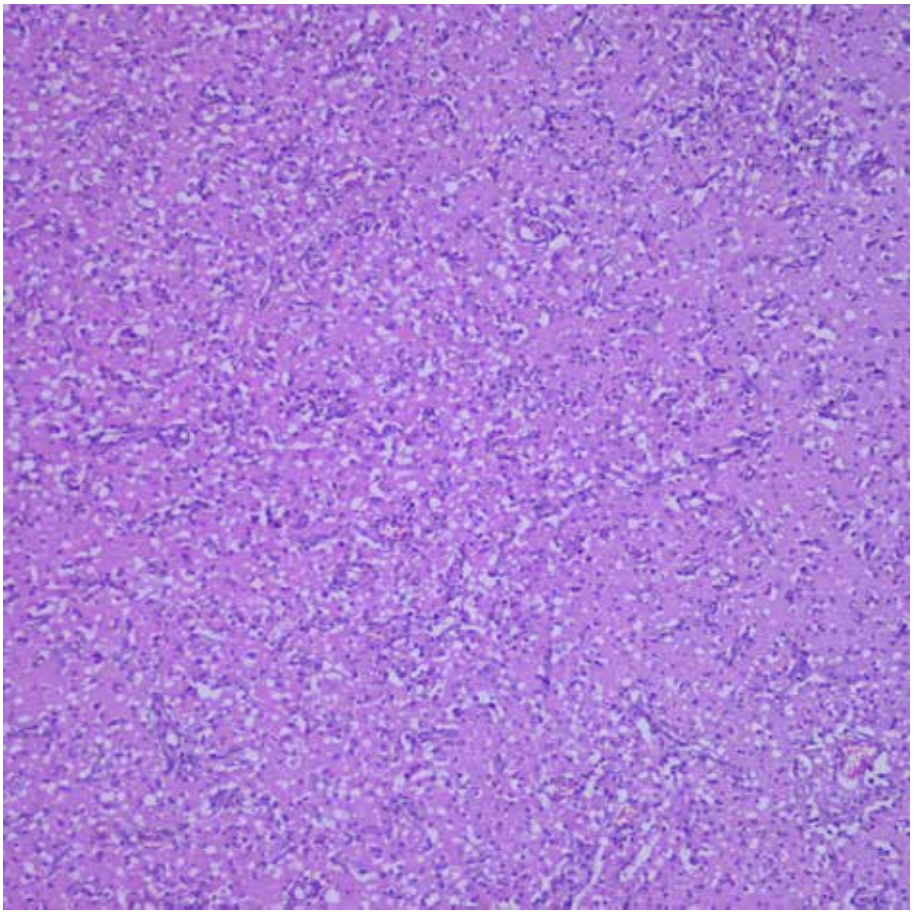

Figure 10.29
Brain, subacute infarction, (H&E, x100). Macrophages within the brain parenchyma, vascular proliferation and gliosis are observed.

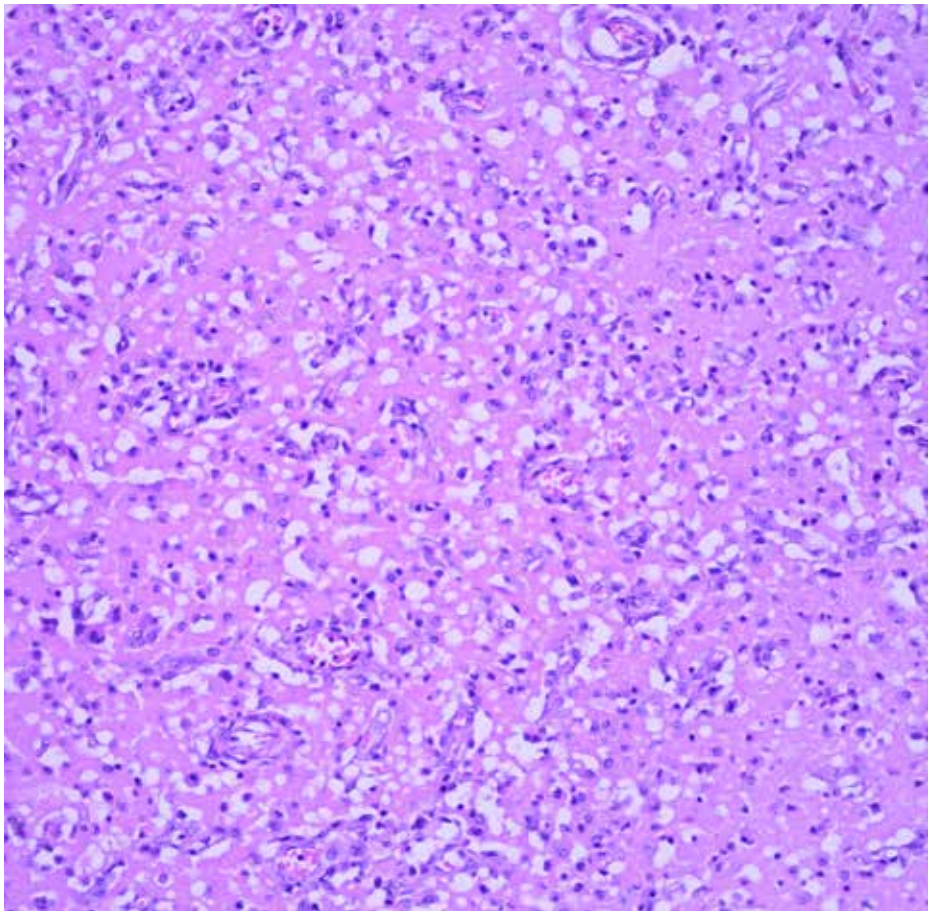

Figure 10.30
Brain, subacute infarction, (H&E, x200). At higher magnification.

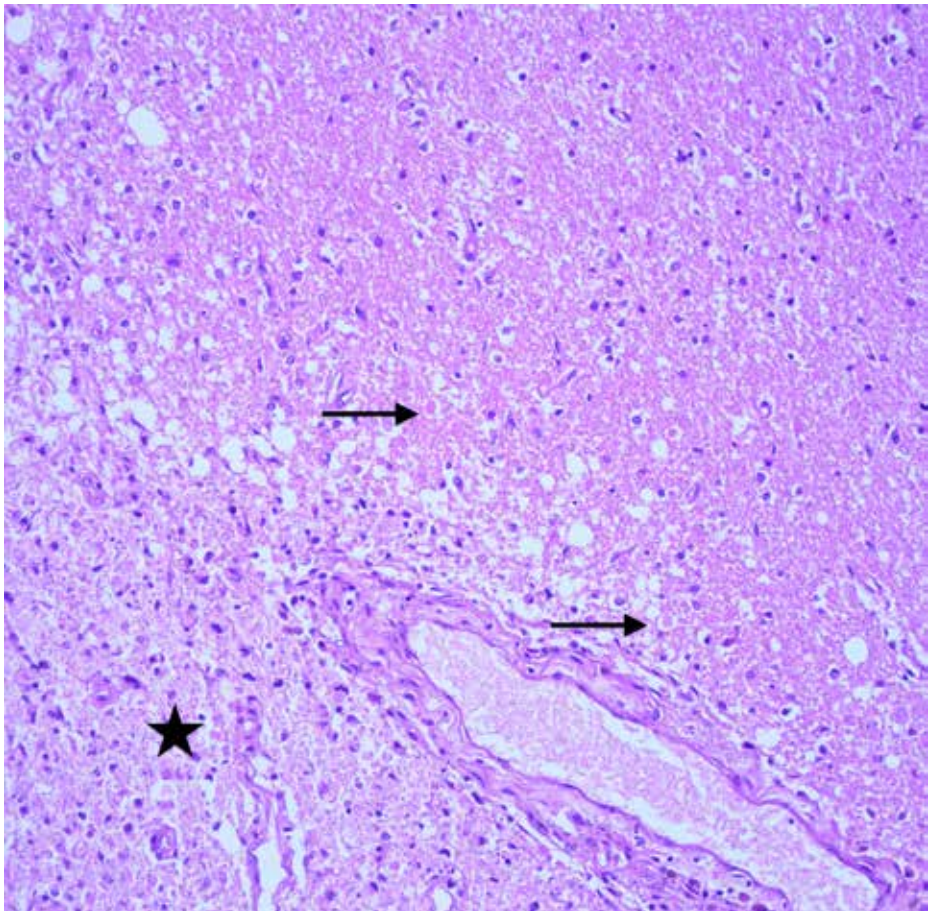

Figure 10.31
Cerebellum, subacute infarction and diffuse axonal damage, (H&E, x200). Round pinkish axonal bulbs (torpedo bodies) (arrows), which are introductory findings of diffuse axonal damage, are seen in the parenchyma adjacent to the subacute infarction (asterisk) where macrophages and increased numbers of vascular structures are observed. Diffuse axonal damage may occur due to brain trauma, especially traffic accidents, degenerative neurological diseases and ischemic conditions.

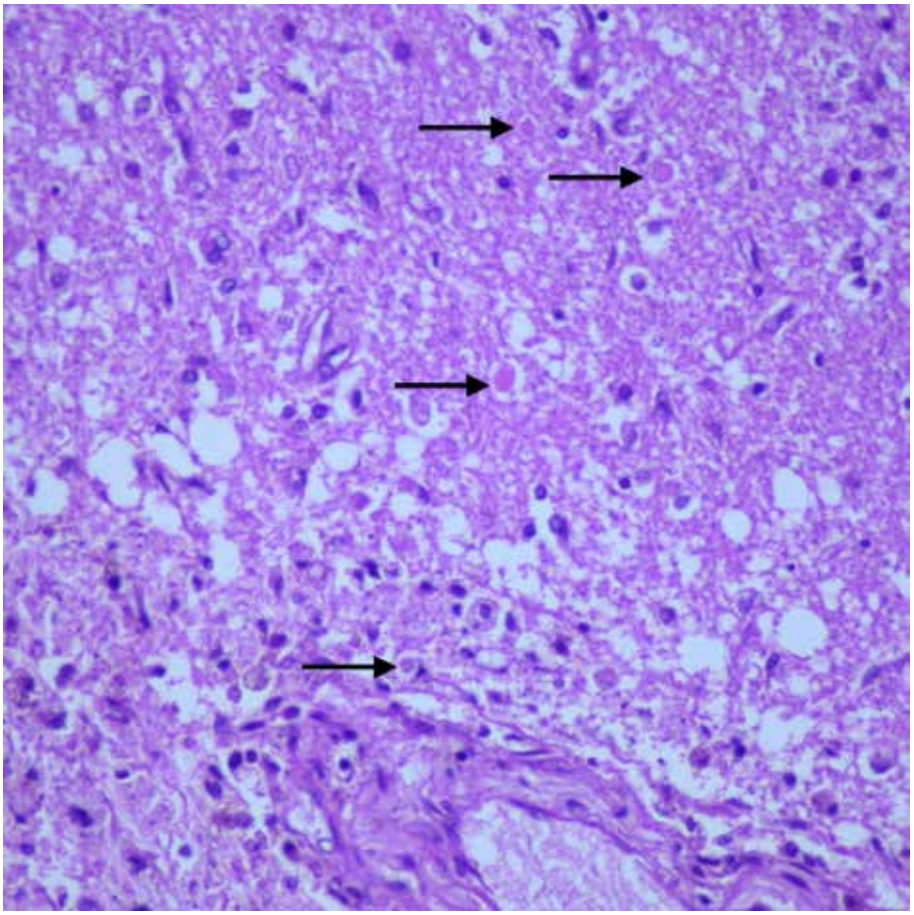

Figure 10.32
Cerebellum, subacute infarction and diffuse axonal damage, (H&E, x400). Axonal bulb (torpedo bodies) at higher magnification (arrows). Torpedo bodies are axonal swellings that develop due to trauma or ischemic damage. These structures can be detected with H&E staining approximately 1 day after incident. However, immunohistochemical staining can be done with ß-APP for earlier detection (2-3 hours). In such cases, findings of axonal damage can be seen most frequently in tissue samples taken from the corpus callosum, brain stem, cerebellum, parasagittal white matter and basal ganglia.

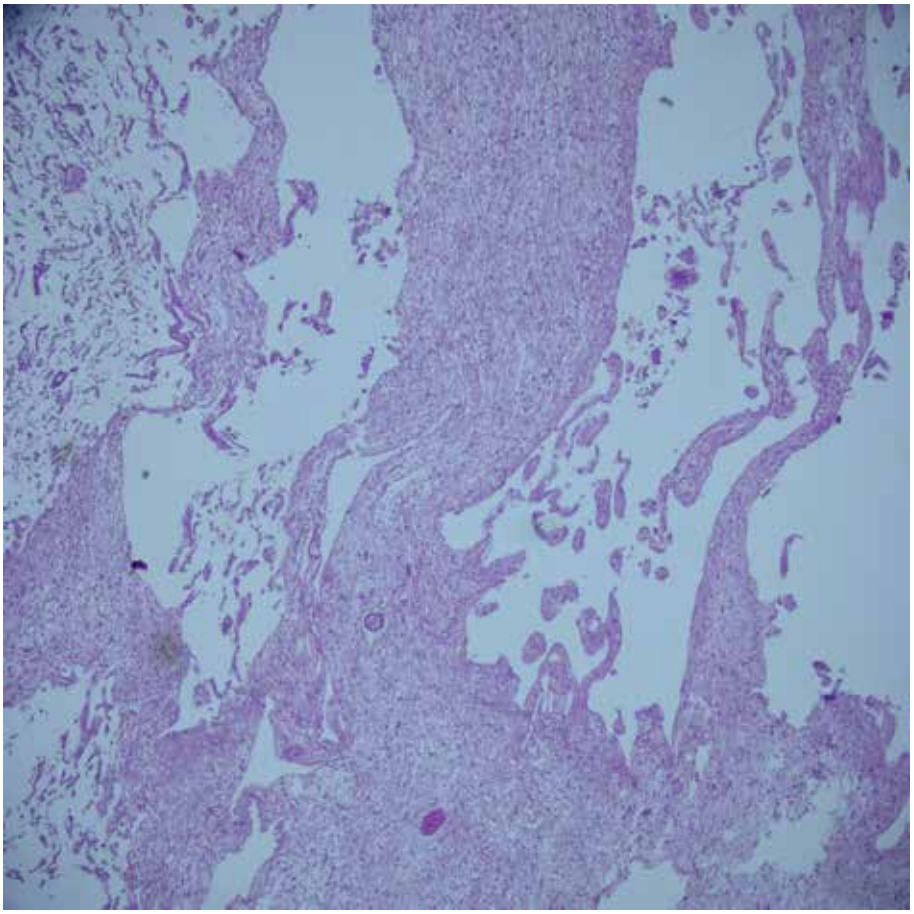

Figure 10.33
Brain infarction, chronic, (H&E, x40). In the microscopic view, loss of parenchyma as a result of glial fibrosis and cavitation is seen. The cells most sensitive to hypoxia in the central nervous system are pyramidal cells of the Sommer sector (CA1 region), Purkinje cells of the cerebellar cortex, and cortical III, V, VI neurons. As a result of chronic (late) stage infarction, astrocyte proliferation and glial scar development, cavitation as a result of clearing of necrotic tissue, glial and fibroblastic tissue proliferation and microglial proliferation are detected.

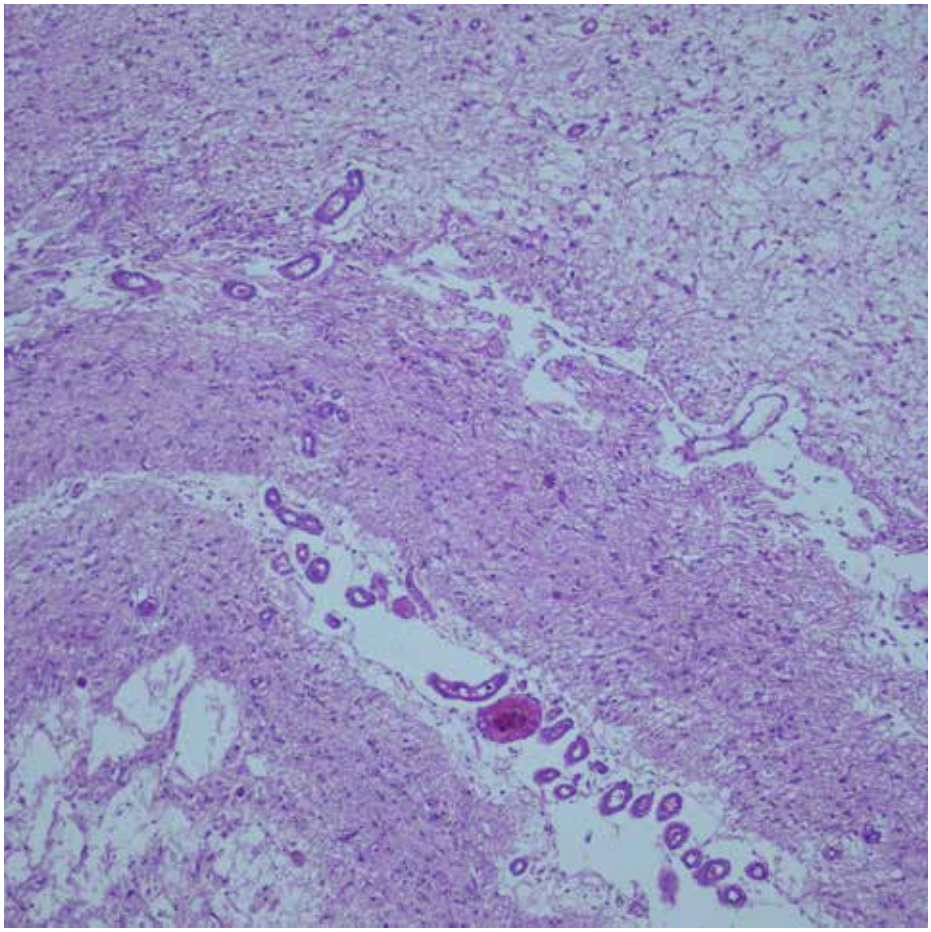

Figure 10.34
Brain infarction, chronic,
(H&E, x100).
In the microscopic view, astrocyte proliferation and glial scar development, cavitation as a result of the clearance of necrotic tissue, glial and fibroblastic tissue proliferation and microglial proliferation are seen.

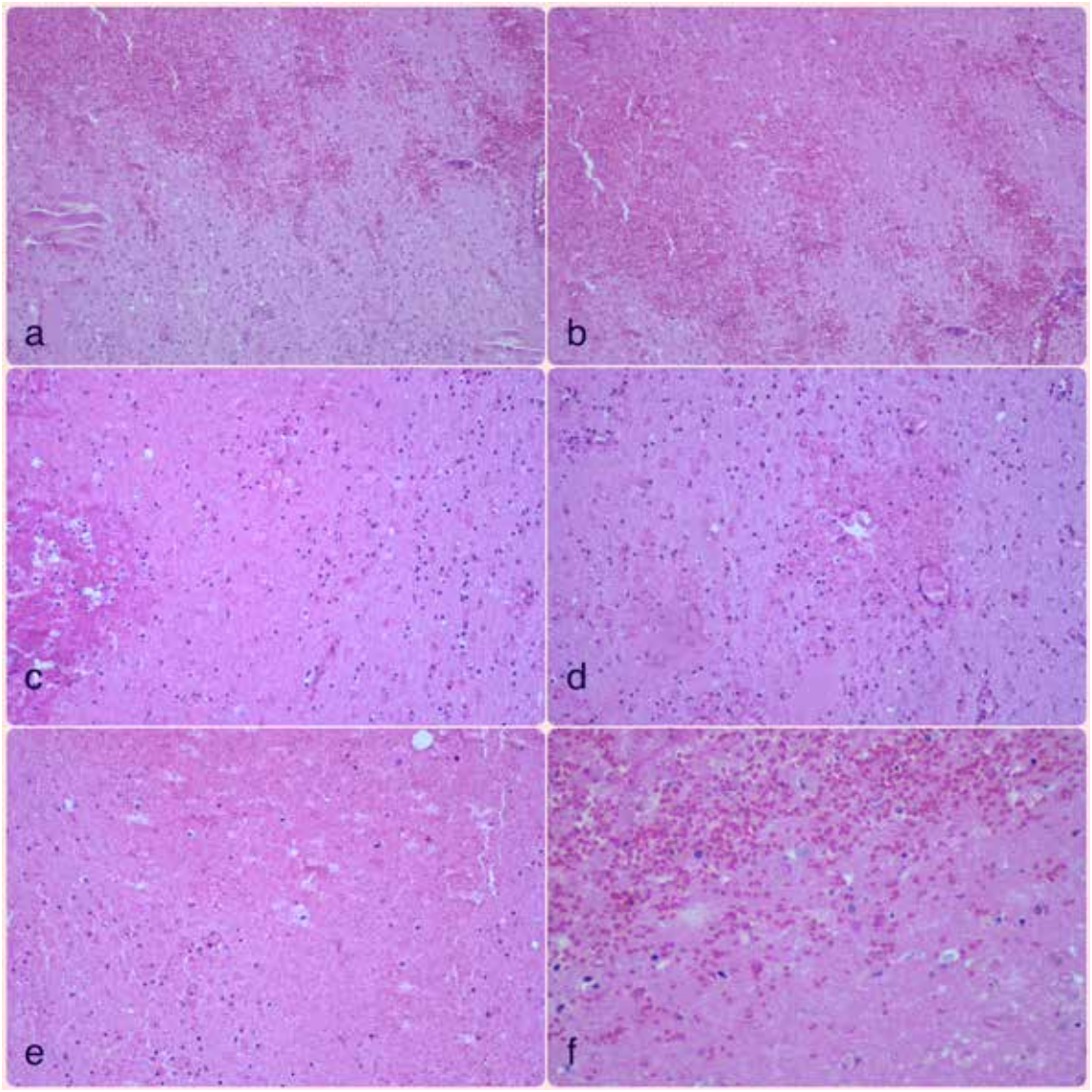

Figure 10.35
Methanol intoxication,
a,b,c,d,e,f) (H&E, x100, x100, x200, x200, x200, x400).
60 years old decedant (25 days hospitalization) after methyl alcohol intoxication. In toxicologic analysis, formic acid and 21 mg/dl methanol were detected in the blood sample. The microscopic view shows hemorrhage and subacute infarction in the tissues sampled from the putamen of the brain.

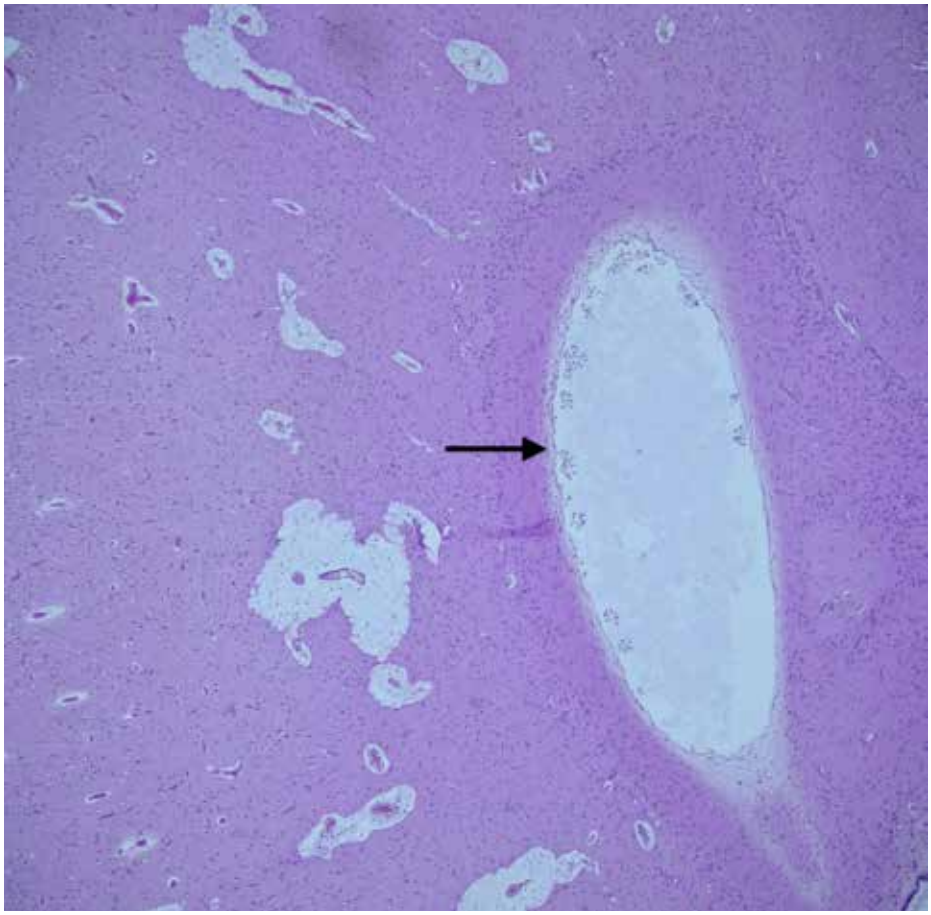

Figure 10.36
Cavitation and lacune formation after chronic brain infarction, (H&E, x40). Chronic period (late period) ischemic changes occur weeks, months, or years after acute ischemic events. Lacunar spaces (cavitation) (liquefaction necrosis) (arrow) are detected as a result of the clearance of necrotic tissue by macrophages.

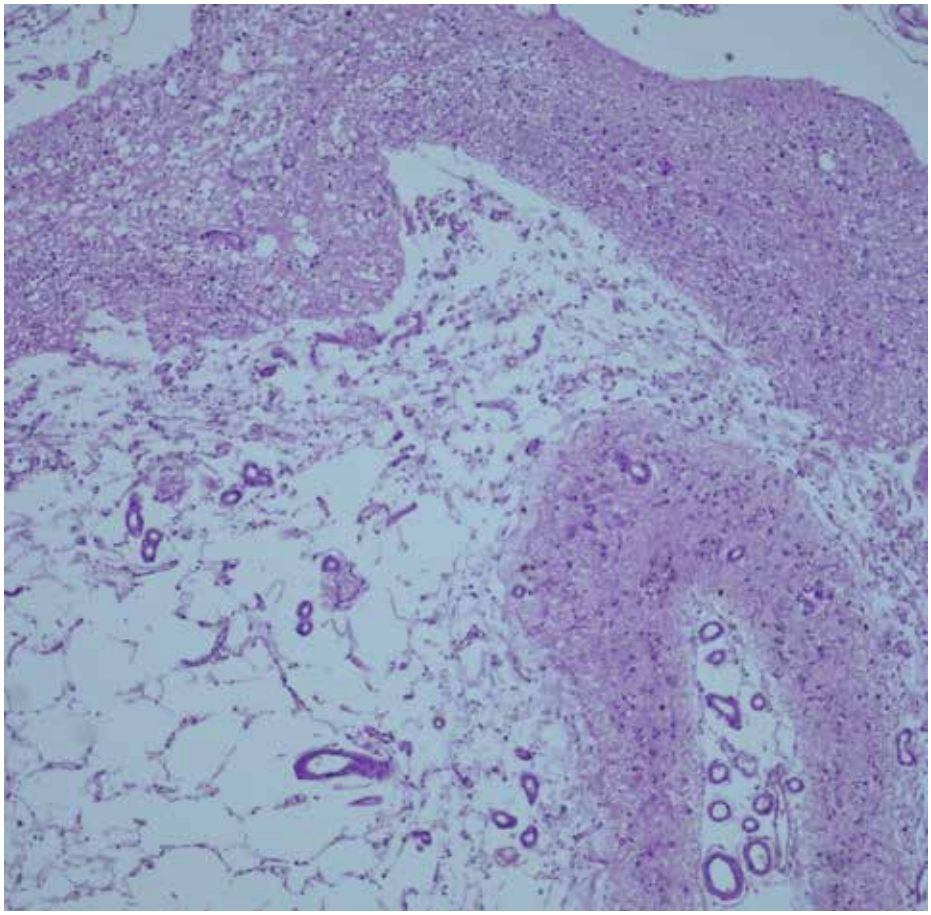

Figure 10.37
Brain infarction, chronic, (H&E, x100). At higher magnification, neuropil damage, gliosis, parenchyma loss and cavitation are seen in the brain.

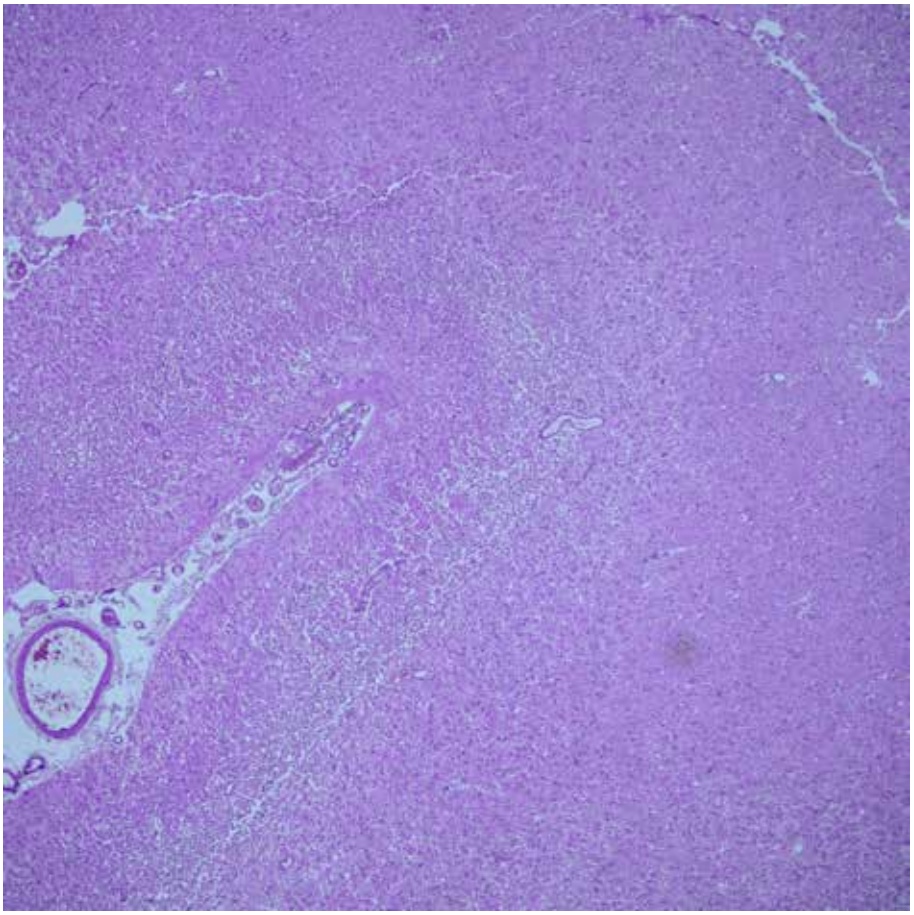

Figure 10.38 Cortical laminar necrosis (Cortical pseudolaminar necrosis) (H&E, x40). It is seen in cerebral hypoxic-ischemic injuries. Microscopically, gray matter is more susceptible to necrosis than white matter due to lack of oxygen. Cortical laminar necrosis is often indicative of severe and widespread brain damage.

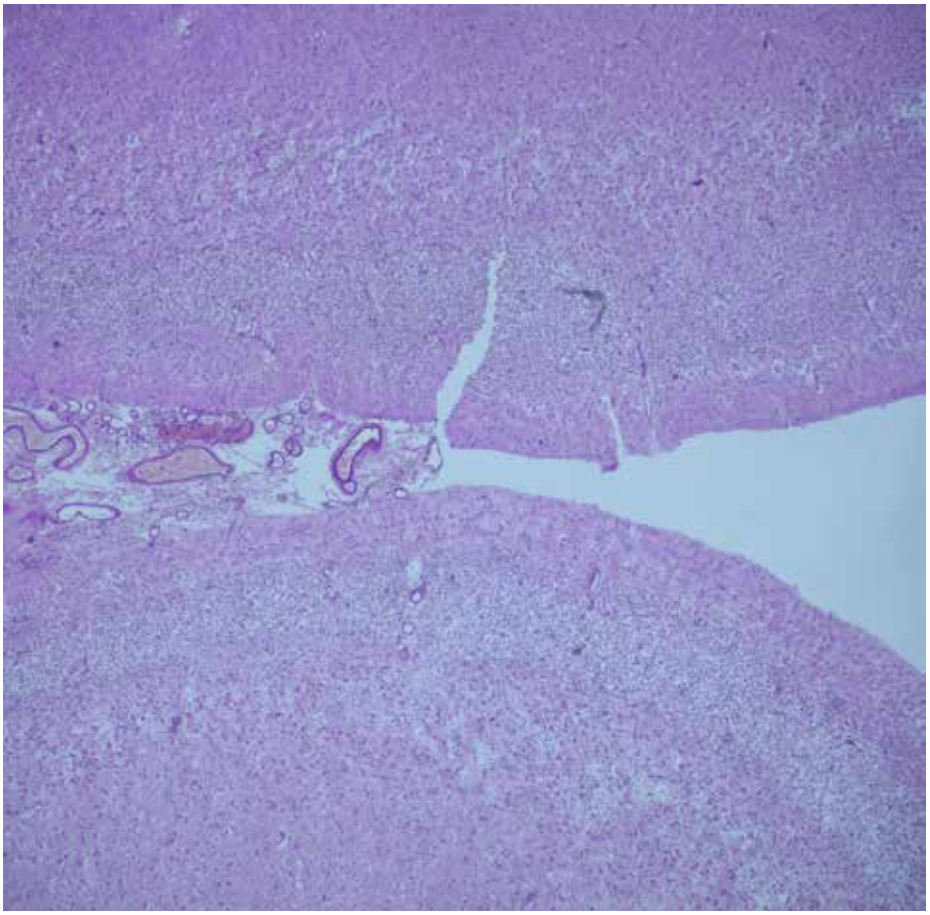

Figure 10.39 Cortical laminar necrosis (Cortical pseudolaminar necrosis), (H&E, x40). In the microscopic view, linear necrotic changes are observed in the cerebral cortical region.

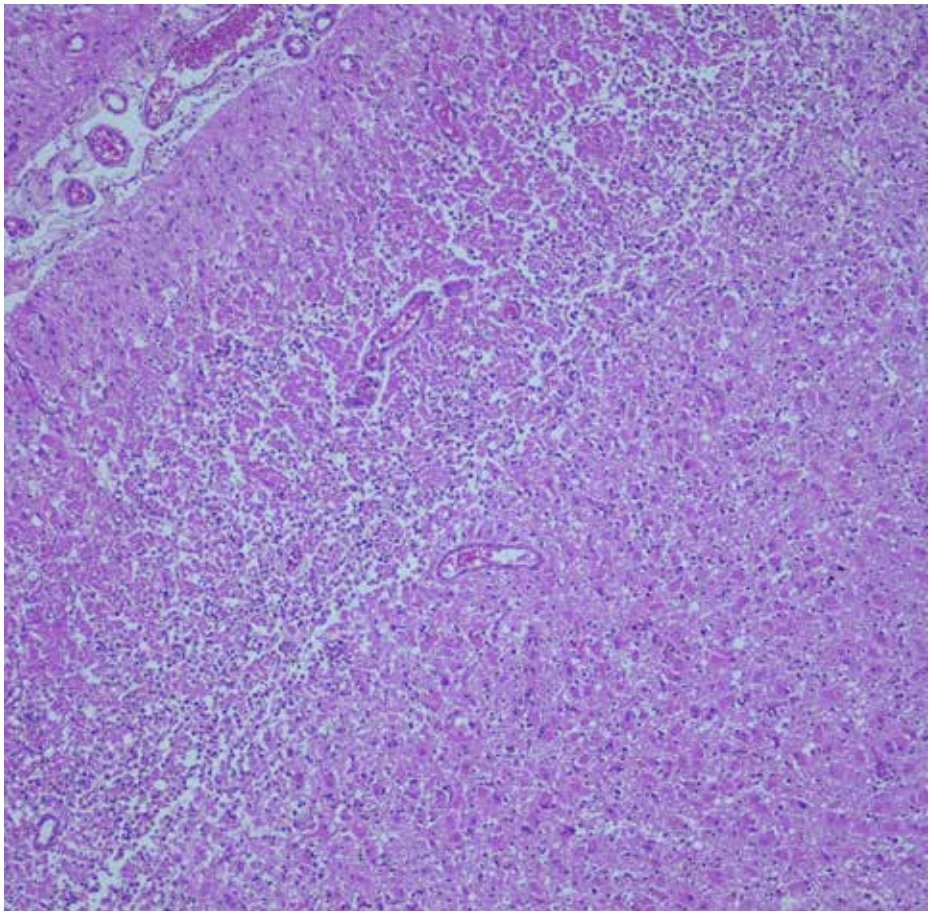

Figure 10.40
Cortical laminar necrosis (Cortical pseudolaminar necrosis), (H&E, x100).
At higher magnification, laminar necrosis is seen in the cortical region.

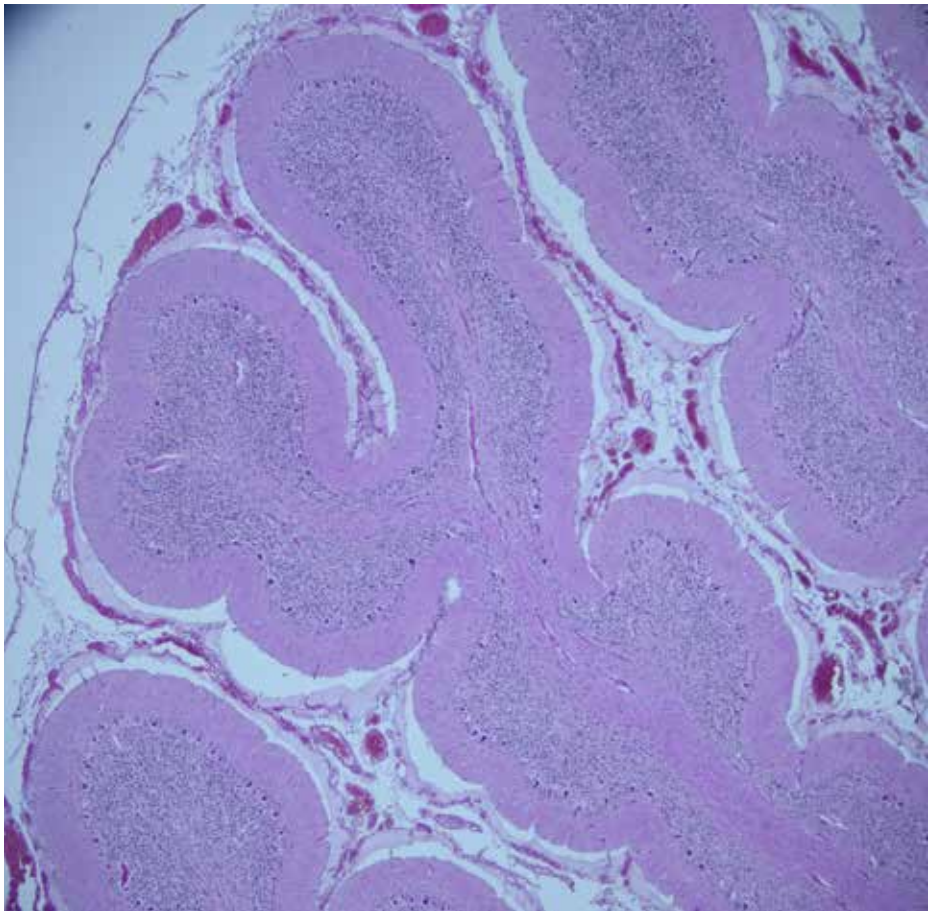

Figure 10.41
Cerebellar cortical degeneration, (H&E, x40).
Cerebellar cortical degeneration is a neurodegenerative disease characterized by neuronal loss and glial proliferation in the cortical structures of the cerebellum.
Marked loss of Purkinje cells, cytoplasmic swelling and eosinophilic changes in the remaining Purkinje cells, marked neuronal loss in the granular layer, and astrocyte proliferation are observed.
Purkinje cell loss and thinning of the granular layer are remarkable in the microscopic view.

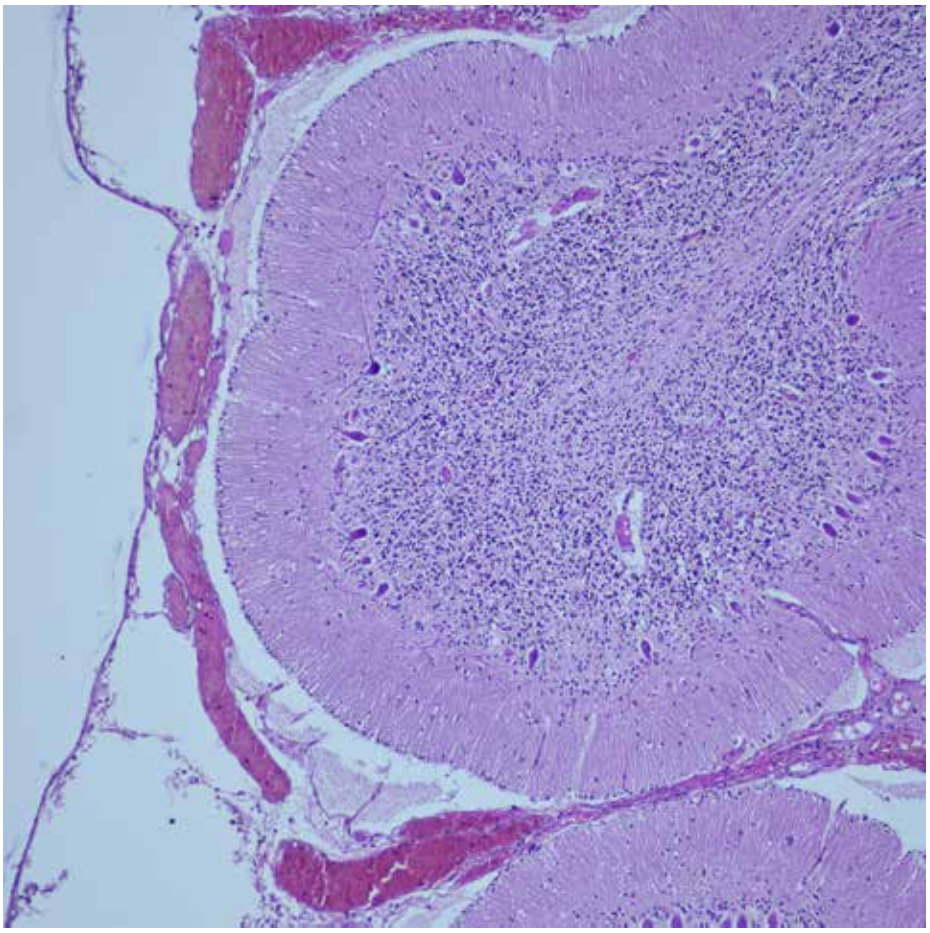

Figure 10.42 Cerebellar cortical degeneration, (H&E, x100). At higher magnification.

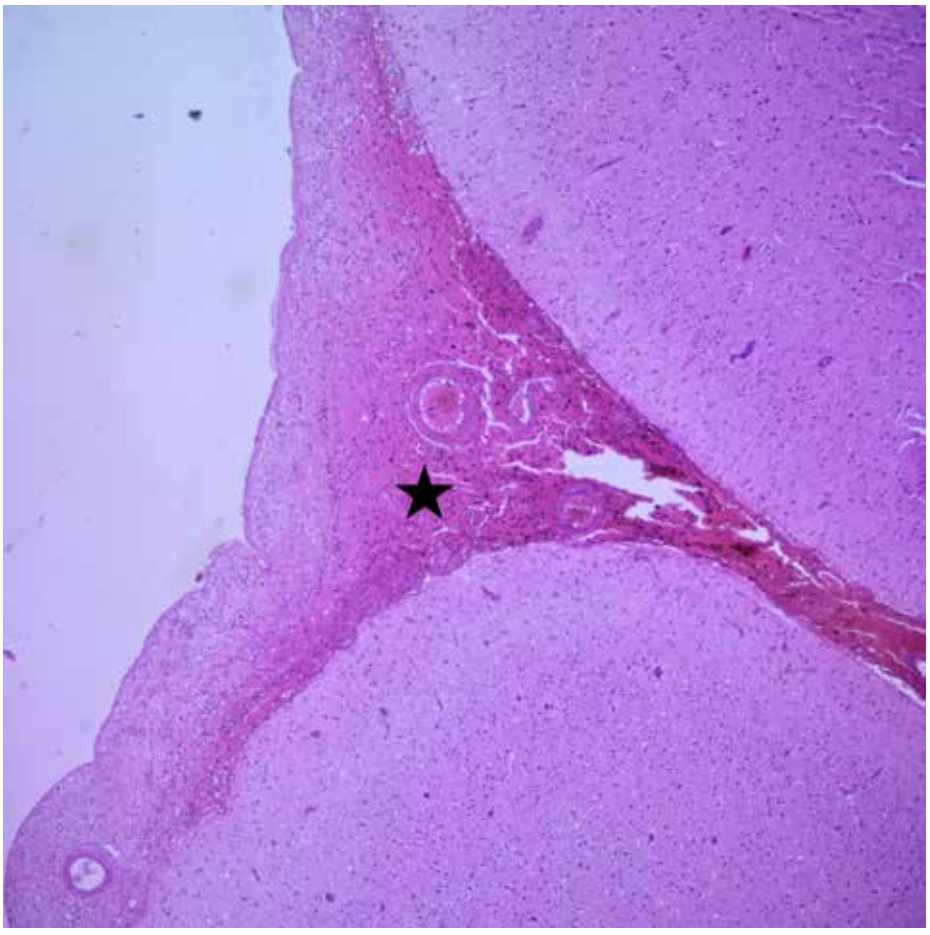

Figure 10.43 Subarachnoid hemorrhage, (H&E, x40). In the microscopic view, fresh extravasated erythrocytes are seen filling the subarachnoidal space (asterisk) and extending into the Wirchow-Robin space. Subarachnoid hemorrhage (SAH) is defined as extravasation of erytrocytes into the subarachnoid space as a result of rupture in the large arteries on the surface of the brain. It can often occur due to traumatic or non-traumatic (spontaneous) causes.

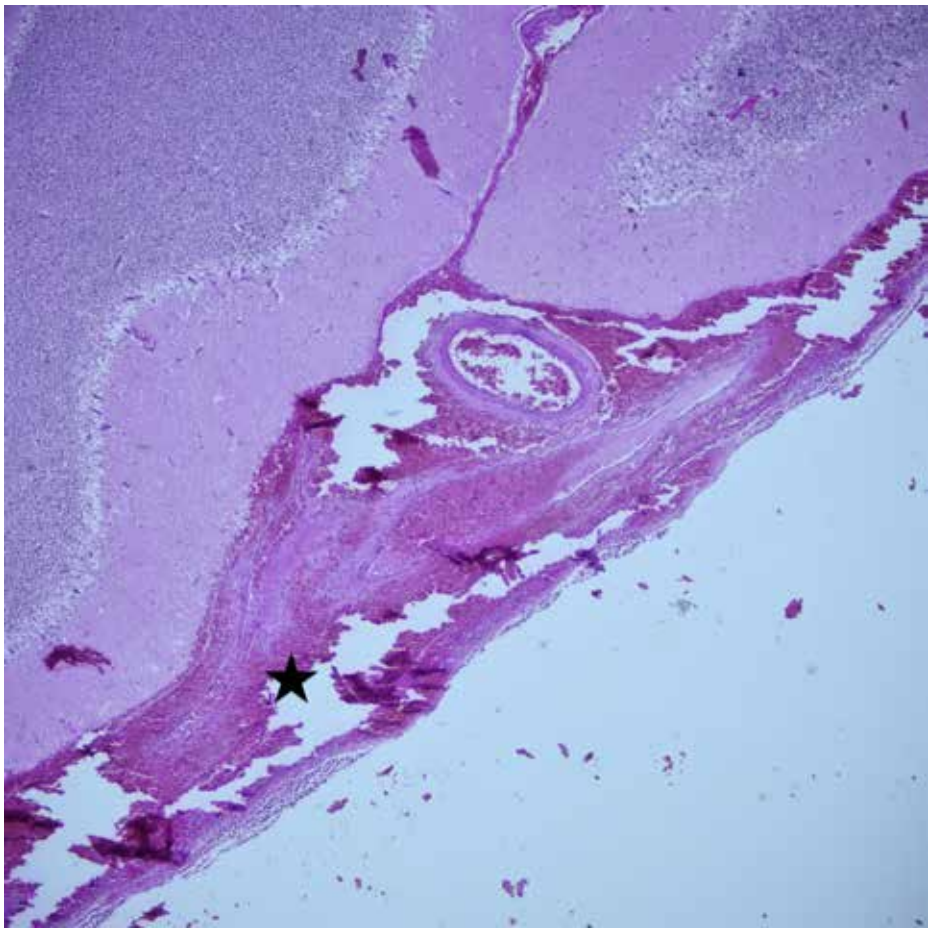

Figure 10.44
Subarachnoid hemorrhage, (H&E, x40). The microscopic view shows fresh extravasated erythrocytes filling the subarachnoid space (asterisk).

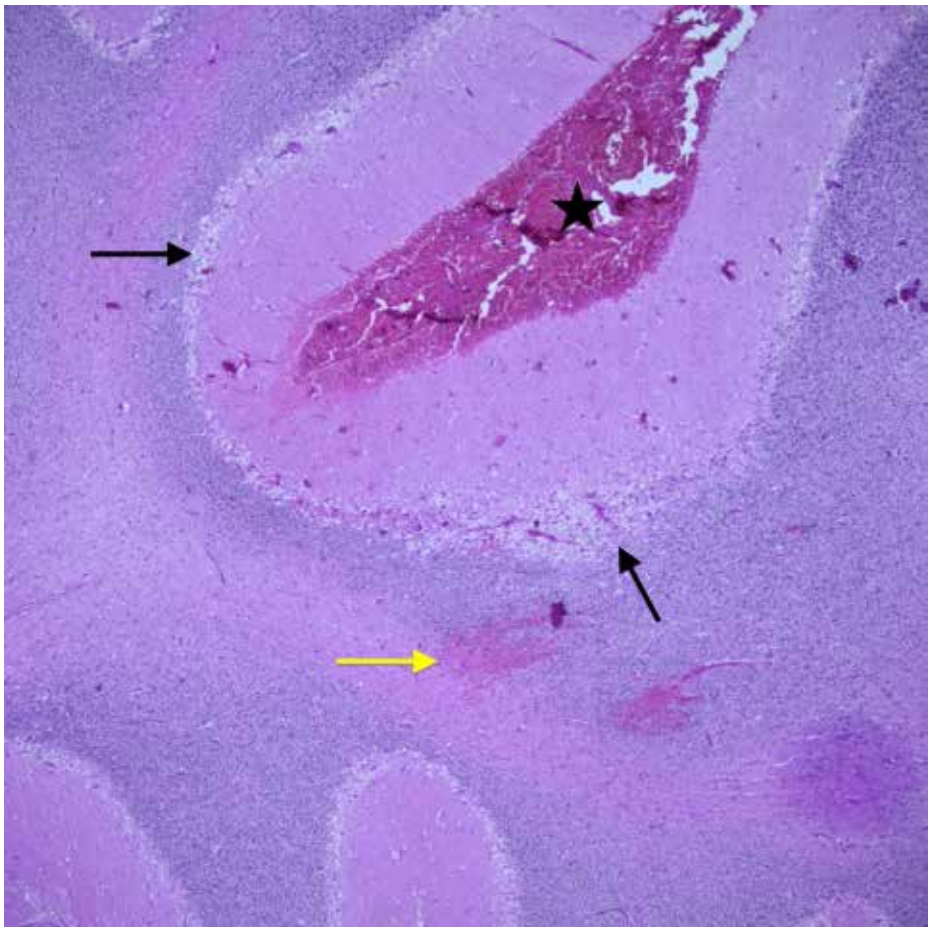

Figure 10.45
Subarachnoid hemorrhage, petechial hemorrhage in the parenchyma, acute hypoxic-ischemic changes, (H&E, x40). The microscopic view shows hemorrhage in the subarachnoid space (asterisk), small-scale hemorrhage areas in the parenchyma (yellow arrow) and acute hypoxic-ischemic changes (black arrow).

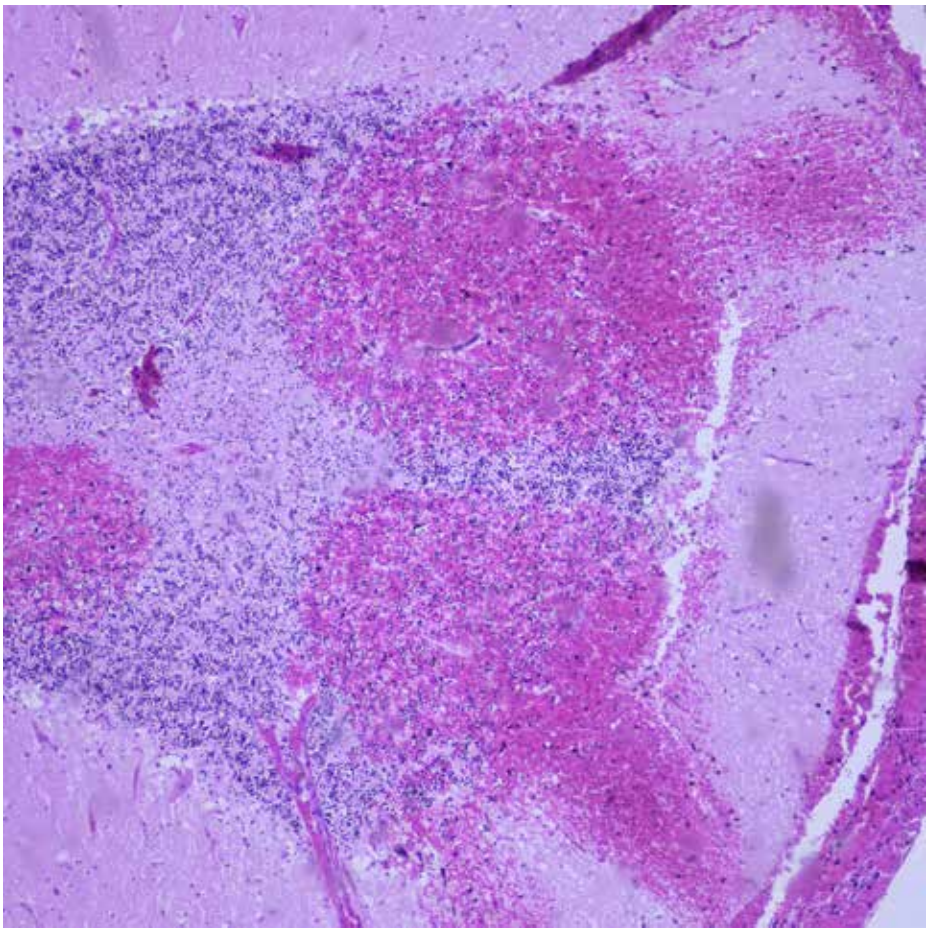

Figure 10.46 Cerebellum, contusion and hemorrhage in parenchyma, (H&E, x100). Contusions are characterized by localized hemorrhages, necrosis and edema in the brain as a result of head trauma. Diffuse erythrocyte extravasation is observed in the parenchyma in the acute period. In the microscopic view, areas of hemorrhage are seen in the cerebellar parenchyma.

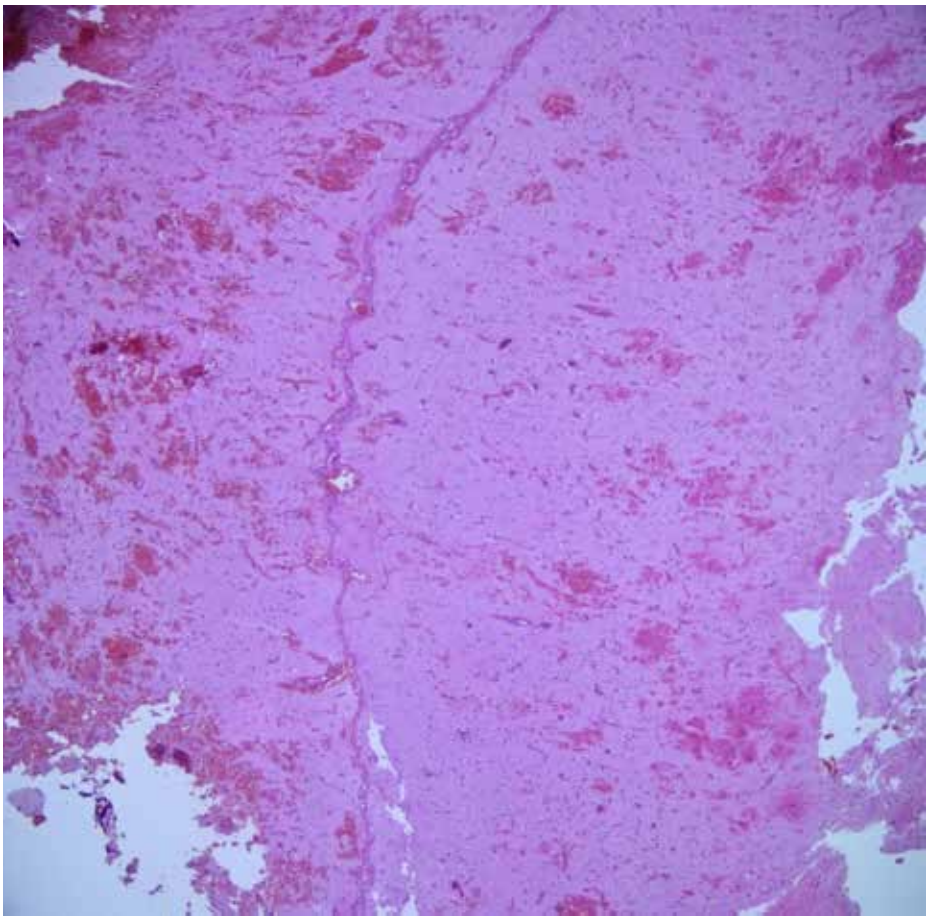

Figure 10.47 Brain contusion, (H&E, x40). The severity of contusions varies depending on their size and location. The microscopic view shows extensive areas of hemorrhage resulting from contusion within the brain parenchyma.

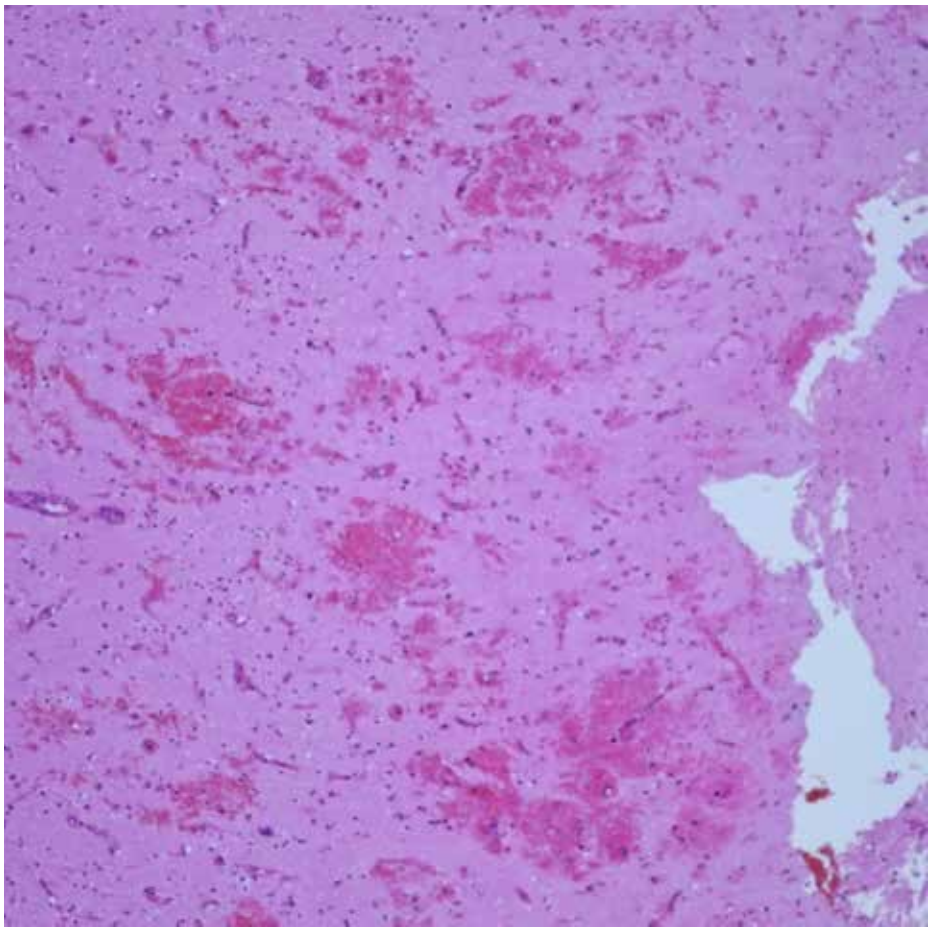

Figure 10.48
Brain contusion,
(H&E, x100).
At higher magnification areas of hemorrhage within the brain parenchyma.

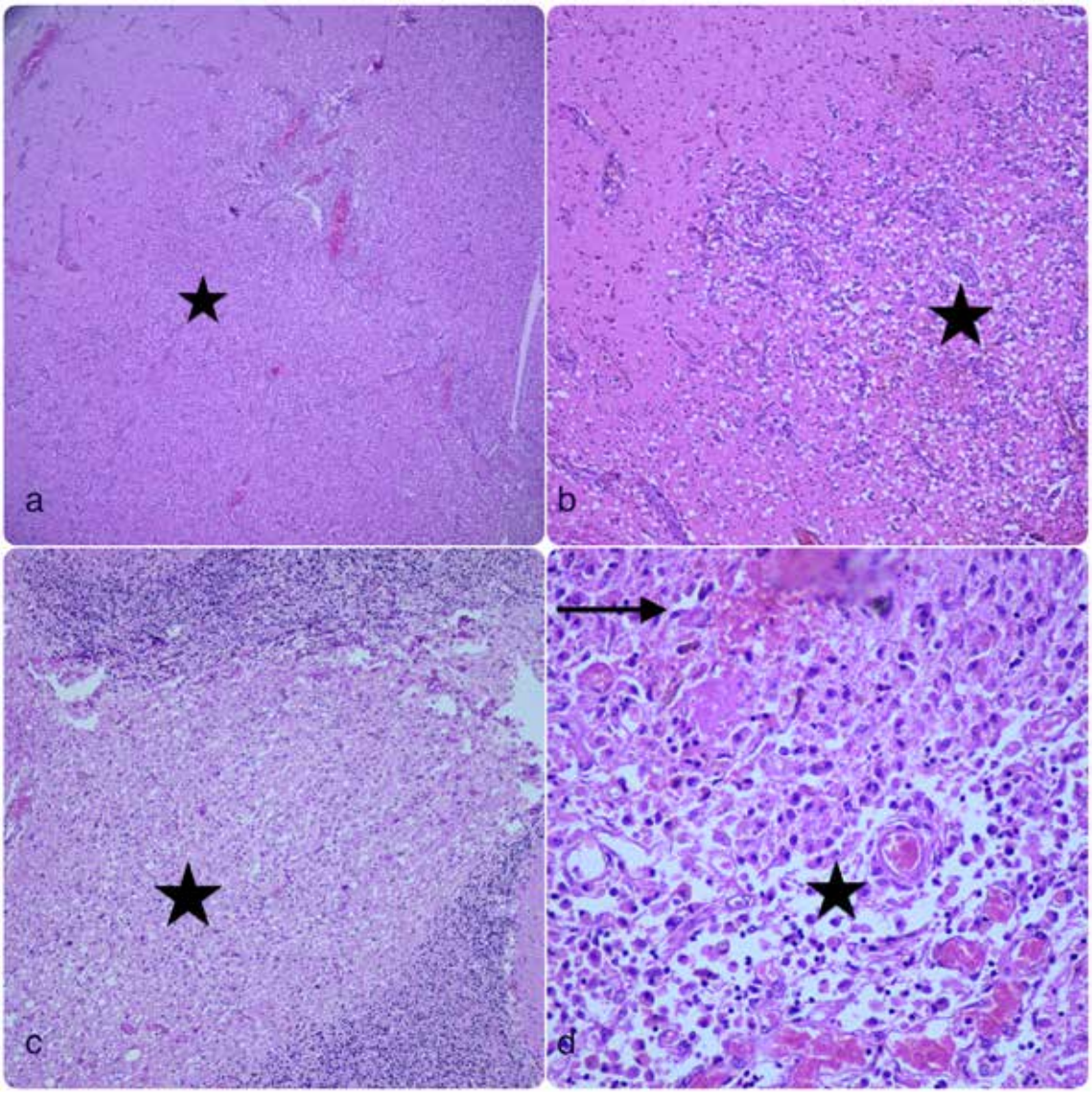

Figure 10.49
Subacute reparative changes around brain hemorrhage.
a) (H&E, x40). Subacute reperation around contusion includes histopathological changes that occur within a few days to a few weeks during the healing process of the trauma. During this period, brain tissue is in the process of repairing the damage. During the subacute period, macrophages (asterisk) migrate to the injury site to phagocytose necrotic tissue and blood cells. The formation of new capillaries (neoangiogenesis), astrocytic proliferation and gliosis are observed in the damage area.
b) (H&E, x100). At higher magnification subacute reperation (asterisk)
c) (H&E, x100). Subacute reparative changes in the cerebellum (asterisk).
d) (H&E, x400). Subacute reperation (asterisk) and adjacent petechial hemorrhage at higher magnification (arrow).

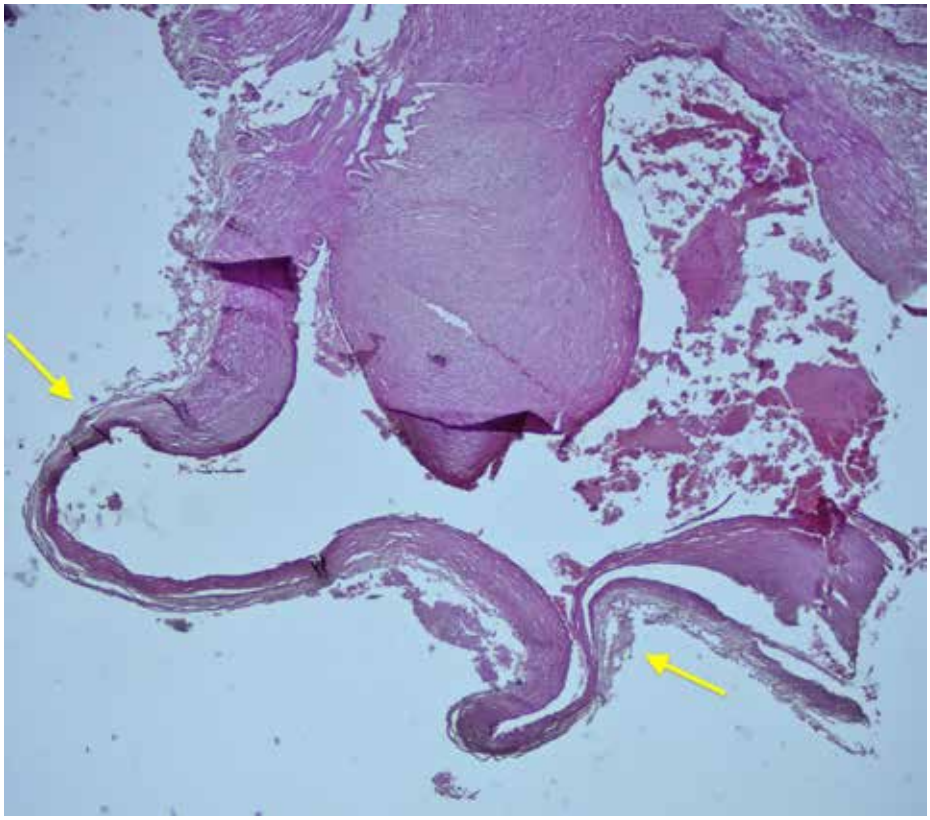

Figure 10.50
Saccular (berry) aneurysm,
(H&E, x40).
Saccular (berry) aneurysms are vascular lesions that occur as balloon-like swelling in a weak area of the blood vessels.
One of the most common causes of non-traumatic subarachnoidal hemorrhage in the brain is Berry aneurysm rupture. 90% of aneurysms occur near major arterial branch points in the anterior circulation.
In the microscopic view, in a case of aneurysm rupture, thinning and weakening of the media layer of the vessel wall
(arrows)
and loss of the elastic lamina are noteworthy.

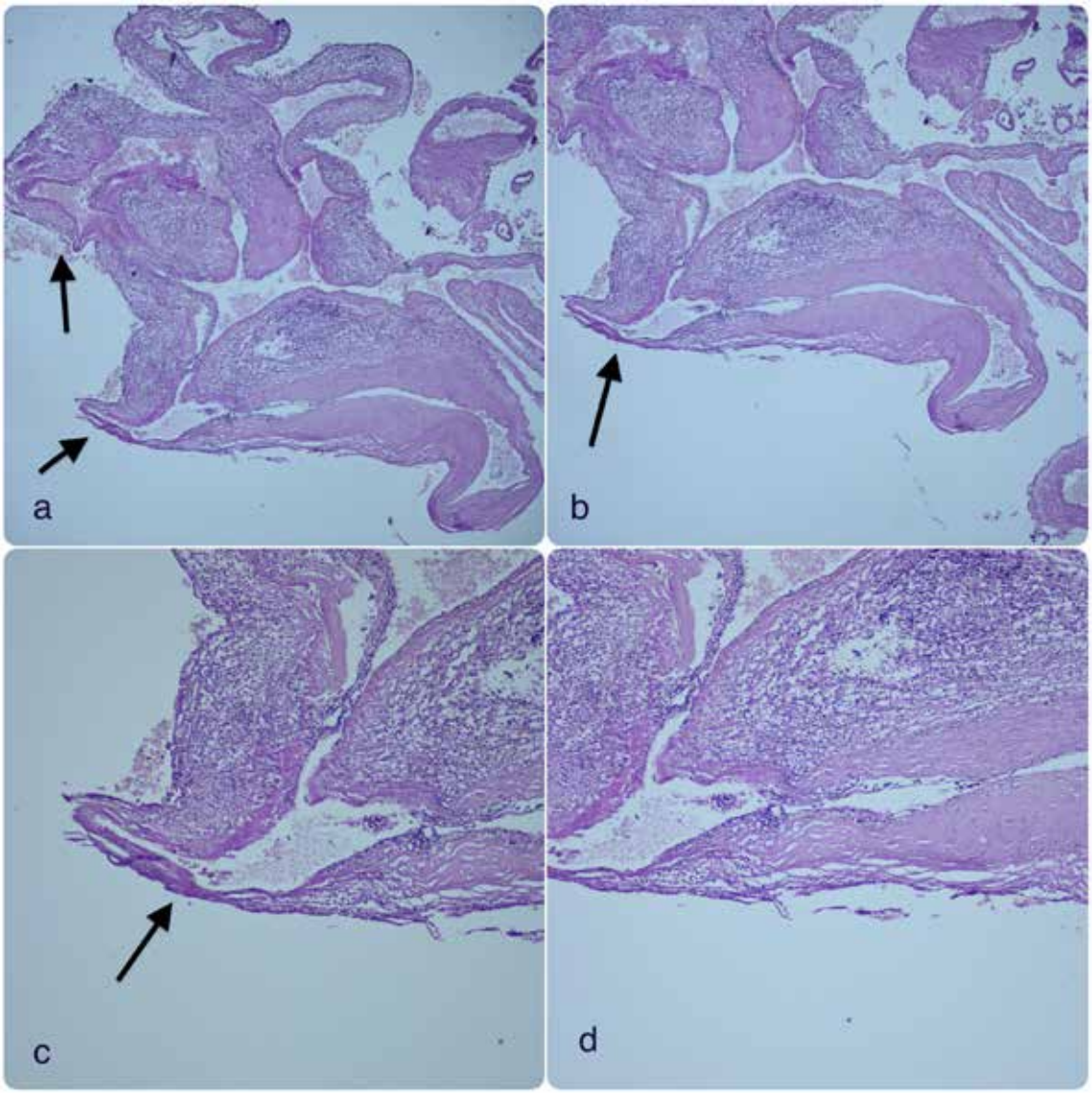

Figure 10.51
Weakening of the vessel wall and aneurysm formation due to vasculitis,
a) (H&E, x40). Vasculitis may cause weakening of the vessel wall and subsequently cause the development of aneurysm. This type of aneurysms often occurs in small and medium-sized arteries and squela varies depending on the severity and location of the vasculitis. The microscopic view shows vasculitis and thinning of the vascular wall, weakening (arrow) and aneurysm development.
b) (H&E, x40). In the microscopic view, the arrow shows the part where the vessel wall becomes extremely thin and loses its strength.
c,d) (H&E, x100). Thinning of the vessel wall at higher magnification (arrow).

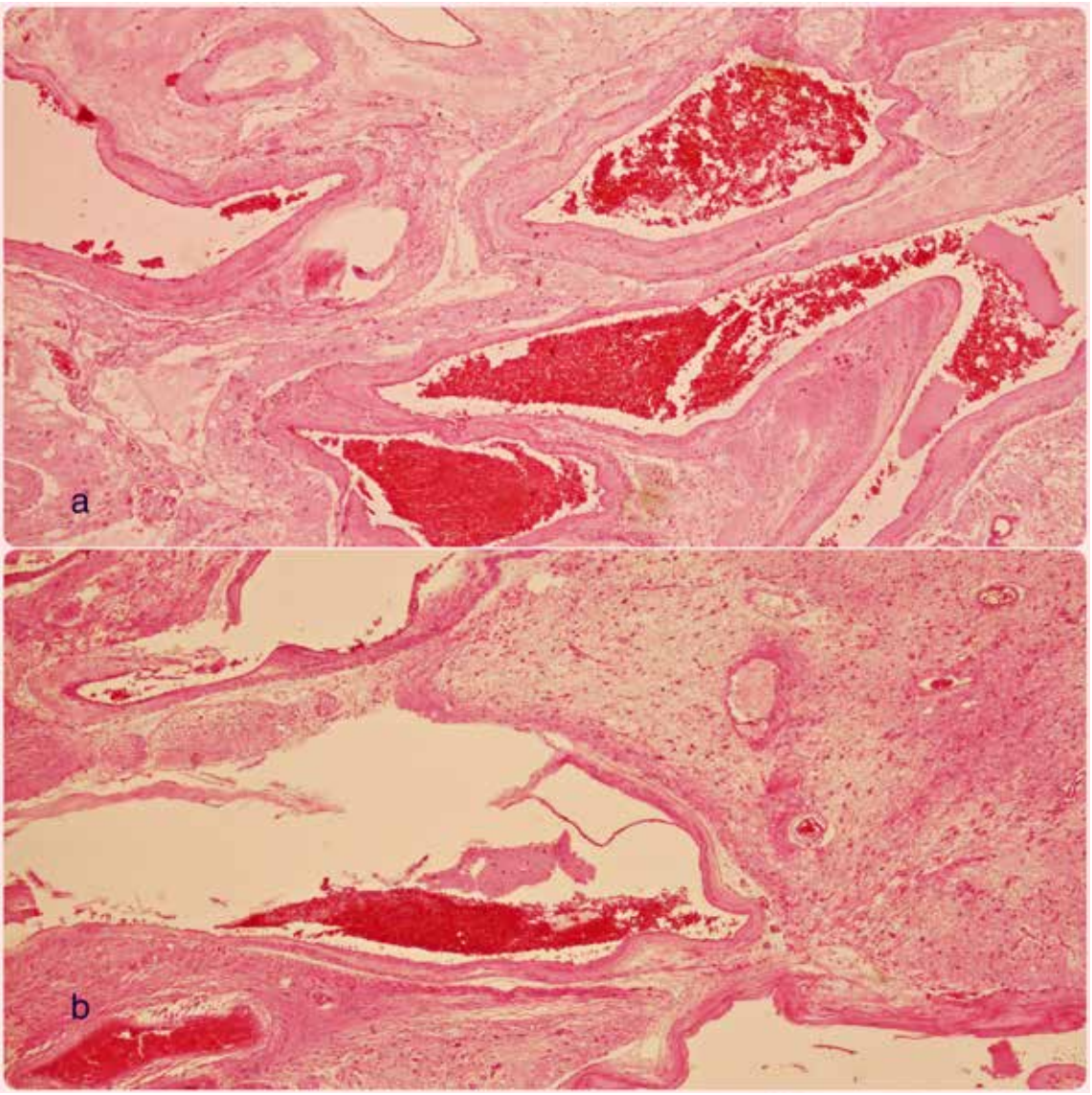

Figure 10.52
Arteriovenous malformation (AVM).
a,b) (H&E, x100). The microscopic views show dilated blood vessels separated by gliotic tissue. While some vessels are arteries others are venous type.
Arteriovenous malformation, which is a relatively less common cause of non-traumatic subarachnoidal hemorrhage in the 10-30 age group, involves the vessels originating from the subarachnoid space and extending towards the brain parenchyma or is only within the brain. Macroscopically, it is in the form of vascular channels that form a complex network.

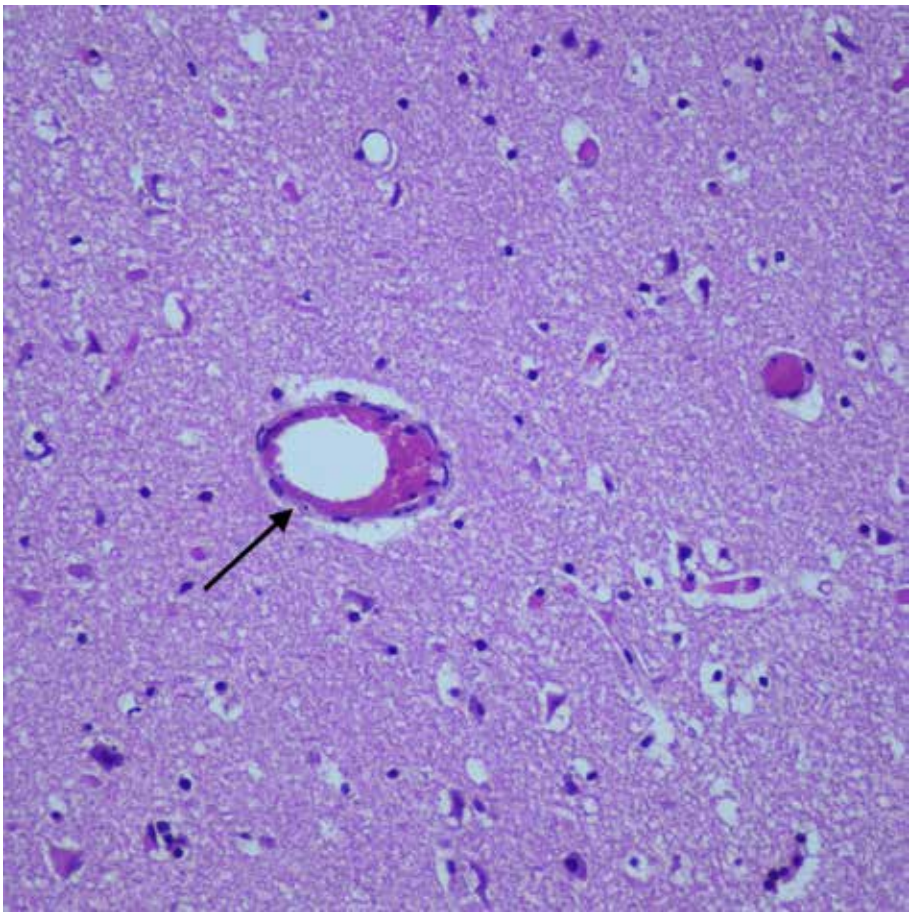

Figure 10.53
Fat embolism,
(H&E, x400).
In the microscopic view, a sharp-lined, hollow appearance
(arrow)
with erythrocytes squeezed aside in the lumen of the capillary vessel within the brain parenchyma is observed. Cerebral fat embolism is rare. It occurs 12-72 hours after onset of insident, especially from multiple long bone fractures of the lower extremity.
Macroscopically, it appears as diffuse punctate hemorrhages in brain sections.

Table 10.1 Microscopic findings of subdural hemorrhage timing and determination of age.

Time	Histopathological findings at dural side
To 24 hours	-Fresh erythrocytes. -Fibrin between the dura mater and hemorrhage.
24-48 hours	-Increased fibrin accumulation. -Neutrophils enter the hemorrhage area.
48-72 hours	-Increase in the amount of fibrin. -Increase in the amount of neutrophils. -Increase in the number of fibroblasts.
3-5 days	–Macrophages appear. -Premature lysis of erythrocytes. -Towards the 3rd day, fibroblasts are 3-4 cells layers thick, and towards the 5th day, they are 7 cells layers thick.
5-10 days	–New capillaries appear in the hemorrhage. -Towards the 10th day, the new membrane (angiofibroblastic proliferation) reaches a thickness of 15 cells.
14 days	-Hemosiderin-laden macrophages are seen. -The new angiofibroblastic membrane thickness is half the thickness of the original membrane. -Very large dilated capillaries.
21 days	–Hemorrhage resorbed. -More pronounces vascular proliferation is observed. -The newly formed membrane is loose fibrovascular tissue.
1 month	-The newly formed membrane is as thick as the dura. -Pigment-laden macrophages are seen.
1-3 months	-The resulting neomembrane consists of fibrous connective tissue similar to the adjacent dura. -Large capillaries appear. -Secondary hemorrhage are seen.
6 months	-Sparse hemosiderin-laden macrophages are seen. -The new membrane and dura unite.
1 year	-The resulting neomembrane consists of fibrous connective tissue similar to the adjacent dura. -Calcification and ossification may be seen. -Hemosiderin-laden macrophages are still seen.

Reference :

1)Di Maio VJM,Dana SE (2007). Handbook of forensic pathology 2 nd edn. Taylor&Francis.Boca Raton,London,New York.

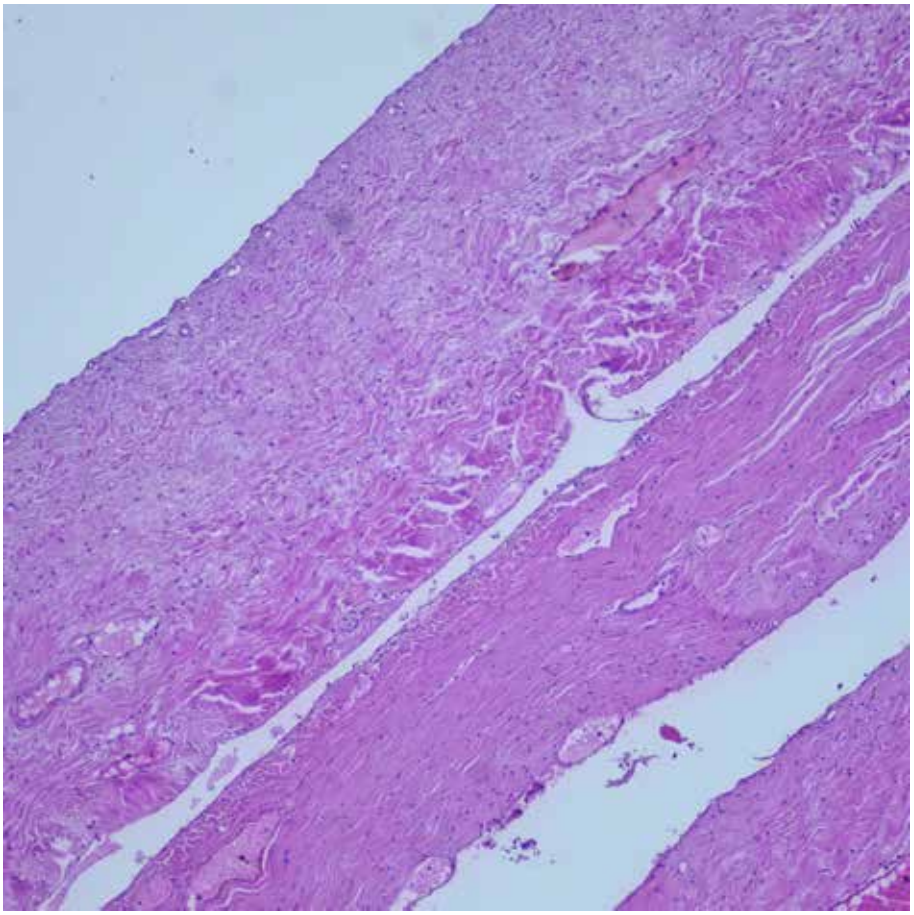

Figure 10.54 Dura mater, (H&E x100). Dura mater consists of thick bundles of collagen fibers. Fibroblasts are found between collagen fibers. The dura mater consists of two layers: periosteal (outer) and meningeal (inner).

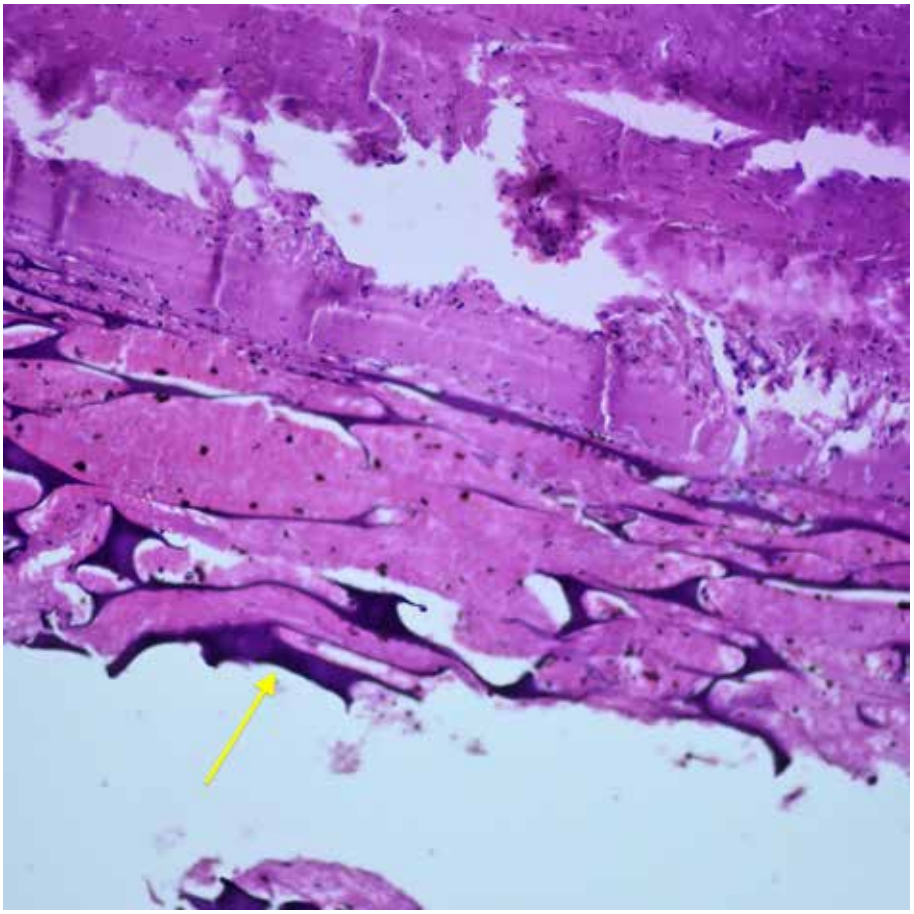

Figure 10.55 Duragel, (H&E, x200). Duragel is a biomaterial used in dural tears and neurosurgery. It is used especially in brain and spinal cord surgeries to repair the dura mater and prevent leaks. The microscopic view shows hemorrhage adjacent to the dura and duragel (arrow) in a person who underwent dural surgery.

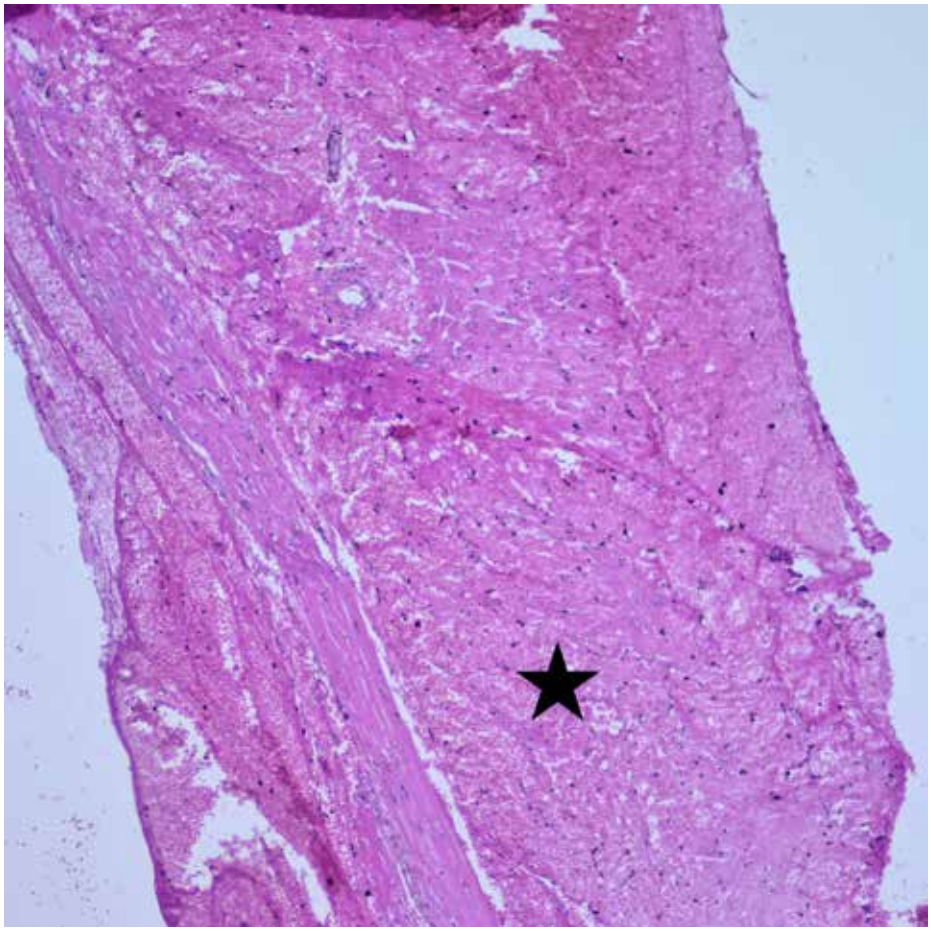

Figure 10.56
Hemorrhage in the dura
(H&E, x100).
The microscopic view shows hemorrhage (asterisk)
in the dura.

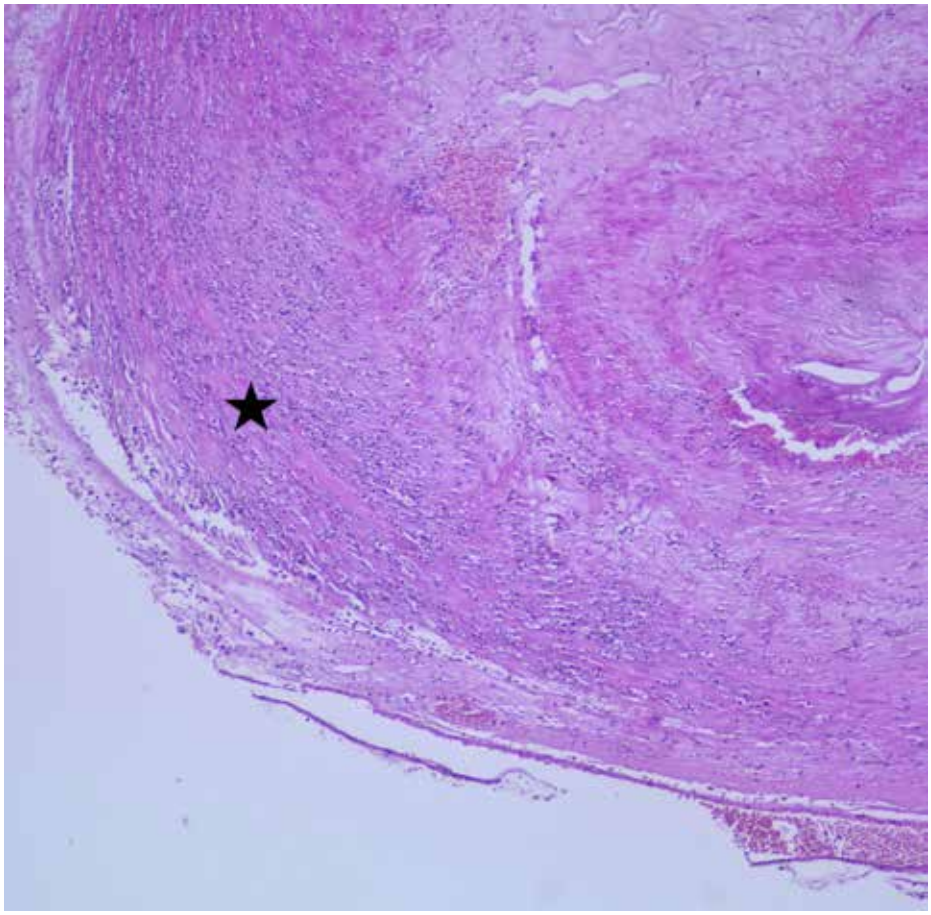

Figure 10.57
Pachymeningitis,
(H&E, x100).
Pachymeningitis means inflammation of the dura mater.
The microscopic view shows neutrophil infiltration
(asterisk)
in the dura mater.

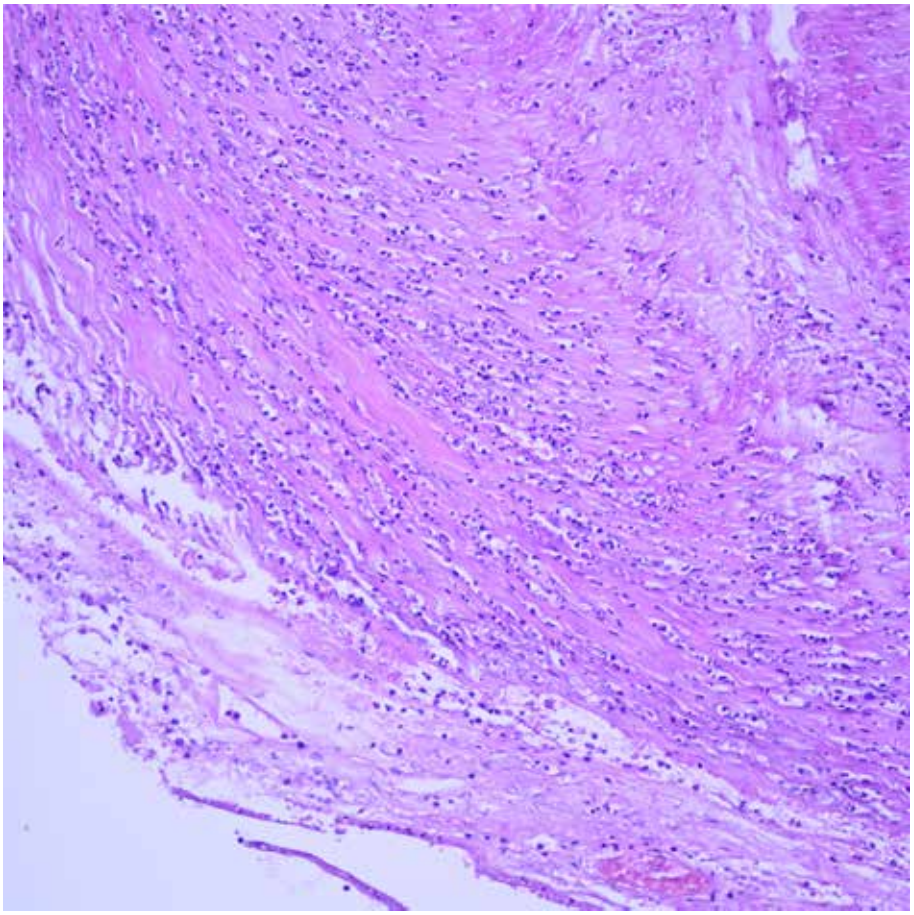

Figure 10.58 Pachymeningitis, (H&E, x200). At higher magnification, neutrophil infiltration within the dura mater.

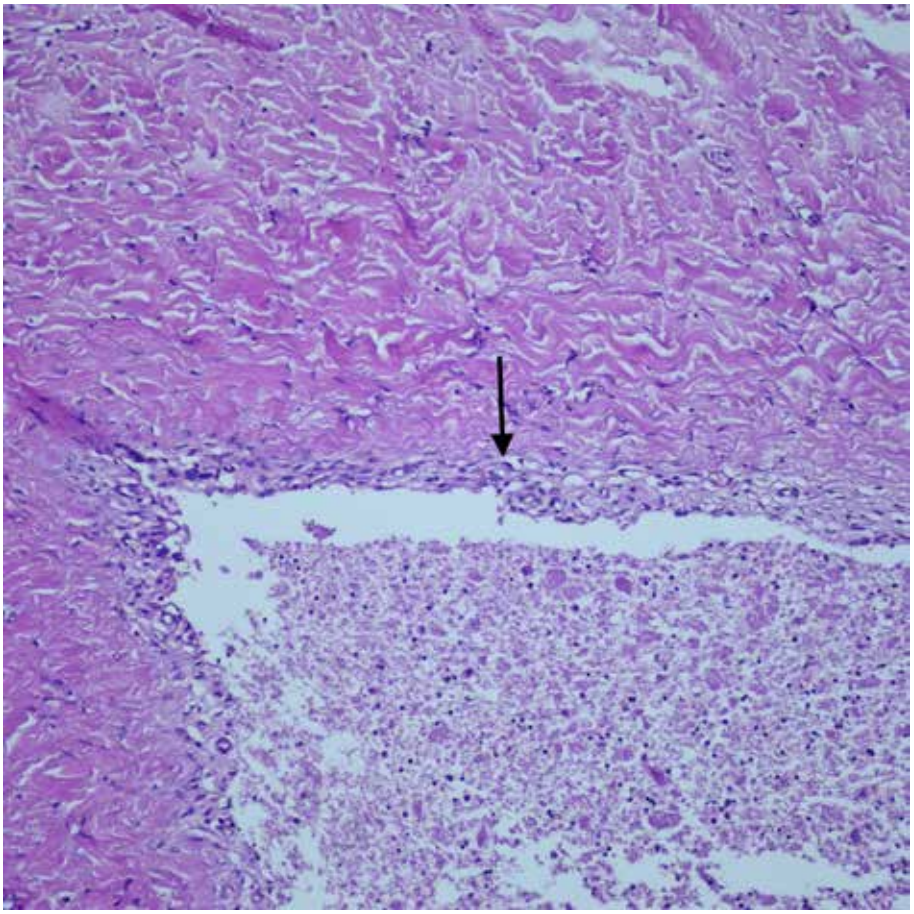

Figure 10.59 Dura mater hemorrhage and organization, (H&E, x200). 4-5 rows of fibroblast proliferation (arrow) are seen adjacent to the dura mater. These findings are compatible with the days 3-5 of hemorrhage.

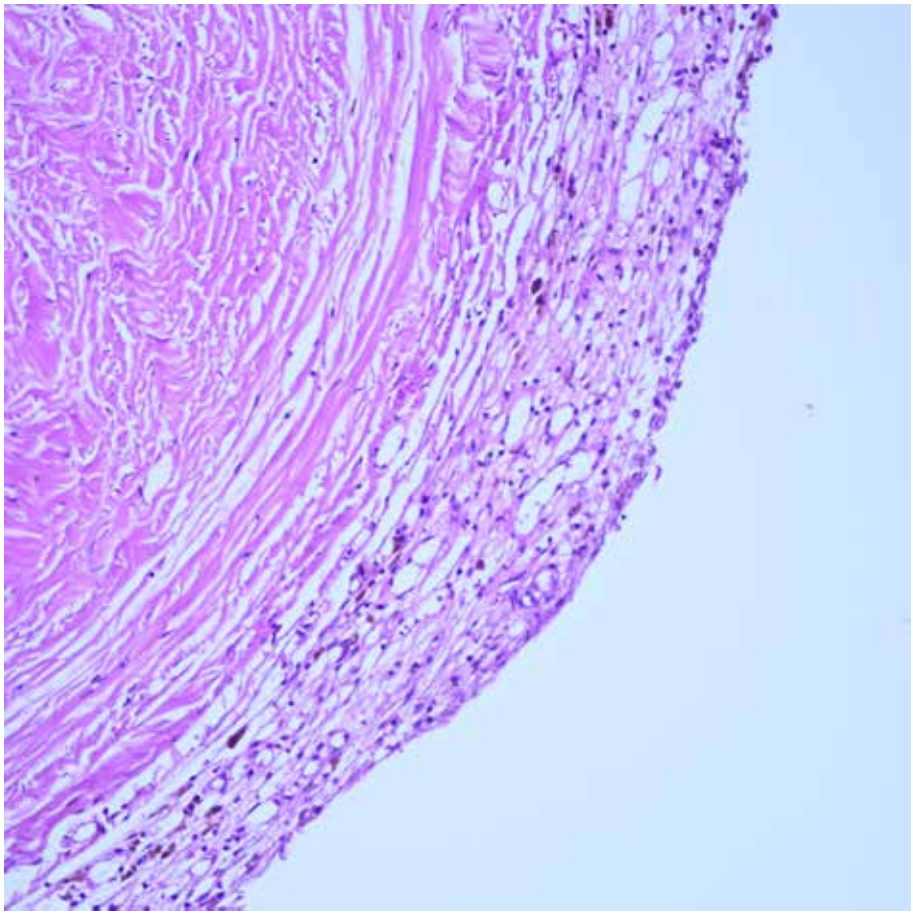

Figure 10.60
Dura mater, hemorrhage organization, (H&E, x200). Approximately 15 rows of fibroblast proliferation and hemosiderin-laden macrophages are seen adjacent to the dura mater.
These findings are consistent with the 10-14th day of hemorrhage.

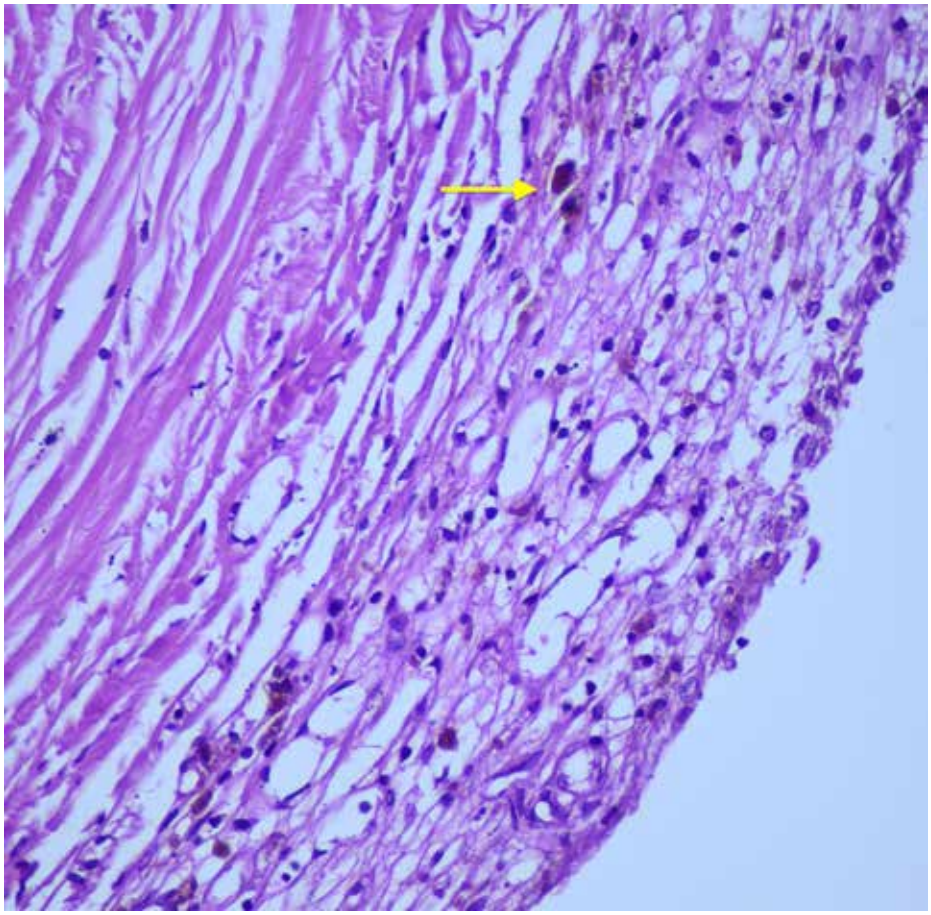

Figure 10.61
Dura mater, hemorrhage organization, (H&E, x400). At higher magnification. Hemosiderin laden macrophages (arrow).

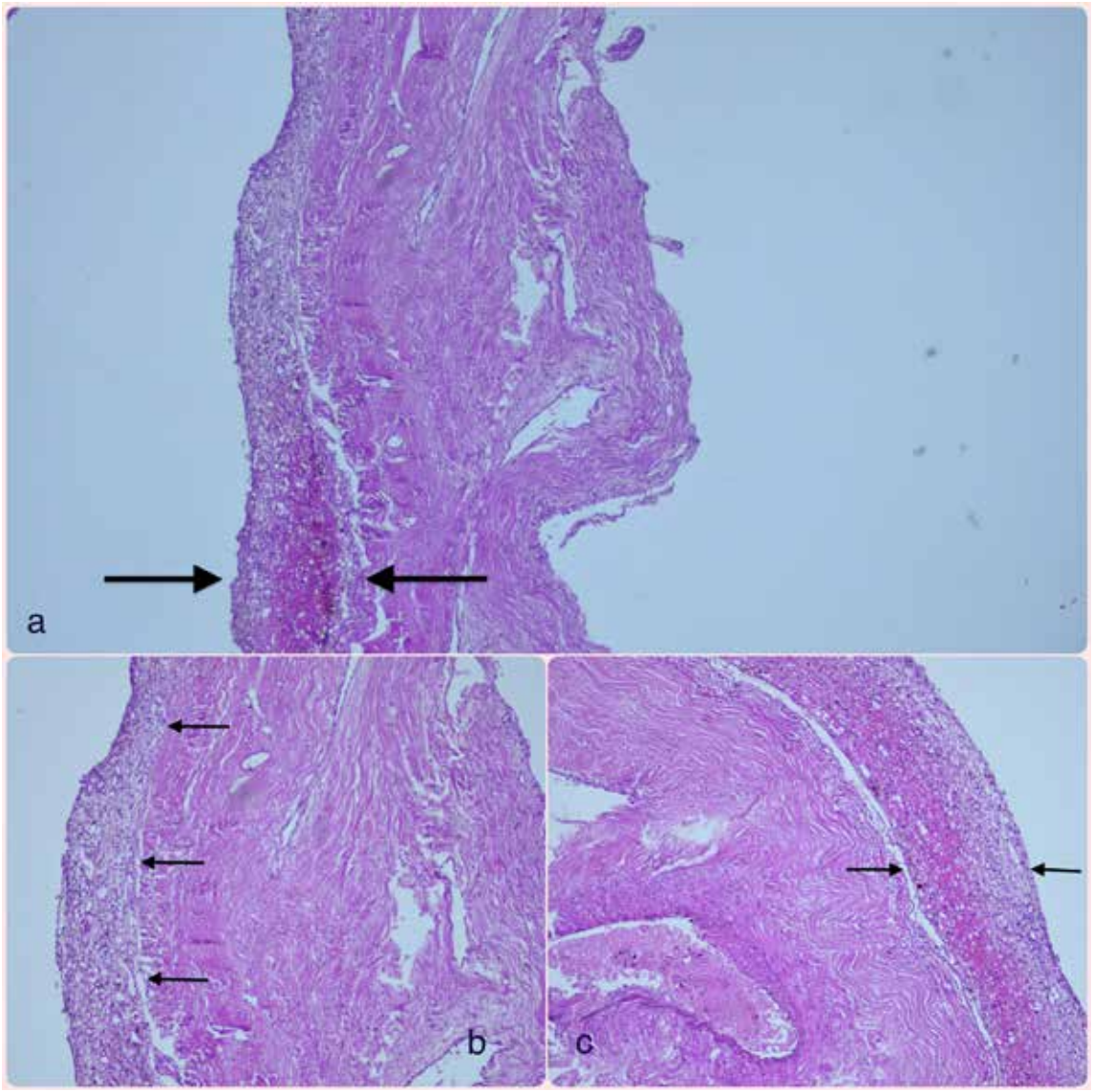

Figure 10.62
Dura mater, hemorrhage organization (14 days)
a) (H&E, x40) Fibroblastic proliferation and new membrane formation adjacent to the dura mater are half the thickness of the dura (arrows).
b,c) (H&E, x100) At higher magnification, dural fibroblastic proliferation and new membrane thickness are indicated by arrows.

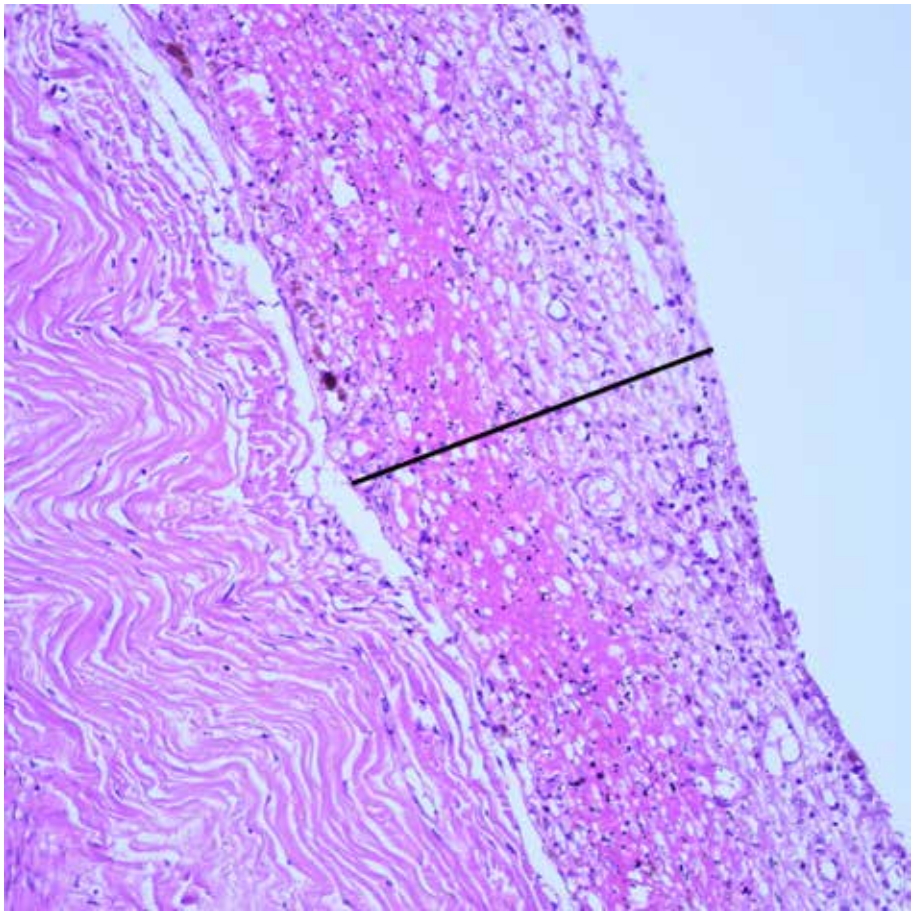

Figure 10.63
Dura mater, hemorrhage organization, (H&E, x200). Fibroblastic proliferation and new membrane formation adjacent to the dura mater have been demonstrated.

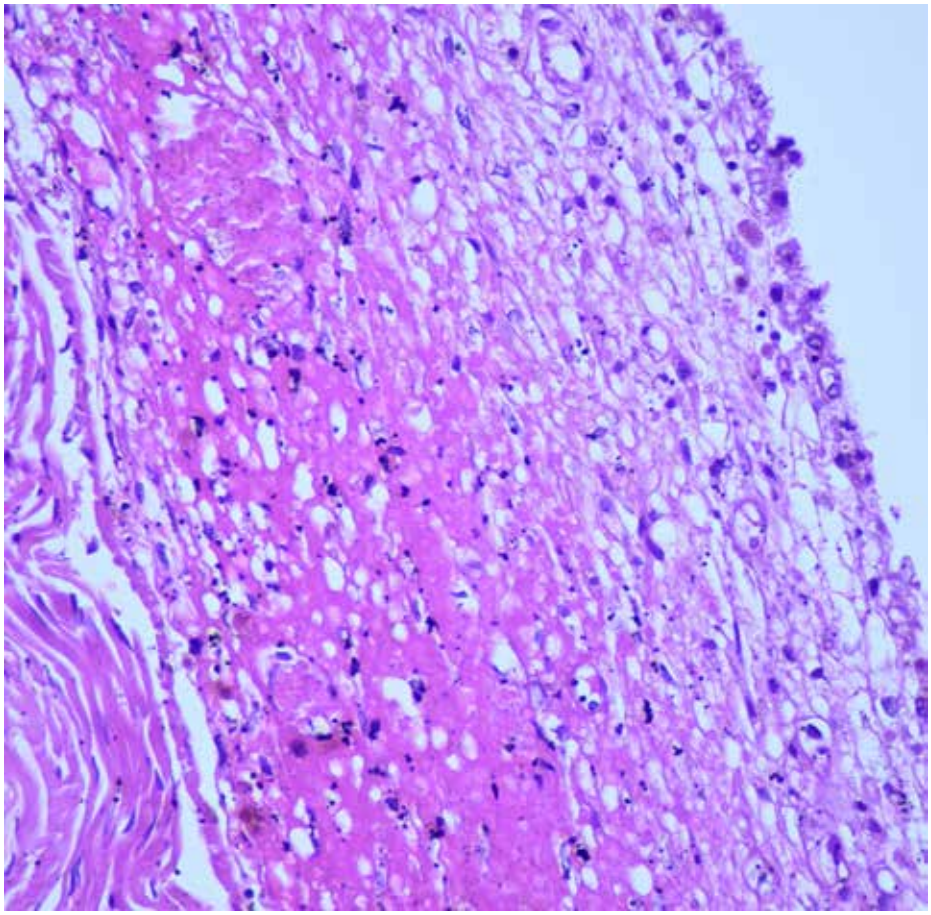

Figure 10.64
Dura mater, hemorrhage organization, (H&E, x400). At higher magnification, fibroblastic proliferation and new membrane formation adjacent to the dura mater have been demonstrated. There are hemosiderin-laden macrophages in the new membrane.

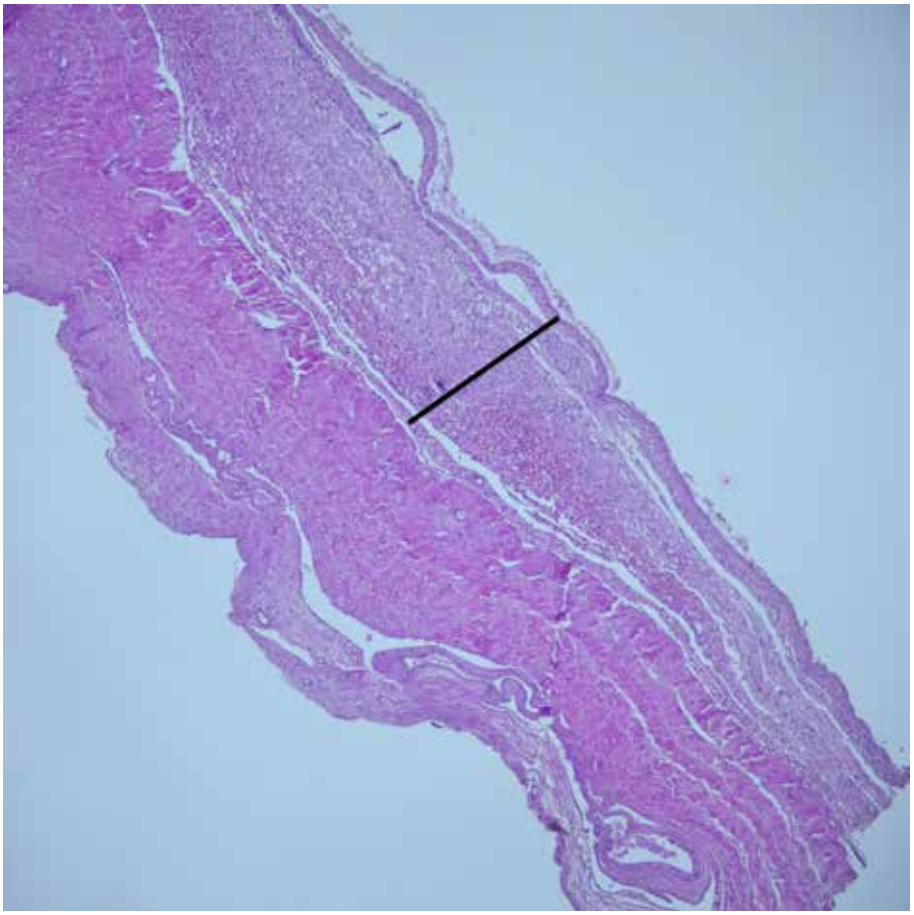

Figure 10.65 Dura mater, hemorrhage organization, (H&E, x40). Fibroblast proliferation is observed adjacent to the dura mater, approximately in the thickness of the dura. These findings are compatible with the 4th week of hemorrhage.

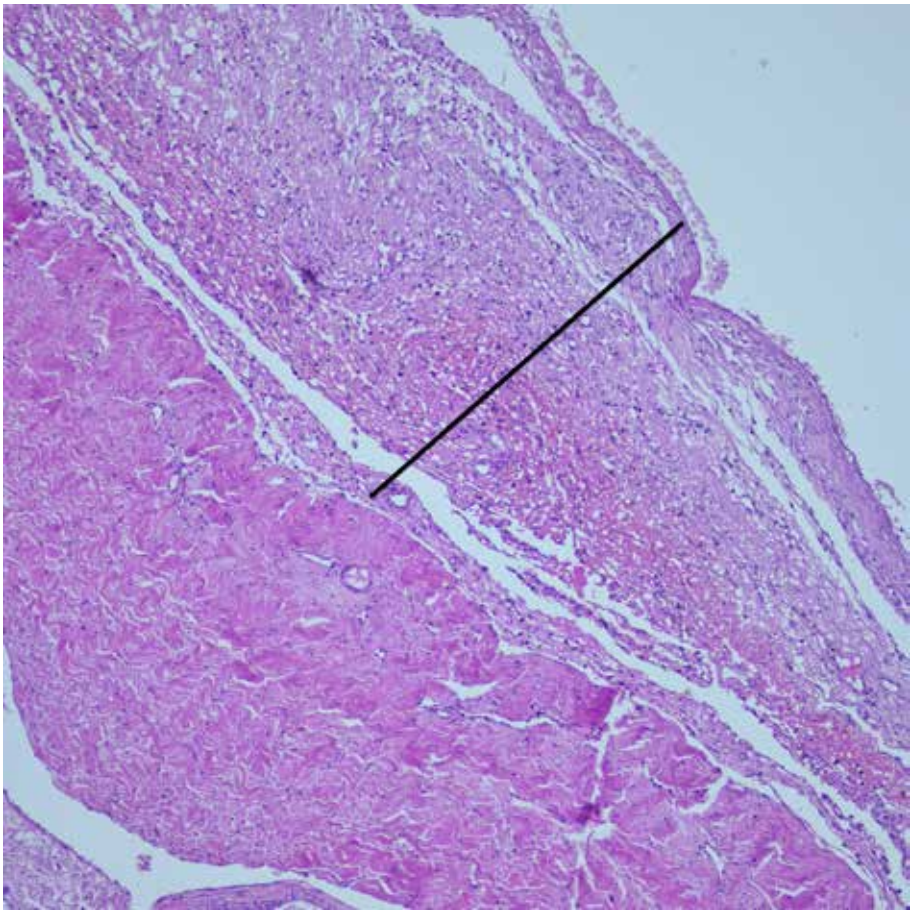

Figure 10.66 Dura mater, hemorrhage organization, (H&E, x100). At higher magnification.

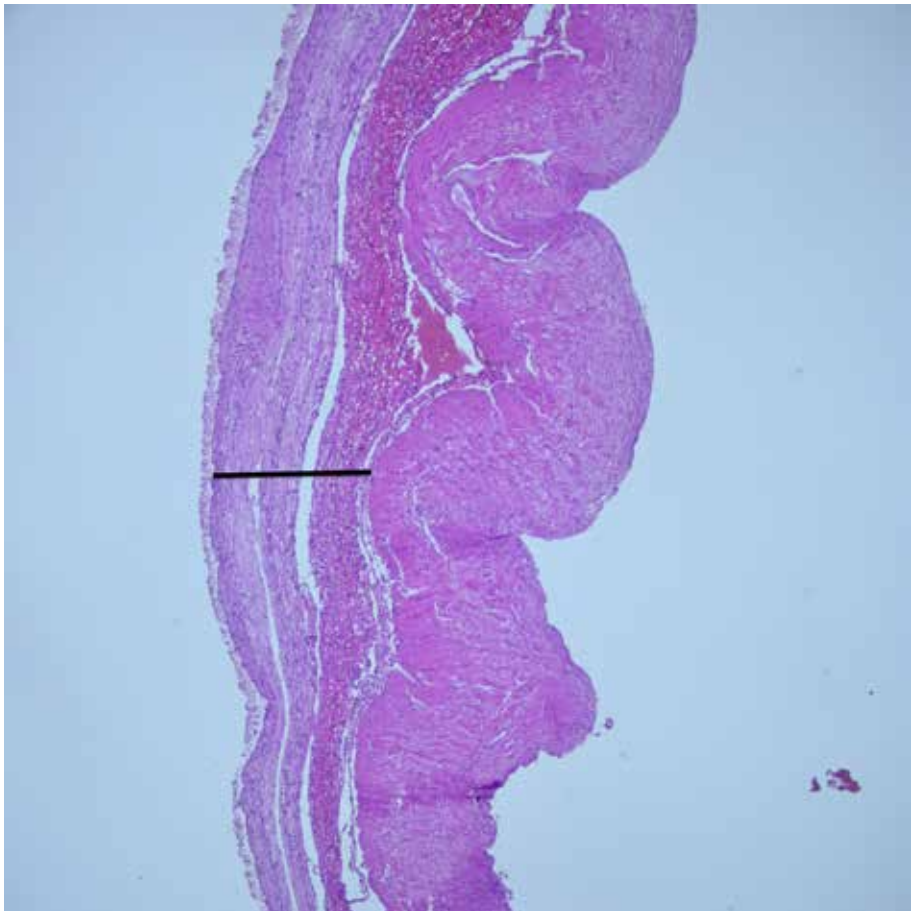

Figure 10.67
Dura mater, hemorrhage organization, (H&E, x40).
In another case, fibroblast proliferation is observed adjacent to the dura mater, approximately in the full thickness of the dura.
These findings are compatible with the 4th week of hemorrhage.

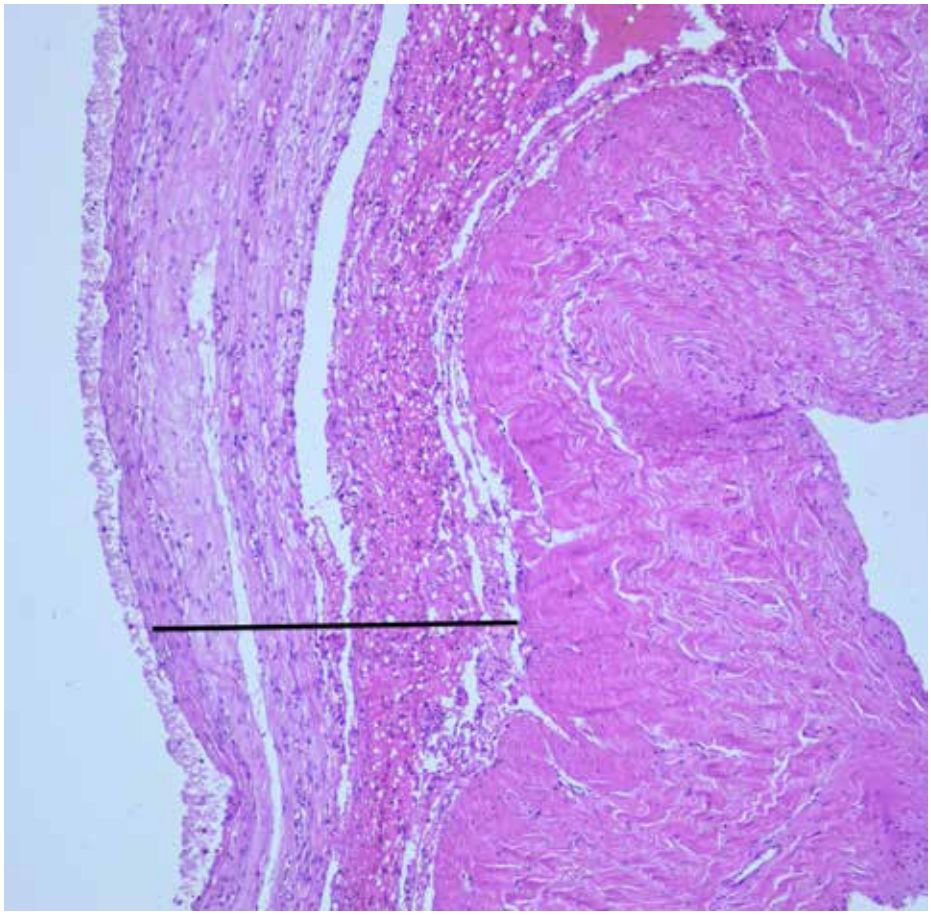

Figure 10.68
Dura mater, hemorrhage organization, (H&E, x100).
At higher magnification.

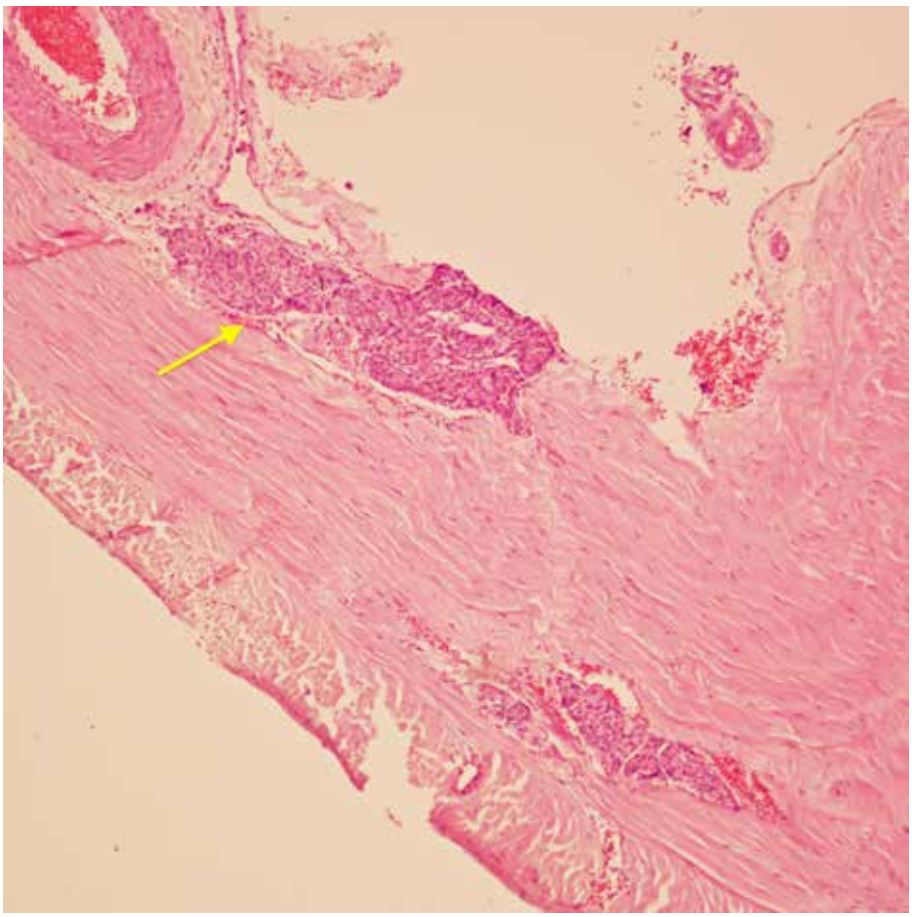

Figure 10.69
Dura mater, meningothelial proliferation,
(H&E, x100).
Meningothelial proliferation
(arrow),
which can be seen adjacent to the dura mater, may occur as a response of these cells to various stimuli. These cells should not be confused with fibroblasts seen in hemorrhage organization.

PEDIATRIC PATHOLOGY

Assoc. Prof. Ferah KARAYEL

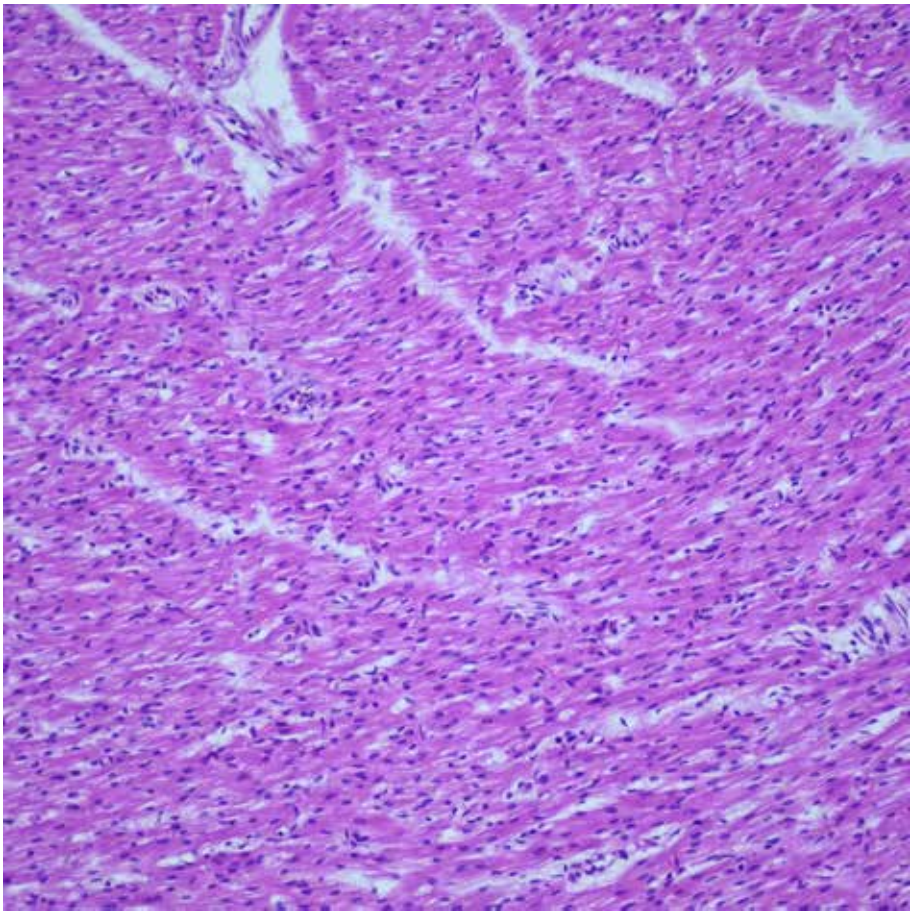

Figure 11.1
Normal myocardium in the stillborn baby, (H&E, x200). The microscopic view shows normal myocardial tissue in a stillborn baby. It has a more cellular appearance than adult myocardial tissue.

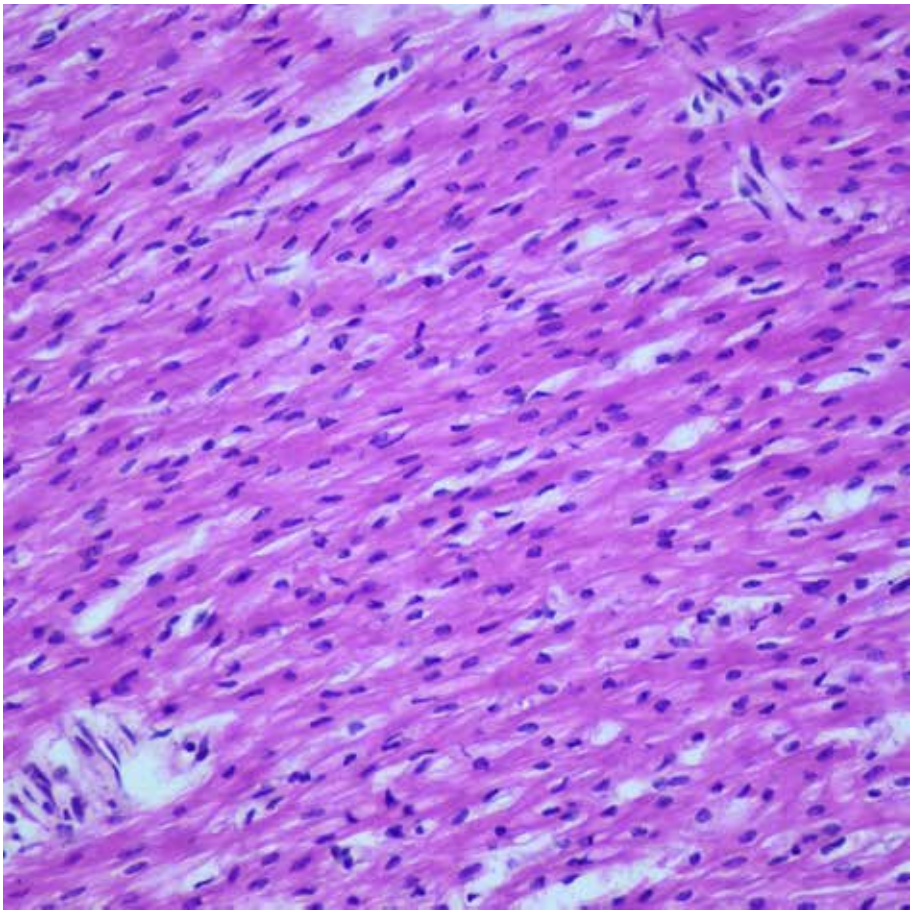

Figure 11.2
Normal myocardium in the stillborn baby, (H&E, x400). At higher magnification.

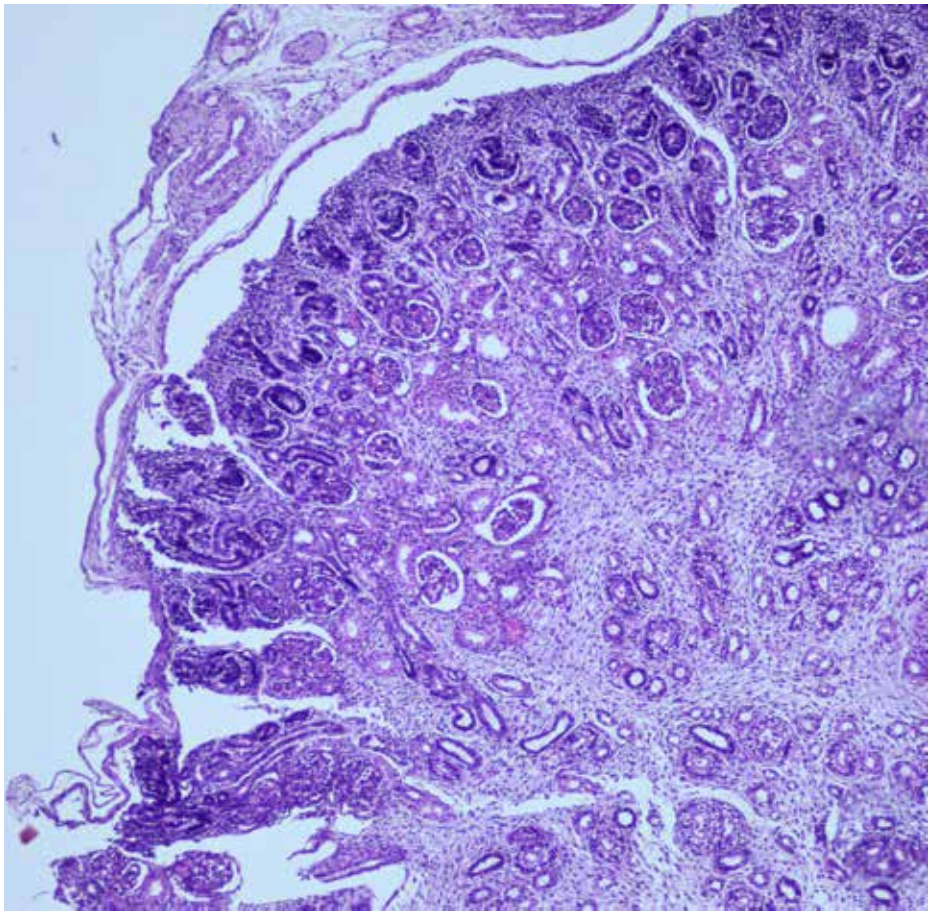

Figure 11.3
Fetal kidney,
(H&E, x100).
Immature kidney in a
16-week fetus.

Figure 11.4
Normal umbilical
cord,
(H&E, x40).
The umbilical cord
containing 2 arteries
and 1 vein with
normal appereance.

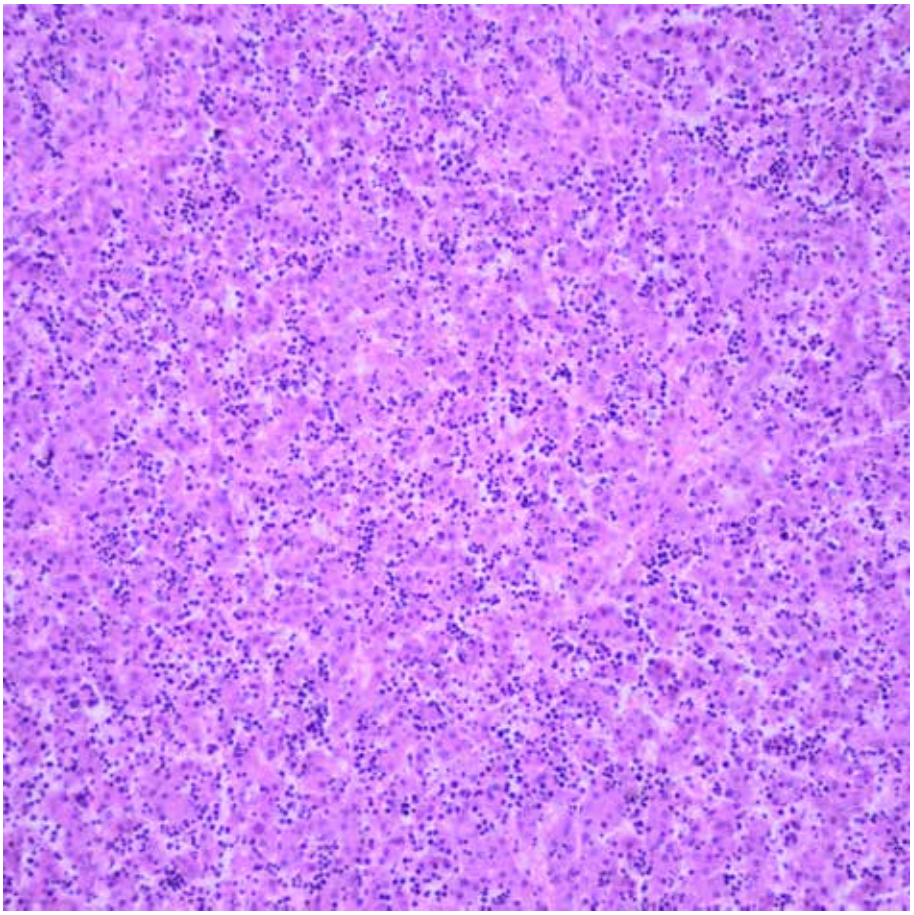

Figure 11.5 Extramedullary hematopoiesis, (H&E, x200). Extramedullary hematopoiesis is the production of hematopoietic cells apart from bone marrow. It is frequently seen in the liver, spleen and lymph nodes. Extramedullary hematopoiesis is considered a finding supporting asphyxia in infants.

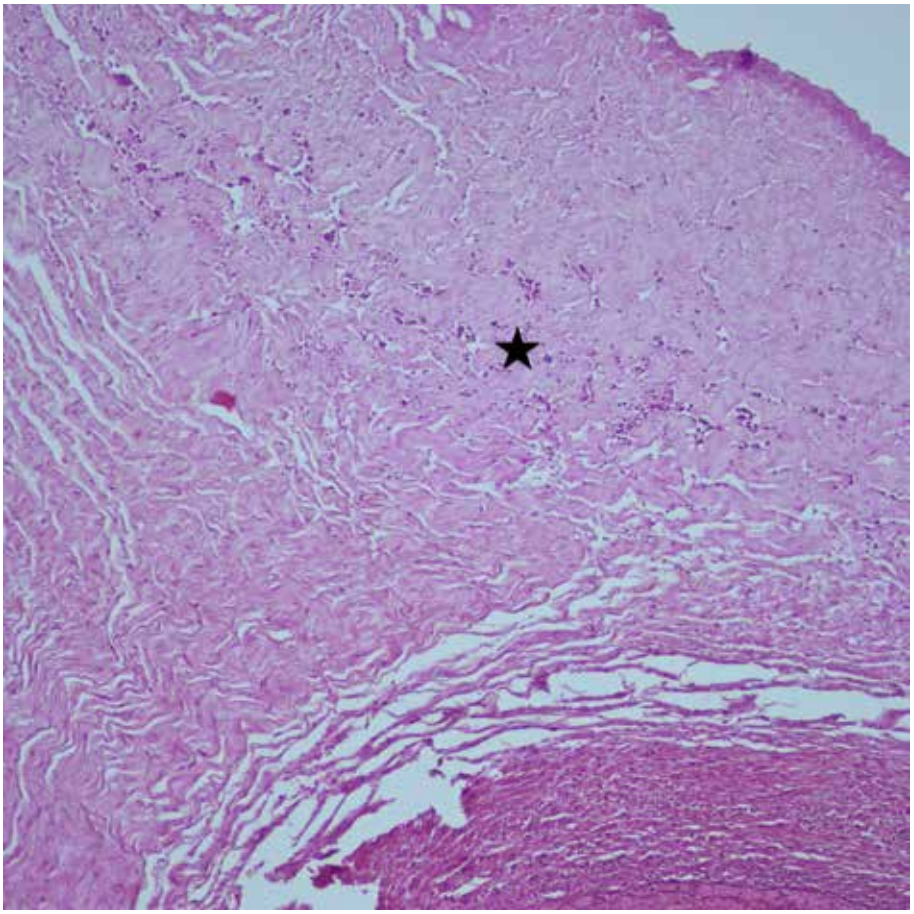

Figure 11.6 Funisitis, (H&E, x100). Neutrophil infiltration (asterisk) is seen in Wharton jelly.

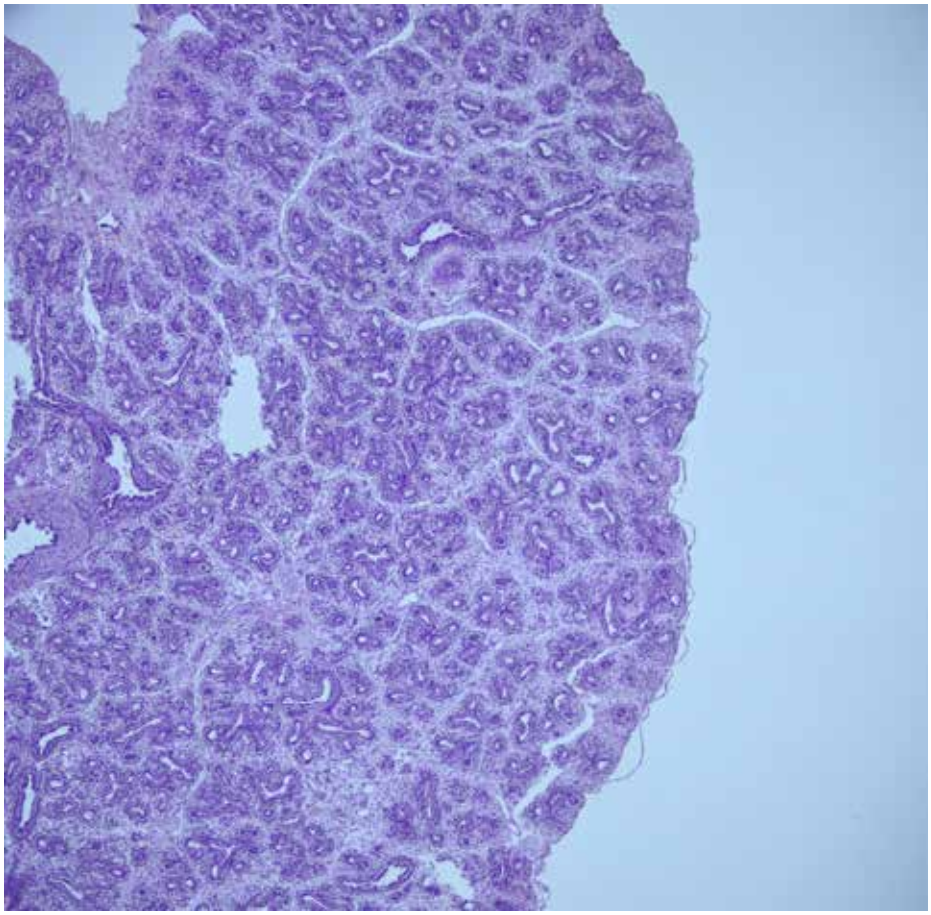

Figure 11.7
Pseudoglandular stage (5-17 weeks), (H&E, x40).
The lung appears similar to exocrine glands due to thick airways lined with cuboidal epithelium.

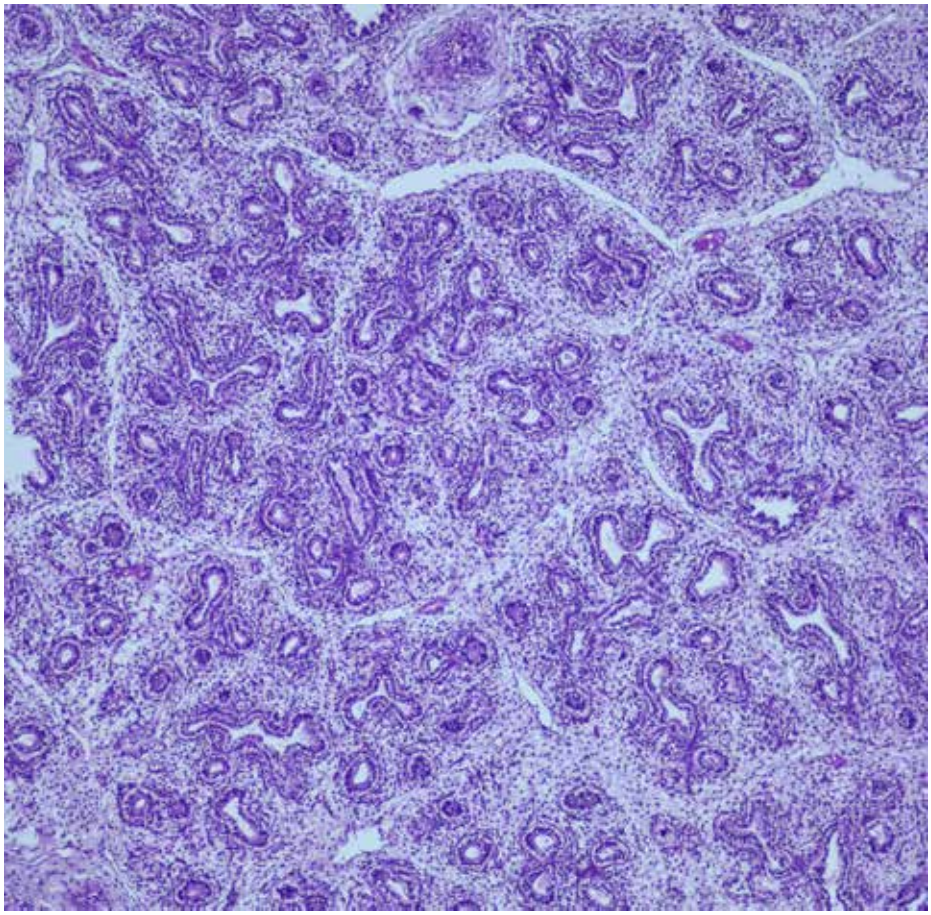

Figure 11.8
Pseudoglandular stage (5-17 weeks), (H&E, x100).
At higher magnification pseudoglandular stage.

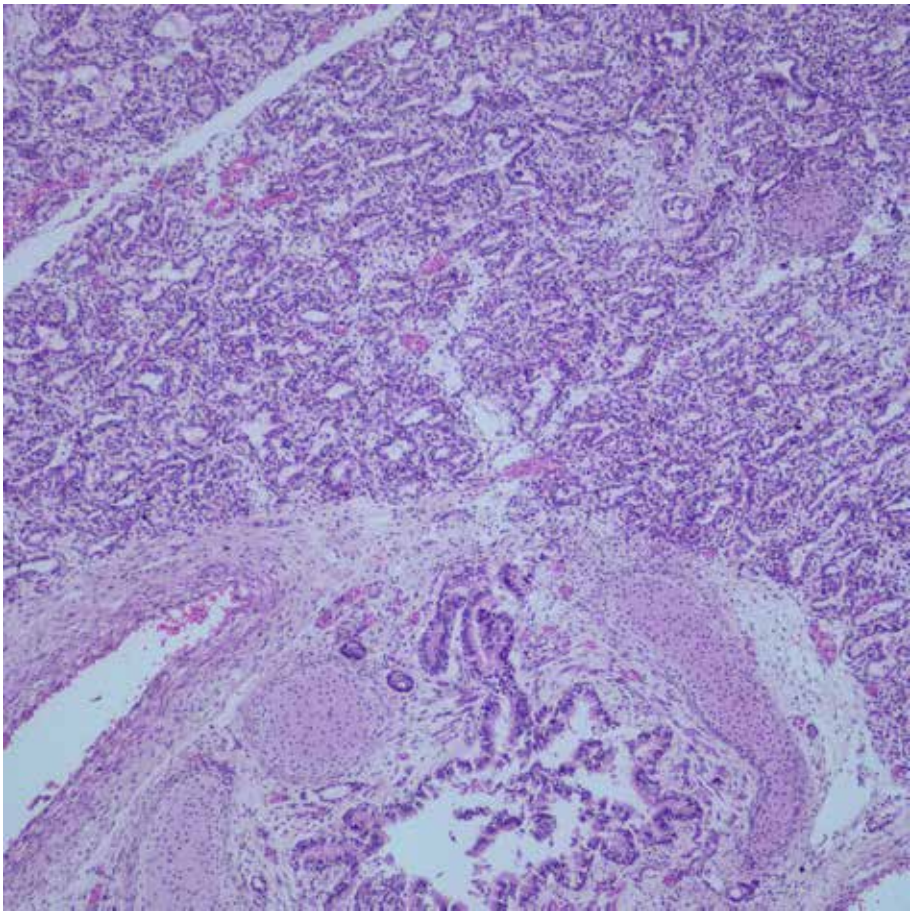

Figure 11.9
Canalicular stage (16-25 weeks), (H&E, x100).
In the canalicular stage, bronchioles and alveolar ducts develop. The interstitial connective tissue thins and alveolar walls develop. Pneumocytes begin to differentiate into type 1 and 2 pneumocytes.

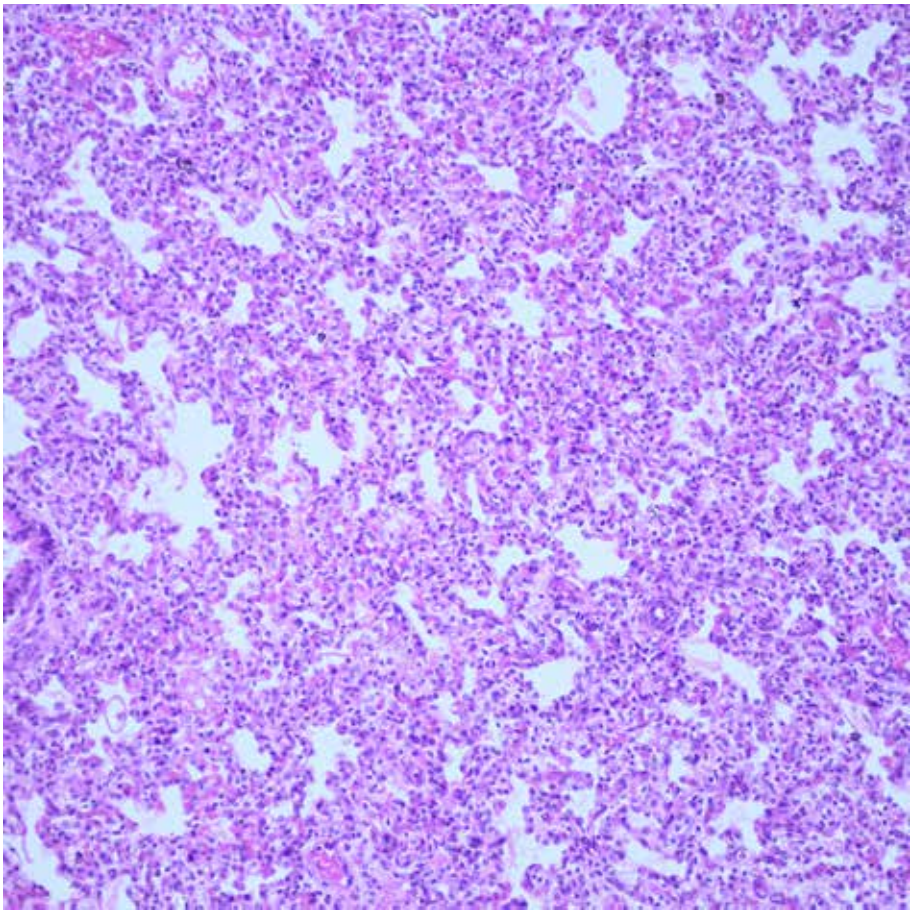

Figure 11.10
Saccular stage (24 weeks-birth), (H&E, x200).
In the saccular stage, saccules (primitive alveoli) are formed. In the microscopic view, amount of connective tissue between the structures differentiated into alveoli decreases and the vascular structures become more prominent.
At this stage, many more terminal sacs develop, and the epithelium of these sacs becomes very thin. Cuboidal epithelium changes into type 1 and type 2 pneumocytes. Capillaries also protrude into these developing alveoli.
The close contact between epithelial and endothelial cells creates the blood-air barrier that will allow sufficient gas exchange for the fetus to survive even in premature birth.

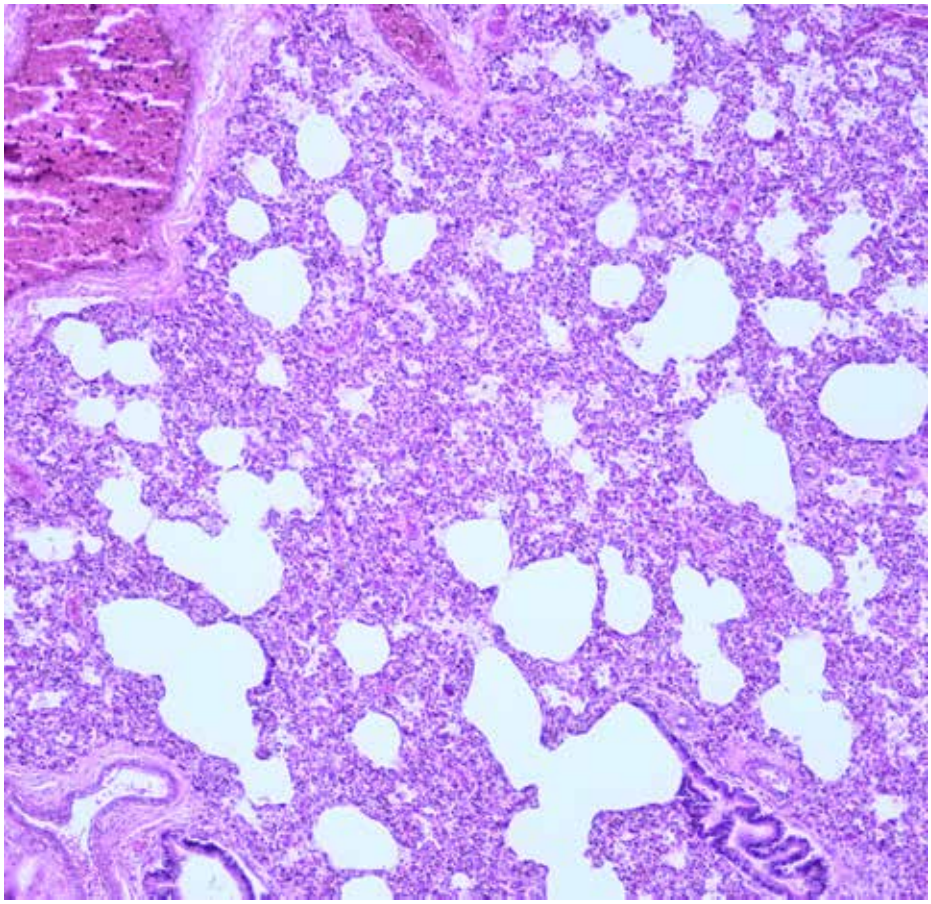

Figure 11.11
Alveolar stage (36 weeks- 8 years), (H&E, x100).
In the microscopic view, alveoli and bronchial structures are formed.
Prior to birth, immature alveoli appear as bulges from the sacculi.
The alveolar stage continues until the age of 8.

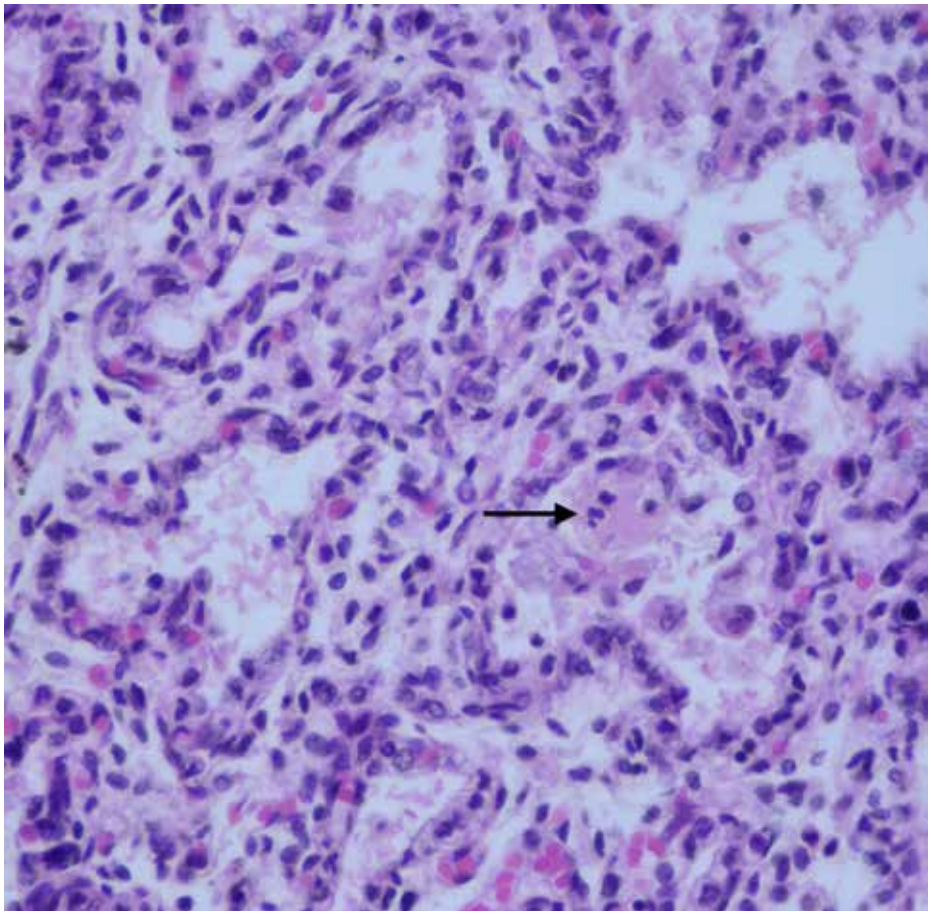

Figure 11.12
Normal myocardium in the stillborn baby, (H&E, x400).
At higher magnification.

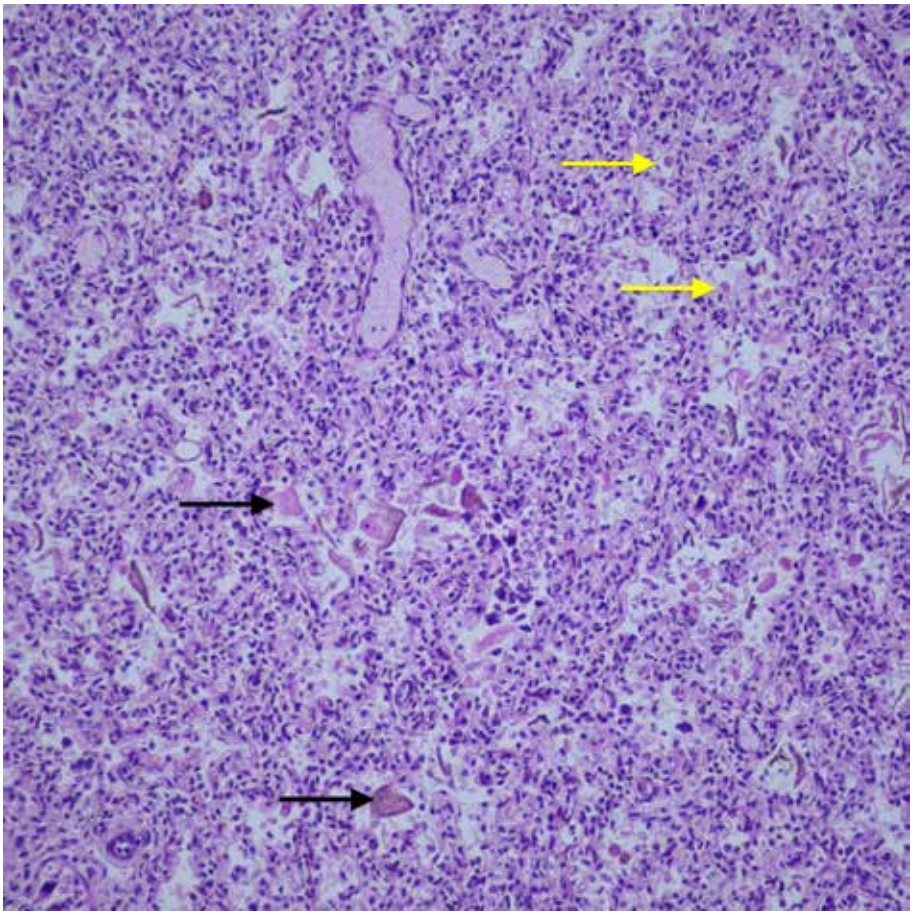

Figure 11.13
Amnion aspiration (Late canalicular-early saccular stage), (H&E, x200). The microscopic view shows widespread anucleated squam particles (black arrows) and light-dark brown meconium (yellow arrows) in the primitive alveolar lumens.

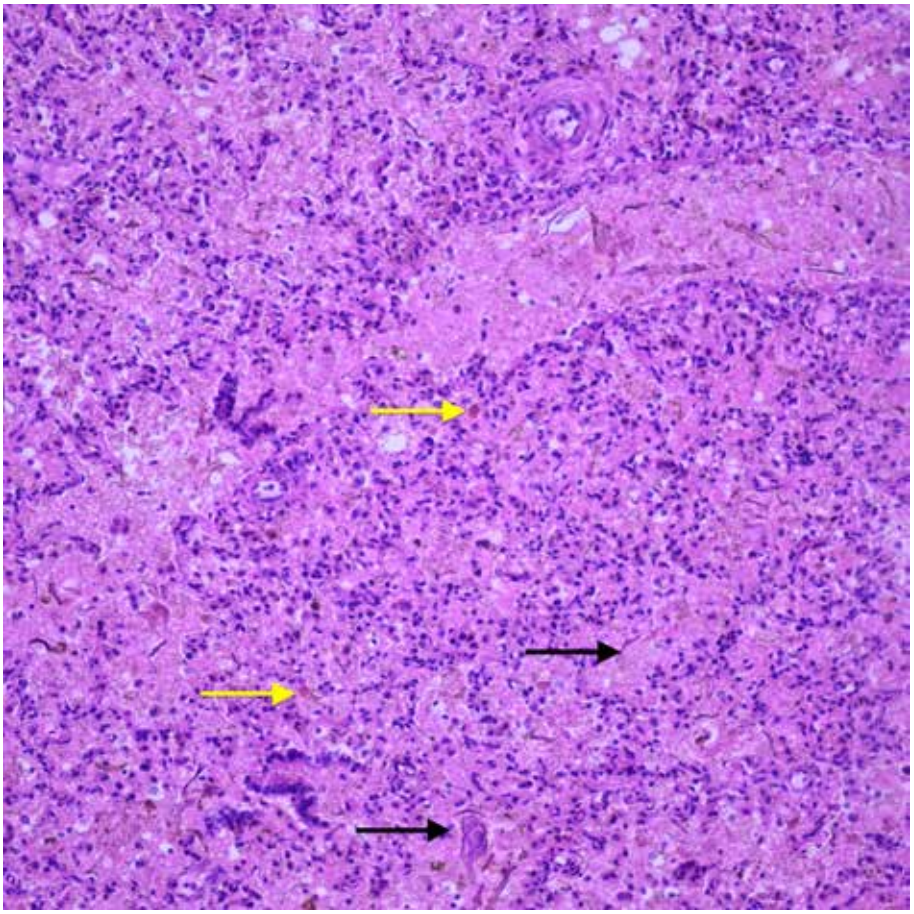

Figure 11.14
Amnion and meconium aspiration, (H&E, x200). The microscopic view shows widespread anucleated squam particles (black arrows) and light-dark brown meconium (yellow arrows) in the alveolar lumens. Amniotic fluid aspiration occurs physiologically in the fetus. After the 34th-36th week, a small amount of squamous epithelial cells belonging to the amniotic fluid can be seen in the lungs of all fetuses. However, it is also accepted that intrauterine anoxia causes significant amniotic fluid aspiration. However, it is known that it is not the sole cause of death. Meconium is the bile-stained intestinal content of the fetus. The presence of meconium in amniotic fluid is widely considered a sign of fetal distress. Morbidity and mortality are quite high in meconium aspiration syndrome.

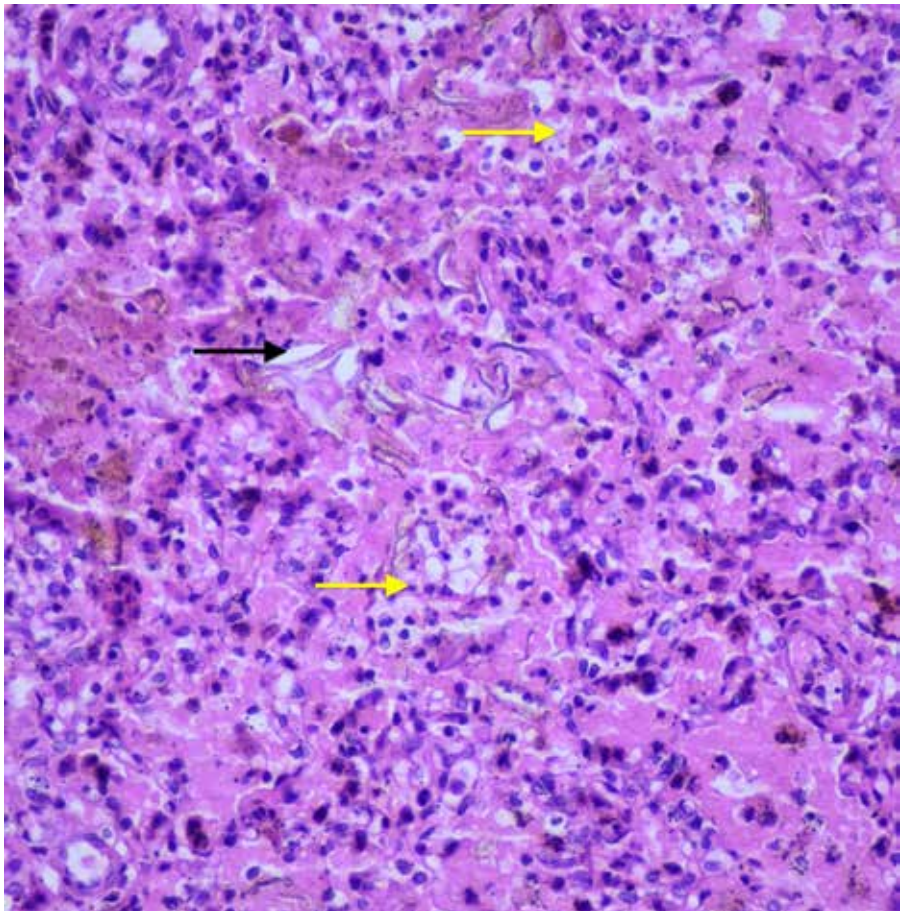

Figure 11.15
Amnion aspiration and perinatal pneumonia, (H&E, x400). The picture shows anucleated squames (black arrow) and neutrophil infiltration (yellow arrows) in the alveolar lumens.

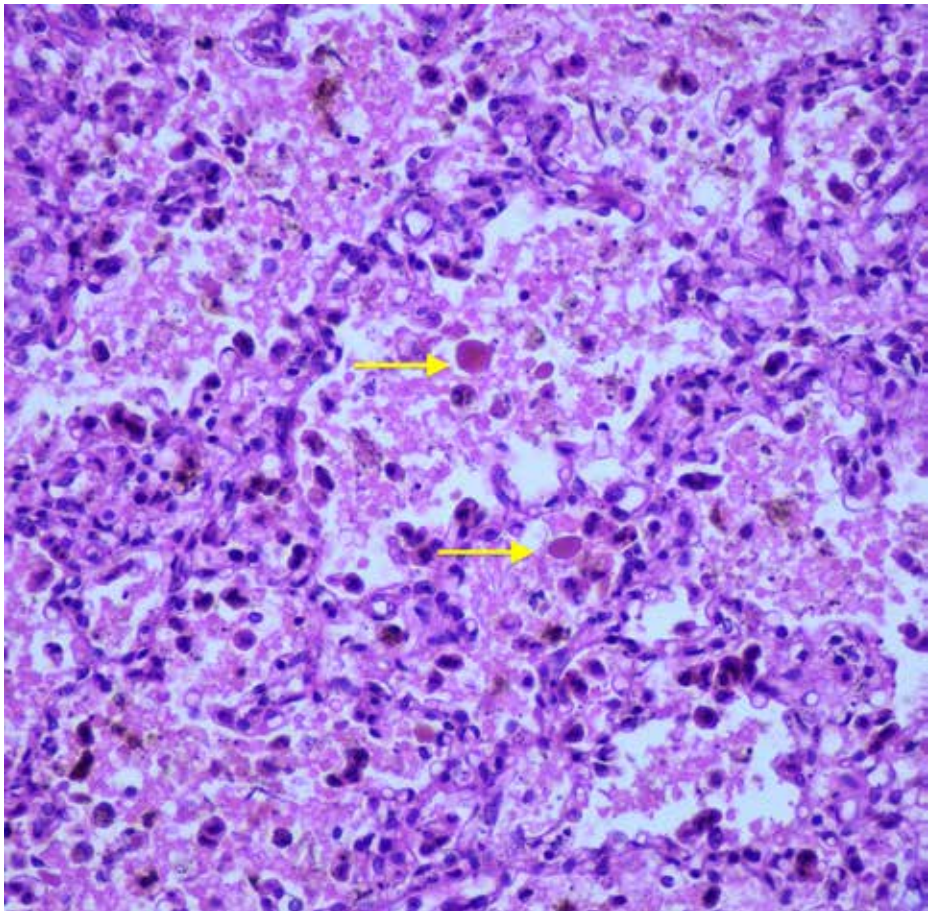

Figure 11.16
Meconium aspiration, (H&E, x400). At high magnification, aspiration of dark brown meconium (yellow arrows) is seen in alveoli.

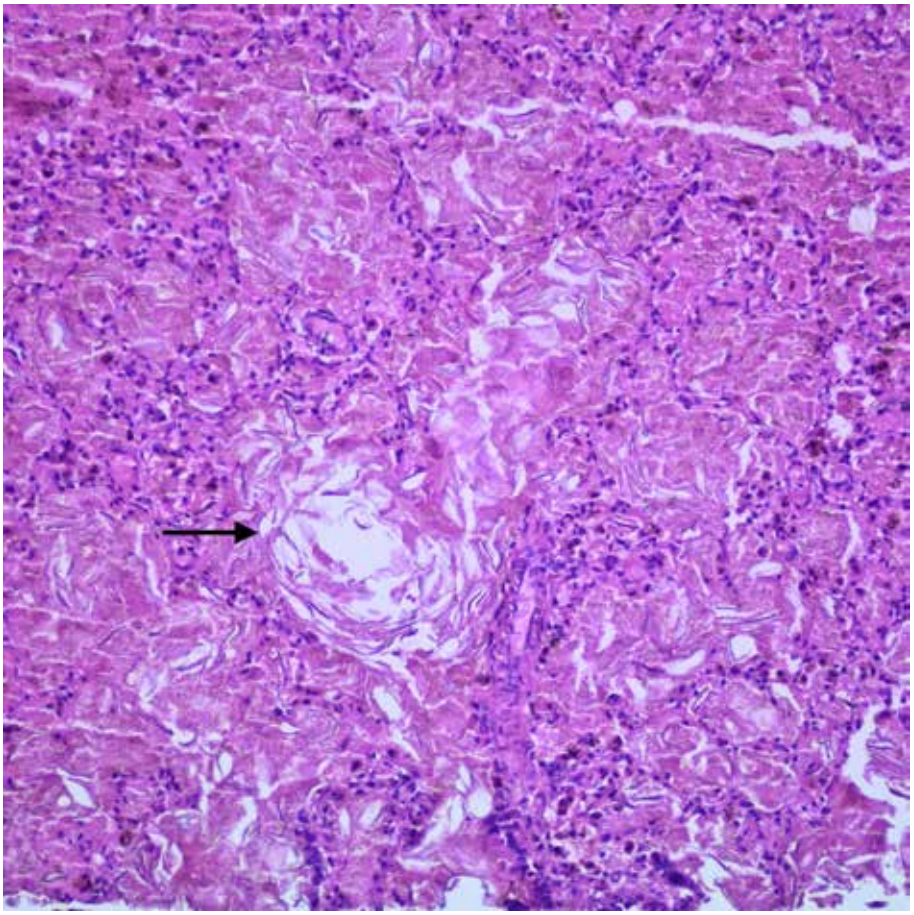

Figure 11.17 Amnion aspiration, (H&E, x200). In the microscopic view, numerous annucleated squames (black arrow) can be seen in the alveolar lumens.

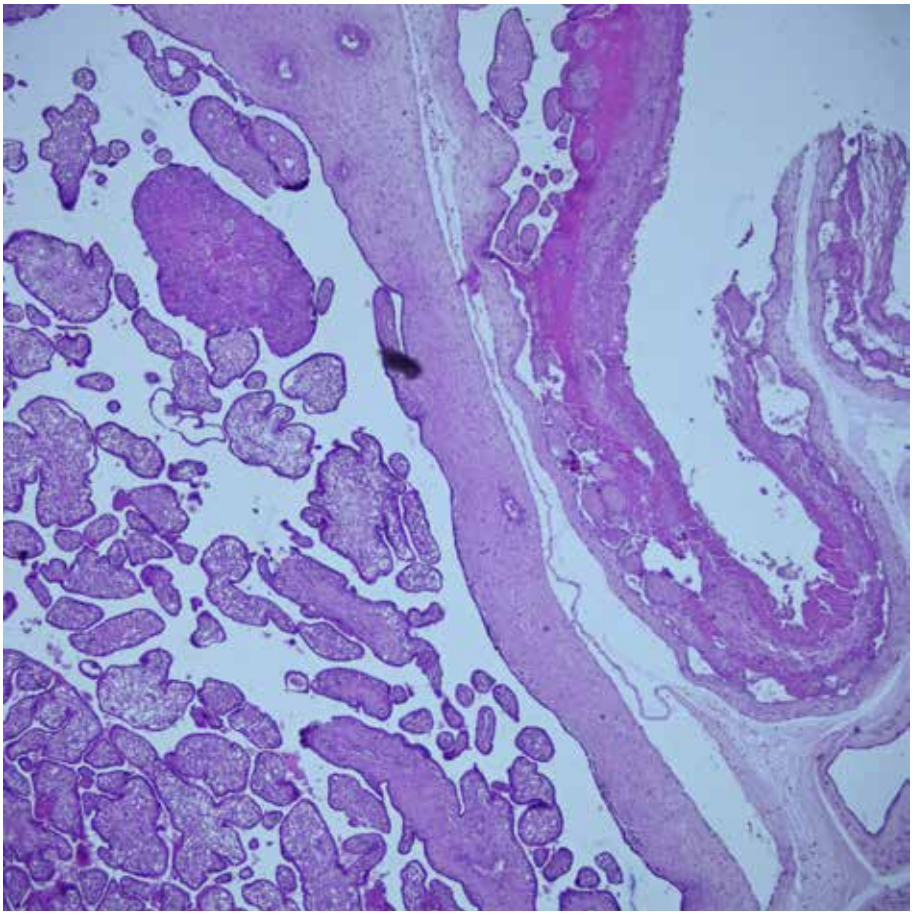

Figure 11.18 Normal placenta, (H&E, x40). Histological appearance of the placenta of a 16-week fetus.

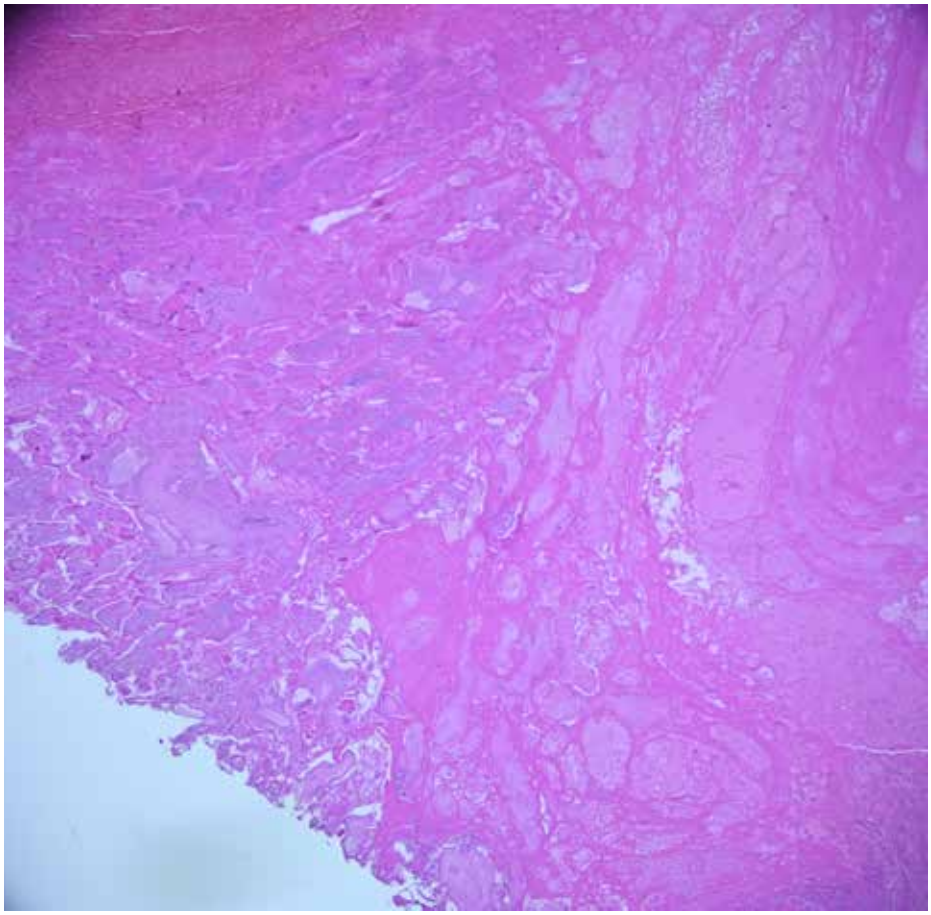

Figure 11.19
Placental infarction, (H&E, x40). Coagulation necrosis in the placental tissue.

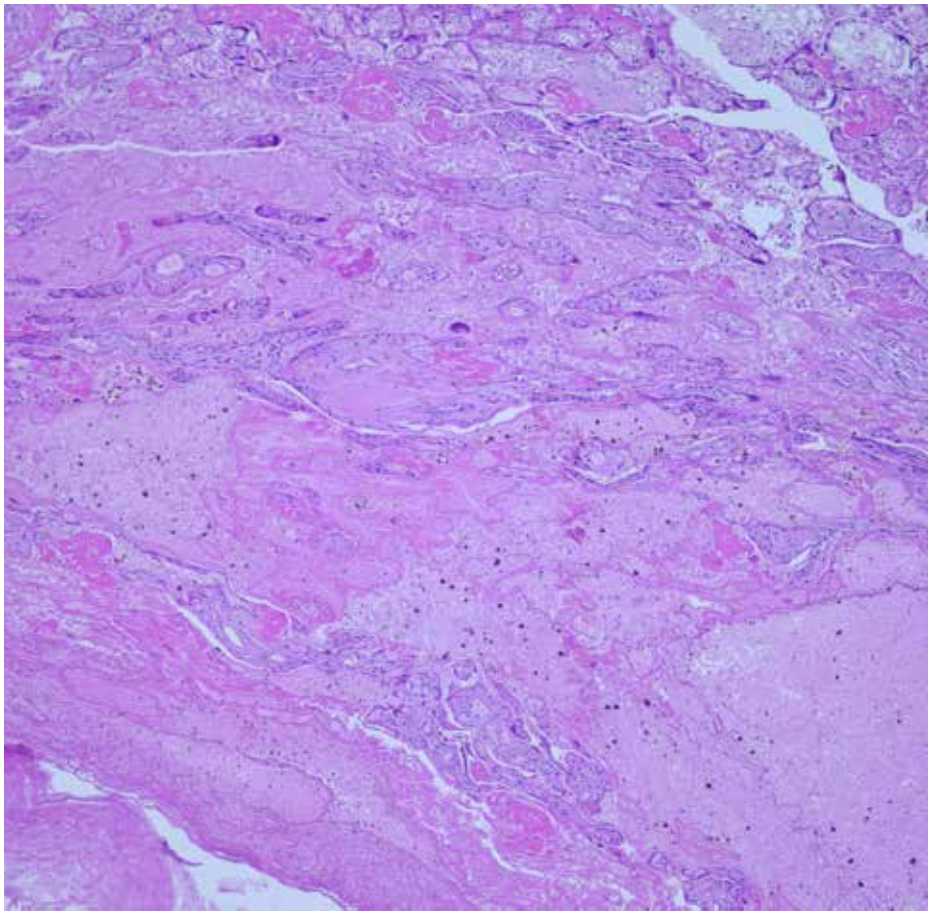

Figure 11.20
Placental infarction, (H&E, x100). At higher magnification. Placental infarction is a sign of maternal uteroplacental insufficiency. It can be seen in normal or prolonged pregnancies. Intrauterine growth retardation, fetal hypoxia, intrauterine fetal death, neonatal mortality and morbidity are among the causes.

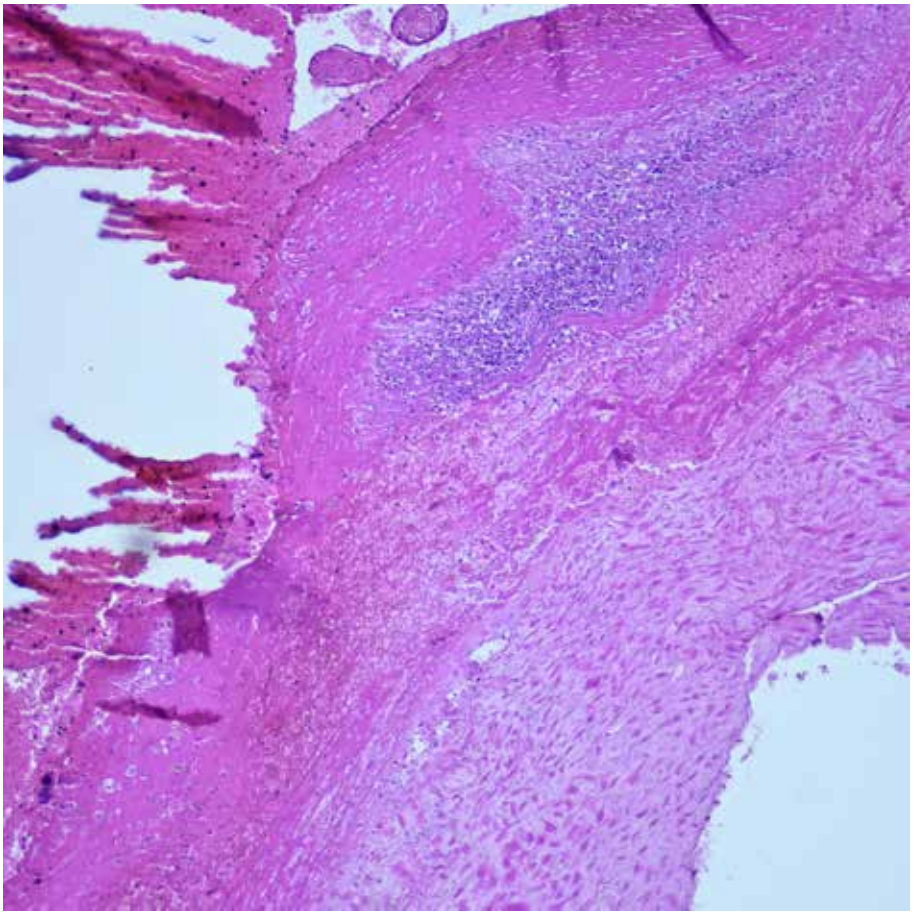

Figure 11.21 Inflamed and necrotic decidua, (H&E, x100). Decidua indicates pregnancy-related change in the endometrium. However, to evaluate it as a definite pregnancy, chorionic villi or trophoblastic cells must be seen.

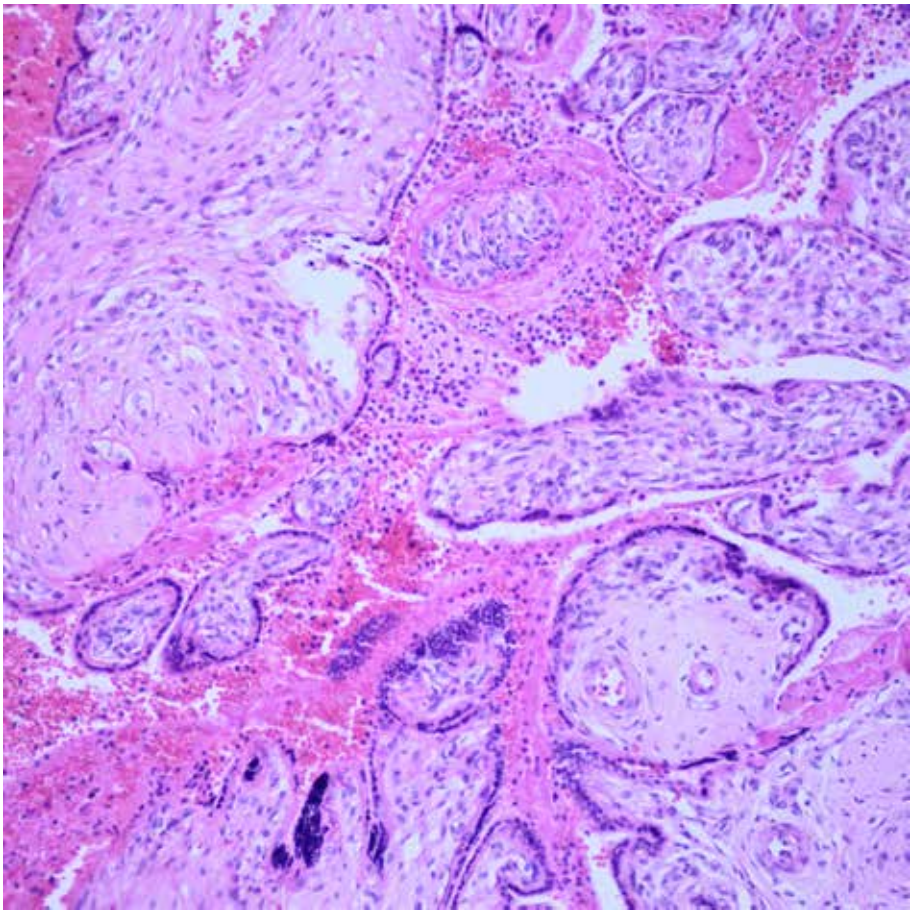

Figure 11.22 Chorioamnionitis, (H&E, x200). Infections in the fetus and newborn may arise from the transcervical (ascending route) or transplacental (hematogenous) route. Fetal infections are usually accompanied by infection of the placental membranes (chorioamnionitis) and umbilical cord infection (funisitis).

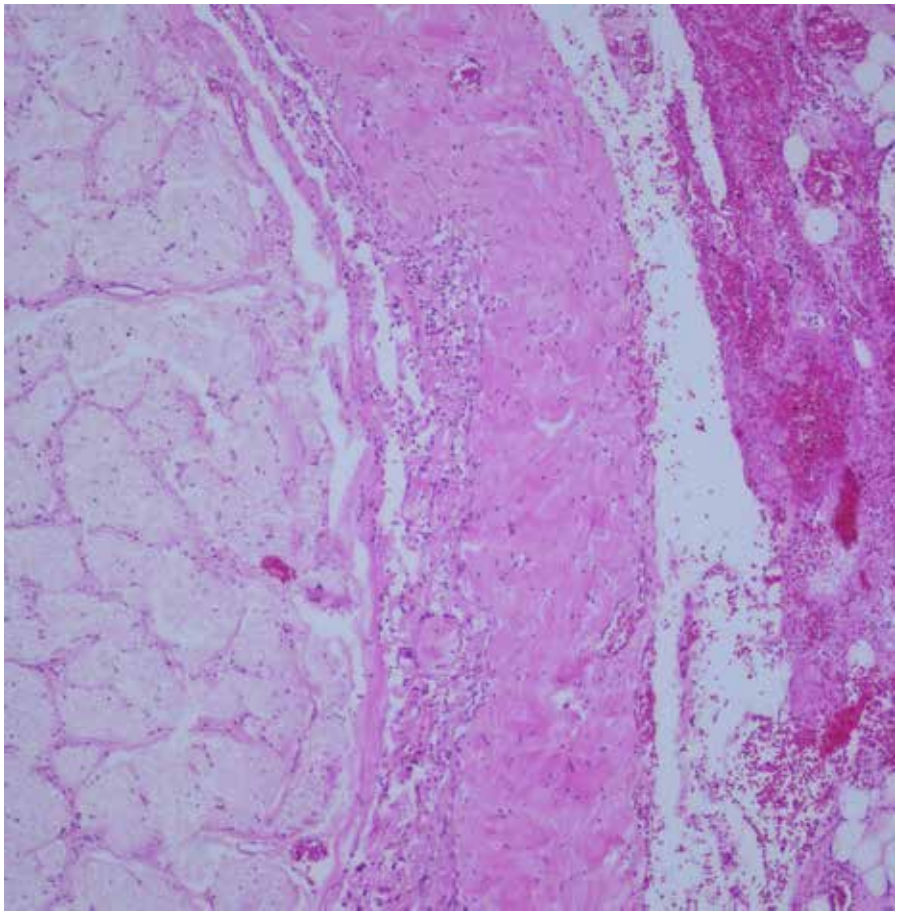

Figure 11.23
Hemorrhage and neutrophil infiltration around the optic nerve,
(H&E, x100).
In cases of child abuse, hemorrhage and neutrophil infiltration are observed around the optic nerve.

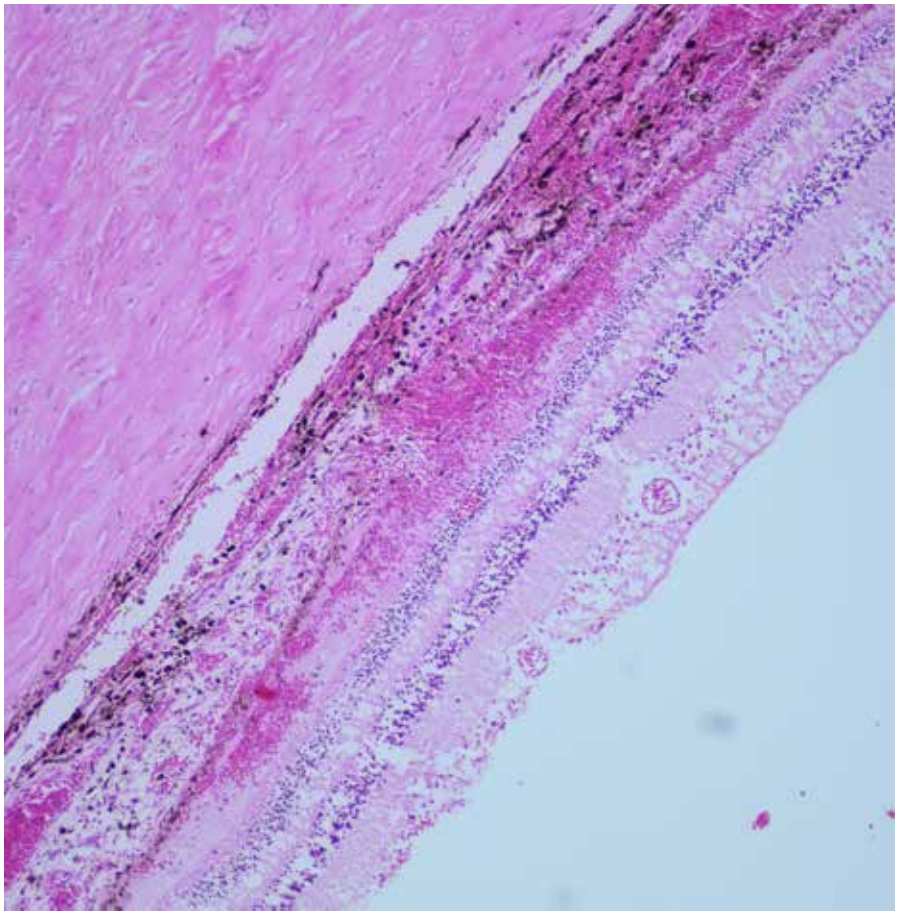

Figure 11.24
Retinal hemorrhage,
(H&E, x100).
In cases of child abuse, hemorrhage is observed in the retina. The most common findings in cases of suspected child abuse are head injuries, acceleration-deceleration injuries in the brain (subdural hemorrhage, diffuse axonal damage), bone fractures occurring at different times with metaphyseal-epiphyseal damage, skin lesions such as burns and ecchymosis, and eye lesions. Vitreous hemorrhage, lens dislocation, retinal tear, and optic nerve sheath hemorrhage may occur in babies.
Retinal hemorrhages are one of the typical findings in babies older than 2 months. This type of hemorrhage occurs when the child is shaken violently.
In such cases, it is very important to evaluate samples taken from different regions of the skin, bone, eyeball and brain for pathological examination at autopsy. Particularly, the pathologist's detection of skin and bone lesions at different times, as well as subdural hemorrhage and diffuse axonal damage through microscopic examination, is of great importance for the correct evaluation of the case.

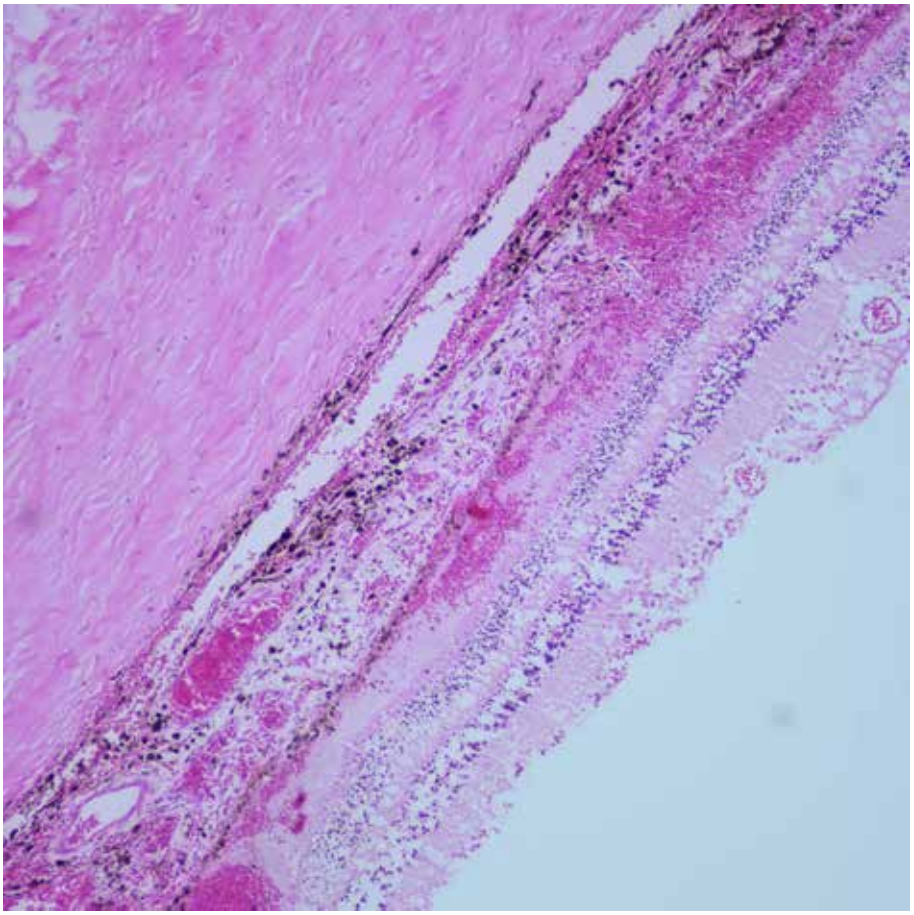

Figure 11.25
Retinal hemorrhage, (H&E, x100). In cases of child abuse, retinal hemorrhage.

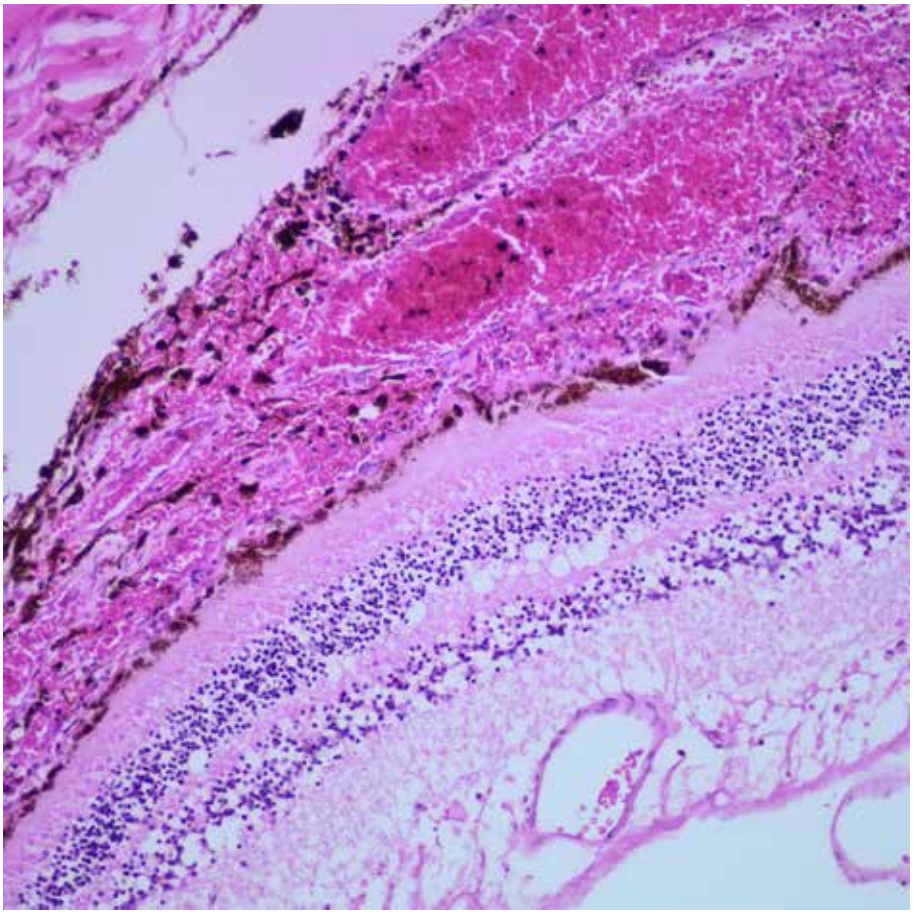

Figure 11.26
Retinal hemorrhage, (H&E, x200). At higher magnification.

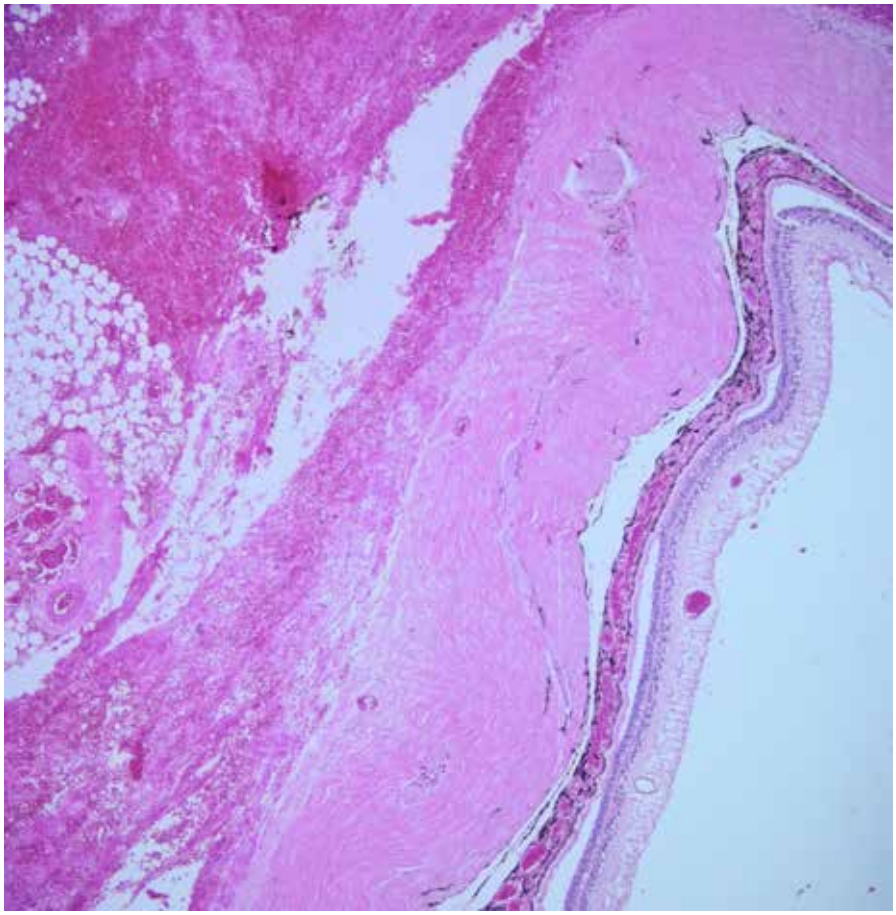

Figure 11.27
Hemorrhage in soft tissues surrounding the retina, (H&E, x40).
Hemorrhage in the soft tissues around the retina in cases of child abuse.

Figure 11.28
Child abuse, callus formation (compatible with 7-14 days), (H&E, x100).
In cases of physical child abuse, new bone formation, granulation tissue and callus formation with hemorrhage are observed.

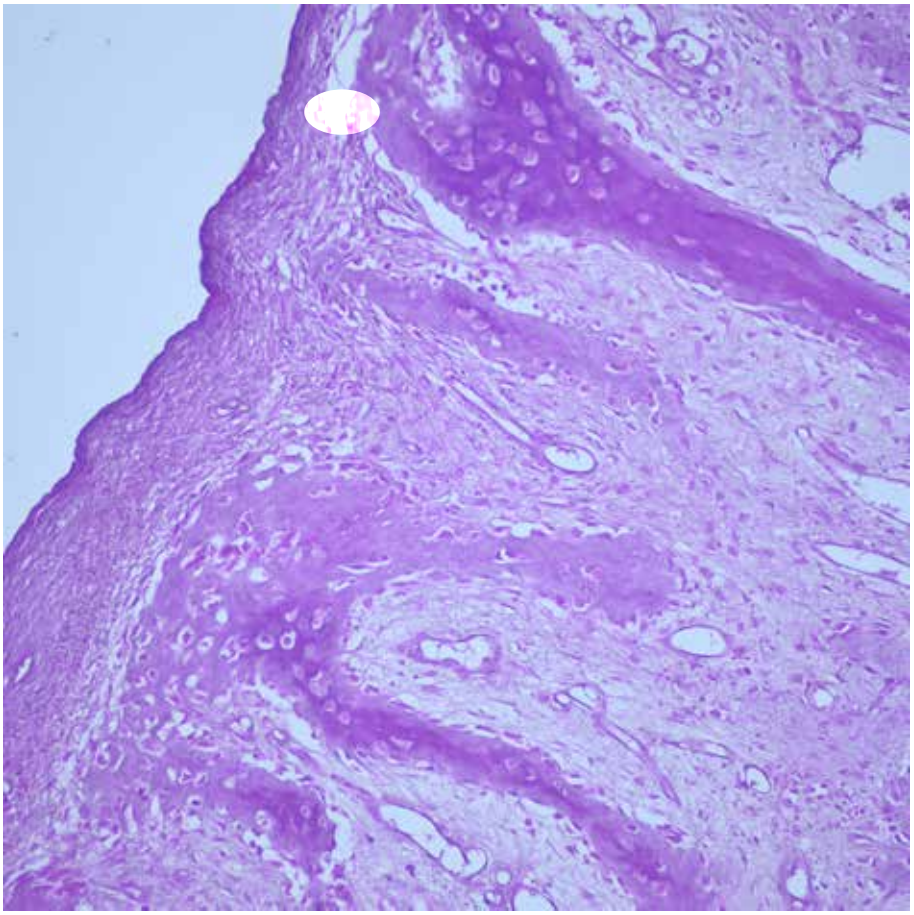

Figure 11.29
Child abuse, callus formation (compatible with 7-14 days), (H&E, x200). At higher magnification.

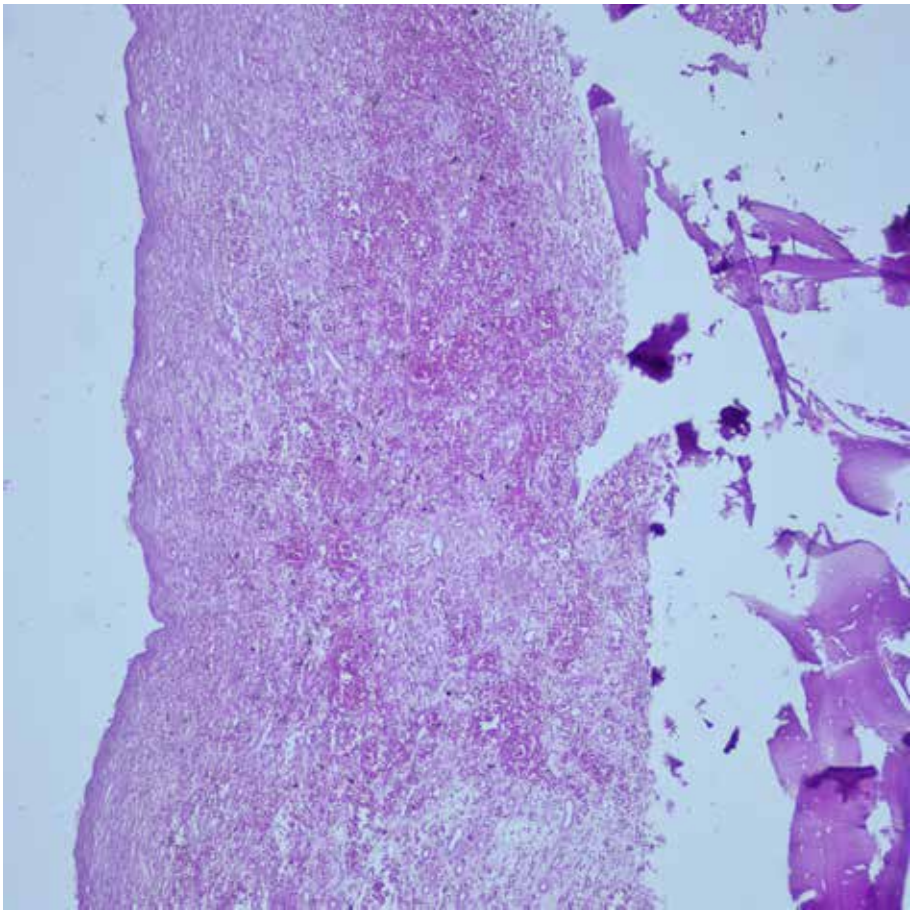

Figure 11.30
Child abuse, callus formation (compatible with 7-14 days), (H&E, x100). In cases of physical child abuse, areas of hemorrhage .

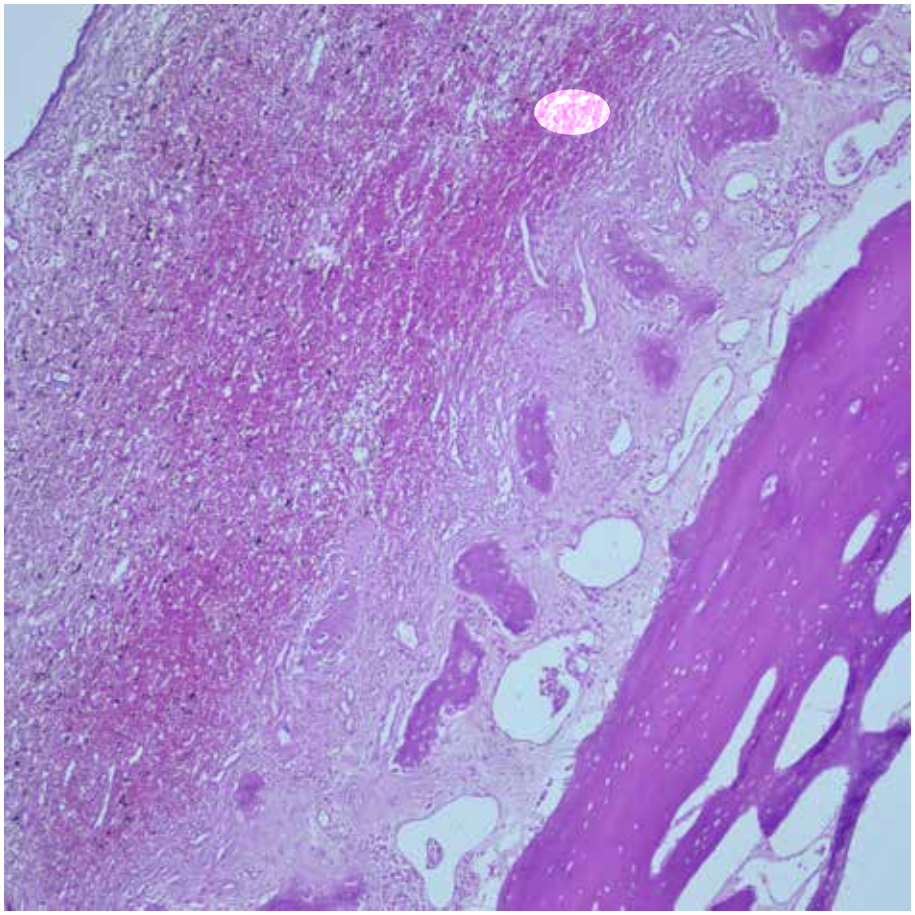

Figure 11.31
Child abuse, callus formation (compatible with 7-14 days), (H&E, x100).
In cases of physical child abuse, new bone formation, and callus formation with hemorrhage are observed.

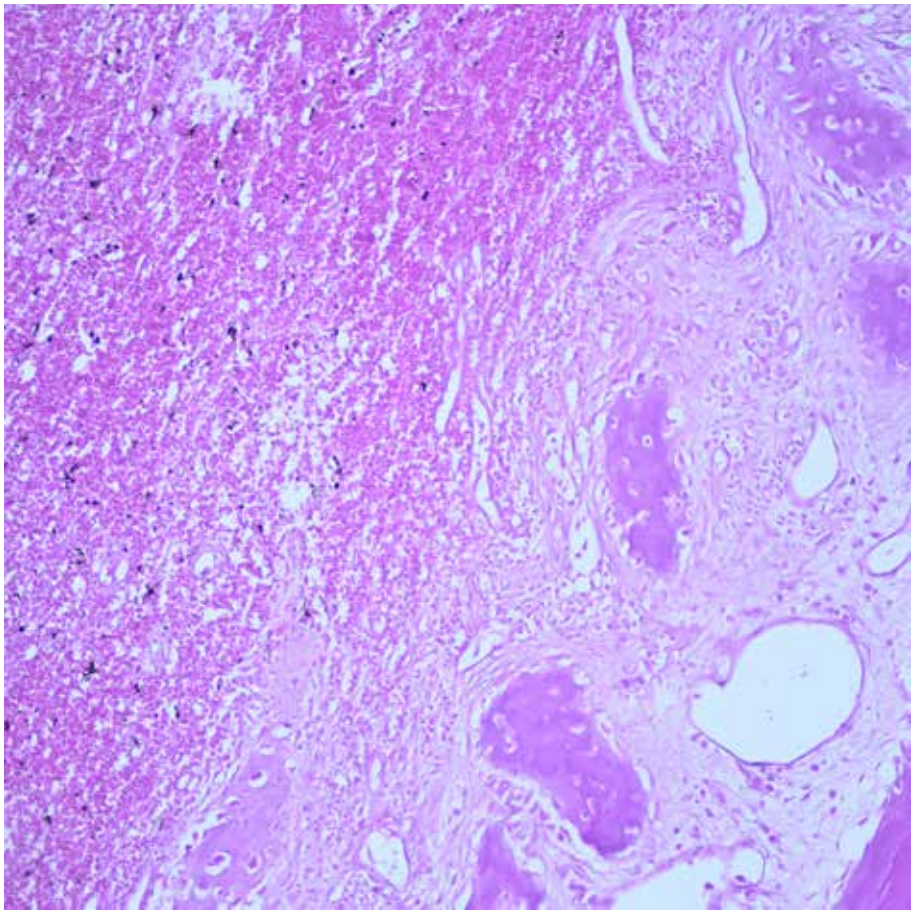

Figure 11.32
Child abuse, callus formation (compatible with 7-14 days), (H&E, x200).
At higher magnification.

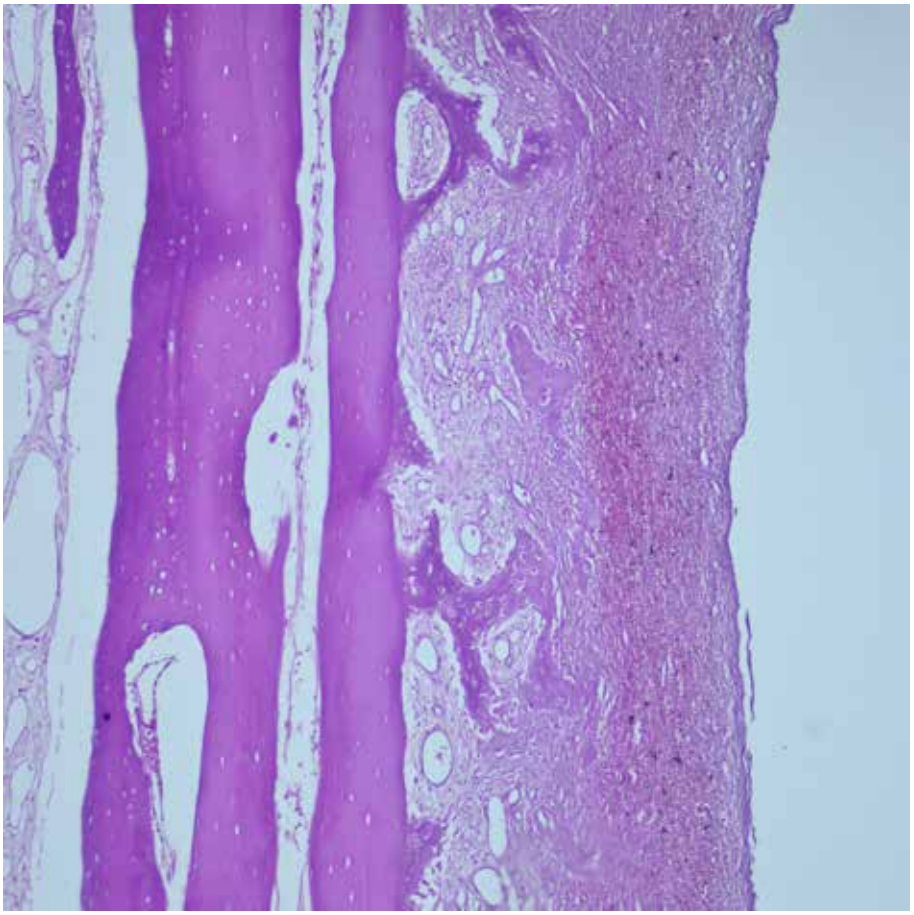

Figure 11.33 Child abuse, callus formation (compatible with 7-14 days), (H&E, x100). In cases of physical child abuse, new bone formation, granulation tissue and callus formation with hemorrhage are observed.

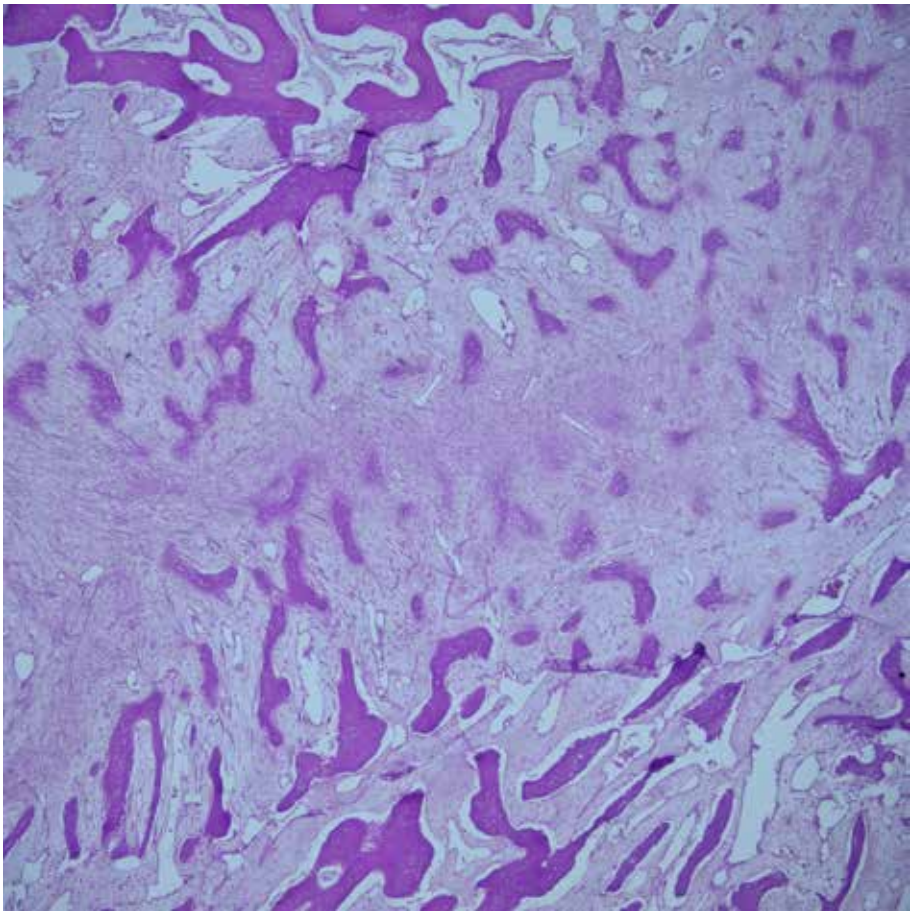

Figure 11.34 Child abuse, callus formation (compatible with 2-3 weeks), (H&E, x40). In cases of physical child abuse, callus formation in which new bone formation is prominent.

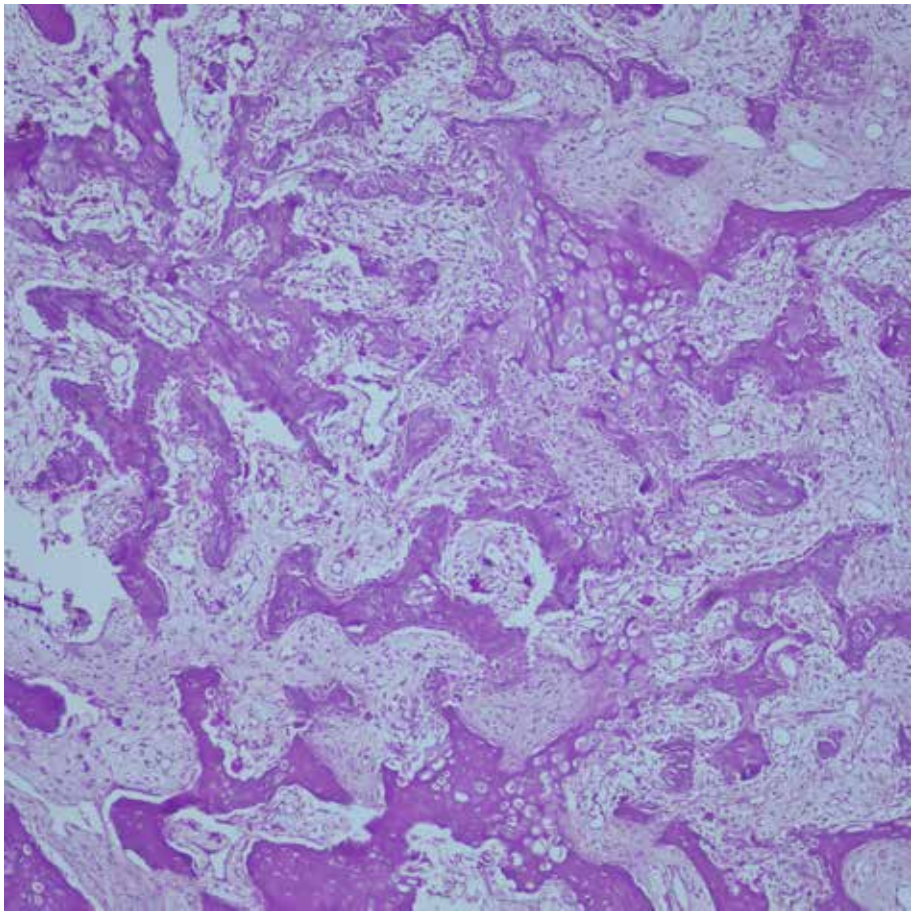

Figure 11.35
Child abuse, callus formation (compatible with 2-3 weeks), (H&E, x100). At higher magnification.

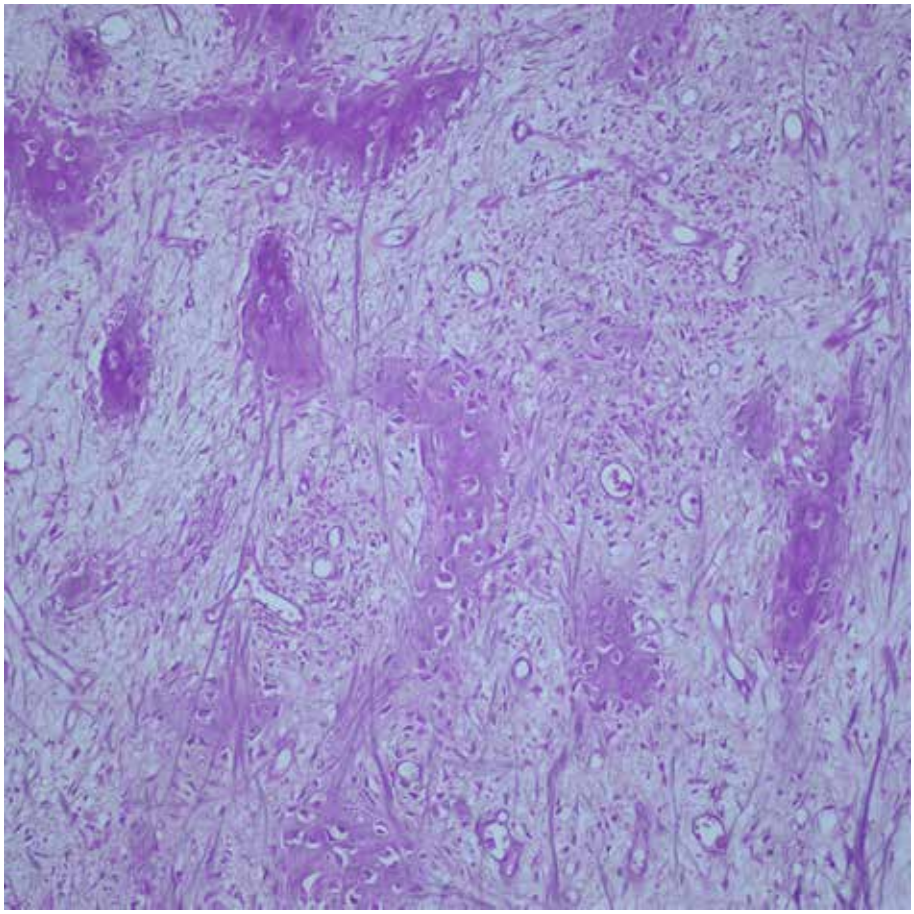

Figure 11.36
Child abuse, callus formation (compatible with 2-3 weeks), (H&E, x200). At higher magnification.

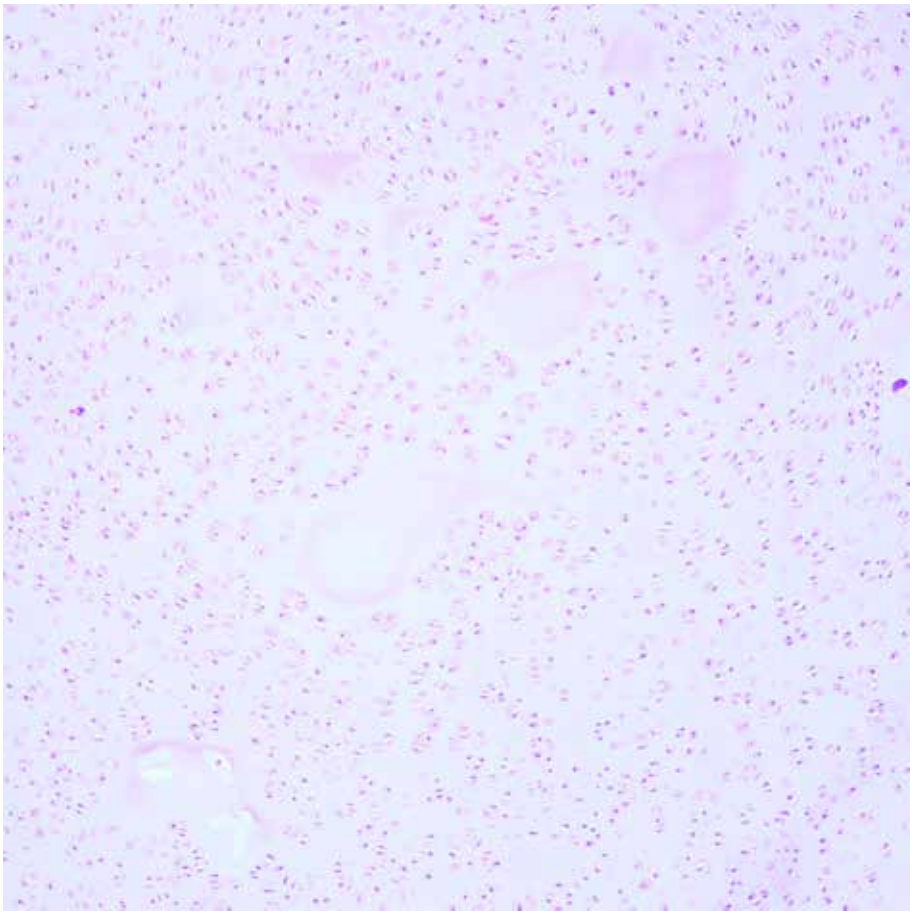

Figure 11.37 Cartilage tissue without ossification area (Calcaneus), (H&E, x100). Ossification points of bones such as calcaneus and femur are important in both forensic medicine and clinical pathology. These points are important for age determination and evaluation of bone traumas.

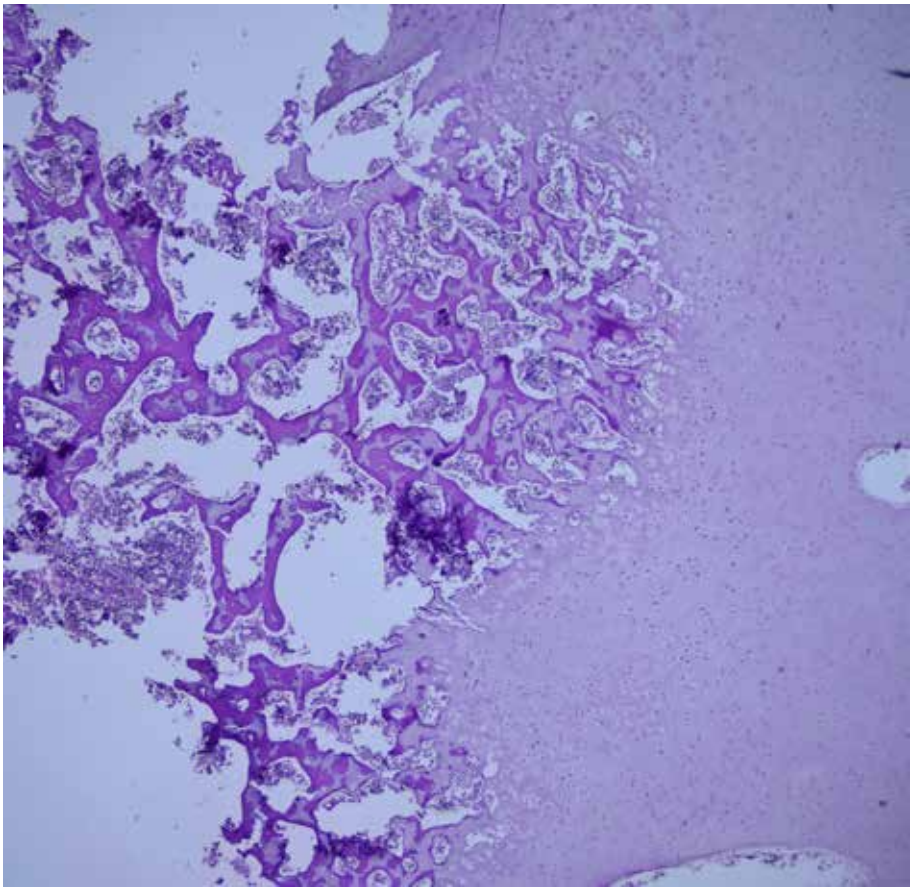

Figure 11.38 Cartilage tissue containing ossification area (Calcaneus), (H&E, x40). In microscopic view, an area of ossification is visible. The calcaneus ossification center appears in the 24th week of gestation, and the femur lower end (Becklard) ossification center appears in the 36th week of gestation.

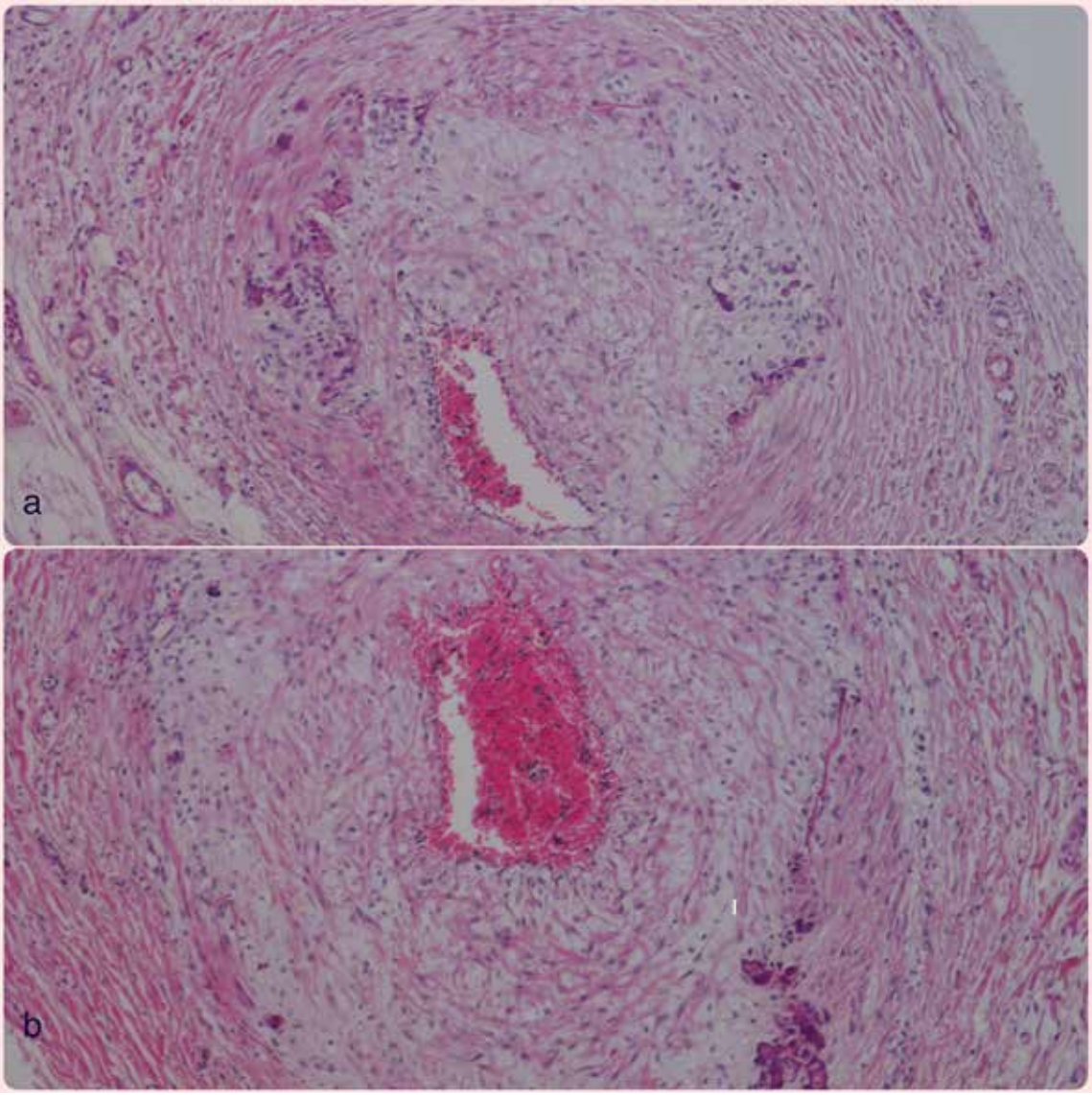

Figure 11.39
Idiopathic Infantile Arterial Calcification,
(H&E, x100).
a,b) It is a rare autosome recessive disease characterized by extensive calcification of medium and large arteries.
In the microscopic view, diffuse calcium deposition within the internal elastic lamina of arteries as well as narrowing of lumen due to myointimal proliferation is seen.

REPUBLIC OF TURKEY MINISTRY OF JUSTICE

COUNCIL OF FORENSIC MEDICINE

A

Abuse 237, 238, 239, 240, 241, 242, 243
Acute myocardial infarction
First 24 hours 24, 25, 26, 27
1-3 days 29
3-7 days 29,30
1-2 weeks 30, 31, 32, 33
2.weeks 33, 34
2-8. weeks 34, 35
2. months 35, 36
Acute Tubular Necrosis (Injury), ... 135, 136
Toxic 137
Alveolar stage 231
Amniotic aspiration 232, 233, 234
Amyloid
kidney 147
liver 120
spleen 153
Aortic dissection 72, 73
Aortitis 74, 75
Arrhythmogenic cardiomyopathy 62, 63, 64, 65
Arteriolosclerosis
hyaline 145
hyperplastic 144
Arteriovenous malformation 213
Asthma 80
Atelectasis 83, 84
Atrioventricular (AV) node 20
cystic tumor (of AV node) ..... 67, 68 ,69
hemorrhage (of AV node) 55, 56
Autolysis
brain 185
heart 21
kidney 128
liver 114
pancreas 156
stomach 166

B

Becklard 244
Bone marrow embolism 104
Bronchiectasis 98
Bronchitis 82
Bronchopneumonia 82

C

Calcaneous 244
Canalicular stage 230
Cardiac amyloidosis 57, 58
Cardiac valves 19
Cerebellar cortical degeneration 205,206
Cerebellum 184
purkinje cells 185
Cirrhosis 121
Colliquative myositolysis 28
Contusion 207, 208, 209
Coronary arteritis 41
Coronary artery dissection 40
Corpora amilesea 186
Cortical laminar necrosis 204, 205
Chorioamnionitis 236
Chronic passive congestion 117
Chronic pericarditis 52
Chronic pyelonephritis 146, 147
Coronary artery
atheroma plaque 37, 38, 39
Coronary artery bridging 36, 37
Cystic medial degeneration 73, 74

D

Diffuse alveolar epithelial injury 88, 89
Diffuse axonal injury 199, 200, 237
Dilated cardiomyopathy 61, 62
Dura mater 216, 217, 218, 219, 220, 221, 222, 223
Duragel 216

E

Electric effect 169, 170, 171
Embolism
brain tissue 107
food 109
Emphysema 97
Encephalitis 189, 190, 191, 192
Endocarditis 43
Esophagus 162
Extramedullary hematopoiesis 228

F

Fat embolism 101, 103, 151, 214
brain 214
fat globules 102
spleen 151
Fat necrosis 158
Fibrin thrombus 104, 105
Food aspiration 96
alveoli 96
bronchiole 96
Foreign body granuloma 95
Funisitis 228

G

Giant cell lymphohistiocytic myocarditis 47, 48, 49, 51, 52
Glomerulosclerosis 142, 143
Granuloma
kidney 133, 134
liver 120

H

Heat effect 169, 170, 171
Hemorrhage, organization 218, 219, 220, 221, 222, 223
Hepatitis
fungal 119
Hippocampus 184
Histiocytoid cardiomyopathy 66, 67
Honeycomb lung 98
Hyaline membrane 85
Hydatid cyst 106, 123, 124
Hypertrophic Cardiomyopathy 59, 60
Hypertrophic cardiomyocytes 42

I

Idiopathic infantile arterial calcification 245
Infarct
late period 200, 201, 203
subacute 197, 198, 199, 200
transmural 165
Infective Endocarditis 53, 54, 55
Intercalated discs 18
Interstitial fibrosis 42

K

Kidney 127, 128

L

Large bowel 163
Laryngeal edema 111
Lipofuskin 21
Liver
normal 114
Lungs 77, 79
Lymphocytic myocarditis 45

M

Malaria 70, 71, 125, 193
Meconium aspiration 232, 233
Megakaryocyte 88
Meningitis 187, 188, 189
Meningoencephalitis 190, 191, 192
Methanol intoxication 202
Microvesicular steatosis 116
Myocarditis
Lymphocytic myocarditis 45
Lymphohistiocytic myocarditis with giant cells 47, 48, 49, 51, 52
Myocarditis with granuloma 49, 50
Neutrophilic myocarditis 46
Toxic myocarditis 46, 47
Myocardium
normal 18
Myxoid degeneration 22

N

Nephritis
Acute tubulointerstitial 129, 130
Fungal 132, 133
Neutrophilic myocarditis 46

O

Optic nerve 237

P

Pancarditis 44
Pancreas 155, 156
Pancreatitis 157, 158, 159
Pachymeningitis 217, 218
Peritonitis 166, 167
Perivascular fibrosis 43
Placenta 234
Placental infarct 235
Pleuritis 83, 84
Pneumonia 81, 84, 86, 87, 93, 94, 233
CMV 86, 87, 94
Fungal 89, 90
Lymphoid 100
Pneumocystis Jiroveci 93, 94
RSV 91
Usual 99
Polycystic Kidney Disease 148
Postmortem bacterial growth
liver 122
Pseudoglandular stage 229
Pulmonary hypertension 110

R

Rabies 193, 194, 195
Renal infarct 140, 141

Retinal hemorrhage 237, 238
Rhabdomyolysis 142
RSV 91

S

SA (Sinoatrial) node 19, 20
Saccular aneurysm 211
Saccular stage 230
Scolex 106, 124
Septic focus
kidney 134, 135
liver 122, 123
Septic splenitis 152
Sinoatrial (SA) node 19, 20
Small intestine 163
Soot 94, 95
Spleen 149, 150
atrophy 150
Splenic infarct 151
Steatohepatitis 115
Stomach 162
Subarachnoid hemorrhage 207, 208
Subdural hemorrhage 215
Submassive necrosis 118

T

Thrombus
renal 139, 141
Toxic myocarditis 46, 47
Tuberculous granuloma 92

U

Umbilical cord 227

V

Vasculitis 212
Vitality 173, 175

W

Wound age 173,174,175,176,177, 178,179,180,181

Note:

Note:

Note:

Note:

Note:

Note:

REPUBLIC OF TURKEY MINISTRY OF JUSTICE

COUNCIL OF FORENSIC MEDICINE

REPUBLIC OF TURKEY MINISTRY OF JUSTICE

COUNCIL OF FORENSIC MEDICINE